Determination of the Size Distribution of Charged Nanoparticles via Capillary Electrophoresis under Variation of Counter-Ion Type and Concentration

Dissertation

zur
Erlangung des Doktorgrades
der Naturwissenschaften
(Dr. rer. nat.)

dem
Fachbereich Chemie der Philipps-Universität Marburg
vorgelegt von

M.Sc.
Alaa Hussein Jalil

aus dem
Irak

Marburg an der Lahn 2018

Die vorliegende Dissertation wurde in der Zeit von Oktober 2013 bis Oktober 2018 am Fachbereich Chemie der Philipps-Universität Marburg unter der Leitung von Prof. Dr. Ute Pyell angefertigt.

Vom Fachbereich Chemie der Philipps-Universität Marburg als Dissertation am .... angenommen.

Erstgutachter: Prof. Dr. Ute Pyell
Zweitgutachter: Prof. Dr. Florian Kraus

Tag der mündlichen Prüfung: ....

Hochschulkennziffer: 1180

Alaa Hussein Jalil (M.Sc.)
Hans-Meerwein Str. 4/FB Chemie
35032 Marburg

Erklärung

Ich erkläre, dass eine Promotion noch an keiner anderen Hochschule als der Philipps-Universität Marburg, Fachbereich Chemie, versucht wurde.

Ich versichere, dass ich meine vorgelegte Dissertation

“*Determination of the Size Distribution of Charged Nanoparticles via Capillary Electrophoresis under Variation of Counter-Ion Type and Concentration*”

selbst und ohne fremde Hilfe verfasst, nicht andere als die in ihr angegebenen Quellen oder Hilfsmittel benutzt, alle vollständig oder sinngemäß übernommenen Zitate als solche gekennzeichnet sowie die Dissertation in der vorliegenden oder einer ähnlichen Form noch bei keiner anderen in- oder ausländischen Hochschule anlässlich eines Promotionsgesuchs oder zu anderen Prüfungszwecken eingereicht habe.

Marburg, Oktober 2018

Unterschrift

(Alaa Hussein Jalil)

To the soul of my

parents

Acknowledgement

First and above all, I give thanks to **Allah** my greatest lord for his protection and inspiration to achieve this work.

My special and heartily thanks to my supervisor, **Professor Dr. Ute Pyell** who encouraged and directed me. Her challenges brought this work towards a completion. It is with her supervision that this work came into existence. I appreciate her helpful scientific instructions and comments that she always offered to me.

I am also very grateful to **Professor Dr. Harbrecht** and his PhD student in his working group **Mr. Alexander Kudielka** for preparing and providing cobalt oxyhydroxide nanoparticles used in this thesis, and for their valuable help to discuss the experimental results for the behavior of these nanoparticles comprehensively. Also, I want to express my deep gratitude to **Professor Dr. Harbrecht** for his cooperation through financial support for contribution to complete the current work.

I am also deeply thankful and express my sincere thanks to **Dr. Firas M. Mustafa**, Duhok Polytechnic University-IRAQ. I want to acknowledge his help during my research. His information has helped me to write many programs in Matlab program for calculating and an estimation of zeta potential and to complete this thesis. Special thanks to **Dr. Abdelhakim El-Hamdan** for the translation of the summary part of the thesis into German.

I am so grateful to the Iraqi Ministry of Higher Education and Scientific Research (**MoHESR**) and the University of Mosul, IRAQ for making it possible for me to study at the University of Marburg, Department of Chemistry, GERMANY, via funding my PhD scholarship.

Nobody has been more important to me in the pursuit of this project than the members of my family. I would like to thank my brother **Thaair** and my sisters for their unconditional love and continuous encouragement throughout the time of my research and for always showing how proud they are of me.

A very special word of thanks goes for my wife and for my beloved children, who have been great over the years and they have given me the extra strength and motivation to get things done. This thesis is dedicated to them.

Also, I thank all who in one way or another contributed to the completion of this work.

Alaa Hussein Jalil

Table of Contents

Abstract

In the current study, three different types of NPs were used with varied size, namely, Ludox silica nanoparticles (SNP), polystyrene sulfate latex nanoparticles (PSSL) and cobalt oxyhydroxide nanoparticles (CoOOH-NPs). SNPs with three different size distributions have the nominal particle diameters 7, 12 and 22 nm. PSSLs with four different size distributions have the mean particle diameters 21, 41, 63 and 80 nm. CoOOH-NPs have a mean domain size of 3.7-4.5 nm. While SNPs and PSSLs are negatively charged in alkaline dispersion medium. COOH-NPs were dispersed in acidic medium having a positively charged surface.

This study focuses on considering the influence of the variation of the counterion type and its concentration on the determination of the particle size distribution (PSD) of charged nanoparticles using capillary electrophoresis (CE). CE provides a suitable method to measure the size of NPs through converting electropherograms into a PSD. This approach is based on an exact determination of the electrokinetic potential ζ by measuring the electrophoretic mobility μ_{ep} in an electrolyte of known composition, in combination with a second independent method that determines the mean particle radius such as TEM or Taylor dispersion analysis (TDA).

TDA measurements were used to determine the mean collective diffusion coefficient and the mean hydrodynamic radius via Stokes-Einstein equation. Later, these values of the mean hydrodynamic radius were used in the calculation of the calibration functions to obtain PSDs for the three types of NPs under this study. In addition, preliminary investigations and UV-Vis spectroscopy measurements were made for CoOOH-NPs in an aqueous solution of a monoprotic acid with varied type of anion as counterion. Results obtained show that the continuous decrease in the colour intensity and the absorbance at band maximum for CoOOH-NPs dispersions are independent of the type of anion.

For electrophoretic mobility measurements, two series of SNPs were used with varied sizes with different counterion types, namely: Li^+, Na^+, K^+, and guanidinium (Gdm^+) with varied ionic strength (I = 20-120 mmol L^{-1}) at 25 °C. For PSSL with varied sizes, electrophoretic mobility measurements were made with Na^+ as counterion in the ionic strength range 10-50 mmol L^{-1} and with Li^+, Na^+ and Gdm^+ as counterion in the ionic strength range 40-120 mmol L^{-1}, at 20 °C. In the case of CoOOH-NPs, the electrophoretic mobility measurements were made in acidic solution of pH 2 at 25 °C using different methods for coating of the inner capillary wall, because these NPs have a positive charge on their surface. Also, the influence of parameters such as injection parameters, applied electric field strength and concentration of

CoOOH-NPs in the sample were investigated. In all investigations, the electrophoretic mobilities for NPs are dependent on the type of counterion, which can be attributed to Hofmeister effects also called the specific ion effects.

The modification proposed by Pyell *et al.* based on an analytic approximation introduced by Ohshima, was used to estimate the electrokinetic potential ζ for all NP types. For the determination of ζ from the obtained electrophoretic mobility, the procedure takes the limiting equivalent conductance of the counterion or its ionic drag coefficient into account neglecting the limiting equivalent conductance or ionic drag coefficient of the co-ion. Results for $|\zeta|$ follow the order $Li^+ > Na^+ > K^+ > Gdm^+$ for SNPs and the order $Li^+ > Na^+ > Gdm^+$ for PSSLs, whereas for CoOOH-NPs there is a decrease in ζ in the order $NO_3^- > Cl^- > CH_3SO_3^-$. This dependence of $|\zeta|$ on the type of the counterion is also reflected by the determined values for the electrokinetic surface charge densities $|\sigma_\zeta|$.

Finally, size distributions of NPs were obtained from using the method developed by Pyell and Pyell *et al.* Electropherograms are converted directly into size distribution functions. The results of using the developed method for SNPs are reliable independent of the type of counterion. There is a good agreement with the results from using TEM analysis for the dispersion (width), which indirectly confirms the validity of the theoretical approach for the calculation of ζ from electrokinetic data and the mean particle size. There are advantages of using Li^+ or Na^+ compared to the use of K^+ or Gdm^+ as counterion with regard to preventing particle aggregation and peak distortion via the stabilizing effect due to higher $|\zeta|$ and higher $|\sigma_\zeta|$. In addition, there is a positive impact of the higher ionic drag coefficients on the size-selectivity of the method.

For PSSLs, results show acceptable values for the width produced from using the developed method within expected experimental errors. High electrophoretic mobility values and corresponding calibration functions result in very large errors with considerable uncertainty if $\zeta > 60$. However, for CoOOH-NPs the value calculated from the moment analysis for the dispersion is excessively large, which might be due to adsorption effects that influence the estimation of ζ and the corresponding calibration functions. In addition, because of the small mean domain size of the CoOOH-NPs and the use of a low ionic strength electrolyte there is a very small value for κa ($\kappa a \ll 1$). Hence, for CoOOH-NPs the results obtained show the limitations of the investigated approach in the case of this very low reduced radius.

Zusammenfassung

Im Rahmen dieser Arbeit wurden drei verschiedene NP-Typen mit unterschiedlichen Größen verwendet, nämlich Ludox-Silica-Nanopartikel (SNP), Polystyrol-Sulfat-Latex-Nanopartikel (PSSL) und Cobaltoxyhydroxid-Nanopartikel (CoOOH-NPs). SNPs mit drei verschiedenen Größenverteilungen haben die nominalen Teilchendurchmesser 7, 12 und 22 nm. PSSL mit vier verschiedenen Größenverteilungen haben die mittleren Teilchendurchmesser 21, 41, 63 und 80 nm. CoOOH-NPs haben eine mittlere Domänengröße von 3,7-4,5 nm. Während SNPs und PSSLs in einem alkalischen Dispersionsmedium negativ geladen sind, wurden COOH-NPs im sauren Medium mit einer positiv geladenen Oberfläche dispergiert.

Diese Arbeit konzentriert sich auf die Berücksichtigung des Einflusses der Variation des Gegenionentyps und dessen Konzentration zur Bestimmung der Partikelgrößenverteilung (PSD) von geladenen Nanopartikeln unter Verwendung der Kapillarelektrophorese (CE). CE ermöglicht eine geeignete Methode zur Messung der Größenverteilung von NPs durch Umwandlung von Elektropherogrammen in eine PSD. Dieser Ansatz basiert auf einer genauen Bestimmung des elektrokinetischen Potential ζ durch Messung der elektrophoretischen Mobilität μ_{ep} in einem Elektrolyten bekannter Zusammensetzung in Kombination mit einer zweiten unabhängigen Methode zur Bestimmung des mittleren Teilchenradius wie TEM oder Taylor-Dispersionsanalyse (TDA).

TDA-Messungen wurden zur Bestimmung des mittleren kollektiven Diffusionskoeffizienten und des mittleren hydrodynamischen Radius über die Stokes-Einstein-Gleichung verwendet. In späteren Rechnungen wurden diese Werte bei der Berechnung der Kalibrierfunktionen verwendet, um PSD für die in der Arbeit verwendeten NPs zu erhalten. Darüberhinaus wurden Voruntersuchungen und UV-Vis-Spektroskopiemessungen für CoOOH-NPs in wässriger Lösung einer monoprotischen Säure mit unterschiedlichen Anionen als Gegenion durchgeführt. Die erhaltenen Ergebnisse zeigen, dass die kontinuierliche Abnahme der Farbintensität und der Extinktion am Bandenmaximum für die CoOOH-NP-Dispersionen unabhängig von der Art des Anions ist.

Für elektrophoretische Mobilitätsmessungen wurden zwei Chargen von SNPs mit den Gegenionen Li^+, Na^+, K^+ und Guanidinium (Gdm^+) bei einer variierten Ionenstärke von 20 bis 120 mmol L^{-1} bei 25°C verwendet. Für PSSLs mit unterschiedlichen Größen wurden elektrophoretische Mobilitätsmessungen mit Na^+ als Gegenion im Bereich der Ionenstärke 10-50 mmol L^{-1} durchgeführt, während Messungen mit Li^+, Na^+ und Gdm^+ als Gegenionen im

Ionenstärkenbereich 40-120 mmol L^{-1} bei 20 ^{o}C durchgeführt wurden. Im Fall von CoOOH-NPs wurden die elektrophoretischen Beweglichkeitsmessungen in saurer Lösung mit einem pH-Wert von 2 bei 25 ° C unter Verwendung verschiedener Methoden zur Beschichtung der inneren Kapillarwand durchgeführt, da diese NPs eine positive Ladung auf ihrer Oberfläche aufweisen. Untersucht wurde auch der Einfluss von Parametern wie Injektionsparametern, angelegter elektrischer Feldstärke und Konzentration von CoOOH-NPs in der Probe. In allen Untersuchungen sind die elektrophoretischen Mobilitäten der NPs von der Art des verwendeten Gegenions abhängig. Diese Abhängigkeit ist auf Hofmeister-Effekte (auch als spezifische Ioneneffekte bezeichnet) zurückzuführen.

Um das elektrokinetische Potential ζ für alle NP-Arten zu bestimmen, wurde die von Pyell *et al.* vorgeschlagene Methode, die auf einer von Ohshima eingeführten analytischen Näherung basiert, verwendet. Zur Bestimmung des ζ-Potentials aus der erhaltenen der elektrophoretischen Mobilität wird bei der vorgeschlagenen Vorgehensweise die Grenzäquivalentleitfähigkeit des Gegenions oder dessen Ionenwiderstandskoeffizient berücksichtgt unter Vernachlässigung der Grenzäquivalentleitfähigkeit oder des Ionenwiderstandskoeffizienten des Co-ions. Ergebnisse für $|\zeta|$ folgen der Reihenfolge Li^+ > Na^+ > K^+ > Gdm^+ für SNPs und der Reihenfolge Li^+ > Na^+ > Gdm^+ für PSSLs, wobei es für CoOOH-NPs eine Reduzierung in ζ in der Reihenfolge NO_3^- > Cl^- > $CH_3SO_3^-$ gibt. Diese Abhängigkeit des Werts für $|\zeta|$ von der Art des Gegenions zeigt sich auch in den berechneten Werten für die elektrokinetische Ladungsdichte $|\sigma_\varsigma|$.

Schließlich wurden durch die von Pyell und Pyell *et al.* entwickelte Methode Größenverteilungen von NPs erhalten. Hier werden Elektropherogramme direkt in Größenverteilungsfunktionen umgewandelt. Die Ergebnisse der Verwendung der entwickelten Methode für SNPs sind zuverlässig unabhängig von der Art des Gegenions. Es gibt eine gute Übereinstimmung mit den Ergebnissen der TEM-Analyse für die Dispersion (Breite), wodurch indirekt die Gültigkeit des theoretischen Ansatzes für die Berechnung von ζ aus elektrokinetischen Daten und der mittleren Partikelgröße bestätigt wird. Es gibt Vorteile bei Verwendung von Li^+- oder Na^+-Ionen verglichen mit der Verwendung von K^+ oder Gdm^+ als Gegenion in Bezug auf die Verhinderung von Partikelaggregation und Peakverzerrung infolge des stabilisierenden Effekts aufgrund höheren $|\varsigma|$ und höheren $|\sigma_\zeta|$. Zusätzlich genutzt wurde der positive Einfluss des höheren Ionenwiderstandskoeffizienten auf die Größenselektivität der Methode.

Für PSSLs zeigen die Ergebnisse der entwickelten Methode akzeptable Werte für die Dispersion der Verteilung mit Abweichungen innerhalb der erwarteten Messunsicherheit. Hohe elektrophoretische Mobilitätswerte und entsprechende Kalibrierungsfunktionen führen bei ζ > 60 zu sehr großen Fehlern mit erheblicher Unsicherheit. Dagegen ist der aus der Momentenanalyse für die Dispersion berechnete Wert für CoOOH-NP übermäßig groß, was auf Adsorptionseffekte zurückgeführt werden kann. Diese beeinflussen die Bestimmung von ζ und die entsprechenden Kalibrierfunktionen. Zusätzlich ergab sich infolge der kleinen mittlere Domänengröße von CoOOH-NPs und der Verwendung eines Elektrolyten mit niedriger Ionenstärke ein sehr kleiner Wert für κa ($\kappa a \ll 1$). Die erhaltenen Ergebnisse zeigen somit die Grenzen der entwickelten Methode im Falle eines sehr niedrigen reduzierten Radius.

List of abbreviations and symbols

Abbreviations

AFM	Atomic force microscopy
APS	Ammonium persulfate
BGE	Background electrolyte
ccc	Critical coagulation concentration
CE	Capillary electrophoresis
CoOOH-NPs	Cobalt oxyhydroxide nanoparticles
CTAB	cetyltrimethylammonium bromide
DADMAC	Diallyldimethylammonium chloride
DDAB	Didodecyldimethylammonium bromide
DLS	Dynamic light scattering
EDL	Electrical double layer
EOF	Electroosmotic flow
FTIR	Fourier-transform infrared spectroscopy
GCAS	Gram-Charlier Type A series
I.D	Inner diameter
IHP	Inner Helmholtz plane
MSA	Methanesulfonic acid
NPs	Nanoparticles
O.D	Outer diameter
OA	Oriented attachment
OHP	Outer Helmholtz plane
OR	Ostwald ripening
PBE	Poisson–Boltzmann equation
PDADMAC	Poly(diallyldimethylammonium chloride)
PS	Particle size
PSD	Particle size distribution

PSS	poly(sodium 4-styrenesulfonate)
PSSL	Polystyrene sulfate latex nanoparticles
PSSL20	Sulfate latex-0.02 µm with mean particle diameter 21 nm
PSSL40	Sulfate latex-0.04 µm with mean particle diameter 41 nm
PSSL60	Sulfate latex-0.06 µm with mean particle diameter 63 nm
PSSL80	Sulfate latex-0.08 µm with mean particle diameter 80 nm
RSD	Relative standard deviation
SAXS	Small-angle X-ray scattering
SEC	Size exclusion chromatography
SEM	Scanning electron microscopy
SMIL	Successive multiple ionic-polymer layer
SNP12	Ludox HS-30 with a nominal particle diameter of 12 nm
SNP22	Ludox TM-40 with a nominal particle diameter of 22 nm
SNP7	Ludox SM-30 with a nominal particle diameter of 7 nm
SNPs	Ludox silica nanoparticles
TDA	Taylor dispersion analysis
TEM	Transmission electron microscopy
TEMED	N,N,N,N-tetramethylethylenediamine
TEOS	Tetraethyl orthosilicate
UV-Vis	Ultra-Violet and Visible Light Spectroscopy
VSFS	Vibrational sum frequency spectroscopy

Symbols

λ_D	Eectrical double layer thickness
σ_ς	Charge density at the shear plane (Electrokinetic surface charge density)
Λ_{+}°	Limiting equivalent conductance of cation
Λ_{-}°	Limiting equivalent conductance of anion
v	Velocity
v_{EOF}	Mean EOF velocity
$\langle v \rangle$	Mean linear velocity
μ_3'	Standardized third central moment
μ_4'	Standardized forth central moment
μ_{ep}	Electrophoretic mobility
a	Sphere radius
A	Area
$A_{(t)}$	Absorbance
B	Jones–Dole Viscosity B coefficient
B	Constant
D_0	Self-diffusion coefficient at infinite dilution
D_c	Collective diffusion coefficient
d	Double layer distance
$d_{\max}$	Diameter at the maximum
d_p	Particle diameter
E	Electric field strength
e	Elementary charge
F_1	Electric force
F_2	Viscous force
H_3	Third Hermite polynomial

H_4	Fourth Hermite polynomial
I	Ionic strength
k	Boltzmann constant
K	Dispersion coefficient
k	Reaction rate constant
k_1	Reaction rate constant for first step
k_2	Reaction rate constant for second step
L_D	Length of capillary to the detector
L_T	Total length of capillary
E_0	Absorbance at time 0
$E_{(t)}$	Absorbance at time t
m	Dimensionless ionic drag coefficient
m_-	Dimensionless ionic drag coefficient of anion
m_+	Dimensionless ionic drag coefficient of cation
m_0	Zeroth moment
$m_{counter}$	Dimensionless ionic drag coefficient of counterion
μ'_n	n^{th} central moment
μ_n	n^{th} absolute moment
m_n	n^{th} moment
n	Number density
n_i	Concentration of the ion i
$p_{(x)}$	Probability density
P_e	Peclet number
pKa	Ionization constant
Q	Charge of particle
R_H	Hydrodynamic radius

$r_{H,N}$	Number-weighted mean hydrodynamic radius
T	Absolute temperature
$t_{1/2}$	Half-life of the reaction
t	time
t_H	Elution time / inflection point
t_{mig}	Migration time of particle
U	Voltage
v_{ep}	Velocity of particle
y_0	Offset
z	charge number
z_i	Valence of the ion i
ε_0	Permittivity of vacuum
ε_r	Relative permittivity of the medium
η	Viscosity of the solution
η_0	Viscosity of pure water
κ	Debye-Hückel parameter
κ^{-1}	Debye length (thickness of the diffusive layer)
κ_3	Skewness = third central moment (μ_3')
κ_4	Excess = kurtosis (E) = fourth central moment (μ_4')
μ_1	First moment
$\rho_{(x)}$	charge density at any point in the solution
σ_0	Surface charge density
σ_t	Width of the distribution
σ^2	Second central moment = second moment (μ_2)
σ_t^2	Variance of the concentration profile
τ	Residence time

ψ	Electrode/electrolyte interface
$\psi_{(x)}$	Electrostatic potential
Φ_0	Electric potential at the surface
C_{GCL}	Integral capacity
μ_{EOF} ; μ_{eo}	Electroosmotic mobility
t_{EOF} ; t_0	Migration time of marker (neutral marker)
$Å$	Ångström
a_c	Capillary radius
C ; $conc.$	Concentration
q	Electric charge
ζ	Zeta potential
ψ_0	Surface potential

Chapter One

Introduction and Remit

Introduction and Remit

Nanoparticles (NPs) can be classified into different classes based on their properties, shapes or sizes. According to their size, nanoparticles can be classified as ultradispersion systems (1–50 nm), high dispersion systems (50–100 nm) or sedimentable particles (100–1000 nm) [1]. In effect, they are a bridge between bulk materials and atomic or molecular structures. A bulk material should have constant physical properties regardless of its size, but at the nanoscale often properties observed are size dependent. The percentage of the surface in relation to the percentage of the volume of a material becomes significant when the properties of materials change as their size approaches the nanoscale [1].

The terms colloid and nanoparticle are not interchangeable. Colloids can contain particles too large to be nanoparticles, and nanoparticles can exist in non-colloidal form, for examples as a powder or in a solid matrix [2]. NPs are surrounded by interfacial layer. Fundamentally, this interfacial layer is affecting all of NPs properties because its an integral part of nanoscale matter.

The characteristics of NPs depend on their size and size distribution. Therefore, the particle size (PS) and particle size distribution (PSD) are of great importance. Therefore, many different methods have been developed for NPs characterization [3]. Also, knowledge of PS and PSD is required to optimize nanoparticle synthesis procedures especially if size selection processes are to be avoided [4].

Different measurement techniques often produce different values for the number-weighted mean radius and for the dispersion. For example, the National Institute of Standards and Technology (NIST) stated that different measurement techniques produced different values for the same particles [5]. Three spherical gold nanoparticle samples provided by NIST as reference standards materials which nominally display radii of 5, 15, and 30 nm, respectively. Reported particle sizes are based on measurements using atomic force microscopy (AFM), scanning electron microscopy (SEM), transmission electron microscopy (TEM), dynamic light scattering (DLS) and small-angle X-ray scattering (SAXS). It was found that the smaller the particles the larger are the differences of the values from different techniques [5].

On this background, this study aims to show that capillary electrophoresis is a powerful separation technique (CE) also in the field of nanoparticle research. In combination with Taylor dispersion analysis (TDA) it can be regarded as a promising alternative to the traditionally used method TEM for determining the size of nanoparticles (NPs) through converting an electropherogram into the particle size distribution (PSD). In addition, the method allows for the precise determination of mean electrophoretic mobilities, electrophoretic mobility distributions, and zeta potentials in a matrix of exactly known composition and the calibration-free determination of number-weighted mean hydrodynamic radii.

The present work intends to investigate, whether the developed concept is applicable to different types of nanoparticles varying in size and surface chemistry. With the aim to make the method also applicable to nanoparticles with positive surface charge density, one part of this work is directed towards the development of different capillary coating method, which will be evaluated in subsequent TDA and CE studies. Particular attention will be given to the influence of the counterion on electrokinetic potential, electrokinetic surface charge density, and relaxation effect-based size selectivity.

Chapter Two

Theoretical Background

Theoretical Background

2.1 Electrokinetic Effects – The Electrical Double Layer

2.1.1 Electroosmosis

Electroosmotic flow (EOF) or electroosmosis is one of the electrokinetic effects and a phenomenon in many electrophoretic separation processes. It can be described as the motion of liquid relative to the wall due to the effect of the electric field on the liquid layer enriched in counterions adjacent to a fixed charged surface (capillary wall). The magnitude and the direction of the resulting electroosmotic flow depend on the chemical composition and structure of the surface of the capillary wall and the chemical composition of the solution within the tube. Because the surface of the wall of a fused-silica capillary is negatively charged (at most pH conditions), there is a build-up of a layer adjacent to the capillary wall enriched in positive counterions while the negative ions (co-ions) are repelled from this layer (electrical double layer (EDL)). When an electric field is applied, this layer of positive charge is accelerated toward the negative electrode, resulting in the bulk flow of liquid toward that electrode. The movement of EDL is transferred to the bulk of the liquid through viscous effect to generate EOF. After reaching steady state conditions, the mean velocity of the EOF is proportional to the applied electric field strength in the following equation:

$$v_{EOF} = \mu_{EOF} \cdot E \qquad (1)$$

where v_{EOF} is the mean EOF velocity, μ_{EOF} is the electroosmotic mobility, and E is the electric field strength.

The electroosmotic mobility depends on the zeta potential, the permittivity of the medium and the viscosity of the solution as following:

$$\mu_{EOF} = -\frac{\varepsilon_0 \varepsilon_r \varsigma}{\eta} \qquad (2)$$

where ε_0 is the permittivity of vacuum, ε_r is the relative permittivity of the medium, ζ is the zeta potential and η is the viscosity of the solution. This equation is only valid, when the thickness of the double layer is much smaller than the diameter of the capillary.

Experimentally, the electroosmotic mobility can be measured using the following equation:

$$\mu_{EOF} = \frac{v_{EOF}}{E} = \frac{L_D \; L_T}{U \; t_{EOF}} \qquad (3)$$

where L_D = length of capillary to the detector, L_T = total length of capillary, U = voltage, t_{EOF} = migration time of a suitable marker of the EOF velocity.

2.1.2 Models of the electrical double layer

The first step in understanding the generation of the EOF is to describe quantitatively the distribution of the surface charge density σ_0 and the volume charge density ρ due to the excess of counterions in the layer of solution near the capillary wall. As already mentioned above, this counterion rich region is called the electrical double layer (EDL). The term EDL was first put forward in 1879 by Helmholtz.

Although there are several theoretical models that describe the structure of the electric double layer, there is no general model that can be used in all experimental situations. However, the most commonly used ones are the Helmholtz model, the Gouy-Chapman model, and the Stern model which are represented in Figure 1. The Helmholtz model assumes the presence of a compact layer of ions in contact with the charged solid surface. The model of Gouy and Chapman involves a diffuse double layer, in which the accumulated ions, due to the thermal energy in accordance with the Boltzmann distribution, extend to some distance from the solid surface. In addition, in the Stern model it is suggested that the solid-liquid interface includes both a rigid (Helmholtz) and a diffuse layer (Gouy-Chapman layer).

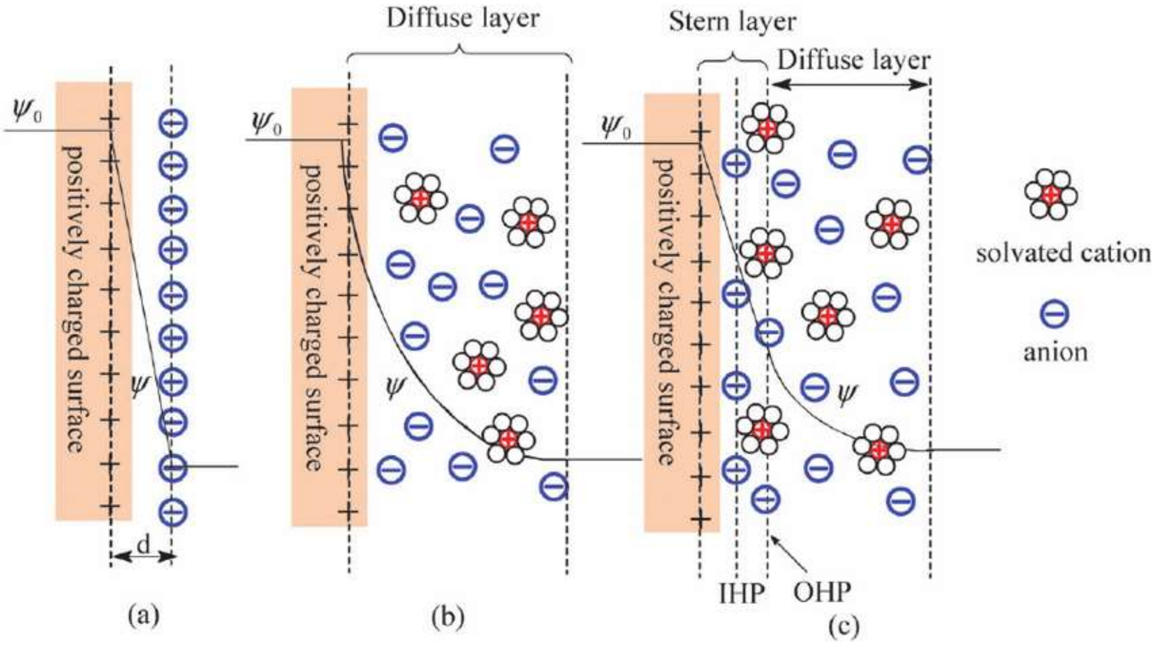

Figure 1: Schematic representation of the (a) Helmholtz model, (b) Gouy-Chapman model, and (c) Stern model for the electrical double layer at a positively charged surface. IHP: the inner Helmholtz plane, OHP: outer Helmholtz plane, d : the double layer distance, ψ_0 : the potentials at the surface, and ψ : the electrode/electrolyte interface (taken from ref. [6]).

In the Stern model, there is a thin region between the surface (having the surface potential ψ_0) and the diffuse layer. This layer of bound or tightly associated solvent molecules and counterions is generally referred to as the Stern layer. The Stern layer can be subdivided into two regions: the inner layer and the outer layer. The inner layer, the outer surface of which is referred to as the inner Helmholtz plane (IHP), that is located at the center of ions which are not hydrated and are specifically adsorbed to the surface. The outer layer passes through the center of hydrated ions; the interface between this and the diffuse layer is referred to as the outer Helmholtz plane (OHP). IHP can contain both co- and counter ions, whilst the OHP contains exclusively solvent molecules and counterions. In this region, it is assumed that there is no charge between the surface and the IHP and between the IHP and the OHP. Therefore, in this region the electrostatic potential decreases linearly. Schematic of the electrical double layer is represented in Figure 2 as a model of the silica surface immersed in an aqueous electrolyte.

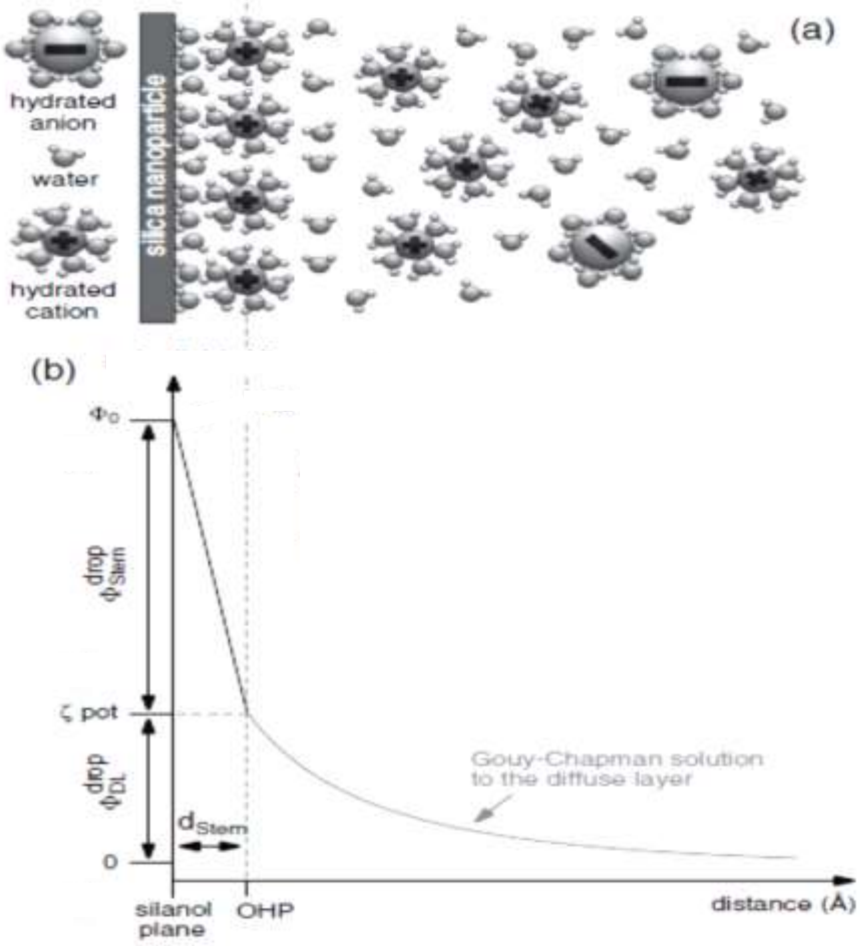

Figure 2: Model of the electrical double layer of a silica surface immersed in an aqueous electrolyte from [7]):

(a) Graphical representation of the liquid layer near the silica surface including bound hydrated counterions and diffusing hydrated ions (co-ions and counterions).

(b) Sketch of involved distances and potentials.

Several processes can be responsible for the acquisition of a surface net charge [8]: *e.g.* the dissociation of chemical groups on the surface of the solid or the adsorption of ions or molecules from the solution onto the surface. This charge creates an electrostatic surface potential ψ_0. When the surface is immersed in an electrolyte, the electrostatic force attracts ions of opposite charge (counterions) from the solution and repels ions with like charge (co-ions). The region of liquid near to the surface has a higher volume density of counterions and a lower volume density of co-ions than the bulk liquid. The surface charge is balanced by an equal amount of excess charge (of opposite sign) within the double layer. The net result is that the countercharge from the solution effectively screens the surface charge so that on the global scale (within the bulk medium), the overall charge is zero.

According to the theory of electrostatics, the Poisson equation describes the relationship between the electrostatic potential $\psi_{(x)}$ and the charge density $\rho_{(x)}$ at any point in the solution:

$$\nabla^2\psi_{(x)} = -\frac{\rho_{(x)}}{\varepsilon_0\varepsilon_r} \tag{4}$$

The change in concentration of the counterions near a charged surface obeys the Boltzmann distribution:

$$n_i = n_i^{\infty}\exp\left(-\frac{z_i e\psi}{kT}\right) \tag{5}$$

where n_i and z_i are the number concentration or number density and the valence of the ion i, respectively, e is the elementary charge, k is the Boltzmann constant and T is the absolute temperature. The volume charge density $\rho_{(x)}$ at position x is thus given by:

$$\rho_{(x)} = \sum_i z_i e n_i = \sum_i z_i e n_i^{\infty}\exp\left(-\frac{ze\psi}{kT}\right) \tag{6}$$

Combining Eq. (4) and Eq. (6) leads to the well-known Poisson–Boltzmann equation (PBE), which describes the distribution of the electrostatic potential in solution near a charged surface:

$$\nabla^2\psi_{(x)} = -\frac{1}{\varepsilon_0\varepsilon_r}\sum_i z_i e n_i^{\infty}\exp\left(-\frac{ze\psi_{(x)}}{kT}\right) \tag{7}$$

The employ of PBE postulates that [9]:

(i) Electrolyte ions are point charges.

(ii) Ion-ion corelation may be neglected.

(iii) Solvent is a structureless dielectric continuum having a uniform dielectric permittivity ε_r.

(iv) Charges on the particle surface are smeared out to give a uniform surface charge density σ_0.

Generally, PBE is commonly solved numerically with certain geometries. For the planar limiting case, it can be solved analytically. If the electrostatic energy is small compared to the thermal energy of the ions, i.e. ($ze\psi / kT \ll 1$), Eq. (7) reduces to the linearized PBE, which is called the Debye–Hückel approximation:

$$\nabla^2\psi \ = \ \kappa^2\psi \qquad (8)$$

with the Debye–Hückel parameter κ is expressed as:

$$\kappa \ = \ \sqrt{\frac{e^2 N_A \sum z_i^2 c_i}{\varepsilon_0 \varepsilon_r kT}} \qquad (9)$$

Moreover, the Debye length (κ^{-1}) is the reciprocal of the Debye–Hückel parameter. It is a measure of the thickness of the diffuse electrical double layer (Chapter 4).

2.1.3 Electrophoretic mobility

The electrophoretic mobility μ_{ep} of a spherical particle (with sphere radius a) moving with a velocity v_{ep} in an electrolyte solution in a homogeneous electric field with the field strength E is given by the ratio v_{ep} / E . The most widely used equation relating the electrophoretic mobility μ_{ep} of a colloidal particle to its zeta potential ζ is the Smoluchowski equation ($\kappa a \gg 1$):

$$\mu_{ep} = \frac{\varepsilon_o \varepsilon_r \varsigma}{\eta} \qquad (10)$$

which corresponds to Equation 2 with reversed sign. The Smoluchowski equation is readily derived on the basis of some approximations from the condition of balance between electric and viscous forces acting on the particle. This formula is only applicable when κa is sufficiently large (where κ is the Debye-Hückel parameter and a is the sphere radius, which can be approximated by the solid particle radius plus the thickness of bound layer).

The electrokinetic potential or zeta potential ζ is defined to be the electrostatic potential at the slipping or shear plane, which is identical to the electrostatic potential at the surface of the model sphere. The electrostatic potential decreases continuously and monotonically across the diffuse layer. It finally converges to the electrostatic potential of the bulk medium.

If the particle is small relative to the size of the double layer ($\kappa a \ll 1$), the Hückel equation (*cf.* Eq. 15) is applicable. In accordance with the electric force on the particle F_1 ($F_1 = QE$; where Q is the particle charge) and the viscous force F_2 ($F_2 = 6\pi\eta a v$ (Stokes law); where v is the velocity), these two forces must be balanced under stationary conditions:

$$QE \;=\; 6\pi\eta a v \qquad \text{and} \qquad v \;=\; \frac{QE}{6\pi\eta a} \tag{11}$$

In order to normalize on the parameter E following definition is valid:

$$\mu_{ep} \;=\; \frac{v}{E} \tag{12}$$

Substituting the velocity (Eq. 11) into Eq. (12) yields to:

$$\mu_{ep} \;=\; \frac{1}{6\pi\eta}\frac{Q}{a} \tag{13}$$

If it is now assumed that ζ is given by the Coulomb potential of the model sphere, ζ can be obtained as follows:

$$\varsigma \;=\; \frac{Q}{4\pi\varepsilon_0\varepsilon_r a} \tag{14}$$

After rearrangement and placing Q into Eq. (13), it results what is known as the Hückel equation, which is applicable for the limiting case where the particle radius a is much smaller than the thickness of the double layer:

$$\mu_{ep} \;=\; \frac{4\pi\varepsilon_0\varepsilon_r\varsigma}{6\pi\eta} \;=\; \frac{2\varepsilon_0\varepsilon_r\varsigma}{3\eta} \tag{15}$$

The Smoluchowski equation (Eq. 10) and the Hückel equation (Eq. 15) differ by a factor of 2/3. As is seen in Figure 3 for $\kappa a \ll 1$, most electrolyte ions in the double layer experience an undistorted original field. For $\kappa a \gg 1$, on the other hand, most electrolyte ions in the double layer experience a distorted field.

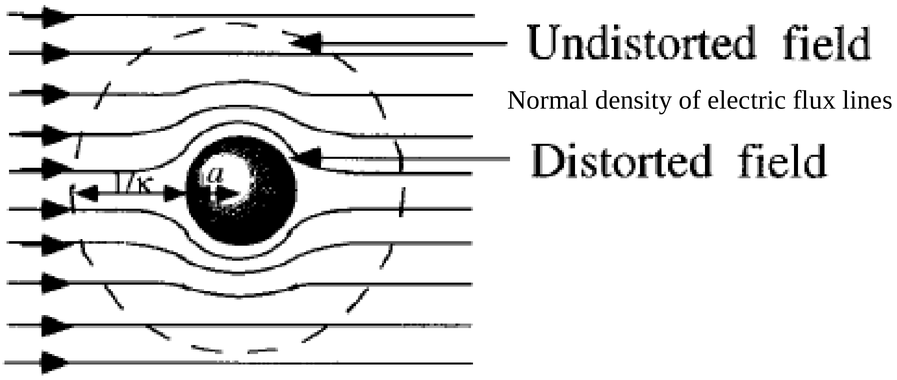

(a) $a \ll 1/\kappa$

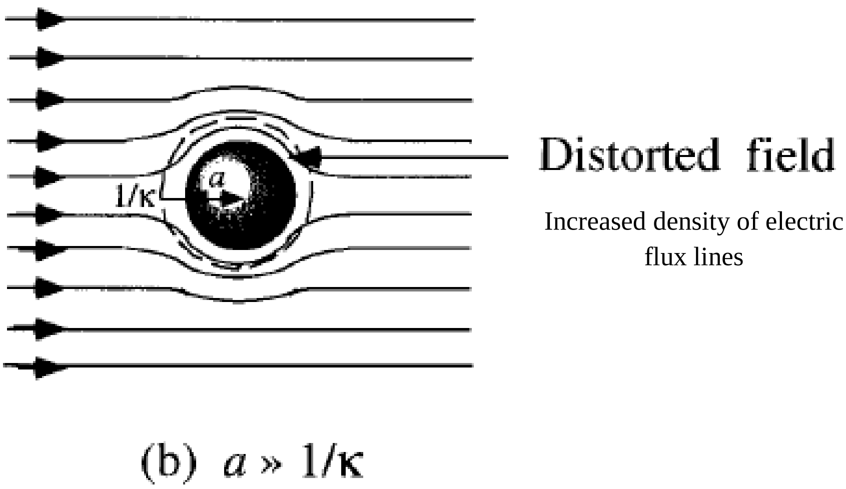

Increased density of electric flux lines

Figure 3: Electric field in the region near the particle surface. Electrolyte ions experience a stronger electric field for $\kappa a \ll 1$ (Condition **b**) than for $\kappa a \gg 1$ (Condition **a**) (taken from ref. [9])

Experimentally, the electrophoretic mobility μ_{ep} can be calculated from recorded electropherograms according to:

$$\mu_{ep} = \frac{L_D \ L_T}{U \ t_{mig}} - \frac{L_D \ L_T}{U \ t_{EOF}} \tag{16}$$

where t_{mig} = migration time of zone investigated. The first term on the right side of Eq. (16) represents the observed mobility, which is the observed velocity normalized on the electric field strength. The second term on the right side of this equation represents the electroosmotic mobility.

2.1.4 The zeta potential

Theoretical treatments generally assume that the solid immersed in a liquid is either a sphere, a cylinder, or a large flat plate. The plane of shear (or shear plane or slipping plane) is an imaginary plane that is considered to lie close to the solid. In the case of a particle undergoing electrophoresis, the plane of shear forms a sheath which envelopes the particle. The analysis of the forces exerted on each liquid element (forces induced by pressure gradients in the system and by the electrical charges it contains, as well as shear forces induced by neighboring parcels of liquid moving with different velocities) can be carried out in terms of either charge or electrostatic potential. In the latter case, one calculates the average potential in the plane of shear, the electrokinetic or zeta potential ζ, which plays a central role for the stability of charged colloidal dispersions. In the absence of strongly adsorbed species, the ζ potential has the same sign as the surface potential, but the absolute value of the ζ potential is lower, especially at higher ionic strength.

Henry [10] derived following equation for spheres of radius a, which is applicable for low ζ and has no restrictions regarding κa:

$$\mu_{ep} = \frac{2\varepsilon_0\varepsilon_r\varsigma}{3\eta} f(\kappa a) \tag{17}$$

where $f(\kappa a)$ is called Henry’s function. Equation (17) bridges between Smoluchowski's equation and Hückel's equation. If $f(\kappa a) = 1$, Equation (17) becomes Smoluchowski’s equation ($\kappa a \to \infty$), while it becomes Hückel’s equation when $f(\kappa a) = 2/3$ ($\kappa a \to 0$). Henry’s function $f(\kappa a)$ can be calculated with a maximum relative error of less than 1% with following approximation [11]:

$$f(\kappa a) = 1 + \frac{1}{2\left(1 + \frac{2.5}{\kappa a\left\{1 + 2e^{-\kappa a}\right\}}\right)^3} \tag{18}$$

where κ = Debye–Hückel parameter = reciprocal thickness of the diffuse layer. Calculating ζ via the Henry equation requires knowledge of the sphere radius a and the ionic strength I. The sphere radius a can be approximated by the number-weighted mean hydrodynamic radius $r_{H,N}$ of the investigated nanoparticle population, while the Debye–Hückel parameter κ is calculated from the ionic strength I (*cf.* Eq. 9).

As the particle moves through the electrolyte, the ions in the double layer will tend to lag behind. The charge density will be less than its equilibrium value in front of the particle, while behind the particle it will be larger. This behavior is called the “relaxation effect” [12]. If ζ> 25 mV, the relaxation effect exerts a noticeable influence on the electrophoretic mobility of nanoparticles [13]. Neglecting the relaxation effect will result in an intolerable error in ζ. Wiersema *et al.* [14] were the first to solve numerically the differential equations. Their calculations were based on the dimensionless ionic drag coefficient m (which is a function of the limiting equivalent conductance) of the co-ion and the counterion. The algorithm developed by Wiersema *et al.* failed to converge for ζ potentials larger than 150 mV for a 1:1 electrolyte [15]. This problem was solved later by O’Brien and White [16]. For fixed κa, they showed that the electrophoretic mobility plotted against ζ goes through a maximum if κa > 3. This maximum is very flat so that mobility measurements in this region cannot be expected to yield accurate values for ζ. In many cases, it is possible to avoid the unfavorable maximum region by increasing the ionic strength of the separation electrolyte, so that ζ can be decreased to values lower than 100 mV.

Several approximate analytic expressions have been developed to avoid numerical calculations [13,17]. The semi-empirical formula developed in 1983 by Ohshima *et al.* [18] is applicable for $\kappa a \geq 10$ with a relative error less than 1%. Later, Ohshima [19,20] presented an approximate analytic expression which has no restrictions regarding κa:

$$\mu_{ep} = \frac{2\varepsilon_0\varepsilon_r\varsigma}{3\eta}\left\{\begin{array}{l}\left[1+\dfrac{1}{2\left[1+2.5/\left\{\kappa a\left(1+2e^{-\kappa a}\right)\right\}\right]^3}\right]-\left[\left(\dfrac{e\varsigma}{kT}\right)^2\left(\dfrac{\kappa a\left(\kappa a+1.3e^{-0.18\kappa a}+2.5\right)}{2\left(\kappa a+1.2e^{-7.4\kappa a}+4.8\right)^3}\right)\right]- \\ \left[\dfrac{m_+ + m_-}{2}\left(\dfrac{e\varsigma}{kT}\right)^2\left(\dfrac{9\kappa a\left(\kappa a+5.2e^{-3.9\kappa a}+5.6\right)}{8\left(\kappa a+1.55e^{-0.32\kappa a}+6.02\right)^3}\right)\right]\end{array}\right\}$$

$$m_{\pm} = \frac{2\varepsilon_0\varepsilon_r kTN_A}{3\eta\Lambda^{\circ}_{\pm}} \qquad (19)$$

where k = Boltzmann constant; T = absolute temperature; m_+ and m_- = the dimensionless ionic drag coefficients; Λ°_{+}, Λ°_{-} = the limiting equivalent conductance of the cation and the anion, respectively.

For nanoparticles (NPs), this approximation is only valid if $\zeta \leq$ 100 mV. This approximation does not distinguish between the stronger influence of the counterion mobility and the lower influence of the co-ion mobility. Therefore, Pyell *et al.* [21] proposed a new approximation that is based on a simplification of Oshima's model [19], extending the applicability of the approximation to the use of any buffered electrolyte (containing one type of strong electrolyte counter-ions).

$$\mu_{ep} = \frac{2\varepsilon_0\varepsilon_r\varsigma}{3\eta}\left\{\begin{array}{l}\left[1+\dfrac{1}{2\left[1+2.5/\left\{\kappa a\left(1+2e^{-\kappa a}\right)\right\}\right]^3}\right]-\left[\left(\dfrac{e\varsigma}{kT}\right)^2\left(\dfrac{\kappa a\left(\kappa a+1.3e^{-0.18\kappa a}+2.5\right)}{2\left(\kappa a+1.2e^{-7.4\kappa a}+4.8\right)^3}\right)\right]- \\ \left[m_{counter}\left(\dfrac{e\varsigma}{kT}\right)^2\left(\dfrac{9\kappa a\left(\kappa a+5.2e^{-3.9\kappa a}+5.6\right)}{8\left(\kappa a+1.55e^{-0.32\kappa a}+6.02\right)^3}\right)\right]\end{array}\right\} \qquad (20)$$

where $m_{counter}$ = dimensionless ionic drag coefficient of the counterion (which has to be a strong electrolyte ion). Equations (17), (19) and (20) are only valid for very diluted nanoparticle dispersions (interparticle interactions are not taken into account).

2.1.5 The surface charge density

The surface charge density σ_0 is defined as the electric charge Q that is present on a surface of given area A :

$$\sigma_0 \;=\; \frac{Q}{A} \tag{21}$$

The surface potential Φ_0 is the electric potential at the surface. The potential ζ is the electric potential at the shear plane. Consequently, it is a function of the charge density σ_ς at the shear plane and the integral capacity C_{GCL} of the outer double layer, which is accessible from solving the PBE. The charge density σ_ς at the shear plane is also called effective or electrokinetic charge density and can be deduced from electrokinetic data. It is much lower (in absolute value) than the surface charge density σ_0 [22,23]. The ζ potential gives access to σ_ς (if the charge density distribution within the diffusive layer is known). In the planar limiting case, the non-linearized Poisson-Boltzmann equation can be analytically solved (Gouy-Chapman equation):

$$\sigma_\varsigma = \frac{2\varepsilon_0\varepsilon_r\kappa kT}{ze}\sinh\left(\frac{ze\varsigma}{2kT}\right) = \sqrt{8n\varepsilon_0\varepsilon_r kT}\,\sinh\left(\frac{ze\varsigma}{2kT}\right) \tag{22}$$

where z = charge number, n = number density.

In the spherical case (curvature effects), the non-linearized Poisson-Boltzmann equation cannot be solved analytically. However, for a 1:1 electrolyte Loeb *et al.* derived an empirical formula for the relationship between σ_ς and ζ (based on a numerical solution) [9].

$$\sigma_\varsigma = \frac{2\varepsilon_0\varepsilon_r\kappa kT}{e}\left[\sinh\left(\frac{e\varsigma}{kT}\right) + \frac{2}{\kappa a}\tanh\left(\frac{e\varsigma}{4kT}\right)\right] \tag{23}$$

According to the mathematical basis quoted by Loeb, Ohshima *et al.* [24] obtained a more exact analytic approximation relating the electrokinetic surface charge density σ_ς to the zeta potential ζ. They showed that their expression results in an excellent approximation of the exact numerical values obtained by Loeb, Overbeek, and Wiersema over a wide range of κa values, with a maximum relative error of 4% at κa = 0.1 and less than 1% for $\kappa a \geq 1$.

$$\sigma_\varsigma = \frac{2\varepsilon_0\varepsilon_r\kappa kT}{ze}\sinh\left(\frac{ze\varsigma}{2kT}\right)\left[1 + \frac{1}{\kappa a}\left(\frac{2}{\cosh^2\left(\frac{ze\varsigma}{4kT}\right)}\right) + \frac{1}{(\kappa a)^2}\left(\frac{8\ln\left(\cosh\left(\frac{ze\varsigma}{4kT}\right)\right)}{\sinh^2\left(\frac{ze\varsigma}{2kT}\right)}\right)\right]^{1/2} \tag{24}$$

2.1.6 Specific ion effect

The influence of aqueous electrolytes on various physicochemical and biological phenomena has been widely studied since the 19th century. Hofmeister showed that different salts increase or decrease the solubility of proteins in aqueous media depending on the type of salt and its concentration [25–30]. This effect is now known as the Hofmeister effect or specific ion effect which is a classification of ions in order of their ability to salt-out or salt-in proteins. More generally, the specific ion effect relates to the stability of colloidal solutions [25–30]. Accordingly, (by measuring the critical coagulation concentration, ccc) the “effectiveness” of different anions (with a fixed cation), or cations (with a fixed anion), can be ordered reproducibly in the so-called Hofmeister series (Figure 4). In colloidal science, there are a growing number of experiments showing that ions with the same valence can induce very different behaviours. Aqueous ion-containing interfaces are found everywhere and play a key role in physical, chemical, atmospheric, and biological processes [30].

For negatively charged colloids such as silica NPs or polystyrene sulfate latex NPs, the influence of the alkali cation on the surface charge density is often interpreted in terms of specific ion adsorption or on site binding, or on the basis of the size of the solvated ions [31,32].

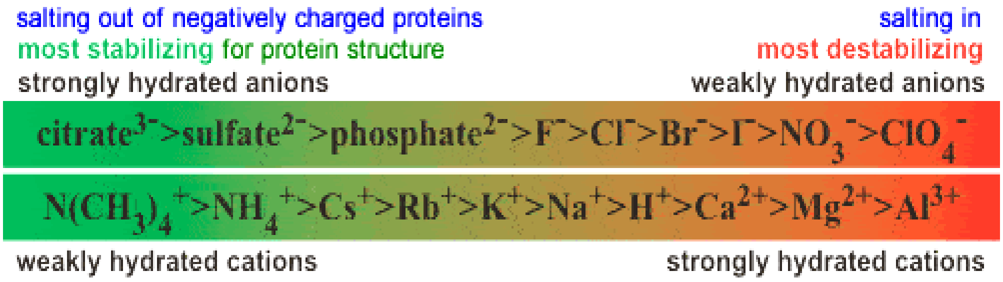

Figure 4: The Hofmeister series

Many investigators found that ζ and σ_ς are not only dependent on κa, $m_{counter}$, ε_0 and T but are also dependent on the type of counterion [33,34]. Tadros and Lyklema [33] determined the specific surface area of porous silica particles with diameter between 50-100 nm by two independent methods of the aqueous chloride solutions of the alkali cations (Li^+, Na^+, K^+ and Cs^+) of various ionic strengths at 20 °C. In their work, they made an investigation on the influence of the type of cation on the surface charge density of porous silica for 0.1 M chloride solutions.

Another systematic investigation dependent on the type of counterion was made by Sonnefeld *et al.* [34]. The surface charge density on AEROSIL 300 was determined in aqueous solutions of different alkali cation (Li^+, Na^+, K^+, Rb^+ and Cs^+) chloride solutions from 0.005 M to 0.3 M in the pH range between 4 and 8 by potentiometric titration at 25 ^{o}C. Their results showed that the alkali sequence for the spherical particles is in agreement with data for porous silica [33]. With respect to nonhydrated radii, the larger counterions show a greater tendency towards surface binding (adsorption); thus, they reduce the critical coagulation concentration (ccc). Milonjic [35] investigated the adsorption of alkali ions (Li^+, Na^+, K^+ and Cs^+) on silica sol particles in a wide concentration and pH range. He found that adsorbed amount of ion on the silica surface increases with increasing of both pH of solution and electrolyte concentration in the order: $Li^+ < Na^+ < K^+ < Cs^+$. Thereby, ccc for these ions increases in the series as follows: $Cs^+ < K^+ < Na^+ < Li^+$. The same sequence was found by Tadros and Lyklema [33] on silica surface in 0.1 N concentrations of alkali ions at pH > 7. Moreover, the electrophoretic mobility measurements generally indicate that the electrophoretic mobilities increase in the order: $K^+ < Na^+ < Li^+$, while the magnitude of the negative ζ potential increases as: $K^+ < Na^+ < Li^+$ [36–39].

On the other hand, ions have been classified as being either kosmotropes (structure makers) or chaotropes (structure breakers). This notion was first introduced by Gurney [39]. The degree of water structuring is determined mainly by two types of quantities: (i) the increase or decrease in viscosity of aqueous solution due to added salt, and (ii) entropy of ion solvation. For example, the viscosity η of an aqueous salt solution typically has the following dependence on ion concentration [40]:

$$\eta / \eta_0 = 1 + Ac^{1/2} + Bc \qquad (25)$$

where η_0 is the viscosity of pure water at the same temperature. A is a an electrostatic parameter about equal for all salts; its corresponding term can be explained by Debye–Hückel theory as being due to counterion screening at low ion concentrations. The constant B, which is an ion specific parameter known as the Jones–Dole Viscosity B coefficient, is the quantity that defines the degree of water structuring [40]. B is positive for kosmotropic ions and negative for chaotropic ions. One issue in interpreting experiments is how to separate the contributions of the anion from the cation. The standard assumption is that K^+ has the same B coefficient as Cl^- ($B_{K^+} = B_{Cl^-}$), because K^+ and Cl^- have approximately the same ion conductance [41] and because the value of B for KCl is approximately zero.

Water structuring is also reflected in entropies of ion solvation. Ions which are kosmotropic in viscosity experiments tend to have a negative hydration component to their solvation entropy, implying that they order the nearby water molecules, while chaotropic ions have a positive hydration component to their solvation entropy. The experiments show that water is ordered by small or multivalent ions and disordered by large monovalent ions. Therefore, water ordering has generally been interpreted in terms of ion charge densities [42].
The ion effects on water structure can be explained by a competition between ion–water interactions, which are dominated by charge density effects, and water– water interactions, which are dominated by hydrogen bonding. This explanation was proposed by Collins [42]. He explained that anions are stronger than cations at water ordering because of the asymmetry of charge in a water molecule: the negative end of water's dipole is nearer to the center of the water molecule than the positive end. The results of Kalyuzhnyi *et al.* [43] indicate that the simple solvation model proposed by Collins yields qualitative agreement with their experimental and theoretical data for simple monovalent ions. By using Collins' model for ion-induced structuring and disordering of water, they obtained the potential of mean force between ions and water molecules from which they calculated the activation energy for transferring a water molecule from near the ion to the bulk. On the basis of water reorientation dynamics, Bakker and co-workers reported that ion−water interactions only extend beyond the first solvation shell in solutions where both ion and counterion are strongly hydrated [44,45].

The guanidinium ion is a weakly hydrated ion, so it was classified as the strongest denaturanting ion. Mason *et al.* [46] applied the first-order difference method of neutron diffraction and isotopic substitution to determine the hydration structure of the guanidinium ion. They noted that the guanidinium ion is planar and contains a carbon atom, surrounded by three nitrogens in a trigonal form. They showed that the guanidinium ion is only weakly interacting with water. Therefore, guanidinium has no recognizable hydration shell and is one of the most weakly hydrated cations yet characterized. Vanderkooi and co-workers [47] presented temperature-dependent FTIR spectra of the OH stretching vibration of the water present in several different concentrations of aqueous guanidinium chloride solutions.

2.2 Taylor Dispersion Analysis

Taylor dispersion analysis (TDA) is a simple and absolute method that allows the determination of the collective diffusion coefficient of entities of virtually any size from molecules with a diameter of several Ångström to particles with a diameter in the submicrometer range. TDA, based on the work of Taylor [48,49] and Aris [50], relies on the analysis of the zone broadening of a solute plug in a laminar Poiseuille flow. Taylor demonstrated that the diffusion coefficient of the solute governs the longitudinal spread of the zone (see Eq. 26 and Eq. 27). Ideal conditions for TDA are described by two dimensionless quantities. (i) The residence time τ which is the ratio of the elution time to the time required for a solute to diffuse a distance equal to the radius of the capillary. (ii) The Peclet number (P_e) which is related to the relative rate of mass transfer along the axis of the capillary due to convection and diffusion. The validity range of TDA is fulfilled when $\tau > 1.4$ and $P_e > 70$ [51]. By using a capillary with small inner diameter (*i.e.* 76 µm in this study), the validity of TDA conditions are fulfilled. Profiles can be fitted to the cumulative Gaussian function:

$$A_{(t)} = \frac{1}{\sigma_t \sqrt{2\pi}} \int_0^t e^{\frac{(t-t_H)^2}{2\sigma_t^2}} dt \tag{26}$$

where $A_{(t)}$ = absorbance, t_H = inflection point, σ_t = parameter describing the width of the distribution.

After that, the collective diffusion coefficient D_c is determined from t_H and σ_t^2. The elution time is the time it takes the solute moving with the mean velocity to reach the detector located at a distance L_D from the inlet of the capillary. The variance σ_t^2 is a measure of the sharpness of the frontal injection profiles and is related to the dispersion coefficient K by $\sigma_t^2 = 2Kt$. The constant K is known as the dispersion coefficient and is related to the capillary radius, a_c, the mean linear velocity, $\langle v \rangle$, and the collective diffusion coefficient D_c.

$$K = \frac{a_c^2 \langle v \rangle^2}{48 D_c} \tag{27}$$

Aris [50] extended the theory of Taylor [48] and found that:

$$K = D_0 + \frac{a_c^2 \langle v \rangle^2}{48 D_c} \tag{28}$$

where D_0 is the self-diffusion coefficient at infinite dilution. If the diffusion coefficient at infinite dilution, D_0, can be approximated by D_c, then D_c is directly related to the hydrodynamic radius R_H via the Stokes-Einstein equation:

$$D_c = \frac{kT}{6\pi\eta R_H} \tag{29}$$

where k = Boltzmann's constant; T = absolute temperature; η = viscosity.

2.3 Gram−Charlier A Series Function

The Gram-Charlier Type A series (GCAS) is one well-known function to approximate the probability density function of a random variable. Usually, the GCAS is represented in terms of the Hermite polynomials as follows:

$$p_{(x)} = y_0 + \frac{B}{\sigma\sqrt{2\pi}} e^{\frac{-(x-\mu_1)^2}{2\sigma^2}} \left(1 + \frac{\kappa_3}{3!\sigma^3} H_3(z) + \frac{\kappa_4}{3!\sigma^4} H_4(z)\right)$$

$$H_3(z) = z^3 - 3z$$

$$H_4(z) = z^4 - 6z^2 + 3$$

$$z = (x - \mu_1)\,\sigma \tag{30}$$

where $p_{(x)}$ is the probability density, y_0 is the offset, B is a constant, μ_1 is the first moment, σ^2 is the second central moment, κ_3 is the skewness, the third Hermite polynomial H_3, κ_4 is the excess, and the fourth Hermite polynomial H_4.

2.4 Moment Analysis

Peak shape can be analyzed by the statistical moments when assuming a recorded eluted peak, $c = f(t)$, c = concentration, t = time. Thereby, the moments for any distribution can be calculated numerically from the following equations [52]:

$$m_n = \int_0^\infty c\, t^n dt \qquad (m_n = n^{th} \text{ moment}) \tag{31}$$

$$\mu_n = \frac{m_n}{m_0} = \frac{\int_0^\infty c\, t^n dt}{\int_0^\infty c\, dt} \qquad (\mu_n = n^{th} \text{ absolute moment}) \tag{32}$$

$$\mu'_n = \frac{\int_0^\infty c(t-\mu_1)^n dt}{\int_0^\infty c\ dt} \qquad (\mu'_n = n^{th} \text{ central moment}) \qquad (33)$$

$$S = \frac{\mu'_3}{\sqrt{(\mu'_2)^3}} \qquad (\text{standardized third central moment } \mu'_3) \qquad (34)$$

$$W = \frac{\mu'_4}{(\mu'_2)^2} \qquad (\text{standardized forth central moment } \mu'_4) \qquad (35)$$

$$E = W - 3 \qquad (\text{3 is the kurtosis of a normal distribution}) \qquad (36)$$

Physical significance of the moments:

i) The zeroth moment (m_0). This is simply the area under the peak.

ii) The first absolute moment (μ_1). This gives the center of gravity or mean of the peak.

iii) The second absolute moment (μ_2). This is the variance (*i.e.*, $\mu_2 = \sigma^2$) of the peak.

iv) The standardized third central moment (μ'_3) is a measure of the degree of asymmetry of peaks and its direction (skewness).

v) The standardized fourth central moment (μ'_4) provides information on the excess or kurtosis of the elution profile.

If $S = 0$ and $E = 0$, then there is no deviation from a Gaussian normal distribution.

2.5 Size distribution of nanoparticles

The methods commonly used for determining the size of nanoparticles are transmission electron microscopy (TEM), size exclusion chromatography (SEC) and dynamic light scattering (DLS). TEM and DLS are measuring the particle size in a powder or in a suspension without involving a separation process [53,54]. For example, average diameter or shape measured by TEM is based on chosen areas of the grid to image and photograph; in addition size separation effects that may occur during the drying process. Also, DLS is not a suitable method for measuring sizes of particles in samples with a broad PSD [55]. Therefore, it needs to use a suitable method to characterize and to measure the size of nanoparticles simultaneously with an ability of separation. Capillary electrophoresis (CE) is one of the most powerful separation techniques with advantages of short analysis times (fast analysis), low operating costs (little sample consumption) and high separation resolution. McCann *et al.* [56] used continuous particle electrophoresis to convert electropherograms of latex particles into PSD rapidly and accurately. They have suggested that in principle the electrophoretic mobility can be used to determine the particle size and particle-size distribution of colloidal particles and to fractionate the particles according to size, after size-selective separation due to the relaxation effect.

2.6 Synthesis of Nanoparticles

Three different types of nanoparticles were used in this study namely: Ludox silica NPs (SNPs) with three different sizes: Ludox TM-40 with a nominal particle diameter of 22 nm (SNP22), Ludox HS-30 with a nominal particle diameter of 12 nm (SNP12), and Ludox SM-30 with a nominal particle diameter of 7 nm (SNP7), purchased from Sigma-Aldrich, Germany; polystyrene sulfate latex NPs (PSSL) with four different sizes: Sulfate latex-0.02 µm with mean particle diameter 21 nm (PSSL20), Sulfate latex-0.04 µm with mean particle diameter 41 nm (PSSL40), Sulfate latex-0.06 µm with mean particle diameter 63 nm (PSSL60), and Sulfate latex-0.08 µm with mean particle diameter 80 nm (PSSL80), purchased from Molecular Probes, USA and cobalt oxyhydroxide NPs (CoOOH-NPs) with mean domain size (3.71-4.49 nm) prepared in Department of Chemistry, University of Marburg, Germany. These NPs carry on their surfaces negative charge for SNPs and PSSL and a positive charge for CoOOH-NPs.

Silica Ludox nanoparticles (SNPs). The quite simple preparation, chemical inertness, and the relatively inexpensive precursors, make SNPs to one of the most important and most studied oxide nanoparticle types in academics and in commercial applications. A pioneering method for the preparation of spherical and monodisperse silica particles from aqueous alcohol solutions of silicon alkoxides in the presence of ammonia as a catalyst was reported by Stöber *et al.* in 1968 [57]. The reaction produces silica particles with diameters ranging from 50 to 2000 nm, depending on conditions. The main advantage of the Stöber method is producing spherical silica particles in a suspension with a narrow particle size distribution under ambient conditions. The reaction can be represented as follows:

$$Si(OC_2H_5)_4 + H_2O \rightarrow HO-Si(OC_2H_5)_3 + C_2H_5OH \tag{37}$$

The products are partially hydrolyzed TEOS and an ethanol molecule. The hydrolysis may go to completion depending on the amount of water and catalyst present or stop after partial hydrolysis. If the hydrolysis reaction is completely carried out silicic acid is obtained [58]:

$$Si(OC_2H_5)_4 + 4H_2O \rightarrow Si(OH)_4 + 4C_2H_5OH \quad (38)$$

In a condensation reaction, two partially hydrolyzed molecules can link together and liberate a small molecule, such as water or alcohol:

$$(OR)_3Si-OH + HO-Si(OR)_3 \rightarrow (OR)_3Si-O-Si(OR)_3 + H_2O \quad (39)$$

or

$$(OR)_3Si-OH + HO-Si(OR)_3 \rightarrow (OR)_3Si-O-Si(OR)_3 + ROH \quad (40)$$

$R = H$ or alkyl, then OR is an alkoxy group.

This type of reaction can continue to build larger and larger molecules by polymerization forming nuclei that are typically in the range of 1−5 nm depending on the conditions of polymerization [59]. Figure 5 illustrates synthesis of colloidal silica.

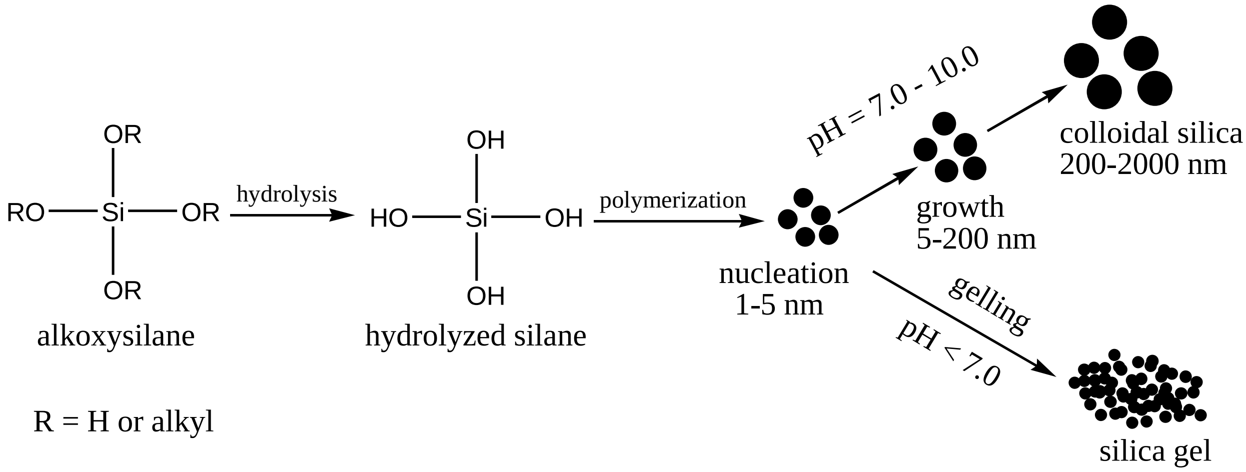

Figure 5: Schematic general method of colloidal silica synthesis *via* the hydrolysis and condensation reactions.

Polystyrene sulfate latex nanoparticles (PSSL). Monodispersity, strong adsorption ability, uniform particle size made these particles to one of the most studied materials. PSSL can be prepared by several methods [60]. As an example, the mechanism of the free radical polymerization is represented in Figure 6.

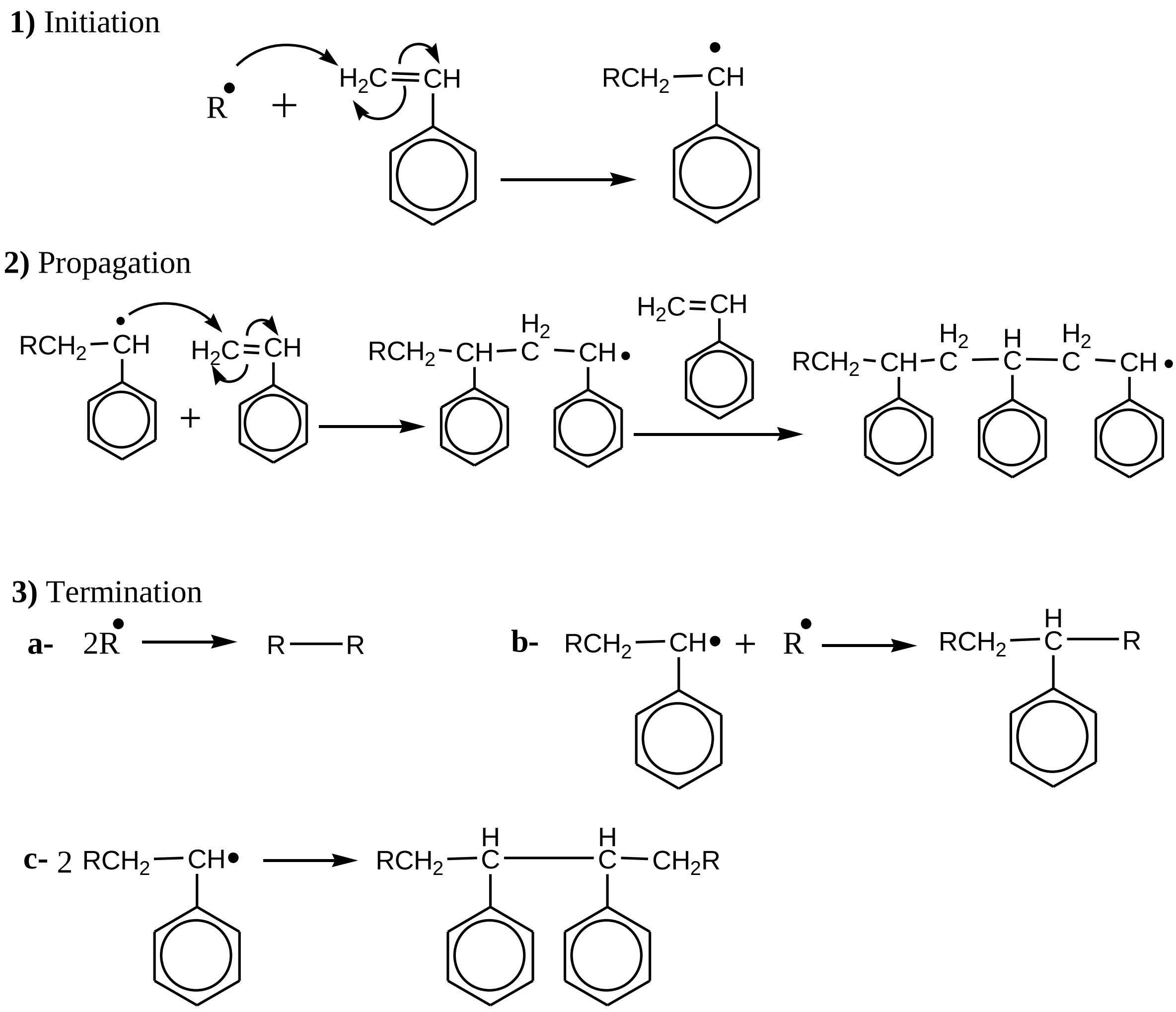

Figure 6: The schematic reaction illustration the free radical polymerization steps of styrene.

In the emulsion polymerization process, PSSL can be produced by either using a surfactant or without added surfactant (‘‘soap-free’’ or emulsifier-free polymerization) [61]. The main components for emulsion polymerization are an initiator (water-soluble inorganic salts), a monomer (such as styrene), a dispersing medium (usually water) and a surfactant [61].

Resulting from surfactant-free emulsion polymerization, the charged groups existing on a polystyrene latex surface are sulfate groups arising from the initiator decomposition [62]. The information for PSSL used in this study was obtained from the manufacturing company. The certificates of analysis for PSSL20, PSSL40, PSSL60, and PSSL80, respectively, are presented in Appendix B1.

Cobalt oxyhydroxide nanoparticles (CoOOH-NPs). CoOOH is one of the transition metal oxides, which have been extensively used as carriers and support for a variety of industrial catalysts at high and low temperatures due to their high surface area, chemical and thermal stablility, and mesoporous properties. CoOOH can be synthesized by several methods such as oxidation of solid $Co(OH)_2$ with O_2 or air at elevated temperature, electrochemically anodic oxidation of cobalt , and hydrothermal oxidation of $Co(OH)_2$ in alkaline medium under elevated pressure [63].

Recently, Kudielka *et al.* [64] presented three preparative routes using atmospheric oxygen or Br_2 dissolved in an aqueous solution of NaOH as oxidising agents to produce nanocrystalline CoOOH [64]. Their procedures start from forming $Co(OH)_2$ as a precursor to produce CoOOH by oxidation. In more details, they prepared CoOOH-NPs from the reaction of cobalt acetate with NaOH to form $Co(OH)_2$. With the first method, this oxidized with atmospheric oxygen under stirring for 24 h at room temperature and was finally heated up to 100 °C for 90 h.

With the second method, they obtained CoOOH-NPs from oxidizing $Co(OH)_2$ by the disproportionation product of Br_2 dissolved in an aqueous solution of NaOH. With the third method, they produced CoOOH-NPs by adding Br_2 to the aqueous solution of NaOH prior to its combination with the solution of cobalt acetate. Those CoOOH-NPs used in this study were prepared by them according to the third procedure [64]. In short, the preparation of CoOOH-NPs according to the third method can be represented in the following equations:

$$3\,Br_2 + 6\,NaOH \rightarrow 3\,OBr^- + 3\,Br^- + 3\,H_2O + 6\,Na^+ \quad \text{(first step of disproportionation)}$$

$$3\,OBr^- \rightarrow 2\,Br^- + BrO_3^- \qquad \text{(second step of disproportionation)}$$

$$6\,Co^{2+} + 21\,H_2O + BrO_3^- \rightarrow 6\,CoOOH + 12\,H_3O^+ + Br^- \qquad \text{(oxidation step)}$$

Chapter Three

Experimental Part

Experimental Part

3.1 Instrumentation

3.1.1 Capillary electrophoresis

The P/ACE MDQ capillary electrophoresis system (Beckman Instruments, Fullerton, CA, USA) equipped with UV-absorbance detector and a liquid-cooled capillary cartridge was used for the CE measurements. Temperature control of the capillary at 20.0 or 25.0 ^{o}C was achieved within the cartridge. The wavelength was set at 200 and 214 nm in the case of the silica NPs, to 214 nm for polystyrene sulfate latex NPs and to 254 nm for cobalt oxyhydroxide NPs. With the silica NPs and with the cobalt oxyhydroxide NPs, experiments were performed in fused-silica capillaries of 39.5 cm total length, 76 μm inner diameter (I.D) and 363.5 μm outer diameter (O.D), externally coated with polyimide (Polymicro Technologies, Phoenix, AZ, USA). The detection window was formed at 29.2 cm (effective capillary length) from the inlet (cathodic or anodic end) of the capillary. With the polystyrene sulfate latex NPs, the total length of the capillary was 60.7 cm and the length to the detector 50.5 cm. New capillaries were conditioned by rinsing them with 0.1 M sodium hydroxide solution for 60 min, 60 min with water, and 10 min with separation electrolyte. The capillary were rinsed 10 min with separation electrolyte between runs and after varying the buffer concentration and/or the buffer composition. Thoiurea was used as a marker to determine the electroosmotic mobility. With the cobalt oxyhydroxide NPs, either a covalently coated capillary or a capillary coated by dynamic procedures was used.

Data were recorded with the Beckman 32 Karat software (v.5.0). Further data treatment (*e.g.*, fitting of data to a Gram-Charlier series of type A, baseline correction, and moment analysis) was done with Origin 8.5G (Northampton, MA, USA). The ζ potential was calculated employing a Matlab (MathWorks, Natick, MA, USA) procedure.

3.1.2 Taylor dispersion analysis

All Taylor dispersion analyses (TDA) were done with the same instrument as that taken for the CE measurements. Temperature of the capillary and the sample tray were kept at 20 or 25 ^{o}C by liquid cooling. Either the total length of the capillary was 60.8 cm and the length to the detector 50.4 cm (uncoated capillaries) or the total length of the capillary was 39.5 cm and the length to the detector 29.2 cm (covalently coated capillaries and capillaries coated by successive multiple ionic-polymer layer (SMIL) procedure, refer to *Section 3.3.2.3*).

3.1.3 UV spectroscopy

UV-Vis spectroscopic measurements were done with a Lambda 35 UV/Vis Spectrometer (Perkin Elmer, Singapore). A quadratic quartz glass cell was used for measurements. Data were recorded with the Perkin Elmer UV Winlab (v.6.0). The wavelength was scanned between 200 - 700 nm. All measurements were made at room temperature.

3.1.4 Miscellaneous

The pH-meter type inoLab pH 720 (Wissenschaftlich-Technische Werkstätten (WTW), Weilheim, Germany) was used for pH measurements. The conductivity meter model LF 191 (Wissenschaftlich-Technische Werkstätten (WTW), Weilheim, Germany) was used for determination of electric conductivity.

3.2 Colloidal Silica Nanoparticles

3.2.1 Materials

Three different silica nanoparticle (SNPs) populations differing in their nominal mean particle diameter were supplied by Sigma-Aldrich (Taufkirchen, Germany), namely Ludox TM-40 with a nominal particle diameter of 22 nm (SNP22), Ludox HS-30 with a nominal particle diameter of 12 nm (SNP12), and Ludox SM-30 with a nominal particle diameter of 7 nm (SNP7). The concentrations of these particles were 40% (w/w) (pH = 9.0), 30% (w/w) (pH = 9.8), and 30% (w/w) (pH = 10) of SNP22, SNP12 and SNP7, respectively. Lithium tetraborate ($Li_2B_4O_7$) (Merck, Darmstadt, Germany), sodium tetraborate decahydrate ($Na_2B_4O_7 \cdot 10H_2O$) (Merck, Darmstadt, Germany) and potassium tetraborate tetrahydrate ($K_2B_4O_7 \cdot 4H_2O$) (Acros Organics, Geel, Belgium) were dissolved in water to prepare aqueous buffers of known ionic strength. Diguanidinium carbonate (Alfa Aesar, Karlsruhe, Germany) and boric acid (Sigma-Aldrich, Steinheim, Germany) were used to prepare aqueous buffers containing guanidinium borate (see *Section 3.2.3*).

3.2.2 Preparation of the buffers

Stock solutions of $Li_2B_4O_7$, $Na_2B_4O_7 \cdot 10H_2O$, or $K_2B_4O_7 \cdot 4H_2O$ were prepared by dissolving a weighed amount of each type of these materials in deionized water. From these stock solutions, the electrophoretic buffers of various salt concentrations (5-60 mmol L^{-1}) were prepared by diluting the stock solution with deionized water. For guanidinium borate, the stock solution was prepared (see the next section). From this stock solution, buffers with a lower concentration of Gdm^+ ion (10-40 mmol L^{-1}) were prepared by dilution with Milli-Q water.

3.2.3 Preparation of diguanidinium tetraborate solutions

A stock solution containing 40 mmol L^{-1} diguanidinium tetraborate was prepared employing following reaction [65]:

$$[C(NH_3)_3]_2CO_3 + 4H_3BO_3 \xrightarrow{2H_2O} 2[C(NH_3)_2]^+ + 2B(OH)_4^- + 2H_3BO_3 + CO_2\uparrow + H_2O$$

The amount of 0.004 mol of diguanidinium carbonate was mixed with 0.016 mol of boric acid in 100 mL deionized water. The mixture was heated for 1 h to boiling to get rid of CO_2 and deionized water was added to keep the final volume of the mixture solution. This solution was left to cooling and after cooling the volume was again completed to 100 mL. The concentration of this solution is then regarded to be exactly 40 mmol L^{-1}. From this stock solution, buffers of lower concentration (molar concentration denoted 5-30 mmol L^{-1}) were prepared by diluting the stock solution with Milli-Q water.

3.2.4 Preparation of samples

Either individual samples were prepared, which included exclusively one of the nanoparticle populations mentioned above, or mixture samples, which included the three nanoparticle populations SNP7, SNP12 and SNP22. The individual samples were prepared by taking 1000 µL from the original sample and completing the volume to 50 mL using one of the salt solutions (c = 5 mmol L^{-1}) described in *Sections 3.2.2* and *3.2.3*. The mixture samples consist of 500 µL SNP22, 1000 µL SNP12 and 2000 µL SNP7 completed to 50 mL by adding one of the salt solutions (c = 5 mmol L^{-1}) described in *Sections 3.2.2* and *3.2.3*. MilliQ water (18 MΩ cm, Merck MilliPore, Darmstadt, Germany) was used for sample preparation.

3.3 Polystyrene Sulfate Latex NPs

3.3.1 Materials

Four different populations of polystyrene sulfate latex nanoparticles (PSSL) were supplied by Molecular Probes (Eugene, USA), namely Sulfate latex-0.02 µm with mean particle diameter 21 nm (PSSL20), Sulfate latex-0.04 µm with mean particle diameter 41 nm (PSSL40), Sulfate latex-0.06 µm with mean particle diameter 63 nm (PSSL60), and Sulfate latex-0.08 µm with mean particle diameter 80 nm (PSSL80).

The concentration of these PSSL was 8% (w/v) in the original samples. Sodium tetraborate decahydrate (Merck, Darmstadt, Germany) was used as a starting material to prepare the buffer solution. MilliQ water (Merck MilliPore, Darmstadt, Germany) was used for sample dilution.

3.3.3 Preparation of the buffers

For TDA measurements, the different borate buffer solutions were prepared in the concentration range (2-10 mmol L^{-1}). For the CE measurements, the various concentrations of the borate buffer (5-25 mmol L^{-1}) were prepared by dissolving a weighed amount of sodium tetraborate in deionized water. MilliQ water was used for sample dilution.

3.3.4 Preparation of samples

For TDA measurements, the stock solution was prepared for each the measured sample by weighing it and diluting with 8 mmol L^{-1} of the buffer solution. From this stock solution, different concentrations of PSSL were prepared by diluting with 8 mmol L^{-1} of the buffer solution. For CE measurements, the same procedure for the preparation of PSSL samples in TDA measurements was followed except the buffer concentration used was 5 mmol L^{-1} instead of 8 mmol L^{-1}.

3.4. Cobalt Oxyhydroxide NPs

3.4.1 Materials

Cobalt oxyhydroxide NPs (CoOOH-NPs) were prepared by Alexander Kudielka (PhD student, Department of Chemistry, Section of Inorganic Chemistry, Workgroup of Prof. Dr. Harbrecht, University of Marburg). Nitric acid 1.0 N standard solution (Alfa Aesar, Karlsruhe, Germany), Hydrochloric acid 1.0 N (Sigma-Aldrich, Steinheim, Germany), or Methanesulfonic acid (MSA) 70% pure (Applichem, Darmstadt, Germany) were used as starting material to prepare non-buffering electrolytes. Sodium hydroxide solution 0.2 M (Sigma-Aldrich, Steinheim, Germany) was used as a reference material to determine exactly the concentrations of the prepared acidic electrolytes. N,N,N,N-tetramethylethylenediamine (TEMED) and 3-(trimethoxysilyl) propyl methacrylate (bind silane) were from Fluka (Buchs, Switzerland). Ammonium persulfate (APS), didodecyldimethylammonium bromide (DDAB), diallyldimethylammonium chloride (DADMAC), poly(diallyldimethylammonium chloride) (PDADMAC, solution 20% (w/w) in water, average molar mass: 400,000 - 500,000 g mol^{-1}), and poly(sodium 4-styrenesulfonate) (PSS, solution 25% (w/w) in water, average molar mass: 1,000,000 g mol^{-1}) were supplied by Sigma-Aldrich (Steinheim, Germany).

3.4.2 Preparation of capillary coatings

3.4.2.1 Covalently bonded (or permanent) coating

Fused-silica capillaries were first conditioned for each 15 min with acetone, 0.1 M hydrochloric acid, 0.1 M sodium hydroxide, water, and finally with acetone. A solution (30% (v/v)) of the bifunctional compound 3-(trimethoxysilyl) propylmethacrylate in acetone was forced by pressure through the capillary for 30 min at room temperature in order to introduce covalently bound vinylic anchoring groups onto the inner wall of the fused silica capillaries. After rinsing, the capillary was left overnight filled with the rinsing solution.

Finally, the pretreated capillary was rinsed successively with acetone and water for each 15 min. Subsequently, a solution of 5% (w/v) of DADMAC monomer was prepared and degassed for 10–15 min using a membrane vacuum pump. After that, 10 µL of 10% (w/v) APS and 10 µL of 10% (v/v) TEMED solution were added to the monomer solution, which was mixed for 3–5 s using a spatula. Afterwards, the capillary was dipped into the reaction mixture, and with help of an argon overpressure (ca. 1–2 bar) the reaction mixture was passed into the capillary. This process was continued until the first drop of the reaction mixture became visible at the opposite end of the capillary. Both ends of the capillary were then sealed with silicone grease and left overnight at room temperature.

Before installing the capillary in the instrument, it was rinsed with distilled water for about 2-5 min with the help of an HPLC pump (50–100 bars) and a flow splitter. The detection window is created during the rinsing process by burning off a small section (5-6 mm in length) of the capillary polyimide coating at a fixed distance from the capillary end using lighter until the polyimide turn from dark brown to black in appearance. A carefully and gently, the charred polyimide coating cleaned by using a wiper moistened with isopropanol over the burned area. Finally, the capillary was installed in the CE apparatus, rinsed and equilibrated with buffer solution for 10 min.

3.4.2.2 Noncovalent coating – dynamic coating

In the dynamic coating procedure, the coating agent DDAB, a double-chained cationic surfactant, is added to the background electrolyte (BGE) to prevent CoOOH-NPs adsorption on the capillary wall. The pre-treating solution containing DDAB (0.1 mmol L^{-1}) was prepared as follows. DDAB was prepared by dissolving DDAB in the appropriate BGE (10 mmol L^{-1}) and stirred for 15 min. Then this solution was sonicated for 10 min. Afterwards the solution was left to cool at room temperature and stirred at room temperature until DDAB completely dissolved. This sonication/stirring cycle was repeated until the solution of DDAB in BGE was clear [66]. New capillaries were pretreated with 0.1 M sodium hydroxide for 10 min rinsed for 5 min with water. After that, the solution of 0.1 mmol L^{-1} DDAB in buffer was rinsed through the capillary for 15 min. Finally, the capillary was washed for 2 min with the buffer. Electrophoretic runs are perfomed with electrolytes that do not contain DDAB. After each run, the capillary was rinsed successively with the electrolyte containing 0.1 mmol L^{-1} DDAB (3 min) and then BGE (2 min) [67,68].

3.4.2.3 Noncovalent coating – static coating

In the static coating procedures, highly charged high molecular weight polymers (polyelectrolytes) were used. In this case, the capillary was rinsed with a solution containing the appropriate coating agent. The capillary was coated with multilayers. This technique is denoted as formation of SMIL, in which a cationic polymer is sandwiched between an anionic polymer such as PSS and the uncoated negative fused-silica capillary. After the process, the capillary is covered with successively alternating layers of a polycation and a polyanion.

The PDADMAC solution 0.2% was prepared as follows: 50 mg PDADMAC, 12.1 mg Tris, and 43.4 mg NaCl were dissolved with small amount of water and then 0.5 mL of 0.1 N HCl were added to this mixture. Afterwards, this solution was adjusted to 5 mL with water. Finally, the solution was sonicated for 5 min and stored at 4 ^{o}C.

The PSS solution 0.2% was prepared in the same way as the preparation of the PDADMAC solution except that the amount of PSS was 10 mg instead of 50 mg. Each new fused-silica capillary was first conditioned with 0.1 M sodium hydroxide for 30 min (20 psi) and with water for 15 min (20 psi). For the SMIL coating, five successive layers on the capillary surface were deposited by using PDADMAC and PSS sequentially. The last deposited layer was PDADMAC, therefore, the inner capillary wall surface will carry a high positive charge density. The capillary coating procedure is as follows. The capillary was rinsed with PDADMAC solution 0.2% for 10 min (first layer), water for 5 min, PSS solution 0.2% for 10 min (second layer) and with water for 5 min. Afterwards, the rinse steps were repeated in the following order: PDADMAC solution for 10 min (third layer), water for 5 min, PSS solution for 10 min (four layer), water for 5 min, PDADMAC solution for 10 min (five layer) and water for 5 min. Finally, the capillary was rinsed with the BGE for 5 min. The voltage of 15 kV was applied for 10 min to stabilize the coating. Then the capillary was equilibrated again for 10 min by rinsing with the BGE.

Finally, the samples of CoOOH-NPs were prepared by dispersing the sample in 10 mmol L^{-1} HCl, HNO_3 and MSA at pH = 2.0 for both TDA and CE measurements.

Chapter Four

Results and Discussion

Results and Discussion

4.1 Colloidal silica nanoparticles

4.1.1 Electrophoretic mobilities

Investigations made with colloidal silica nanoparticles (SNPs) are divided into two groups. Experiments of the first group are called 1st series (containing the individual measurements of SNP12 and SNP22, first batch SNPs) and experiments of the second group are called 2nd series (second batch SNPs, including the investigations of SNP7, SNP12 and SNP22 added to a mixture solution except for the measurements with buffers of 20 mmol L^{-1}, which were repeated with individual measurements for all sizes of SNPs due to the observed overlap of peaks for SNP7 and SNP12). The migration time of the neutral marker (t_0) was calculated by using two methods. For the first method, the migration time was determined from the positive peak of thiourea, whereas in the second method was used the negative system peak to determinate the migration time. For different counterions (Li^+, Na^+ and K^+) with different concentrations, typical electropherograms of SNPs for 1st series are presented in Figure 7 (also see Appendix A1).

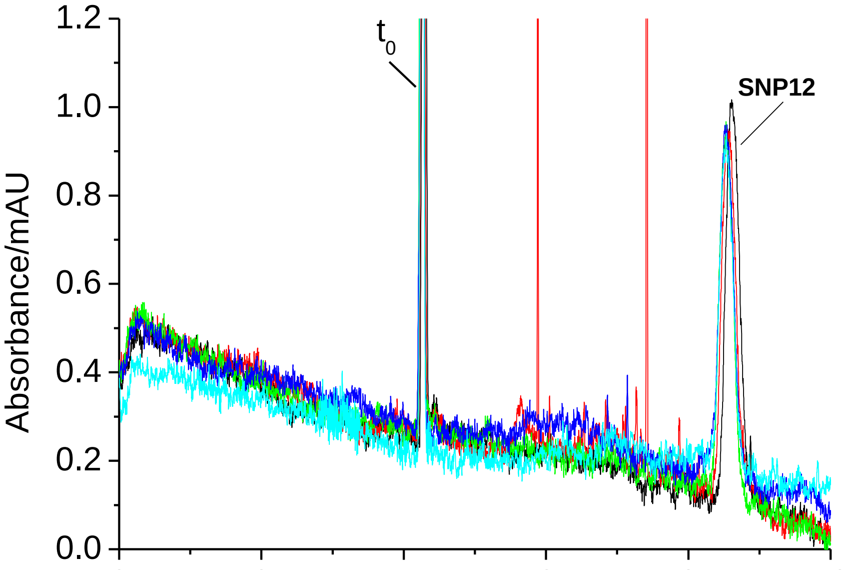

Figure 7: Recorded electropherogram obtained for SNP12, 1st series, c(Na^+) = 20 mmol L^{-1} . Experimental conditions: T = 25°C, total length of capillary = 39.5 cm, capillary length to detector = 29.2 cm, inner diameter of fused silica capillary = 76 μm, separation voltage 7 kV, sample injection 0.1 psi (6.89 mbar) 6 s, data rate 16 Hz, absorbance detection at the wavelength of 214 nm.

Figure 8 shows the overlap of the peaks between SNP7 and SNP12 of the 2nd series. Therefore, the migration time for these series is determined separately to distinguish exactly the migration time for each size. The electropherograms are measured in 20 mmol L^{-1} a concentration of different counterions (Li^+, Na^+, K^+ and Gdm^+) (refer to Appendix A2). It is clear from Figure 8 that SNP7 and SNP12 were comigrated as a one peak.

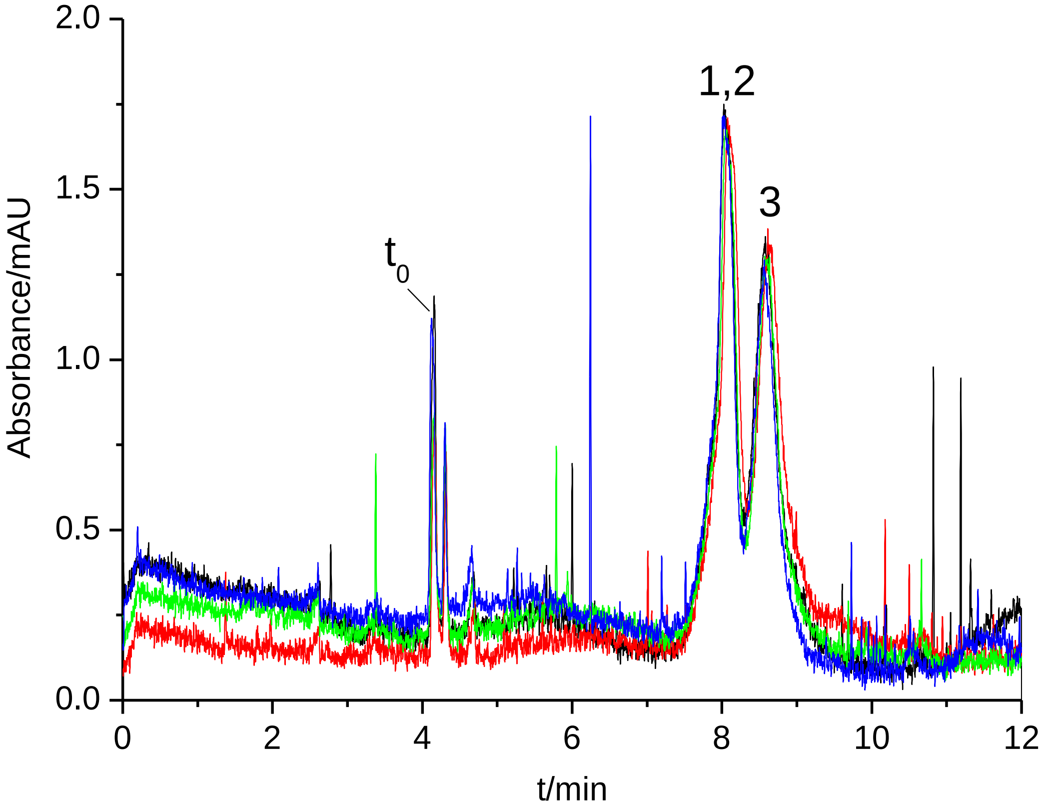

Figure 8: Superimposed recorded electropherograms obtained for: (t_0) thiourea as neutral marker, (1) SNP7 (w= 1.2%, w/w in mixture), (2) SNP12 (w= 0.6%, w/w in mixture) and (3) SNP22 (w= 0.4%, w/w in mixture), 2nd series, c(Li^+) = 20 mmol L^{-1}. Experimental conditions: T = 25°C, total length of capillary = 39.5 cm, capillary length to detector = 29.2 cm, inner diameter of fused silica capillary = 76 µm, separation voltage 7 kV, sample injection 0.1 psi (6.89 mbar) 6 s, data rate 16 Hz, absorbance detection at the wavelength of 200 nm.

On the other hand, the separation of the mixture of 2nd series was demonstrated for different concentrations of different counterions (Li^+, Na^+, K^+ and Gdm^+). The experimental results are presented as electropherograms of the mixture of SNPs (2nd series) in Figure 9 and Appendix A3. The repeatability of the data was confirmed by repeated injections (3-5 repeated runs).

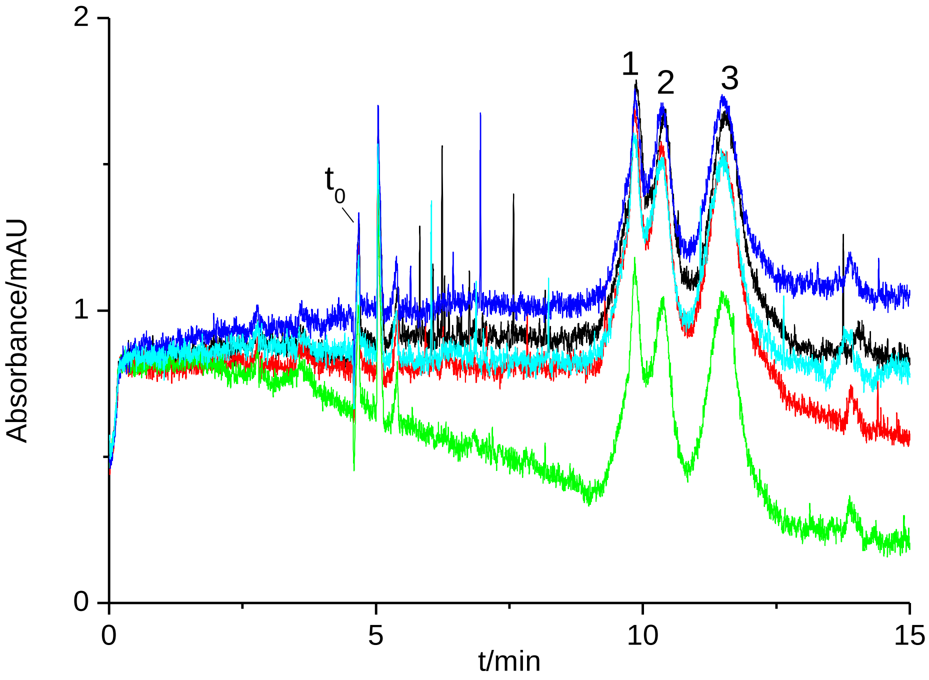

Figure 9: Superimposed recorded electropherograms obtained for: (t_0) thiourea as neutral marker, (1) SNP7 (w= 0.4%, w/w in mixture), (2) SNP12 (w= 0.9%, w/w in mixture) and (3) SNP22 (w= 1.7%, w/w in mixture) with 40 mmol L^{-1} of a concentration of Li^+ at the wavelength of 200 nm. Experimental conditions: T = 25°C, total length of capillary = 39.5 cm, capillary length to detector = 29.2 cm, inner diameter of fused silica capillary = 76 µm, separation voltage 7 kV, sample injection 0.1 psi (6.89 mbar) 6 s, data rate 16 Hz, absorbance detection at the wavelength of 200 nm.

The calculated electrophoretic mobilities are given in Table 1. The results for repeated runs under variation of the ionic strength are listed in Appendix A4. Good agreement was obtained between the migration times observed for 1st series and for 2nd series. Drift in the intensity of the Deuterium-lamp employed for absorbance detection causes drift of the baseline which is observed in several electropherograms. This drift can be easily corrected and is not inferring the developed data evaluation scheme. The relative standard deviation for five consecutive runs is between (0.01-0.31%) for Li^+, (0.02-0.42%) for Na^+, (0.01-0.69%) for K^+ and (0.06-0.70%) for Gdm^+ (refer to Appendix A4). Figure 10 shows that the electrophoretic mobility of SNPs is dependent on the particle size and dependent on the type of counterion and decreases with increasing the ionic strength. The absolute values of the electrophoretic mobility of SNPs decrease in the series: $Li^+ > Na^+ > K^+ > Gdm^+$.

Adsorption of SNPs onto the capillary wall can be excluded because the electroosmotic velocity remained very constant. The electroosmotic velocity of SNPs follows the same trend as that of the electrophoretic mobility of the SNPs with regard to type of counterion and ionic strength. The results are presented in Figure 11.

Table 1: Electrophoretic mobility μ_{ep} calculated from migration times obtained in consecutive runs (mean values, standard deviations in brackets, single values are listed in Appendix 4, for number of consecutive runs refer to Tables 1-18 in Appendix 4).

Cation	c/ (mmol L^{-1})	μ_{ep} (SNP7[**])/ ($mm^2\,kV^{-1}\,s^{-1}$)	μ_{ep} (SNP12[*])/ ($mm^2\,kV^{-1}\,s^{-1}$)	μ_{ep} (SNP12[**])/ ($mm^2\,kV^{-1}\,s^{-1}$)	μ_{ep} (SNP22[*])/ ($mm^2\,kV^{-1}\,s^{-1}$)	μ_{ep} (SNP22[**])/ ($mm^2\,kV^{-1}\,s^{-1}$)
Li^+	20	-32.96 (±0.03)	-33.18 (±0.10)	-33.13 (±0.04)	-33.51 (±0.07)	-35.16 (±0.03)
	40	-30.89 (±0.03)	-31.93 (±0.01)	-32.24 (±0.02)	-33.33 (±0.03)	-34.88 (±0.02)
	60	-29.94 (±0.04)	-31.55 (±0.05)	-31.72 (±0.03)	-34.16 (±0.07)	-34.47 (±0.05)
	80	-29.04 (±0.03)	-30.91 (±0.01)	-30.93 (±0.02)	-33.56 (±0.03)	-33.54 (±0.05)
	100	-28.17 (±0.07)	-30.14 (±0.01)	-30.15 (±0.05)	-32.64 (±0.08)	-32.63 (±0.05)
	120	-27.54 (±0.06)	-29.55 (±0.10)	-29.54 (±0.08)	-31.84 (±0.04)	-31.81 (±0.08)
Na^+	20	-32.63 (±0.02)	-30.71 (±0.13)	-32.79 (±0.03)	-34.20 (±0.11)	-34.72 (±0.08)
	40	-30.53 (±0.03)	-31.93 (±0.01)	-31.82 (±0.02)	-34.01 (±0.06)	-34.33 (±0.02)
	60	-29.39 (±0.01)	-30.39 (±0.03)	-31.00 (±0.01)	-32.53 (±0.04)	-33.58 (±0.04)
	80	-28.23 (±0.01)	-29.74 (±0.01)	-29.92 (±0.02)	-32.00 (±0.05)	-32.36 (±0.04)
	100	-27.21 (±0.04)	-28.44 (±0.08)	-28.92 (±0.03)	-30.96 (±0.05)	-31.15 (±0.04)
	120	----------[a]	-27.23 (±0.04)	----------[a]	----------[a]	----------[a]
K^+	20	-32.49 (±0.02)	-32.36 (±0.03)	-32.22 (±0.01)	-34.80 (±0.13)	-33.67 (±0.05)
	40	-29.89 (±0.08)	-31.15 (±0.02)	-30.93 (±0.05)	-34.22 (±0.06)	-32.19 (±0.03)
	60	-28.72 (±0.11)	----------[a]	-29.78 (±0.08)	-33.28 (±0.19)	-31.35 (±0.02)
	80	-27.25 (±0.07)	----------[a]	-28.79 (±0.19)	-32.53 (±0.01)	-30.46 (±0.21)
Gdm^+	20	----------[a]	----------[a]	-30.35 (±0.02)	----------[a]	-32.04 (±0.02)
	40	-27.47 (±0.03)	----------[a]	-28.71 (±0.05)	----------[a]	-30.72 (±0.11)
	60	-25.50 (±0.18)	----------[a]	-26.90 (±0.15)	----------[a]	-28.70 (±0.19)
	80	-23.90 (±0.05)	----------[a]	-25.36 (±0.30)	----------[a]	-26.88 (±n.d.)

[*] 1st series, [**] 2nd series, [a] not determined.

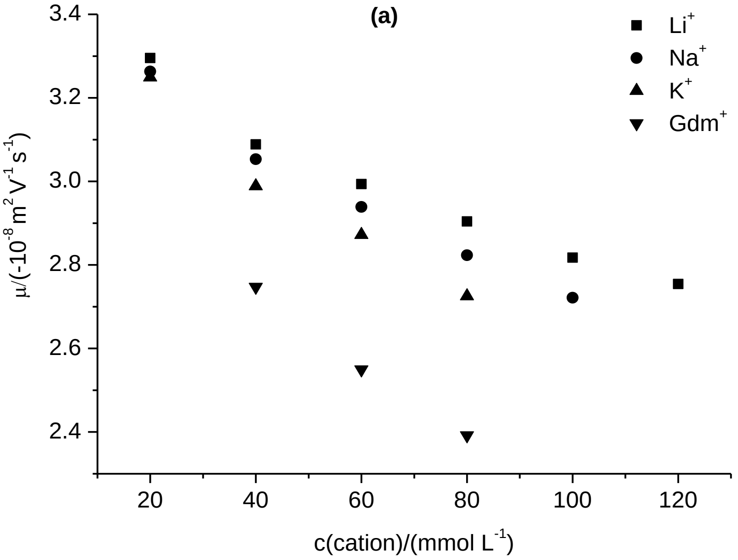

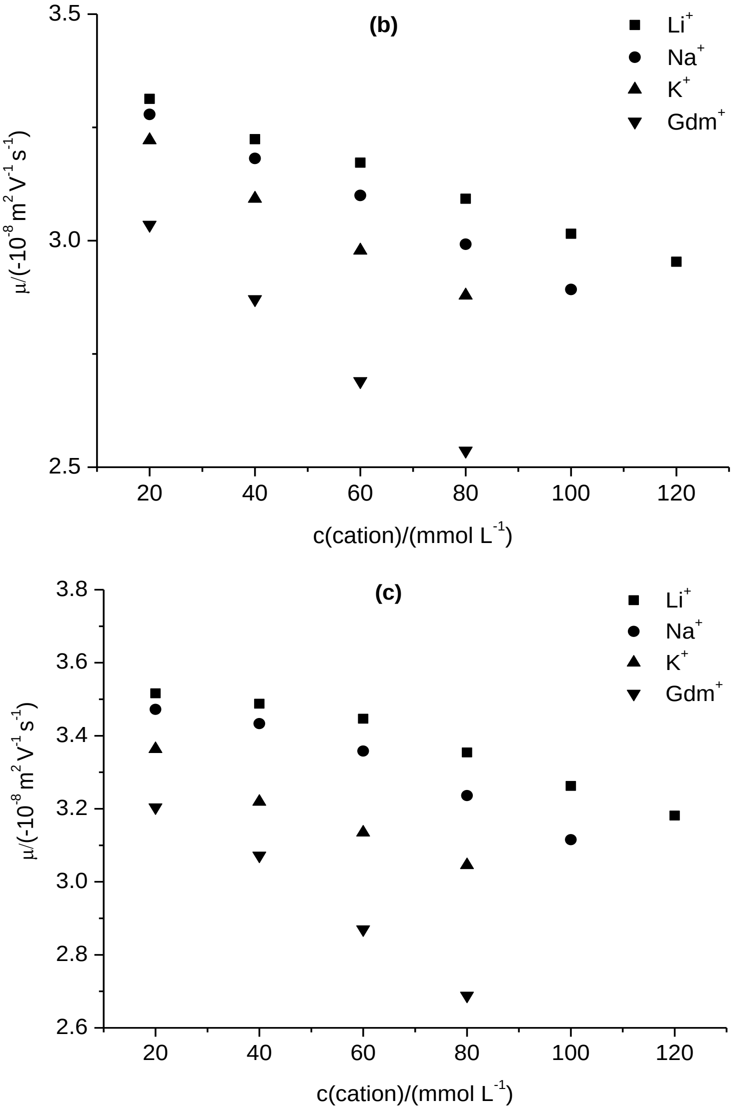

Figure 10: Electrophoretic mobilities of (a) SNP7, (b) SNP12 and (c) SNP22 in electrolytes differing in ionic strength and type of counterion. For experimental conditions refer to Figure 8, 2nd series.

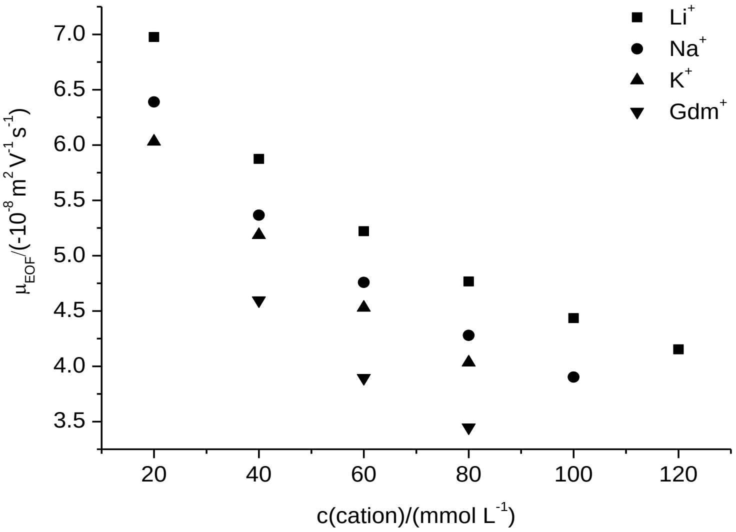

Figure 11: Electroosmotic mobilities of SNPs, 2nd series with different concentrations of different counterions. For experimental conditions refer to Figure 8, 2nd series.

In consideration of the limited stability of SNPs suspensions, the reproducibility of migration times was excellent. The overlay plots in Figures 9, 10 and 11 (see also Appendix A1, A2 and A3) demonstrate the excellent reproducibility in peak width, peak height, peak shape and migration time that was typically observed. However, SNPs with a nominal diameter of 7 nm cannot be separated completely from particles with a nominal diameter of 12 nm at low ionic strength (refer Figure 8 and Appendix A3). It can also be deduced that for the separation or measurement of small particles a high ionic strength should be chosen, while for the separation or measurement of large particles a lower ionic strength can have advantages. However, variation of counterion may lead to different critical coagulation concentrations (ccc). Allen and Matijevic [69] found that the ccc of Ludox HS and AM particles in alkali halide solutions at fixed salt concentration at pH = 9 followed the series $Li^+ > Na^+ > K^+ > Cs^+$. The SNPs and capillary wall are of the same material. Therefore, it is interesting to make a comparison of data obtained from electrophoresis with those obtained for the electroosmotic mobility μ_{eo}. As shown in Figure 11, the absolute electroosmotic mobility $|\mu_{eo}|$ is decreasing with increasing ionic strength and strongly dependent on the type of counterion. By using the wide capillaries for $|\mu_{eo}|$, the validity range of the Helmholtz-Smoluchowski equation is reached, hence here the relaxation effect is expected to be negligible. This does not hold for $|\mu_{ep}|$ of the nanoparticles, therefore $|\mu_{ep}| << |\mu_{eo}|$ and $d|\mu_{ep}|/dI << d|\mu_{eo}|/dI$. Beside this, the dependence of $|\mu_{eo}|$ on the type of counterion follows the same order as that observed for $|\mu_{ep}|$. An inhomogeneity of the electric field strength in the capillary can be neglected because there is no systematic deviation of the results obtained between the two series of SNPs. This gives indication that the results are independent of the mass fraction of particles in the sample because a higher mass fraction of particles is present in mixed samples for 2nd series, while a lower mass fraction of particles is given with samples that contain only one type of SNP (1st series).

A comparison of the recorded electropherograms dependent on the size of the nanoparticles, the ionic strength, and the type of counterion (refer to Appendix A1, A2 and A3) shows the strong influence of aggregation processes on the peak shape. Narrow peaks are observed under low ionic strength for all counterions, whereas broad and distorted peaks are obtained with the increasing of the ionic strength. It can be noticed that the aggregation is low at low ionic strength and increased with increasing the ionic strength. The reason is that the increase in ionic strength induces a reduction in the repulsive forces between the particles.

Distorted, skewed or even bimodal peaks were obtained in cases of insufficient colloidal stability. It is apparent that the second peak can be attributed to aggregated particles. Generally, overestimated electrophoretic mobilities and peak distortions point to pronounced particle aggregation [70] under conditions of low ζ potential [71]. On the other hand, aggregation and peak shape are affected by the type and concentration of counterion which follow the series: $Li^+ < Na^+ < K^+ < Gdm^+$ (refer to Appendix A1, A2 and A3).

4.1.2 Evaluation of zeta potential

The modification proposed by Pyell *et al.* [21] for the determination of ζ potential from the electrophoretic mobility (*cf.* Eq. (20)) was employed, taking the mobility of the counterion via its ionic drag coefficient into account neglecting the mobility or ionic drag coefficient of the co-ion. The limiting equivalent conductance values for the ions Li^+, Na^+, K^+ [72] and Gdm^+ [73] at 25 °C were taken from literature data. The electrophoretic mobilities can be calculated dependent on the reduced sphere radius κa and the ζ potential (refer to Figure 12). These calculated values are compared to the experimental values obtained by capillary electrophoresis (refer to Appendix 4). Figure 12 shows the superposition of calculated and experimental data. All experimental data exceed the threshold value (ζ = 25-50 mV) defined for the validity range of the Henry equation ($1 \ll \kappa a \ll 100$ for 1:1 electrolyte [9]). Apparently, ζ is significantly influenced by the ionic strength and strongly dependent on the type of counterion. Independent of the type of counterion, the estimated values for ζ of SNP7 and SNP12 are very close, while those for SNP22 seem to be somewhat lower. Moreover, the less mobile ions give a larger relaxation effect because the time needed for relaxation increases with decreasing ionic mobility.

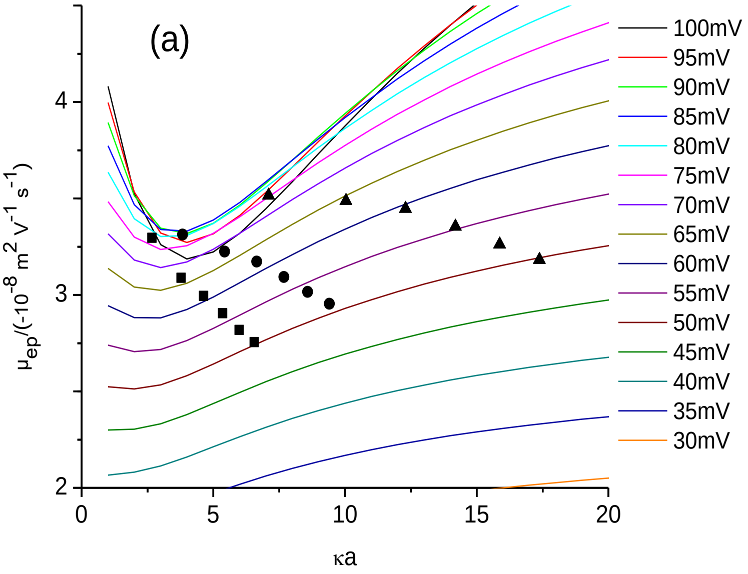

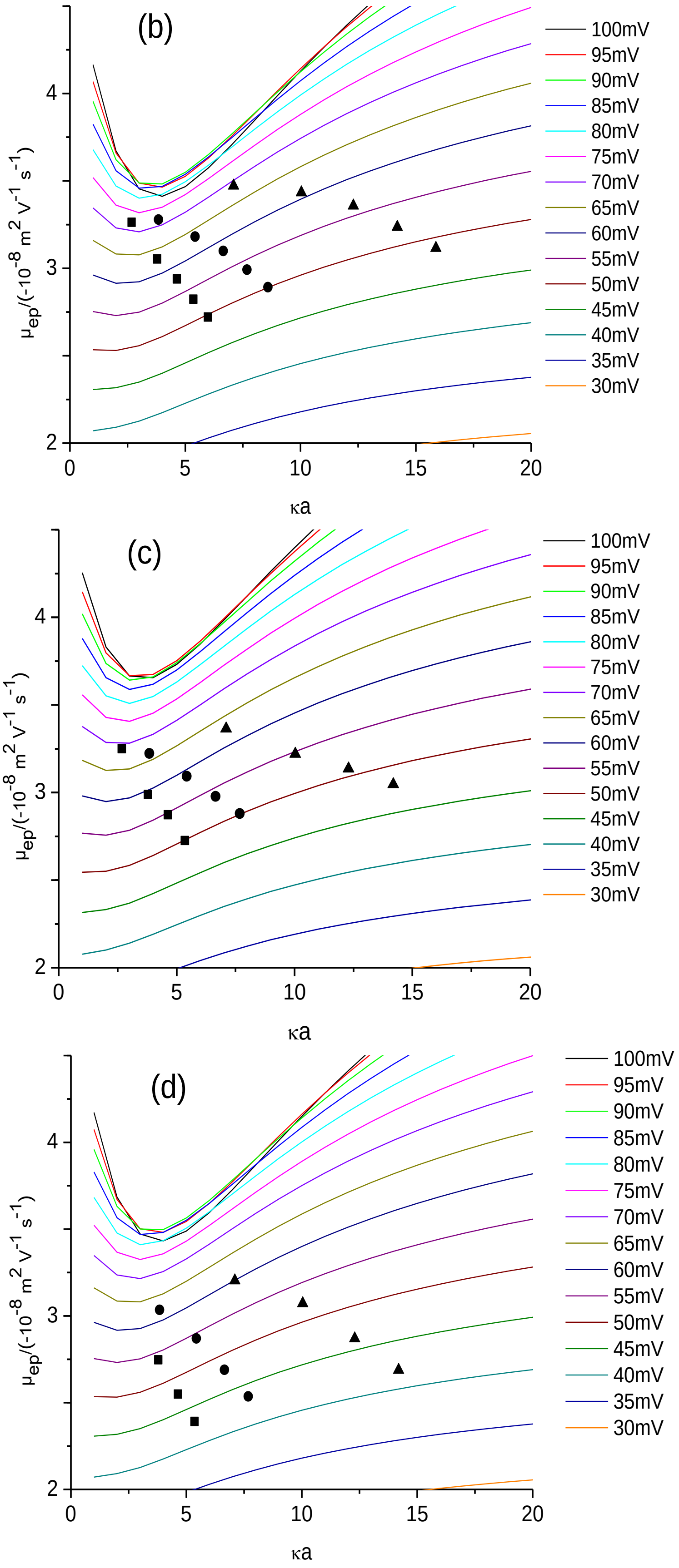

Figure 12: Calculated electrophoretic mobilities μ_{ep} for: (■) SNP7, (●) SNP12 and (▲) SNP22 with: (a) Li^+, (b) Na^+, (c) K^+ and (d) Gdm^+ cations for varied reduced sphere radius κa and varied ζ with superimposed experimental data for different counterions and varied ionic strength.

By using an iterative scheme described in [74], calculated ζ values were attained from the measured electrophoretic mobility (refer to Appendix 4), which constitute more precise data than those obtainable with a graphical procedure. This iterative procedure is based on a procedure, in which μ is calculated with varied ζ at fixed κa and $m_{counter}$ (refer to Table 2:1-4). The results are given in Table 3. Table 3 also contains those values calculated for ζ at the inner capillary wall/electrolyte interface from the experimentally measured electroosmotic mobilities μ_{eo} (refer to Appendix 4) via the Helmholtz-Smoluchowski equation (Eq. 10).

Table 2-1: Illustration of the iterative scheme employed for the determination of ζ via the modified analytic approximation for: SNP7, SNP12 and SNP22 nm with Li-cation as counterion.

c(Li$^+$)/ (mmol L^{-1})	κa	μ_{ep} (measured/ (10^{-8} m^2 s^{-1} V^{-1})	μ_{ep} (calculated)/ (10^{-8} m^2 s^{-1} V^{-1})	ζ/mV	
20	2.67620	-3.29546	-3.29528	-78.20	**SNP7****
			-3.29542	-78.21	
			-3.29556	-78.22	
40	3.78472	-3.08852	-3.08823	-66.62	
			-3.08847	-66.63	
			-3.08870	-66.64	
60	4.63531	-2.99373	-2.99353	-61.02	
			-2.99382	-61.03	
			-2.99411	-61.04	
80	5.35240	-2.90424	-2.90407	-56.55	
			-2.90440	-56.56	
			-2.90474	-56.57	
100	5.98416	-2.81732	-2.81702	-52.89	
			-2.81740	-52.90	
			-2.81777	-52.91	
120	6.55532	-2.75440	-2.75419	-50.34	
			-2.75459	-50.35	
			-2.75500	-50.36	
20	3.83976	-3.31280	-3.31274	-81.49	**SNP12****
			-3.31280	-81.50	
			-3.31286	-81.51	
40	5.43024	-3.22383	-3.22368	-67.72	
			-3.22390	-67.73	
			-3.22412	-67.74	
60	6.65066	-3.17204	-3.17168	-61.96	
			-3.17198	-61.97	
			-3.17227	-61.98	
80	7.67953	-3.09251	-3.09234	-57.27	
			-3.09270	-57.28	
			-3.09306	-57.29	
100	8.58597	-3.01521	-3.01498	-53.74	
			-3.01539	-53.75	
			-3.01579	-53.76	
120	9.40546	-2.95352	-2.95304	-51.19	
			-2.95348	-51.20	
			-2.95391	-51.21	

20	3.83976	-3.31839	-3.31835	-82.54	**SNP12***
			-3.31839	-82.55	
			-3.31844	-82.56	
40	5.43024	-3.19338	-3.19319	-66.39	
			-3.19343	-66.40	
			-3.19365	-66.41	
60	6.65066	-3.15490	-3.15454	-61.39	
			-3.15484	-61.40	
			-3.15515	-61.41	
80	7.67953	-3.09067	-3.09019	-57.21	
			-3.09056	-57.22	
			-3.09091	-57.23	
100	8.58597	-3.01393	-3.01337	-53.70	
			-3.01377	-53.71	
			-3.01418	-53.72	
120	9.40546	-2.95498	-2.95435	-51.22	
			-2.95478	-51.23	
			-2.95522	-51.24	
20	7.09774	-3.51610	-3.51603	-75.53	**SNP22****
			-3.51617	-75.54	
			-3.51632	-75.55	
40	10.03772	-3.48775	-3.48749	-64.16	
			-3.48782	-64.17	
			-3.48814	-64.18	
60	12.29365	-3.44654	-3.44629	-59.41	
			-3.44669	-59.42	
			-3.44709	-59.43	
80	14.19549	-3.35408	-3.35353	-55.31	
			-3.35399	-55.32	
			-3.35445	-55.33	
100	15.87104	-3.26249	-3.26195	-52.19	
			-3.26245	-52.20	
			-3.26295	-52.21	
120	17.38585	-3.18137	-3.18075	-49.78	
			-3.18128	-49.79	
			-3.18181	-49.80	
20	7.09774	-3.35058	-3.35031	-67.19	**SNP22***
			-3.35055	-67.20	
			-3.35180	-67.21	
40	10.03772	-3.33294	-3.33257	-59.71	
			-3.33294	-59.72	
			-3.33331	-59.73	
60	12.29365	-3.41552	-3.41491	-58.64	
			-3.41532	-58.65	
			-3.41573	-58.66	
80	14.19549	-3.35641	-3.35584	-55.36	
			-3.35630	-55.37	
			-3.35676	-55.38	
100	15.87104	-3.26360	-3.26295	-52.21	
			-3.26345	-52.22	
			-3.26395	-52.23	
120	17.38585	-3.18375	-3.18341	-49.83	
			-3.18394	-49.84	
			-3.18447	-49.85	

* 1st series. ** 2nd series.

Table 2-2: Illustration of the iterative scheme employed for the determination of ζ via the modified analytic approximation for: SNP7, SNP12 and SNP22 nm with Na-cation as counterion.

c(Na^+)/ (mmol L^{-1})	κa	μ_{ep} (measured/ (10^{-8} m^2 s^{-1} V^{-1})	μ_{ep} (calculated)/ (10^{-8} m^2 s^{-1} V^{-1})	ζ/mV	
20	2.67620	-3.26319	-3.26295	-72.30	**SNP7****
			-3.26318	-72.31	
			-3.26341	-72.32	
40	3.78472	-3.05304	-3.05284	-63.02	
			-3.05314	-63.03	
			-3.05343	-63.04	
60	4.63531	-2.93900	-2.93861	-57.71	
			-2.93895	-57.72	
			-2.93930	-57.73	
80	5.35240	-2.82333	-2.82281	-53.18	
			-2.82320	-53.19	
			-2.82359	-53.20	
100	5.98416	-2.72136	-2.72110	-49.64	
			-2.72152	-49.65	
			-2.72194	-49.66	
20	3.83976	-3.27863	-3.27832	-71.77	**SNP12****
			-3.27853	-71.78	
			-3.27874	-71.79	
40	5.43024	-3.18164	-3.18141	-63.41	
			-3.18170	-63.42	
			-3.18200	-63.43	
60	6.65066	-3.09975	-3.09927	-58.09	
			-3.09963	-58.10	
			-3.09999	-58.11	
80	7.67953	-2.99201	-2.99178	-53.54	
			-2.99219	-53.55	
			-2.99261	-53.56	
100	8.58597	-2.89224	-2.89195	-50.04	
			-2.89240	-50.05	
			-2.89286	-50.06	
20	3.83976	-3.23131	-3.23108	-69.64	**SNP12***
			-2.23131	-69.65	
			-2.23155	-69.66	
40	5.43024	-3.07055	-3.07004	-59.88	
			-3.07037	-59.89	
			-3.07071	-59.90	

60	6.65066	-3.03943	-3.03900	-56.46	
			-3.03938	-56.47	
			-3.03976	-56.48	
80	7.67953	-2.97421	-2.97386	-53.11	
			-2.97427	-53.12	
			-2.97470	-53.13	
100	8.58597	-2.84395	-2.84338	-48.98	
			-2.84384	-48.99	
			-2.84430	-49.00	
120	9.40546	-2.72253	-2.72227	-45.63	
			-2.72277	-45.64	
			-2.72326	-45.65	
20	7.09774	-3.47218	-3.47194	-68.77	**SNP22**[**]
			-3.47221	-68.78	
			-3.47248	-68.79	
40	10.03772	-3.43336	-3.43303	-60.91	
			-3.43341	-60.92	
			-3.43380	-60.93	
60	12.29365	-3.35806	-3.35767	-56.27	
			-3.35812	-56.28	
			-3.35858	-56.29	
80	14.19549	-3.23606	-3.23558	-52.14	
			-3.23609	-52.15	
			-3.23659	-52.16	
100	15.87104	-3.11538	-3.11467	-48.83	
			-3.11522	-48.84	
			-3.11576	-48.85	
20	7.09774	-3.41966	-3.41923	-66.86	**SNP22**[*]
			-3.41952	-66.87	
			-3.41981	-66.88	
40	10.03772	-3.40085	-3.40028	-60.07	
			-3.40067	-60.08	
			-3.40107	-60.09	
60	12.29365	-3.25322	-3.25269	-54.00	
			-3.25316	-54.01	
			-3.25363	-54.02	
80	14.19549	-3.20022	-3.19961	-51.43	
			-3.20012	-51.44	
			-3.20063	-51.45	
100	15.87104	-3.09559	-3.09517	-48.47	
			-3.09572	-48.48	
			-3.09626	-48.49	

[*] 1st series. [**] 2nd series.

Table 2-3: Illustration of the iterative scheme employed for the determination of ζ via the modified analytic approximation for: SNP7, SNP12 and SNP22 nm with K-cation as counterion.

c(K^+)/ (mmol L^{-1})	κa	μ_{ep} (measured/ (10^{-8} m^2 s^{-1} V^{-1})	μ_{ep} (calculated)/ (10^{-8} m^2 s^{-1} V^{-1})	ζ/mV	
20	2.67620	-3.24942	-3.24905	-69.09	**SNP7****
			-3.24933	-69.10	
			-3.24962	-69.11	
40	3.78472	-2.98892	-2.98875	-59.37	
			-2.98910	-59.38	
			-2.98945	-59.39	
60	4.63531	-2.87209	-2.87172	-54.66	
			-2.87211	-54.67	
			-2.87251	-54.68	
80	5.35240	-2.72538	-2.72494	-49.91	
			-2.72537	-49.92	
			-2.72581	-49.93	
20	3.83976	-3.22202	-3.22170	-66.44	**SNP12****
			-3.22200	-66.45	
			-3.22229	-66.46	
40	5.43024	-3.09270	-3.09238	-58.91	
			-3.09275	-58.92	
			-3.09312	-58.93	
60	6.65066	-2.97828	-2.97769	-53.77	
			-2.97811	-53.78	
			-2.97854	-53.79	
80	7.67953	-2.87910	-2.87843	-50.08	
			-2.87889	-50.09	
			-2.87936	-50.10	
20	3.83976	-3.23574	-3.23549	-66.91	**SNP12***
			-3.23578	-66.92	
			-3.23607	-66.93	
40	5.43024	-3.11529	-3.11507	-59.53	
			-3.11543	-59.54	
			-3.11580	-59.55	
100	8.58597	-2.87689	-2.87640	-48.99	
			-2.87688	-49.00	
			-2.87736	-49.01	

20	7.09774	-3.36387	-3.36363	-62.79	**SNP22****
			-3.36399	-62.80	
			-3.36434	-62.81	
40	10.03772	-3.21927	-3.21894	-54.65	
			-3.21940	-54.66	
			-3.21986	-54.67	
60	12.29365	-3.13516	-3.13468	-50.85	
			-3.13519	-50.86	
			-3.13571	-50.87	
80	14.19549	-3.04595	-3.04505	-47.94	
			-3.04560	-47.95	
			-3.04615	-47.96	
20	7.09774	-3.48002	-3.47959	-66.16	**SNP22***
			-3.47991	-66.17	
			-3.48024	-66.18	
40	10.03772	-3.42210	-3.42149	-59.19	
			-3.42192	-59.20	
			-3.42235	-59.21	
60	12.29365	-3.32828	-3.32763	-54.70	
			-3.32812	-54.71	
			-3.32861	-54.72	
80	14.19549	-3.25326	-3.25249	-51.80	
			-3.25302	-51.81	
			-3.25354	-51.82	

* 1st series. ** 2nd series.

Table 2-4: Illustration of the iterative scheme employed for the determination of ζ via the modified analytic approximation for: SNP7, SNP12 and SNP22 nm with Gdm-cation as counterion.

c(Gdm$^+$)/ (mmol L^{-1})	κa	μ_{ep} (measured/ (10^{-8} m^2 s^{-1} V^{-1})	μ_{ep} (calculated)/ (10^{-8} m^2 s^{-1} V^{-1})	ζ/mV	
20	3.78472	-2.74739	-2.74701	-53.80	**SNP7****
			-2.74739	-53.81	
			-2.74776	-53.82	
30	4.63531	-2.54948	-2.54911	-47.54	
			-2.54953	-47.55	
			-2.54996	-47.56	
40	5.35240	-2.39191	-2.39122	-43.02	
			-2.39168	-43.03	
			-2.39215	-43.04	
10	3.83976	-3.03484	-3.03466	-62.15	**SNP12****
			-3.03497	-62.16	
			-3.03523	-62.17	
20	5.43024	-2.87051	-2.87016	-54.18	
			-2.87055	-54.19	
			-2.87093	-54.20	
30	6.65066	-2.68971	-2.68912	-47.90	
			-2.68956	-47.91	
			-2.69001	-47.92	
40	7.67953	-2.53644	-2.53593	-43.44	
			-2.53642	-43.45	
			-2.53691	-43.46	
10	7.09774	-3.20373	-3.20336	-59.95	**SNP22****
			-3.20372	-59.96	
			-3.20407	-59.97	
20	10.03772	-3.07193	-3.07144	-52.27	
			-3.07189	-52.28	
			-3.07235	-52.29	
30	12.29365	-2.86976	-2.86896	-46.25	
			-2.86948	-46.26	
			-2.87001	-46.27	
40	14.19549	-2.68819	-2.68787	-41.90	
			-2.68844	-41.91	
			-2.68900	-41.92	

** 2nd series.

Table 3: Electrokinetic potential calculated from the data in Appendix 4 with the iterative procedure illustrated in Table 1:1-4 and electrokinetic potential of the capillary wall/electrolyte interface calculated via Helmholtz-Smoluchowski equation.

cation counterion	**c(cation)/ (mmol L^{-1})**	**SNP7** ζ/mV**	**SNP12** ζ/mV**	**SNP12* ζ/mV**	**SNP22** ζ/mV**	**SNP22* ζ/mV**	**Capillary(a) ζ/mV**	**Capillary(b) ζ/mV**
Li^{+}	20	-78.21	-81.50	-82.55	-75.54	-67.20	-87.16	-88.22
	40	-66.63	-67.73	-66.40	-64.17	-59.72	-73.78	-75.42
	60	-61.03	-61.97	-61.40	-59.42	-58.65	-70.68	-67.05
	80	-56.56	-57.28	-57.22	-55.32	-55.37	-64.07	-61.21
	100	-52.90	-53.75	-53.71	-52.20	-52.22	-59.63	-56.96
	120	-50.35	-51.20	-51.23	-49.79	-49.84	-55.65	-53.33
Na^{+}	20	-72.31	-71.78	-69.65	-68.78	-66.87	-80.75	-82.01
	40	-63.03	-63.42	-59.89	-60.92	-60.08	-66.97	-68.92
	60	-57.72	-58.10	-56.47	-56.28	-54.01	-59.09	-61.10
	80	-53.19	-53.55	-53.12	-52.15	-51.44	-53.80	-54.95
	100	-49.65	-50.05	-48.99	-48.84	-48.48	-50.85	-50.12
	120	--------(c)	--------(c)	-45.64	--------(c)	-------(c)	-46.56	-46.70
K^{+}	20	-69.10	-66.45	-66.92	-62.80	-66.17	-81.25	-76.75
	40	-59.38	-58.92	-59.54	-54.66	-59.20	-67.09	-66.61
	60	-54.67	-53.78	-------(c)	-50.86	-54.71	-58.20	-58.17
	80	-49.92	-50.09	-------(c)	-47.95	-51.81	-51.33	-51.81
	100	--------(c)	--------(c)	-49.00	--------(c)	-------(c)	-46.26	-48.04
	120	--------(c)	--------(c)	--------	--------(c)	-------(c)	-45.14	-44.65
Gdm^{+}	20	--------(c)	-62.16	-------(c)	-59.96	-------(c)	-------(c)	-71.56
	40	-53.81	-54.19	-------(c)	-52.28	-------(c)	-------(c)	-59.01
	60	-47.55	-47.91	-------(c)	-46.26	-------(c)	-------(c)	-50.01
	80	-43.03	-43.45	-------(c)	-41.91	-------(c)	-------(c)	-44.33

* 1st series. ** 2nd series. (a) mean value of ζ for 1st series from first method. (b) mean value of ζ for 2nd series from second method. (c) not determined.

The validity of the employed approximate analytic approach can be confirmed through a comparison between SNPs data and capillary data (both materials are amorphous silica), so that similar values for ζ would be expected independent of size and geometry. There is good agreement of ζ calculated for the fused silica wall and the SNPs as shown in Figure 13 dependent on concentration and type of counterion. Figure 13 and Table 3 show a discrepancy in $|\zeta|$ calculated for SNPs with those for the capillary wall, particularly at lower ionic strength. This can be attributed to a difference in the diffuse layer specific capacitance, which is curvature-dependent [75].

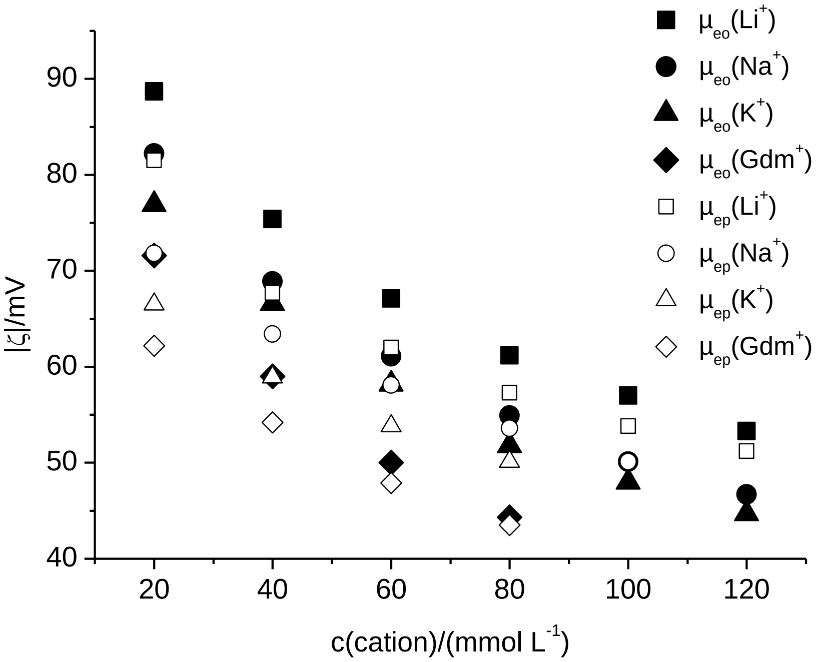

Figure 13: Comparison of $|\zeta|$ calculated from the electroosmotic mobility (closed symbols) to $|\zeta|$ calculated from the electrophoretic mobility determined for SNP12/2nd series (open symbols) dependent on concentration and type of counterion. For experimental conditions refer to Figure 9 and Appendix 3.

Figure 14 presents the ζ potential of different SNP populations as a function of the counterion concentration. Although the individual ζ potentials are somewhat scattered, the increase in the ionic strength clearly produced a decrease in the absolute value of ζ for all four types of counterions and this result complies with the expectations due to the compression of the diffuse layer. The results indicate that at any electrolyte concentration, the absolute value of the ζ potential decreases in the series $Li^+ > Na^+ > K^+ > Gdm^+$. This series is identical to that determined for quartz [76]. The experimental data demonstrated that the magnitude of ζ at any pH value follows the Hofmeister series, so that ζ values are most negative in the presence of lithium and least negative in the presence of cesium.

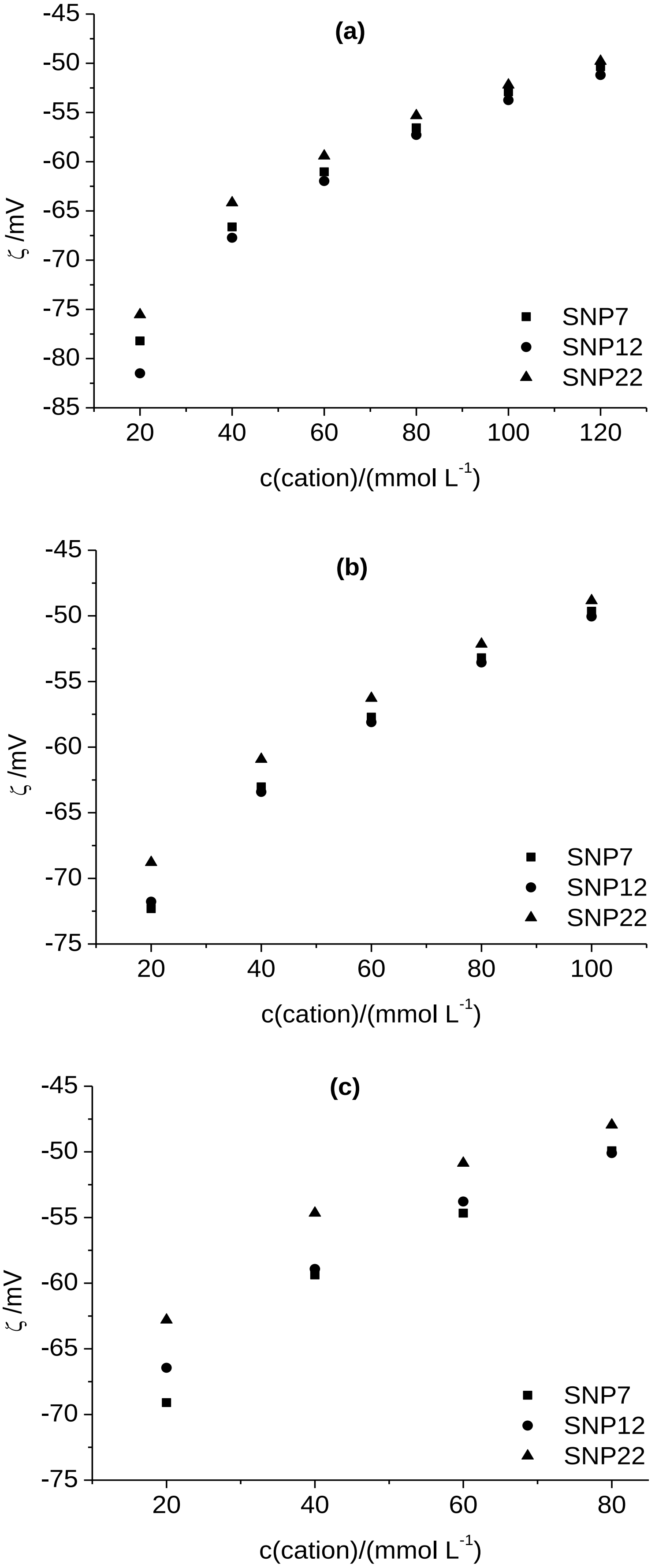
(a)
ζ /mV
-45
-50
-55
-60
-65
-70
-75
-80
-85
20
40
60
80
100
120
c(cation)/(mmol L-1)
SNP7
SNP12
SNP22
(b)
ζ /mV
-45
-50
-55
-60
-65
-70
-75
20
40
60
80
100
c(cation)/(mmol L-1)
SNP7
SNP12
SNP22
(c)
ζ /mV
-45
-50
-55
-60
-65
-70
-75
20
40
60
80
c(cation)/(mmol L-1)
SNP7
SNP12
SNP22

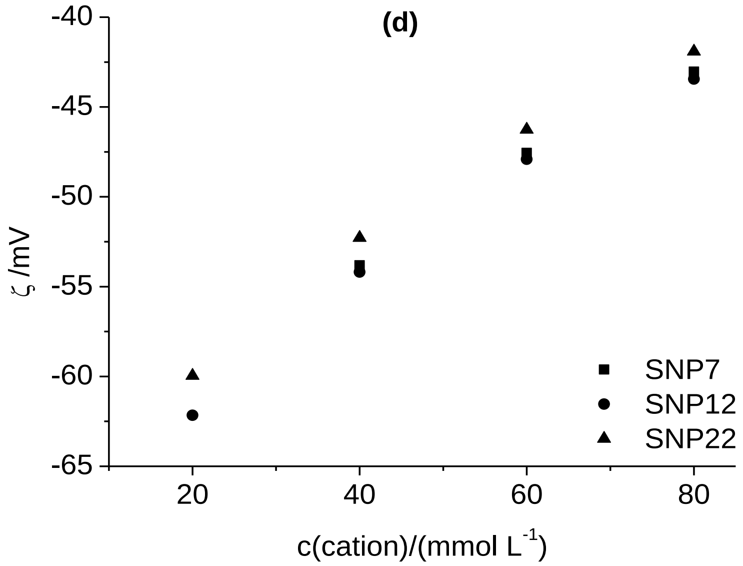

Figure 14: Zeta potential of SNPs as a function of the monovalent counterions concentration, at 25°C: (a) Li^+, (b) Na^+, (c) K^+ and (d) Gdm^+.

The two series of SNPs demonstrate a good reproducibility. However, the limited accuracy of this method does not allow to observe a dependence of ζ on the particle radius, which might be predicted from the curvature-dependence of the diffuse layer specific capacitance [75]. Furthermore, as the ζ potential of SNPs decreases, the electrostatic repulsion between particles will also decrease, allowing particles to approach one another more closely. However, when the minimum separation distance is reduced to within the range of van der Waals or other attractive forces, the suspension starts to aggregate. Finally, as can be seen in Figure 12 the largest variation of data is observed at low ionic strength (for $c(cation)$ = 20 mmol L^{-1}) resulting from the nonlinearity of the function $\mu = f\ (\varsigma)$ under conditions of a strong impact of the relaxation effect. Therefore, at this low ionic strength the estimation of ζ is associated with the highest imprecision. For Li^+ as counterion, a distinct maximum of the function $\mu = f\ (\varsigma)$ is observed.

4.1.3 Estimation of electrokinetic surface charge densities

As outlined in *Section 2.1.5*, with the purpose of calculating the electrokinetic surface charge densities of SNPs, Eq. (24) was used. The significant errors are resulting from using Eq. (24) for $\kappa a < 0.5$, can be neglected because $\kappa a \gg 0.5$ for all experimental data (refer to Figure 7). Therefore, correct values for σ_ς are expected by using this equation with a maximum relative error much smaller than 5%. The results of the electrokinetic surface charge density σ_ς (nanoparticles and planar limiting case) are represented in Figure 15 and Table 4.

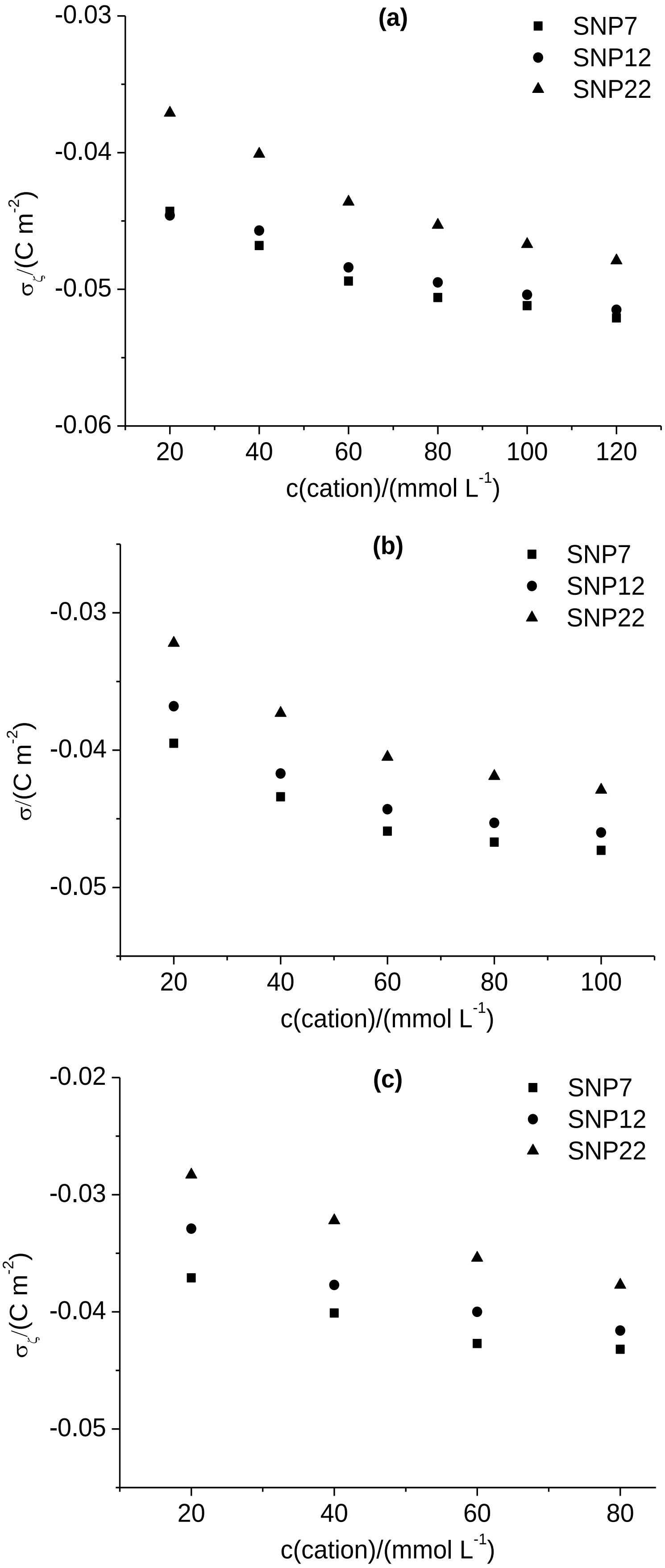
(a)
SNP7
SNP12
SNP22
-0.03
-0.04
-0.05
-0.06
σ_ζ/(C m^-2)
20
40
60
80
100
120
c(cation)/(mmol L^-1)
(b)
SNP7
SNP12
SNP22
-0.03
-0.04
-0.05
σ/(C m^-2)
20
40
60
80
100
c(cation)/(mmol L^-1)
(c)
SNP7
SNP12
SNP22
-0.02
-0.03
-0.04
-0.05
σ_ζ/(C m^-2)
20
40
60
80
c(cation)/(mmol L^-1)

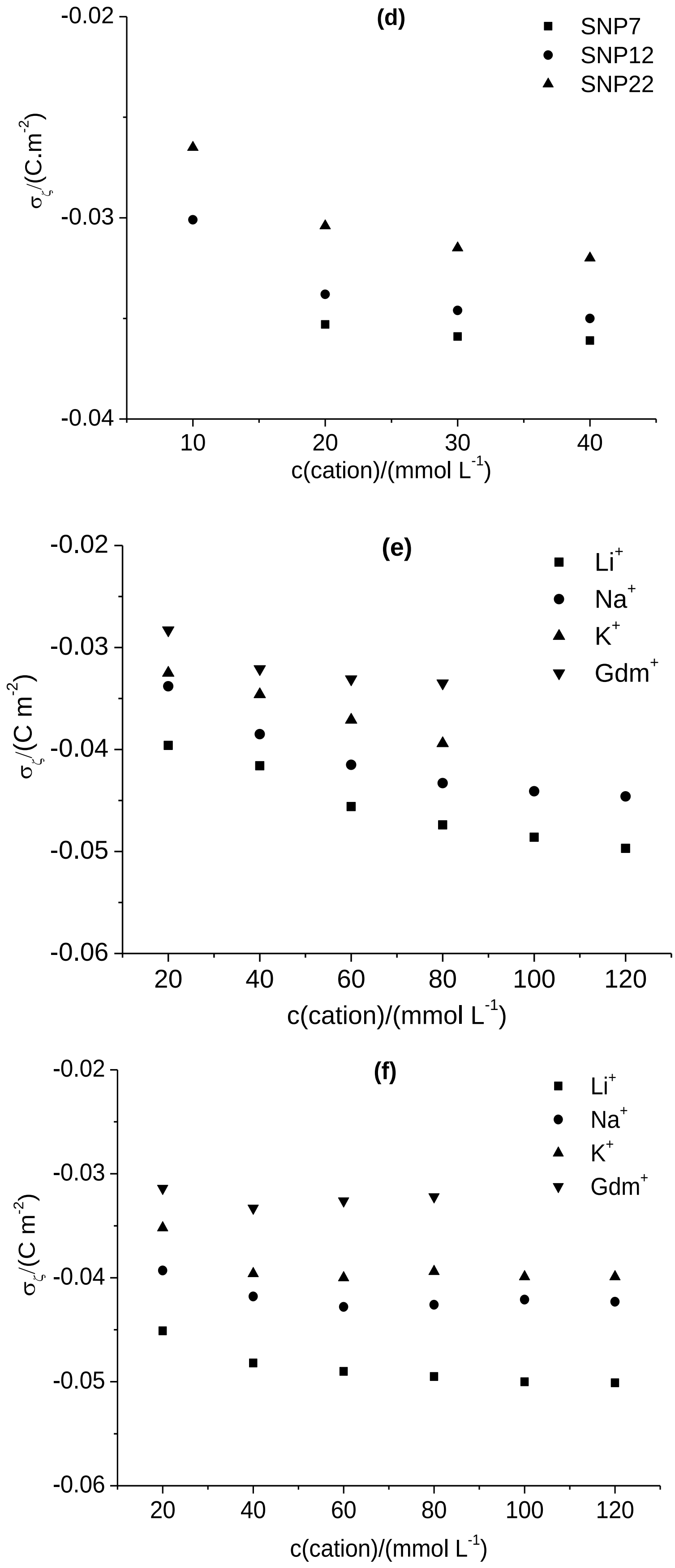

Figure 15: Electrokinetic surface charge densities of SNPs as a function of the monovalent counterions concentration, at 25°C: (a) Li^+, (b) Na^+, (c) K^+ and (d) Gdm^+ for 2nd series; (e) mean values of SNPs and (f) planar limiting case.

Table 4: Electrokinetic surface charge density σ_{ς} (obtained *via* Eq. (20)) for the nanoparticles investigated compared to the surface charge density σ_{ς} of capillary inner wall (Gouy-Chapman equation).

Cation	c/ (mmol L^{-1})	SNP7** σ_{ς} / (C m^{-2})	SNP12* σ_{ς} / (C m^{-2})	SNP12** σ_{ς} / (C m^{-2})	SNP22* σ_{ς} / (C m^{-2})	SNP22** σ_{ς} / (C m^{-2})	Mean[b] σ_{ς} / (C m^{-2})	Capillary σ_{ς} / (C m^{-2})	rel. dev.[c]/ %
Li$^+$	20	-0.0443	-0.0455	-0.0446	-0.0311	-0.0371	-0.0396	-0.0451	-12.3
	40	-0.0468	-0.0444	-0.0457	-0.0363	-0.0401	-0.0416	-0.0482	-13.6
	60	-0.0494	-0.0477	-0.0484	-0.0428	-0.0436	-0.0456	-0.0490	-6.9
	80	-0.0506	-0.0494	-0.0495	-0.0454	-0.0453	-0.0474	-0.0495	-4.2
	100	-0.0512	-0.0504	-0.0504	-0.0467	-0.0467	-0.0486	-0.0500	-2.9
	120	-0.0521	-0.0515	-0.0515	-0.0480	-0.0479	-0.0497	-0.0501	-0.7
	Mean[d]	-------[a]	-0.0487	-0.0491	-0.0438	-0.0447	-0.0466	-0.0494	-5.6
	SD[d]	-------[a]	0.0028	0.0022	0.0046	0.0030	0.0032	0.0008	
	RSD[e]/%	-------[a]	5.6917	4.5152	10.5676	6.7980	6.7804	1.5862	
Na$^+$	20	-0.0395	-0.0352	-0.0368	-0.0309	-0.0322	-0.0338	-0.0393	-14.1
	40	-0.0434	-0.0385	-0.0417	-0.0366	-0.0373	-0.0385	-0.0418	-7.8
	60	-0.0459	-0.0427	-0.0443	-0.0383	-0.0405	-0.0415	-0.0428	-3.2
	80	-0.0467	-0.0448	-0.0453	-0.0412	-0.0419	-0.0433	-0.0426	1.6
	100	-0.0473	-0.0448	-0.0460	-0.0425	-0.0429	-0.0441	-0.0421	4.6
	120	-------[a]	-0.0446	-------[a]	-------[a]	-------[a]	-0.0446	-0.0423	5.4
	Mean[d]	-------[a]	-0.0431	-0.0443	-0.0397	-0.0407	-0.0424	-0.0423	0.2
	SD[d]	-------[a]	0.0027	0.0019	0.0027	0.0024	0.0025	0.0004	
	RSD[e]/%	-------[a]	6.2876	4.2502	6.7752	6.0040	5.8139	0.9363	
K$^+$	20	-0.0371	-0.0333	-0.0329	-0.0354	-0.0283	-0.0325	-0.0352	-7.7
	40	-0.0401	-0.0382	-0.0377	-0.0304	-0.0322	-0.0346	-0.0396	-12.6
	60	-0.0427	-------[a]	-0.0400	-0.0358	-0.0354	-0.0371	-0.0400	-7.3
	80	-0.0432	-------[a]	-0.0416	-0.0390	-0.0377	-0.0394	-0.0394	0.1
	100	-------[a]	-------[a]	-------[a]	-------[a]	-------[a]	-------[a]	-0.0399	-------[a]
	120	-------[a]	-------[a]	-------[a]	-------[a]	-------[a]	-------[a]	-0.0399	-------[a]
	Mean[d]	-------[a]	-0.0382	-0.0398	-0.0351	-0.0351	-0.0370	-0.0398	-6.8
	SD[d]	-------[a]	-------[a]	0.0020	0.0043	0.0028	0.0024	0.0003	
	RSD[e]/%	-------[a]	-------[a]	4.9299	12.3954	7.8696	6.4907	0.6313	
Gdm$^+$	20	-------[a]	-------[a]	-0.0301	-------[a]	-0.0265	-0.0283	-0.0314	-9.9
	40	-0.0353	-------[a]	-0.0338	-------[a]	-0.0304	-0.0321	-0.0333	-3.6
	60	-0.0359	-------[a]	-0.0346	-------[a]	-0.0315	-0.0331	-0.0326	1.4
	80	-0.0361	-------[a]	-0.0350	-------[a]	-0.0320	-0.0335	-0.0322	4.0
	Mean[d]	-------[a]	-------[a]	-0.0345	-------[a]	-0.0313	-0.0329	-0.0327	0.6
	SD[d]	-------[a]	-------[a]	0.0006	-------[a]	0.0008	0.0007	0.0006	
	RSD[e]/%	-------[a]	-------[a]	1.7728	-------[a]	2.6151	2.1735	1.7027	

* 1st series, ** 2nd series, [a] not determined, [b] arithmetic mean of values determined for SNP12 and SNP22, [c] rel. dev. = relative deviation in percent = {[σ_{ς} (Capillary) – σζ(Mean)]/ σ_{ς} (Capillary)} (-100), [d] without value for c = 20 mmol L^{-1}, [e] RSD = relative standard deviation.

Table 4 clearly shows that σ_{ς} (nanoparticles and planar limiting case) is dependent on the type of the counterion. The stability of the negatively charged SNPs will decrease in the order Li^+ > Na^+ > K^+ > Gdm^+ at fixed ionic strength. For fixed electrolyte concentration, peak distortion is increasing in the order Li^+ < Na^+ < K^+ < Gdm^+ with the recorded peaks dependent on the type of counterion. These results are in accord with the manufacturer's information on colloidal stability of different populations, peak distortion is increasing in the order SNP22 < SNP12 < SNP7 (at fixed type of counterion and ionic strength). These considerations are allowing to predict the order of the critical coagulation concentration (ccc) for a given nanoparticle population to be Li^+ > Na^+ > K^+ > Gdm^+, which corresponds to the Hofmeister series [77] (or lyotropic sequence [78]) and exactly matches those data determined experimentally for silica nanoparticles by other workers [69,79]. Also, these data confirm that the observed differences in ccc can be ascribed to differences in ζ induced by differences in σ_{ς}.

There is a significant increase for SNPs in σ_{ς} with ionic strength for all counterions that is not observed in the planar limiting case. This observation can be attributed to the influence of aggregation that is more pronounced with higher I and lower σ_{ς}. This result confirms that a correct measurement of μ_{ep} by CE requires the absence of aggregation during the electrophoretic run. However, in spite of a small mean relative deviation (less than 7% in all instances) between the results for SNPs and for the interface fused silica capillary/buffer, these results as an indirect confirmation of the validity of the modified analytic approximation presented by Pyell *et al.* [74], which consider that the effective ionic drag coefficient should be approximated with the ionic drag coefficient of the counterion in the case of a buffered solution with a weak electrolyte co-ion and a strong electrolyte counterion. In addition, comparison of the results obtained for different series gives an indication of the precision of the method. Variation of results obtained for different nanoparticle populations reflects differences in the colloidal stability but also inaccuracies due to the imprecision in the determination of ζ.

According to Barisik *et al.* [80] the surface charge density is independent of the particle size if the ratio of electrical double layer thickness to the particle diameter ($\lambda_D / d_p < 0.2$) (which was reached in the current investigations), regardless of the pH and the ionic strength. Therefore, it would be expected that σ_{ς} is invariant with the particle diameter (and identical with that of the planar limiting case). Hence if the measured values for μ_{ep} and μ_{eo} do not show significant deviations from the true values, the comparison between σ_{ς} for SNPs with those for the inner capillary wall (planar limiting case) should provide an unbiased confirmation of the correctness of the applied approach (with regard to the calculation of ζ and σ_{ς}). This prerequisite is not given in all cases due to particle aggregation during the electrophoretic run resulting in distorted peaks. However, the data obtained for μ_{eo} are expected to be very accurate, while those data obtained from distorted electrophoretic zones are systematically higher than the true values. A more pronounced (upwards) shift due to aggregation effects under conditions of higher ionic strength is expected. As shown in Table 4, σ_{ς} can be regarded to be independent of the ionic strength (within the selected parameter range, I = 40-120 mmol L^{-1}) for the inner capillary surface with all counterions with relative standard deviation between 0.7-2 %.

4.1.4 Calculation of size distribution functions

The approach proposed by Pyell [81] and Pyell *et al.* [82] to convert electropherograms directly into size distribution functions was used. They succeeded in avoiding experimental calibration curves. Their method is based on an exact determination of the electrokinetic potential ζ by measuring the electrophoretic mobility in an electrolyte of known composition. In addition, the mean particle radius has to be determined by a second independent method (*e.g.*, TEM or Taylor dispersion analysis (TDA)). The signal-to-noise ratio was improved by a cumulative superposition of consecutive runs. Figure 16 (refer to Appendix A5) illustrates the principle for a sample containing SNP22 (1st series) and for a sample containing a mixture of SNPs (2nd series). Direct superposition is possible because of the very small variation in migration times. The cumulative superposition of five runs results in at least a two-fold improvement of the signal-to-noise ratio.

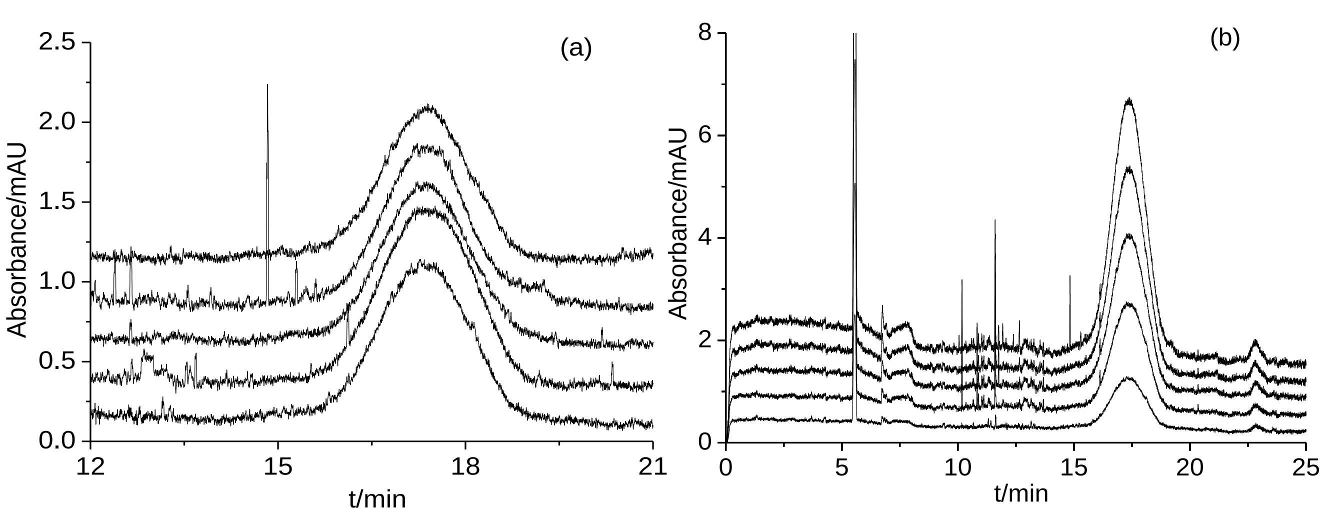

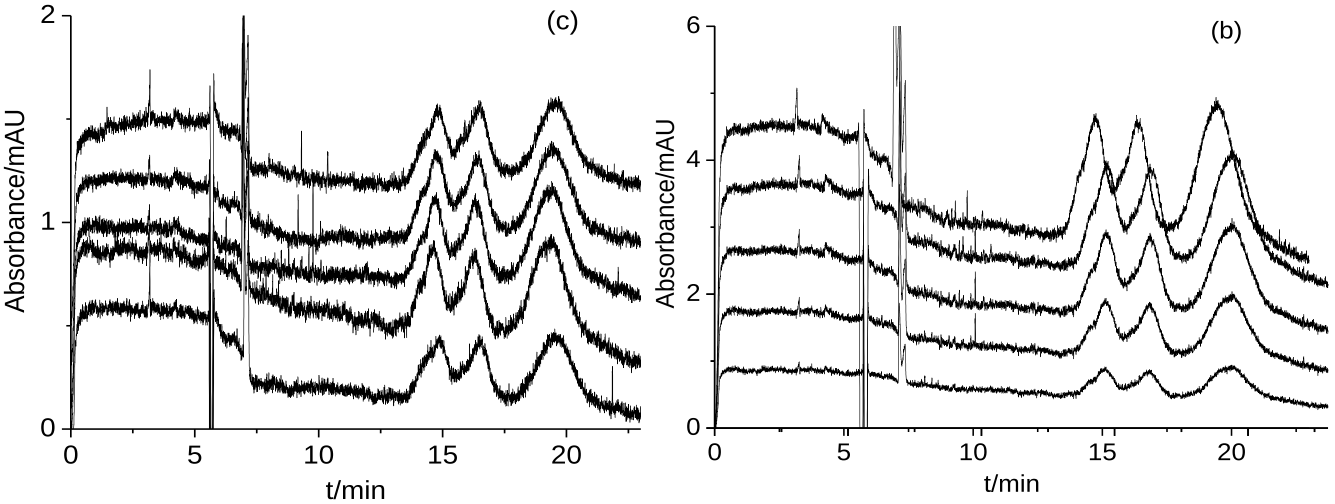

Figure 16: Electropherograms obtained: (a) superposition of consecutive runs, and (b) cumulative superposition for SNP22 (1st series), c(Li^+) = 80 mmol L^{-1}; (c) superposition of consecutive runs, and (d) cumulative superposition for a mixture of SNPs (2nd series), c(Li^+) = 80 mmol L^{-1}. Experimental conditions (refer to Figs. 5 and 6).

After that, the recorded electropherograms can be easily converted into intensity-weighted electrophoretic mobility distributions (see Figure 17). Therefore, the regression lines which were calculated by using the (modified) analytic approximation presented by Ohshima [19,20] permit to calculate functions (see Appendix A6) that relate the electrophoretic mobility μ_{ep} to the reduced radius κa at fixed value for ζ (refer to Table 3 and Appendix A7).

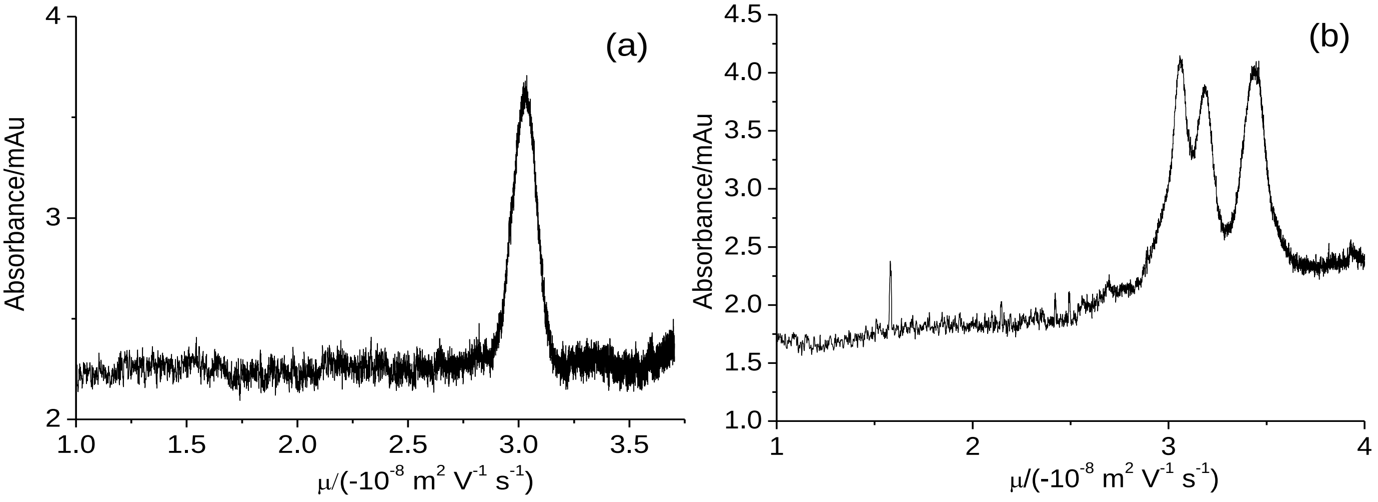

Figure 17: Intensity-weighted distribution of the electrophoretic mobility resulting from an electropherogram obtained: (a) for SNP12 (1st series), c(Na^+) = 60 mmol L^{-1}, (b) for SNPs mixture (2nd series), 40 mmol L^{-1}. Experimental conditions (refer to Figures. 5 and 6).

Within the selected ranges for the reduced sphere radius κa, the function $\mu_{ep} = f\ (\kappa a)$ can be approximated with a straight line, although this function is inherently nonlinear (refer to Figure 15). The resulting constants and the associated standard errors are listed in Appendix A7. In general, there is a decrease in the calculated constants for SNP12 and SNP22 with increasing ionic strength (which reflects the decrease in $|\zeta|$ with increasing ionic strength).

This comparison shows that from the viewpoint of maximizing sensitivity, better measurement conditions are reached with higher ionic strength. An improved accuracy of the method would be reached by the calculation of a larger set of data points and fitting to a polynomial function.

Size distribution functions can now be obtained by converting the mobility *x*-axis of the converted electropherograms (refer to Figure 17) into a size coordinate via rearranging the regression function $\mu = f\ (\kappa a)$ into $\kappa a = f\ (\mu)$ or $a = f\ (\mu)$ with a fixed κ. The following procedure was finally selected for the conversion of recorded electropherograms into size distribution functions:

1. Traces with an improved signal-to-noise-ratio were obtained by the cumulative superposition of subsequently recorded electropherograms (refer to Figure 16 and Appendix A5).
2. These traces were converted into functions $A = f\ (\mu)$ (A = apparent absorbance, refer to Figure 14) and then to $A = f\ (d)$ (d = particle diameter) by applying the regression lines depicted in Appendix 6.
3. After smoothing of the obtained traces using Savitzky−Golay algorithm (100−3500 points) and baseline subtraction, the resultant lines were fitted to Gram−Charlier A series function (*cf.* Eq.(30)). The obtained regression parameters are listed in Table 5.
4. Subsequently, new data points were calculated with a step length of 0.01 nm by using Gram−Charlier A series function and the regression parameters listed in Table 5. After weighing the data points with the correction factor $d_{\max}/d$, $d_{\max} = d$ at the maximum, the parameters μ_1 (μ_1 = first moment), σ (σ = second central moment), κ_3 (κ_3 = skewness), and κ_4 (κ_4 = excess) (refer to Tables 6 and 7) were calculated using moment analysis [71].
5. Superposition of the resulting size distribution curves with size distribution histograms obtained via TEM from ref. [71] are depicted in Figure 18 and Appendix A8.

The results presented in Tables 5-7, Figure 18 and Appendix 8 confirm that the developed method to convert electropherograms into size distribution functions works reliably independent of the type of counterion. The results obtained for σ (Table 6) are in good agreement with these resulting from TEM analysis (Table 7). The type of counterion has no significant effect on the determined σ. This result indirectly confirms the validity of the theoretical approach for the calculation of ς from electrokinetic data and the mean particle size (based on a second independent method such as TEM or TDA). It also confirms that reliable values can be easily obtained from mixtures of NP populations, which is difficult with TEM and often impossible with DLS [71]. However, the imprecision of the values obtained for κ_3 and κ_4 (Tables 5 and 6) does not allow determining skewness and/or kurtosis.

Using Li^+ or Na^+ has advantages with regard to the use of K^+ or Gdm^+ as counterion, due to the stabilizing effect of Li^+ and Na^+ (higher ccc due to higher $|\varsigma|$ and higher $|\sigma|$), which prevents particle aggregation and peak distortion. Li^+ as counterion might have advantages for NPs with lower $|\varsigma|$, while Na^+ as counterion might have advantages for NPs with very high $|\varsigma|$.

In addition, the higher $m_{counter}$ of Li^+ with regard to the $m_{counter}$ of Na^+ has a positive impact on the size-selectivity of the method, which is based on the size-dependent relaxation effect. This impact on the size-selectivity, which is dependent on $m_{counter}$, further justifies the conclusion that using Li^+ or Na^+ as counterion has advantages over K^+ or Gdm^+. Borate as co-ion permits the exact definition of pH and ionic strength. The role of the co-ion is expected to be very low [71,83]. This influence might be elucidated in further studies.

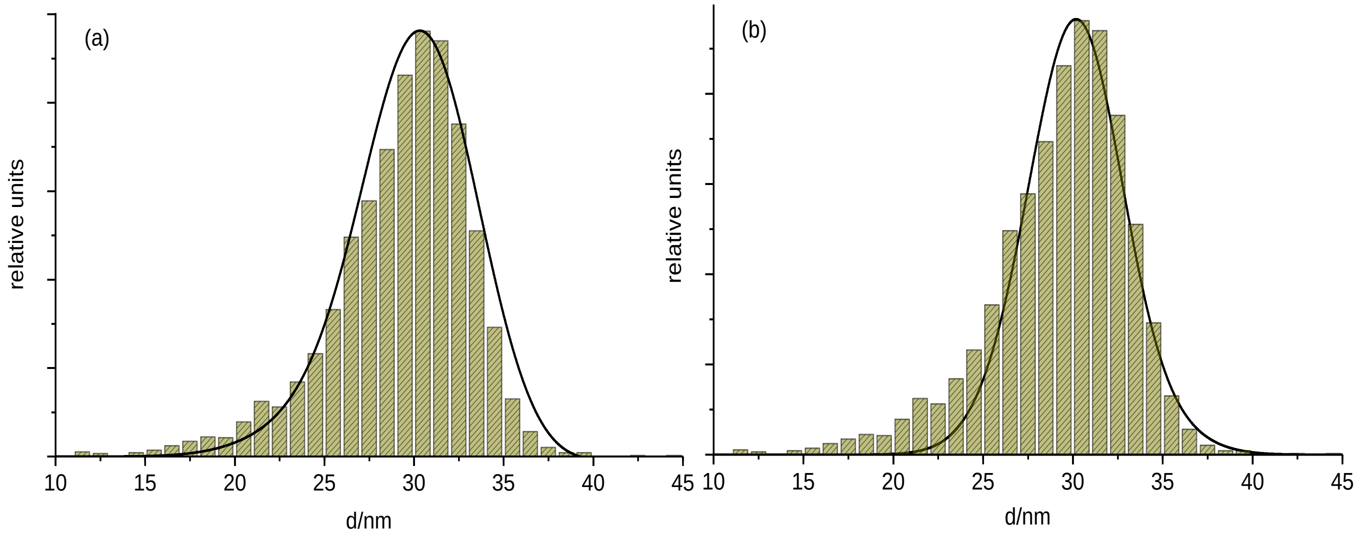

Figure 18: Superposition of size distribution functions calculated from electropherograms (black solid line) obtained for (a) SNP22 (1st series) and (b) SNP22 (2nd series), $c(Li^+) = 60$ mmol L^{-1}, T = 25 °C with histograms calculated from TEM data.

Table 5: Calculated parameters obtained via nonlinear fitting to Gram-Charlier A Series function.

Cation counterion	SNP	$c(cation)$ / (mmol L^{-1})	R	μ_1 /nm	σ /nm	κ_3	κ_4
Li$^+$	**SNP7****	40	0.9965	11.39 (±0.09)	1.15 (±0.02)	-0.057 (±0.15)	0.042 (±0.10)
		60	0.9983	11.41 (±0.02)	1.18 (±0.01)	0.140 (±0.03)	0.474 (±0.02)
	SNP12*	40	0.9988	16.84 (±0.03)	2.13 (±0.01)	0.667 (±0.04)	0.631 (±0.02)
		60	0.9997	16.66 (±0.01)	1.64 (±0.01)	-0.348 (±0.01)	0.021 (±0.01)
		80	0.9997	16.10 (±0.01)	1.73 (±0.01)	-0.328 (±0.01)	0.057 (±0.01)
		100	0.9995	16.30 (±0.02)	1.89 (±0.01)	-0.123 (±0.02)	-0.013 (±0.02)
		120	0.9991	17.28 (±0.06)	1.99 (±0.01)	1.427 (±0.01)	0.760 (±0.01)
	SNP12**	40	0.9997	16.90 (±0.02)	1.22 (±0.01)	0.509 (±0.04)	0.385 (±0.03)
		60	0.9990	16.67 (±0.03)	1.05 (±0.01)	0.217 (±0.06)	0.213 (±0.04)
		80	0.9991	16.22 (±0.01)	1.13 (±0.01)	-0.072 (±0.01)	0.286 (±0.01)
	SNP22*	20	0.9999	30.47 (±0.02)	3.11 (±0.01)	0.202 (±0.01)	0.114 (±0.01)
		40	0.9988	31.37 (±0.02)	3.53 (±0.01)	0.125 (±0.01)	-0.102 (±0.01)
		60	0.9995	29.20 (±0.02)	3.75 (±0.01)	-0.978 (±0.01)	-0.328 (±0.01)
		80	0.9997	29.50 (±0.03)	3.63 (±0.01)	-0.506 (±0.02)	-0.148 (±0.01)
		100	0.9992	29.71 (±0.05)	4.04 (±0.02)	-0.576 (±0.03)	-0.229 (±0.01)
	SNP22**	20	0.9991	31.45 (±0.01)	2.83 (±0.01)	0.993 (±0.01)	0.441 (±0.01)
		40	0.9997	30.80 (±0.04)	2.29 (±0.01)	0.021 (±0.03)	0.178 (±0.02)
		60	0.9999	31.00 (±0.01)	2.69 (±0.01)	0.479 (±0.01)	0.296 (±0.01)
		80	0.9996	29.23 (±0.04)	2.82 (±0.01)	-0.499 (±0.03)	-0.140 (±0.01)
Na$^+$	**SNP7****	40	0.9982	11.32 (±0.12)	1.34 (±0.04)	-0.582 (±0.18)	-0.337 (±0.09)
		60	0.9980	10.79 (±0.04)	1.31 (±0.03)	-0.869 (±0.09)	-0.265 (±0.02)
		80	0.9985	11.82 (±0.63)	1.24 (±0.08)	0.859 (±1.5)	0.752 (±0.78)
	SNP12*	20	0.9995	15.65 (±0.03)	2.69 (±0.01)	-0.254 (±0.02)	-0.242 (±0.01)
		40	0.9994	15.98 (±0.02)	2.26 (±0.01)	-0.140 (±0.01)	-0.151 (±0.01)
		60	0.9993	15.15 (±0.01)	2.35 (±0.01)	-1.132 (±0.01)	-0.407 (±0.01)
		80	0.9997	15.67 (±0.01)	2.18 (±0.01)	-0.907 (±0.02)	-0.415 (±0.01)
		100	0.9994	17.72 (±0.00)	1.99 (±0.01)	0.800 (±0.01)	1.068 (±0.01)
		120	0.9981	17.66 (±0.01)	2.74 (±0.00)	0.690 (±0.01)	0.438 (±0.01)
	SNP12**	40	0.9995	17.09 (±0.03)	1.40 (±0.01)	0.607 (±0.04)	0.209 (±0.01)
		60	0.9995	16.80 (±0.01)	1.17 (±0.01)	0.960 (±0.02)	0.450 (±0.01)
		80	0.9985	16.90 (±0.02)	1.28 (±0.01)	0.675(±0.06)	0.227 (±0.01)
		100	0.9996	16.86 (±0.01)	0.96 (±0.01)	0.486 (±0.02)	0.220 (±0.01)
	SNP22*	20	0.9993	31.22 (±0.03)	3.35 (±0.01)	0.762 (±0.03)	0.640 (±0.02)
		40	0.9996	30.55 (±0.02)	4.28 (±0.01)	-0.799 (±0.01)	-0.291 (±0.01)
		60	0.9995	29.47 (±0.01)	3.91 (±0.01)	-1.056 (±0.01)	-0.365 (±0.01)
		80	0.9987	28.80 (±0.01)	4.85 (±0.01)	-1.423 (±0.01)	-0.475 (±0.01)
		100	0.9959	30.98 (±0.22)	4.78 (±0.01)	-0.156 (±0.09)	-0.096 (±0.06)
	SNP22**	20	0.9991	31.96 (±0.02)	3.07 (±0.01)	0.864 (±0.02)	0.388 (±0.01)
		40	0.9987	32.13 (±0.01)	3.00 (±0.01)	1.086 (±0.01)	0.410 (±0.01)
		60	0.9996	31.45 (±0.01)	2.88 (±0.01)	1.446 (±0.01)	0.765 (±0.01)
		80	0.9988	31.25 (±0.01)	2.78 (±0.01)	0.871 (±0.01)	0.467 (±0.01)
		100	0.9991	29.41 (±0.01)	3.15 (±0.01)	-0.911 (±0.18)	-0.266 (±0.01)
K$^+$	**SNP12***	20	0.9989	16.44 (±0.02)	2.30 (±0.01)	-0.314 (±0.02)	0.229 (±0.01)
		40	0.9978	16.67 (±0.01)	2.04 (±0.01)	-0.577 (±0.01)	0.429 (±0.01)
	SNP22*	20	0.9991	32.11 (±0.02)	3.02(±0.01)	0.948 (±0.02)	0.704 (±0.01)
		40	0.9987	30.62 (±0.01)	2.86 (±0.01)	0.006 (±0.01)	0.466 (±0.01)
		60	0.9977	30.80 (±0.01)	3.38 (±0.01)	0.023 (±0.01)	0.818 (±0.01)

R = correlation coefficient, standard errors in brackets

Table 6: Parameters characterizing the obtained size distribution functions obtained from moment analysis.

counterion	SNP	$c(cation)$ / (mmol L^{-1})	μ_1 /nm	σ /nm	κ_3	κ_4
Li$^+$	**SNP7****	40	11.23	1.18	-0.119	0.027
		60	10.88	1.28	-0.290	-0.176
		Mean value		**1.23 (±0.05)**		
	SNP12*	40	16.45	1.69	-0.358	-0.007
		60	15.83	1.80	-0.371	-0.026
		80	16.09	1.91	-0.108	-0.002
		100	16.06	2.05	0.292	0.965
		120	15.63	2.28	-0.071	0.163
		Mean value		**1.94 (±0.20)**		
	SNP22*	20	29.87	3.20	0.044	0.111
		40	31.28	3.37	0.385	-0.306
		60	29.83	3.37	-0.498	0.068
		80	29.49	3.55	-0.286	-0.044
		100	29.97	3.80	-0.180	-0.160
		Mean value		**3.46 (±0.20)**		
	SNP22**	20	30.32	2.95	0.318	0.655
		40	30.32	2.39	-0.103	0.074
		60	30.18	2.82	0.065	0.246
		80	29.28	2.75	-0.302	-0.027
		Mean value		**2.73 (±0.21)**		
Na$^+$	**SNP7****	40	11.57	1.14	0.334	-1.461
		60	10.93	1.23	-0.517	0.101
		80	11.06	1.31	-0.029	0.284
		Mean value		**1.22 (±0.07)**		
	SNP12*	20	15.79	2.41	0.439	-0.977
		40	15.94	2.15	0.197	-0.372
		60	15.69	1.98	-0.437	-0.186
		80	16.22	1.76	0.156	-0.516
		100	16.19	2.07	-0.297	-0.327
		120	16.32	2.92	0.063	0.326
		Mean value		**2.21 (±0.37)**		
	SNP22*	20	29.41	3.54	-0.016	0.249
		40	31.01	3.93	-0.288	-0.040
		60	30.27	3.42	-0.478	0.009
		80	30.33	3.85	-0.483	0.101
		100	30.62	4.69	0.014	-0.127
		Mean value		**3.89 (±0.46)**		
	SNP22**	20	30.81	3.20	0.263	0.519
		40	30.99	3.10	0.416	0.727
		60	29.76	2.97	0.346	1.094
		80	30.09	2.92	0.202	0.523
		100	29.79	2.93	-0.572	0.146
		Mean value		**3.02 (±0.11)**		
K$^+$	**SNP12***	20	15.67	2.52	-0.437	-0.191
		40	15.73	2.29	-0.640	-0.658
		Mean value		**2.41 (±0.12)**		
	SNP22*	20	30.43	3.17	0.061	0.435
		40	29.39	3.09	-0.370	-0.279
		60	28.61	3.66	-0.507	-0.807
		Mean value		**3.31 (±0.25)**		

Table 7: Parameters (in nm, if not dimensionless) obtained by different procedures for the size (diameter) distribution functions evaluated from TEM measurements (standard errors in brackets) from ref. [71].

	SNP7	**SNP12**	**SNP22**
Histogram[a]			
Arithmetic mean	11.17	16.28	29.32
Median	11.10	16.42	29.91
Maximum	11.5	16.5	30.5
Standard deviation	1.87	2.30	3.85
Gauß			
μ_1	11.11 (± 0.02)	16.51 (± 0.05)	30.17 (± 0.09)
σ	1.67 (± 0.03)	2.18 (± 0.06)	3.02 (± 0.10)
GCSA[b]			
μ_1	11.47 (± 0.18)	15.45 (± 0.16)	29.99 (± 0.17)
σ	1.67 (± 0.03)	2.42 (± 0.08)	3.00 (± 0.08)
κ_3	0.49 (± 0.25)	-0.67 (± 0.15)	-0.54 (± 0.11)
κ_4	0.27 (± 0.16)	-0.15 (± 0.07)	0.20 (± 0.08)
Moment analysis			
μ_1	11.16	15.77	29.61
σ	1.91	2.40	3.25
κ_3	0.25	-0.42	-0.57
κ_4	1.68	0.71	0.35

[a] bin-width = 0.1 nm. [b] Gram-Charlier series of type A

4.2 Polystyrene Sulfate Latex Nanoparticles

4.2.1 Taylor dispersion analysis (TDA)

The mean hydrodynamic radius R_H of selected polystyrene sulfate latex NPs (PSSL) was determined after dilution of the original sample with borate buffer (5 mmol L^{-1}). The prepared sample was loaded into CE instrument and pumped at a constant pressure through a fused-silica capillary. To increase the sensitivity of detection by avoiding the effect of dilution, TDA measurements were implemented in the frontal mode. Three wavelengths (214, 254 and 280 nm) were tested to find the best wavelength for all measurements (see Figure 19). Figure 19 shows that the signal-to-noise ratio was best at a detection wavelength of 214 nm. Therefore, this detection wavelength was selected for subsequent measurements.

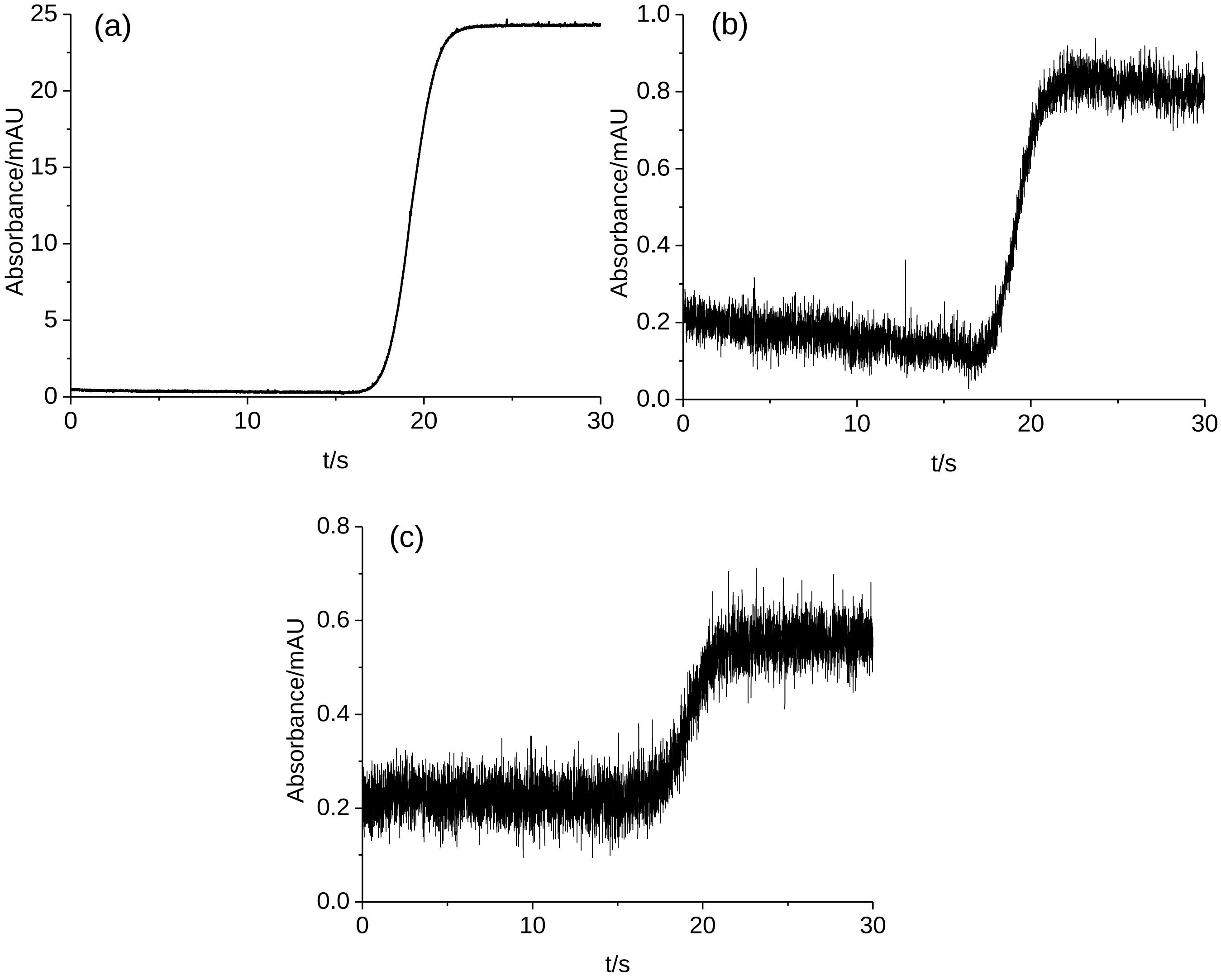

Figure 19: Recorded eluent traces (absorbance versus time) at wavelength: (a) 214, (b) 254 and (c) 280 nm for PSSL20. Experimental conditions: T = 20 ^{o}C, total length of capillary = 60.8 cm, capillary length to the detector 50.4 cm, inner diameter of the fused-silica capillary = 76 μm, electrolyte = 8 mmol L^{-1} borax, frontal method, pressure difference = 0.2 psi (13.8 mbar), original PSSL20 suspension against 5 mmol L^{-1} borax.

The linearity range of the detector was examined with a sample containing PSSL20 (see Figure 20). Figure 20 shows that the recorded absorbances are within the linearity range of the detector. The correlation coefficient for plotting the step height against PSSL concentration within the range depicted in Figure 20b, is: 1.00 for PSSL20; 0.9999 for each of PSSL40 and PSSL60; and 0.9945 for PSSL80.

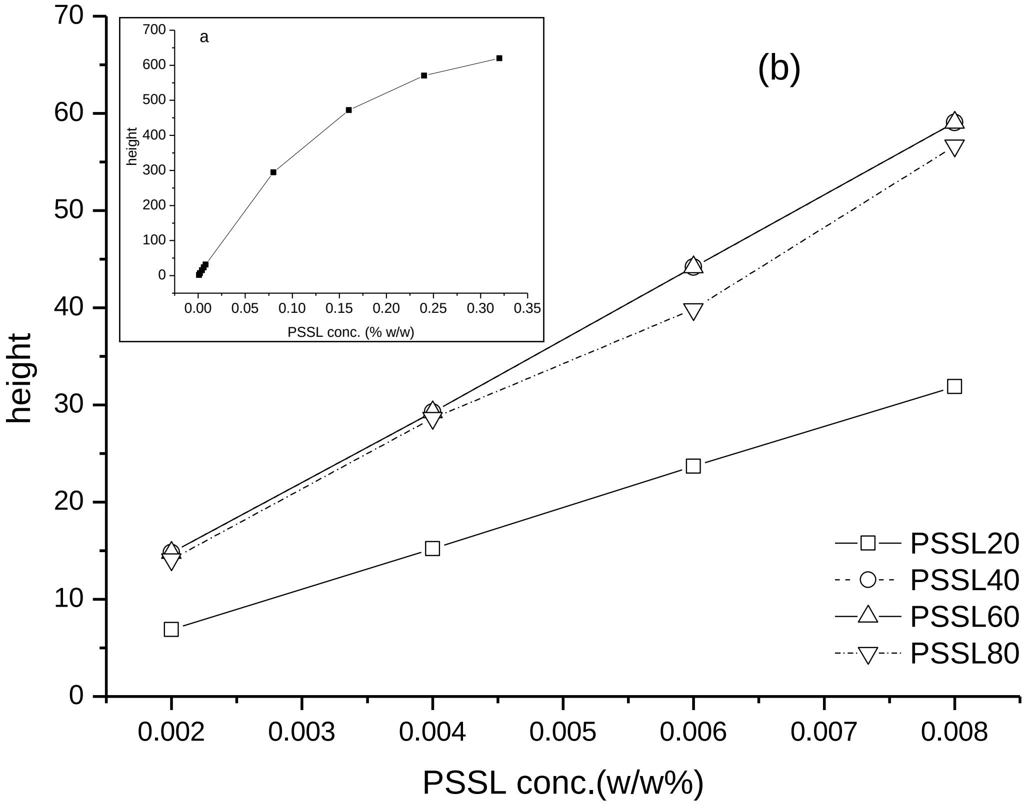

Figure 20: Investigation of linearity of detection for: (a) PSSL20 and (b) all sizes used in this study of PSSL (the height of recorded eluent traces against concentration). Experimental conditions (refer to Figure 19).

With elution times around 30 min for a capillary with a single detection window no correction of variances is not required because the effects of ramping up in velocity at this long residence times can be neglected (the velocity remains constant during the measurement) [51]. The experimental scheme also does not require a correction for the finite length of the injected sample zone (as there is no finite sample zone length).

All absorbance traces (absorbance $A = f(t)$) were fitted to the cumulative Gaussian function (Eq. 26) by non-linear regression (refer to Appendix B2 and B3). The collective diffusion coefficient D_c can be determined by using Eq. (27) from the determined parameters σ_t^2 and t which are obtained from fitting the concentration profiles to the cumulative Gaussian function (Eq. (26)). After that, the hydrodynamic radius R_H was calculated from the obtained diffusion coefficients by applying the Stokes-Einstein equation (Eq. 29).

The resulting hydrodynamic diameters for different mass fraction of PSSL in the sample (obtained from TDA measurements in 8 mmol L^{-1} borax) are reported in Figure 21 and Table 7. Figure 21 shows that the diameter for each size of PSSL is approximately invariant of the mass fraction of particles in the sample. The recorded traces, as shown in Appendix B2 and B3, do not show a systematic deviation from the cumulative Gaussian function (the fitted curve).

The obtained mean particle diameters are as follows: PSSL20: 24.62 (2.81%) nm; PSSL40: 46.81 (3.16%) nm; PSSL60: 67.44 (1.82%) nm; and PSSL80: 89.38 (3.05%) nm. RSD in brackets represent the repeatability of the method for twelve runs for PSSL20 and PSSL40; eleven runs for PSSL60; and nine runs for PSSL80.

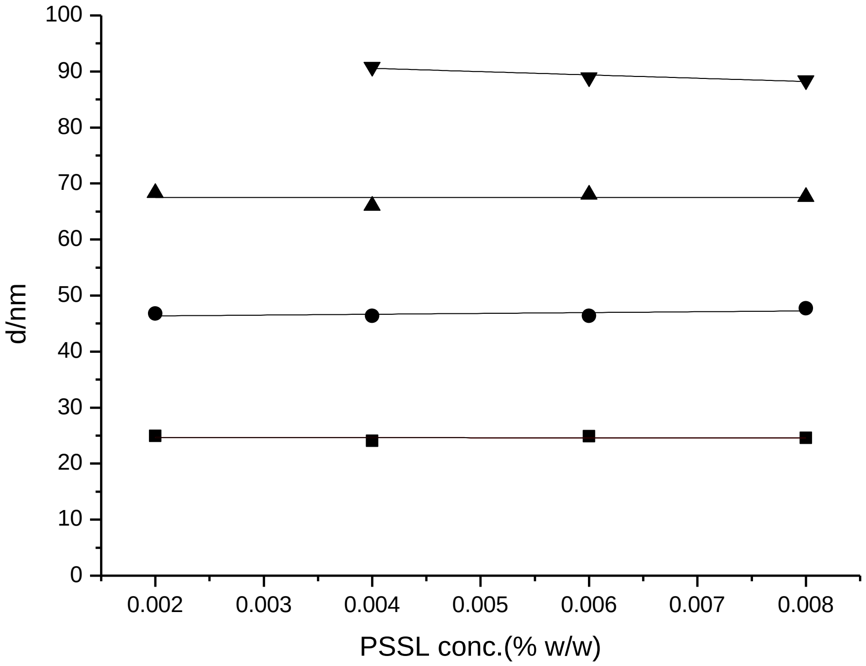

Figure 21: Calculated hydrodynamic particle diameter with different mass fraction of PSSL in the sample in 8 mmol L^{-1} borax from TDA measurements using the cumulative Gaussian function. ■ PSSL20; ● PSSL40; ▲ PSSL60; and ▼ PSSL80. Each point is the mean of three repeated runs (except for two runs with 2x10^{-3} % w/w for PSSL60).

Table 7: Results of Taylor dispersion analysis measurements with different mass fraction of PSSL in the sample in 8 mmol L^{-1} borax.

PSSL	conc. (%w/w)	run	t_H/ min	$SE(t_H)$/ min	σ_t/ min	$SE(\sigma_t)$/ min	$D.10^{-12}$/ ($m^2\ s^{-1}$)	R_H/ nm	d/ nm	R^2
PSSL20	0.002	1	19.306	0.0696	1.046	0.0962	17.679	12.131	24.262	0.99857
		2	19.370	0.0447	1.060	0.0617	17.282	12.410	24.820	0.99942
		3	19.342	0.0328	1.079	0.0453	16.646	12.884	25.767	0.99969
	0.004	1	19.253	0.0238	1.033	0.0329	18.085	11.859	23.717	0.99983
		2	19.261	0.0227	1.046	0.0313	17.642	12.156	24.312	0.99985
		3	19.165	0.0176	1.040	0.0244	17.772	12.067	24.135	0.99991
	0.006	1	19.270	0.0293	1.041	0.0405	17.815	12.038	24.077	0.99975
		2	19.276	0.0249	1.054	0.0343	17.398	12.327	24.654	0.99982
		3	19.317	0.0134	1.082	0.0184	16.540	12.966	25.933	0.99995
	0.008	1	19.316	0.0130	1.067	0.0180	17.025	12.597	25.194	0.99995
		2	19.341	0.0240	1.044	0.0332	17.788	12.057	24.113	0.99983
		3	19.354	0.0144	1.051	0.0199	17.557	12.215	24.430	0.99994
	MW		**19.298**		**1.054**		**17.436**	**12.309**	**24.618**	
	SD		**0.057**		**0.016**		**0.480**	**0.346**	**0.692**	
	RSD		**0.29%**		**1.47%**		**2.76%**	**2.81%**	**2.81%**	
PSSL40	0.002	1	19.534	0.0260	1.460	0.0356	9.186	23.340	46.679	0.99986
		2	19.402	0.0184	1.458	0.0252	9.151	23.429	46.858	0.99993
		3	19.466	0.0212	1.458	0.0290	9.179	23.365	46.731	0.99991
	0.004	1	19.519	0.0143	1.461	0.0195	9.166	23.396	46.793	0.99996
		2	19.552	0.0122	1.452	0.0166	9.299	23.063	46.126	0.99997
		3	19.612	0.0138	1.455	0.0189	9.290	23.086	46.171	0.99996
	0.006	1	19.390	0.0135	1.443	0.0185	9.341	22.958	45.916	0.99996
		2	19.690	0.0285	1.504	0.0390	8.734	24.555	49.109	0.99984
		3	19.492	0.0118	1.418	0.0162	9.719	22.067	44.133	0.99997
	0.008	1	19.549	0.0209	1.486	0.0286	8.880	24.151	48.303	0.99991
		2	19.458	0.0163	1.440	0.0223	9.405	22.803	45.606	0.99994
		3	19.569	0.0199	1.502	0.0272	8.701	24.648	49.297	0.99992
	MW		**19.519**		**1.461**		**9.171**	**23.405**	**46.810**	
	SD		**0.085**		**0.025**		**0.288**	**0.739**	**1.478**	
	RSD		**0.44%**		**1.70%**		**3.14%**	**3.16%**	**3.16%**	
PSSL60	0.002	1	19.786	0.0770	1.942	0.1043	5.262	--------	--------	0.99911
		2	19.604	0.0484	1.762	0.0658	6.332	33.863	67.727	0.99961
		3	19.615	0.0367	1.778	0.0499	6.225	34.450	68.901	0.99978
	0.004	1	19.452	0.0282	1.753	0.0384	6.345	33.803	67.605	0.99987
		2	19.365	0.0209	1.721	0.0285	6.559	32.699	65.399	0.99993
		3	19.449	0.0168	1.720	0.0229	6.594	32.524	65.049	0.99995
	0.006	1	20.556	0.0160	1.808	0.0217	6.309	33.992	67.984	0.99996
		2	19.511	0.0232	1.756	0.0315	6.348	33.784	67.568	0.99991
		3	19.611	0.0207	1.774	0.0281	6.250	34.316	68.632	0.99993
	0.008	1	19.691	0.0207	1.758	0.0282	6.387	33.575	67.151	0.99993
		2	19.579	0.0206	1.771	0.0280	6.260	34.258	68.517	0.99993
		3	19.452	0.0178	1.749	0.0242	6.377	33.628	67.256	0.99995
	MW		**19.639**		**1.774**		**6.271**	**33.718**	**67.435**	
	SD		**0.312**		**0.058**		**0.337**	**0.615**	**1.230**	
	RSD		**1.59%**		**3.26%**		**5.37%**	**1.82%**	**1.82%**	

PSSL80	0.002	1	19.669	0.0959	2.252	0.1292	3.890	55.113	--------	0.99885
		2	19.622	0.0534	2.065	0.0722	4.612	46.485	--------	0.9996
		3	19.653	0.0581	2.147	0.0785	4.274	50.179	--------	0.99955
	0.004	1	19.615	0.0354	2.051	0.0479	4.677	45.855	91.711	0.99982
		2	19.662	0.0463	2.054	0.0626	4.674	45.887	91.773	0.9997
		3	19.616	0.0306	2.019	0.0414	4.826	44.437	88.875	0.99987
	0.006	1	19.467	0.0229	1.996	0.0310	4.902	43.750	87.501	0.99992
		2	19.542	0.0351	2.045	0.0475	4.685	45.777	91.554	0.99983
		3	19.490	0.0320	1.999	0.0434	4.889	43.868	87.735	0.99985
	0.008	1	19.544	0.0208	1.977	0.0282	5.013	42.782	85.564	0.99994
		2	19.498	0.0182	1.986	0.0247	4.956	43.277	86.555	0.99995
		3	19.427	0.0399	2.057	0.0540	4.603	46.589	93.177	0.99978
	MW		**19.567**		**2.054**		**4.667**	**44.691**	**89.383**	
	SD		**0.083**		**0.078**		**0.316**	**1.362**	**2.724**	
	RSD		**0.42%**		**3.77%**		**6.77%**	**3.05%**	**3.05%**	

MW = arithmetic mean; SD = standard deviation; RSD = relative standard deviation; R = correlation coefficient; SE = standard error resulting from regression analysis, R_H = hydrodynamic radius.

Furthermore, the influence of the ionic strength of the borax buffer solution on the resulting hydrodynamic diameter was studied for PSSL20 and PSSL40. The results are given in Figure 22 and Table 8. The calculated hydrodynamic diameter was found to be (within experimental error) independent of the ionic strength in the range $I = 4 – 20$ mmol L^{-1}.

The experimental results show at a given PSSL size that in the ionic strength range $I = 4 – 20$ mmol L^{-1}, the diffusion coefficient is independent of the ionic strength and there is no dependence on the PSSL concentration in the concentration range 0.002 – 0.008 % (w/w) (refer to Tables 7 and 8). It is noticed that there is a small difference in the mean size value for PSSL20 and PSSL40 as shown in Tables 7 and 8 reflecting the precision of the method [84].

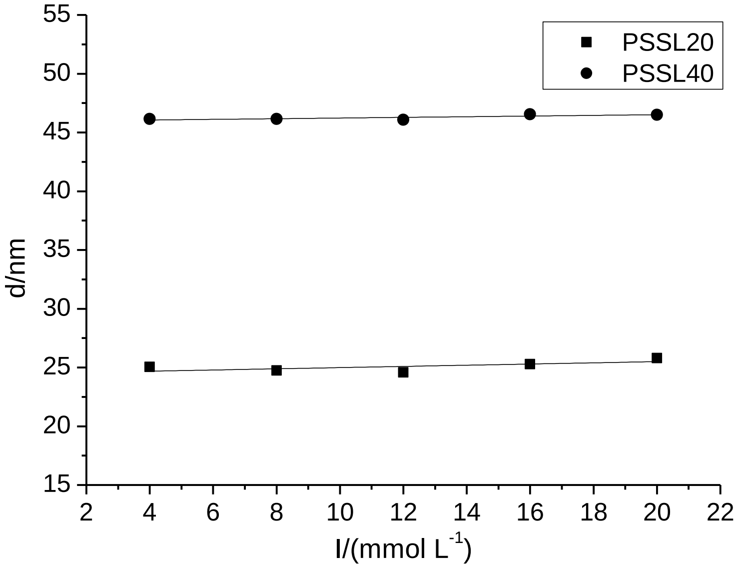

Figure 22: Calculated hydrodynamic diameters for PSSL20 and PSSL40 as a function of the ionic strength of borax buffer solution from TDA measurements using the cumulative Gaussian function. Each experimental point is the mean of three replicates.

Table 8: Results obtained from Taylor dispersion analysis measurements for PSSL20 and PSSL40 in buffers of different ionic strength.

PSSL	**I/ (mmol L^{-1})**	**run**	**t_H/** min	**SE(t_H)/** min	**σ_t/** min	**SE(σ_t)/** min	**D/(10^{-12}** m² s^{-1})	**R_H/** nm	**d/** nm	**R^2**
PSSL20	4	1	19.138	0.01954	1.076	0.02697	16.566	12.946	25.891	0.99989
		2	19.141	0.01787	1.037	0.02469	17.839	12.022	24.044	0.99991
		3	19.061	0.01768	1.060	0.02441	17.021	12.600	25.200	0.99991
	8	1	19.205	0.01739	1.049	0.02402	17.490	12.262	24.525	0.99991
		2	19.134	0.0171	1.051	0.02363	17.386	12.335	24.671	0.99991
		3	19.238	0.01675	1.061	0.02313	17.131	12.519	25.038	0.99992
	12	1	19.085	0.01572	1.040	0.02172	17.682	12.129	24.258	0.99993
		2	19.009	0.01576	1.047	0.02178	17.377	12.342	24.683	0.99993
		3	19.035	0.01739	1.051	0.02403	17.274	12.416	24.831	0.99991
	16	1	19.165	0.01497	1.067	0.02066	16.878	12.707	25.414	0.99994
		2	19.152	0.01675	1.058	0.02314	17.152	12.504	25.008	0.99992
		3	19.228	0.01781	1.069	0.02459	16.858	12.722	25.443	0.99991
	20	1	19.232	0.01421	1.072	0.01961	16.767	12.791	25.582	0.99994
		2	19.247	0.0128	1.067	0.01767	16.968	12.639	25.278	0.99995
		3	18.550	0.01386	1.072	0.01915	16.177	13.257	26.514	0.99995
	MW		**19.108**		**1.059**		**17.104**	**12.546**	**25.092**	
	SD		**0.172**		**0.012**		**0.432**	**0.319**	**0.639**	
	RSD		**0.90%**		**1.15%**		**2.52%**	**2.55%**	**2.55%**	
PSSL40	4	1	19.073	0.99993	1.436	0.02434	9.275	23.124	46.248	0.01776
		2	18.987	0.99995	1.435	0.02137	9.241	23.208	46.415	0.01559
		3	19.012	0.99988	1.427	0.03246	9.367	22.896	45.792	0.02368
	8	1	19.076	0.99995	1.431	0.02072	9.348	22.943	45.886	0.01511
		2	19.233	0.99996	1.441	0.0186	9.288	23.091	46.182	0.01358
		3	19.090	0.99996	1.438	0.01943	9.252	23.179	46.358	0.01417
	12	1	19.083	0.99994	1.429	0.02267	9.367	22.896	45.792	0.01654
		2	19.033	0.99992	1.431	0.02661	9.319	23.014	46.028	0.01941
		3	19.121	0.99994	1.440	0.02367	9.248	23.191	46.383	0.01727
	16	1	19.211	0.99997	1.434	0.01761	9.365	22.901	45.801	0.01285
		2	19.205	0.99994	1.463	0.02426	9.003	23.821	47.643	0.01771
		3	19.329	0.99995	1.445	0.02125	9.286	23.096	46.192	0.01551
	20	1	19.252	0.99986	1.489	0.03626	8.705	24.635	49.271	0.02649
		2	19.266	0.99996	1.427	0.01943	9.487	22.607	45.214	0.01418
		3	19.296	0.99996	1.426	0.01824	9.520	22.526	45.053	0.01331
	MW		**19.151**		**1.439**		**9.271**	**23.142**	**46.284**	
	SD		**0.110**		**0.017**		**0.196**	**0.508**	**1.015**	
	RSD		**0.58%**		**1.15%**		**2.11%**	**2.19%**	**2.19%**	

MW = arithmetic mean; SD = standard deviation; RSD = relative standard deviation; R = correlation coefficient; SE = standard error resulting from regression analysis, R_H = hydrodynamic radius.

4.2.2 Capillary electrophoresis

4.2.2.1 Electrophoretic mobilities

As a first step, runs were recorded for PSSL40 at varied detection wavelength (214, 254 and 280 nm) and fixed electrolyte composition (5 mmol L^{-1} borax). Experimental results show that the electropherogram recorded at the wavelength of 214 nm has an improved signal-to-noise ratio with respect to those recorded at a wavelength of 254 nm or 280 nm. Thus, the wavelength of 214 nm was selected for all subsequent capillary electrophoresis measurements. In addition, the injection conditions were varied taking PSSL40 with 5 mmol L^{-1} borax as an example. Figure 23 shows the overlay of recorded electropherograms which reveals that the resulting peak shape is asymmetric which can be related to the phenomenon of electromigration dispersion (also called overloading) [52]. It is a consequence of differences in the electric conductivities in the zone of the sample and in the running buffer. There is a shift in the migration time of PSSL40. These measurements confirm the presence of induced local electric field inhomogeneities. To reduce the capillary overloading and to obtain a good peak height, the concentration of PSSL was decreased and the injection time was selected to be at 6 s within the subsequent measurements.

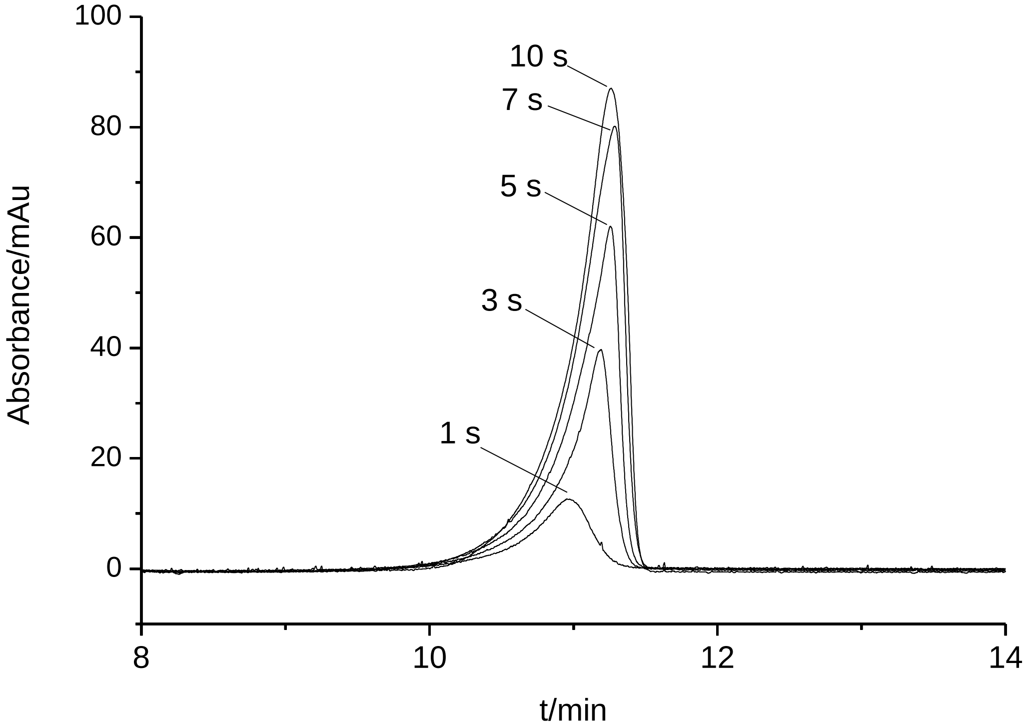

Figure 23: Overlay of electropherograms obtained for PSSL40 with varied injection parameters. The absorbance recorded in the detection volume is plotted against the migration time. Experimental conditions: T= 20°C, sample concentration = 8 $x10^{-3}$ (w/w %) background electrolyte = 5 mmol L^{-1} borax, total length of capillary = 60.7 cm, capillary length to detector = 50.5 cm, inner diameter of fused silica capillary = 76 μm, separation voltage 14 kV, sample injection 0.1 psi (6.89 mbar), data rate 16 Hz, absorbance detection at 214 nm.

The electrophoretic mobilities of PSSL were determined experimentally from the parameters that are given in Eq. 16. Typical electropherograms for different sizes of PSSL particles are shown in Figure 24 (see Appendix B4). The repeatability of the data was confirmed by repeated injections. The precision of the electroosmotic mobility determined for three runs had a relative standard deviation of (< 0.17%) for the runs with PSSL20; (< 0.13%) for the runs with PSSL40; (< 1.08%) for the runs with PSSL60, and (0.05-0.18%) for the runs with PSSL80, which confirms the conclusion drawn from the electropherograms that adsorption of PSSL particles on the wall of capillary can be excluded (refer to Appendix B5). Good repeatability is also observed for the migration times of the NPs. The relative standard deviation for three consecutive runs is < 0.17% for PSSL20; < 0.75% for PSSL40; < 0.40% for PSSL60 and< 0.73% for PSSL80 (refer to Appendix B5).

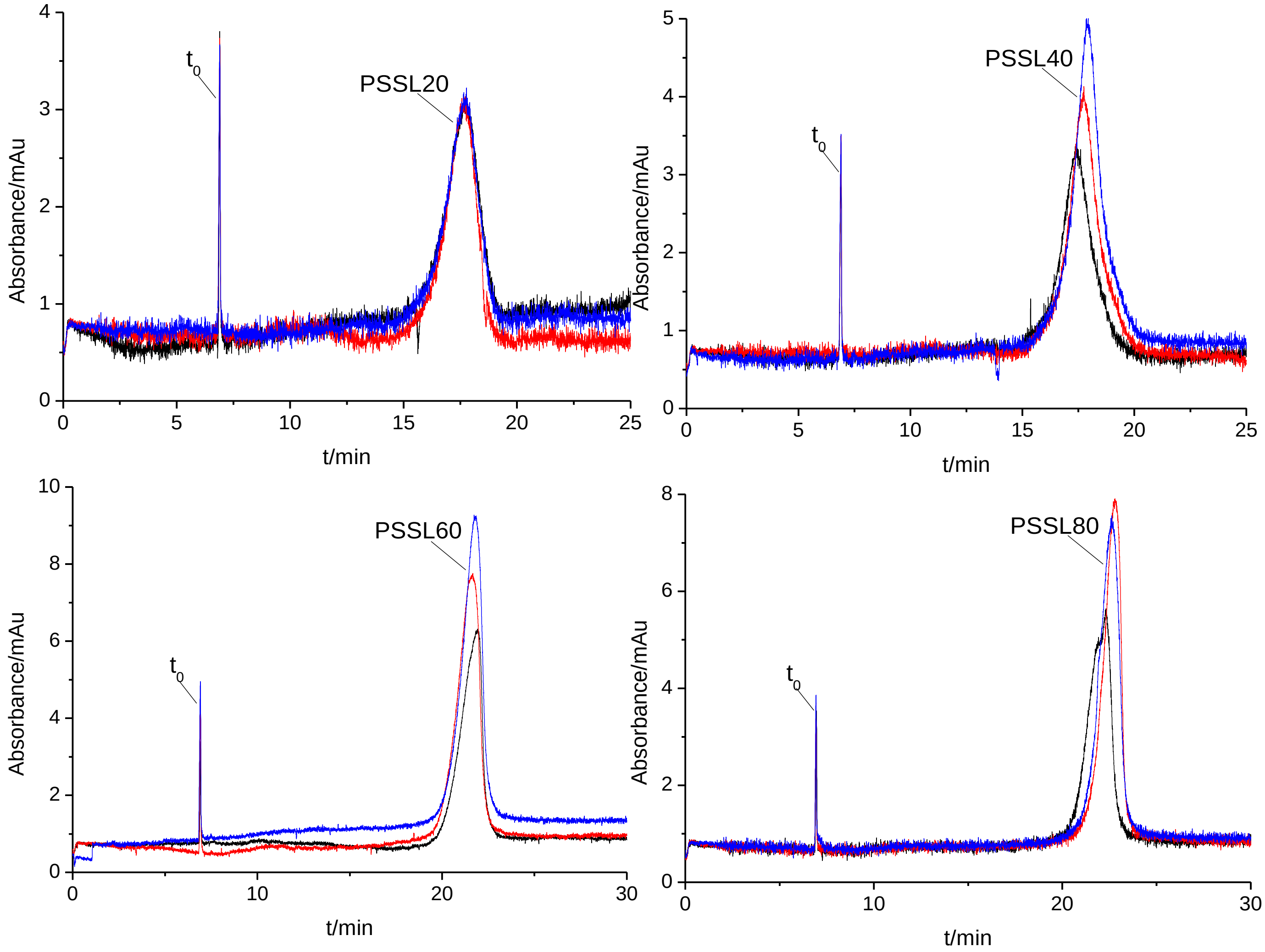

Figure 24: Superimposed electropherograms obtained in consecutive runs for different sizes of PSSL particles with 15 mmol L^{-1} borax; t_o= thiourea as a neutral marker. Experimental conditions: T= 20°C, total length of capillary = 60.7 cm, capillary length to detector = 50.5 cm, inner diameter of fused silica capillary = 76 µm, separation voltage 14 kV, sample injection 0.1 psi (6.89 mbar) 6 s, data rate 16 Hz, absorbance detection at 214 nm.

Three different counterion cations (Li^+, Na^+, and guanidinium (Gdm^+)) are used to investigate the influence of the type of the cations on the electrophoretic mobility of PSSL20 and PSSL40 at 20 °C with different ionic strength (I = 40-120 mmol L^{-1}). The electropherograms of these measurements are represented in Figure 25. The experimental data are shown in Appendix B6. The reproducibility of measurements is proved by repeated injections. This reproducibility of PSSL20 and PSSL40 relates to the precision of measurements via the calculation of RSD from four repeated runs. RSDs of the electroosmotic mobility (for PSSL20 and PSSL40) with different cations in the ionic strength ranges (I = 40-120 mmol L^{-1}) are: (< 0.67%) with Li^+; (< 1.24%) with Na^+; and (< 3.17%) with Gdm^+; respectively. The RSD of the electrophoretic mobility for both PSSL20 and PSSL40 with different cations in the ionic strength ranges (I = 40-120 mmol L^{-1}) are: (< 3.79%) with Li^+; (< 2.49) with Na^+; (< 4.06%) with Gdm^+; respectively. Asymmetric peaks due to overloading of recorded electropherograms, inhomogeneities of the electric field and adsorption of particles onto the capillary wall are observed (see Figure 25). Within experimental error, the migration times for the neutral marker (t_0) and for both PSSL size are increasing with increase in the ionic strength as expected. In some of the measurements, an irregular behavior was observed.

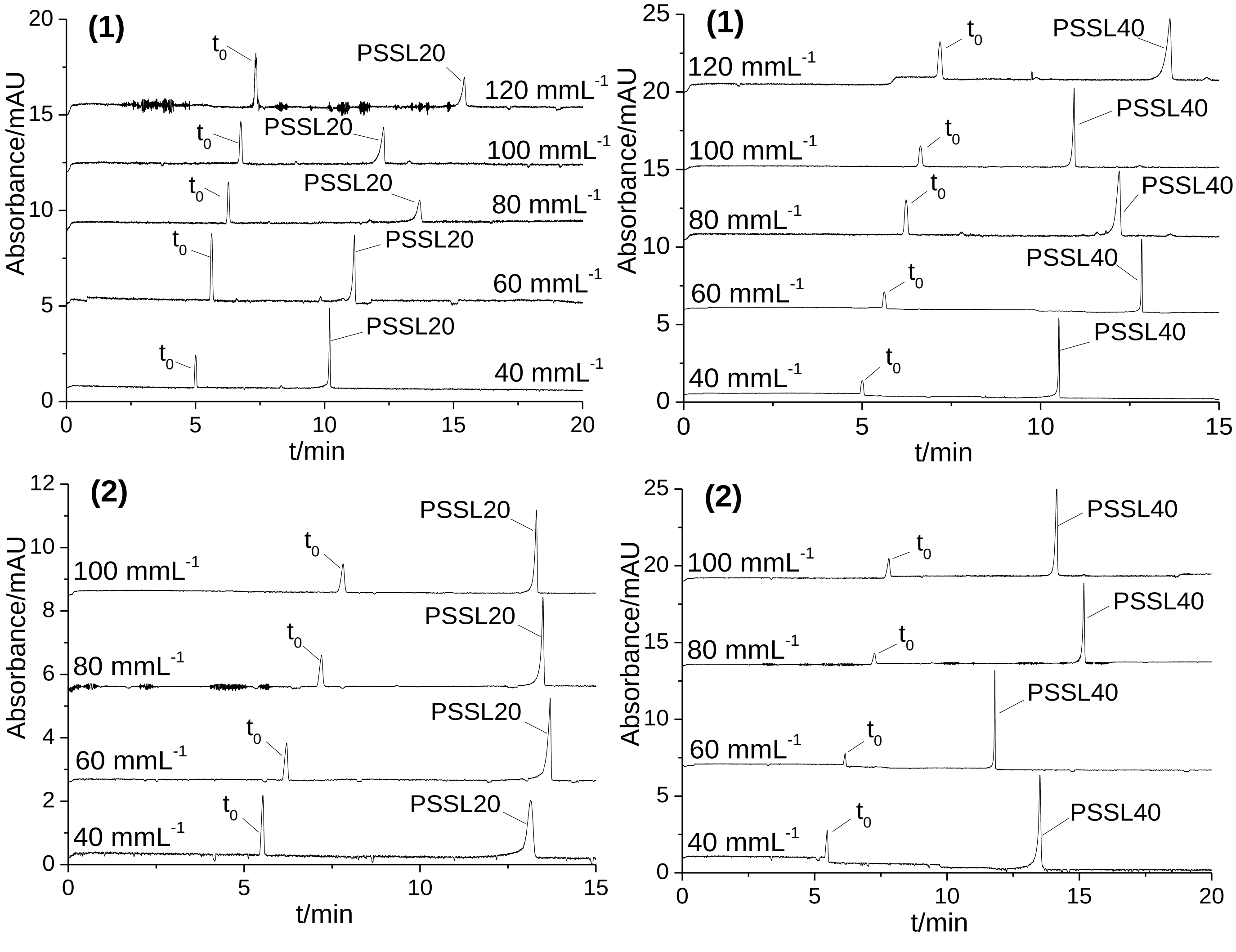

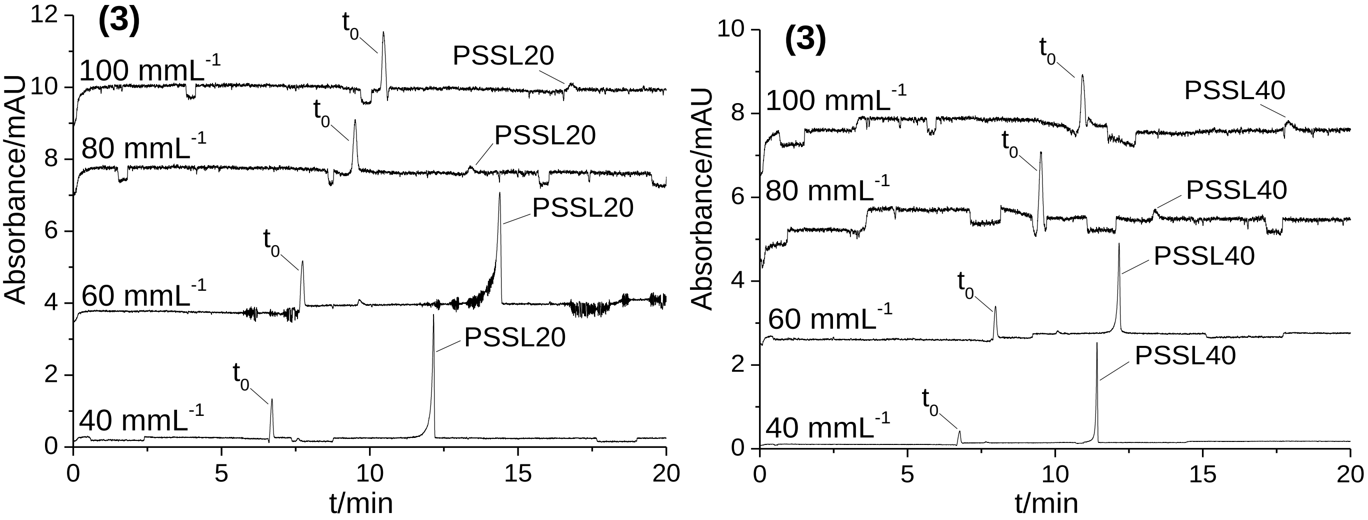

Figure 25: Superimposed electropherograms obtained for PSSL20 and PSSL40 with different ionic strength (I = 40-120 mmol L^{-1}) of different counterion cation: (1) Li^+, (2) Na^+, and (3) Gdm^+; t_o= thiourea as a neutral marker. Experimental conditions: T = 20°C, total length of capillary = 39.5 cm, capillary length to detector = 29.1 cm, inner diameter of the capillary = 76 μm, separation voltage 7 kV, sample injection 0.1 psi (6.89 mbar) 6 s, data rate 16 Hz, absorbance detection at 214 nm.

The electrophoretic mobility values were obtained by taking the average of three measurements in the ionic strength ranges 10-50 mmol L^{-1} and four measurements in the ionic strength ranges 40-120 mmol L^{-1}. A summary of the experimental results of the electrophoretic mobility data in borax buffer dependent of the concentration of the buffer is presented in Appendix B5. In Appendix B6 a summary of the experimental results of the electrophoretic mobility data in different counterion cations with different ionic strength is displayed. The results indicate a decrease in the absolute electrophoretic mobility of the PSSL with increase the ionic strength as expected.

Figure 26 depicts the electrophoretic mobility for various sizes of PSSL as a function of the ionic strength for Na^+ cation as counterion. Figure 27 depicts the electrophoretic mobility for PSSL20 and PSSL40 as a function of the ionic strength for different counterion cations. Theoretically, it is expected that increasing the ionic strength will result in a continuous decrease in the absolute value of the electrophoretic mobility due to a reduction of the electrokinetic potential. The electrolyte concentration is increased; the absolute electrophoretic mobility is decreased. Figure 26 shows that the absolute electrophoretic mobility increases with size and follows the series: PSSL20 < PSSL40 < PSSL60 < PSSL80. Furthermore, the absolute values of the electrophoretic mobility at a given ionic strength decrease as follows: $Li^+ > Na^+ > Gdm^+$ (refer to Figure 27). This trend in the electrophoretic mobility reflects the expected direct Hofmeister series as shown in the investigation of Oncsik *et al.* [32] for negatively charged polystyrene sulfate latex particles in the presence of various monovalent electrolytes by electrophoresis and time-resolved light scattering. They concluded that the affinity of the different monovalent cations to adsorb on the PSSL surface follows the direct Hofmeister series so that the poorly hydrated cation adsorbs the most on the PSSL surface than the more hydrated cation which adsorbs weakly on the particle surface. Thus they observed a decrease in the electrophoretic mobility according to the sequence: $N(CH3)_4^+ < NH_4^+ < Cs^+ < K^+ < Na^+ < Li^+$. This trend of the influence of these counterions on the electrophoretic mobility was observed also with SNPs (refer to *Section 4.1.1* and ref. [83]). It was found to be strongly dependent on the type of counterion.

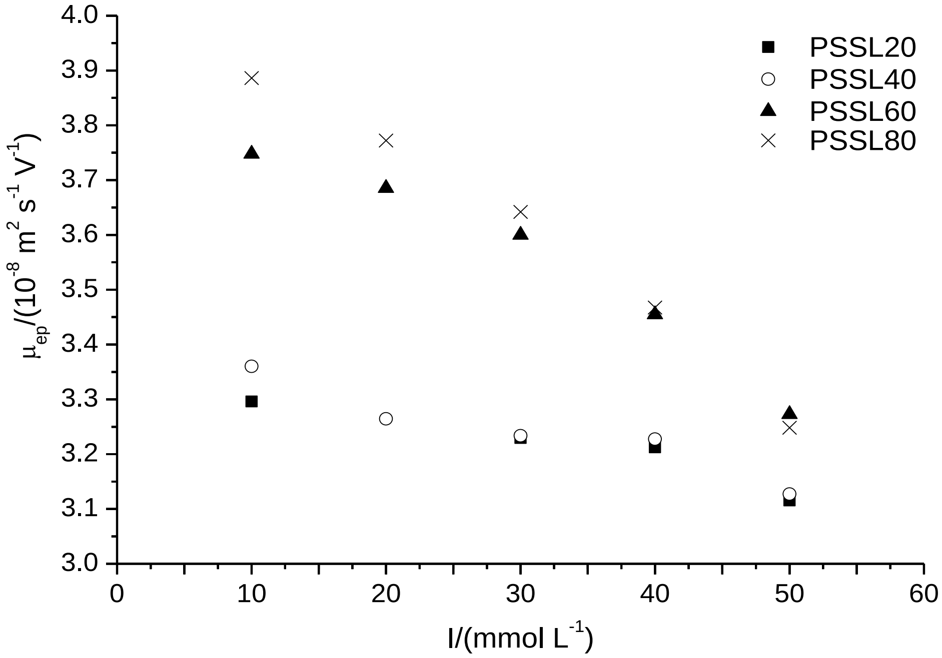

Figure 26: The electrophoretic mobility (T = 20°C) in Na^+ cation for different PSSL populations as a function of the ionic strength. Experimental conditions see Figure 24.

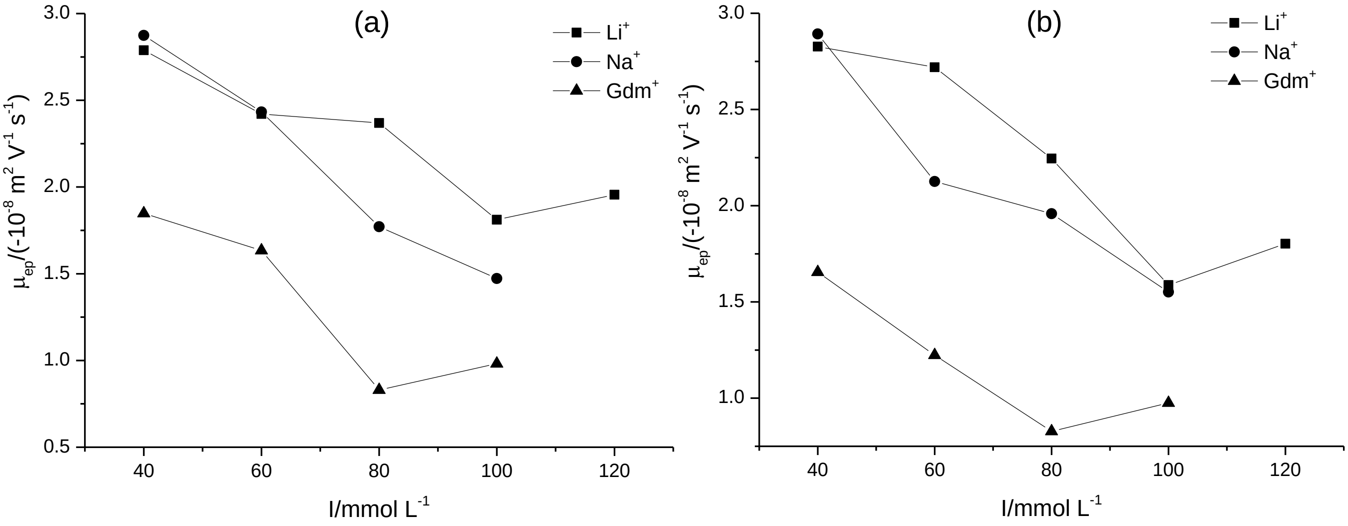

Figure 27: The electrophoretic mobility (T = 20°C) in different counterion cations for: (a) PSSL20, and (b) PSSL40 as a function of the ionic strength. Experimental conditions refer to Figure 29.

4.2.2.2 Evaluation of zeta potential ζ

Calculation of the zeta potential from the measured electrophoretic mobility is done by using the modified procedure proposed by Pyell *et al.* [21] based on an analytic approximation introduced by Ohshima [19] (refer to Eq. 20). The dimensionless ionic drag coefficients for Li^+ (m_+ = 0.330), for Na^+ (m_+ = 0.245), and for Gdm^+ (m_+ = 0.248) are obtained from the limiting equivalent conductivities of these ions at 20 °C (Λ^o_+ = 34.94 S cm^2 mol^{-1} for Li^+; 45.36 S cm^2 mol^{-1} for Na^+; and 46.55 for S cm^2 mol^{-1} for Gdm^+; refer to Eq. 19). Figure 28 represents the electrophoretic mobilities for different size of PSSL with varied ionic strength for Na^+ as counterion. Figure 29 represents the electrophoretic mobilities for PSSL20 and PSSL40 with varied ionic strength for different counterions. Figures 28 and 29 illustrate the dependence of electrophoretic mobilities of PSSL on the reduced sphere radius κa and ζ. The ζ potential decreases with increasing the ionic strength of the counterion. At all ionic strengths for various counterion cations, the radius (a) of PSSL is considered to be constant. Also, the PSSL carry on their surface a constant surface charge density as reported by certificates of analysis supported by molecular probes company as following: 3.3 μC/cm^2 for PSSL20, 0.6 μC/cm^2 for PSSL40, 1.7 μC/cm^2 for PSSL60, and 1.2 μC/cm^2 for PSSL80. However, at low borax concentration (see Figure 28), the ζ potential of PSSL20 (ζ >100 mV) cannot be estimated, because Eq. 20 is only valid if $\zeta \leq$ 100 mV.

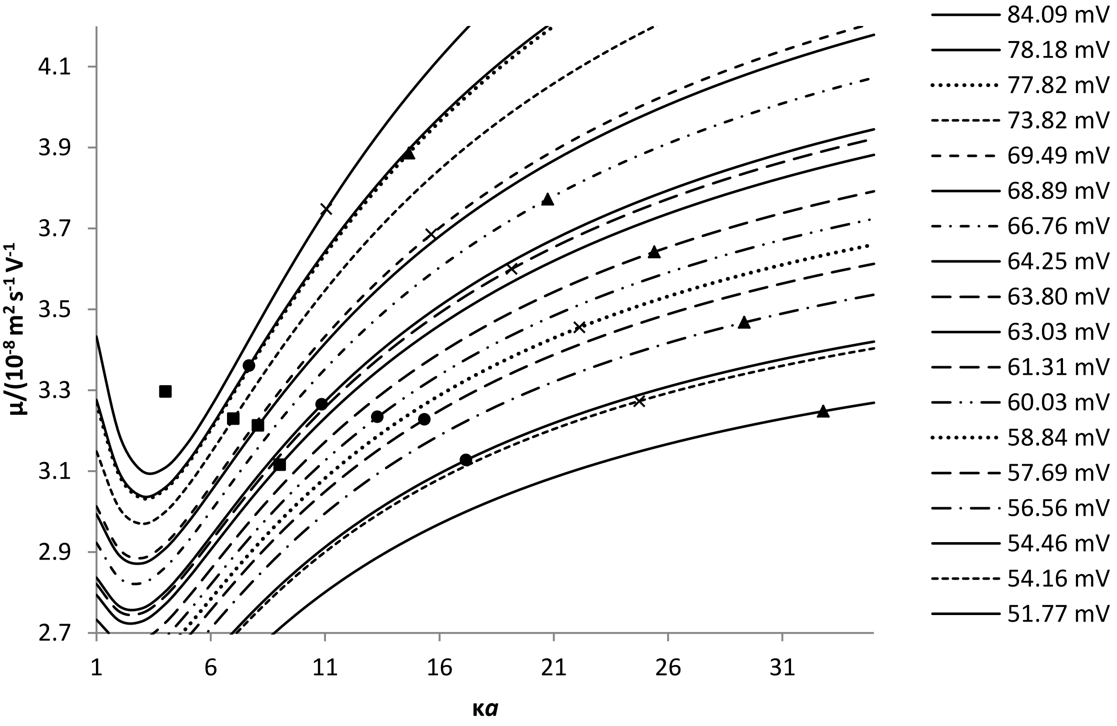

Figure 28: The electrophoretic mobilities for PSSL particles as a function of reduced sphere radius κa and varied ζ with superimposed experimental data for different particle sizes and varied ionic strength of borax buffer. (■) PSSL20; (●) PSSL40; (×) PSSL60 and (▲) PSSL80.

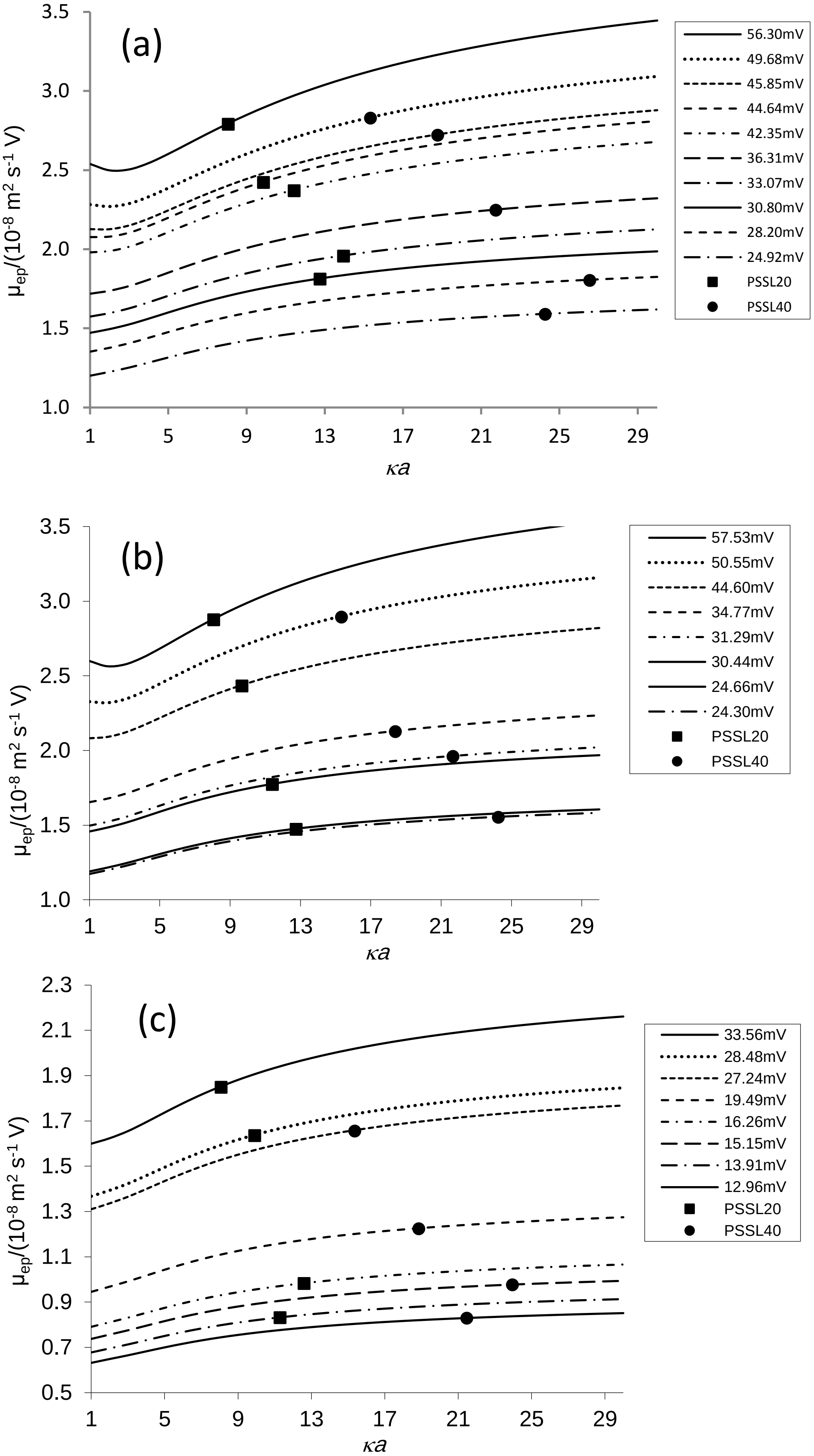

Figure 29: The electrophoretic mobilities for PSSL20 and PSSL40 with varied ionic strength of different counterion cations: (a) Li^+, (b) Na^+ and Gdm^+ as a function of reduced sphere radius κa and varied ζ with superimposed experimental data.

If ζ is higher than a threshold value, the mobility begins to drop with increasing ζ, giving rise to a maximum in the mobility. This maximum is due to the retardation effect, which increases as ζ increases. This increase overcompensates the increase in the electrical force on the particle.

In Figure 30 the calculated zeta potentials are plotted against the normalized decadic logarithm of the concentration with correlation coefficients: 0.9701 for PSSL20; 0.9555 for PSSL40; 0.9933 for PSSL60; and 0.9953 for PSSL80. These results show that PSSL60 and PSSL80 give a better correlation than PSSL40.

Figure 31 shows the decrease of ζ for PSSL20 and PSSL40 as a function of the ionic strength with different counterions. In general, absolute ζ potentials decrease with an increase in the ionic strength due to the compression of the diffuse layer (increase in the specific capacitance of the diffuse part of the electric double layer). As expected, the ζ potential is dependent on the size of PSSL as shown in Figure 30. The colloidal stability of PSSL is decreasing with decreasing $|\zeta|$ (refer to Table 11). Furthermore, the data depicted in Figures 30 and 31 are the results of the iterative procedure based on a Matlab script described in ref. [21]. The resulting values are listed in Tables 10 and 11 (refer to Appendix B5 and B6).

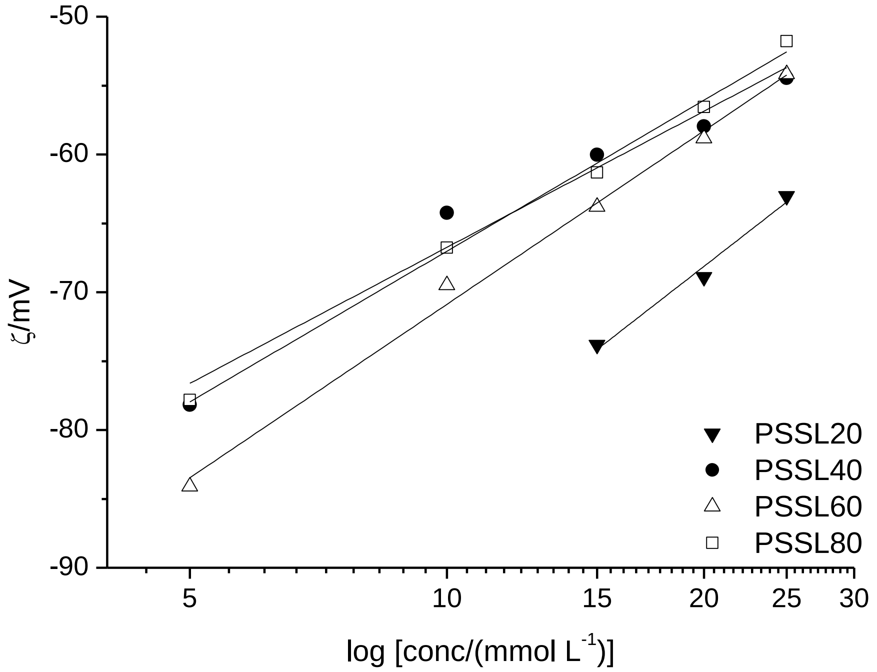

Figure 30: Plotting of ζ against log[conc/(mmol L^{-1})] with borax buffer.

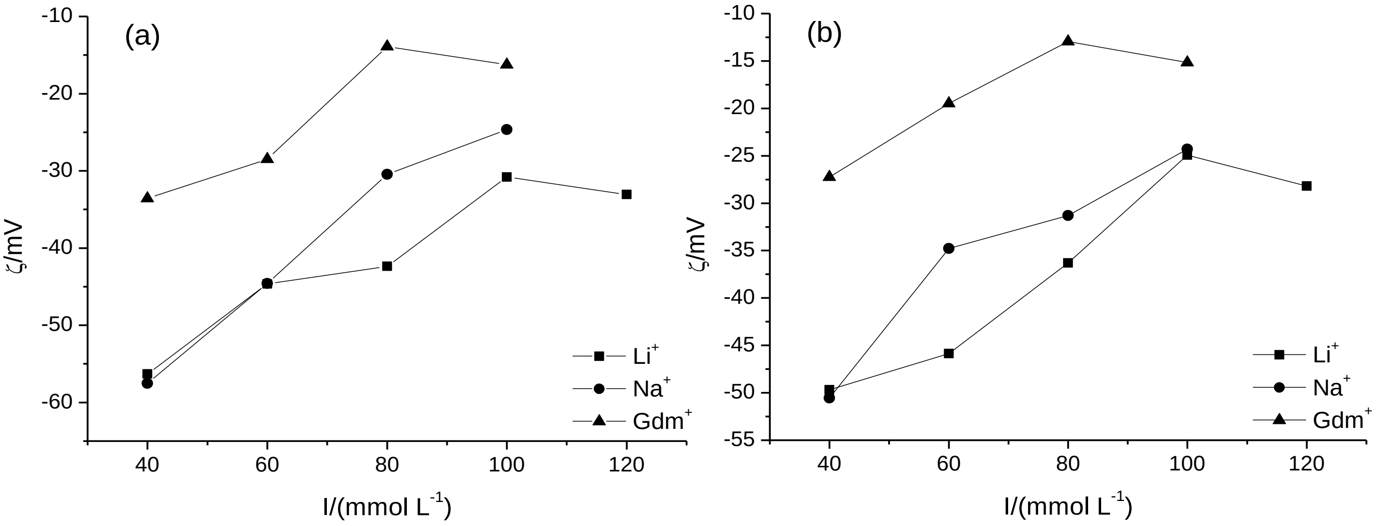

Figure 31: The zeta potential for: (a) PSSL20; and (b) PSSL40 as a function of the ionic strength for different counterions at 20 °C.

Table 10: Illustration of the iterative procedure employed for the determination of $|\zeta|$ via the modified analytic approximation for PSSLs with varied borax concentration at 20°C.

borax conc. (mmol L^{-1})	**κ*a***	$\lvert\mu_{\mathrm{measured}}\rvert$/ (x10^{-8} m^2 s^{-1} V^{-1})	$\lvert\mu_{\mathrm{calculated}}\rvert$/ (x10^{-8} m^2 s^{-1} V^{-1})	$\lvert\zeta_{\mathrm{calculated}}\rvert$/ mV	**PSSL**
15	6.99610	3.22931	3.22915	73.81	**PSSL20**
			3.22933	73.82	
			3.22951	73.83	
20	8.07840	3.21236	3.21217	68.88	
			3.21242	68.89	
			3.21266	68.90	
25	9.03193	3.11533	3.11489	63.02	
			3.11530	63.03	
			3.11561	63.04	
5	7.68035	3.36032	3.36021	78.17	**PSSL40**
			3.36035	78.18	
			3.36050	78.19	
10	10.86166	3.26448	3.26423	64.24	
			3.26455	64.25	
			3.26488	64.26	
15	13.30276	3.23358	3.23321	60.02	
			3.23360	60.03	
			3.23399	60.04	

20	15.36071	3.22753	3.22731	57.95	
			3.22774	57.96	
			3.22817	57.97	
25	17.17379	3.12712	3.12664	54.45	
			3.12711	54.46	
			3.12757	54.47	
5	11.06457	3.74794	3.74786	84.08	**PSSL60**
			3.74800	84.09	
			3.74814	84.10	
10	15.64766	3.68557	3.68506	69.48	
			3.68540	69.49	
			3.68575	69.50	
15	19.16439	3.59987	3.59933	63.79	
			3.59975	63.80	
			3.60017	63.81	
20	22.12913	3.45485	3.45444	58.83	
			3.45491	58.84	
			3.45539	58.85	
25	24.74112	3.27274	3.27243	54.15	
			3.27294	54.16	
			3.27346	54.17	
5	14.66536	3.88628	3.88615	77.81	**PSSL80**
			3.88641	77.82	
			3.88667	77.83	
10	20.73995	3.77239	3.77186	66.75	
			3.77228	66.76	
			3.77270	66.77	
15	25.40115	3.64190	3.64141	61.30	
			3.64189	61.31	
			3.64237	61.32	
20	29.33072	3.46754	3.46685	56.55	
			3.46738	56.56	
			3.46790	56.57	
25	32.79274	3.24804	3.24736	51.76	
			3.24792	51.77	
			3.24848	51.78	

Table 11: Illustration of the iterative procedure employed for the determination of $|\zeta|$ via the modified analytic approximation for PSSL20 and PSSL40 with varied counterion at 20^{o}C.

counterion	**PSSL**	**c(cation)** /(mM)	**κa**	$|\mu_{measured}|$/ (x10^{-8} m^{2}.s^{-1}.V)	$|\mu_{calculated}|$/ (x10^{-8} m^{2}.s^{-1}.V)	$|\zeta_{calculated}|$/ /mV
Li^{+}	**PSSL20**	40	8.06833	2.78838	2.78817	56.29
					2.78850	56.30
					2.78883	56.31
		60	9.87819	2.42103	2.42038	44.63
					2.42082	44.64
					2.42126	44.65
		80	11.43998	2.36900	2.36872	42.34
					2.36920	42.35
					2.36967	42.36
		100	12.76774	1.81113	1.81043	30.79
					1.81098	30.80
					1.81152	30.81
		120	13.96708	1.95588	1.95539	33.06
					1.95593	33.07
					1.95647	33.08
	PSSL40	40	15.34157	2.82669	2.82602	49.67
					2.82648	49.68
					2.82694	49.69
		60	18.78293	2.71923	2.71859	45.84
					2.71910	45.85
					2.71961	45.86
		80	21.75259	2.24487	2.24457	36.30
					2.24514	36.31
					2.24571	36.32
		100	24.27727	1.58760	1.58724	24.91
					1.58786	24.92
					1.58847	24.93
		120	26.55776	1.80249	1.80207	28.19
					1.80268	28.20
					1.80330	28.21
Na^{+}	**PSSL20**	40	8.06127	2.87445	2.87398	57.52
					2.87432	57.53
					2.87467	57.54
		60	9.67612	2.43249	2.43190	44.59
					2.43236	44.60
					2.43281	44.61
		80	11.40336	1.77136	1.77109	30.43
					1.77163	30.44
					1.77218	30.45
		100	12.75435	1.47227	1.47187	24.65
					1.47244	24.66
					1.47301	24.67

	PSSL40	40	15.32814	2.89291	2.89241	50.54
					2.89288	50.55
					2.89336	50.56
		60	18.39869	2.12586	2.12503	34.76
					2.12560	34.77
					2.12616	34.78
		80	21.68296	1.95873	1.95802	31.28
					1.95861	31.29
					1.95921	31.30
		100	24.25181	1.55188	1.55120	24.29
					1.55182	24.30
					1.55244	24.31
Gdm$^+$	**PSSL20**	40	8.07922	1.84799	1.84772	33.55
					1.84821	33.56
					1.84871	33.57
		60	9.91470	1.63441	1.63373	28.47
					1.63427	28.48
					1.63481	28.49
		80	11.29549	0.83042	0.83008	13.90
					0.83067	13.91
					0.83126	13.92
		100	12.60353	0.98125	0.98058	16.25
					0.98117	16.26
					0.98176	16.27
	PSSL40	40	15.36227	1.65479	1.65446	27.23
					1.65504	27.24
					1.65561	27.25
		60	18.85235	1.22341	1.22251	19.48
					1.22312	19.49
					1.22374	19.50
		80	21.47787	0.82800	0.82708	12.95
					0.82771	12.96
					0.82834	12.97
		100	23.96503	0.97510	0.97428	15.14
					0.97492	15.15
					0.97556	15.16

4.2.2.3 Electrokinetic surface charge densities of PSSL

Under the assumption that the nanoparticles are ideal rigid spheres having a uniform distribution of charge on the shear surface, the electrokinetic surface charge density σ_ζ of a charged colloidal particle can be calculated numerically from its ζ potential by using the approximate formula derived by Ohshima *et al.* [24] (see Eq. 24). In Figure 32, the electrokinetic charge densities $\left|\sigma_\varsigma\right|$ are plotted against the ionic strength. The absolute electrokinetic surface charge density $\left|\sigma_\varsigma\right|$ can be assumed to be invariant of the ionic strength within the range of 10–50 mmol L^{-1}, although of there is a small increase in $\left|\sigma_\varsigma\right|$ for each series of PSSL in this range with increasing ionic strength as expected theoretically. Figure 33 shows that $\left|\sigma_\varsigma\right|$ can be regarded to be a constant although there is a random variation in their values in the ionic strength range of 40-120 mmol L^{-1} obtained with borate buffers containing either Li^+, Na^+ or Gdm^+ as counterion. Variation might be attributed to the experimental error due to an inexact determination of the migration time of the nanoparticles zone (refer to Table 11).

Differences in the electrokinetic charge density can be explained to be due to differences in the size of the hydrated cation and the hydration state of the particle surface as was observed with electrokinetic data measurements for dilute aqueous dispersions of amorphous silica nanoparticles of various size with different counterions including Li^+, Na^+, K^+ and Gdm^+ [83]. These results constitute a direct confirmation of Hofmeister effects. The colloidal stability of negatively charged colloidal nanoparticles will decrease in the order $Li^+ > Na^+ > Gdm^+$, at fixed ionic strength. These results follow the same trend with regard to the dependency of the electrokinetic charge density on the type of the counterion as that found with amorphous silica nanoparticles of various size with different counterions [83]. It is, also, expected that the effect of the particle size on the surface charge density can be neglected, regardless of the pH and the ionic strength because the range of the ratio of electrical double layer thickness to the particle diameter of $\lambda_D / d_p < 0.2$ was reached as reported by Barisik *et al.* [80].

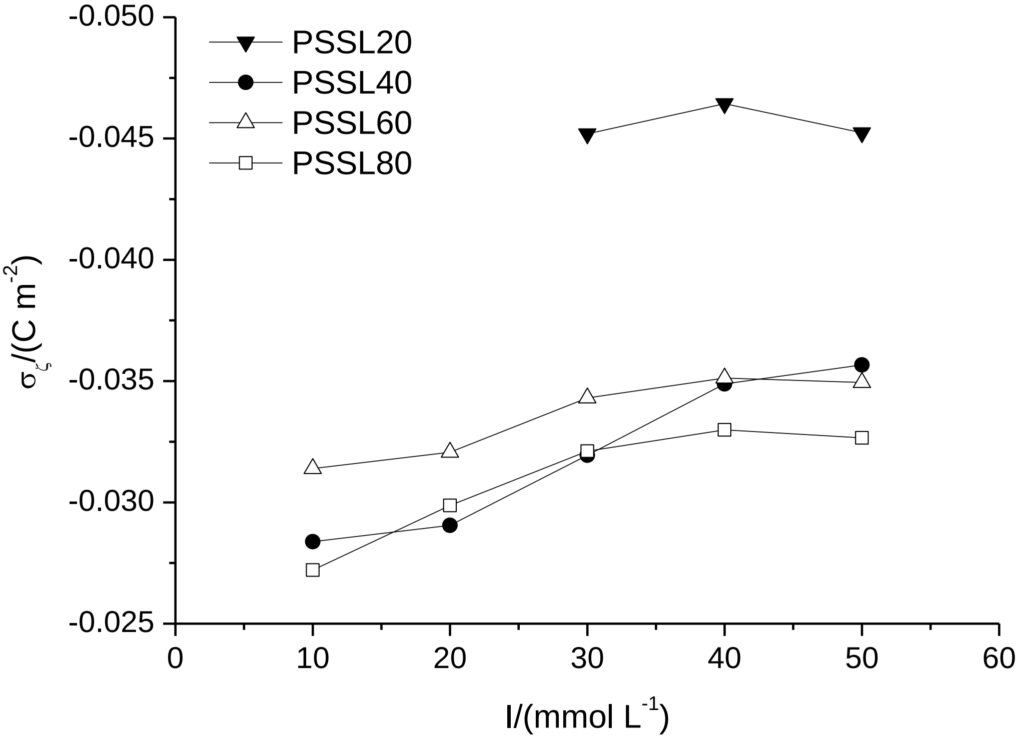

Figure 32: The electrokinetic surface charge densities plotted against the ionic strength (borax buffer) at 20 ^{o}C according to the formula derived by Ohshima (Eq. 15).

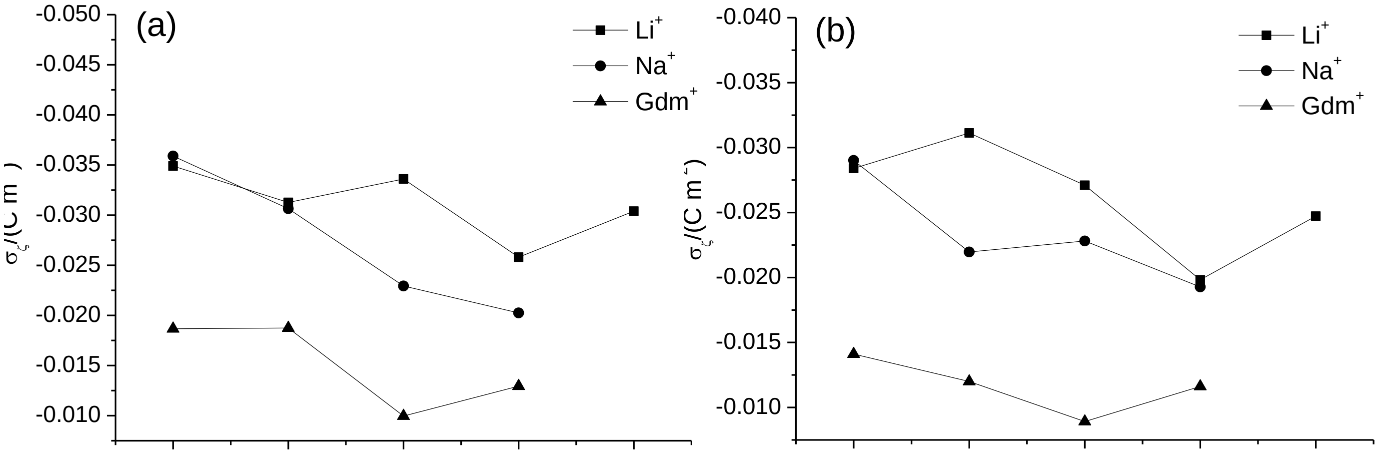

Figure 33: The electrokinetic surface charge densities for: (a) PSSL20; and (b) PSSL40 as a function of the ionic strength with Li^+, Na^+ and Gdm^+ as a counterion at 20 ^{o}C according to the formula derived by Ohshima (Eq. 15).

4.2.3 Calculation of size distribution functions

With TEM or TDA as a second independent method to determine the mean particle radius, an exact determination of the electrokinetic potential ζ by measuring the electrophoretic mobility in an electrolyte of known composition was taken by Pyell [81] and Pyell *et al.* [82] to convert electropherograms obtained from SNPs and coated gold nanopaeticles directly into size distribution functions. The same approach was applied to calculate the size distribution of PSSL of various size according to the procedure described in detail by Pyell and co-authors [71]. Figure 34 shows the cumulative superposition of three runs resulting in a significant improvement of the signal-to-noise ratio. This is the first step to convert electropherograms directly into size distribution functions. Then the recorded electropherograms are converted into a distribution of the intensity-weighted electrophoretic mobility as a second step as shown in Figure 35.

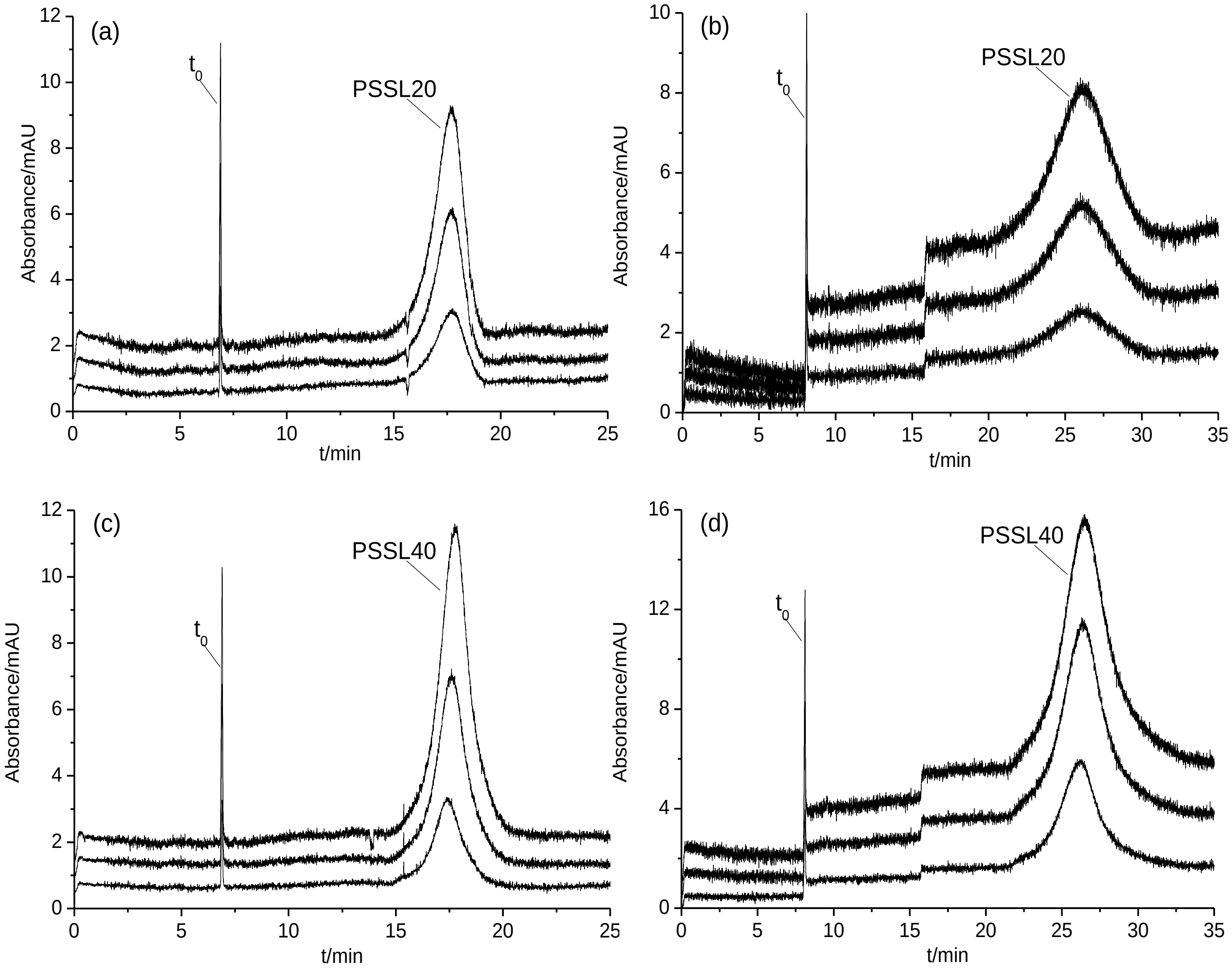

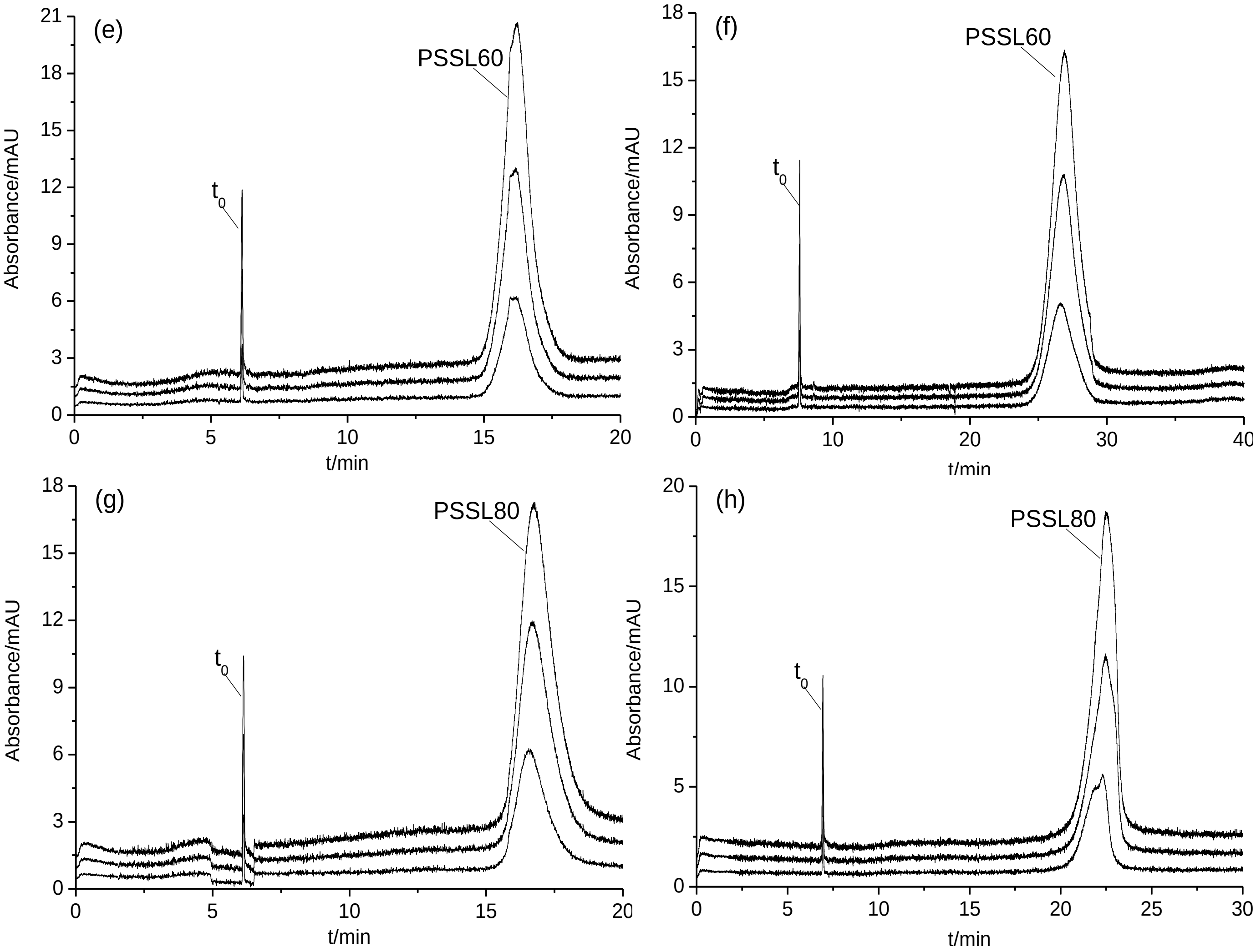

Figure 34: Electropherograms obtained from the superposition of consecutive runs for PSSL with different size with varied borax concentration: (e) and (g) 10 mmol L^{-1}; (a), (c) and (h) 15 mmol L^{-1}; (f) 20 mmol L^{-1}; (b) and (d) 25 mmol L^{-1}, respectively; t_o= thiourea as a neutral marker. For experimental conditions refer to Figure 24.

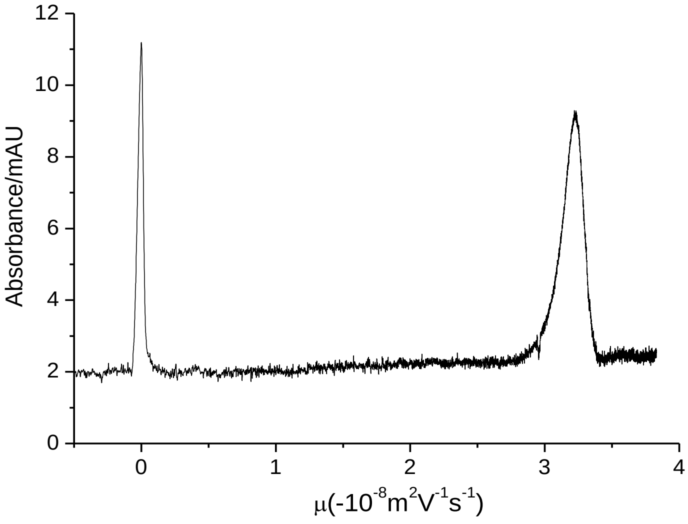

Figure 35: Intensity-weighted distribution of the electrophoretic mobility resulting from the cumulative superposition of different runs (Figure 34) obtained for PSSL20 with 15 mmol L^{-1} borax. For experimental conditions refer to Figure 24.

The third step is converting the mobility trace of the converted electropherograms (x axis in Figure 35) into a size distribution via the regression function $\kappa a = f(\mu)$ or $a = f(\mu)$ with a fixed κ. The regression function was obtained by using Eq. 20 which relates the electrophoretic mobility to the reduced radius κa at a fixed value for ζ. The data points of this regression function were calculated in a range which is expected for the particle size distribution by varying the sphere radius a at fixed κ and ζ. The resulting data points of this regression functions are given in Appendix B7. The fourth step is fitting the trace to Gram-Charlier series A function (see Eq.(30)) after baseline subtraction to obtain the regression parameters listed in Table 12.

Table 12: Calculated parameters obtained via Gram-Charlier series A function for PSSL at 20 °C.

PSSL	**c(borax)/ mmol L^{-1}**	**R**	**μ_1/nm**	**σ/nm**	**k_3**	**k_4**
PSSL20	15	0.99800	23.61(±0.011)	3.269(±0.007)	-0.531	0.228
	25	0.99264	23.40(±0.040)	4.138(±0.020)	-0.445	0.056
PSSL40	15	0.99176	47.84(±0.163)	5.941(±0.013)	0.372	0.382
	25	0.99018	48.39(±0.058)	7.750(±0.024)	0.819	0.429
PSSL60	10	0.99825	70.11(±0.024)	6.208(±0.010)	0.916	0.443
	20	0.99716	68.52(±0.068)	5.901(±0.006)	0.346	0.282
PSSL80	10	0.99946	91.55(±0.026)	10.275(±0.009)	0.482	-0.025
	15	0.99446	88.95(±0.026)	6.347(±0.014)	-0.422	0.500

R = correlation coefficient, standard errors in brackets

As a fifth step, new data points were calculated with a step length of 0.01 nm by using Gram-Charlier series A function and the regression parameters listed in Table 12. In the next step, the data points of the probability density function were weighted with the correction factor d_{max}/d, $d_{max} = d$ at the maximum. The type of detection used will underestimate the fraction of smaller particles and overestimate the fraction of larger particles. Therefore, the apparent absorbance value of each data point of the initially calculated intensity-weighted size distribution was multiplied with a correction factor. Finally, moment analysis was used to calculate the parameters μ_1, σ, k_3, k_4 listed in Table 13.

Under the selected measurement conditions within the ionic strength range (I = 20-50 mmol L^{-1}), estimation of ζ potential (approximately ≥ 60 mV (see Table 13)) from high electrophoretic mobility values (refer to Appendix 5) and corresponding calibration functions are resulting in very large errors with considerable uncertainty. Small deviations in the calculated slope of the calibration line will result in significant errors in the width of the determined size distribution function. In according to the certificates of analysis provided by Molecular Probes, the calculation of the spread of PSSLs from the mean diameter and the coefficient of variation (refer to Appendix B1), is obtained: 3.8 nm for PSSL20, 6.2 nm for PSSL40, 5.0 nm for PSSL60, and 6.6 nm for PSSL80 (see Table 13). These data agree very well with those depicted in Table 13 for σ within expected experimental errors. Apparently that the developed procedure introduced by Pyell *et al.* [82] to calculate the particle size distribution functions has given values could be a reliable as displayed in Table 13. It should be reminded that the absence of electromigration dispersion due to the field strength inhomogeneities and the colloidal stability of the dispersed particles under the measurement conditions are required to estimate the size distribution from converted electropherograms [71].

Table 13: Parameters characterizing the obtained size distribution functions obtained from moment analysis for PSSL at 20 °C and mean diameter obtained from each of TEM and TDA.

PSSL	**c(borax)/ mmol L^{-1}**	**$|\zeta|$ mV**	**σ/ nm**	**k_3**	**k_4**	**μ_1/ nm**	**d_{TEM}/ nm**	**d_{TDA}/ nm**	**σ_{TEM}/ nm**
PSSL20	15	73.82	3.618	-0.571	-0.337	22.50	21	24.62	3.8
	25	63.03	4.507	-0.458	-0.040	22.32			
PSSL40	15	60.03	6.352	-0.093	0.102	45.40	41	46.81	6.2
	25	54.46	8.183	0.151	0.461	44.64			
PSSL60	10	84.09	6.489	0.258	0.570	67.63	63	67.44	5.0
	20	58.84	6.191	-0.031	0.111	66.78			
PSSL80	10	77.82	9.941	0.607	-0.127	90.65	80	89.38	6.6
	15	61.31	6.896	-0.655	-0.685	86.28			

4.3 Cobalt oxyhydroxide nanoparticles

4.3.1 Preliminary investigations

Cobalt oxyhydroxide nanoparticles (CoOOH-NPs) have a positive charge on their surface. Preliminary investigations for CoOOH-NPs were made with borax buffer (pH 9.2) to prepare a dispersed solution, which did not result in a successful peptization of the precipitate. Therefore, the solubility of CoOOH-NPs was tested with an aqueous solution of HCl at low pH. The preliminary investigations regarding the behavior of CoOOH-NPs indicate that peptization is only possible at low pH.

Figure 36 illustrates the decrease in the colour intensity for a 10 mmol L^{-1} HCl solution. Firstly the brownish turbid solution of CoOOH-NPs was homogenized by shaking the original stock solution. This colour corresponds to the dark brown of CoOOH-NPs, which passes within 10 minutes into a clear brown solution. With the time, in the CoOOH-NPs solution appears a slow discoloration to yellow and then to colorless. Within this process, the solution remains clear. There is neither visible precipitation nor turbidity.

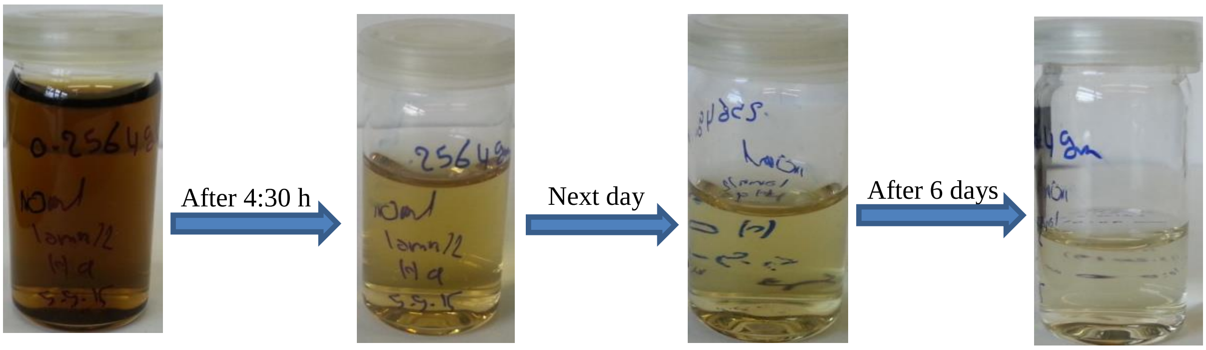

Figure 36: The decrease in colour intensity of CoOOH-NPs in 10 mmol L^{-1} HCl electrolyte at pH 2.0 and room temperature.

At pH 4.0, the CoOOH-NPs dispersion shows a fast aggregation of the nanoparticles followed by a precipitation of the aggregates. This behavior of aggregation and precipitation was observed for different HCl concentrations (e.g. 1.0, 3.0 and 5.0 mmol L^{-1}). Based on these observations, in subsequent experiments dispersion of the CoOOH-NPs was made in an aqueous solution of a monoprotic acid at a molar concentration of 10 mmol L^{-1} at pH 2.0 and at a temperature of 25 ^{o}C following monoprotic acids were used in further studies: HCl, HNO_3, and methanesulfonic acid (MSA). These acids are strong acids that differ in the complex formation properties of the formed anion. Studies with different monoprotic acids aim act quantifying the impact of surface complexation on the dissolution process.

In Figure 37, the pH of the solution (determined with a pH combination electrode) is plotted as a function of the time (at a fixed concentration of CoOOH-NPs) for different starting concentrations of HCl. As expected the pH increases as the concentration of HCl solution decreases. This increase in pH can be attributed to a decrease in the concentration of H^+ ions in the aqueous solution due to the dissolution of the CoOOH-NPs. The Co^{3+} ion is a powerful oxidizing agent since it liberates oxygen from water and is reduced to Co^{2+} [85].

$$\overset{3+}{Co}OOH \; + \; 3\,H^{+} \; \rightarrow \; Co^{3+}_{(aq)} + \; 2\,H_2O$$

$$4\,Co^{3+}_{(aq)} \; + \; 2\,H_2O^{-2} \; \rightarrow \; 4\,Co^{2+}_{(aq)} \; + \; \overset{0}{O}_2 \; + 4\,H^{+}$$

$$Co^{3+}_{(aq)} \; + \; e^{-} \; \rightarrow \; Co^{2+}_{(aq)} \qquad\qquad E^{o} \; = \; +1.81\,V$$

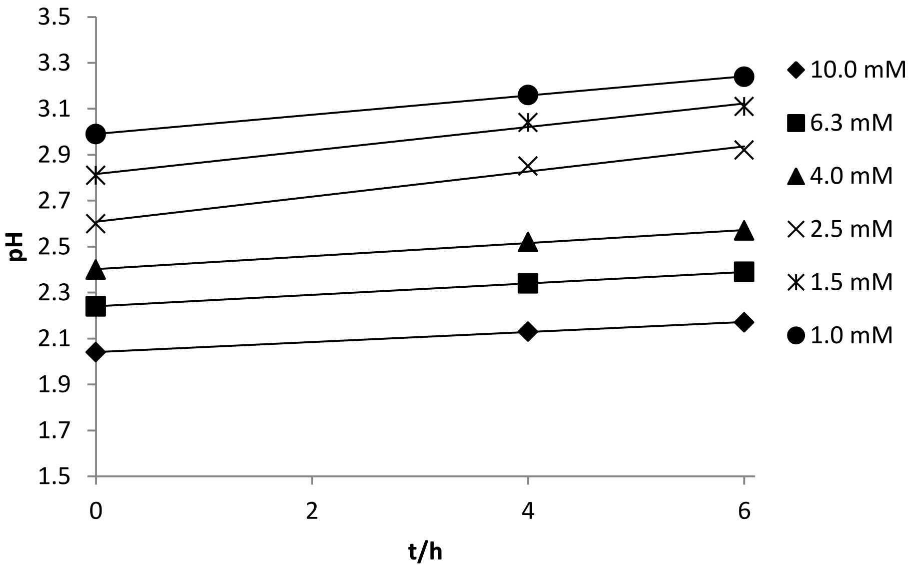

Figure 37: Measurements of pH for CoOOH-NPs in different HCl concentrations as a function of time at room temperature.

4.3.2 UV-Visible spectroscopy

UV/Vis spectroscopy was used to study the spontaneous dissolution of the CoOOH-NPs under the conditions selected. The experimental results depicted in Figure 38 confirm a monotonous decrease in the absorbance (at fixed wavelength) observed for the dispersion of CoOOH-NPs when plotting the absorbance against the time. The results were fitted to a mono-exponential decay function. During the dissolution process, the peak due to the CoOOH-NPs will decrease and broaden with the time observed as decrease in colour intensity of the solution. Maximum wavelengths of CoOOH-NPs with Cl^-, NO_3^- and $CH_3SO_3^-$ are: 358 (0.50%) nm; 360 (0.87%) nm and 362 (0.57%) nm, respectively. RSD represented in brackets. Hence, the absorbance spectrum can be regarded to be independent of the type of anion.

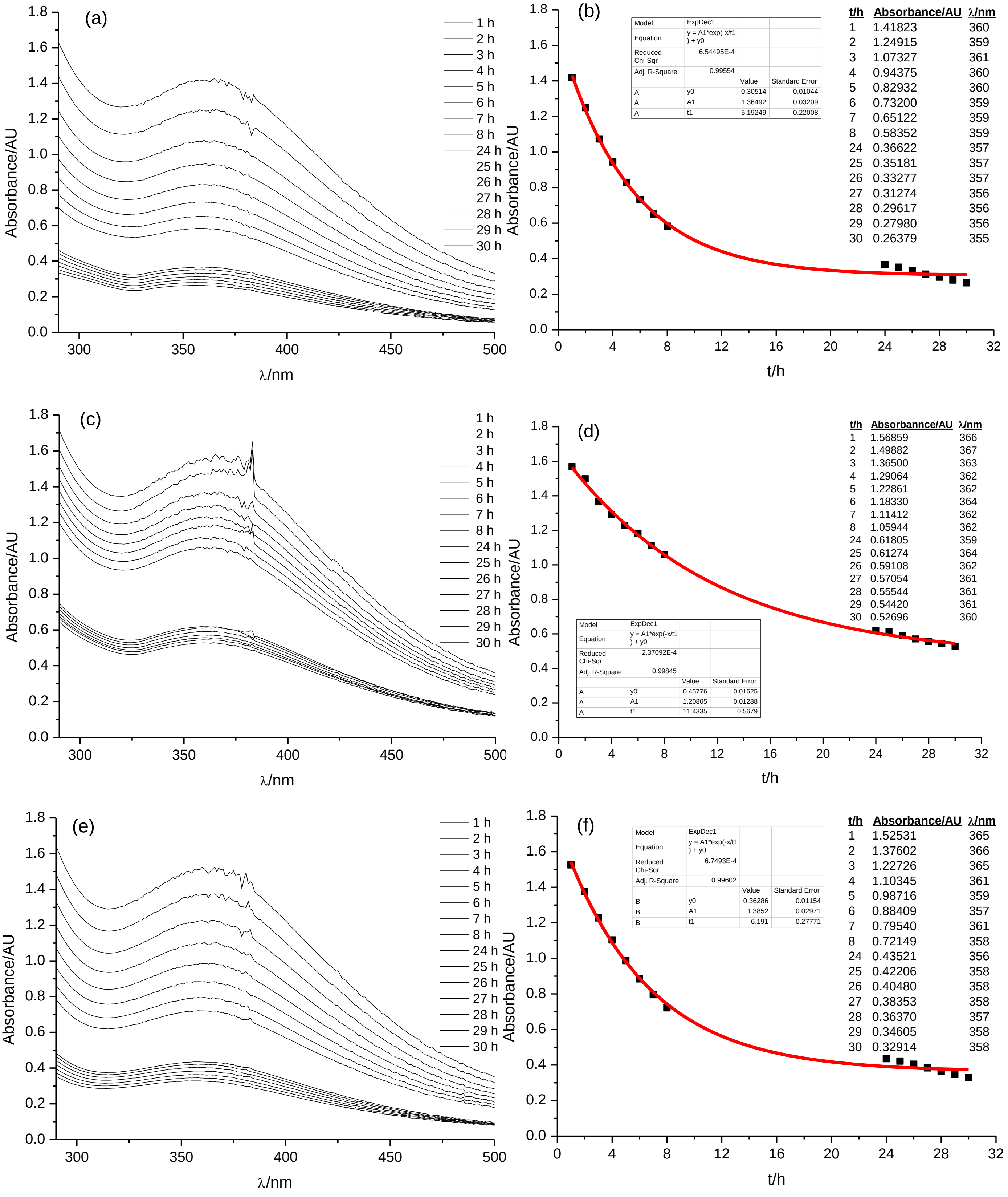

(b)

Model	ExpDec1		
Equation	y = A1*exp(-x/t1) + y0		
Reduced Chi-Sqr	6.54495E-4		
Adj. R-Square	0.99554		
		Value	Standard Error
A	y0	0.30514	0.01044
A	A1	1.36492	0.03209
A	t1	5.19249	0.22008

t/h	Absorbance/AU	λ/nm
1	1.41823	360
2	1.24915	359
3	1.07327	361
4	0.94375	360
5	0.82932	360
6	0.73200	359
7	0.65122	359
8	0.58352	359
24	0.36622	357
25	0.35181	357
26	0.33277	357
27	0.31274	356
28	0.29617	356
29	0.27980	356
30	0.26379	355

(d)

t/h	Absorbannce/AU	λ/nm
1	1.56859	366
2	1.49882	367
3	1.36500	363
4	1.29064	362
5	1.22861	362
6	1.18330	364
7	1.11412	362
8	1.05944	362
24	0.61805	359
25	0.61274	364
26	0.59108	362
27	0.57054	361
28	0.55544	361
29	0.54420	361
30	0.52696	360

Model	ExpDec1		
Equation	y = A1*exp(-x/t1) + y0		
Reduced Chi-Sqr	2.37092E-4		
Adj. R-Square	0.99845		
		Value	Standard Error
A	y0	0.45776	0.01625
A	A1	1.20805	0.01288
A	t1	11.4335	0.5679

(f)

Model	ExpDec1		
Equation	y = A1*exp(-x/t1) + y0		
Reduced Chi-Sqr	6.7493E-4		
Adj. R-Square	0.99602		
		Value	Standard Error
B	y0	0.36286	0.01154
B	A1	1.3852	0.02971
B	t1	6.191	0.27771

t/h	Absorbance/AU	λ/nm
1	1.52531	365
2	1.37602	366
3	1.22726	365
4	1.10345	361
5	0.98716	359
6	0.88409	357
7	0.79540	361
8	0.72149	358
24	0.43521	356
25	0.42206	358
26	0.40480	358
27	0.38353	358
28	0.36370	357
29	0.34605	358
30	0.32914	358

Figure 38: UV-Vis absorbance spectra of dispersions of CoOOH-NPs in 10 mmol L^{-1} (a) HCl; (c) HNO_3; and (e) MSA at a starting pH of 2.0 and a temperature of 25 °C (no temperature control overnight). The second column depicts the fitting functions obtained for dispersions of CoOOH-NPs in 10 mmol L^{-1} (b) HCl; (d) HNO_3; and (f) MSA. Fitting of absorbance at band maximum against time.

For all anions, the maximum wavelength decreases slightly with time. Comparison of the results obtained for chloride, nitrate or $CH_3SO_3^-$ as counterion shows that the type of anion only has a marginal influence on the dissolution process, as the recorded lines are very similar. In addition, there is a good agreement between the experimental data and the fitting line of a mono-exponential decay function. There is a better agreement in the case of NO_3^- (Figure 38c+d) than in the cases of Cl^- or $CH_3SO_3^-$ (Figure 38a+b and e+f). The change in the absorbance at the band maximum over time was also monitored when using different mass fractions of CoOOH-NPs as shown in Figure 39. The observations indicate that the decrease in the absorbance follows the same trend.

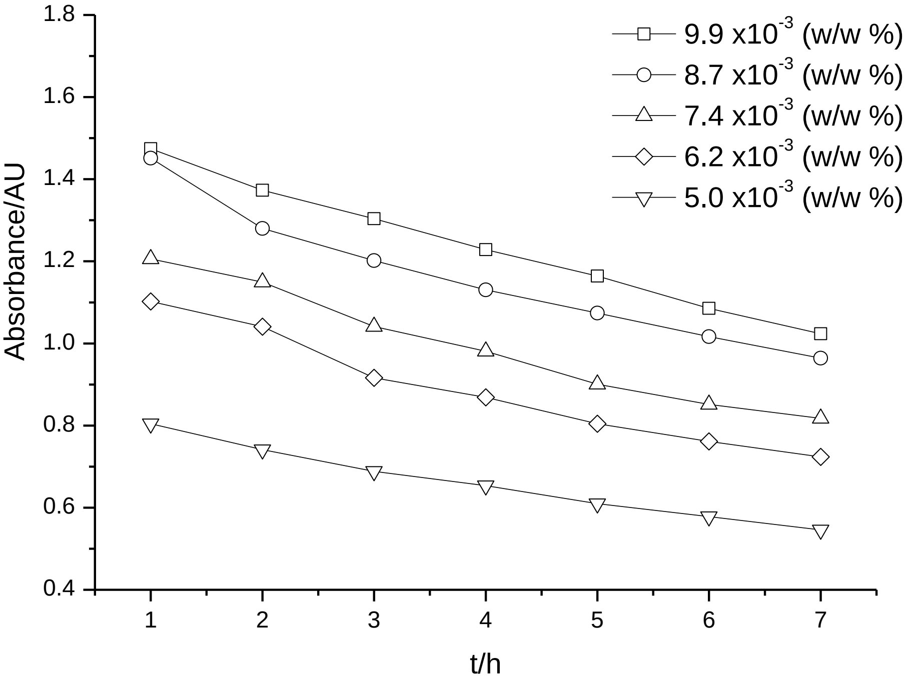

Figure 39: Decrease of UV-Vis absorbance at the band maximum with time in different mass fraction of CoOOH-NPs dispersion in 10 mmol L^{-1} HNO_3 at pH 2.0 and ambient temperature.

Reaction rate constants for each of Cl^-, NO_3^- and $CH_3SO_3^-$ anions are obtained directly from the recorded spectra. Data treatment assumes a consecutive or sequential reaction [86]. A two-step mechanism where an intermediate from the first step is consumed in the second step. Both steps are assumed are modeled as pseudo first-order reaction with negligible reverse reaction rate. Because H_2O is present in large excess, the equation of the pseudo first-order reaction for the dissolution of CoOOH-NPs can be:

$$CoOOH\ +3\,\mathrm{H}^{+}\xrightarrow{k_1}Co^{3+}_{(aq)}+2\,H_2\mathrm{O}\xrightarrow{k_2}Co^{2+}_{(aq)}+\ 1/4\,O_2\ +H^{+}+\ 3/2\,H_2O$$

where k_1 is the rate constant for the first step and k_2 is the rate constant for the second step. The second step is assumed to be slower than the first step. However, spectroscopically only the first step is monitored.

The differential rate laws are:

$$-\frac{d[A]}{dt} = k[A]$$

where the square brackets denote molar concentrations, A in brackets is the concentration of reactant A, k is the reaction rate constant (k_1 for first step and k_2 for second step) and t is time. The negative sign indicates that the concentration reduced over time (A is consumed). Accordingly, the decrease in the absorbance E due to the dissolution of CoOOH-NPs with time ($-\frac{dE}{dt}$) can be related to the decrease in the concentration over time ($E = const. \cdot [A]$). Therefore, the differential rate law can be written:

$$-\frac{dE}{dt} = k_1 E$$

After rearrangement and integration, this equation is converted to:

$$\ln\left(\frac{E_{(t)}}{E_0}\right) = -k_1 t \qquad \underline{\text{OR}} \qquad \ln\left(\frac{E_0}{E_{(t)}}\right) = k_1 t$$

where $E_{(t)}$ is the absorbance at time t and E_0 is the absorbance at time 0. Plotting $\ln(E_0 / E_{(t)})$ with respect to time gives a straight line as shown in Figure 40 with the slope of the line equal to (k) in unit s^{-1} or min^{-1}. Another form of the previous equation follows an exponential law:

$$E_{(t)} = E_0 \, e^{-k_1 t}$$

Furthermore, Figure 40 illustrates the assumption of a pseudo first-order reaction to get the values of the reaction rate constant for the first step (k_1) from the slope by fitting the experimental data using linear regression. Values of the reaction rate constant for CoOOH-NPs: 2.13 x10^{-3} min^{-1} for Cl^-; 9.34 x10^{-4} min^{-1} for NO_3^- and 1.80 x10^{-3} min^{-1} for $CH_3SO_3^-$. According to the rate constants calculated for the dispersed CoOOH-NPs following "order of stability" can be deduced: $NO_3^- > CH_3SO_3^- > Cl^-$.

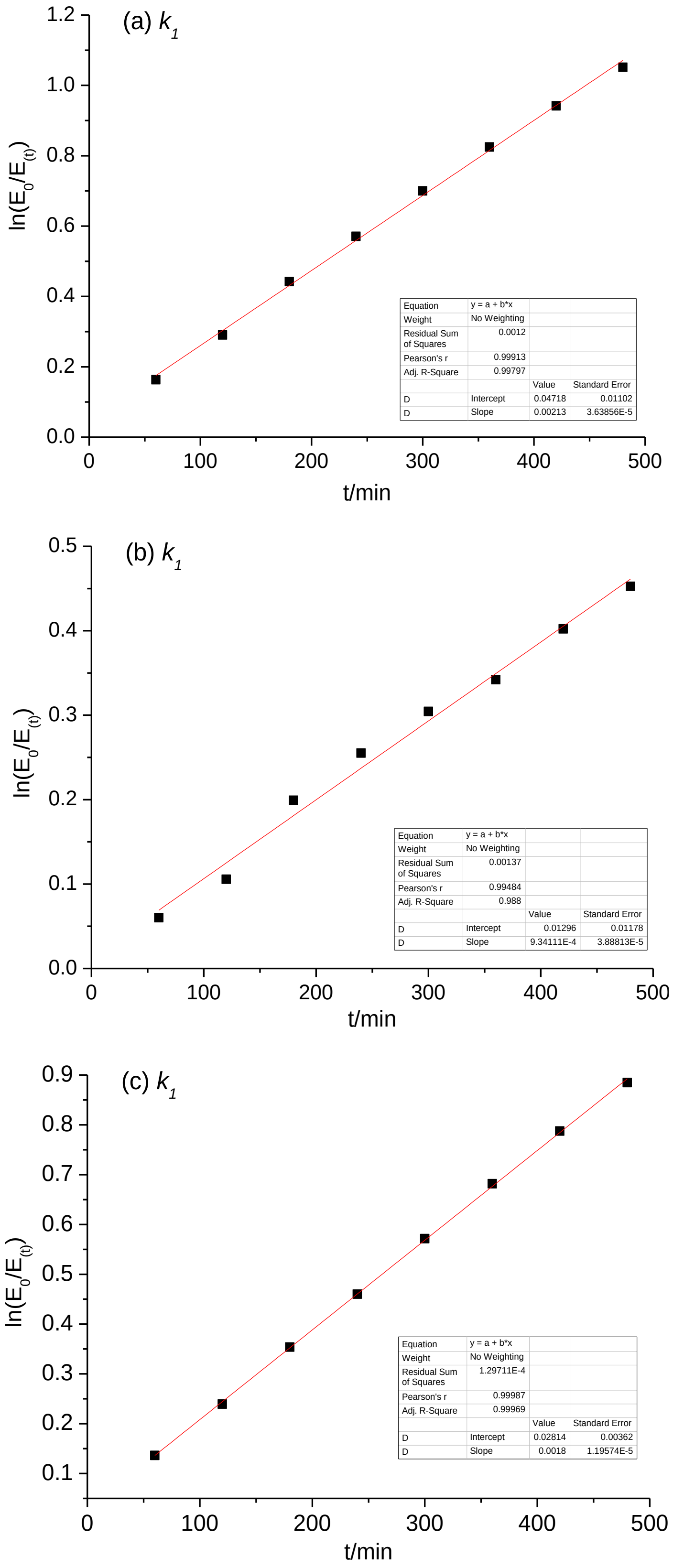

Equation	y = a + b*x		
Weight	No Weighting		
Residual Sum of Squares	0.0012		
Pearson's r	0.99913		
Adj. R-Square	0.99797		
		Value	Standard Error
D	Intercept	0.04718	0.01102
D	Slope	0.00213	3.63856E-5

Equation	y = a + b*x		
Weight	No Weighting		
Residual Sum of Squares	0.00137		
Pearson's r	0.99484		
Adj. R-Square	0.988		
		Value	Standard Error
D	Intercept	0.01296	0.01178
D	Slope	9.34111E-4	3.88813E-5

Equation	y = a + b*x		
Weight	No Weighting		
Residual Sum of Squares	1.29711E-4		
Pearson's r	0.99987		
Adj. R-Square	0.99969		
		Value	Standard Error
D	Intercept	0.02814	0.00362
D	Slope	0.0018	1.19574E-5

Figure 40: Reaction rate constants obtained from plot $\ln(E_0 / E_{(t)})$ versus time t from UV-Vis spectroscopy measurements assumed as pseudo first-order reaction for: (a) HCl; (b) HNO_3; and (c) MSA. Experimental conditions (refer to Figure 38).

In the dissolution of CoOOH-NPs at pH 2.0 with different acids can be assumed that the acid anion primarily reacts with the surface O-H groups followed by a proton attack yielding surface protonation. The "neutralization" of the surface O-H groups with protons of the solution will destabilize the crystal lattice, which results in the detachment of the Co^{3+} cation that enters (primarily as the hexaquocobalt(III) complex) into the solution [87]. Typically, Co^{3+} complexes are octahedral complexes (d^6 electron configuration), which makes them kinetically inert towards ligand exchange. This means that the ligand is not labile and the ligand exchange reaction takes significantly longer time than that of labile complexes ($t_{1/2} \leq 1$ min.; $t_{1/2}$ = half-life of the reaction) at 25 ^{o}C [88]. The values of $t_{1/2}$ of pseudo first-order reaction for CoOOH-NPs in different anions acid are: 325 min for Cl^-; 742 min for NO_3^-; and 385 min for $CH_3SO_3^-$. The $t_{1/2}$ values are calculated via $t_{1/2} = (\ln 2)/k$ (k is the rate constant of the pseudo first-order reaction).

The influence of the anion of the acid affecting the dissolution process of CoOOH-NPs can be attributed to their complexing ability influencing the CoOOH-NPs surface [89]. For example, the Cl^- ions have a higher complexing ability to form complexes than the NO_3^- ions to form cobalt–comlpexes [89]. Therefore, the dissolution rate increases in the presence of HCl compared to that in the presence of HNO_3.

As mentioned above Co^{3+} in aqueous solution containing no complexing agent is very instable and Co^{3+} reduces to Co^{2+} producing O_2. To prove this, the sample of CoOOH-NPs was dissolved in 10 mmol L^{-1} HCl. The dispersion solution has been left several days until it had been become completely colorless or nearly colorless, due to the dissolution process. After that, this solution was tested with a few drops of a saturated solution of sodium thiocyanate in acetone. The results are documented in Figure 41a. A green to blue colouration appears owing to the formation of tetrathiocyanatocobaltate (II) according to:

$$Co^{2+}_{(aq)} + 4\,SCN^{2+}_{(aq)} \rightarrow \left[Co\left(SCN\right)_4\right]^{2-}_{(aq)}$$

Also, the sample of CoOOH-NPs, after dissolving in 10 mmol L^{-1} HCl, tested with 0.1 M NaOH. The results are depicted in Figure 41b. With the increased the amount of NaOH, an insoluble precipitate was formed. This is attributed due to the peptized CoOOH-NPs solution reprecipitated with increasing pH [90]:

$$CoOOH_{peptized} \rightarrow CoOOH\,)_{precipitated}$$

Figure 41c shows a formation of insoluble cobalt hydroxide precipitates by removing hydrogen ions from acidic CoOOH-NPs solution via reacting with ammonia solution:

$$Co^{2+}_{(aq)} + 2\,OH^{-} \rightarrow Co(OH)_2$$

Figure 41 consists of three parts (a, b and c). Each part includes two pictures, one on the left and another on the right. The pictures on the left show the solution at the beginning of the reaction. The pictures on the right display the result of the reaction.

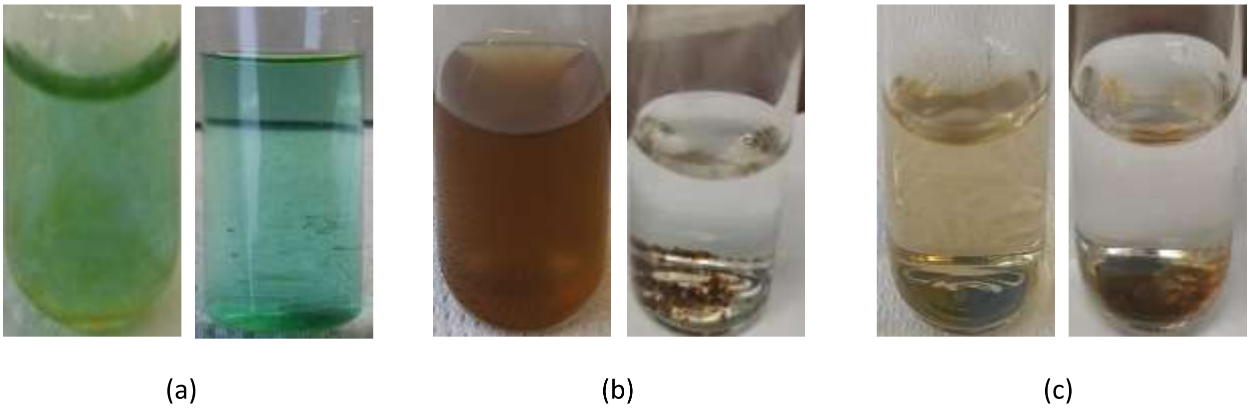
(a) (b) (c)

Figure 41: Experimental testing results of CoOOH-NPs dissolved in 10 mmol L^{-1} HCl (pH 2.0 and at ambient temperature) with: (a) saturated solution of sodium thiocyanate in acetone; (b) 0.1 M NaOH; and (c) ammonia solution.

4.3.3 Capillary coating

The inner surface of the untreated fused-silica capillaries possesses a negative charge due to the presence of dissociated silanol groups at its surface. These groups are immobilized on the surface as a polyanion, having an ionization constant pKa between 2 and 9 [91]. Positively charged solutes or particles can be adsorbed via electrostatic forces. Adsorption of the NPs onto the capillary wall will produce band-broadening, asymmetry and non-reproducible migration times. CoOOH-NPs dispersed by peptization in acidic solution have a positive charge surface. Therefore, strategies must be developed with the aim to eliminate their adsorption onto the inner wall and minimize interactions with the wall. These strategies are focused on changing the sign of the surface charge density of the inner capillary wall. To this end, different strategies have been employed for the coating of capillaries by either a static or a dynamic method of attachment of the coating onto the capillary wall surface. Static coatings can be either covalently anchored or statically adsorbed onto the silica surface, which eliminates the need to add the coating agent into the background electrolyte (BGE), while dynamic coatings involve weaker adsorptive interactions of the coating agent (a polyelectrolyte, a double-chained detergent or a multivalent ion), which is added to the BGE to obtain a constant density of the coating via dynamic equilibrium.

(A) Static, covalently attached (also denoted: permanent) capillary wall coating typically is produced via two steps. In the first step, double bonds covalently fixed to the capillary wall are introduced by rinsing the capillary with a bifunctional reagent such as γ-methacryloxy propyl trimethoxy silane to form a sub-layer [92]. The surface silanol groups react with one or two of the methoxysilane groups of the reagent, the other functional group (methacrylate group) is used to attach the coating agent to the capillary. In the second step, a monomer such as diallyldimethylammonium chloride (DADMAC) is polymerized via free radical polymerization incorporating the methacryloxy group of the previously immobilized bifunctional reagent into the formed polymeric chain. This procedure gives a thin layer of a polymer covalently bound to the capillary wall. Figure 42 represents the scheme of covalently capillary wall coating. DADMAC is a quaternary ammonium compound having two allyl groups as functional groups. The polymer of DADMAC (PDADMAC), as shown in Figure 43, has a cyclic pyrrolidinium structure unit. Alternating intra-intermolecular chain propagation (cyclopolymerization) is obtained by the free radical polymerization with ammonium persulfate (APS) in water. The size of the ring structure that can be formed determines whether intermolecular polymerization or intramolecular cyclization is the predominant reaction. PDADMAC consists exclusively of five-membered rings [93].

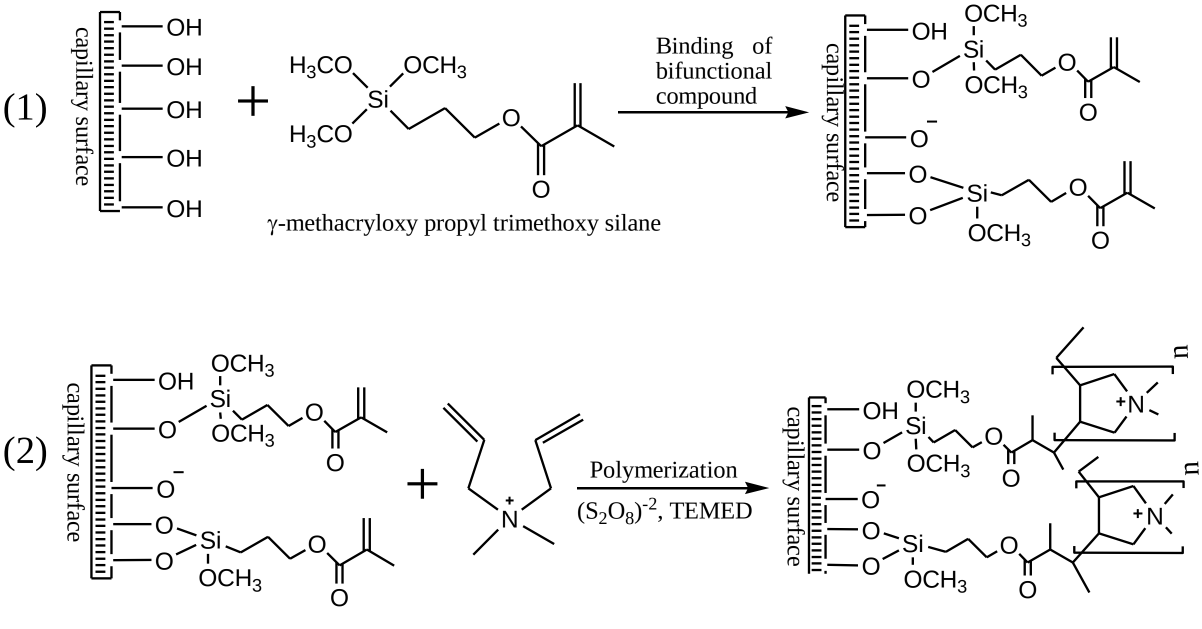

Figure 42: Schematic for the polymerization of DADMAC monomer for producing a covalently coated capillary.

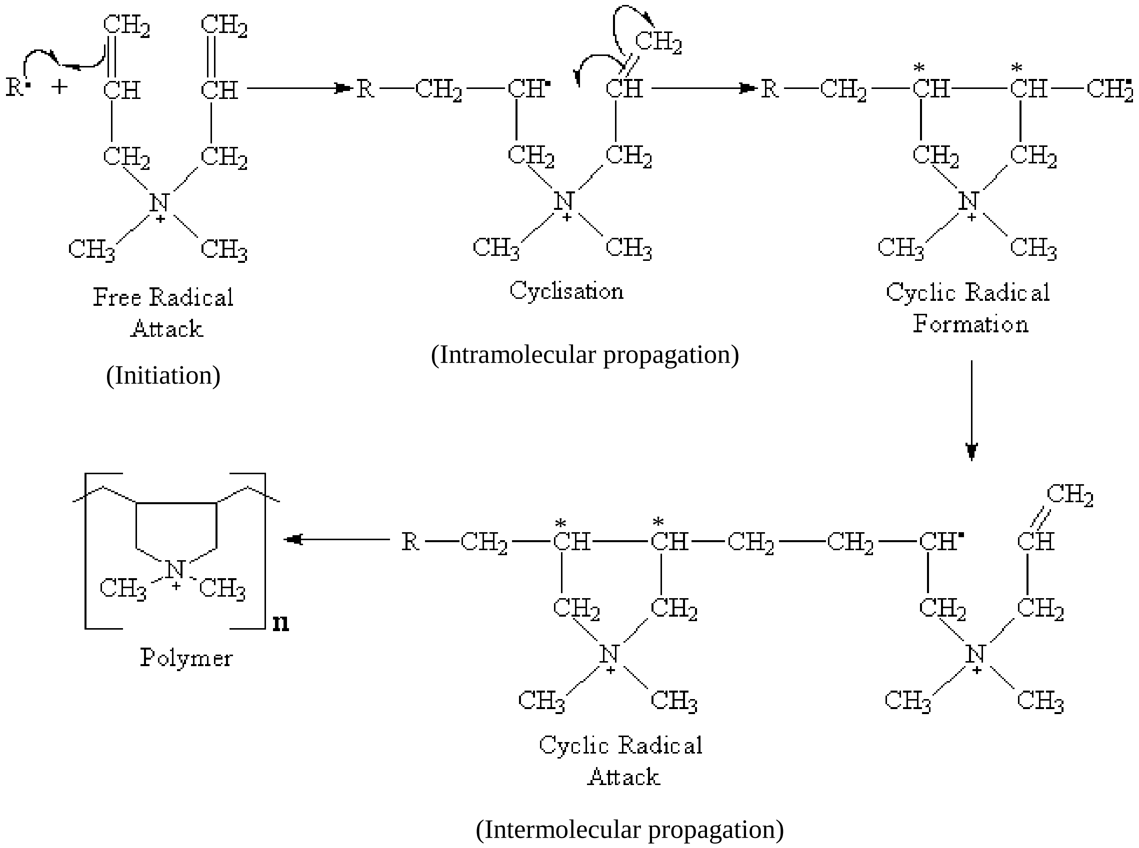

Figure 43: Reaction mechanism for the polymerization of DADMAC to form the five-member pyrrolidinium ring system [94].

(B) Statically adsorbed capillary wall coating is performed by using one or two highly charged high-molecular weight polymers (polyelectrolytes) to obtain coating of the capillary wall with a cationic monolayer such as poly(diallyldimethylammonium) chloride (PDADMAC) [95] or with successive multiple ionic polymer layers (SMIL) in which a cationic polymer is sandwiched between an anionic polymer and the uncoated negatively charged fused-silica capillary [96]. This coating procedure is very simple since it consists of rinsing the capillary with the appropriate solution of a polycationic polymer to obtain a monolayer coating or alternately first with a solution of a polycationic and then with a solution of a polyanionic polymer to obtain a SMIL coating, which adheres strongly to the negatively charged capillary. Figure 44 illustrates how capillary coating with a monolayer or a SMIL coating is achieved. SMIL can increase to several layers by rinsing the capillary successively (and alternately) with solutions containing either a cationic or an anionic polymer to make the capillary wall positively or negatively charged.

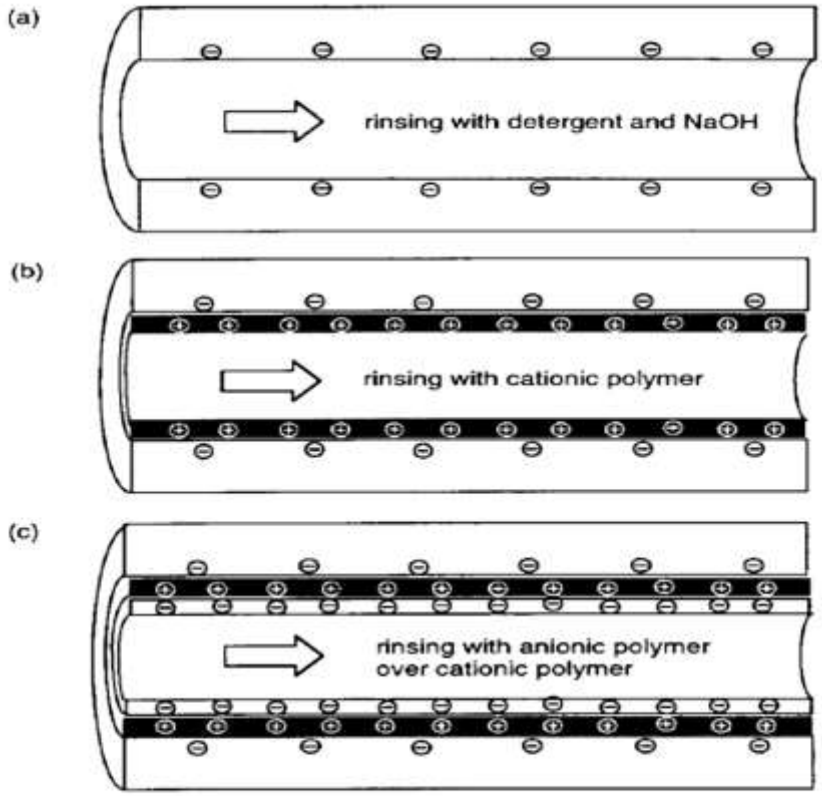

Figure 44: Static coating procedure with polyelectrolytes. (a) Activation of the silanol groups; (b) first layer coating; (c) second layer coating (SMIL coating) [96].

(C) Dynamic coating was examined with didodecyldimethyl ammonium bromide (DDAB), which is a cationic double-chained surfactant that provides a homogeneous cationic bilayer coating of the capillary wall preventing adsorption (see Figure 45B). Ideally, the geometry of the surfactant molecule should be cylindrical in shape such as DDAB to form a homogeneous bilayer [97]. If the surfactant geometry is conical in shape, such as with single-chained surfactants (e.g., cetyltrimethylammonium bromide, CTAB), the surfactant will form spherical micelles which cannot provide a complete surface coverage (see Figure 45A) [98].

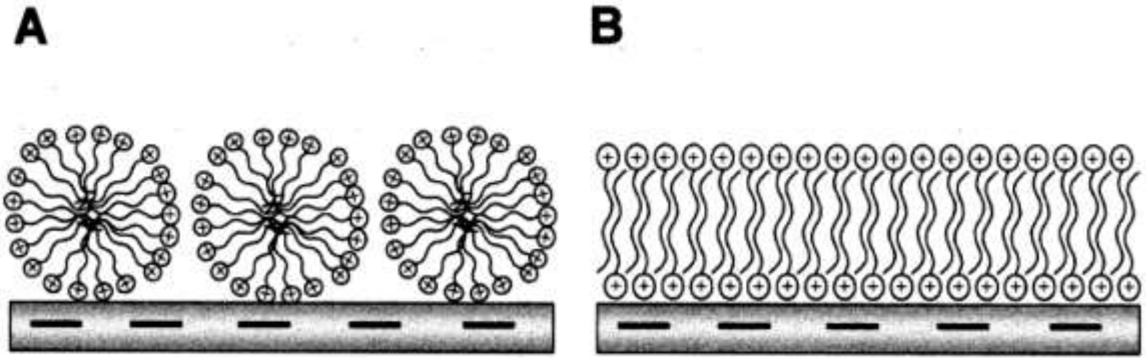

Figure 45: Structures previously depicted for surfactant aggregates at the capillary wall with (A) CTAB or (B) DDAB [99].

With this type of coating, the solution of a surfactant is rinsed through the capillary to form a noncovalent dynamic wall coating. Between the runs, the capillary can be regenerated to maintain a reproducible EOF. The excess of the surfactant is flushed out of the capillary prior to the measurement and replaced with the run BGE solution which does not contain the surfactant, thereby eliminating unwanted interactions such as ion-pairing between the analyte and the surfactant molecule [100,68]. On the other hand, after the run the coating can be removed and then regenerated.

4.3.4 Taylor dispersion analysis

To avoid the adsorption of CoOOH-NPs onto the capillary wall (due to their positive charge) different coating procedures were examined, namely covalently attached coating or SMIL coating. The experimental results are depicted in Figure 46. This Figure shows the impact of the reaction time on the recorded taylorgrams and on the resulting mean hydrodynamic diameter (obtained with two different coatings).

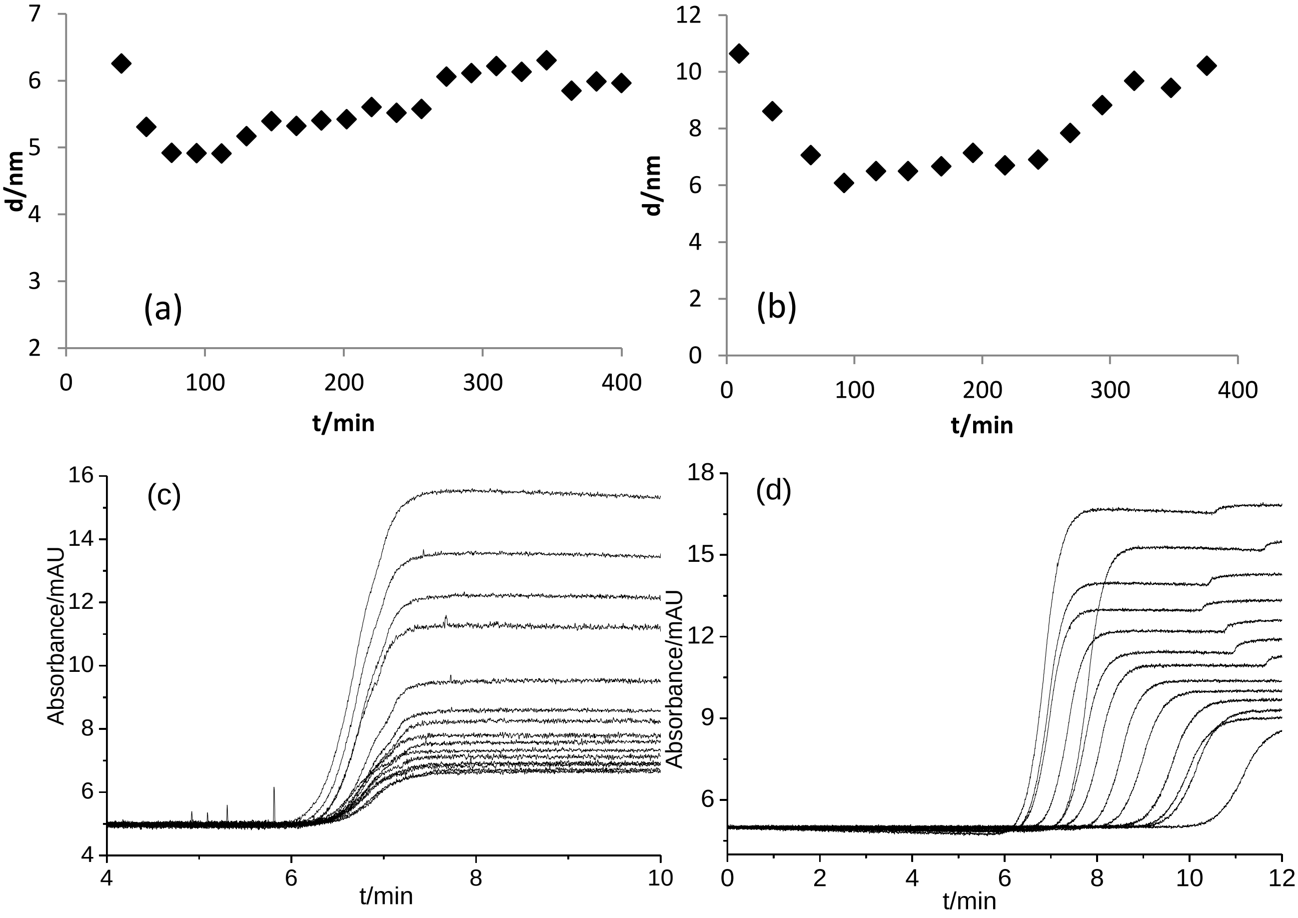

Figure 46: TDA measurements for CoOOH-NPs dissolved in 10 mmol L^{-1} HCl with coated capillary wall: (a) covalently bonded and (b) SMIL. Decrease in the absorbance of CoOOH-NPs with time was obtained from TDA measurements by using: (c) covalently coating, and (d) SMIL coating. Experimental conditions: fused-silica capillary (76 µm I.D., 363.5 µm O.D.); total length of the capillary was 39.5 cm and the length to the detector 29.2 cm; T = 25 ^{o} C; frontal method; pressure difference = 0.2 psi (13.8 mbar) 6 s; and absorbance detection at 254 nm.

The results reveal that there is a measurable initial decrease in the mean size of the CoOOH-NPs (in accord with the assumed dissolution process) followed after about 70-100 min by a significant increase of the determined mean particle size. Also, the recorded taylorgrams resulting from using SMIL coating as shown in Figure 46d show a deviation from the typical shape. This might be attributed to the interaction between the coating agent and CoOOH-NPs. Therefore, subsequent TDA measurements of CoOOH-NPs with Cl^-, NO_3^-, and $CH_3SO_3^-$ anions as counterion were made with the covalent capillary coating.

The stability of the covalent coating was examined with thiourea as a neutral marker. The experimental results are represented in Figure 47. Recorded taylorgrams show a good repeatability for five repeated runs (refer to Figure 47a). This repeatability gives an indication about the stability of the covalently bonded inner capillary coating. Recorded taylorgrams are fitted to the cumulative Gaussian function (Eq. 26) by non-linear regression (Figure 47b). An excellent accordance between the recorded taylorgram of thiourea (black line) and the fitting line (red line) resulting from the cumulative Gaussian function gives a typical S-like shape with a correlation coefficient of 0.99996.

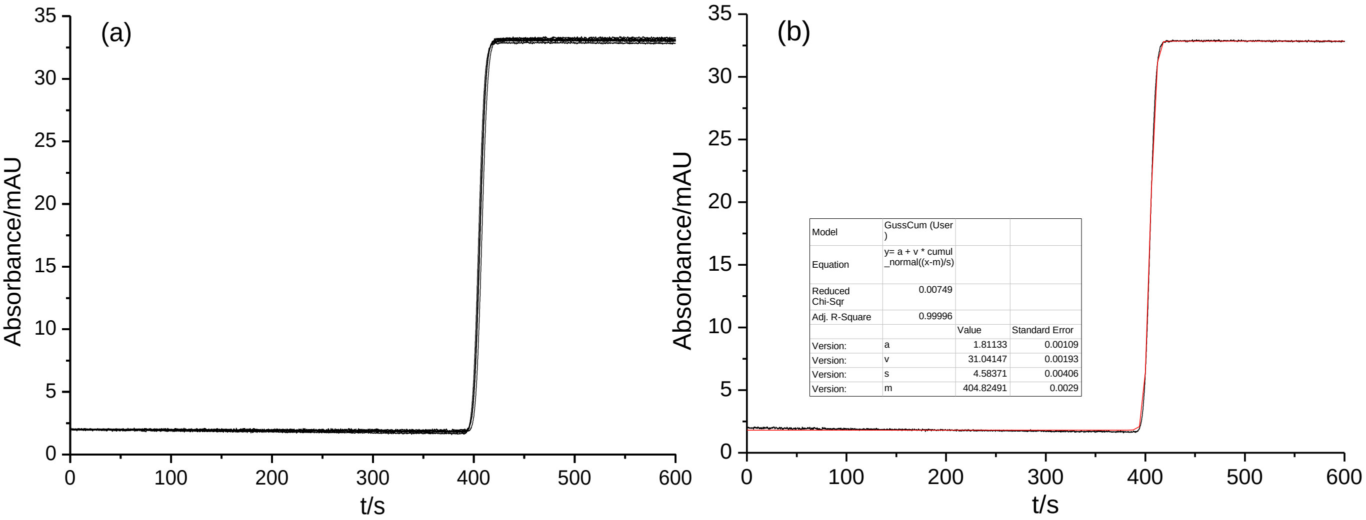

Model	GussCum (User)		
Equation	y= a + v * cumul _normal((x-m)/s)		
Reduced Chi-Sqr	0.00749		
Adj. R-Square	0.99996		
		Value	Standard Error
Version:	a	1.81133	0.00109
Version:	v	31.04147	0.00193
Version:	s	4.58371	0.00406
Version:	m	404.82491	0.0029

Figure 47: Recorded taylorgram of thiourea in 10 mmol L^{-1} HCl: (a) Superimposed taylorgrams obtained in consecutive runs; and (b) Taylorgram is fitted to the cumulative Gaussian function. Experimental conditions: fused-silica capillary (76 µm I.D., 363.5 µm O.D.); total length of the capillary was 39.5 cm and the length to the detector 29.2 cm; T = 25 ^{o} C; frontal method; pressure difference = 0.1 psi (6.89 mbar) 6 s; and absorbance detection at 254 nm.

The average diameter value of CoOOH-NPs from using the covalent coating is 5.78 ± 0.5 nm, while it becomes 7.92 ± 1.5 nm by using SMIL coating in 10 mmol L^{-1} HCl. Those values for CoOOH-NPs diameter were obtained by fitting taylorgrams of both covalent and SMIL coatings to the cumulative Gaussian function (Eq. 26) by non-linear regression. Difference in the diameter values of CoOOH-NPs obtained from the two types of coating might be attributed to the influence of the coating on the viscosity. The mean diffusion coefficient values are: 8.56 x10^{-11} m^2 s^{-1} for covalent bonded coating and 5.99 x10^{-11} m^2 s^{-1} for SMIL coating. It seems that SMIL coatings are very thick because five successive layers of alternatively PDADMAC and PSS were deposited on the capillary surface. Figure 48 illustrates recorded taylorgrams with decreasing absorbance of CoOOH-NPs against time and fitting experimental data to a mono-exponential decay function in different acids. For fitting data to the mono-exponential decay function, data of absorbance is selected at 8 min. from each taylorgram. Recorded taylorgrams of CoOOH-NPs in MSA solution (Figure 48e) are shown high values of absorbance compared with those of CoOOH-NPs in both of HCl and HNO_3 (Figure 48a+c). The deviation can be attributed to the higher initial concentration used for CoOOH-NPs sample with MSA in TDA measurements, compared to that used with HCl or HNO_3 solutions (refer to Figure 48).

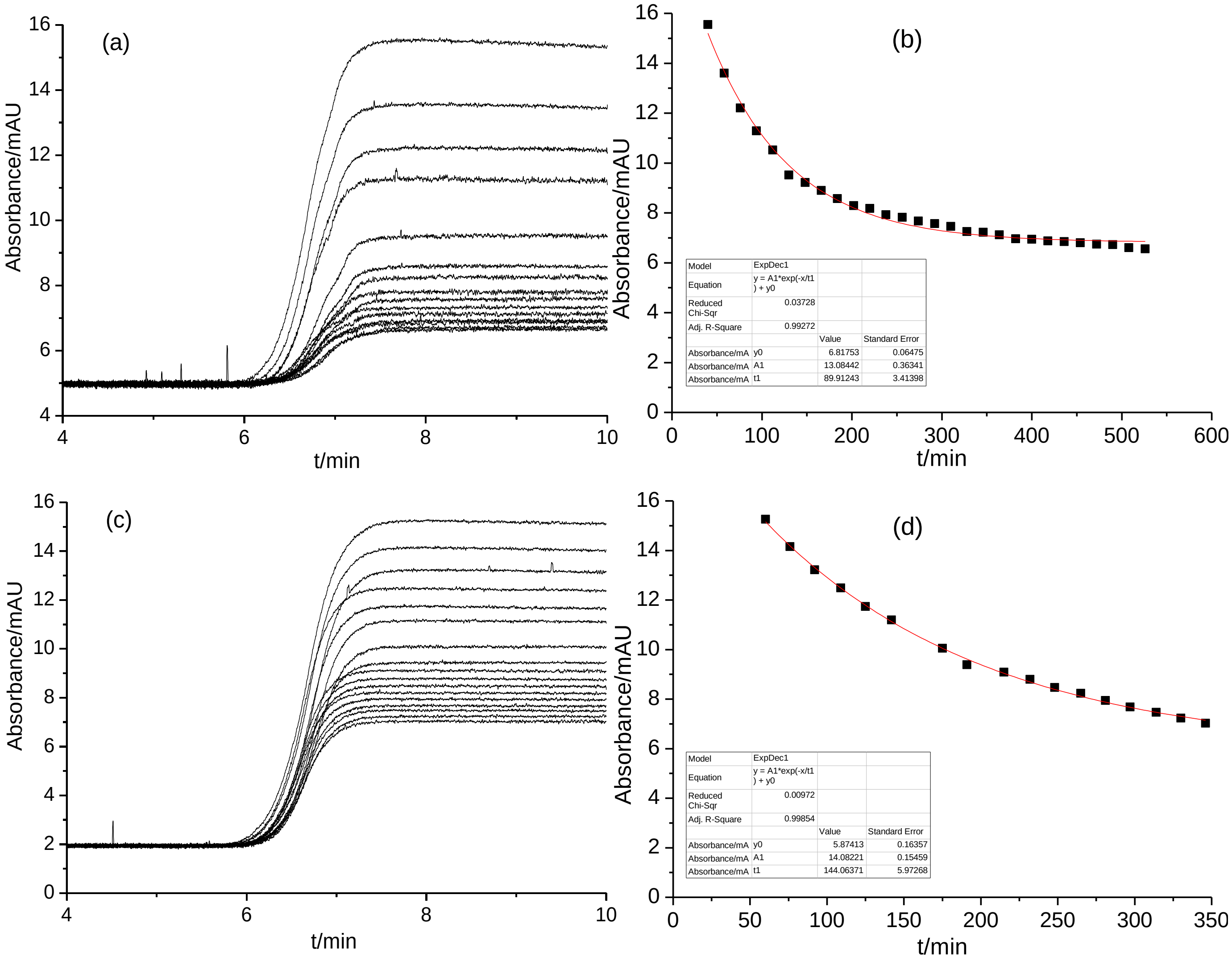

Model	ExpDec1		
Equation	y = A1*exp(-x/t1) + y0		
Reduced Chi-Sqr	0.03728		
Adj. R-Square	0.99272		
		Value	Standard Error
Absorbance/mA	y0	6.81753	0.06475
Absorbance/mA	A1	13.08442	0.36341
Absorbance/mA	t1	89.91243	3.41398

Model	ExpDec1		
Equation	y = A1*exp(-x/t1) + y0		
Reduced Chi-Sqr	0.00972		
Adj. R-Square	0.99854		
		Value	Standard Error
Absorbance/mA	y0	5.87413	0.16357
Absorbance/mA	A1	14.08221	0.15459
Absorbance/mA	t1	144.06371	5.97268

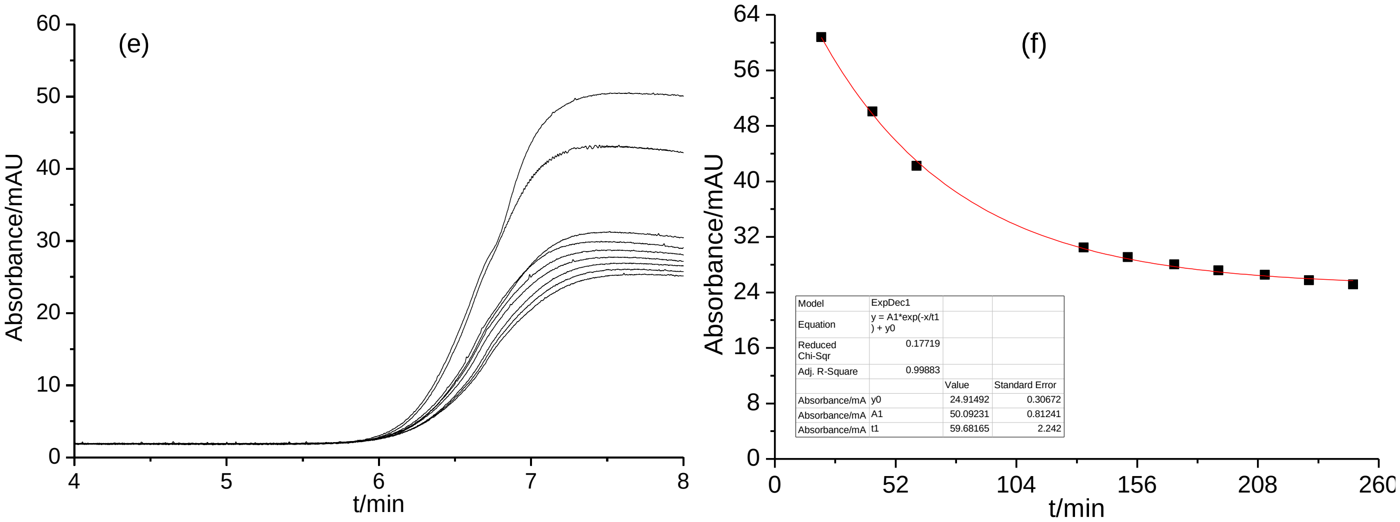

Model	ExpDec1		
Equation	y = A1*exp(-x/t1) + y0		
Reduced Chi-Sqr	0.17719		
Adj. R-Square	0.99883		
		Value	Standard Error
Absorbance/mA	y0	24.91492	0.30672
Absorbance/mA	A1	50.09231	0.81241
Absorbance/mA	t1	59.68165	2.242

Figure 48: Absorbance of CoOOH-NPs decreasing with time via TDA measurements in 10 mmol L^{-1} for: (a) HCl, (c) HNO_3 and (e) MSA. Experimental data fitted to a mono-exponential decay function represented in: (b) HCl; (d) HNO_3; and (f) MSA. Fitting data of absorbance against time was chosen at 8 min. Experimental conditions: fused-silica capillary (76 µm I.D., 363.5 µm O.D.), L_T = 39.5 cm, L_D = 29.2 cm, capillary coating with covalent bonded, T = 25 ^{o} C, pH = 2 and CoOOH-NPs concentrations in three acids are: 0.11 mmol L^{-1} in both HCl and HNO_3; and 0.55 mmol L^{-1} in MSA.

There is a good agreement between the experimental data and the fitting lines of a mono-exponential decay function as shown in Figure 48b, d+f, with the correlation coefficients are: 0.99272 for Cl^{-}; 0.99854 for NO_3^{-}; and 0.99883 for $CH_3SO_3^{-}$. From recorded taylorgrams, reaction rate constants for each of Cl^{-}, NO_3^{-} and $CH_3SO_3^{-}$ anions are calculated directly from plotting the absorbance value against time by assuming that the reacting system follows a two-step consecutive pseudo first-order reaction. Experimental results are depicted in Figure 49. Values of the reaction rate constants for CoOOH-NPs are obtained from fitting experimental data to an exponential decay function via linear regression. Thereby, these values are as the follows: k = 5.37 x10^{-3} min^{-1} for Cl^{-}; k = 3.77 x10^{-3} min^{-1} for NO_3^{-} and k = 8.87 x10^{-3} min^{-1} for $CH_3SO_3^{-}$. Values of the reaction rate for CoOOH-NPs with these anions at 25 ^{o}C are: 3.5 x10^{-5} mol L^{-1} s^{-1} for Cl^{-}; 2.5 x10^{-5} mol L^{-1} s^{-1} for NO_3^{-} and 2.9 x10^{-4} mol L^{-1} s^{-1} for $CH_3SO_3^{-}$. The same results were observed with UV-Vis measurements. Furthermore, the values of the reaction rate in TDA measurements (also in UV-Vis measurements) reveal that the dissolution process of CoOOH-NPs was slower in HNO_3 solution than that in both of HCl and MSA solutions.

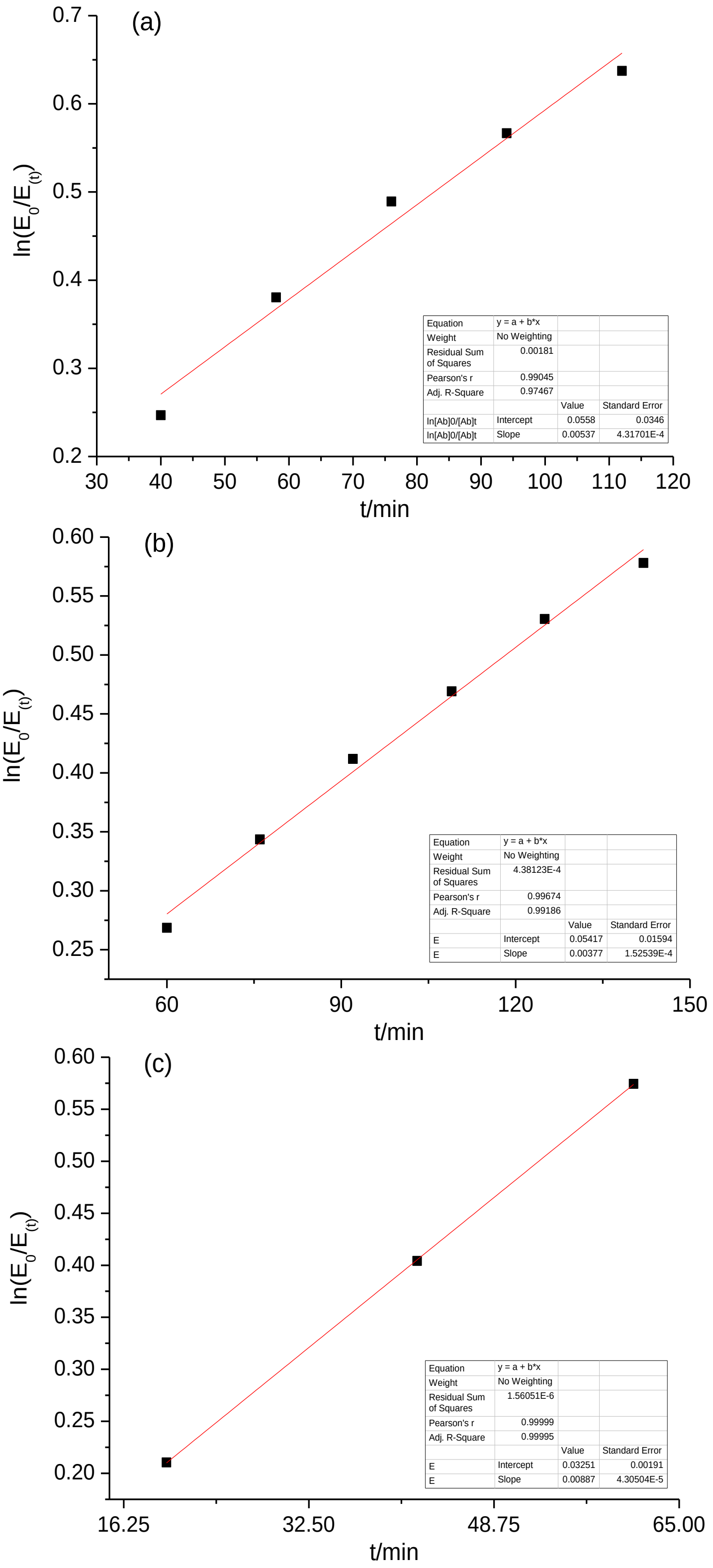

Equation	y = a + b*x		
Weight	No Weighting		
Residual Sum of Squares	0.00181		
Pearson's r	0.99045		
Adj. R-Square	0.97467		
		Value	Standard Error
ln[Ab]0/[Ab]t	Intercept	0.0558	0.0346
ln[Ab]0/[Ab]t	Slope	0.00537	4.31701E-4

Equation	y = a + b*x		
Weight	No Weighting		
Residual Sum of Squares	4.38123E-4		
Pearson's r	0.99674		
Adj. R-Square	0.99186		
		Value	Standard Error
E	Intercept	0.05417	0.01594
E	Slope	0.00377	1.52539E-4

Equation	y = a + b*x		
Weight	No Weighting		
Residual Sum of Squares	1.56051E-6		
Pearson's r	0.99999		
Adj. R-Square	0.99995		
		Value	Standard Error
E	Intercept	0.03251	0.00191
E	Slope	0.00887	4.30504E-5

Figure 49: Reaction rate constants obtained from plotting $\ln(E_0/E_{(t)})$ versus time from TDA measurements assumed as pseudo first-order reaction for: (a) HCl; (b) HNO_3; and (c) MSA. For experimental conditions refer to Figure 48.

Further, the influence the type of anion on the measured CoOOH-NPs size is recorded as illustrated in Figure 50. The average diameters of CoOOH-NPs with Cl^-, NO_3^-, and $CH_3SO_3^-$ anions are: 5.8 ± 0.5 nm for 28 runs; 5.0 ± 0.6 nm for 17 runs; and 8.0 ± 1.3 nm for 10 runs, respectively. The increase in diameter follows the series: $CH_3SO_3^- > Cl^- > NO_3^-$. Results reveal that the type of anion impacts on CoOOH-NPs size, and this might not be attributed to the hydrated radius of the anion, because the hydrated radius of Cl^- (3.32 Å) and NO_3^- (3.35 Å) [101] are quite close and thus not likely to produce much of an effect. Another reason might be related to significant mechanism named ‘‘oriented attachment (OA)’’ [102], where spontaneous self-organization of adjacent particles occurs so that they share a common crystallographic orientation, followed by joining of these particles at a planar interface to form larger ones (particle collisions lead to the formation of complexes (*i.e.*, agglomerates), where coalescence may take place). This mechanism can give rise to homogeneous single crystals or to crystals separated by twin boundaries or other planar defects. This postulation was considered because coarsening behavior often cannot be explained by classical Ostwald ripening (OR) when the nanoparticles are sufficiently small [103]. Classical Ostwald ripening mechanism can be described as a diffusion-limited growth of nanoparticles at the expense of smaller ones [104]. Figure 51 illustrates the scheme of nanoparticles growth by either of classical Ostwald ripening mechanism (OR) or by the oriented attachment mechanism (OA).

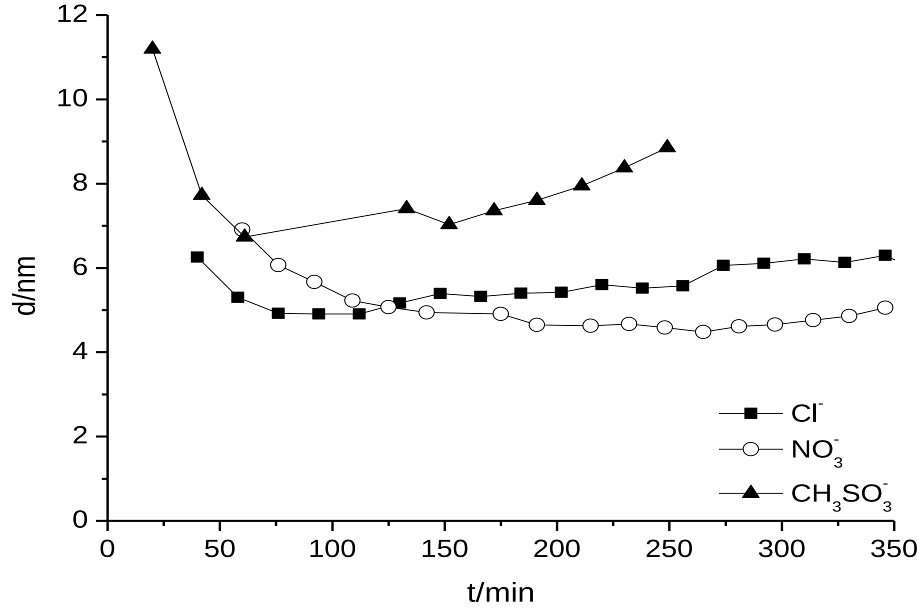

Figure 50: The determined mean diameter of the CoOOH-NPs as a function to of the time in 10 mmol L^{-1} monoprotic acid with either Cl^-, NO_3^- or $CH_3SO_3^-$ as counterion, for experimental conditions refer to Figure 48.

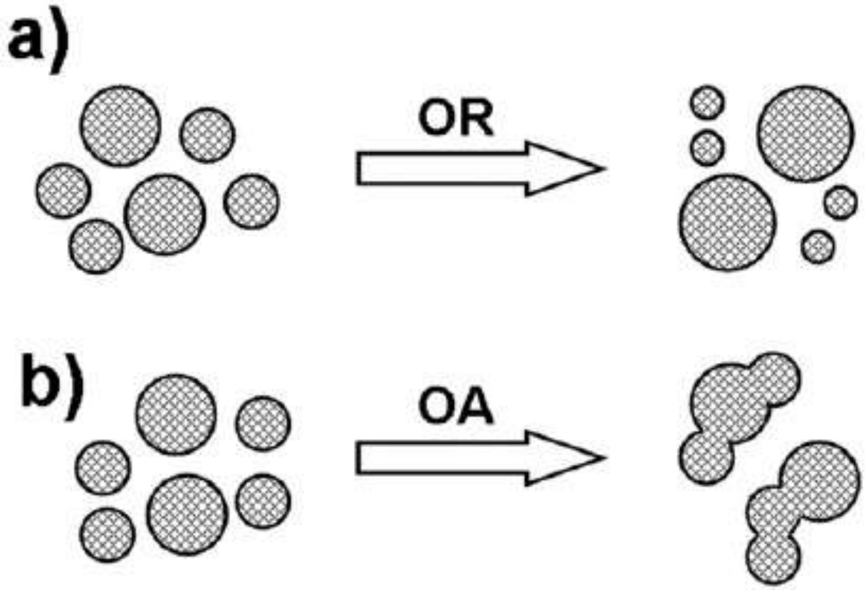

Figure 51: The mechanism of nanoparticles growth by: (a) Ostwald ripening mechanism (OR); (b) oriented attachment mechanism (OA) from [105].

4.3.5 Capillary electrophoresis

4.3.5.1 Electrophoretic mobility measurements

The CoOOH-NPs dispersed in acidic solution of pH 2 carry a positive charge and have the tendency to adsorb on the bare silica wall. Thus, modification of the capillary wall either by covalent coating (via polymerization of DADMAC) or by dynamic coating (via the double-chained cationic surfactant DDAB) was considered to reduce adsorption of CoOOH-NPs on the wall during the capillary electrophoresis measurements. The stability of the coating was indirectly evaluated by monitoring the EOF as a function of time. RSD was 1.74% (n=8); and 1.58% (n=4) for covalent coating and dynamic coating, respectively. These results indicate that both methods provide a suitable stability and repeatability of the velocity of the EOF.

With 10 mmol L^{-1} HCl as background electrolyte, CoOOH-NPs were measured at varied detection wavelength. The electropherograms for CoOOH-NPs recorded at the wavelengths 214, 254, and 280 nm, respectively, as shown in Figure 52. The recorded electropherograms at different wavelengths show that recorded electropherograms at 254 and 280 nm have two peaks yielded by CoOOH-NPs and neutral marker, whereas recorded electropherogram at 214 nm clearly shows an additional peak. This additional zone might be attributed to anionic impurities produced from the capillary coating. In both cases, the zone has a lower migration time than that of CoOOH-NPs or EOF marker. Therefore, the electropherograms were recorded at 254 nm to avoid unwanted recorded co-migration peak and to improve the signal-to-noise ratio.

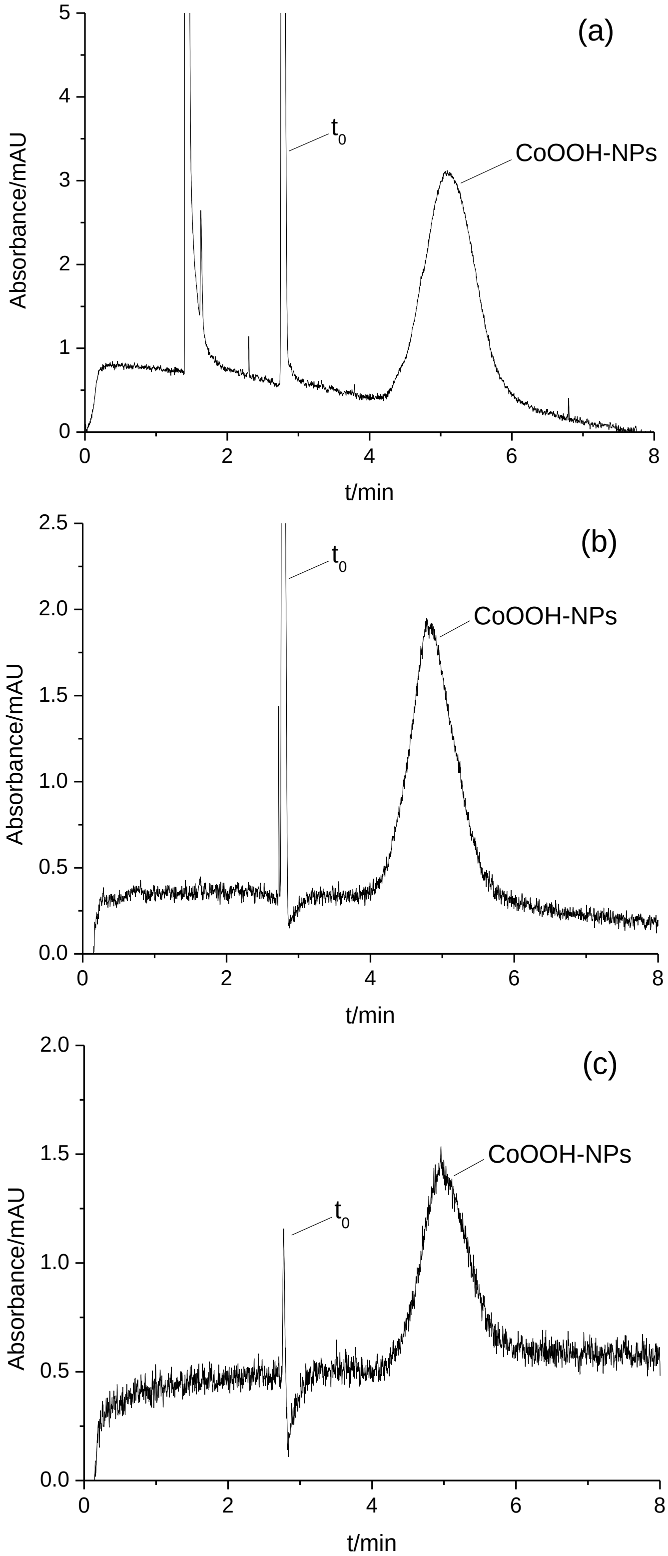

Figure 52: Comparison of electropherograms obtained for CoOOH-NPs at different wavelength: (a) 214 nm, (b) 254 nm, and (c) 280 nm. t_0 = signal assigned to marker of the electroosmotic flow. Experimental conditions: capillary coated with 0.1 mmol L^{-1} DDAB in 10 mmol L^{-1} HCl (pH = 2) , T = 25 ^oC, inner diameter of fused silica capillary = 76 μm, total length of capillary = 39.5 cm, capillary length to detector = 29.2 cm, background electrolyte = 10 mmol L^{-1} HCl (pH = 2), separation voltage = -10 kV, sample injection = 0.1 psi (6.89 mbar) 5 s, date rate = 16 Hz, absorbance detection.

Additionally, the effect of the injection time on the peak recorded for the CoOOH-NPs was investigated. Experimental results are represented in Figure 53, where recorded traces obtained are compared under variation of both the injection time and the electric field strength by using either covalent or dynamic capillary coatings. This comparison reveals the dramatic effect of volume overloading with a negative effect on peak width. The broad distorted peaks, also, could be attributed to differing in the conductivity between sample zone and buffer zone. These overloading and electrodispersion phenomena frequently cause asymmetric peaks. A significant difference in migration time of CoOOH-NPs between the two coating systems was observed. The faster migration of CoOOH-NPs in the dynamic coated capillary can likely be attributed to the higher absolute values of EOF velocity (6.22 x10^{-8} m^2 s^{-1} V^{-1} compared with 4.36 x10^{-8} m^2 s^{-1} V^{-1} for covalent coating in low electric field; and 7.63 x10^{-8} m^2 s^{-1} V^{-1} compared with 4.94 x10^{-8} m^2 s^{-1} V^{-1} for covalent coating in high electric field).

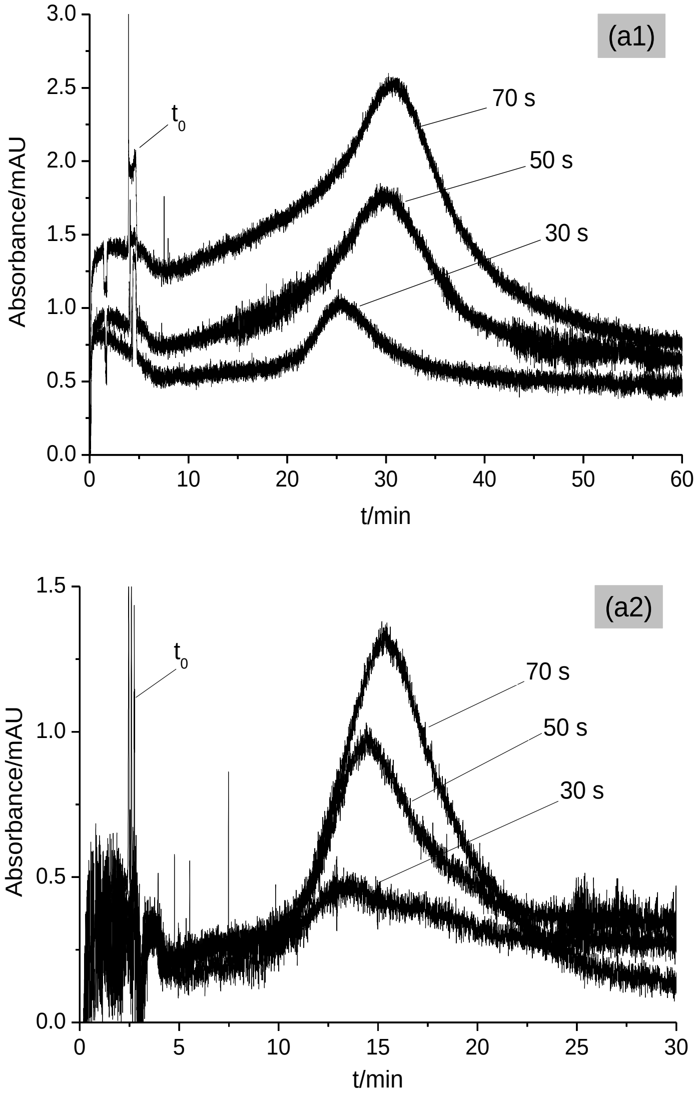

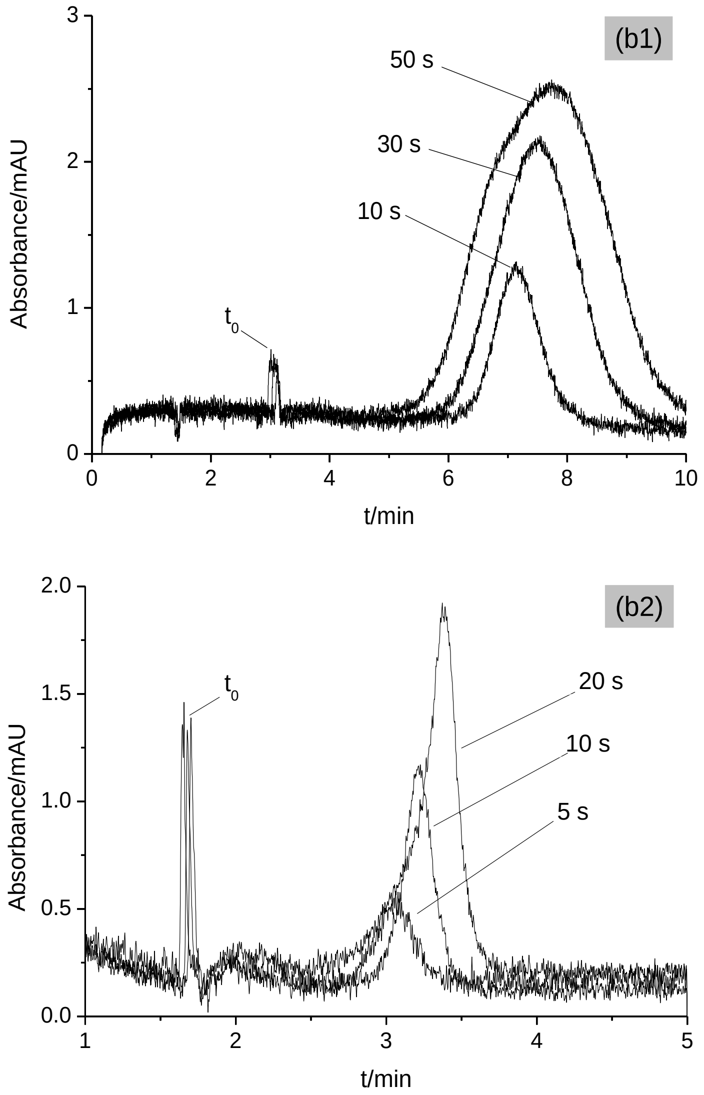

Figure 53: Comparison of electropherograms obtained for CoOOH-NPs with varied injection parameters using: (a) covalent coating (via polymerization); and (b) dynamic coating (via cationic surfactant) at different electric field strength. Experimental conditions: T = 25 ^{o}C, inner diameter of fused silica capillary = 76 µm, total length of capillary = 39.5 cm, capillary length to detector = 29.2 cm, background electrolyte = 10 mmol L^{-1} HNO_3 (pH = 2), separation voltage = (1) -10 kV; (2) -15 kV, injection pressure: 0.1 psi (6.89 mbar) for b1 and 0.2 psi (13.8 mbar) for a1, a2+b2, date rate = 16 Hz, absorbance detection at 254 nm.

In a second series, the effect of the electric field strength E on the peak position (migration time, mean electrophoretic mobility), peak height, peak area, and peak shape was investigated. Experimental results are presented in Figure 54. The electric field strength ranged between 177, 253, 380 and 456 V cm^{-1}. The peak position shift was found to be corresponding to the variation in electric field strength. The electrophoretic mobility values of CoOOH-NPs are 3.74 x 10^{-8}; 3.70 x 10^{-8}; 3.64 x 10^{-8} and 3.89 x 10^{-8} m^{2} s^{-1} V^{-1} relative to E = 177, 253, 380 and 456 V cm^{-1}, respectively, which can be considered to be constant within experimental error. Values of those parameters are calculated via integration of the recorded electropherograms (see upper plot in Figure 54) by using Origin 8.5 program. Experimental data are illustrated in Figure 54. The migration times of CoOOH-NPs decrease with increasing the electric field strength as expected. Whereas the observations of both peaks dispersion and peaks area of CoOOH-NPs are decreasing with increasing the electric field strength. Random variations in some data might be related to adsorption effects of CoOOH-NPs on the inner capillary wall (induced by the covalently attached coating).

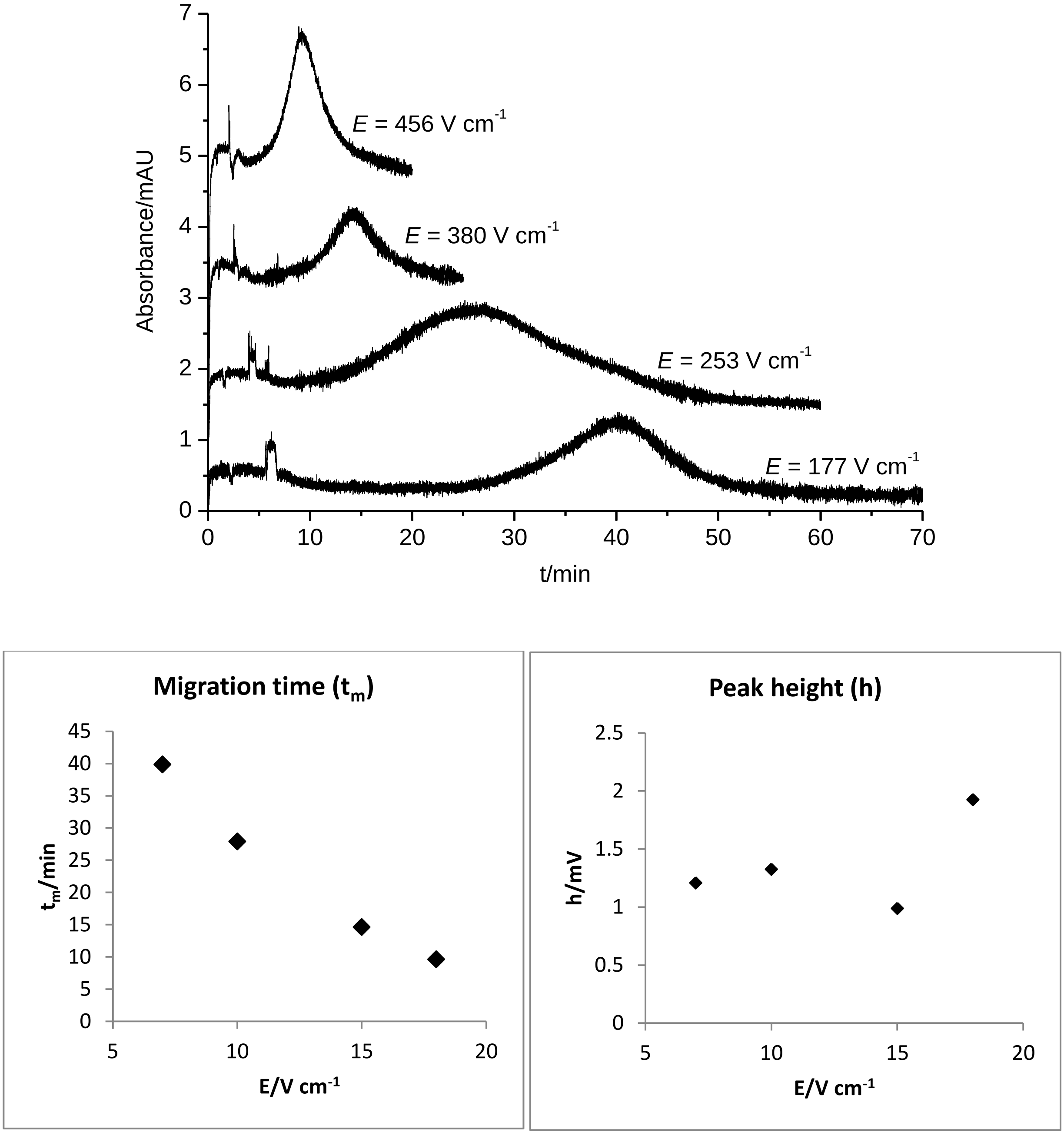

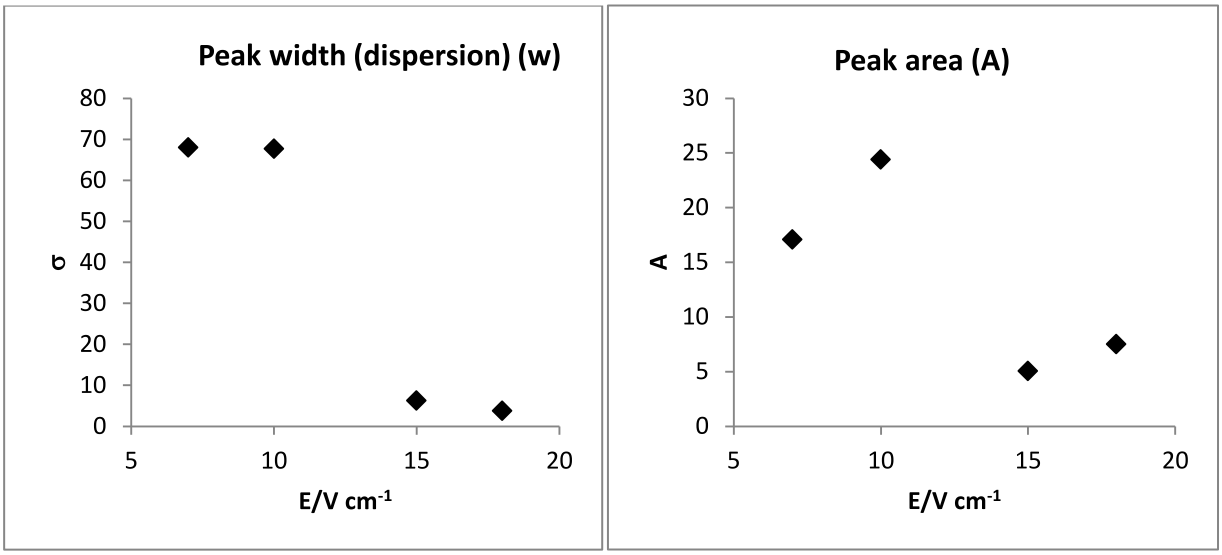

Figure 54 Overlay of electropherograms recorded for CoOOH-NPs with varied electric field strength (E) (upper plot). Parameters (migration time, peak height, peak width (dispersion) and peak area) are obtained from using integration tool for recorded electropherograms. Experimental conditions: capillary coated with covalently bonded via polymerization, T = 25 °C, inner diameter of fused silica capillary = 76 µm, total length of capillary = 39.5 cm, capillary length to detector = 29.2 cm, background electrolyte = 10 mmol L^{-1} HNO_3 (pH = 2), separation voltage varied, sample injection = 0.2 psi (13.8 mbar) 50 s, date rate = 16 Hz, absorbance detection at 254 nm.

In a third series, the influence of the concentration of the CoOOH-NPs in the sample was studied. Recorded electropherograms with varied CoOOH-NPs concentration in the sample are shown in Figure 55. From those recorded electropherograms, μ_{ep} values of CoOOH-NPs are calculated based on μ_{eo} values of the neutral marker. Results are presented in Figure 56. It can be seen that the measured μ_{ep} values increase with the CoOOH-NPs concentration for both types of the capillary coating and that the determined μ_{ep} values are larger for the capillary with covalently attached coating than for the capillary with dynamic coating. In addition, differences between μ_{ep} values are smaller with covalent coating than those with dynamic coating. Also, adsorption of CoOOH-NPs on the capillary wall can be of influence. To find out this discrepancy in the CoOOH-NPs behavior according to the coating capillary type, electric field strength or both, Gram−Charlier A series function (GCAS function - (*cf.* Eq.(30))) was applied to fit recorded electropherograms as shown in Appendix C. This function can give information about peak height, peak width (peak dispersion), peak area, peak skewness (peak asymmetry) and peak excess (peak flattening). Particularly, the information getting from peak height, peak width and peak skewness are helpful, because these quantities demonstrate the influence of coating capillary type, electric field strength, and varied CoOOH-NPs concentration in the sample. Data obtained by fitting recorded electropherograms to GCAS function are tabulated in Table 14. In general, results reveal that peak height, peak width and peak area are increasing with increase in CoOOH-NPs concentration in the sample independent of coating capillary type and electric field strength as expected.

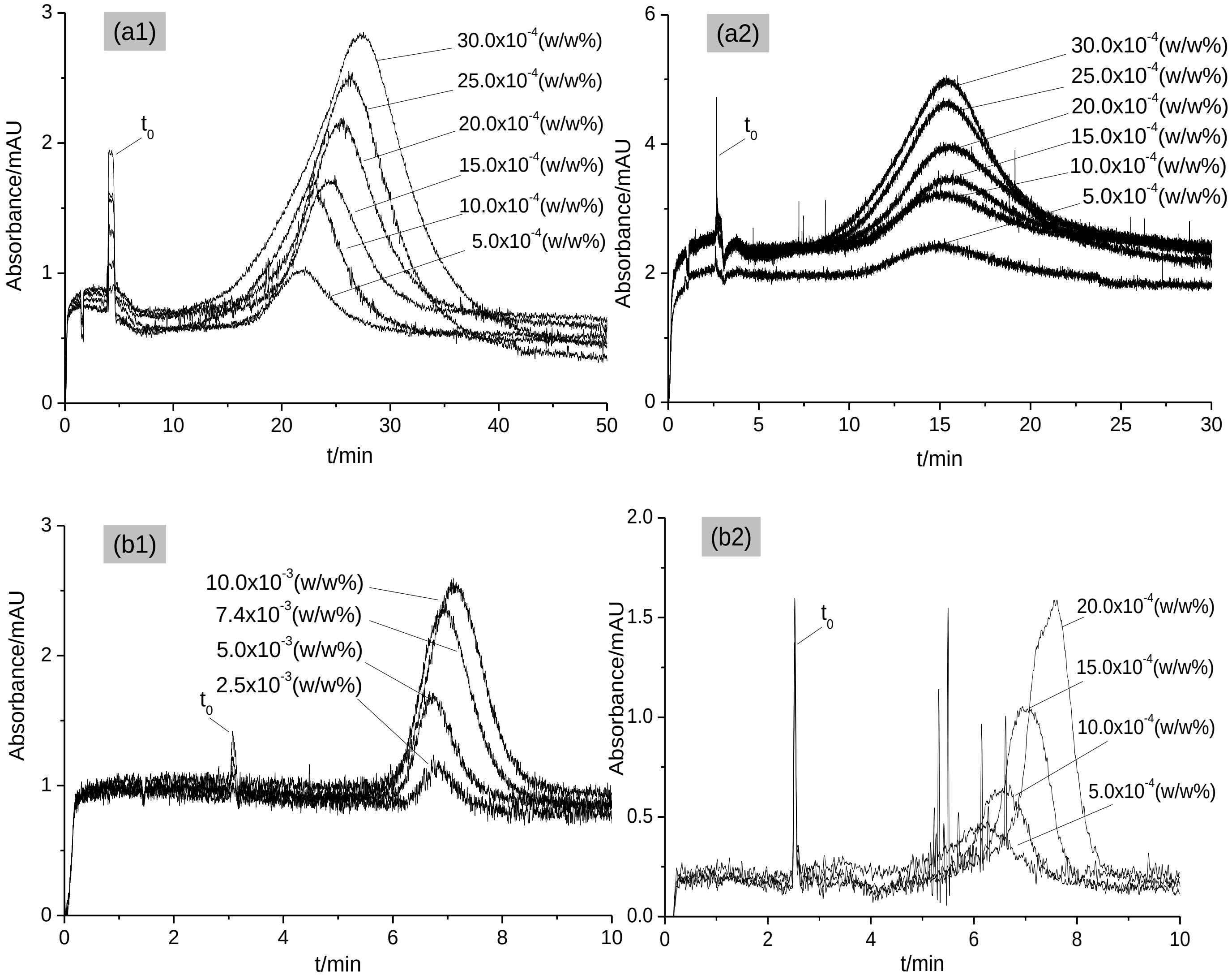

Figure 55: Superposition of electropherograms recorded for CoOOH-NPs with varied particle concentration: (a1) covalent coating with *E* = 253 V cm^{-1} (smoothing via Savitzky-Golay algorithm, 100 points); (a2) covalent coating with *E* = 380 V cm^{-1}; (b1) dynamic coating with *E* = 253 V cm^{-1} and (b2) dynamic coating with *E* = 380 V cm^{-1} (smoothing via Savitzky-Golay algorithm, 50 points). Experimental conditions: T = 25 ^{o}C, I. D. = 76 μm, L_T = 39.5 cm, L_D = 29.2 cm, background electrolyte = 10 mmol L^{-1} HNO3 (pH = 2), injection pressure: 0.1 psi (6.89 mbar) 3 s for b1 and 0.2 psi (13.8 mbar) 50 s for a1, a2+b2, date rate = 16 Hz, absorbance detection at 254 nm.

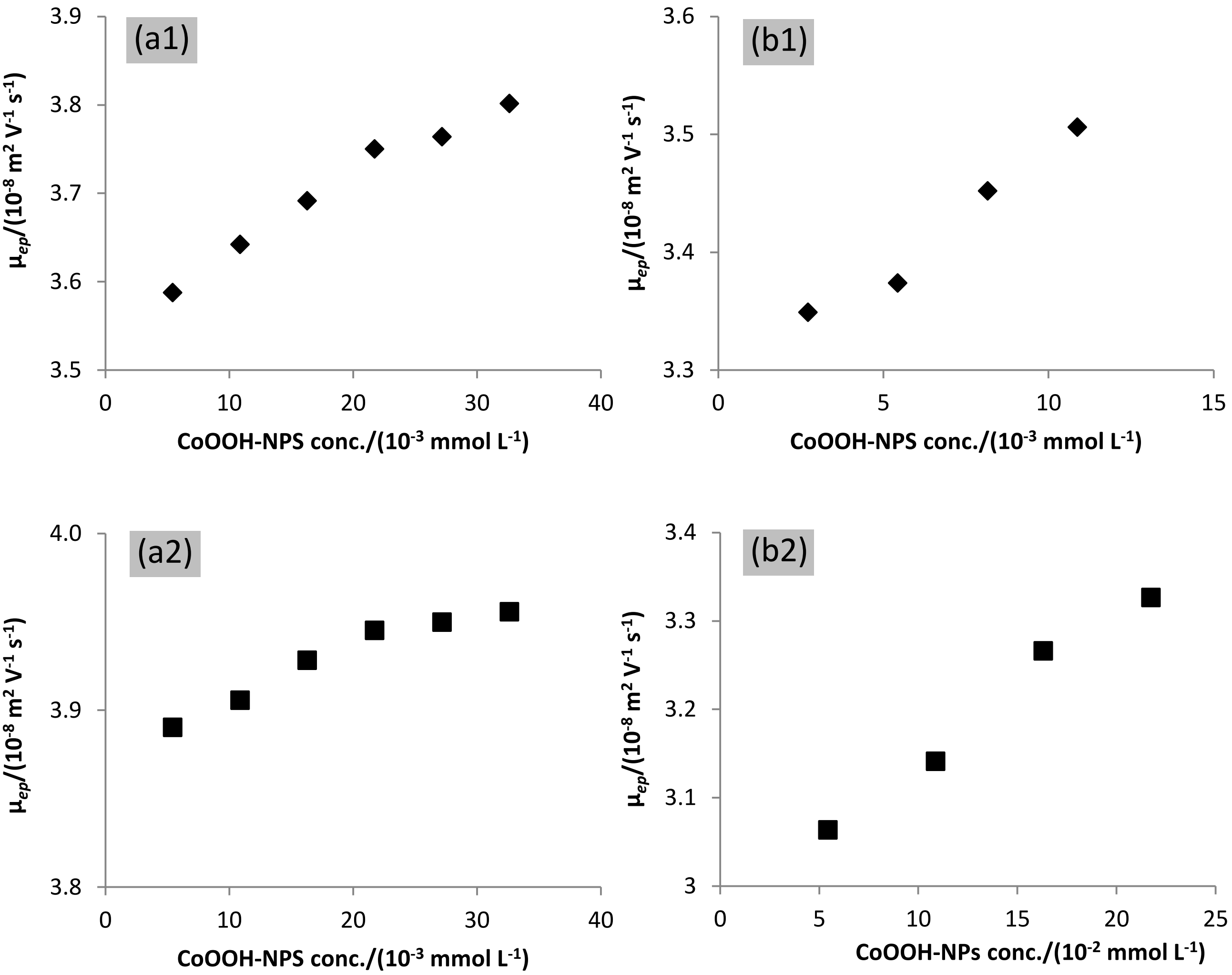

Figure 56: Apparent electrophoretic mobility as a function of the concentration of CoOOH-NPs in the sample. (a1) covalent coating with E = 253 V cm^{-1}; (a2) covalent coating with E = 380 V cm^{-1}; (b1) dynamic coating with E = 253 V cm^{-1} and (b2) dynamic coating with E = 380 V cm^{-1}; (refer to Figure 53 for experimental condition).

However, values of peak height are varied in some data, specifically, in covalent bonded coating at high CoOOH-NPs concentrations for both electric field strength values used. In addition, peak height, peak width and peak area values for covalent bonded coating are larger than that for dynamic coating with independent electric field strength values. Further, residence time in the detector is directly related to peak width. Therefore, peak width or peak dispersion values as shown in Table 14 indicate that the overall residence time of CoOOH-NPs in dynamic capillary coating is less than that in covalent bonded capillary coating because anodic EOF values for dynamic coating are larger than for covalent coating. EOF magnitudes for dynamic capillary coating are: – 5.08 $x10^{-8}$ m^2 s^{-1} V^{-1} for high electric field strength and – 6.22 $x10^{-8}$ m^2 s^{-1} V^{-1} for low electric field strength, whereas for covalent capillary coating are: – 4.76 x10^{-8} m^{2} s^{-1} V^{-1} for high electric field strength and – 4.49 x10^{-8} m^{2} s^{-1} V^{-1} for low electric field strength. The magnitude of EOF for dynamic capillary coating at low electric field strength is larger than that at high electric field strength, in contrary with covalent bonded coating for both electric field strength values (refer to Figure 55).

Table 14: Parameters are estimated by fitting recorded electropherograms of different CoOOH-NPs concentration in the sample to GCAS function for two capillary coating types with electric field strength values.

Type of capillary coating	**Electric field strength/ V cm^{-1}**	**CoOOH-NPs conc./ (x10^{-3} mmol L^{-1})**	**R^{2}**	**Peak height (h)**	**Peak width (w)**	**Peak area (A)**	**Peak skewness (κ_3)**	**Peak excess (κ_4)**
Covalent bonding coating	**253**	5.44	0.9916	22.36	2.39	2.48	0.49	0.18
		10.88	0.9851	24.00	2.40	5.44	0.85	0.36
		16.31	0.9946	25.40	2.86	6.32	0.77	0.31
		21.75	0.9934	26.46	3.24	10.07	0.68	0.39
		27.19	0.9926	24.99	4.22	18.45	- 0.70	- 0.06
		32.63	0.9923	25.91	4.89	24.30	- 0.61	- 0.02
	380	5.44	0.9979	15.32	2.51	2.80	0.28	- 0.16
		10.88	0.7967	16.10	2.89	5.19	0.80	- 0.20
		16.31	0.9891	16.69	2.99	7.21	0.91	- 0.17
		21.75	0.9942	16.66	2.99	10.06	0.90	- 0.04
		27.19	0.9949	16.61	3.07	14.66	1.03	0.19
		32.63	0.9947	16.48	2.92	16.03	1.02	0.47
Dynamic coating	**253**	27.19	0.9816	6.85	0.28	0.20	0.15	0.10
		54.38	0.9713	6.55	0.43	0.69	- 1.58	- 0.66
		81.58	0.9963	7.04	0.46	1.60	0.50	0.12
		108.77	0.9963	7.21	0.49	1.86	0.33	0.06
	380	5.44	0.9934	6.14	0.53	0.28	- 0.24	0.28
		10.88	0.9723	6.40	0.51	0.57	- 0.85	- 0.13
		16.31	0.9700	6.84	0.49	1.00	- 1.12	- 0.19
		21.75	0.9806	7.28	0.49	1.45	- 1.33	- 0.26

4.3.5.2 Estimation of zeta potential

The ζ potential of CoOOH-NPs is determined by measuring the electrophoretic mobility via using the analytic approximation presented by Ohshima [19,20] modified by Pyell *et al.* [74]. This approach is considered to take the relaxation effect into account with $\zeta > 25$ mV to calculate the electrophoretic mobility for a known hydrodynamic radius at fixed ionic strength. Also, this approach involves the approximation of the effective ionic drag coefficient with the counterion ionic drag coefficient [74].

Firstly, the electrophoretic mobilities of CoOOH-NPs are calculated dependent on the reduced sphere radius κa and ζ potential (*cf.* Eq. (20)) taking the ionic drag coefficient calculated from the limiting conductance value. Three anions of three different acids (HCl, HNO_3 and CH_3SO_3H) at 10 mmol L^{-1}, pH 2.0 and 25 °C are used in this study. The limiting conductance values are: 76.35 S cm^2 mol^{-1} for Cl^-, 71.44 S cm^2 mol^{-1} for HNO_3^- and 50.00 S cm^2 mol^{-1} for $CH_3SO_3^-$ [72,106,107]. Secondly, the calculated values are compared to the experimental values obtained from capillary electrophoresis measurements with identical ionic strength.

Because the solution has a very low electrolyte concentration (10 mmol L^{-1}), the value of κ is a small value (0.3291 nm^{-1}). In spite of that, it is possible to use the modified analytic approximation to estimate ζ in this region. Results are represented in Figure 57. Results show the influence of the anion as counterion on ζ. An increase in absolute values of ζ follows the series: $CH_3SO_3^- < Cl^- < NO_3^-$. It is worth mentioning that values of the hydrodynamic radius a used to estimate ζ potential for CoOOH-NPs were obtained from TDA measurements: 2.9 nm with Cl^-, 2.5 nm with NO_3^- and 4.0 nm with $CH_3SO_3^-$ (refer to *Section 4.3.4*).

The effect of anion variation on ζ might be attributed to the ion-specific effect related to the ability of ions to modify the water structure (Hofmeister series). The order of anions in this study is as follows: nitrate > chloride > methanesulfonate [108]. This means that the interaction between methanesulfonate and water is stronger than the interaction between nitrate and chloride with water. Allen *et al.* [109] reported using surface vibrational sum frequency spectroscopy (VSFS) that the presence of small amounts of MSA affects the hydrogen bonding of water. With small amounts of MSA added to bulk water, the surface water molecule vibrational modes shift to lower energy due to enhanced hydrogen bonding between surface water molecules. This shift is indicative of stronger coupling between the water molecules caused by the presence of MSA.

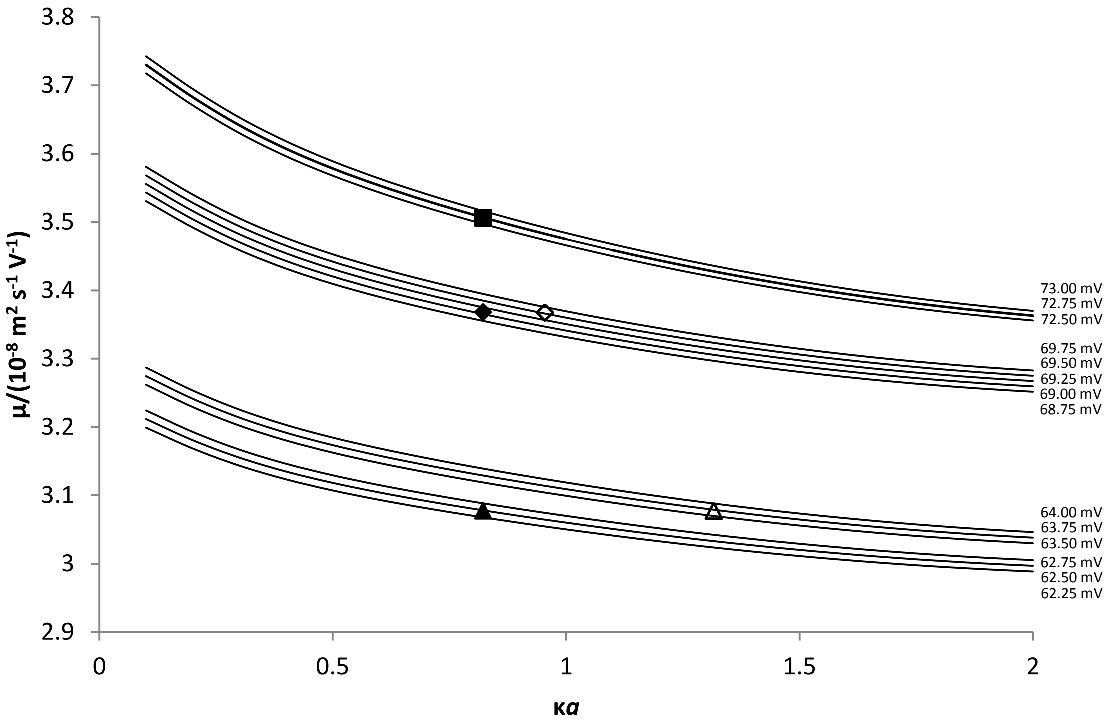

Figure 57: Calculated electrophoretic mobilities μ_{ep} for CoOOH-NPs with different anions as a counterion for varied reduced sphere radius κa and varied ζ with superimposed experimental data obtained by using capillary electrophoretic: ■ NO_3^-, ♦ Cl^- and ▲ $CH_3SO_3^-$ at fixed κa; ◊ Cl^- and Δ $CH_3SO_3^-$ at fixed κ. Capillary coating with dynamic coating and applied electric field strength value is 253 V cm^{-1}.

Furthermore, CoOOH-NPs concentration in the sample has been varied. Their influence on ζ potential is studied in 10 mmol L^{-1} HNO_3 with two types of capillary wall coating. As mentioned above, κ has a small value (< 1) suggesting that Hückel equation can be used in this limiting range. Therefore, ζ potentials for CoOOH-NPs are calculated by using both the modified analytic approximation (*cf.* Eq. (20)) and the Hückel equation (*cf.* Eq. (15)). Results are depicted in Figure 58 in which ζ potential is a function of the CoOOH-NPs concentration. In general, the comparison between the two approaches shows that ζ values increase for both approaches with increasing CoOOH-NPs concentration in the sample independent of the capillary wall coating type and of the electric field strength.

On the other hand, the covalently attached capillary wall coating gives higher ζ values than that with dynamic coating. This might be attributed to adsorption of CoOOH-NPs on the capillary wall. In dynamic coating, ζ values at applied high electric field strength are lower than that with low electric field strength. Values of ζ potential at different electric field strengths are: 79.03, 77.88 and 76.38 mV for 177, 253 and 380 V cm^{-1}, respectively. These values were estimated by applying the modified analytic approximation. ζ values evaluated via the modified analytic approximation show higher values than those estimated from using Hückel equation. The reason behind that is the relaxation effect, which must be accounted when κa is in the range of 0.1 to 300[110]. To obtain more precise data than those obtainable with a graphical procedure, an iterative procedure described in ref. [74] is used. The results are given in Table 15.

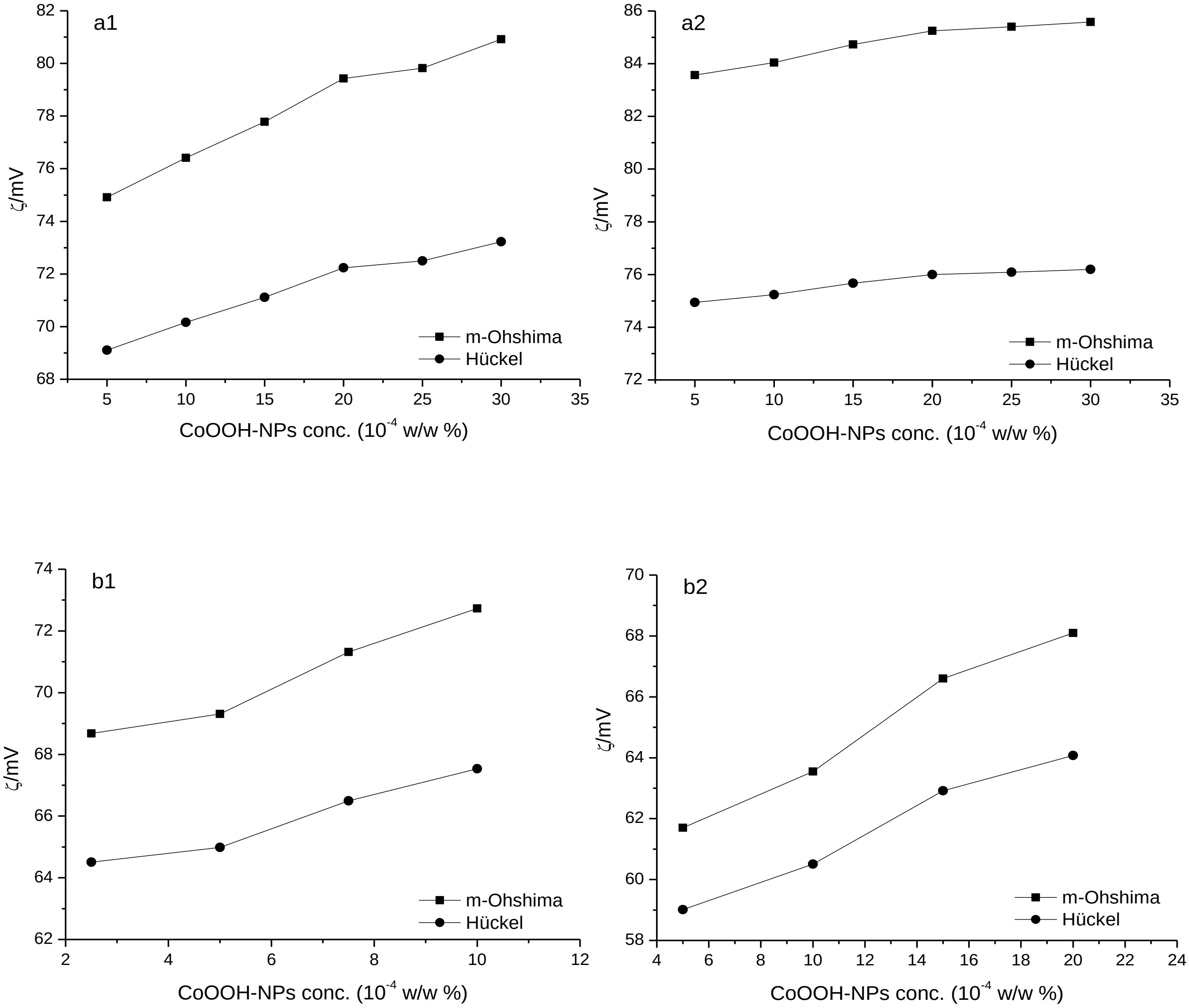

Figure 58: Comparison of the modified analytic approximation (m-Ohshima) and Hückel equation to estimate ζ potential as a function of CoOOH-NPs concentration using two types of the capillary coating: (a) covalent bonded capillary and (b) dynamic coating at: (1) low electric field strength and (2) high electric field strength. 10 mmol L^{-1} HNO_3 is used as BGE in CE measurements.

Table 15: Illustration of the iterative scheme depending on the values estimated of ζ potential from the values calculated of the electrophoretic mobility (μ_{ep}) of CoOOH-NPs in 10 mmol L^{-1} of different acids type (HNO_3, HCl and MSA) using two types of capillary coating at high and low electric field strengths and the values measured of μ_{ep} at κa = constant at 25°C. (a = 2.5 nm for CoOOH-NPs calculated via TDA in HNO_3 electrolyte).

Type of acid	**Electric field strength/** V cm^{-1}	**CoOOH-NPs conc./** mM	κa	$\mu_{ep\text{-measured}}$/ (10^{-8} m^2 s^{-1} V^{-1})	$\mu_{ep\text{-calculated}}$/ ($10^{-8}$ m^2 s^{-1} V^{-1})	$\zeta_{calculated}$/ mV	**capillary coating type**
HNO_3	253	5.44	0.8228	3.5875	3.5871	74.90	covalent bonded coating
					3.5874	74.91	
					3.5878	74.92	
		10.88	0.8228	3.6422	3.6420	76.40	
					3.6423	76.41	
					3.6427	76.42	
		16.31	0.8228	3.6915	3.6913	77.77	
					3.6916	77.78	
					3.6920	77.79	
		21.75	0.8228	3.7500	3.7495	79.42	
					3.7499	79.43	
					3.7502	79.44	
		27.19	0.8228	3.7636	3.7631	79.81	
					3.7635	79.82	
					3.7638	79.83	
		32.63	0.8228	3.8013	3.8010	80.91	
					3.8014	80.92	
					3.8017	80.93	
	380	5.44	0.8228	3.8904	3.8900	83.56	
					3.8903	83.57	
					3.8907	83.58	
		10.88	0.8228	3.9057	3.9054	84.03	
					3.9058	84.04	
					3.9061	84.05	
		16.31	0.8228	3.9283	3.9279	84.72	
					3.9282	84.73	
					3.9285	84.74	
		21.75	0.8228	3.9451	3.9447	85.24	
					3.9450	85.25	
					3.9453	85.26	
		27.19	0.8228	3.9498	3.9495	85.39	
					3.9498	85.40	
					3.9501	85.41	
		32.63	0.8228	3.9557	3.9552	85.57	
					3.9556	85.58	
					3.9559	85.59	
	253	27.19	0.8228	3.3488	3.3486	68.67	dynamic coating
					3.3490	68.68	
					3.3494	68.69	
		54.38	0.8228	3.3737	3.3734	69.30	
					3.3738	69.31	
					3.3742	69.32	
		81.58	0.8228	3.4519	3.4516	71.31	
					3.4520	71.32	
					3.4524	71.33	
		108.77	0.8228	3.5059	3.5055	72.72	
					3.5058	72.73	
					3.5062	72.74	

	380	5.44	0.8228	3.0634	3.0629	61.69
					3.0633	61.70
					3.0638	61.71
		10.88	0.8228	3.1410	3.1404	63.54
					3.1408	63.55
					3.1413	63.56
		16.31	0.8228	3.2659	3.2654	66.59
					3.2658	66.60
					3.2662	66.61
		21.75	0.8228	3.3261	3.3255	68.09
					3.3259	68.10
					3.3263	68.11
HCl	235	108.77	0.95441*	3.3676	3.3672	69.53
					3.3676	69.54
					3.3680	69.55
		108.77	0.8228	3.3676	3.3671	69.05
					3.3675	69.06
					3.3679	69.07
	380	5.44	0.95441*	3.3999	3.3994	70.38
					3.3998	70.39
					3.4002	70.40
		5.44	0.8228	3.3999	3.3994	69.87
					3.3998	69.88
					3.4002	69.89
MSA	253	108.77	1.2835*	3.0777	3.0775	63.71
					3.0779	63.72
					3.0782	63.73
		108.77	0.8228	3.0777	3.0772	62.48
					3.0776	62.49
					3.0780	62.50
	380	5.44	1.2835*	2.9698	2.9695	60.81
					2.9699	60.82
					2.9703	60.83
		5.44	0.8228	2.9698	2.9696	59.89
					2.9700	59.90
					2.9705	59.91

* κa is calculated from TDA for CoOOH-NPs separately in HCl (a = 2.9 nm) and MSA (a = 4.0 nm) electrolytes.

4.3.5.3 Electrokinetic surface charge density of CoOOH-NPs

The relation between electrokinetic surface charge density (σ_ς) and ζ potential gives access to calculate σ_ς by using the formula derived by Ohshima *et al.*[24] (*cf.* Eq. (24)) assuming ideal rigid spheres with a uniform distribution of charge on the shear surface. Eq. (24) is producing significant errors when $\kappa a < 0.5$. However, these errors can be neglected when evaluated σ_ς for CoOOH-NPs because $\kappa a > 0.5$ (refer to Table 15). σ_ς for CoOOH-NPs is calculated from ζ values estimated via both the modified analytic approximation and the Hückel equation depending on experimentally μ_{ep}.

Results of σ_ς as a function of the CoOOH-NPs concentration are represented in Figure 59. Results show that σ_ς is invariant with CoOOH-NPs concentration, regardless of the electric field strength and the capillary coating type. This conclusion is considered depending on the value of the ratio of electrical double layer thickness to the particle diameter (λ_D/d_p), which is 0.165. This value is less than 0.2, thus the surface charge density is expected to be independent of the particle size according to Barisik *et al.* [80]. The determined σ_ς is larger with covalent bonding coating than with that of dynamic coating. In addition, the measured σ_ς is larger in the high applied electric field than that in the low applied electric field. Applying the Hückel equation introduces a significant error.

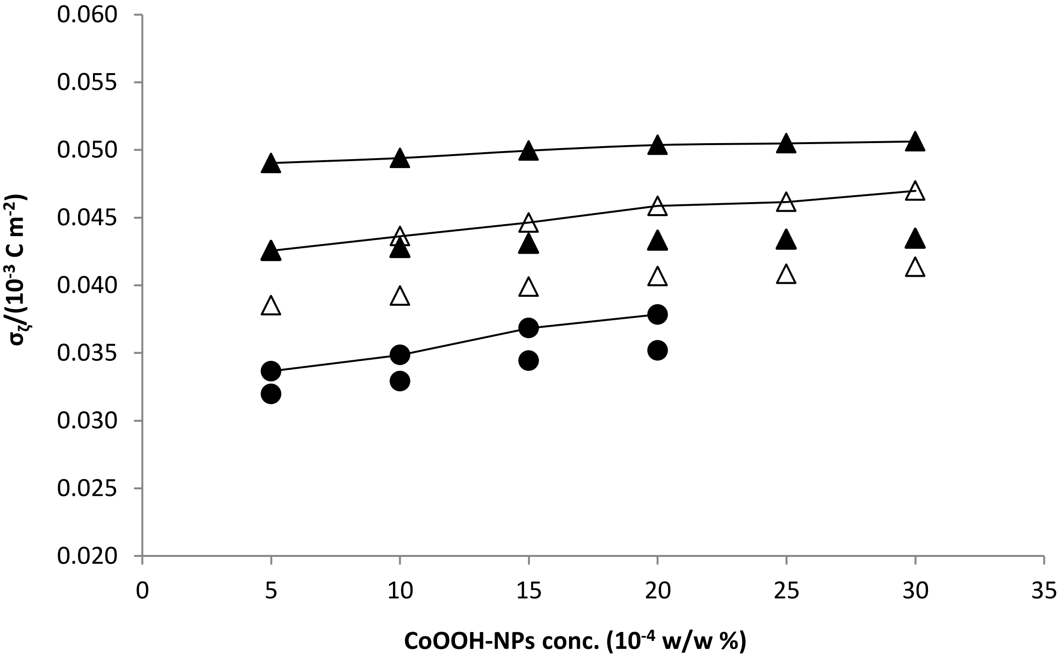

Figure 59: Electrokinetic surface charge densities (σ_ζ) as a function of CoOOH-NPs concentration at pH 2.0 and 25 °C in 10 mmol L^{-1} HNO_3, depending on ζ values evaluated from modified analytic approximation (symbols with lines) and from Hückel equation (symbols without lines) at high (closed symbols) and low (opened symbols) of electric field strength for each of covalent bonded (triangle shape) and dynamic coating (cycle shapes).

Moreover, for CoOOH-NPs, σ_ς is calculated with different anions as counterion by using ζ values estimated via the modified analytic approximation depending on experimentally μ_{ep}. σ_ς as a function of CoOOH-NPs diameter is illustrated in Figure 60. Figure 60 shows the influence of the type of anion as counterion on σ_ζ for CoOOH-NPs for a fixed particle size and for a varied particle size. σ_ς decreases as follows: NO_3^- > Cl^- > $CH_3SO_3^-$, regardless of the particle size.

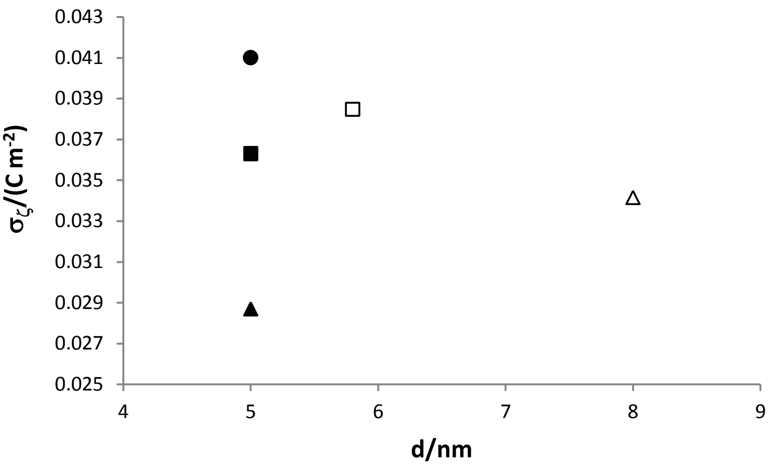

Figure 60: Effect of an anion of acids type as a counterion on electrokinetic surface charge densities (σ_ζ) of CoOOH-NPs at pH 2 and 25 °C with 10 mmol L^{-1} of: ● NO_3^-, ■ Cl^- and ▲ $CH_3SO_3^-$ at fixed κa (a = 2.5 nm for NO_3^- from TDA measurements); □ Cl^- and Δ $CH_3SO_3^-$ at fixed κ (a = 2.9 and 4 nm for Cl^- and $CH_3SO_3^-$, respectively, from TDA measurements). Capillary coating with dynamic coating and applied electric field strength value is 253 V cm^{-1}.

4.3.5.4 Size distribution of CoOOH-NPs

As described before, it is investigated whether electropherograms can be directly converted into size distribution functions by using the approach was suggested by Pyell [81] and Pyell *et al.* [82]. This method depends on an exact determination of the electrokinetic potential ζ by measuring the electrophoretic mobility in an electrolyte of known composition complemented with a second independent method to determine the mean particle radius like TEM or TDA. The steps of how to convert the electropherograms to the size distribution function can be summarized as follows [71]:

1. The cumulative superposition of experimental runs to improvement of the signal-to-noise ratio is not possible in the case of CoOOH-NPs. Therefore, one run not the cumulative superposition runs was taken to convert an electropherogram into a size distribution function. The recorded electropherogram is depicted in Figure 61a.
2. The recorded electropherogram is converted into the intensity-weighted electrophoretic mobility distribution trace (refer to Figure 61b).
3. The data points of the regression function are calculated in a range which is expected for the particle size distribution by varying the sphere radius a at fixed κ and ζ. Results are presented in Figure 61c. The regression function relates the electrophoretic mobility to the reduced radius κa at fixed value for ζ.
4. The regression function is converted into $\kappa a = f(\mu)$ or $a = f(\mu)$ with a fixed κ. The mobility of the converted electropherogram is converted into a size coordinate using constants (see Figure 61d).

5. The resulting trace is fitted to the Gram-Charlier series A function (*cf.* Eq. (30)) after baseline subtraction (refer to Figure 61e).
6. New data points are created with a step length of 0.01 nm by using the GCAS function (refer to Figure 61f) with the obtained regression parameters (Figure 61e).
7. Moment analysis is used to calculate the parameters μ_1, σ, κ_3, κ_4. Values of these parameters are: 5.32 nm, 5.90 nm, 0.1482 and 0.2114, respectively.

The value calculated from the moment analysis for σ is excessively large. The reason might be adsorption of CoOOH-NPs on the inner wall of the capillary. Adsorption might result in higher electrophoretic mobility values, which influence the estimation of ζ and the corresponding calibration functions. This can produce considerable uncertainty with significant errors in the width of the determined size distribution function. In addition, CoOOH-NPs have a small mean domain size (3.7-4.5 nm) and their electrophoretic mobility was determined in a low ionic strength electrolyte (10 mmol L^{-1}). Hence, κa value is very small ($\kappa a \ll 1$), so that the proposed method of converting electropherograms into size distribution functions might be inappropriate with this very low reduced radius. Possibly electrolytes with higher ionic strength have to be used so that κa can be increased. It must be also seen that CoOOH-NPs are nanocrystalline, whereas SNPs and PSSLs are noncrystalline (amorphous). Hence, with COOH-NPs neither the prerequisite of a constant ζ independent of particle size nor the prerequisite of a uniform surface charge density σ_0 with smeared out surface charge will be approximated. Further studies have to be conducted to investigate whether the proposed procedure is principally applicable to nanocrystalline materials.

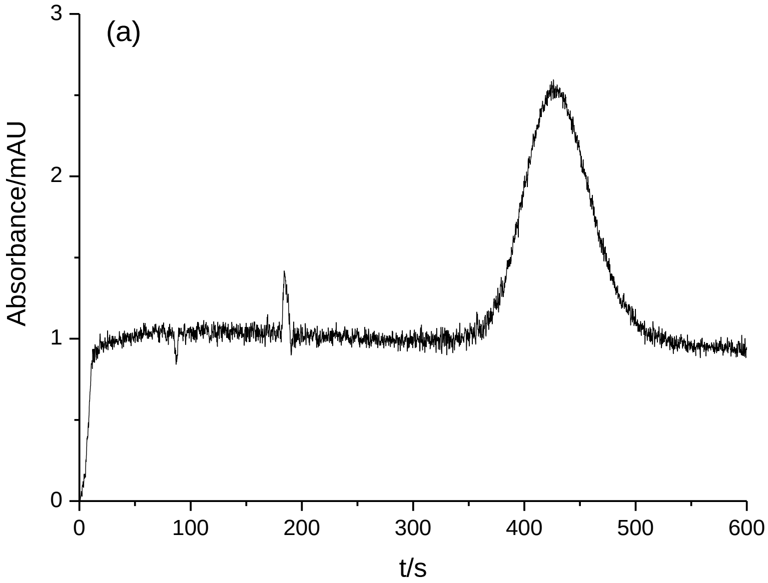

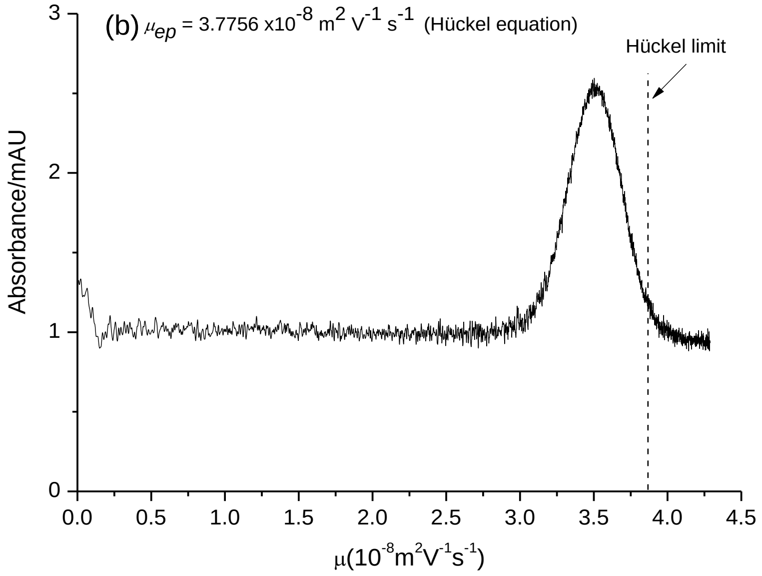

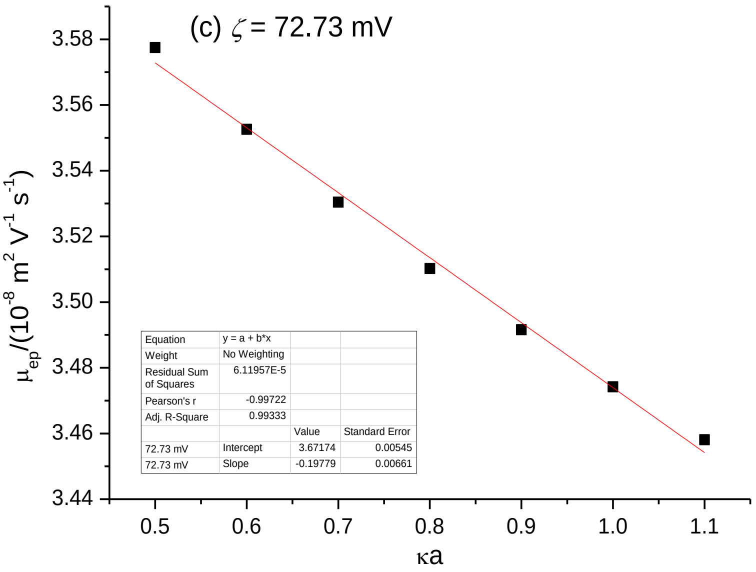

Equation	y = a + b*x		
Weight	No Weighting		
Residual Sum of Squares	6.11957E-5		
Pearson's r	-0.99722		
Adj. R-Square	0.99333		
		Value	Standard Error
72.73 mV	Intercept	3.67174	0.00545
72.73 mV	Slope	-0.19779	0.00661

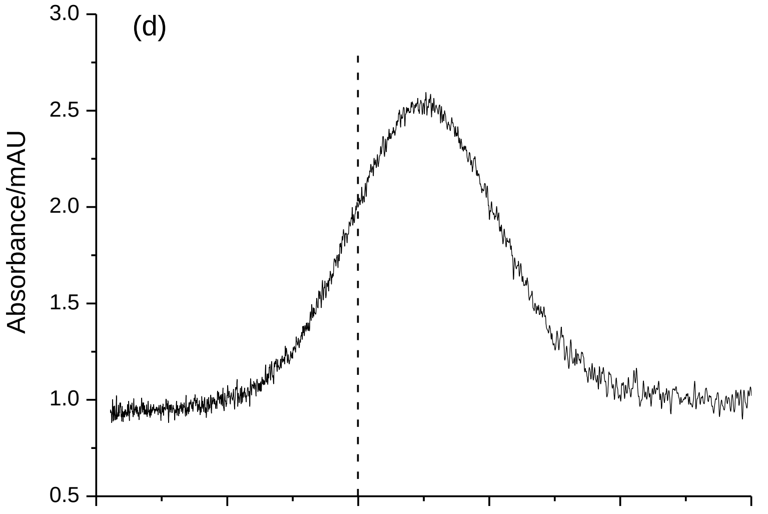

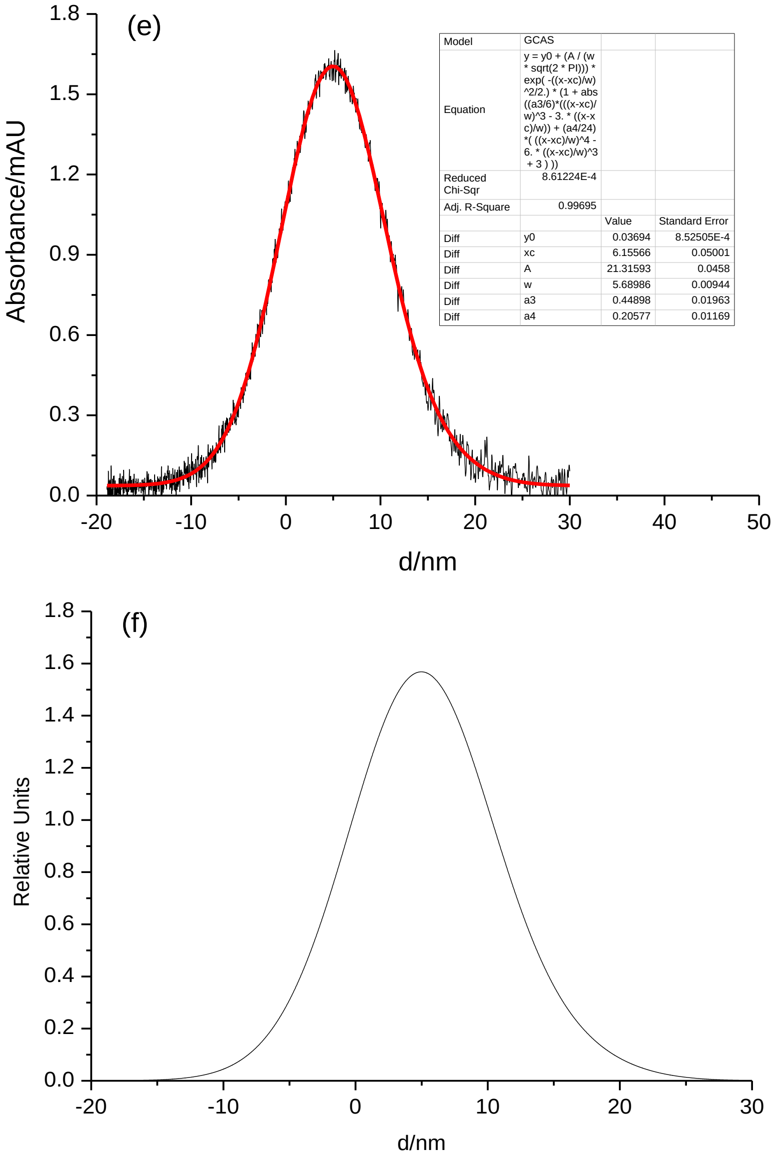

Model	GCAS		
Equation	y = y0 + (A / (w * sqrt(2 * PI))) * exp(-((x-xc)/w)^2/2.) * (1 + abs((a3/6)*(((x-xc)/w)^3 - 3. * ((x-xc)/w)) + (a4/24)*(((x-xc)/w)^4 - 6. * ((x-xc)/w)^3 + 3)))		
Reduced Chi-Sqr	8.61224E-4		
Adj. R-Square	0.99695		
		Value	Standard Error
Diff	y0	0.03694	8.52505E-4
Diff	xc	6.15566	0.05001
Diff	A	21.31593	0.0458
Diff	w	5.68986	0.00944
Diff	a3	0.44898	0.01963
Diff	a4	0.20577	0.01169

Figure 61: Steps of directly converting an electropherogram into a size distribution functions by using the approach introduced by Pyell [81] and Pyell *et al.* [82]: (a) recorded electropherogram of CoOOH-NPs; (b) intensity-weighted distribution of the electrophoretic mobility μ; (c) regression line resulting from using Eq. (20); (d) size coordinate via rearranging the regression function; (e) the resultant lines from fitting to Gram−Charlier series of type A; and (f) new data points calculated with a step length of 0.01 nm by using Gram−Charlier series of type A. Experimental conditions: T = 25 ^{o}C, inner diameter of fused silica capillary = 76 μm, total length of capillary = 39.5 cm, capillary length to detector = 29.2 cm, capillary coating with dynamic coating, background electrolyte = 10 mmol L^{-1} HNO_3 (pH = 2), separation voltage = -10 kV, injection pressure: 0.1 psi (6.89 mbar), date rate = 16 Hz, absorbance detection at 254 nm.

References

References

1. Strambeanu, N.; Demetrovici, L.; Dragos, D.; Lungu, M., Nanoparticles: Definition, Classification and General Physical Properties. In *Nanoparticles' Promises and Risks: Characterization, Manipulation, and Potential Hazards to Humanity and the Environment*, Lungu, M.; Neculae, A.; Bunoiu, M.; Biris, C., Eds. Springer International Publishing: Switzerland, 2015.
2. Alemán, J.; Chadwick, A. V.; He, J.; Hess, M.; Horie, K.; Jones, R. G.; Kratochvíl, P.; Meisel, I.; Mita, I.; Moad, G., Definitions of Terms Relating to the Structure and Processing of Sols, Gels, Networks, and Inorganic-Organic Hybrid Materials (IUPAC Recommendations 2007). *Pure Appl. Chem.* **2007,** *79* (10), 1801-1829.
3. Fisker, R.; Carstensen, J. M.; Hansen, M. F.; Bødker, F.; Mørup, S., Estimation of Nanoparticle Size Distributions by Image Analysis. *J. Nanopar. Res.* **2000,** *2* (3), 267-277.
4. Park, J.; Joo, J.; Kwon, S. G.; Jang, Y.; Hyeon, T., Synthesis of Monodisperse Spherical Nanocrystals. *Angew. Chem. Int. Ed.* **2007,** *46* (25), 4630-4660.
5. Bienert, R.; Emmerling, F.; Thünemann, A. F., The Size Distribution of 'Gold Standard' Nanoparticles. *Anal. Bioanal. Chem.* **2009,** *395* (6), 1651.
6. Zhang, L. L.; Zhao, X. S., Carbon-Based Materials as Supercapacitor Electrodes. *Chem. Soc. Rev.* **2009,** *38* (9), 2520-2531.
7. Brown, M. A.; Abbas, Z.; Kleibert, A.; Green, R. G.; Goel, A.; May, S.; Squires, T. M., Determination of Surface Potential and Electrical Double-Layer Structure at the Aqueous Electrolyte-Nanoparticle Interface. *Phys. Rev. X* **2016,** *6* (1), 011007.
8. Hunter, R., *Zeta Potential in Colloid Science: Principles and Applications*. Academic Press: 1981.
9. Ohshima, H., *Theory of Colloid and Interfacial Electric Phenomena*. Elsevier: Amsterdam, 2006.
10. Medrzycka, K. B., The Effect of Particle Concentration on Zeta Potential in Extremely Dilute Solutions. *Colloid Polym. Sci.* **1991,** *269* (1), 85-90.
11. Ohshima, H., A Simple Expression for Henry's Function for the Retardation Effect in Electrophoresis of Spherical Colloidal Particles. *J. Colloid Interface Sci.* **1994,** *168* (1), 269-271.

12. Tantra, R.; Schulze, P.; Quincey, P., Effect of Nanoparticle Concentration on Zeta-Potential Measurement Results and Reproducibility. *Particuology* **2010,** *8* (3), 279-285.
13. Delgado, A. V.; González-Caballero, F.; Hunter, R. J.; Koopal, L. K.; Lyklema, J., Measurement and Interpretation of Electrokinetic Phenomena. *J. Colloid Interface Sci.* **2007,** *309* (2), 194-224.
14. Wiersema, P.; Loeb, A.; Overbeek, J., Calculation of the Electrophoretic Mobility of a Spherical Colloid Particle. *J. Colloid Interface Sci.* **1966,** *22* (1), 78-99.
15. Masliyah, J. H.; Bhattacharjee, S., *Electrokinetic and Colloid Transport Phenomena*. Wiley: 2006.
16. O'Brien, R.; White, L., Electrophoretic Mobility of a Spherical Colloidal Particle. *J. Chem. Soc. Faraday Trans. 2.* **1978,** *74* (0), 1607-1626.
17. O'Brien, R.; Hunter, R., The Electrophoretic Mobility of Large Colloidal Particles. *Can. J. Chem.* **1981,** *59* (13), 1878-1887.
18. Ohshima, H.; Healy, T. W.; White, L. R., Approximate Analytic Expressions for the Electrophoretic Mobility of Spherical Colloidal Particles and the Conductivity of their Dilute Suspensions. *J. Chem. Soc. Faraday Trans. 2.* **1983,** *79* (11), 1613-1628.
19. Ohshima, H., Approximate Analytic Expression for the Electrophoretic Mobility of a Spherical Colloidal Particle. *J. Colloid Interface Sci.* **2001,** *239* (2), 587-590.
20. Kimura, K.; Takashima, S.; Ohshima, H., Molecular Approach to the Surface Potential Estimate of Thiolate-Modified Gold Nanoparticles. *J. Phys.l Chem. B* **2002,** *106* (29), 7260-7266.
21. Pyell, U.; Jalil, A.; Pfeiffer, C.; Pelaz, B.; Parak, W., Characterization of Gold Nanoparticles with Different Hydrophilic Coatings via Capillary Electrophoresis and Taylor Dispersion Analysis. Part I: Determination of the Zeta Potential Employing a Modified Analytic Approximation. *J. Colloid Interface Sci.* **2015,** *450*, 288-300.
22. Bocquet, L.; Trizac, E.; Aubouy, M., Effective Charge Saturation in Colloidal Suspensions. *J. Chem. Phys.* **2002,** *117* (17), 8138-8152.
23. Stigter, D., Kinetic Charge of Colloidal Electrolytes from Conductance and Electrophoresis. Detergent Micelles, Poly(methacrylates), and DNA in Univalent Salt Solutions. *J. Phys. Chem.* **1979,** *83* (12), 1670–1675.

24. Ohshima, H.; Healy, T.; White, L., Accurate Analytic Expressions for the Surface Charge Density/Surface Potential Relationship and Double-Layer Potential Distribution for a Spherical Colloidal Particle. *J. Colloid Interface Sci.* **1982,** *90* (1), 17-26.
25. Salis, A.; Ninham, B. W., Models and Mechanisms of Hofmeister Effects in Electrolyte Solutions, and Colloid and Protein Systems Revisited. *Chem. Soc. Rev.* **2014,** *43* (21), 7358-7377.
26. Salis, A.; Cugia, F.; Parsons, D. F.; Ninham, B. W.; Monduzzi, M., Hofmeister Series Reversal for Lysozyme by Change in pH and Salt Concentration: Insights from Electrophoretic Mobility Measurements. *Phys. Chem. Chem. Phys.* **2012,** *14* (13), 4343-4346.
27. Lo Nostro, P.; Ninham, B. W., Hofmeister Phenomena: An Update on Ion Specificity in Biology. *Chem. Rev.* **2012,** *112* (4), 2286-2322.
28. Parsons, D. F.; Bostrom, M.; Nostro, P. L.; Ninham, B. W., Hofmeister Effects: Interplay of Hydration, Nonelectrostatic Potentials, and Ion Size. *Phys. Chem. Chem. Phys.* **2011,** *13* (27), 12352-12367.
29. Lyklema, J., Simple Hofmeister Series. *Chem. Phys. Lett.* **2009,** *467* (4–6), 217-222.
30. Jungwirth, P.; Tobias, D. J., Specific Ion Effects at the Air/Water Interface. *Chem. Rev.* **2006,** *106* (4), 1259-1281.
31. Dove, P. M.; Craven, C. M., Surface Charge Density on Silica in Alkali and Alkaline Earth Chloride Electrolyte Solutions. *Geochim. Cosmochim. Acta* **2005,** *69* (21), 4963-4970.
32. Oncsik, T.; Trefalt, G.; Borkovec, M.; Szilagyi, I., Specific Ion Effects on Particle Aggregation Induced by Monovalent Salts within the Hofmeister Series. *Langmuir* **2015,** *31* (13), 3799-3807.
33. Tadros, T.; Lyklema, J., Adsorption of Potential-Determining Ions at the Silica-Aqueous Electrolyte Interface and the Role of Some Cations. *J. Electroanal. Chem.* **1968,** *17* (3), 267-275.
34. Sonnefeld, J.; Göbel, A.; Vogelsberger, W., Surface Charge Density on Spherical Silica Particles in Aqueous Alkali Chloride Solutions-Part 1. Experimental Results. *Colloid Polym. Sci.* **1995,** *273* (10), 926-931.
35. Milonjić, S. K., A Relation between the Amounts of Sorbed Alkali Cations and the Stability of Colloidal Silica. *Colloids Surf.* **1992,** *63* (1–2), 113-119.

36. Kosmulski, M.; Matijević, E., Formation of the Surface Charge on Silica in Mixed Solvents. *Colloid Polym. Sci.* **1992,** *270* (10), 1046-1048.

37. Depasse, J.; Watillon, A., The Stability of Amorphous Colloidal Silica. *J. Colloid Interface Sc.* **1970,** *33* (3), 430-438.

38. Kosmulski, M., Positive Electrokinetic Charge of Silica in the Presence of Chlorides. *J. Colloid Interface Sci.* **1998,** *208* (2), 543-545.

39. Gurney, R. W., *Ionic processes in solution*. McGraw-Hill: New York, 1953.

40. Robinson, R. A.; Stokes, R. H., *Electrolyte Solutions: Second Revised Edition*. Dover Publications, Incorporated: Butterworth: London, 2012.

41. Kaminsky, M., Ion-Solvent Interaction and the Viscosity of Strong-Electrolyte Solutions. *Discuss. Faraday Soc.* **1957,** *24* (0), 171-179.

42. Collins, K., Charge density-Dependent Strength of Hydration and Biological Structure. *Biophys. J.* **1997,** *72* (1), 65-76.

43. Kalyuzhnyi, Y. V.; Vlachy, V.; Dill, K. A., Hydration of Simple Ions. Effect of the Charge Density. *Acta Chim. Slov.* **2001,** *3* (48), 309-316.

44. Tielrooij, K. J.; Garcia-Araez, N.; Bonn, M.; Bakker, H. J., Cooperativity in Ion Hydration. *Science* **2010,** *328* (5981), 1006-1009.

45. Tielrooij, K. J.; van der Post, S. T.; Hunger, J.; Bonn, M.; Bakker, H. J., Anisotropic Water Reorientation around Ions. *J. Phys. Chem. B* **2011,** *115* (43), 12638-12647.

46. Mason, P. E.; Neilson, G. W.; Dempsey, C. E.; Barnes, A. C.; Cruickshank, J. M., The Hydration Structure of Guanidinium and Thiocyanate Ions: Implications for Protein Stability in Aqueous Solution. *Proc. Natl. Acad. Sci. USA* **2003,** *100* (8), 4557-4561.

47. Scott, J. N.; Nucci, N. V.; Vanderkooi, J. M., Changes in Water Structure Induced by the Guanidinium Cation and Implications for Protein Denaturation. *J. Phys. Chem. A* **2008,** *112* (43), 10939-10948.

48. Taylor, G., Dispersion of Soluble Matter in Solvent Flowing Slowly through a Tube. *Proc. R. Soc. London. A.* **1953,** *219* (1137), 186-203.

49. Taylor, G., Conditions under Which Dispersion of a Solute in a Stream of Solvent can be Used to Measure Molecular Diffusion. *Proc. R. Soc. Lond. A* **1954,** *225* (1163), 473-477.

50. Aris, R., On the Dispersion of a Solute in a Fluid Flowing through a Tube. *Proc. R. Soc. London A* **1956,** *235* (1200), 67-77.

51. Sharma, U.; Gleason, N. J.; Carbeck, J. D., Diffusivity of Solutes Measured in Glass Capillaries Using Taylor's Analysis of Dispersion and a Commercial CE Instrument. *Anal. Chem.* **2005,** *77* (3), 806-813.
52. Kok, W., *Capillary Electrophoresis: Instrumentation and Operation*. Vieweg & Sohn Verlagsgesellschaft mbH: Wiesbaden, Germany, 2013.
53. Liu, F.-K.; Wei, G.-T., Adding Sodium Dodecylsulfate to the Running Electrolyte Enhances the Separation of Gold Nanoparticles by Capillary Electrophoresis. *Anal. Chim. Acta* **2004,** *510* (1), 77-83.
54. Hoo, C. M.; Starostin, N.; West, P.; Mecartney, M. L., A Comparison of Atomic Force Microscopy (AFM) and Dynamic Light Scattering (DLS) Methods to Characterize Nanoparticle Size Distributions. *J. Nanopart. Res.* **2008,** *10* (1), 89-96.
55. Peternelj, A. Charge and Size of Particles in Surface Waters. Master’s Thesis, University of Lund, Sweden, 2009.
56. McCann, G.; Vanderhoff, J.; Strickler, A.; Sacks, T., Separation of Latex Particles According to Size by Continuous Electrophoresis. *Sep. Purif. Methods* **1973,** *2* (1), 153-198.
57. Stöber, W.; Fink, A.; Bohn, E., Controlled Growth of Monodisperse Silica Spheres in the Micron Size Range. *J. Colloid Interface Sci.* **1968,** *26* (1), 62-69.
58. Brinker, C. J.; J, B. C.; C. Jeffrey Brinker, G. W. S.; Scherer, G. W.; W, S. G., *Sol-Gel Science: The Physics and Chemistry of Sol-Gel Processing*. Academic Press: San Diego, 1990.
59. Neville, F.; Mohd. Zin, A.; Jameson, G. J.; Wanless, E. J., Preparation and Characterization of Colloidal Silica Particles under Mild Conditions. *J. Chem. Educ.* **2012,** *89* (7), 940-942.
60. Lynwood, C., *Polystyrene: Synthesis, Characteristics and Applications*. Nova Science Publishers, Incorporated: New York, 2014.
61. Odian, G., *Principles of Polymerization*. 4th ed.; Wiley: Hoboken, New Jersey, 2004.
62. Goodwin, J. W.; Hearn, J.; Ho, C. C.; Ottewill, R. H., The Preparation and Characterisation of Polymer Latices Formed in the Absence of Surface Active Agents. *Brit. Polymer J.* **1973,** *5* (5), 347-362.

63. Bardé, F.; Palacin, M. R.; Beaudoin, B.; Delahaye-Vidal, A.; Tarascon, J. M., New Approaches for Synthesizing γIII-CoOOH by Soft Chemistry. *Chem. Mater.* **2004,** *16* (2), 299-306.

64. Kudielka, A.; Bette, S.; Dinnebier, R. E.; Abeykoon, M.; Pietzonka, C.; Harbrecht, B., Variability of Composition and Structural Disorder of Nanocrystalline CoOOH Materials. *J. Mater. Chem. C* **2017,** *5* (11), 2899-2909.

65. Weakley, T., Guanidinium tetraborate(2-) dihydrate, (CH6N3)2[B4O5(OH)4].2H2O. *Acta Cryst. C* **1985,** *41* (3), 377-379.

66. Baryla, N. E.; Lucy, C. A., Semi-Permanent Surfactant Coatings for Inorganic Anion Analysis in Capillary Electrophoresis. *J. Chromatogr. A* **2002,** *956* (1), 271-277.

67. d'Orlyé, F.; Varenne, A.; Gareil, P., Determination of Nanoparticle Diffusion Coefficients by Taylor Dispersion Analysis using a Capillary Electrophoresis Instrument. *J. Chromatogr. A* **2008,** *1204* (2), 226-232.

68. Lucy, C. A.; Baryla, N. E.; Yeung, K. K.-C., Surfactant-Based Methods for Prevention of Protein Adsorption in Capillary Electrophoresis. In *Capillary Electrophoresis of Proteins and Peptides*, Strege, M. A.; Lagu, A. L., Eds. Humana Press: Totowa, New Jersey, 2004.

69. Allen, L. H.; Matijević, E., Stability of Colloidal Silica: I. Effect of Simple Electrolytes. *J. Colloid Interface Sci.* **1969,** *31* (3), 287-296.

70. Nichols, S. C.; Loewenberg, M.; Davis, R. H., Electrophoretic Particle Aggregation. *J. Colloid Interface Sci.* **1995,** *176* (2), 342-351.

71. Fichtner, A.; Jalil, A.; Pyell, U., Determination of the Exact Particle Radius Distribution for Silica Nanoparticles via Capillary Electrophoresis and Modeling the Electrophoretic Mobility with a Modified Analytic Approximation. *Langmuir* **2017,** *33* (9), 2325-2339.

72. Appel, R.; Cruse, K.; Drossbach, P.; Falkenhagen, H.; Grau, G. G.; schmutzer, E.; Strehlow, H., *Landolt-Börnstein, Zahlenwerte und Funktionen aus Physik Chemie Astronomie Geophysik Technik, 6 Auflage, II. Band, 7. Teil, Elektrische Eigenschaften II (Elektrochemische Systeme)*. Springer-Verlag: Berlin, 1960.

73. Hunger, J.; Neueder, R.; Buchner, R.; Apelblat, A., A Conductance Study of Guanidinium Chloride, Thiocyanate, Sulfate, and Carbonate in Dilute Aqueous Solutions: Ion-Association and Carbonate Hydrolysis Effects. *J. Phys. Chem. B* **2013,** *117* (2), 615-622.

74. Pyell, U.; Jalil, A. H.; Pfeiffer, C.; Pelaz, B.; Parak, W. J., Characterization of Gold Nanoparticles with Different Hydrophilic Coatings via Capillary Electrophoresis and Taylor Dispersion Analysis. Part I: Determination of the Zeta Potential Employing a Modified Analytic Approximation. *J. Colloid Interface Sci.* **2015,** *450*, 288-300.

75. Wang, H.; Pilon, L., Accurate Simulations of Electric Double Layer Capacitance of Ultramicroelectrodes. *J. Phys. Chem. C* **2011,** *115* (33), 16711-16719.

76. Ma, X.; Pawlik, M., Effect of Alkali Metal Cations on Adsorption of Guar Gum onto Quartz. *J. Colloid Interface Sci.* **2005,** *289* (1), 48-55.

77. Kunz, W.; Lo Nostro, P.; Ninham, B. W., The Present State of Affairs with Hofmeister Effects. *Curr. Opin. Colloid Interface Sci.* **2004,** *9* (1–2), 1-18.

78. Lyklema, J., Lyotropic Sequences in Colloid Stability Revisited. *Adv. Colloid Interface Sci.* **2003,** *100-102*, 1-12.

79. van der Linden, M.; Conchúir, B. O.; Spigone, E.; Niranjan, A.; Zaccone, A.; Cicuta, P., Microscopic Origin of the Hofmeister Effect in Gelation Kinetics of Colloidal Silica. *J. Phys. Chem. Lett.* **2015,** *6* (15), 2881-2887.

80. Barisik, M.; Atalay, S.; Beskok, A.; Qian, S., Size Dependent Surface Charge Properties of Silica Nanoparticles. *J. Phys. Chem. C* **2014,** *118* (4), 1836-1842.

81. Pyell, U., CE Characterization of Semiconductor Nanocrystals Encapsulated with Amorphous Silicium Dioxide. *ELECTROPHORESIS* **2008,** *29* (3), 576-589.

82. Pyell, U.; Jalil, A. H.; Urban, D. A.; Pfeiffer, C.; Pelaz, B.; Parak, W. J., Characterization of Hydrophilic Coated Gold Nanoparticles via Capillary Electrophoresis and Taylor Dispersion Analysis. Part II: Determination of the Hydrodynamic Radius Distribution - Comparison with Asymmetric Flow Field-Flow Fractionation. *J. Colloid Interface Sci.* **2015,** *457*, 131-140.

83. Jalil, A. H.; Pyell, U., Quantification of Zeta-Potential and Electrokinetic Surface Charge Density for Colloidal Silica Nanoparticles Dependent on Type and Concentration of the Counterion: Probing the Outer Helmholtz Plane. *J. Phys. Chem. C* **2018,** *122* (8), 4437-4453.

84. Chung, H. S.; Hogg, R., The Effect of Brownian Motion on Particle Size Analysis by Sedimentation. *Powder Technology* **1985,** *41* (3), 211-216.

85. Cotton, A. F.; Wilkinson, G.; Bochmann, M.; Murillo, C. A., *Advanced Inorganic Chemistry*. Wiley: 1999.

86. Mortimer, R. G., *Physical Chemistry*. Elsevier Science: 2008.
87. SURANA, V. S. Leaching of Goethite in Acid Solutions, Master Thesis. The University of British Columbia, Vancouver 8, Canada, 1969.
88. Hay, R. W., *Reaction Mechanisms of Metal Complexes*. Horwood Publishing: UK, 2000.
89. Abdus-Salam, N.; Adekola, F., Comparative Dissolution of Natural Goethite Samples in HCl and HNO3. *J. Appl. Sci. Environ. Mgt.* **2006,** *10* (2), 11 - 17.
90. F. Albert Cotton; Geoffrey Wilkinson; Carlos A. Murillo; Bochmann, M., *Advanced Inorganic Chemistry*. John Wiley & Sons, Inc.: New York, 1999.
91. Horvath, J.; Dolník, V., Polymer Wall Coatings for Capillary Electrophoresis. *ELECTROPHORESIS* **2001,** *22* (4), 644-655.
92. Hjertén, S., High-Performance Electrophoresis. *J. Chromatogr. A* **1985,** *347*, 191-198.
93. Craig, M. T.; R., D. N.; G., W. D.; Dietmar, S., Investigation of the Microstructure of Poly(diallyldimethyl-ammonium chloride) by Nitrogen-14(15) NMR Spectroscopy. *J. Polym. Sci. Part B: Polym Physics* **1994,** *32* (13), 2263-2270.
94. John, W. Synthesis, Properties and Analysis of PolyDADMAC for Water Purification. Stellenbosch: Stellenbosch University, 2008.
95. Córdova, E.; Gao, J.; Whitesides, G. M., Noncovalent Polycationic Coatings for Capillaries in Capillary Electrophoresis of Proteins. *Anal. Chem.* **1997,** *69* (7), 1370-1379.
96. Katayama, H.; Ishihama, Y.; Asakawa, N., Stable Capillary Coating with Successive Multiple Ionic Polymer Layers. *Anal. Chem.* **1998,** *70* (11), 2254-2260.
97. Melanson, J. E.; Baryla, N. E.; Lucy, C. A., Double-Chained Surfactants for Semipermanent Wall Coatings in Capillary Electrophoresis. *Anal. Chem.* **2000,** *72* (17), 4110-4114.
98. Baryla, N. E.; Melanson, J. E.; McDermott, M. T.; Lucy, C. A., Characterization of Surfactant Coatings in Capillary Electrophoresis by Atomic Force Microscopy. *Anal. Chem.* **2001,** *73* (19), 4558-4565.
99. Melanson, J. E.; Baryla, N. E.; Lucy, C. A., Dynamic Capillary Coatings for Electroosmotic Flow Control in Capillary Electrophoresis. *Trends Anal. Chem.* **2001,** *20* (6), 365-374.

100. Kaneta, T.; Tanaka, S.; Taga, M.; Yoshida, H., Migration Behavior of Inorganic Anions in Micellar Electrokinetic Capillary Chromatography Using Cationic Surfactant. *Anal. Chem.* **1992,** *64* (7), 798-801.
101. Nightingale, E. R., Phenomenological Theory of Ion Solvation. Effective Radii of Hydrated Ions. *J. Phys. Chem.* **1959,** *63* (9), 1381-1387.
102. Penn, R. L.; Banfield, J. F., Imperfect Oriented Attachment: Dislocation Generation in Defect-Free Nanocrystals. *Science* **1998,** *281* (5379), 969-971.
103. Huang, F.; Zhang, H.; Banfield, J. F., Two-Stage Crystal-Growth Kinetics Observed during Hydrothermal Coarsening of Nanocrystalline ZnS. *Nano Lett.* **2003,** *3* (3), 373-378.
104. Tadros, T., *Encyclopedia of Colloid and Interface Science*. Springer-Verlag Berlin Heidelberg: 2013.
105. Zhang, J.; Huang, F.; Lin, Z., Progress of Nanocrystalline Growth Kinetics Based on Oriented Attachment. *Nanoscale* **2010,** *2* (1), 18-34.
106. Dean, J. A.; Lange, N. A., *Lange's Handbook of Chemistry*. 15th ed.; McGraw-Hill: New York, 1999.
107. Dawson, L. R.; Golben, M.; Leader, G. R.; Zimmerman, H. K., The Limiting Equivalent Conductances of Aqueous Barium Alkanesulfonates. *J. Phys. Chem.* **1951,** *55* (9), 1499-1502.
108. Paul, B. K.; Moulik, S. P.; Kunz, W., *Ionic Liquid-Based Surfactant Science: Formulation, Characterization, and Applications*. Wiley: Hoboken, New Jersey, 2015.
109. Allen, H. C.; Raymond, E. A.; Richmond, G. L., Surface Structural Studies of Methanesulfonic Acid at Air /Aqueous Solution Interfaces Using Vibrational Sum Frequency Spectroscopy. *J. Phys. Chem. A* **2001,** *105* (9), 1649-1655.
110. Chang, Q., *Colloid and Interface Chemistry for Water Quality Control*. Elsevier Science: London, 2016.

Appendix

Appendix A1

Superimposed electropherograms obtained in consecutive runs for SNP12 and SNP22 with different concentrations of different counterions at the wavelength of 214 nm. Experimental conditions: T= 25°C, total length of capillary = 39.5 cm, capillary length to detector = 29.2 cm, inner diameter of fused silica capillary = 76 µm, separation voltage 7 kV, sample injection 0.1 psi (6.89 mbar) 6 s, data rate 16 Hz, absorbance detection.

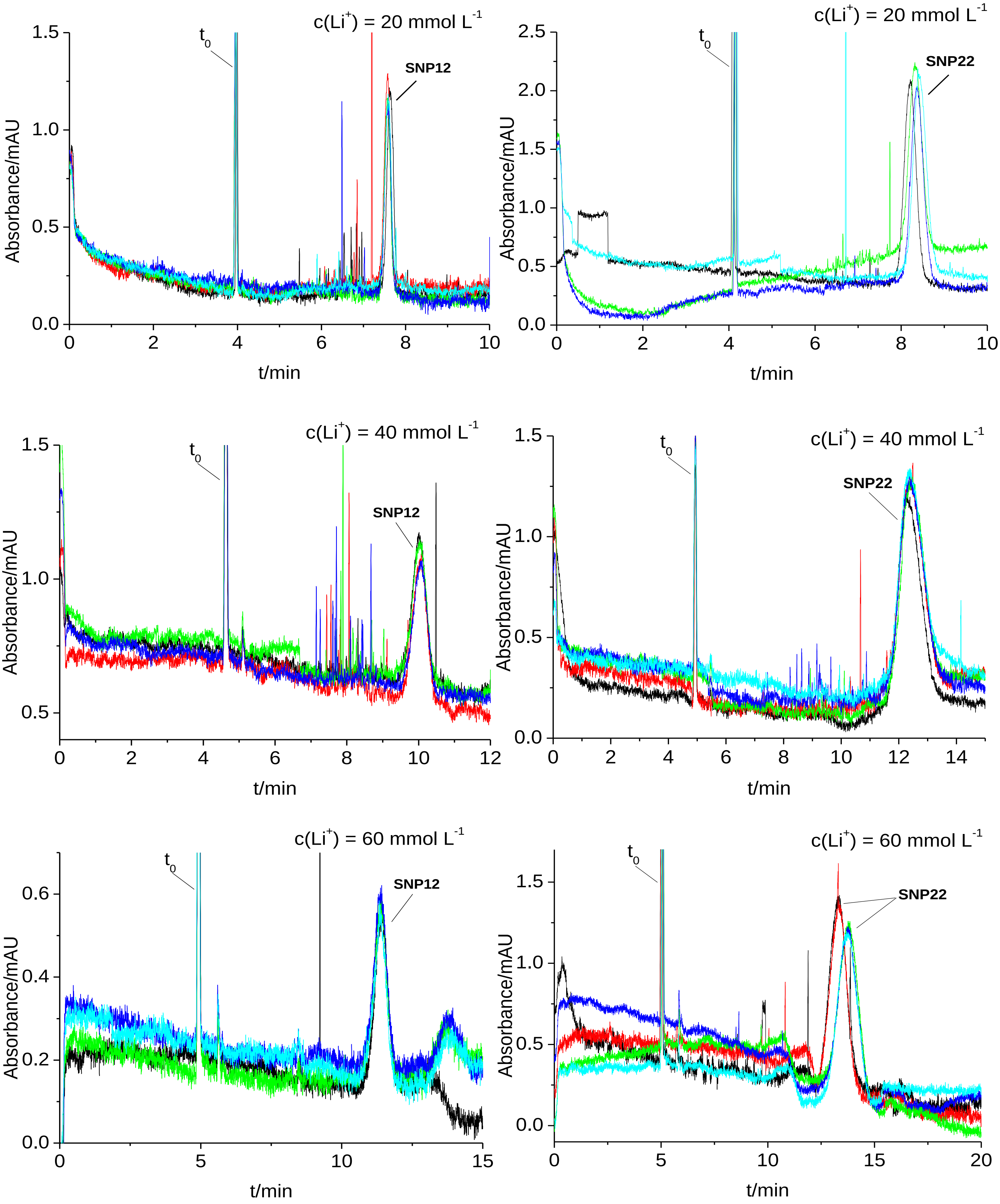

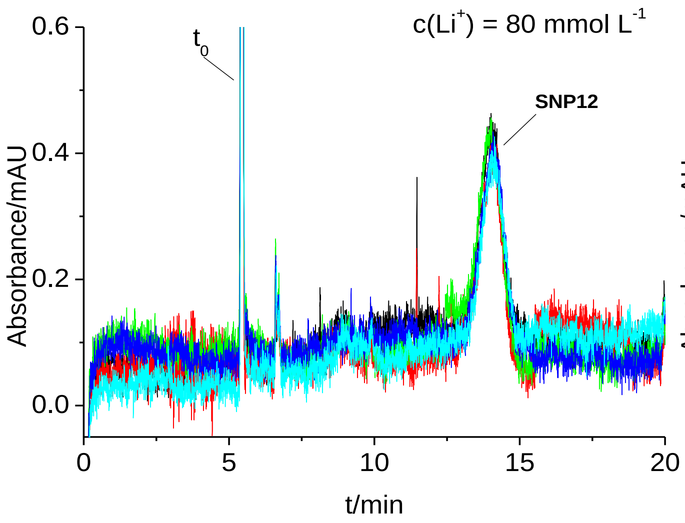
c(Li$^+$) = 80 mmol L^{-1}
t$_0$
SNP12
Absorbance/mAU
0.0
0.2
0.4
0.6
0
5
10
15
20
t/min

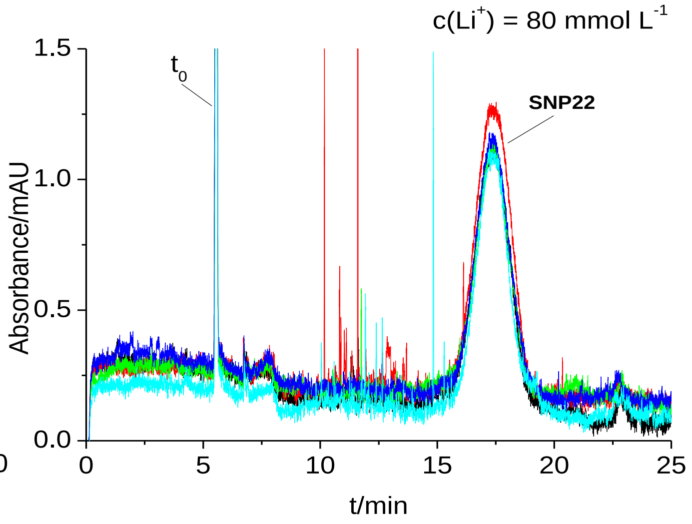
c(Li$^+$) = 80 mmol L^{-1}
t$_0$
SNP22
Absorbance/mAU
0.0
0.5
1.0
1.5
0
5
10
15
20
25
t/min

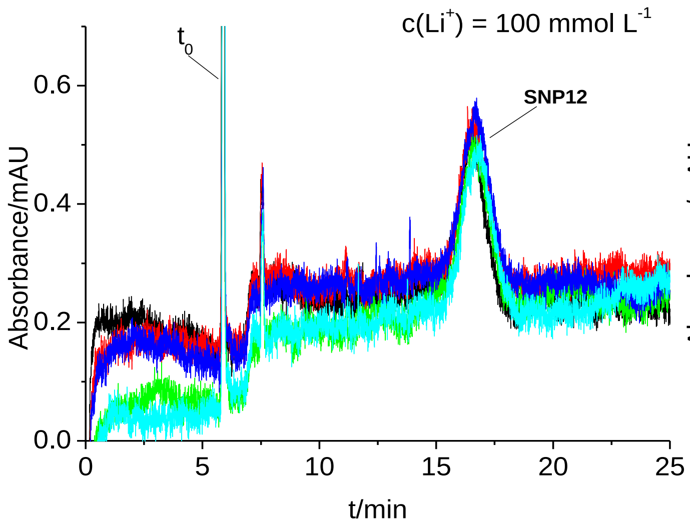
c(Li$^+$) = 100 mmol L^{-1}
t$_0$
SNP12
Absorbance/mAU
0.0
0.2
0.4
0.6
0
5
10
15
20
25
t/min

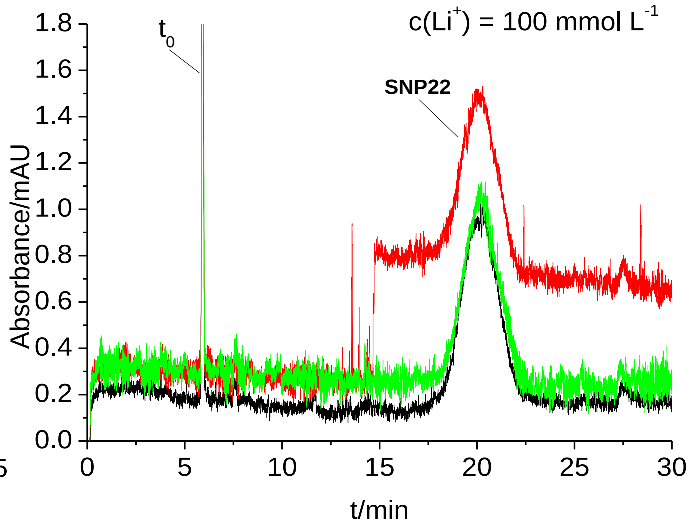
c(Li$^+$) = 100 mmol L^{-1}
t$_0$
SNP22
Absorbance/mAU
0.0
0.2
0.4
0.6
0.8
1.0
1.2
1.4
1.6
1.8
0
5
10
15
20
25
30
t/min

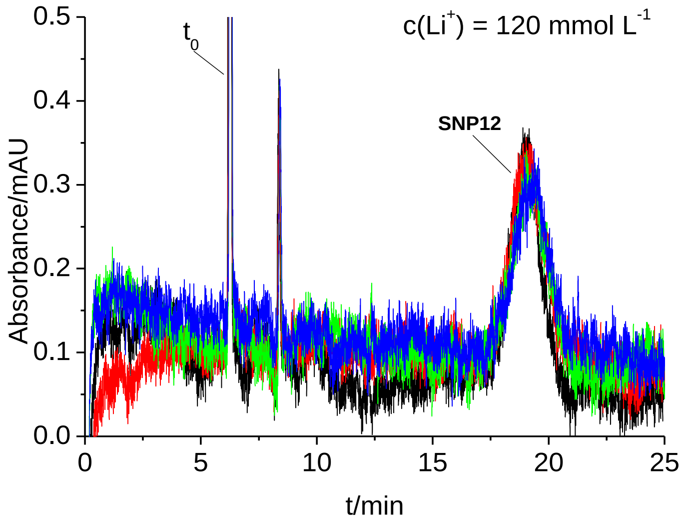
c(Li$^+$) = 120 mmol L^{-1}
t$_0$
SNP12
Absorbance/mAU
0.0
0.1
0.2
0.3
0.4
0.5
0
5
10
15
20
25
t/min

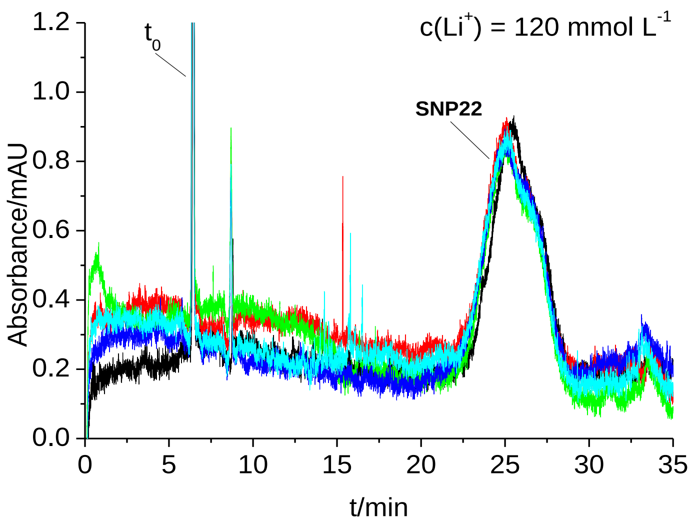
c(Li$^+$) = 120 mmol L^{-1}
t$_0$
SNP22
Absorbance/mAU
0.0
0.2
0.4
0.6
0.8
1.0
1.2
0
5
10
15
20
25
30
35
t/min

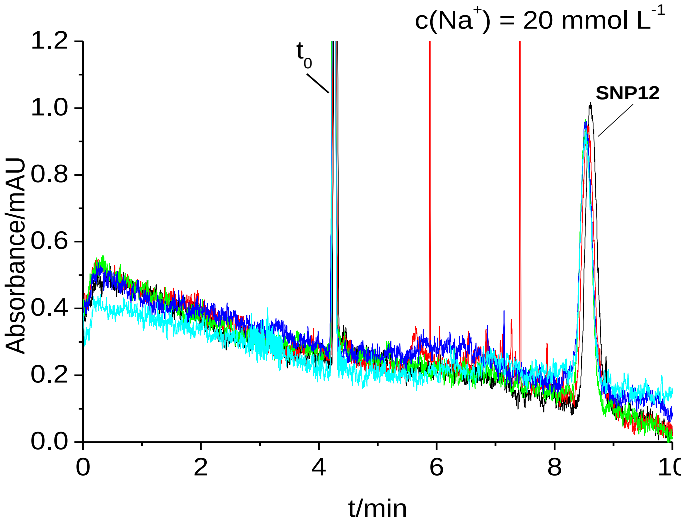
c(Na⁺) = 20 mmol L⁻¹
t₀
SNP12
Absorbance/mAU
t/min
0.0
0.2
0.4
0.6
0.8
1.0
1.2
0
2
4
6
8
10

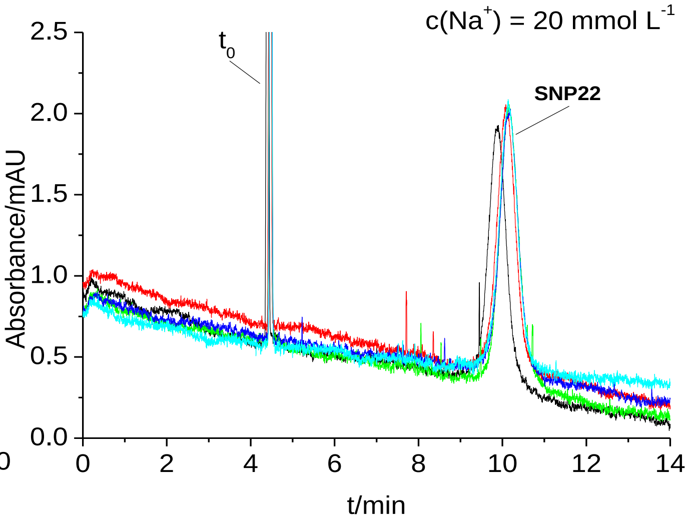
c(Na⁺) = 20 mmol L⁻¹
t₀
SNP22
Absorbance/mAU
t/min
0.0
0.5
1.0
1.5
2.0
2.5
0
2
4
6
8
10
12
14

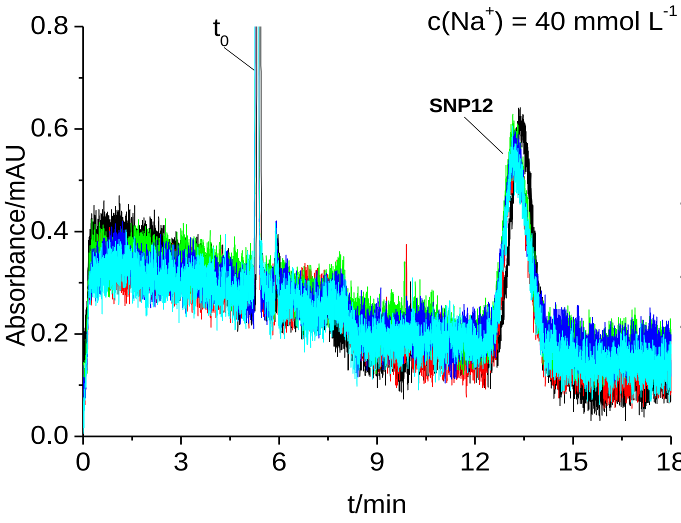
c(Na⁺) = 40 mmol L⁻¹
t₀
SNP12
Absorbance/mAU
t/min
0.0
0.2
0.4
0.6
0.8
0
3
6
9
12
15
18

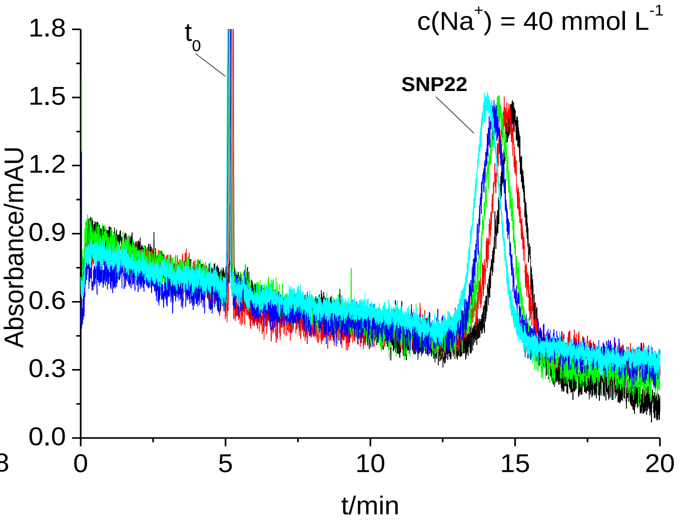
c(Na⁺) = 40 mmol L⁻¹
t₀
SNP22
Absorbance/mAU
t/min
0.0
0.3
0.6
0.9
1.2
1.5
1.8
0
5
10
15
20

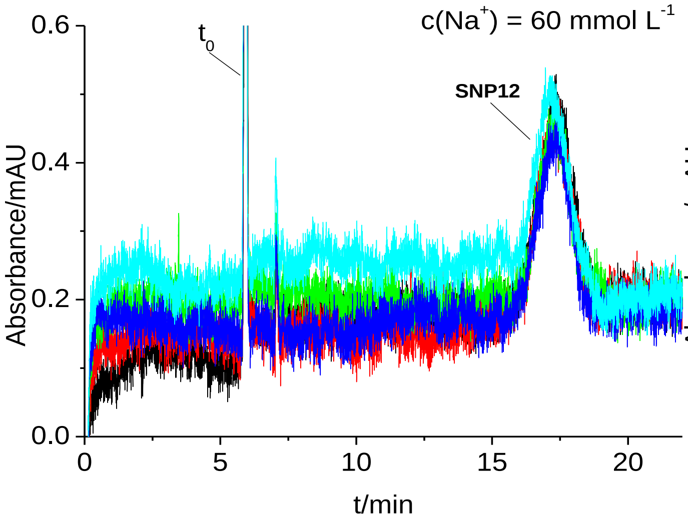
c(Na⁺) = 60 mmol L⁻¹
t₀
SNP12
Absorbance/mAU
t/min
0.0
0.2
0.4
0.6
0
5
10
15
20

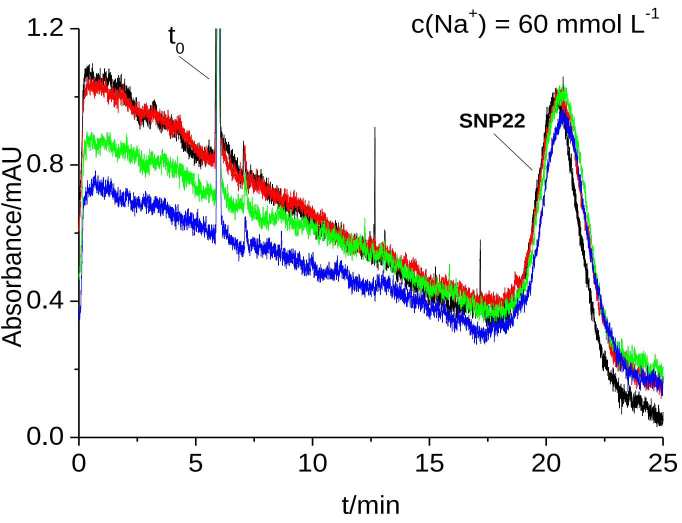
c(Na⁺) = 60 mmol L⁻¹
t₀
SNP22
Absorbance/mAU
t/min
0.0
0.4
0.8
1.2
0
5
10
15
20
25

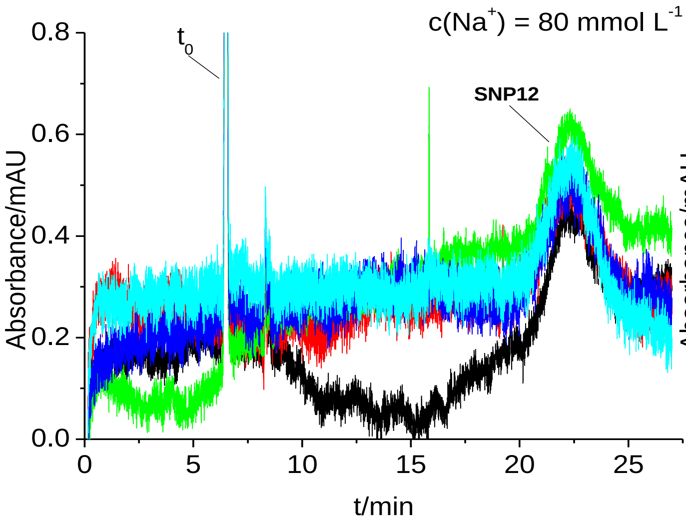
c(Na+) = 80 mmol L-1
t0
SNP12
Absorbance/mAU
0.0
0.2
0.4
0.6
0.8
t/min
0
5
10
15
20
25

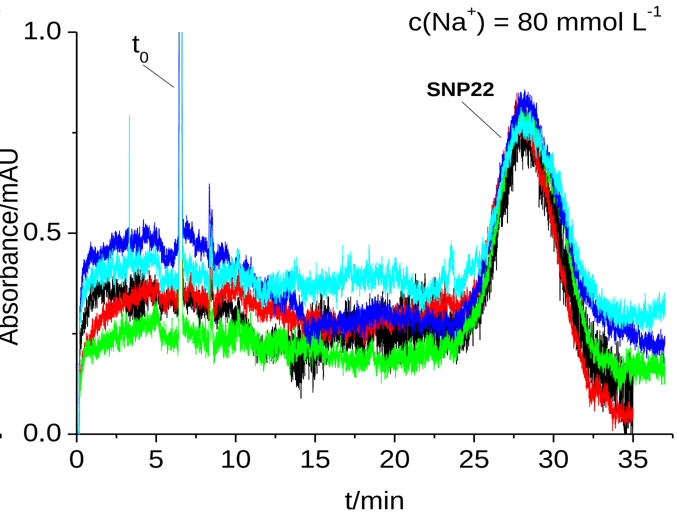
c(Na+) = 80 mmol L-1
t0
SNP22
Absorbance/mAU
0.0
0.5
1.0
t/min
0
5
10
15
20
25
30
35

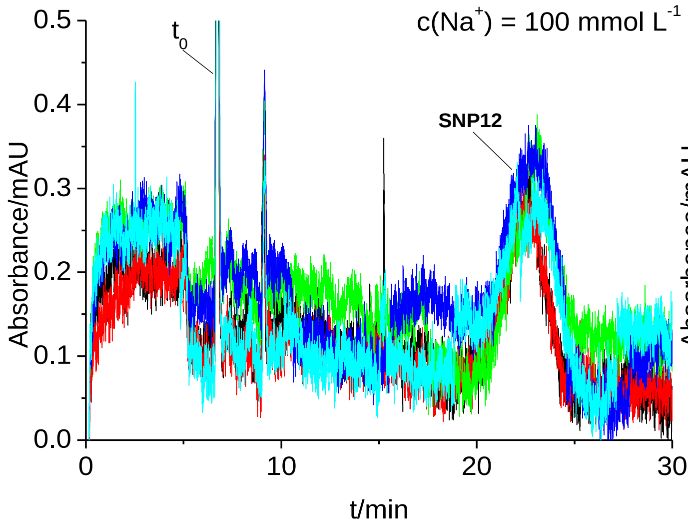
c(Na+) = 100 mmol L-1
t0
SNP12
Absorbance/mAU
0.0
0.1
0.2
0.3
0.4
0.5
t/min
0
10
20
30

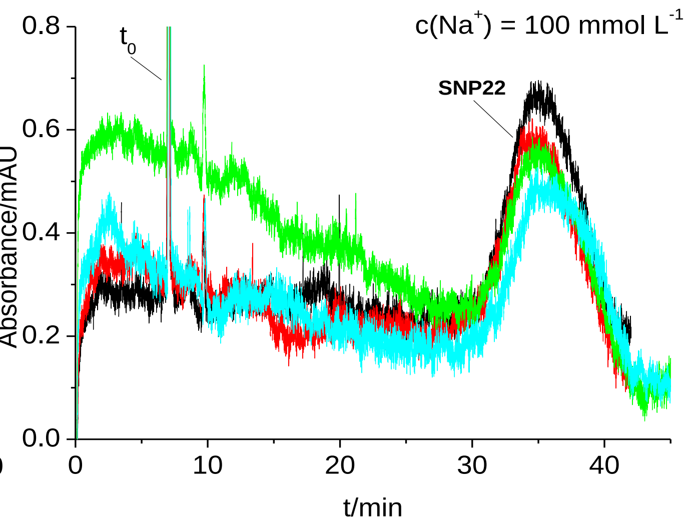
c(Na+) = 100 mmol L-1
t0
SNP22
Absorbance/mAU
0.0
0.2
0.4
0.6
0.8
t/min
0
10
20
30
40

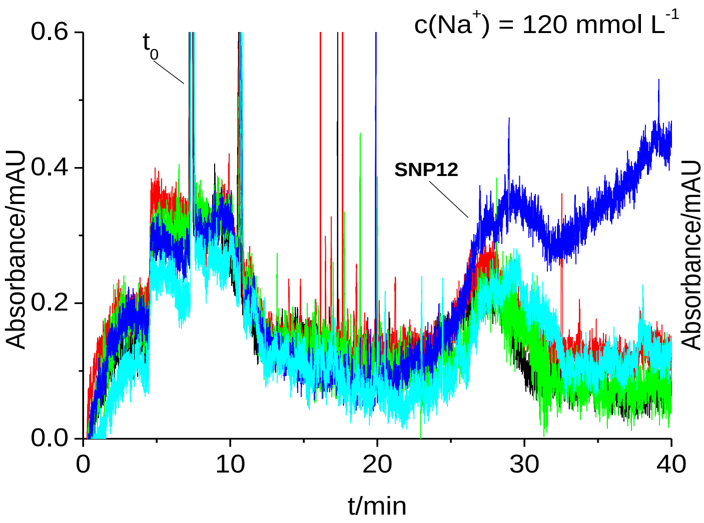
c(Na+) = 120 mmol L-1
t0
SNP12
Absorbance/mAU
0.0
0.2
0.4
0.6
t/min
0
10
20
30
40

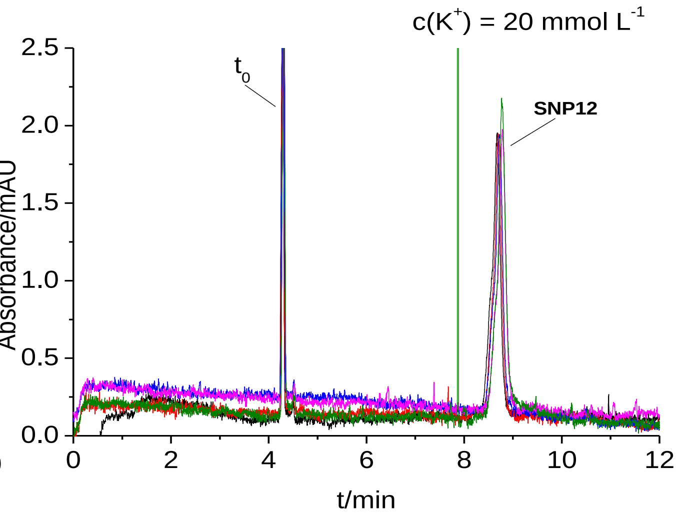
c(K+) = 20 mmol L-1
t0
SNP12
Absorbance/mAU
0.0
0.5
1.0
1.5
2.0
2.5
t/min
0
2
4
6
8
10
12

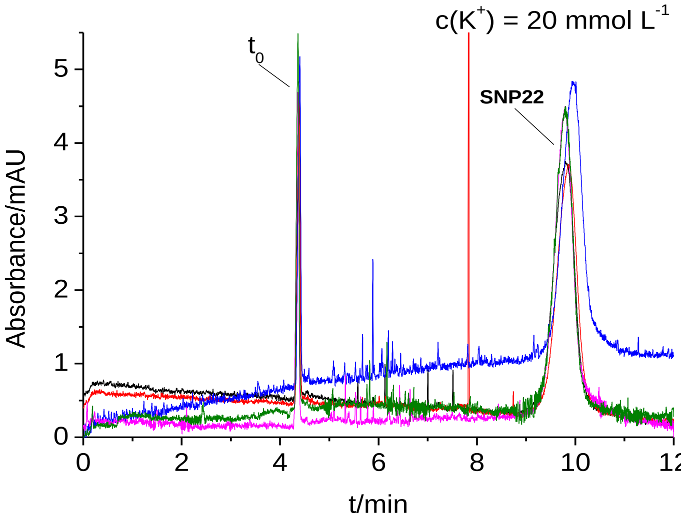
c(K$^+$) = 20 mmol L^{-1}
t$_0$
SNP22
Absorbance/mAU
0
1
2
3
4
5
t/min
0
2
4
6
8
10
12

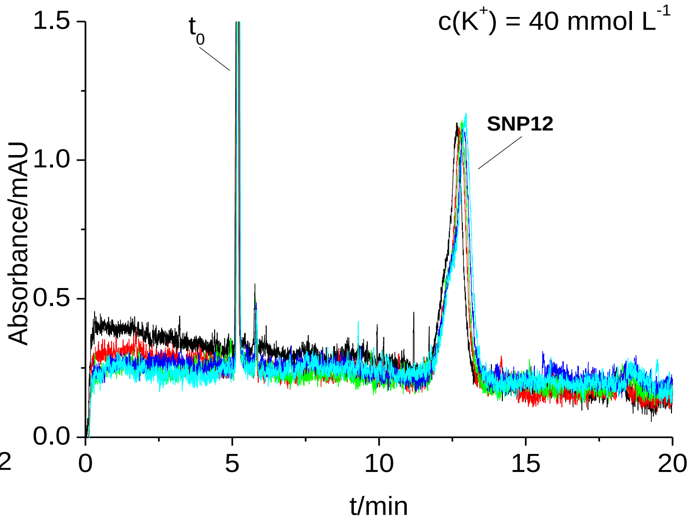
c(K$^+$) = 40 mmol L^{-1}
t$_0$
SNP12
Absorbance/mAU
0.0
0.5
1.0
1.5
t/min
0
5
10
15
20

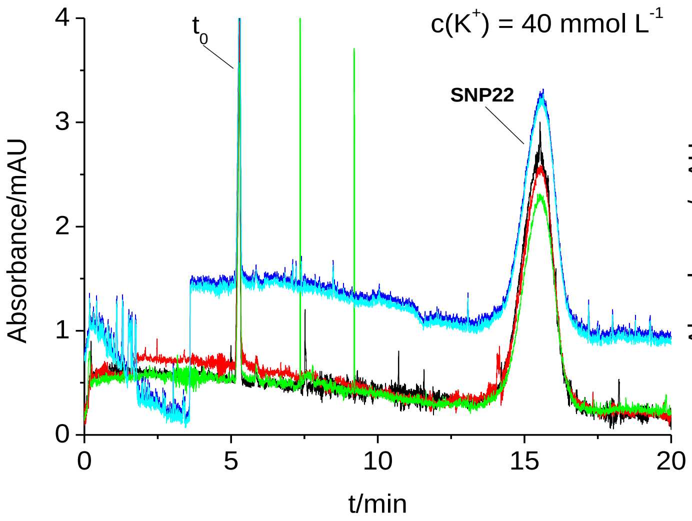
c(K$^+$) = 40 mmol L^{-1}
t$_0$
SNP22
Absorbance/mAU
0
1
2
3
4
t/min
0
5
10
15
20

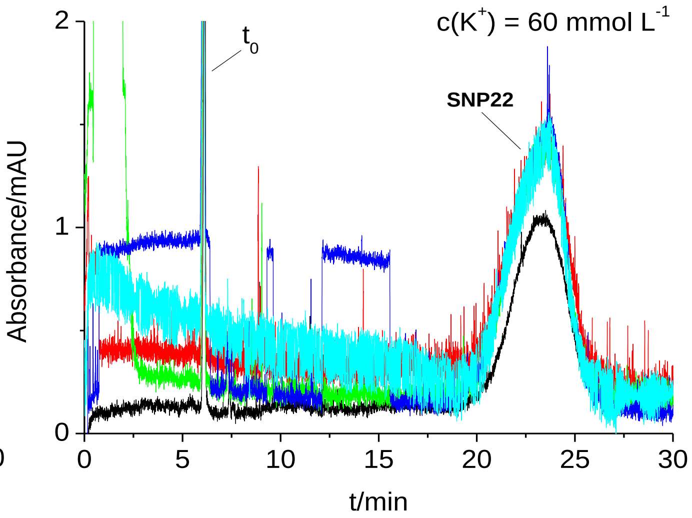
c(K$^+$) = 60 mmol L^{-1}
t$_0$
SNP22
Absorbance/mAU
0
1
2
t/min
0
5
10
15
20
25
30

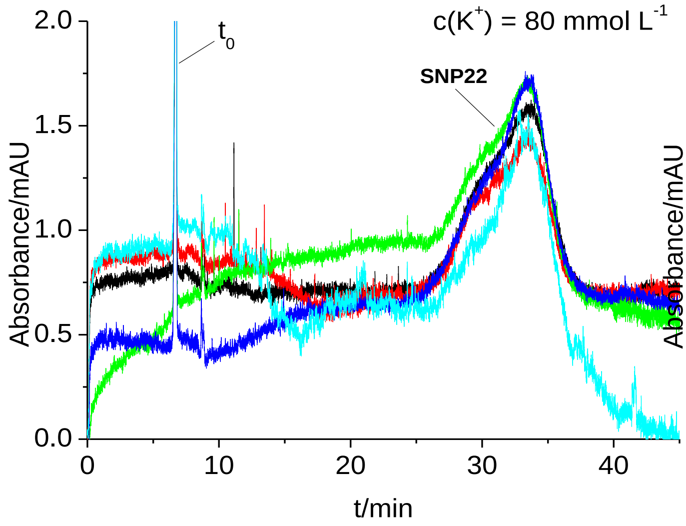
c(K$^+$) = 80 mmol L^{-1}
t$_0$
SNP22
Absorbance/mAU
0.0
0.5
1.0
1.5
2.0
t/min
0
10
20
30
40

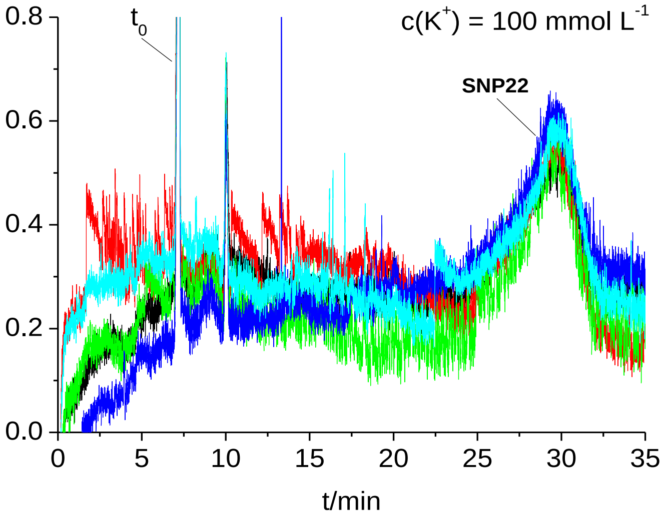
c(K$^+$) = 100 mmol L^{-1}
t$_0$
SNP22
Absorbance/mAU
0.0
0.2
0.4
0.6
0.8
t/min
0
5
10
15
20
25
30
35

Appendix A2

Superimposed electropherograms obtained in consecutive runs for: SNP7, SNP12 and SNP22 with a 20 mmol L^{-1} of different monovalent counterions at the wavelength of 200 nm. Experimental conditions: T= 25°C, total length of capillary = 39.5 cm, capillary length to detector = 29.2 cm, inner diameter of fused silica capillary = 76 μm, separation voltage 7 kV, sample injection 0.1 psi (6.89 mbar) 6 s, data rate 16 Hz, absorbance detection.

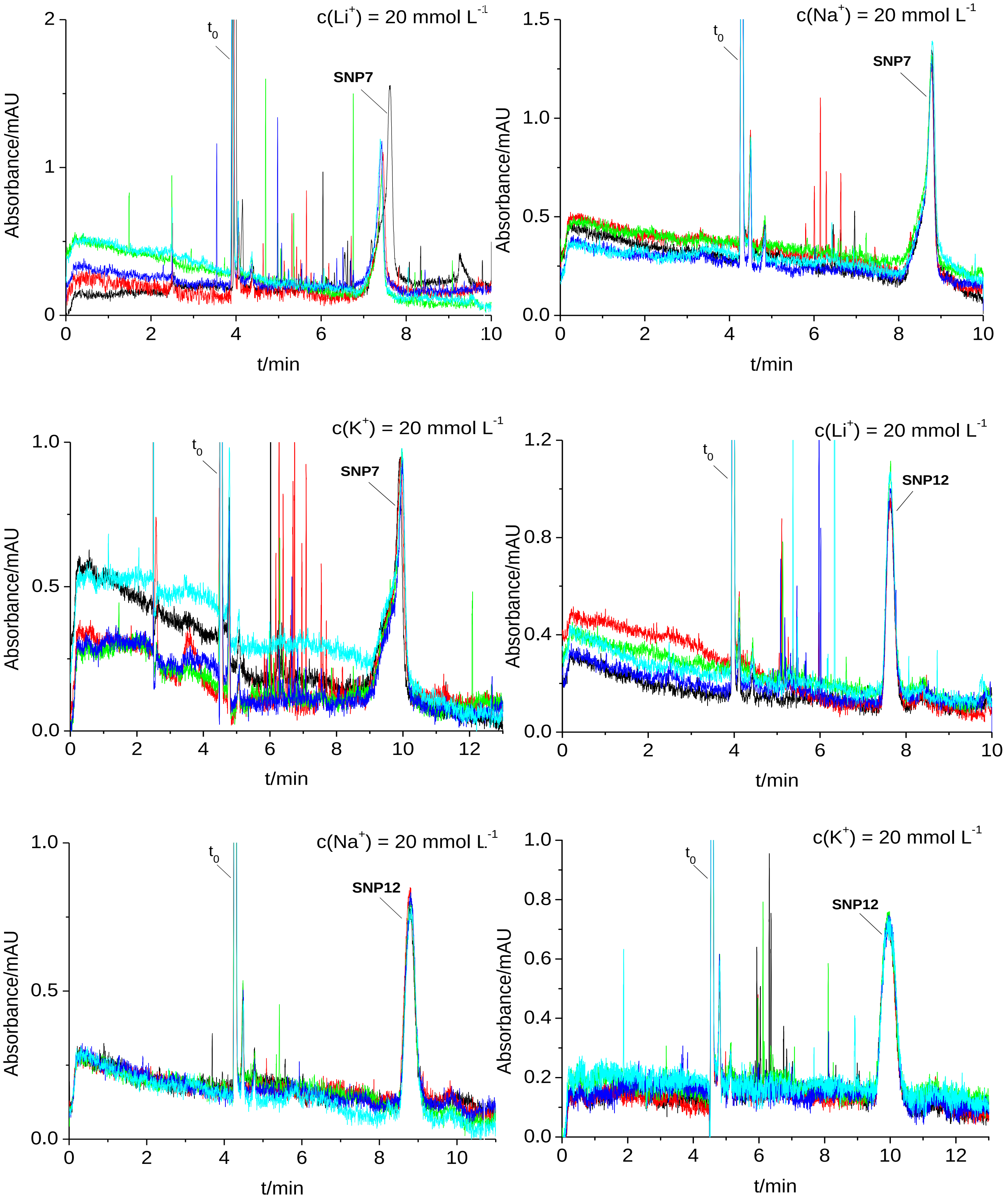

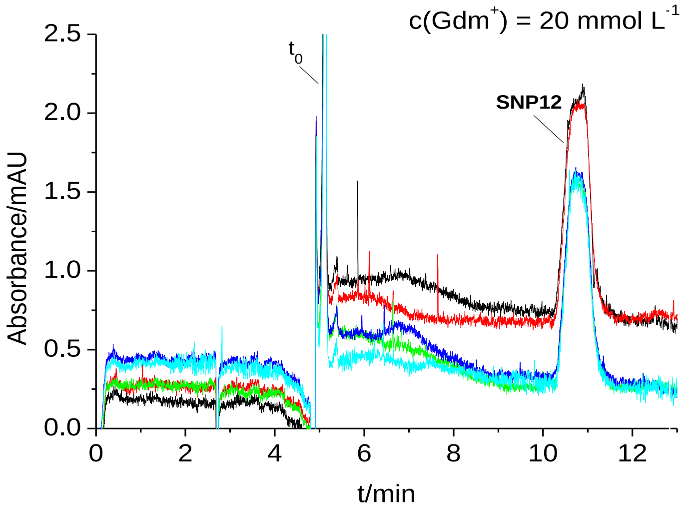
c(Gdm$^+$) = 20 mmol L^{-1}
t$_0$
SNP12
Absorbance/mAU
0.0
0.5
1.0
1.5
2.0
2.5
0
2
4
6
8
10
12
t/min

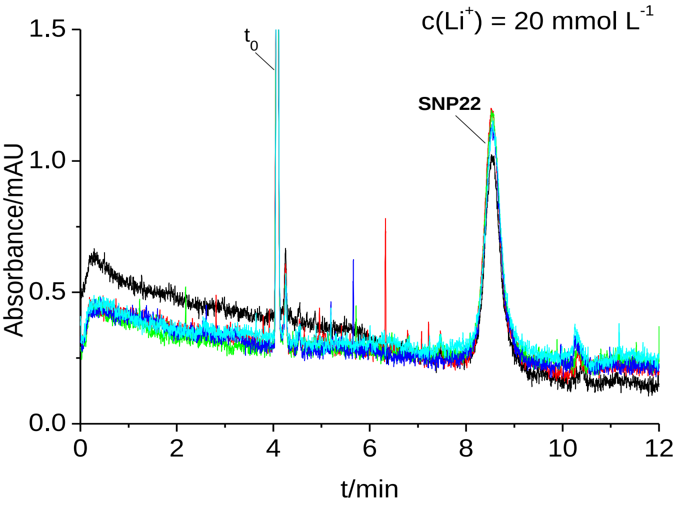
c(Li$^+$) = 20 mmol L^{-1}
t$_0$
SNP22
Absorbance/mAU
0.0
0.5
1.0
1.5
0
2
4
6
8
10
12
t/min

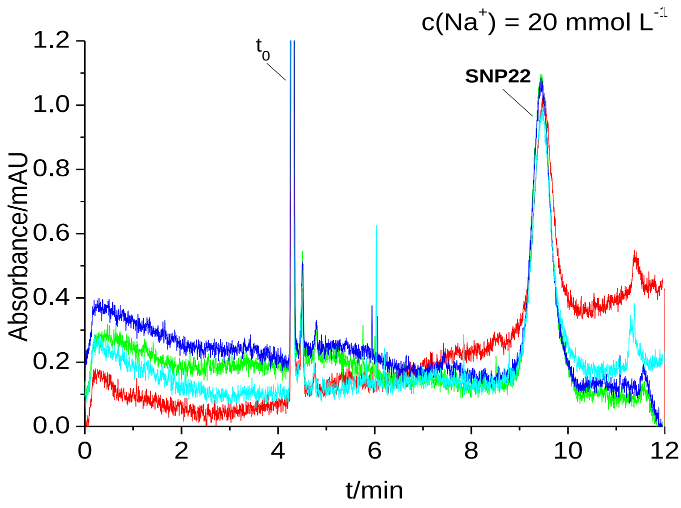
c(Na$^+$) = 20 mmol L^{-1}
t$_0$
SNP22
Absorbance/mAU
0.0
0.2
0.4
0.6
0.8
1.0
1.2
0
2
4
6
8
10
12
t/min

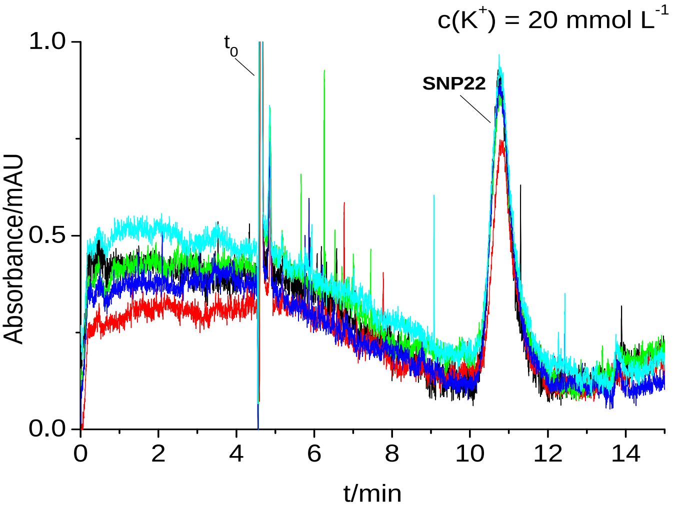
c(K$^+$) = 20 mmol L^{-1}
t$_0$
SNP22
Absorbance/mAU
0.0
0.5
1.0
0
2
4
6
8
10
12
14
t/min

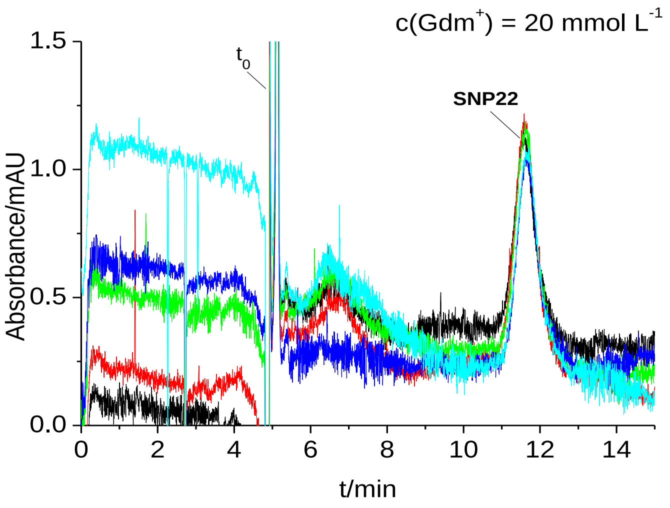
c(Gdm$^+$) = 20 mmol L^{-1}
t$_0$
SNP22
Absorbance/mAU
0.0
0.5
1.0
1.5
0
2
4
6
8
10
12
14
t/min

Appendix A3

Superimposed electropherograms obtained in consecutive runs for: (1) SNP7 (w= 0.4%, w/w in mixture), (2) SNP12 (w= 0.9%, w/w in mixture) and (3) SNP22 (w= 1.7%, w/w in mixture) with a separation electrolyte of different counterions at the wavelength of 200 nm. Experimental conditions: T= 25°C, total length of capillary = 39.5 cm, capillary length to detector = 29.2 cm, inner diameter of fused silica capillary = 76 µm, separation voltage 7 kV, sample injection 0.1 psi (6.89 mbar) 6 s, data rate 16 Hz, absorbance detection.

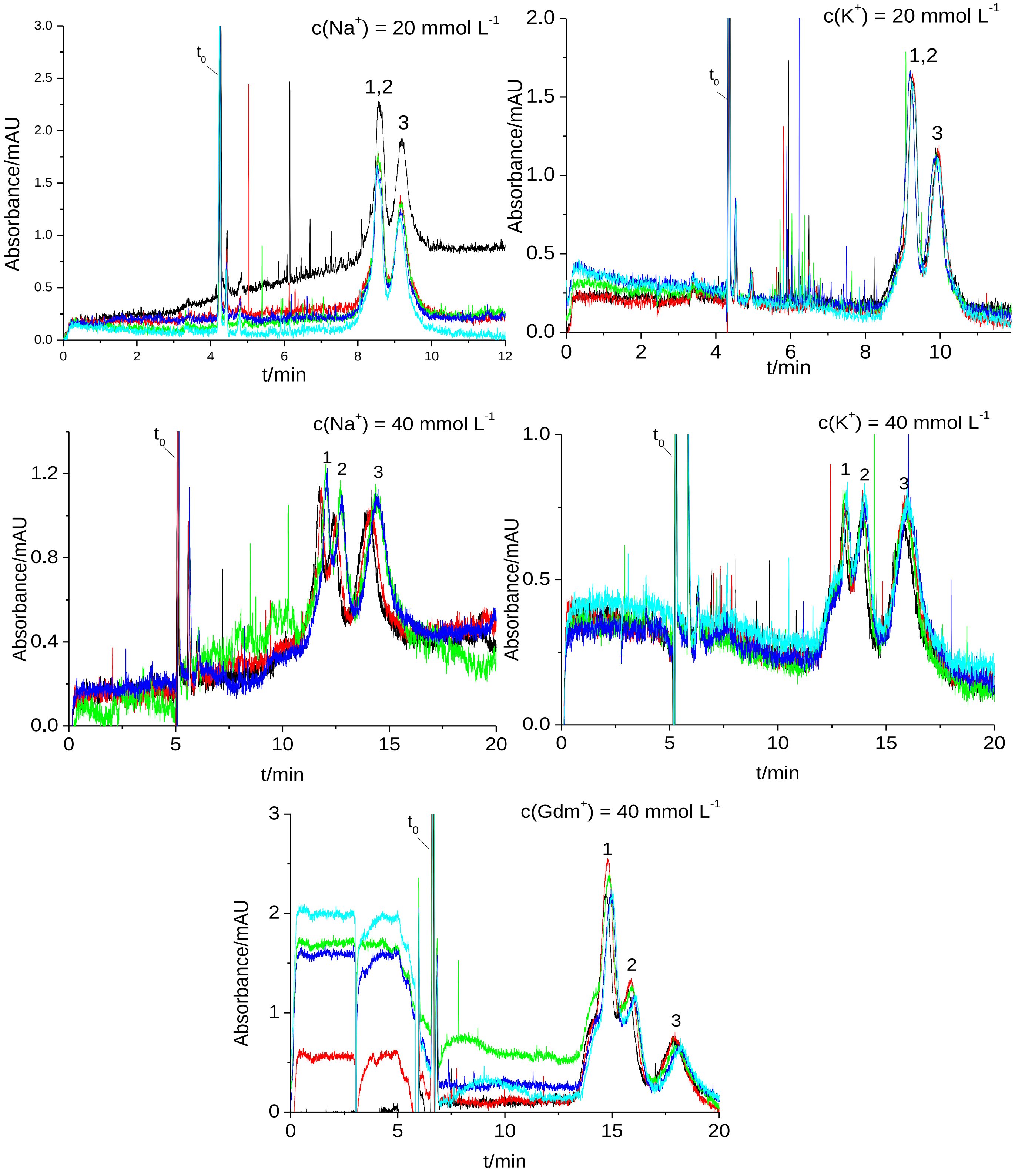

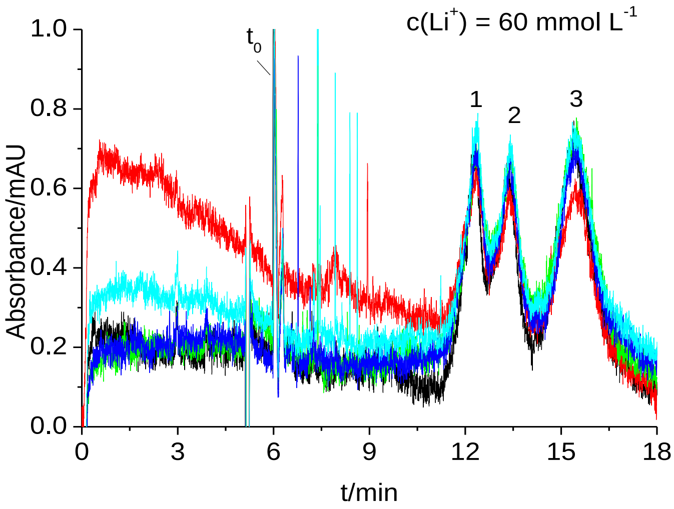
c(Li$^+$) = 60 mmol L^{-1}
Absorbance/mAU
t/min
t$_0$
1
2
3
0.0
0.2
0.4
0.6
0.8
1.0
0
3
6
9
12
15
18

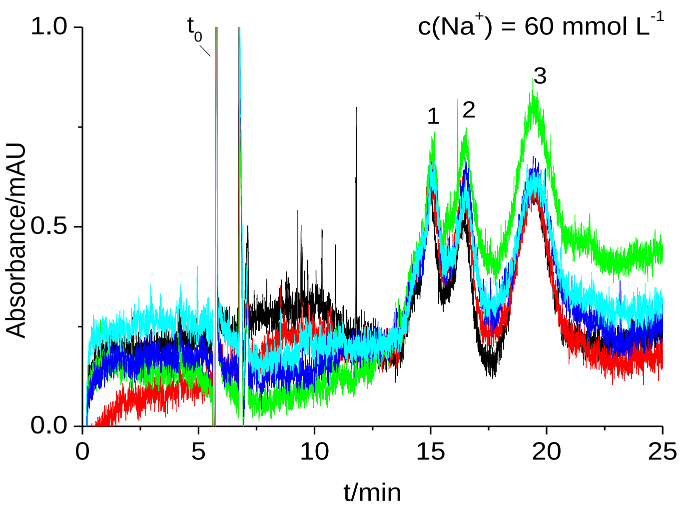
c(Na$^+$) = 60 mmol L^{-1}
Absorbance/mAU
t/min
t$_0$
1
2
3
0.0
0.5
1.0
0
5
10
15
20
25

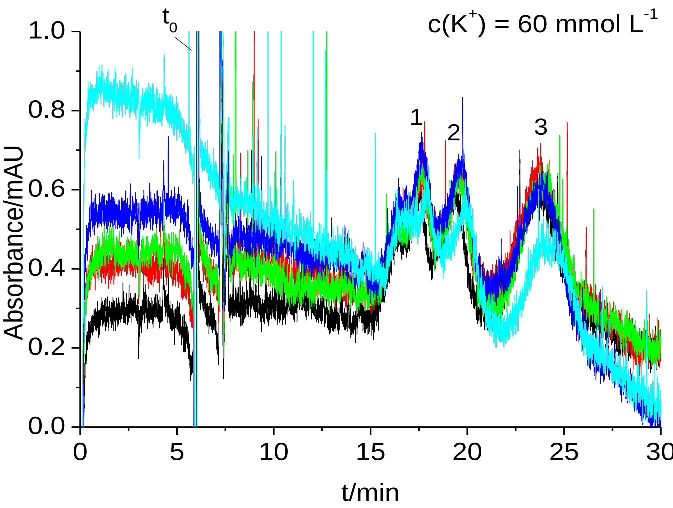
c(K$^+$) = 60 mmol L^{-1}
Absorbance/mAU
t/min
t$_0$
1
2
3
0.0
0.2
0.4
0.6
0.8
1.0
0
5
10
15
20
25
30

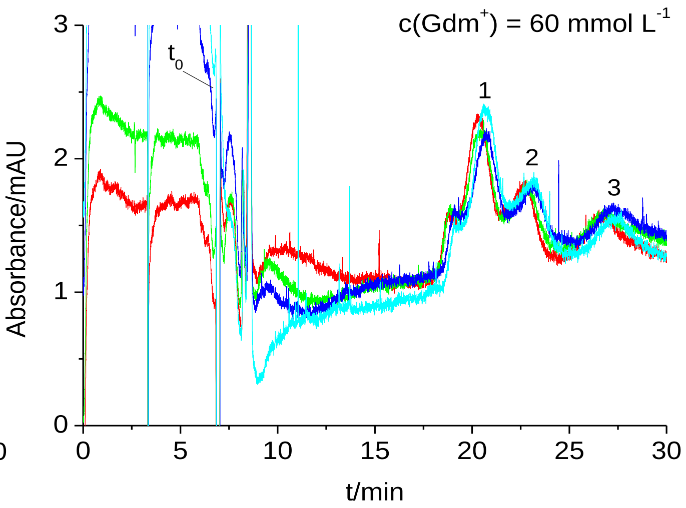
c(Gdm$^+$) = 60 mmol L^{-1}
Absorbance/mAU
t/min
t$_0$
1
2
3
0
1
2
3
0
5
10
15
20
25
30

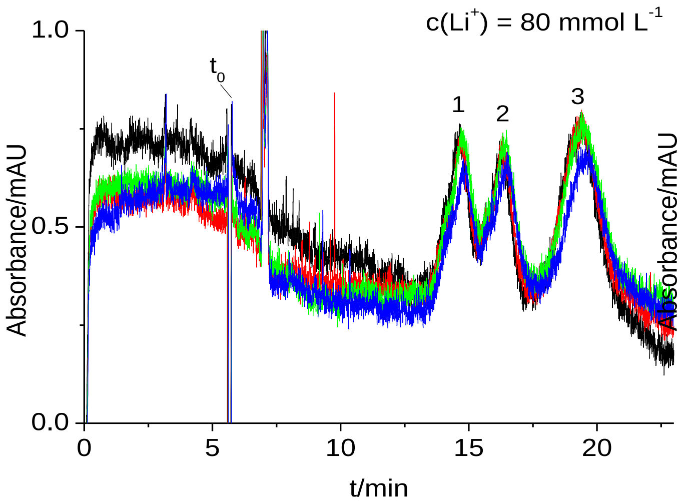
c(Li$^+$) = 80 mmol L^{-1}
Absorbance/mAU
t/min
t$_0$
1
2
3
0.0
0.5
1.0
0
5
10
15
20

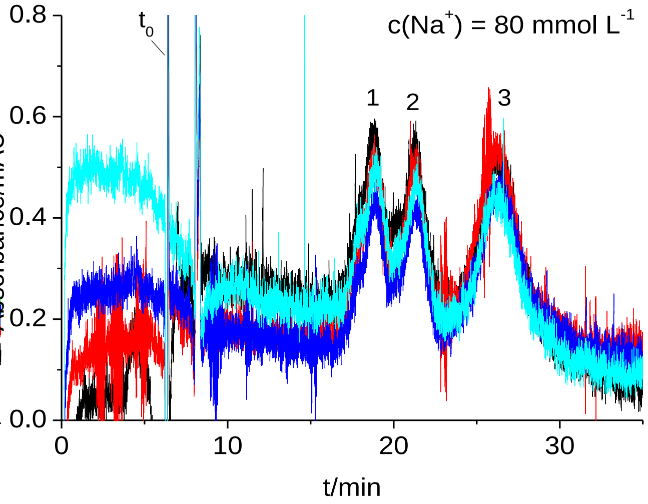
c(Na$^+$) = 80 mmol L^{-1}
Absorbance/mAU
t/min
t$_0$
1
2
3
0.0
0.2
0.4
0.6
0.8
0
10
20
30

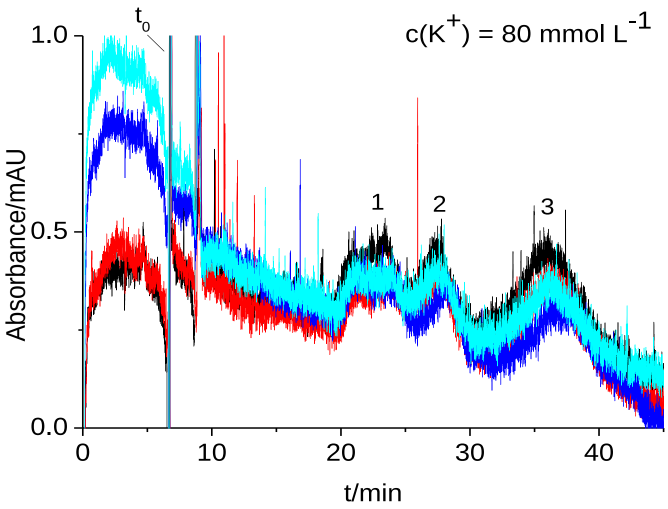
c(K$^+$) = 80 mmol L^{-1}
t$_0$
1
2
3
Absorbance/mAU
0.0
0.5
1.0
t/min
0
10
20
30
40

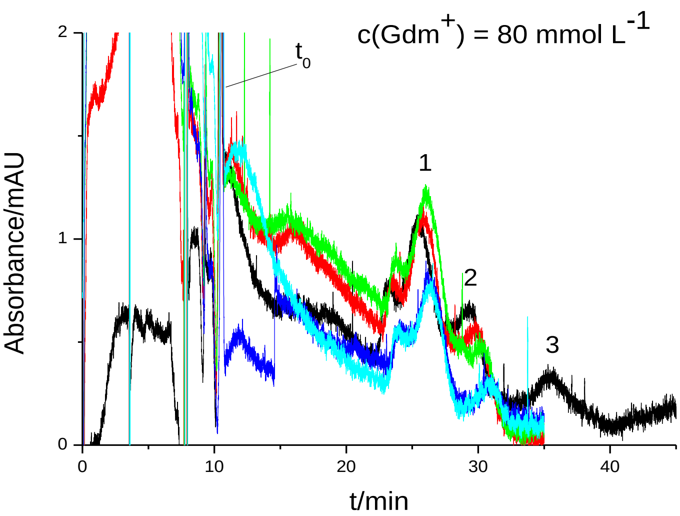
c(Gdm$^+$) = 80 mmol L^{-1}
t$_0$
1
2
3
Absorbance/mAU
0
1
2
t/min
0
10
20
30
40

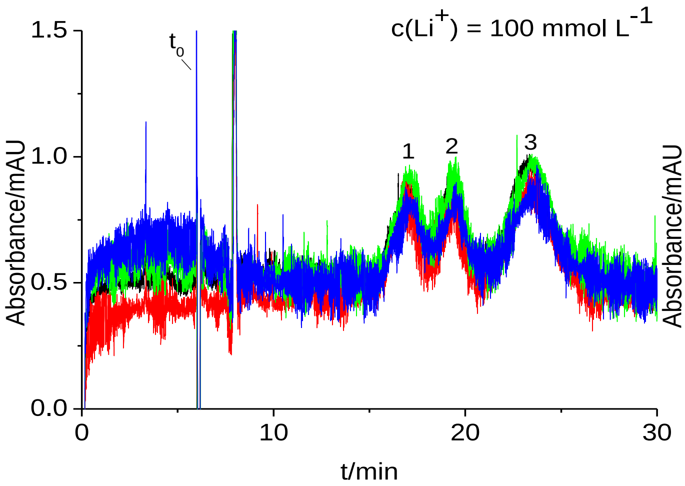
c(Li$^+$) = 100 mmol L^{-1}
t$_0$
1
2
3
Absorbance/mAU
0.0
0.5
1.0
1.5
t/min
0
10
20
30

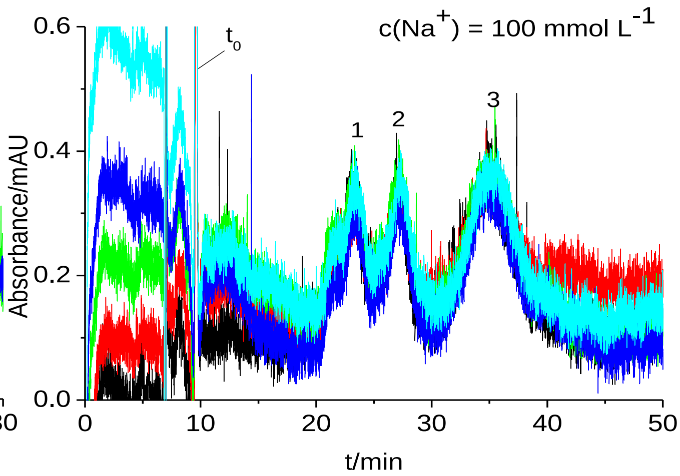
c(Na$^+$) = 100 mmol L^{-1}
t$_0$
1
2
3
Absorbance/mAU
0.0
0.2
0.4
0.6
t/min
0
10
20
30
40
50

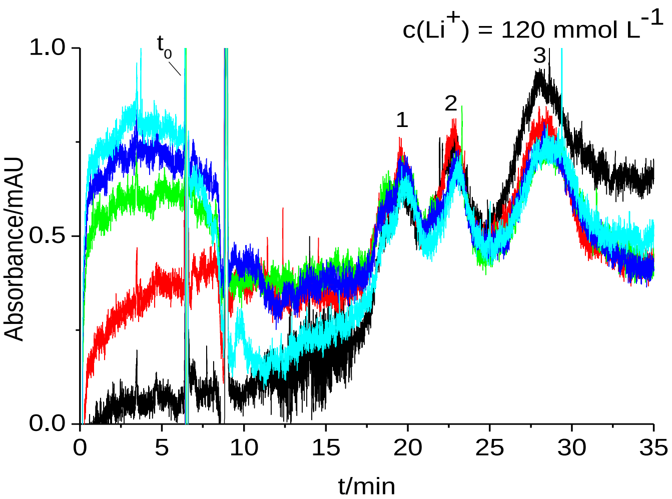
c(Li$^+$) = 120 mmol L^{-1}
t$_0$
1
2
3
Absorbance/mAU
0.0
0.5
1.0
t/min
0
5
10
15
20
25
30
35

Appendix A4

Table 1: Measured electrophoretic mobilities μ and calculated ζ potentials for SNP7 nm with a concentration of Li-cation counterion (20, 40, 60, 80, 100 or 120 mmol L^{-1}) (2^{nd} series), the following experimental conditions: T= 25°C, total length of capillary = 39.5 cm, capillary length to detector = 29.2 cm, inner diameter of fused silica capillary = 76 µm, separation voltage 7 kV, sample injection 0.1 psi (6.89 mbar) 6 s, data rate 16 Hz, absorbance detection.

$c(\mathrm{Li}^{+})/(\mathrm{mmol\ L}^{-1})$	Run	$\mu_{eo}/(\mathrm{mm}^{2}\ \mathrm{kV}^{-1}\ \mathrm{s}^{-1})$	$\mu_{ep}/(\mathrm{mm}^{2}\ \mathrm{kV}^{-1}\ \mathrm{s}^{-1})$	ζ/mV
20	1	69.014	-32.989	
	2	69.763	-32.943	
	3	69.930	-32.923	
	4	69.985	-32.948	
	5	70.134	-32.971	
	MW	69.765	-32.955	-78.21
	SD	0.440	0.026	
	RSD	0.631%	0.078%	
40	1	58.716	-30.906	
	2	58.768	-30.900	
	3	58.768	-30.906	
	4	58.703	-30.852	
	5	58.742	-30.862	
	MW	58.739	-30.885	-66.63
	SD	0.030	0.026	
	RSD	0.051%	0.084%	
60	1	52.225	-29.963	
	2	52.277	-29.977	
	3	52.184	-29.931	
	4	52.215	-29.934	
	5	52.163	-29.882	
	MW	52.213	-29.937	-61.03
	SD	0.044	0.037	
	RSD	0.083%	0.122%	
80	1	47.812	-29.034	
	2	47.743	-29.029	
	3	47.656	-29.049	
	4	47.622	-29.087	
	5	47.485	-29.012	
	MW	47.663	-29.042	-56.56
	SD	0.125	0.028	
	RSD	0.261%	0.097%	
100	1	44.413	-28.159	
	2	44.368	-28.094	
	3	44.293	-28.175	
	4	44.346	-28.264	
	MW	44.355	-28.173	-52.90
	SD	0.050	0.070	
	RSD	0.112%	0.249%	
120	1	41.478	-27.479	
	2	41.530	-27.494	
	3	41.556	-27.554	
	4	41.570	-27.625	
	5	41.517	-27.568	
	MW	41.530	-27.544	-50.53
	SD	0.036	0.059	
	RSD	0.086%	0.215%	

Table 2: Measured electrophoretic mobilities μ and calculated ζ potentials for SNP12 nm with a concentration of Li-cation counterion (20, 40, 60, 80, 100 or 120 mmol L^{-1}) (2nd series), the following experimental conditions: T= 25°C, total length of capillary = 39.5 cm, capillary length to detector = 29.2 cm, inner diameter of fused silica capillary = 76 μm, separation voltage 7 kV, sample injection 0.1 psi (6.89 mbar) 6 s, data rate 16 Hz, absorbance detection.

$c(Li^+)/(mmol\ L^{-1})$	Run	$\mu_{eo}/(mm^2\ kV^{-1}\ s^{-1})$	$\mu_{ep}/(mm^2\ kV^{-1}\ s^{-1})$	ζ/mV
20	1	69.123	-33.176	
	2	68.978	-33.109	
	3	69.014	-33.082	
	4	69.068	-33.131	
	5	69.068	-33.141	
	MW	69.050	-33.128	-81.50
	SD	0.056	0.035	
	RSD	0.081%	0.106	
40	1	58.664	-32.237	
	2	58.768	-32.224	
	3	58.768	-32.272	
	4	58.703	-32.228	
	5	58.742	-32.230	
	MW	58.729	-32.238	-67.73
	SD	0.045	0.020	
	RSD	0.077%	0.061	
60	1	52.225	-31.712	
	2	52.277	-31.764	
	3	52.184	-31.703	
	4	52.215	-31.715	
	5	52.163	-31.708	
	MW	52.213	-31.720	-61.97
	SD	0.044	0.025	
	RSD	0.083%	0.078	
80	1	47.812	-30.925	
	2	47.743	-30.903	
	3	47.656	-30.928	
	4	47.622	-30.932	
	5	47.485	-30.937	
	MW	47.663	-30.925	-57.28
	SD	0.125	0.013	
	RSD	0.261%	0.042	
100	1	44.413	-30.131	
	2	44.368	-30.108	
	3	44.293	-30.150	
	4	44.346	-30.219	
	MW	44.355	-30.152	-53.75
	SD	0.050	0.048	
	RSD	0.112%	0.158	
120	1	41.478	-29.423	
	2	41.530	-29.486	
	3	41.556	-29.586	
	4	41.570	-29.594	
	5	41.517	-29.587	
	MW	41.530	-29.535	-51.20
	SD	0.036	0.077	
	RSD	0.086%	0.260	

Table 3: Measured electrophoretic mobilities μ and calculated ζ potentials for SNP12 nm with a concentration of Li-cation counterion (20, 40, 60, 80, 100 or 120 mmol L^{-1}) (1st series), the following experimental conditions: T= 25°C, total length of capillary = 39.5 cm, capillary length to detector = 29.2 cm, inner diameter of fused silica capillary = 76 µm, separation voltage 7 kV, sample injection 0.1 psi (6.89 mbar) 6 s, data rate 16 Hz, absorbance detection.

c(Li^+)/(mmol L^{-1})	Run	μ_{eo}/(mm^2 kV^{-1} s^{-1})	μ_{ep}/(mm^2 kV^{-1} s^{-1})	ζ/mV
20	1	68.942	-33.015	
	2	69.451	-33.207	
	3	69.414	-33.191	
	4	69.487	-33.294	
	5	69.377	-33.214	
	MW	69.334	-33.184	-82.55
	SD	0.223	0.103	
	RSD	0.322%	0.309%	
40	1	59.350	-31.923	
	2	59.297	-31.938	
	3	59.297	-31.938	
	4	59.217	-31.937	
	MW	59.290	-31.934	-66.40
	SD	0.055	0.007	
	RSD	0.093%	0.023%	
60	1	55.549	-31.503	
	2	55.713	-31.540	
	3	55.690	-31.530	
	4	55.713	-31.531	
	5	55.819	-31.642	
	MW	55.697	-31.549	-61.40
	SD	0.097	0.053	
	RSD	0.174%	0.169%	
80	1	50.447	-30.907	
	2	50.447	-30.907	
	3	50.427	-30.908	
	4	50.350	-30.908	
	5	50.312	-30.904	
	MW	50.397	-30.907	-57.22
	SD	0.062	0.002	
	RSD	0.123%	0.005%	
100	1	46.744	-30.132	
	2	46.719	-30.138	
	3	46.678	-30.151	
	4	46.546	-30.134	
	5	46.521	-30.142	
	MW	46.641	-30.139	-53.71
	SD	0.102	0.008	
	RSD	0.218%	0.025%	
120	1	43.983	-29.574	
	2	43.910	-29.540	
	3	43.808	-29.534	
	4	43.735	-29.552	
	MW	43.859	-29.550	-51.23
	SD	0.110	0.018	
	RSD	0.250%	0.059%	

Table 4: Measured electrophoretic mobilities μ and calculated ζ potentials for SNP22 nm with a concentration of Li-cation counterion (20, 40, 60, 80, 100 or 120 mmol L^{-1}) (2nd series), the following experimental conditions: T= 25°C, total length of capillary = 39.5 cm, capillary length to detector = 29.2 cm, inner diameter of fused silica capillary = 76 µm, separation voltage 7 kV, sample injection 0.1 psi (6.89 mbar) 6 s, data rate 16 Hz, absorbance detection.

$c(Li^+)/(mmol\ L^{-1})$	Run	$\mu_{eo}/(mm^2\ kV^{-1}\ s^{-1})$	$\mu_{ep}/(mm^2\ kV^{-1}\ s^{-1})$	ζ/mV
20	1	67.305	-35.202	
	2	67.288	-35.138	
	3	67.254	-35.142	
	4	67.288	-35.184	
	5	67.219	-35.139	
	MW	67.271	-35.161	-75.54
	SD	0.034	0.030	
	RSD	0.051%	0.085%	
40	1	58.664	-34.861	
	2	58.768	-34.888	
	3	58.768	-34.893	
	4	58.703	-34.870	
	5	58.742	-34.875	
	MW	58.729	-34.878	-64.17
	SD	0.045	0.013	
	RSD	0.077%	0.037%	
60	1	52.225	-34.456	
	2	52.277	-34.550	
	3	52.184	-34.454	
	4	52.215	-34.450	
	5	52.163	-34.418	
	MW	52.213	-34.465	-59.42
	SD	0.044	0.050	
	RSD	0.083%	0.145%	
80	1	47.812	-33.595	
	2	47.743	-33.569	
	3	47.656	-33.531	
	4	47.622	-33.542	
	5	47.485	-33.467	
	MW	47.663	-33.541	-55.32
	SD	0.125	0.048	
	RSD	0.261%	0.143%	
100	1	44.413	-32.618	
	2	44.368	-32.646	
	3	44.293	-32.614	
	4	44.346	-32.622	
	MW	44.355	-32.625	-52.20
	SD	0.050	0.014	
	RSD	0.112%	0.044%	
120	1	41.478	-31.677	
	2	41.530	-31.793	
	3	41.556	-31.889	
	4	41.570	-31.847	
	5	41.517	-31.862	
	MW	41.530	-31.814	-49.79
	SD	0.036	0.084	
	RSD	0.086%	0.264%	

Table 5: Measured electrophoretic mobilities μ and calculated ζ potentials for SNP22 nm with a concentration of Li-cation counterion (20, 40, 60, 80, 100 or 120 mmol L^{-1}) (1st series), the following experimental conditions: T= 25°C, total length of capillary = 39.5 cm, capillary length to detector = 29.2 cm, inner diameter of fused silica capillary = 76 µm, separation voltage 7 kV, sample injection 0.1 psi (6.89 mbar) 6 s, data rate 16 Hz, absorbance detection.

c(Li$^+$)/(mmol L^{-1})	Run	μ_{eo}/(mm^2 kV^{-1} s^{-1})	μ_{ep}/(mm^2 kV^{-1} s^{-1})	ζ/mV
20	1	66.980	-33.592	
	2	66.574	-33.537	
	3	66.373	-33.501	
	4	66.207	-33.489	
	5	65.909	-33.409	
	MW	66.409	-33.506	-67.20
	SD	0.402	0.067	
	RSD	0.605%	0.200%	
40	1	55.737	-33.330	
	2	55.584	-33.306	
	3	55.502	-33.348	
	4	55.596	-33.359	
	5	55.619	-33.304	
	MW	55.607	-33.329	-59.72
	SD	0.085	0.025	
	RSD	0.152%	0.074%	
60	1	54.696	-34.099	
	2	54.662	-34.094	
	3	54.057	-34.160	
	4	54.157	-34.151	
	5	54.335	-34.272	
	MW	54.381	-34.155	-58.65
	SD	0.290	0.071	
	RSD	0.533%	0.209%	
80	1	49.388	-33.549	
	2	49.333	-33.537	
	3	49.351	-33.557	
	4	49.444	-33.600	
	5	49.370	-33.578	
	MW	49.377	-33.564	-55.37
	SD	0.043	0.025	
	RSD	0.086%	0.075%	
100	1	46.382	-32.716	
	2	46.284	-32.627	
	3	46.235	-32.664	
	4	46.026	-32.536	
	MW	46.232	-32.636	-52.22
	SD	0.150	0.076	
	RSD	0.325%	0.233%	
120	1	42.590	-31.784	
	2	42.840	-31.817	
	3	42.867	-31.887	
	4	42.881	-31.850	
	5	42.881	-31.850	
	MW	42.812	-31.837	-49.84
	SD	0.125	0.039	
	RSD	0.292%	0.122%	

Table 6: Measured electrophoretic mobilities μ and calculated ζ potentials for SNP7 nm with a concentration of Na-cation counterion (20, 40, 60, 80 or 100 mmol L^{-1}) (2nd series), the following experimental conditions: T= 25°C, total length of capillary = 39.5 cm, capillary length to detector = 29.2 cm, inner diameter of fused silica capillary = 76 μm, separation voltage 7 kV, sample injection 0.1 psi (6.89 mbar) 6 s, data rate 16 Hz, absorbance detection.

c(Na$^+$)/(mmol L^{-1})	Run	μ_{eo}/(mm^2 kV^{-1} s^{-1})	μ_{ep}/(mm^2 kV^{-1} s^{-1})	ζ/mV
20	1	63.911	-32.660	
	2	63.927	-32.624	
	3	63.896	-32.623	
	4	63.896	-32.634	
	5	63.819	-32.619	
	MW	63.890	-32.632	-72.31
	SD	0.042	0.017	
	RSD	0.065%	0.051%	
40	1	53.880	-30.516	
	2	53.693	-30.511	
	3	53.346	-30.532	
	4	53.238	-30.519	
	5	54.168	-30.574	
	MW	53.665	-30.530	-63.03
	SD	0.382	0.026	
	RSD	0.712%	0.084%	
60	1	47.656	-29.399	
	2	47.613	-29.379	
	3	47.596	-29.382	
	4	47.502	-29.385	
	5	47.527	-29.406	
	MW	47.579	-29.390	-57.72
	SD	0.063	0.012	
	RSD	0.133%	0.040	
80	1	42.812	-28.235	
	2	42.819	-28.239	
	3	42.819	-28.239	
	4	42.763	-28.232	
	5	42.735	-28.222	
	MW	42.789	-28.233	-53.19
	SD	0.038	0.007	
	RSD	0.089%	0.024%	
100	1	39.097	-27.276	
	2	39.034	-27.223	
	3	39.017	-27.211	
	4	38.976	-27.168	
	5	38.999	-27.189	
	MW	39.025	-27.214	-49.65
	SD	0.046	0.041	
	RSD	0.118%	0.150%	

Table 7: Measured electrophoretic mobilities μ and calculated ζ potentials for SNP12 nm with a concentration of Na-cation counterion (20, 40, 60, 80 or 100 mmol L^{-1}) (2nd series), the following experimental conditions: T= 25°C, total length of capillary = 39.5 cm, capillary length to detector = 29.2 cm, inner diameter of fused silica capillary = 76 µm, separation voltage 7 kV, sample injection 0.1 psi (6.89 mbar) 6 s, data rate 16 Hz, absorbance detection.

$c(Na^+)/(mmol\ L^{-1})$	Run	$\mu_{eo}/(mm^2\ kV^{-1}\ s^{-1})$	$\mu_{ep}/(mm^2\ kV^{-1}\ s^{-1})$	ζ/mV
20	1	64.004	-32.768	
	2	64.020	-32.776	
	3	64.004	-32.790	
	4	63.973	-32.826	
	5	63.911	-32.771	
	MW	63.983	-32.786	-71.78
	SD	0.043	0.024	
	RSD	0.068%	0.072%	
40	1	53.880	-31.807	
	2	53.693	-31.804	
	3	53.346	-31.807	
	4	53.238	-31.808	
	5	54.168	-31.856	
	MW	53.665	-31.816	-63.42
	SD	0.382	0.022	
	RSD	0.712%	0.070%	
60	1	47.656	-31.013	
	2	47.613	-30.991	
	3	47.596	-31.003	
	4	47.502	-30.998	
	5	47.527	-30.984	
	MW	47.579	-30.998	-58.10
	SD	0.063	0.011	
	RSD	0.133%	0.036%	
80	1	42.812	-29.926	
	2	42.819	-29.935	
	3	42.819	-29.935	
	4	42.763	-29.897	
	5	42.735	-29.909	
	MW	42.789	-29.920	-53.55
	SD	0.038	0.017	
	RSD	0.089%	0.056%	
100	1	39.098	-28.957	
	2	39.034	-28.942	
	3	39.017	-28.924	
	4	38.976	-28.880	
	5	38.999	-28.909	
	MW	39.025	-28.922	-50.05
	SD	0.046	0.030	
	RSD	0.118%	0.104%	

Table 8: Measured electrophoretic mobilities μ and calculated ζ potentials for SNP12 nm with a concentration of Na-cation counterion (20, 40, 60, 80, 100 or 120 mmol L^{-1}) (1st series), the following experimental conditions: T= 25°C, total length of capillary = 39.5 cm, capillary length to detector = 29.2 cm, inner diameter of fused silica capillary = 76 µm, separation voltage 7 kV, sample injection 0.1 psi (6.89 mbar) 6 s, data rate 16 Hz, absorbance detection.

$c(Na^+)/(mmol\ L^{-1})$	Run	$\mu_{eo}/(mm^2\ kV^{-1}\ s^{-1})$	$\mu_{ep}/(mm^2\ kV^{-1}\ s^{-1})$	ζ/mV
20	1	63.911	-32.164	
	2	64.238	-32.259	
	3	64.490	-32.394	
	4	64.458	-32.370	
	5	64.458	-32.378	
	MW	64.311	-32.313	-69.65
	SD	0.245	0.099	
	RSD	0.381%	0.307%	
40	1	50.855	-30.488	
	2	51.331	-30.689	
	3	51.411	-30.760	
	4	51.431	-30.802	
	5	51.411	-30.789	
	MW	51.288	-30.705	-59.89
	SD	0.245	0.129	
	RSD	0.477%	0.421%	
60	1	46.106	-30.372	
	2	46.122	-30.400	
	3	46.219	-30.401	
	4	46.219	-30.437	
	5	46.252	-30.362	
	MW	46.184	-30.394	-56.47
	SD	0.065	0.029	
	RSD	0.141%	0.095%	
80	1	42.067	-29.762	
	2	42.007	-29.738	
	3	41.993	-29.736	
	4	41.980	-29.742	
	5	41.953	-29.733	
	MW	42.000	-29.742	-53.12
	SD	0.042	0.011	
	RSD	0.101%	0.038%	
100	1	40.709	-28.564	
	2	40.584	-28.444	
	3	40.509	-28.389	
	4	40.484	-28.369	
	5	40.472	-28.432	
	MW	40.552	-28.439	-48.99
	SD	0.098	0.076	
	RSD	0.242%	0.267%	
120	1	37.279	-27.273	
	2	37.106	-27.166	
	3	36.965	-27.202	
	4	36.831	-27.251	
	5	36.718	-27.235	
	MW	36.980	-27.225	-45.64
	SD	0.221	0.042	
	RSD	0.599%	0.154%	

Table 9: Measured electrophoretic mobilities μ and calculated ζ potentials for SNP22 nm with a concentration of Na-cation counterion (20, 40, 60, 80 or 100 mmol L^{-1}) (2nd series), the following experimental conditions: T= 25°C, total length of capillary = 39.5 cm, capillary length to detector = 29.2 cm, inner diameter of fused silica capillary = 76 µm, separation voltage 7 kV, sample injection 0.1 psi (6.89 mbar) 6 s, data rate 16 Hz, absorbance detection.

$c(Na^+)/(mmol\ L^{-1})$	Run	$\mu_{eo}/(mm^2\ kV^{-1}\ s^{-1})$	$\mu_{ep}/(mm^2\ kV^{-1}\ s^{-1})$	ζ/mV
20	1	63.649	-34.710	
	2	63.772	-34.859	
	3	63.711	-34.670	
	4	63.711	-34.670	
	5	63.711	-34.702	
	MW	63.711	-34.722	-68.78
	SD	0.044	0.079	
	RSD	0.068%	0.226%	
40	1	53.880	-34.346	
	2	53.693	-34.331	
	3	53.346	-34.341	
	4	53.238	-34.299	
	5	54.168	-34.352	
	MW	53.665	-34.334	-60.92
	SD	0.382	0.021	
	RSD	0.712%	0.061%	
60	1	47.656	-33.612	
	2	47.613	-33.602	
	3	47.596	-33.612	
	4	47.502	-33.538	
	5	47.527	-33.540	
	MW	47.579	-33.581	-56.28
	SD	0.063	0.038	
	RSD	0.133%	0.114%	
80	1	42.812	-32.379	
	2	42.819	-32.385	
	3	42.819	-32.385	
	4	42.763	-32.349	
	5	42.735	-32.305	
	MW	42.789	-32.361	-52.15
	SD	0.038	0.034	
	RSD	0.089%	0.106%	
100	1	39.098	-31.210	
	2	39.034	-31.168	
	3	39.017	-31.149	
	4	38.976	-31.111	
	5	38.999	-31.131	
	MW	39.025	-31.154	-48.84
	SD	0.046	0.038	
	RSD	0.118%	0.122%	

Table 10: Measured electrophoretic mobilities μ and calculated ζ potentials for SNP22 nm with a concentration of Na-cation counterion (20, 40, 60, 80 or 100 mmol L^{-1}) (1st series), the following experimental conditions: T= 25°C, total length of capillary = 39.5 cm, capillary length to detector = 29.2 cm, inner diameter of fused silica capillary = 76 µm, separation voltage 7 kV, sample injection 0.1 psi (6.89 mbar) 6 s, data rate 16 Hz, absorbance detection.

c(Na$^+$)/(mmol L^{-1})	Run	μ_{eo}/(mm^2 kV^{-1} s^{-1})	μ_{ep}/(mm^2 kV^{-1} s^{-1})	ζ/mV
20	1	62.207	-34.374	
	2	61.425	-34.212	
	3	61.196	-34.168	
	4	61.182	-34.087	
	5	61.239	-34.141	
	MW	61.450	-34.197	-66.87
	SD	0.434	0.109	
	RSD	0.707%	0.319%	
40	1	52.340	-33.926	
	2	52.748	-34.032	
	3	53.024	-33.978	
	4	53.324	-34.086	
	5	53.584	-34.021	
	MW	53.004	-34.008	-60.08
	SD	0.486	0.060	
	RSD	0.918%	0.178%	
60	1	46.042	-32.580	
	2	45.881	-32.523	
	3	45.738	-32.506	
	4	45.722	-32.519	
	MW	45.846	-32.532	-54.01
	SD	0.149	0.033	
	RSD	0.325%	0.100%	
80	1	41.728	-31.989	
	2	41.754	-31.938	
	3	41.767	-32.019	
	4	41.860	-32.081	
	5	41.807	-31.984	
	MW	41.783	-32.002	-51.44
	SD	0.052	0.053	
	RSD	0.124%	0.165%	
100	1	38.884	-31.036	
	2	38.781	-30.910	
	3	38.702	-30.972	
	4	38.386	-30.912	
	5	38.442	-30.951	
	MW	38.639	-30.956	-48.48
	SD	0.216	0.052	
	RSD	0.560%	0.168%	

Table 11: Measured electrophoretic mobilities μ and calculated ζ potentials for SNP7 nm with a concentration of K-cation counterion (20, 40, 60 or 80 mmol L^{-1}) (2nd series), the following experimental conditions: T= 25°C, total length of capillary = 39.5 cm, capillary length to detector = 29.2 cm, inner diameter of fused silica capillary = 76 μm, separation voltage 7 kV, sample injection 0.1 psi (6.89 mbar) 6 s, data rate 16 Hz, absorbance detection.

c(K$^+$)/(mmol L^{-1})	Run	μ_{eo}/(mm^2 kV^{-1} s^{-1})	μ_{ep}/(mm^2 kV^{-1} s^{-1})	ζ/mV
20	1	60.425	-32.527	
	2	60.342	-32.491	
	3	60.287	-32.483	
	4	60.259	-32.485	
	5	60.218	-32.485	
	MW	60.306	-32.494	-69.10
	SD	0.080	0.019	
	RSD	0.133%	0.058%	
40	1	52.030	-29.872	
	2	51.927	-29.980	
	3	51.897	-29.960	
	4	51.764	-29.824	
	5	51.693	-29.811	
	MW	51.862	-29.889	-59.38
	SD	0.134	0.077	
	RSD	0.258%	0.258%	
60	1	45.462	-28.653	
	2	45.376	-28.915	
	3	45.298	-28.678	
	4	45.267	-28.649	
	5	45.081	-28.710	
	MW	45.297	-28.721	-54.67
	SD	0.142	0.111	
	RSD	0.314%	0.388%	
80	1	40.659	-27.339	
	2	40.090	-27.168	
	3	40.250	-27.246	
	4	40.373	-27.262	
	MW	40.343	-27.254	-49.92
	SD	0.240	0.070	
	RSD	0.596%	0.257%	

Table 12: Measured electrophoretic mobilities μ and calculated ζ potentials for SNP12 nm with a concentration of K-cation counterion (20, 40, 60 or 80 mmol L^{-1}) (2nd series), the following experimental conditions: T= 25°C, total length of capillary = 39.5 cm, capillary length to detector = 29.2 cm, inner diameter of fused silica capillary = 76 μm, separation voltage 7 kV, sample injection 0.1 psi (6.89 mbar) 6 s, data rate 16 Hz, absorbance detection.

$c(K^+)/(mmol\ L^{-1})$	Run	$\mu_{eo}/(mm^2\ kV^{-1}\ s^{-1})$	$\mu_{ep}/(mm^2\ kV^{-1}\ s^{-1})$	ζ/mV
20	1	59.890	-32.220	
	2	59.890	-32.220	
	3	59.890	-32.220	
	4	59.863	-32.216	
	5	59.835	-32.224	
	MW	59.873	-32.220	-66.45
	SD	0.024	0.003	
	RSD	0.041%	0.008%	
40	1	52.030	-30.946	
	2	51.927	-30.964	
	3	51.897	-30.940	
	4	51.764	-30.940	
	5	51.693	-30.846	
	MW	51.862	-30.927	-58.92
	SD	0.134	0.046	
	RSD	0.258%	0.150%	
60	1	45.454	-29.758	
	2	45.376	-29.895	
	3	45.298	-29.755	
	4	45.267	-29.722	
	MW	45.349	-29.783	-53.78
	SD	0.084	0.077	
	RSD	0.185%	0.258%	
80	1	40.659	-28.900	
	2	40.090	-28.515	
	3	40.250	-28.834	
	4	40.373	-28.914	
	MW	40.343	-28.791	-50.09
	SD	0.240	0.187	
	RSD	0.596%	0.650%	

Table 13: Measured electrophoretic mobilities μ and calculated ζ potentials for SNP12 nm with a concentration of K-cation counterion (20, 40 or 100 mmol L^{-1}) (1st series), the following experimental conditions: T= 25°C, total length of capillary = 39.5 cm, capillary length to detector = 29.2 cm, inner diameter of fused silica capillary = 76 μm, separation voltage 7 kV, sample injection 0.1 psi (6.89 mbar) 6 s, data rate 16 Hz, absorbance detection.

c(K$^+$)/(mmol L^{-1})	Run	μ_{eo}/(mm^2 kV^{-1} s^{-1})	μ_{ep}/(mm^2 kV^{-1} s^{-1})	ζ/mV
20	1	64.036	-32.341	
	2	63.989	-32.393	
	3	63.865	-32.345	
	4	63.680	-32.384	
	5	63.649	-32.324	
	MW	63.844	-32.357	-66.92
	SD	0.175	0.030	
	RSD	0.275%	0.092%	
40	1	52.939	-31.158	
	2	52.769	-31.170	
	3	52.664	-31.167	
	4	52.423	-31.135	
	5	52.423	-31.135	
	MW	52.643	-31.153	-59.54
	SD	0.224	0.017	
	RSD	0.425%	0.056%	
100	1	38.010	-28.714	
	2	38.097	-28.777	
	3	38.075	-28.777	
	4	38.092	-28.788	
	5	38.092	-28.788	
	MW	45.676	-28.769	-49.00
	SD	0.771	0.031	
	RSD	1.689%	0.108%	

Table 14: Measured electrophoretic mobilities μ and calculated ζ potentials for SNP22 nm with a concentration of K-cation counterion (20, 40, 60 or 80 mmol L^{-1}) (2nd series), the following experimental conditions: T= 25°C, total length of capillary = 39.5 cm, capillary length to detector = 29.2 cm, inner diameter of fused silica capillary = 76 μm, separation voltage 7 kV, sample injection 0.1 psi (6.89 mbar) 6 s, data rate 16 Hz, absorbance detection.

$c(K^+)/(mmol\ L^{-1})$	Run	$\mu_{eo}/(mm^2\ kV^{-1}\ s^{-1})$	$\mu_{ep}/(mm^2\ kV^{-1}\ s^{-1})$	ζ/mV
20	1	59.111	-33.580	
	2	58.979	-33.585	
	3	59.111	-33.664	
	4	59.191	-33.694	
	5	59.217	-33.671	
	MW	59.122	-33.639	-62.80
	SD	0.093	0.053	
	RSD	0.157%	0.156%	
40	1	52.030	-32.217	
	2	51.927	-32.232	
	3	51.897	-32.187	
	4	51.764	-32.166	
	5	51.774	-32.161	
	MW	51.878	-32.193	-54.66
	SD	0.111	0.031	
	RSD	0.214%	0.097%	
60	1	45.462	-31.367	
	2	45.376	-31.363	
	3	45.298	-31.339	
	4	45.267	-31.350	
	5	45.081	-31.339	
	MW	45.297	-31.352	-50.86
	SD	0.142	0.013	
	RSD	0.314%	0.042%	
80	1	40.659	-30.672	
	2	40.090	-30.182	
	3	40.250	-30.559	
	4	40.373	-30.426	
	MW	40.343	-30.460	-47.95
	SD	0.240	0.210	
	RSD	0.596%	0.691%	

Table 15: Measured electrophoretic mobilities μ and calculated ζ potentials for SNP22 nm with a concentration of K-cation counterion (20, 40, 60 or 80 mmol L^{-1}) (1^{st} series), the following experimental conditions: T= 25°C, total length of capillary = 39.5 cm, capillary length to detector = 29.2 cm, inner diameter of fused silica capillary = 76 μm, separation voltage 7 kV, sample injection 0.1 psi (6.89 mbar) 6 s, data rate 16 Hz, absorbance detection.

$c(K^+)/(\text{mmol L}^{-1})$	Run	$\mu_{eo}/(\text{mm}^2\ \text{kV}^{-1}\ \text{s}^{-1})$	$\mu_{ep}/(\text{mm}^2\ \text{kV}^{-1}\ \text{s}^{-1})$	ζ/mV
20	1	62.591	-34.593	
	2	62.591	-34.782	
	3	62.413	-34.814	
	4	62.950	-34.904	
	5	62.920	-34.909	
	MW	62.693	-34.800	-66.17
	SD	0.233	0.129	
	RSD	0.371%	0.370%	
40	1	51.958	-34.271	
	2	51.835	-34.203	
	3	51.835	-34.203	
	4	51.897	-34.283	
	5	51.673	-34.144	
	MW	51.840	-34.221	-59.20
	SD	0.106	0.057	
	RSD	0.205%	0.167%	
60	1	44.737	-32.986	
	2	44.920	-33.218	
	3	44.996	-33.327	
	4	45.081	-33.446	
	5	45.112	-33.436	
	MW	44.969	-33.283	-54.71
	SD	0.150	0.190	
	RSD	0.334%	0.570%	
80	1	40.697	-32.534	
	2	40.709	-32.530	
	3	40.747	-32.536	
	4	40.772	-32.538	
	5	40.722	-32.524	
	MW	40.730	-32.533	-51.81
	SD	0.030	0.005	
	RSD	0.074%	0.017%	

Table 16: Measured electrophoretic mobilities μ and calculated ζ potentials for SNP7 nm with a concentration of Gdm-cation counterion (40, 60 or 80 mmol L^{-1}) (2^{nd} series), the following experimental conditions: T= 25°C, total length of capillary = 39.5 cm, capillary length to detector = 29.2 cm, inner diameter of fused silica capillary = 76 µm, separation voltage 7 kV, sample injection 0.1 psi (6.89 mbar) 6 s, data rate 16 Hz, absorbance detection.

$c(Gdm^+)/(mmol\ L^{-1})$	Run	$\mu_{eo}/(mm^2\ kV^{-1}\ s^{-1})$	$\mu_{ep}/(mm^2\ kV^{-1}\ s^{-1})$	ζ/mV
40	1	46.106	-27.456	
	2	46.026	-27.475	
	3	45.929	-27.447	
	4	45.849	-27.475	
	5	45.849	-27.516	
	MW	45.952	-27.474	-53.81
	SD	0.113	0.027	
	RSD	0.245%	0.097%	
60	1	38.907	-25.208	
	2	38.988	-25.455	
	3	38.988	-25.526	
	4	38.896	-25.646	
	5	38.942	-25.639	
	MW	38.944	-25.495	-47.55
	SD	0.043	0.179	
	RSD	0.111%	0.704%	
80	1	34.643	-23.846	
	2	34.571	-23.950	
	3	34.471	-23.942	
	4	34.336	-23.960	
	5	34.292	-23.898	
	MW	34.463	-23.919	-43.03
	SD	0.150	0.047	
	RSD	0.434%	0.198%	

Table 17: Measured electrophoretic mobilities μ and calculated ζ potentials for SNP12 nm with a concentration of Gdm-cation counterion (20, 40, 60 or 80 mmol L^{-1}) (2nd series), the following experimental conditions: T= 25°C, total length of capillary = 39.5 cm, capillary length to detector = 29.2 cm, inner diameter of fused silica capillary = 76 μm, separation voltage 7 kV, sample injection 0.1 psi (6.89 mbar) 6 s, data rate 16 Hz, absorbance detection.

$c(Gdm^+)/(mmol\ L^{-1})$	Run	$\mu_{eo}/(mm^2\ kV^{-1}\ s^{-1})$	$\mu_{ep}/(mm^2\ kV^{-1}\ s^{-1})$	ζ/mV
20	1	55.807	-30.350	
	2	55.760	-30.367	
	3	55.784	-30.356	
	4	55.784	-30.356	
	5	55.760	-30.313	
	MW	55.779	-30.348	-62.16
	SD	0.020	0.021	
	RSD	0.035%	0.068%	
40	1	46.106	-28.658	
	2	46.026	-28.709	
	3	45.929	-28.680	
	4	45.849	-28.704	
	5	45.849	-28.775	
	MW	45.952	-28.705	-54.19
	SD	0.113	0.044	
	RSD	0.245%	0.152%	
60	1	38.907	-26.652	
	2	38.988	-26.878	
	3	38.988	-26.934	
	4	38.896	-26.986	
	5	38.942	-27.036	
	MW	38.944	-26.897	-47.91
	SD	0.043	0.149	
	RSD	0.111%	0.555%	
80	1	34.643	-25.244	
	2	34.570	-25.337	
	3	34.471	-25.395	
	4	34.336	-25.433	
	5	34.292	-25.413	
	MW	34.463	-25.364	-43.45
	SD	0.150	0.076	
	RSD	0.434%	0.301%	

Table 18: Measured electrophoretic mobilities μ and calculated ζ potentials for SNP22 nm with a concentration of Gdm-cation counterion (20, 40, or 60 mmol L^{-1}) (2nd series), the following experimental conditions: T= 25°C, total length of capillary = 39.5 cm, capillary length to detector = 29.2 cm, inner diameter of fused silica capillary = 76 μm, separation voltage 7 kV, sample injection 0.1 psi (6.89 mbar) 6 s, data rate 16 Hz, absorbance detection.

$c(Gdm^+)/(mmol\ L^{-1})$	Run	$\mu_{eo}/(mm^2\ kV^{-1}\ s^{-1})$	$\mu_{ep}/(mm^2\ kV^{-1}\ s^{-1})$	ζ/mV
20	1	55.737	-32.029	
	2	55.737	-32.058	
	3	55.666	-32.043	
	4	55.619	-32.047	
	5	55.549	-32.010	
	MW	55.661	-32.037	-59.96
	SD	0.080	0.019	
	RSD	0.144%	0.058%	
40	1	46.106	-30.755	
	2	46.026	-30.684	
	3	45.929	-30.701	
	4	45.849	-30.702	
	5	45.849	-30.755	
	MW	45.952	-30.719	-52.28
	SD	0.113	0.034	
	RSD	0.245%	0.109%	
60	1	38.907	-28.380	
	2	38.988	-28.686	
	3	38.988	-28.723	
	4	38.896	-28.807	
	5	38.942	-28.891	
	MW	38.944	-28.698	-46.26
	SD	0.043	0.194	
	RSD	0.111%	0.677%	

Appendix A5

Electropherograms obtained: (a) superposition of consecutive runs, and (b) cumulative superposition for SNPs (1st series) and (2nd series) with different concentrations of different monovalent counterions. Experimental conditions (refer to Figs. 5 and 6).

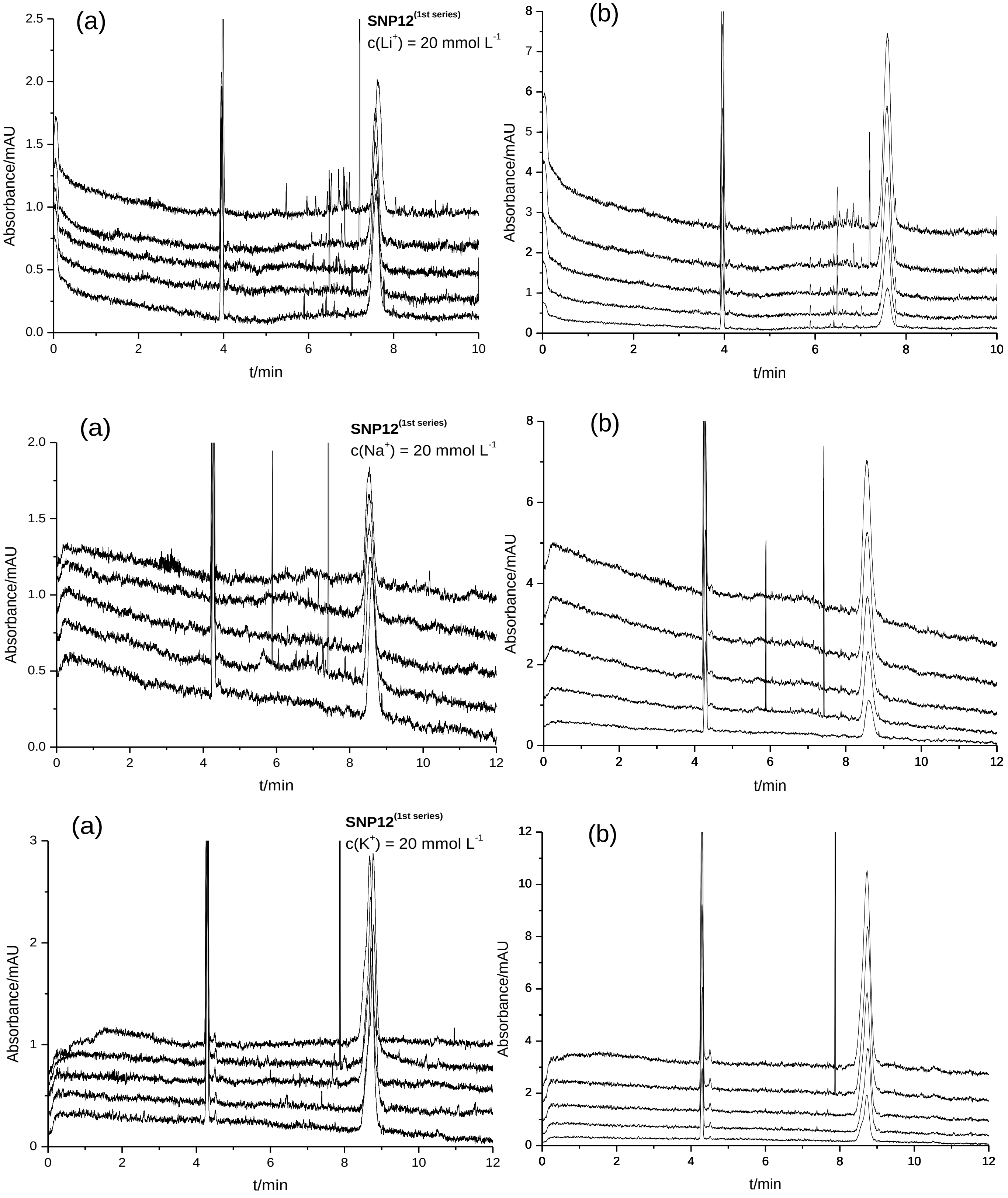

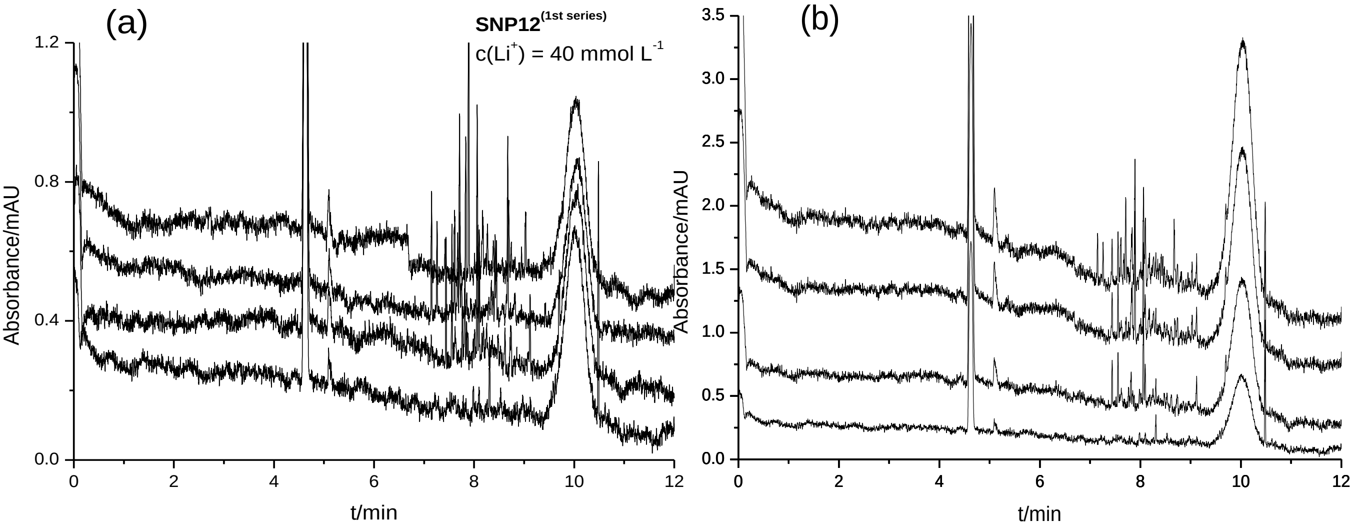
(a)
SNP12$^{(1st\ series)}$
c(Li^{+}) = 40 mmol L^{-1}
Absorbance/mAU
0.0
0.4
0.8
1.2
t/min
0
2
4
6
8
10
12
(b)
Absorbance/mAU
0.0
0.5
1.0
1.5
2.0
2.5
3.0
3.5
t/min
0
2
4
6
8
10
12

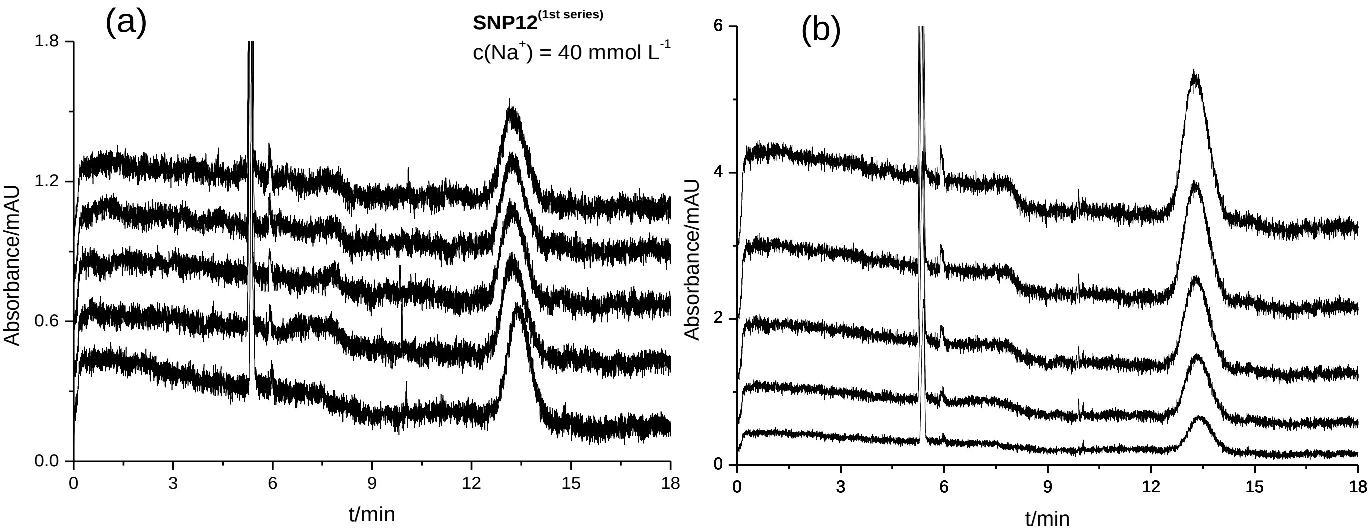
(a)
SNP12$^{(1st\ series)}$
c(Na^{+}) = 40 mmol L^{-1}
Absorbance/mAU
0.0
0.6
1.2
1.8
t/min
0
3
6
9
12
15
18
(b)
Absorbance/mAU
0
2
4
6
t/min
0
3
6
9
12
15
18

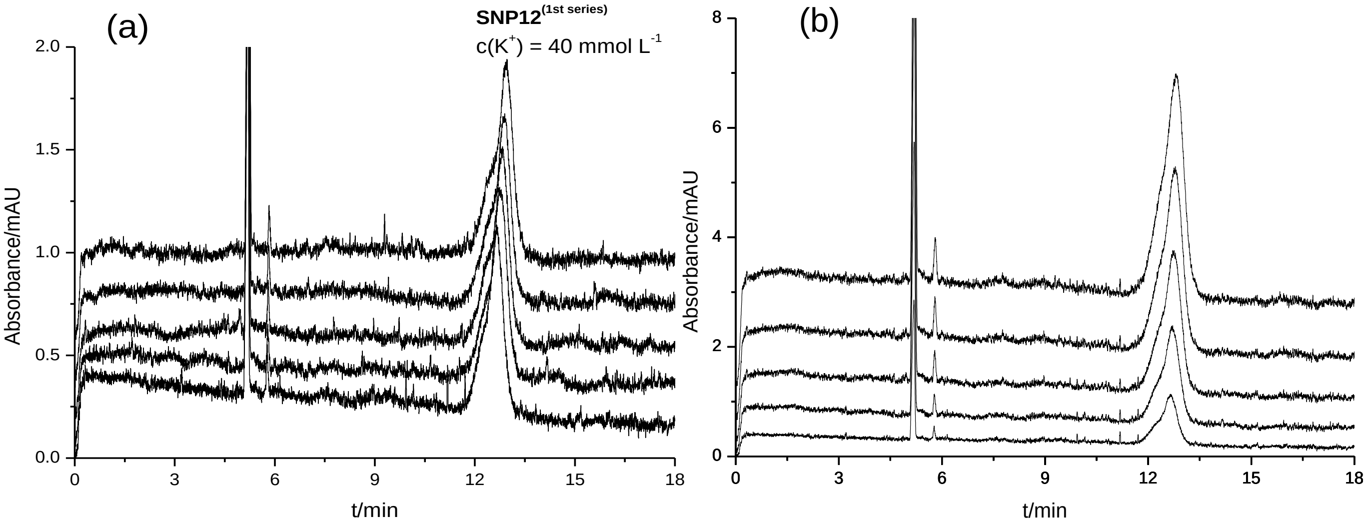
(a)
SNP12$^{(1st\ series)}$
c(K^{+}) = 40 mmol L^{-1}
Absorbance/mAU
0.0
0.5
1.0
1.5
2.0
t/min
0
3
6
9
12
15
18
(b)
Absorbance/mAU
0
2
4
6
8
t/min
0
3
6
9
12
15
18

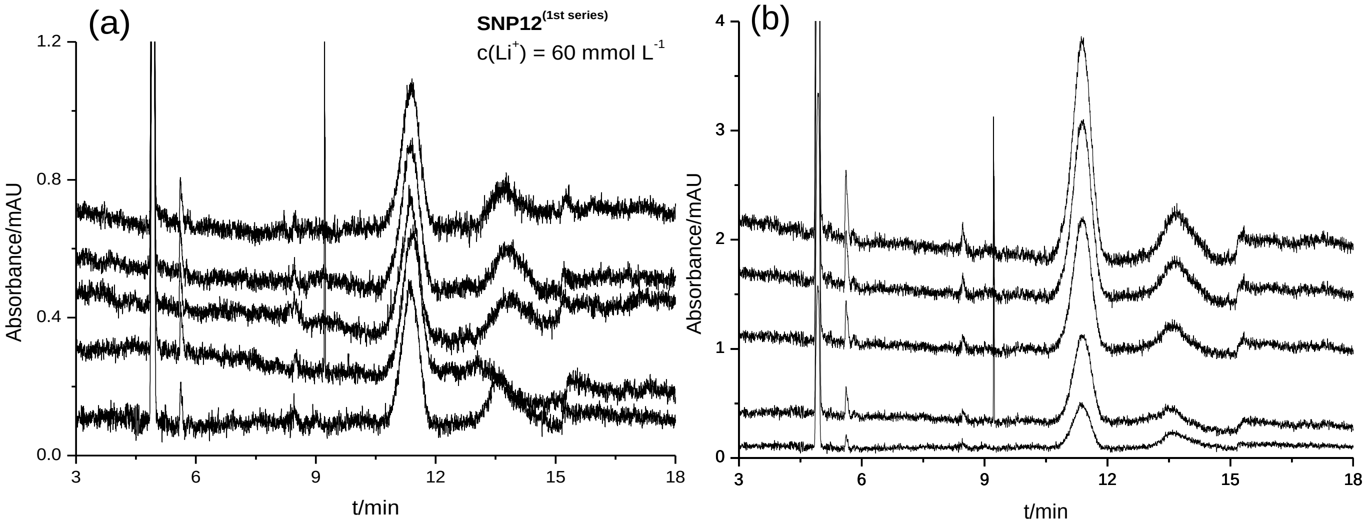
(a)
SNP12$^{(1st\ series)}$
c(Li$^+$) = 60 mmol L^{-1}
Absorbance/mAU
0.0
0.4
0.8
1.2
3
6
9
12
15
18
t/min
(b)
Absorbance/mAU
0
1
2
3
4
3
6
9
12
15
18
t/min

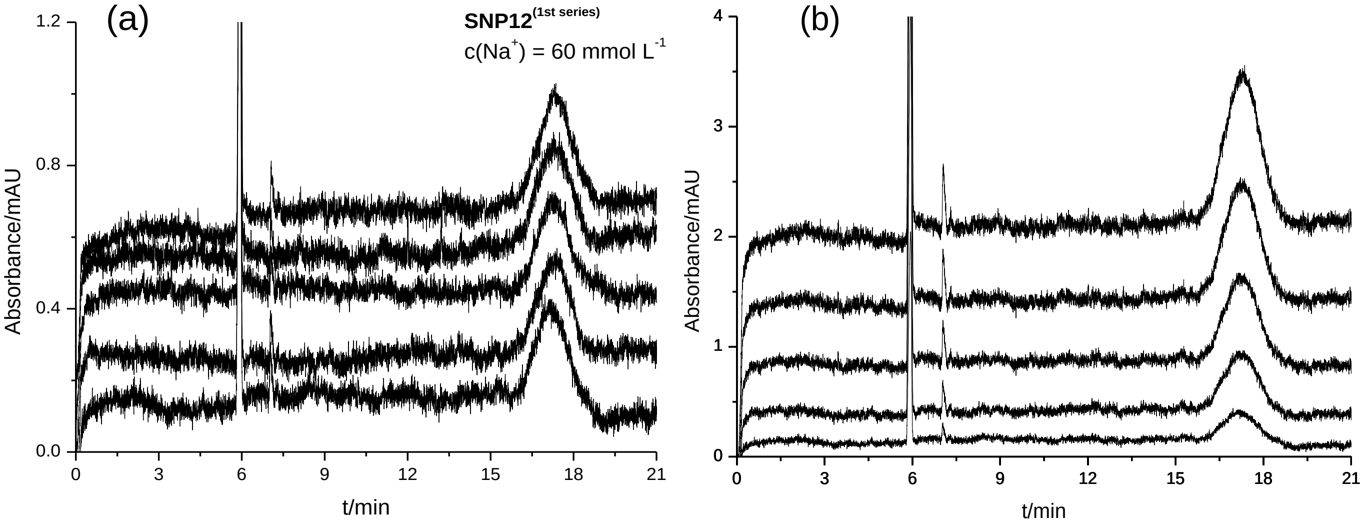
(a)
SNP12$^{(1st\ series)}$
c(Na$^+$) = 60 mmol L^{-1}
Absorbance/mAU
0.0
0.4
0.8
1.2
0
3
6
9
12
15
18
21
t/min
(b)
Absorbance/mAU
0
1
2
3
4
0
3
6
9
12
15
18
21
t/min

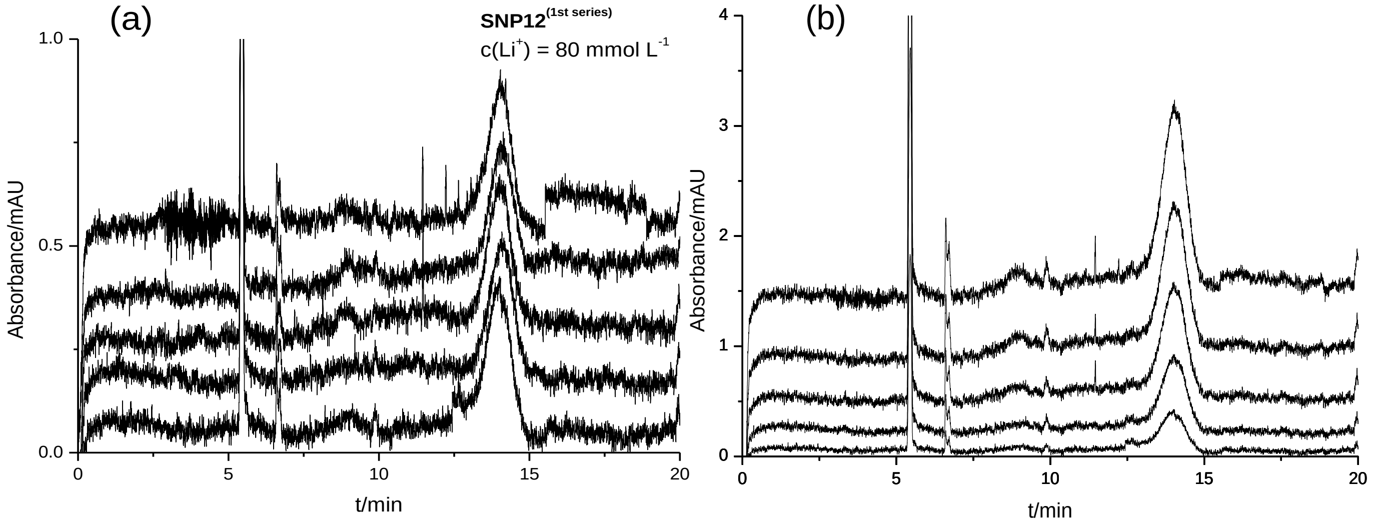
(a)
SNP12$^{(1st\ series)}$
c(Li$^+$) = 80 mmol L^{-1}
Absorbance/mAU
0.0
0.5
1.0
0
5
10
15
20
t/min
(b)
Absorbance/mAU
0
1
2
3
4
0
5
10
15
20
t/min

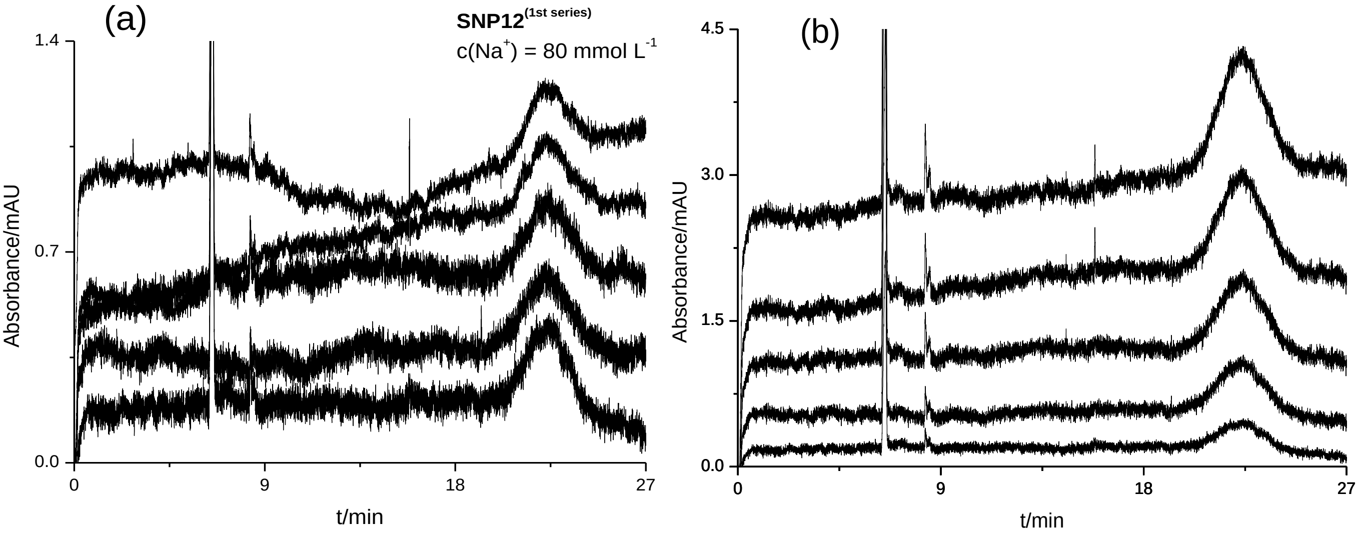
(a)
SNP12$^{(1st\ series)}$
c(Na^{+}) = 80 mmol L^{-1}
Absorbance/mAU
1.4
0.7
0.0
0
9
18
27
t/min
(b)
Absorbance/mAU
4.5
3.0
1.5
0.0
0
9
18
27
t/min

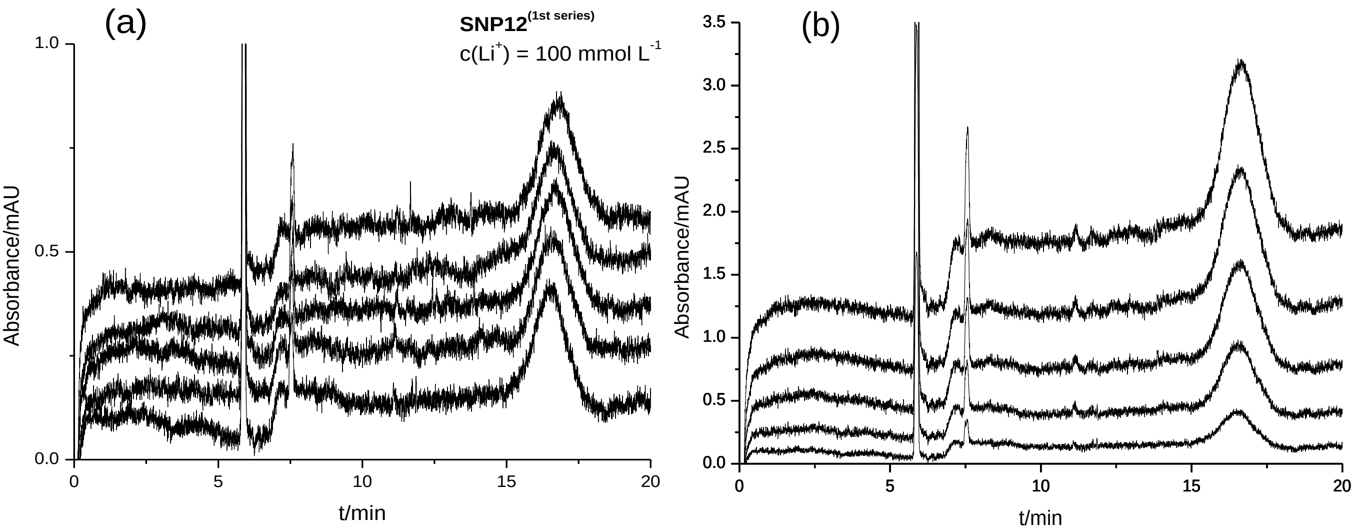
(a)
SNP12$^{(1st\ series)}$
c(Li^{+}) = 100 mmol L^{-1}
Absorbance/mAU
1.0
0.5
0.0
0
5
10
15
20
t/min
(b)
Absorbance/mAU
3.5
3.0
2.5
2.0
1.5
1.0
0.5
0.0
0
5
10
15
20
t/min

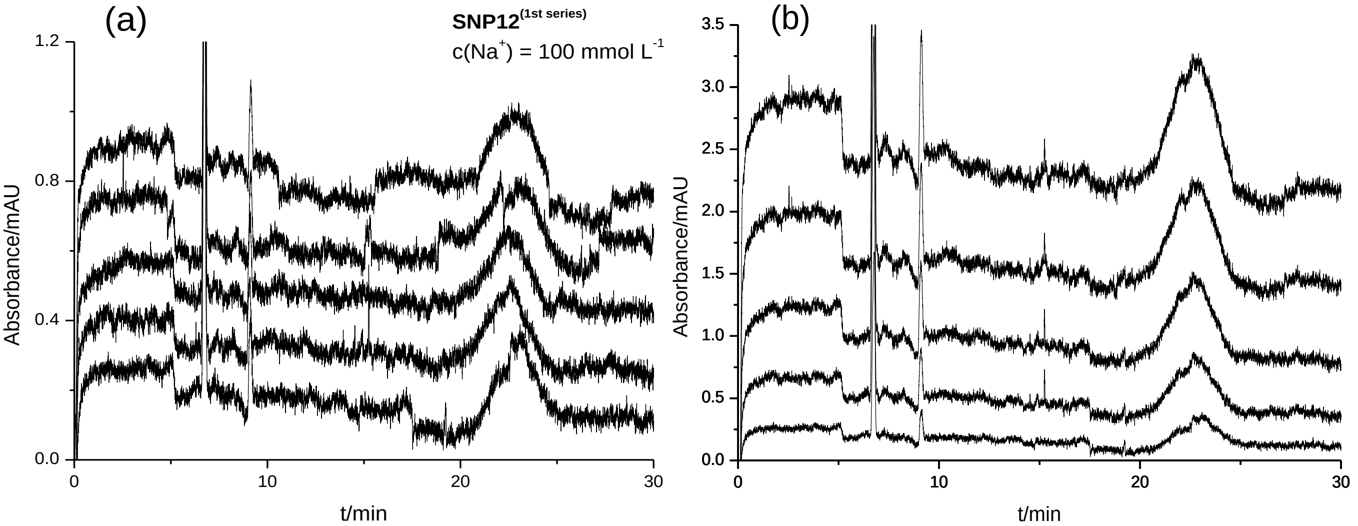
(a)
SNP12$^{(1st\ series)}$
c(Na^{+}) = 100 mmol L^{-1}
Absorbance/mAU
1.2
0.8
0.4
0.0
0
10
20
30
t/min
(b)
Absorbance/mAU
3.5
3.0
2.5
2.0
1.5
1.0
0.5
0.0
0
10
20
30
t/min

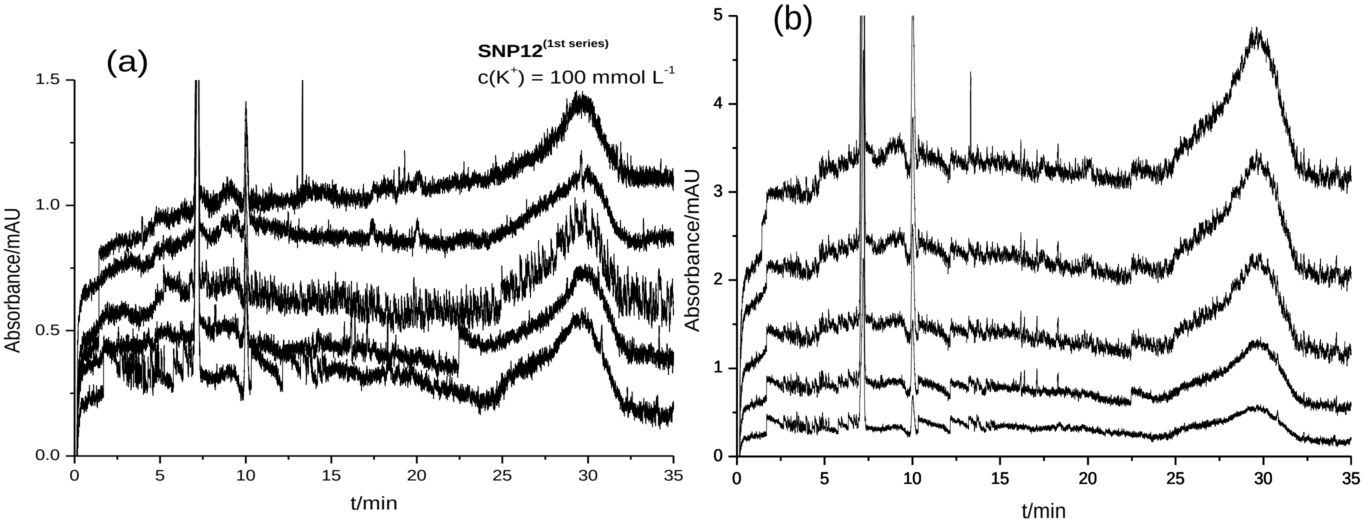
(a)
SNP12$^{(1st series)}$
c(K$^+$) = 100 mmol L^{-1}
Absorbance/mAU
0.0
0.5
1.0
1.5
0
5
10
15
20
25
30
35
t/min
(b)
Absorbance/mAU
0
1
2
3
4
5
0
5
10
15
20
25
30
35
t/min

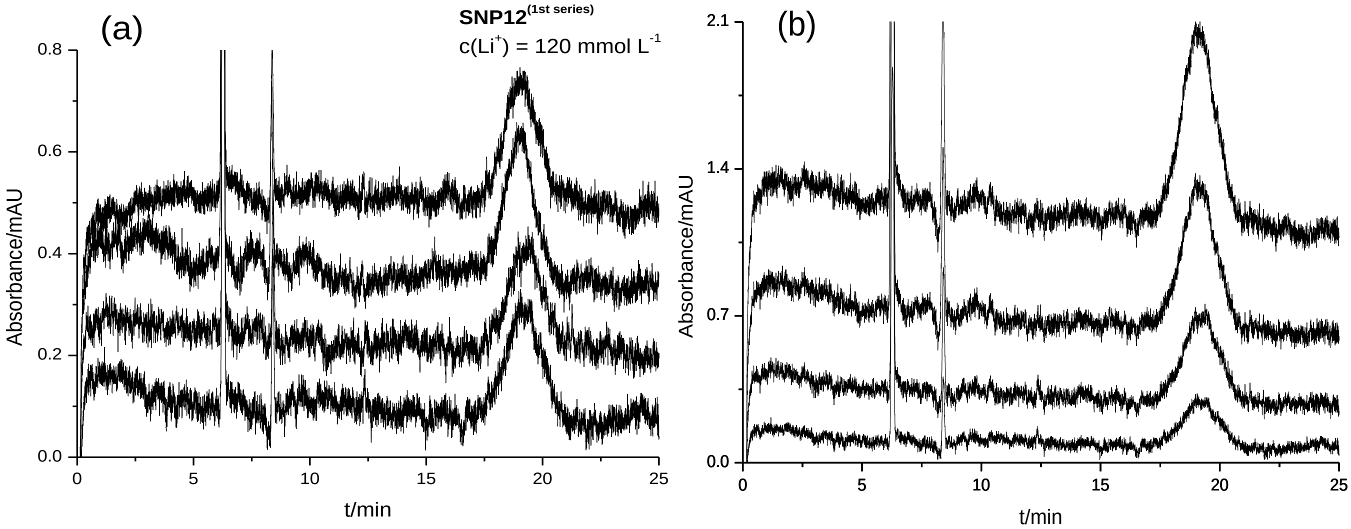
(a)
SNP12$^{(1st series)}$
c(Li$^+$) = 120 mmol L^{-1}
Absorbance/mAU
0.0
0.2
0.4
0.6
0.8
0
5
10
15
20
25
t/min
(b)
Absorbance/mAU
0.0
0.7
1.4
2.1
0
5
10
15
20
25
t/min

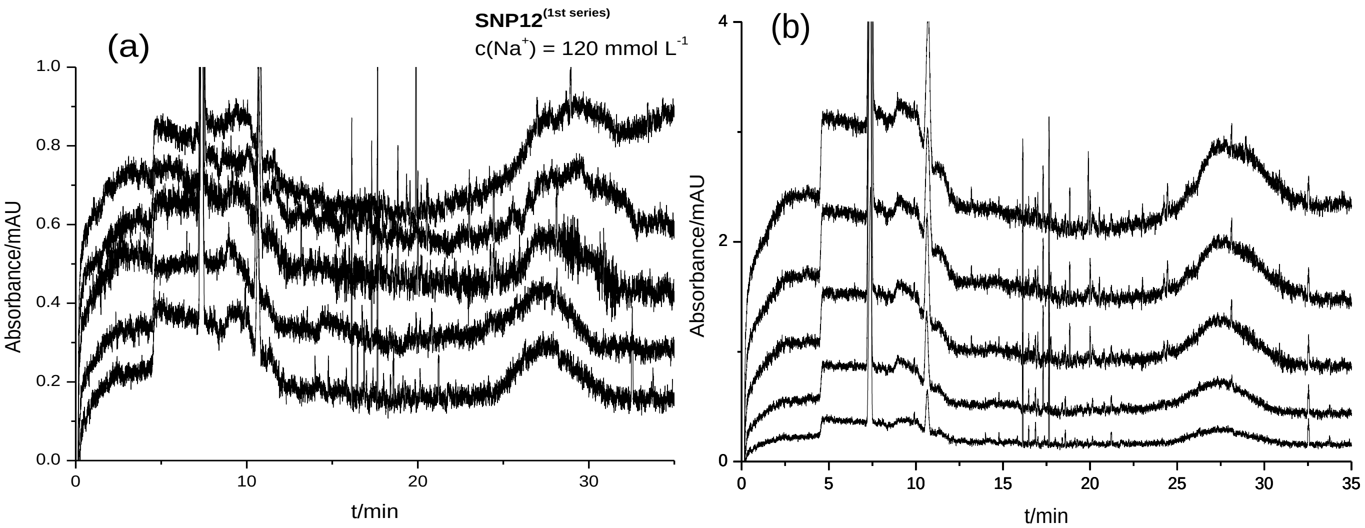
(a)
SNP12$^{(1st series)}$
c(Na$^+$) = 120 mmol L^{-1}
Absorbance/mAU
0.0
0.2
0.4
0.6
0.8
1.0
0
10
20
30
t/min
(b)
Absorbance/mAU
0
2
4
0
5
10
15
20
25
30
35
t/min

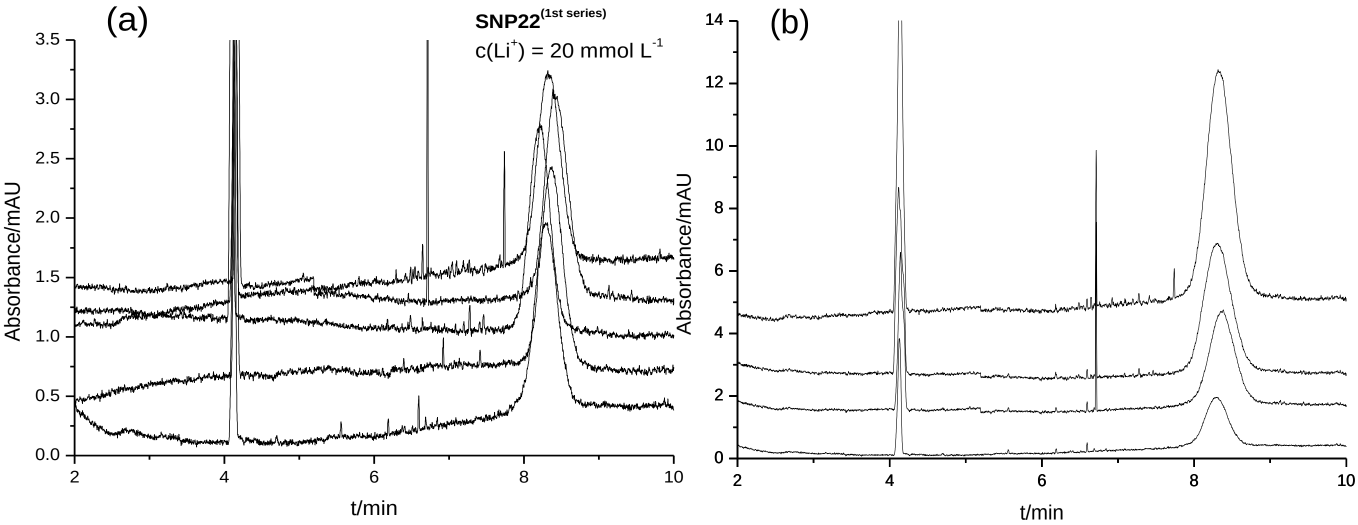
(a)
SNP22$^{(1st\ series)}$
c(Li^{+}) = 20 mmol L^{-1}
Absorbance/mAU
t/min
0.0
0.5
1.0
1.5
2.0
2.5
3.0
3.5
2
4
6
8
10
(b)
Absorbance/mAU
t/min
0
2
4
6
8
10
12
14
2
4
6
8
10

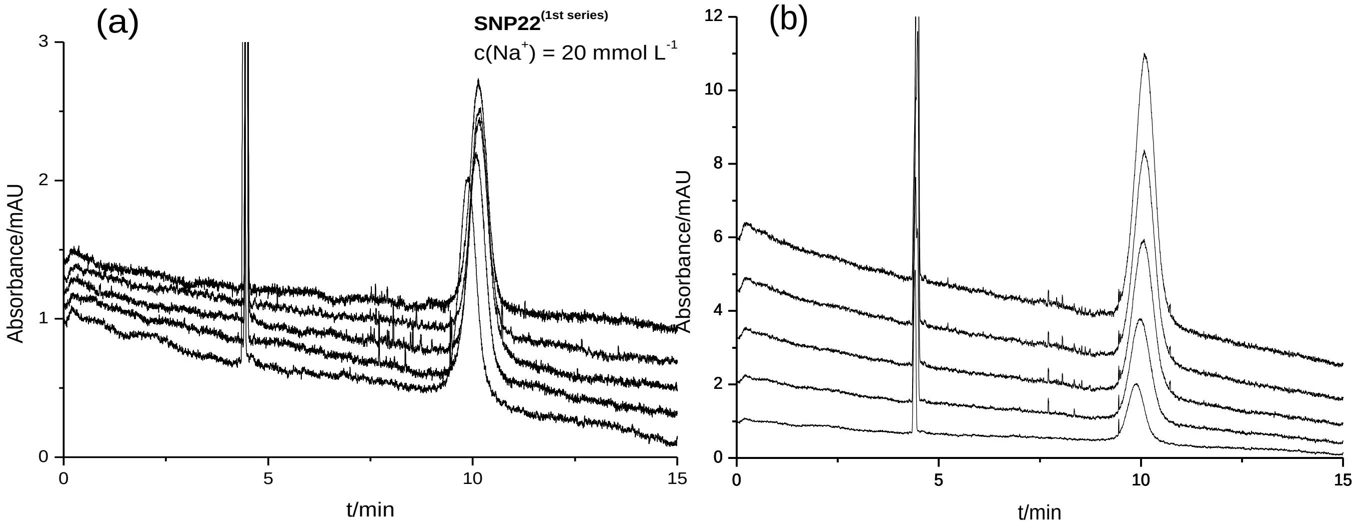
(a)
SNP22$^{(1st\ series)}$
c(Na^{+}) = 20 mmol L^{-1}
Absorbance/mAU
t/min
0
1
2
3
0
5
10
15
(b)
Absorbance/mAU
t/min
0
2
4
6
8
10
12
0
5
10
15

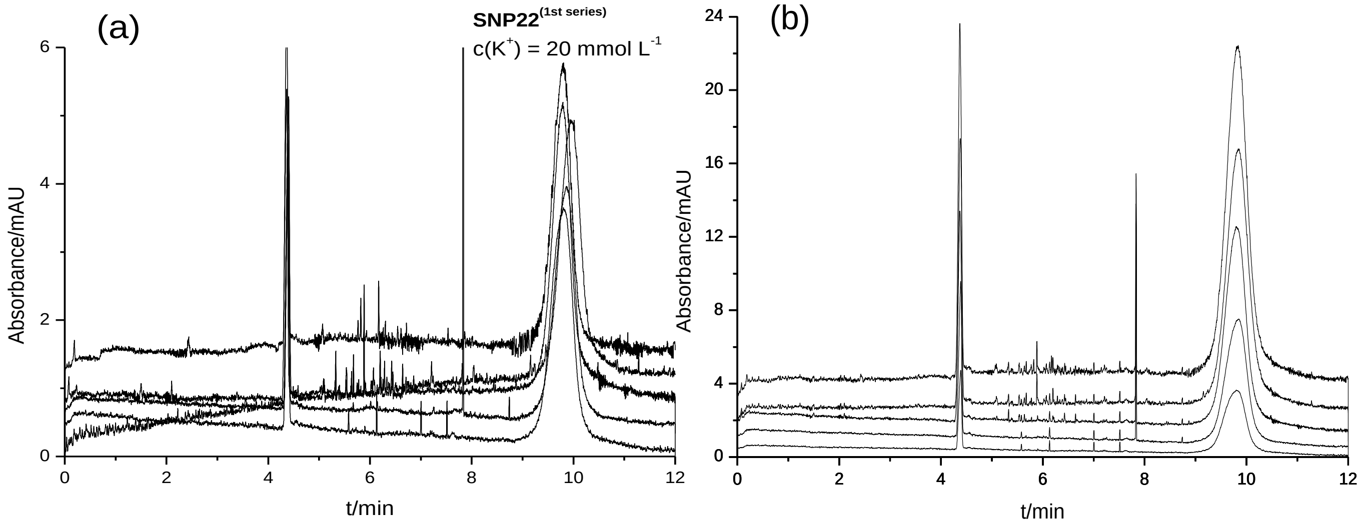
(a)
SNP22$^{(1st\ series)}$
c(K^{+}) = 20 mmol L^{-1}
Absorbance/mAU
t/min
0
2
4
6
0
2
4
6
8
10
12
(b)
Absorbance/mAU
t/min
0
4
8
12
16
20
24
0
2
4
6
8
10
12

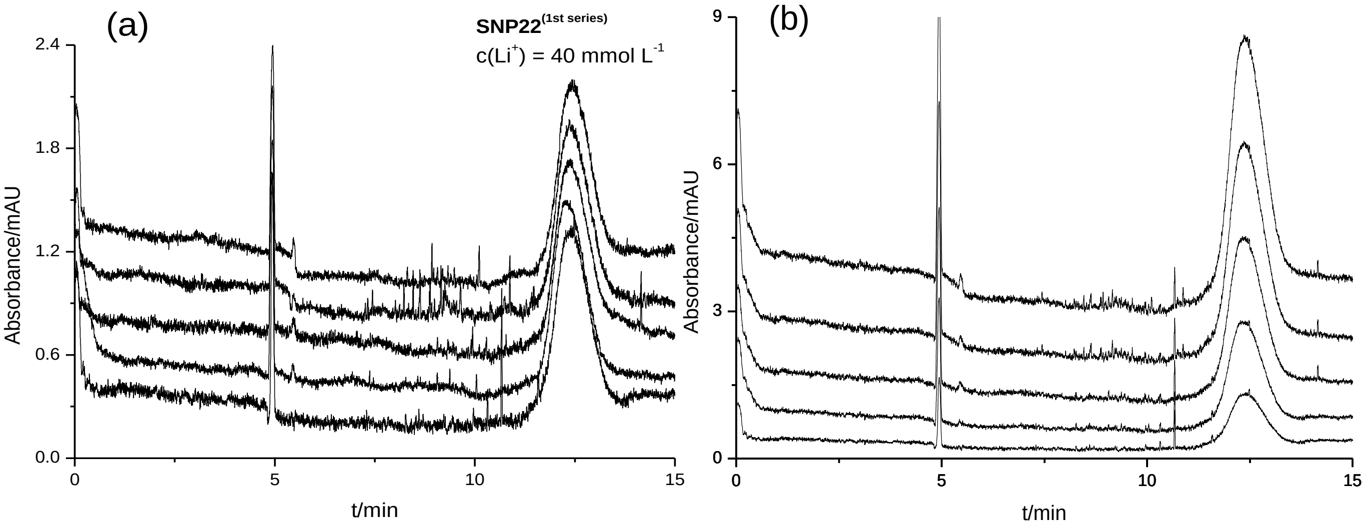
(a)
SNP22(1st series)
c(Li+) = 40 mmol L-1
Absorbance/mAU
0.0
0.6
1.2
1.8
2.4
0
5
10
15
t/min
(b)
Absorbance/mAU
0
3
6
9
0
5
10
15
t/min

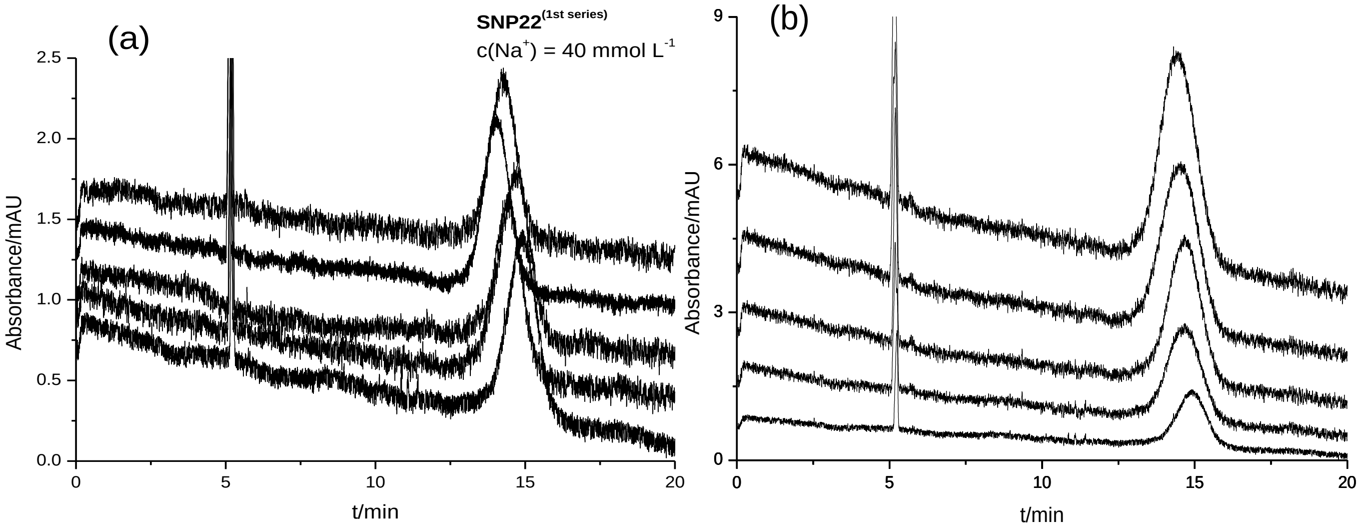
(a)
SNP22(1st series)
c(Na+) = 40 mmol L-1
Absorbance/mAU
0.0
0.5
1.0
1.5
2.0
2.5
0
5
10
15
20
t/min
(b)
Absorbance/mAU
0
3
6
9
0
5
10
15
20
t/min

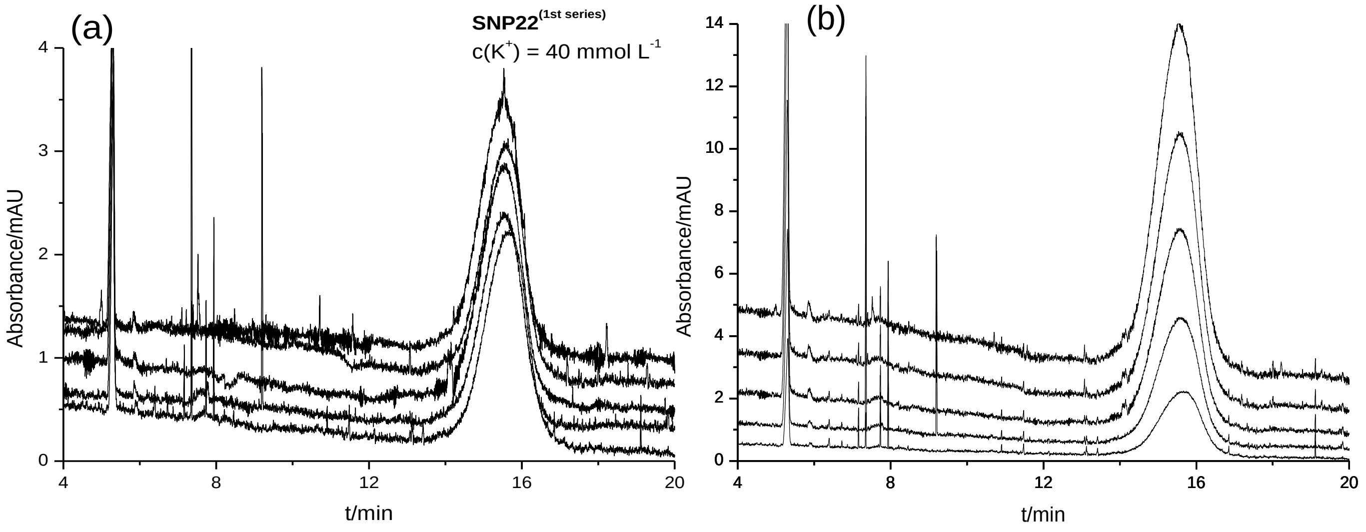
(a)
SNP22(1st series)
c(K+) = 40 mmol L-1
Absorbance/mAU
0
1
2
3
4
4
8
12
16
20
t/min
(b)
Absorbance/mAU
0
2
4
6
8
10
12
14
4
8
12
16
20
t/min

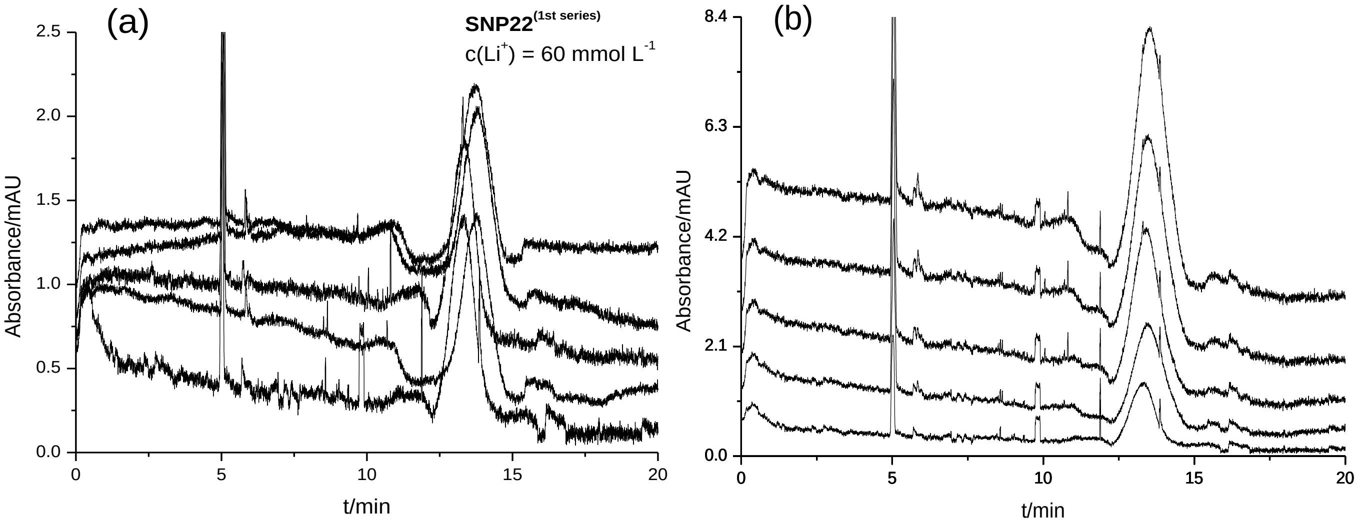
(a)
SNP22$^{(1st\ series)}$
c(Li^{+}) = 60 mmol L^{-1}
Absorbance/mAU
2.5
2.0
1.5
1.0
0.5
0.0
0
5
10
15
20
t/min
(b)
8.4
6.3
4.2
2.1
0.0
Absorbance/mAU
0
5
10
15
20
t/min

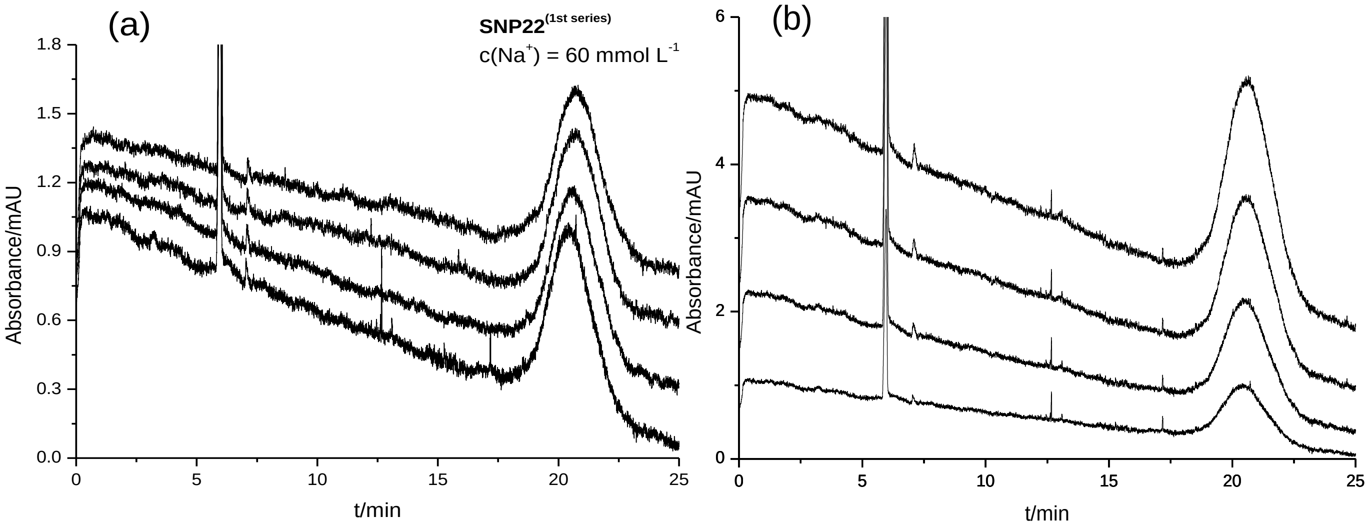
(a)
SNP22$^{(1st\ series)}$
c(Na^{+}) = 60 mmol L^{-1}
Absorbance/mAU
1.8
1.5
1.2
0.9
0.6
0.3
0.0
0
5
10
15
20
25
t/min
(b)
6
4
2
0
Absorbance/mAU
0
5
10
15
20
25
t/min

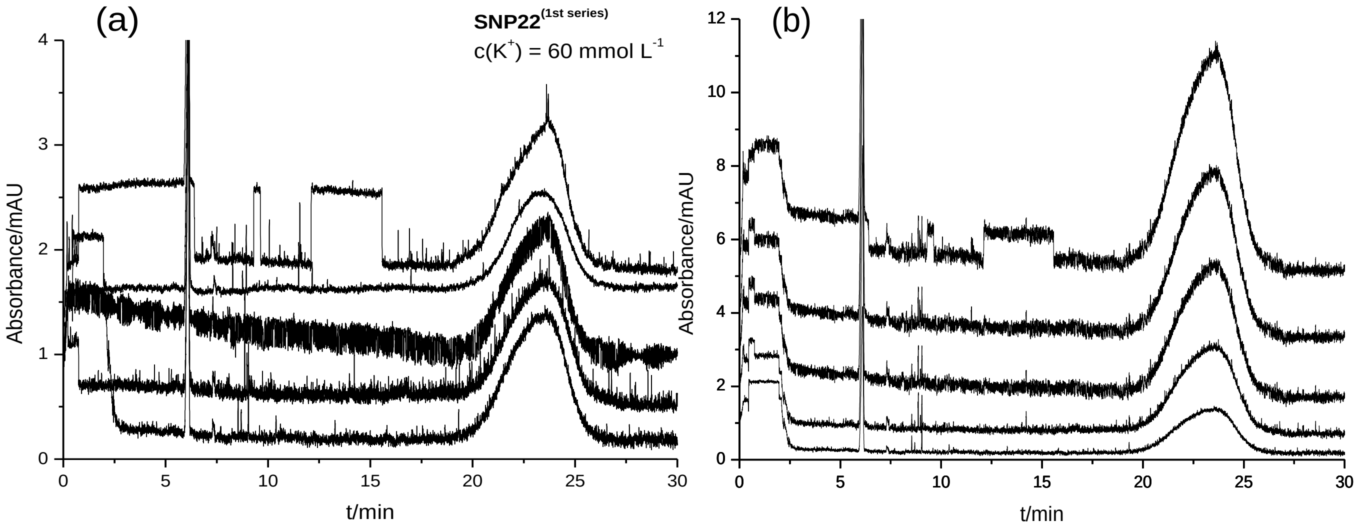
(a)
SNP22$^{(1st\ series)}$
c(K^{+}) = 60 mmol L^{-1}
Absorbance/mAU
4
3
2
1
0
0
5
10
15
20
25
30
t/min
(b)
12
10
8
6
4
2
0
Absorbance/mAU
0
5
10
15
20
25
30
t/min

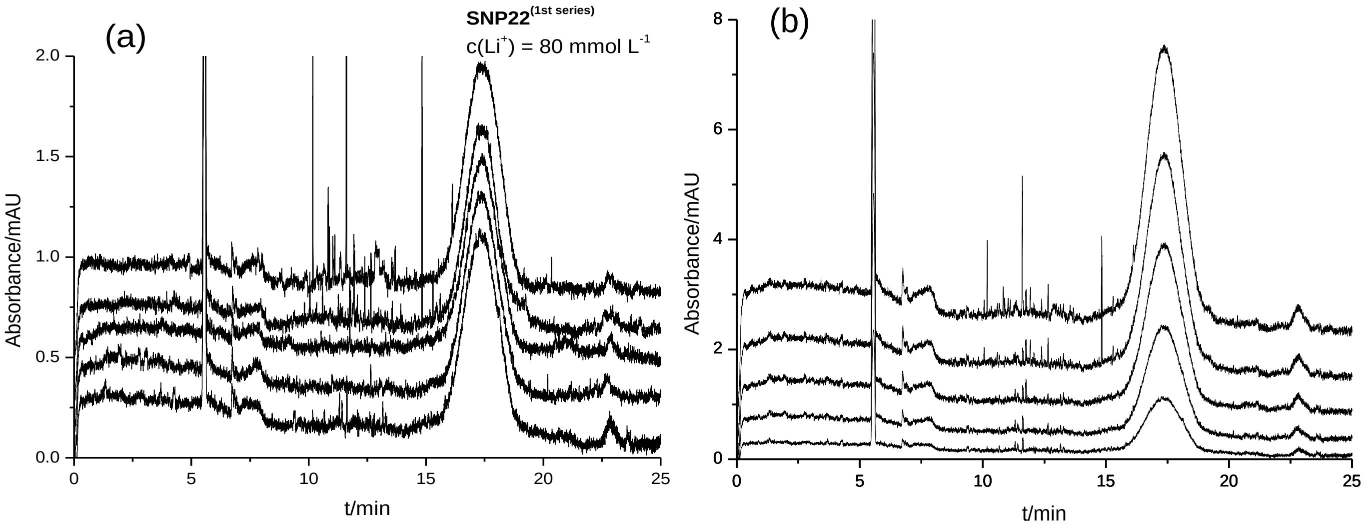
(a)
SNP22$^{(1st\ series)}$
c(Li$^+$) = 80 mmol L^{-1}
Absorbance/mAU
0.0
0.5
1.0
1.5
2.0
t/min
0
5
10
15
20
25
(b)
Absorbance/mAU
0
2
4
6
8
t/min
0
5
10
15
20
25

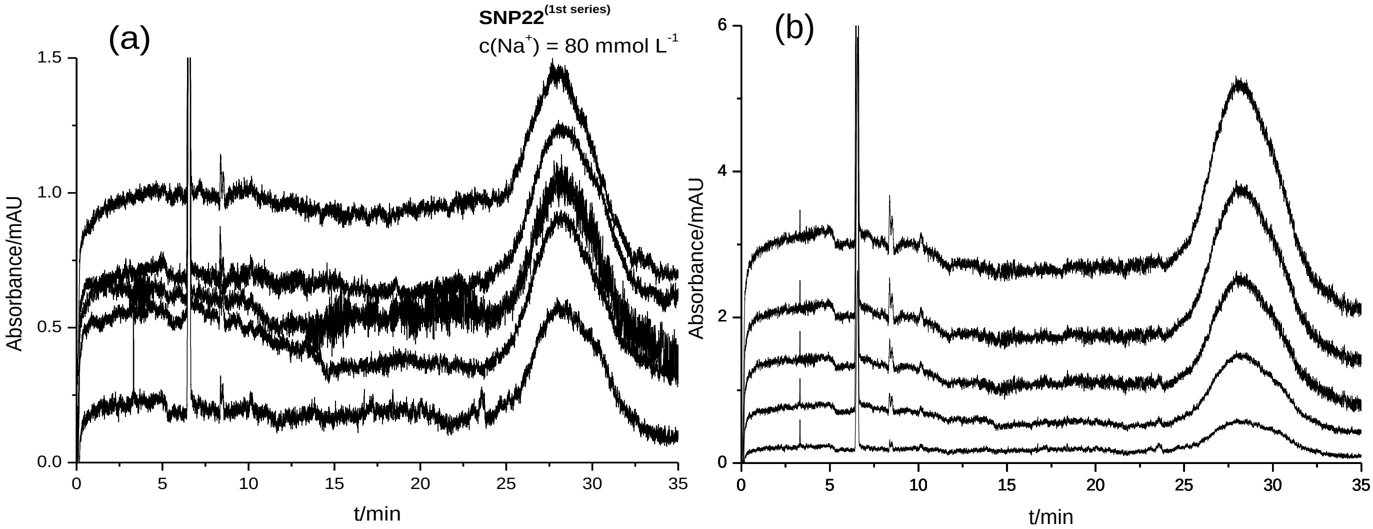
(a)
SNP22$^{(1st\ series)}$
c(Na$^+$) = 80 mmol L^{-1}
Absorbance/mAU
0.0
0.5
1.0
1.5
t/min
0
5
10
15
20
25
30
35
(b)
Absorbance/mAU
0
2
4
6
t/min
0
5
10
15
20
25
30
35

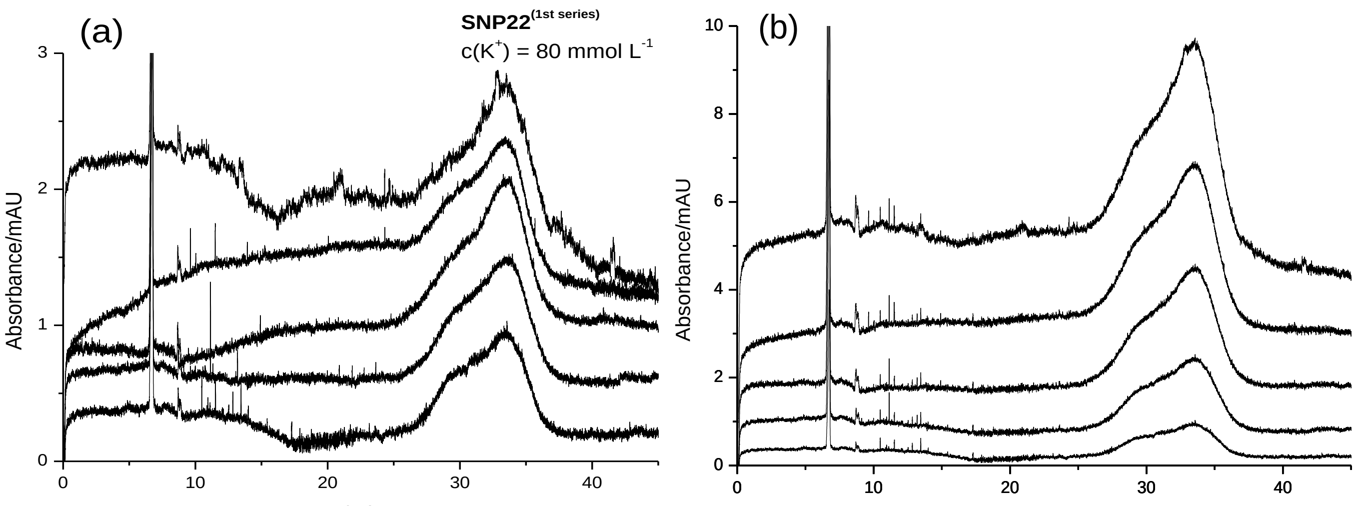
(a)
SNP22$^{(1st\ series)}$
c(K$^+$) = 80 mmol L^{-1}
Absorbance/mAU
0
1
2
3
t/min
0
10
20
30
40
(b)
Absorbance/mAU
0
2
4
6
8
10
t/min
0
10
20
30
40

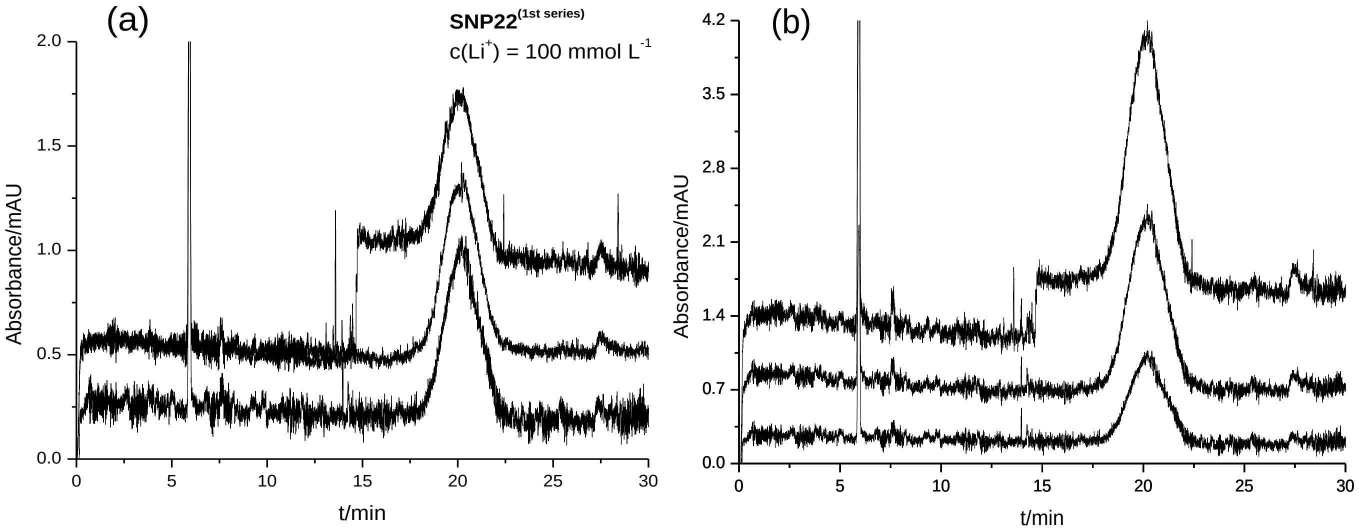
(a)
SNP22$^{(1st\ series)}$
c(Li$^+$) = 100 mmol L^{-1}
Absorbance/mAU
0.0
0.5
1.0
1.5
2.0
t/min
0
5
10
15
20
25
30
(b)
Absorbance/mAU
0.0
0.7
1.4
2.1
2.8
3.5
4.2
t/min
0
5
10
15
20
25
30

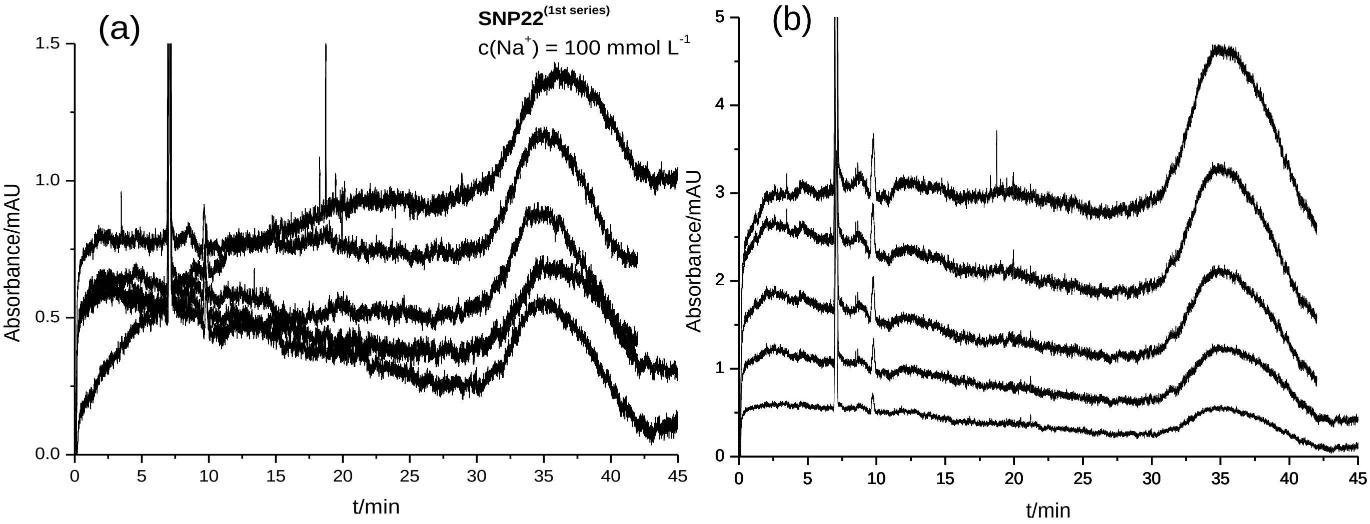
(a)
SNP22$^{(1st\ series)}$
c(Na$^+$) = 100 mmol L^{-1}
Absorbance/mAU
0.0
0.5
1.0
1.5
t/min
0
5
10
15
20
25
30
35
40
45
(b)
Absorbance/mAU
0
1
2
3
4
5
t/min
0
5
10
15
20
25
30
35
40
45

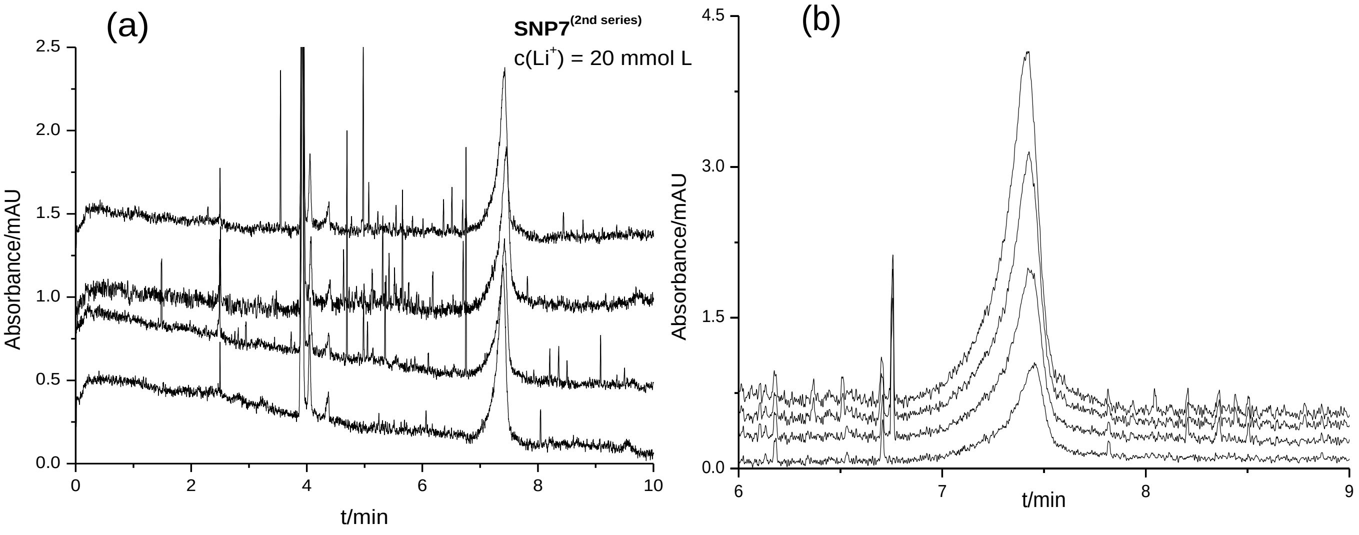
(a)
SNP7$^{(2nd\ series)}$
c(Li$^+$) = 20 mmol L
Absorbance/mAU
0.0
0.5
1.0
1.5
2.0
2.5
t/min
0
2
4
6
8
10
(b)
Absorbance/mAU
0.0
1.5
3.0
4.5
t/min
6
7
8
9

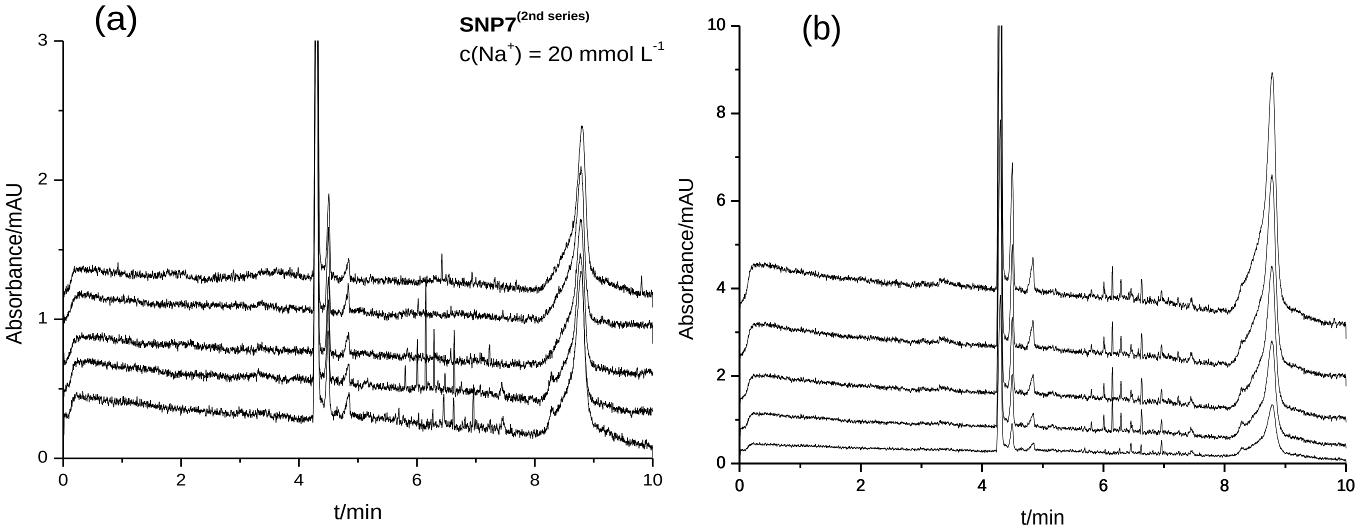
(a)
SNP7$^{(2nd\ series)}$
c(Na$^+$) = 20 mmol L^{-1}
Absorbance/mAU
t/min
0
1
2
3
0
2
4
6
8
10
(b)
Absorbance/mAU
t/min
0
2
4
6
8
10
0
2
4
6
8
10

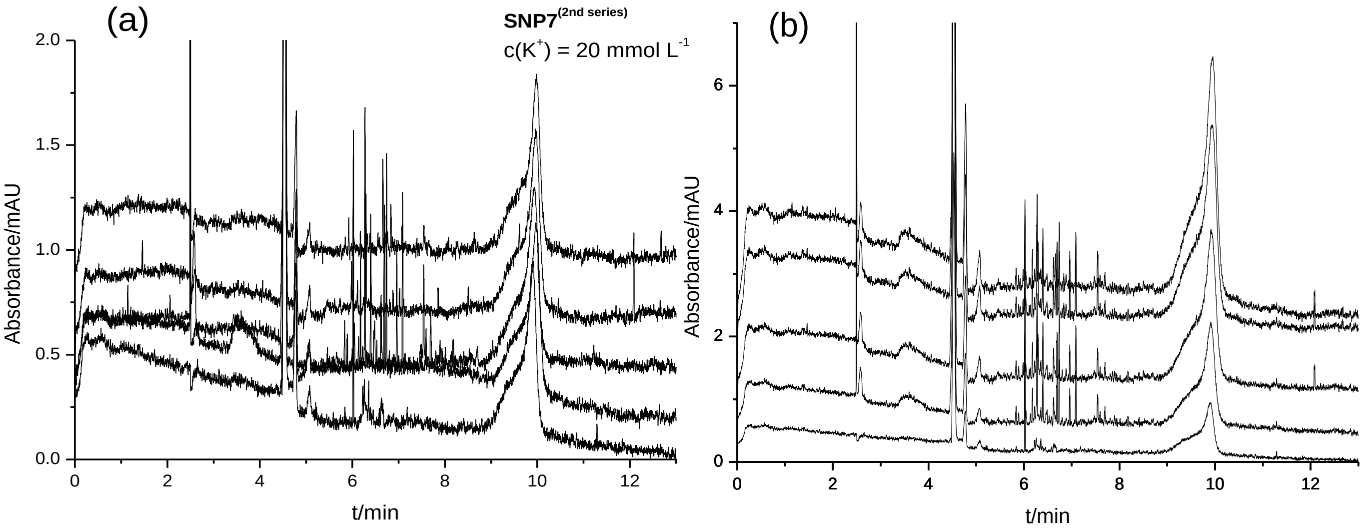
(a)
SNP7$^{(2nd\ series)}$
c(K$^+$) = 20 mmol L^{-1}
Absorbance/mAU
t/min
0.0
0.5
1.0
1.5
2.0
0
2
4
6
8
10
12
(b)
Absorbance/mAU
t/min
0
2
4
6
0
2
4
6
8
10
12

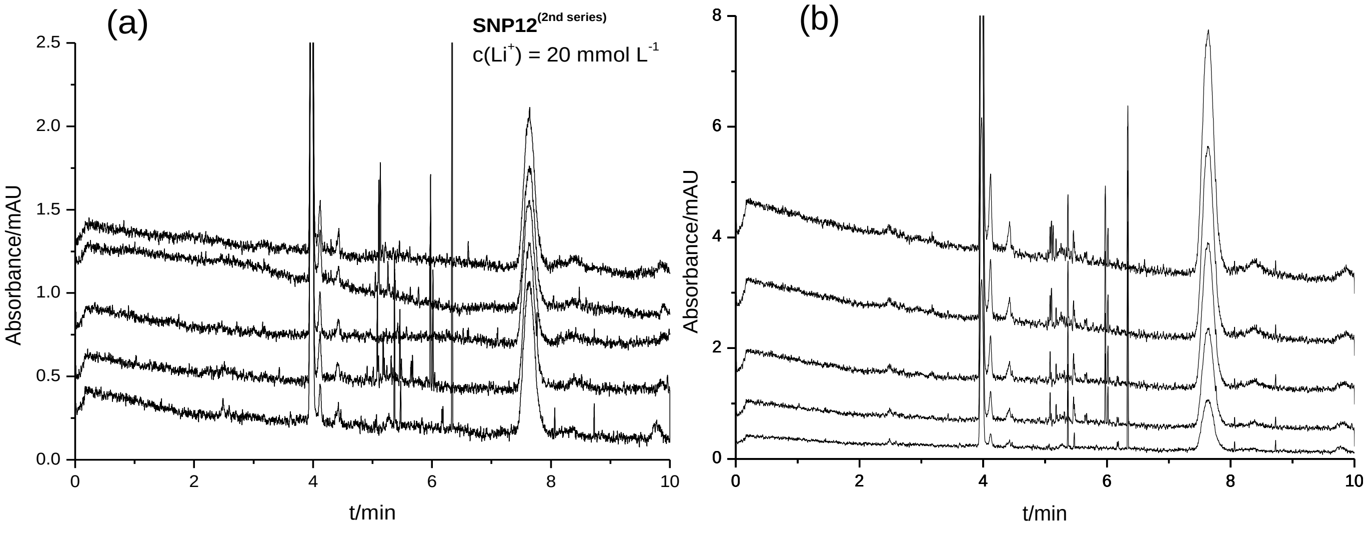
(a)
SNP12$^{(2nd\ series)}$
c(Li$^+$) = 20 mmol L^{-1}
Absorbance/mAU
t/min
0.0
0.5
1.0
1.5
2.0
2.5
0
2
4
6
8
10
(b)
Absorbance/mAU
t/min
0
2
4
6
8
0
2
4
6
8
10

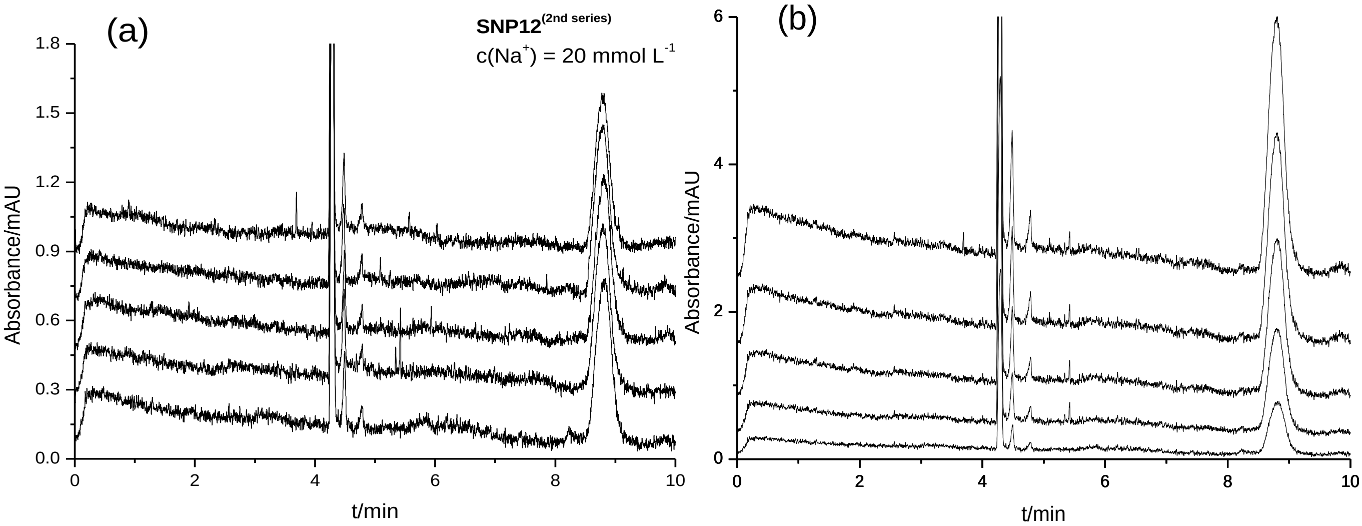
(a)
SNP12$^{(2nd\ series)}$
c(Na$^+$) = 20 mmol L^{-1}
Absorbance/mAU
0.0
0.3
0.6
0.9
1.2
1.5
1.8
0
2
4
6
8
10
t/min
(b)
Absorbance/mAU
0
2
4
6
0
2
4
6
8
10
t/min

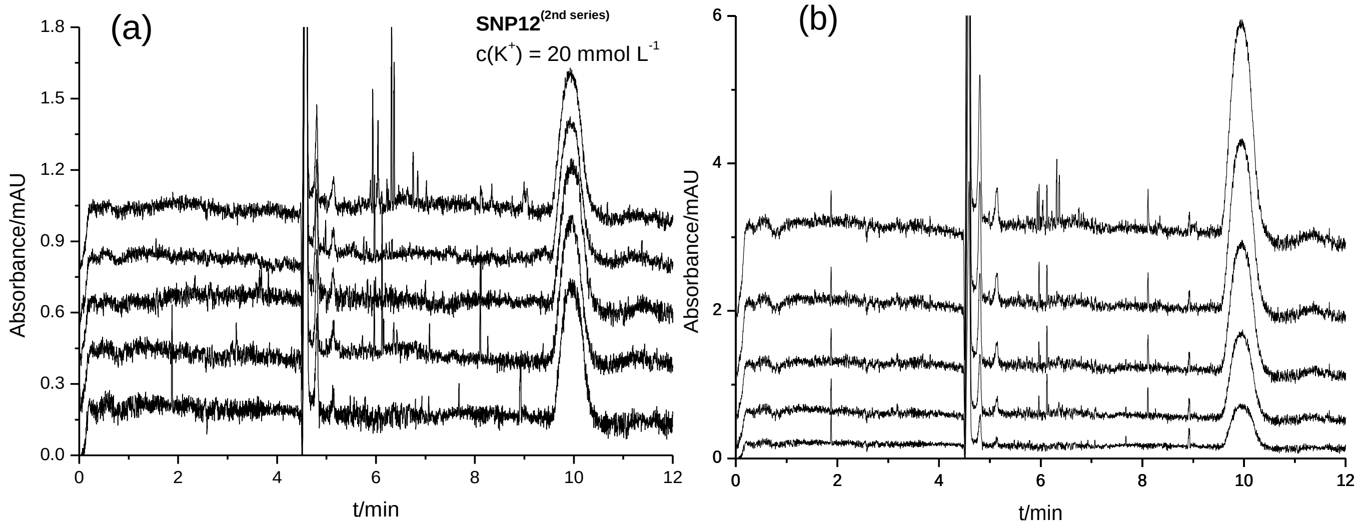
(a)
SNP12$^{(2nd\ series)}$
c(K$^+$) = 20 mmol L^{-1}
Absorbance/mAU
0.0
0.3
0.6
0.9
1.2
1.5
1.8
0
2
4
6
8
10
12
t/min
(b)
Absorbance/mAU
0
2
4
6
0
2
4
6
8
10
12
t/min

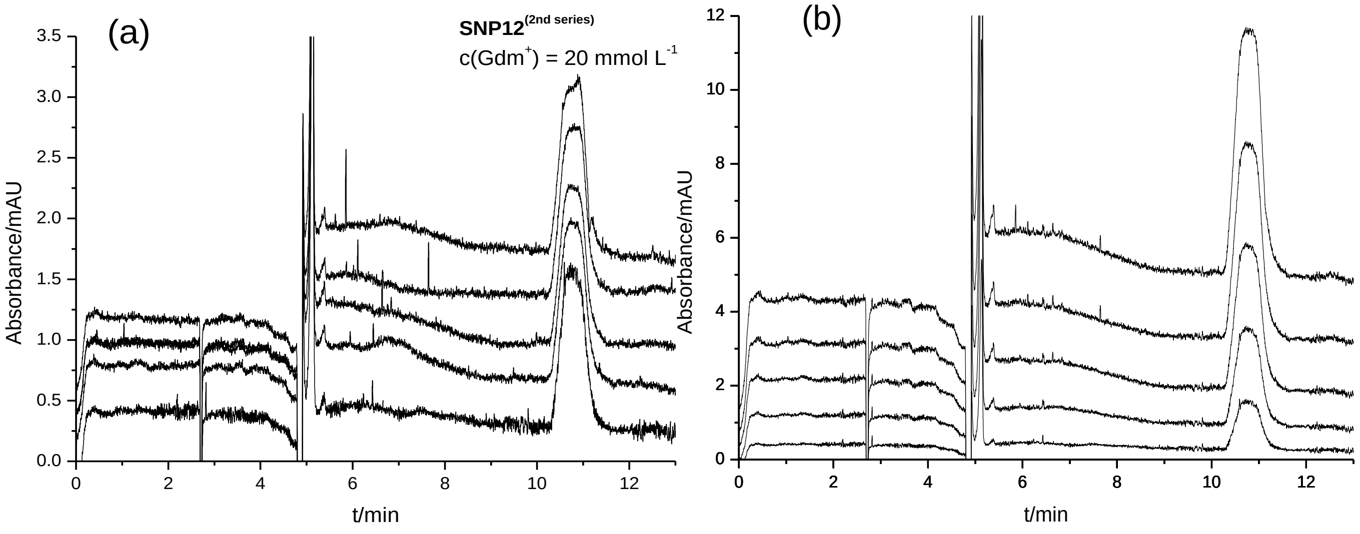
(a)
SNP12$^{(2nd\ series)}$
c(Gdm$^+$) = 20 mmol L^{-1}
Absorbance/mAU
0.0
0.5
1.0
1.5
2.0
2.5
3.0
3.5
0
2
4
6
8
10
12
t/min
(b)
Absorbance/mAU
0
2
4
6
8
10
12
0
2
4
6
8
10
12
t/min

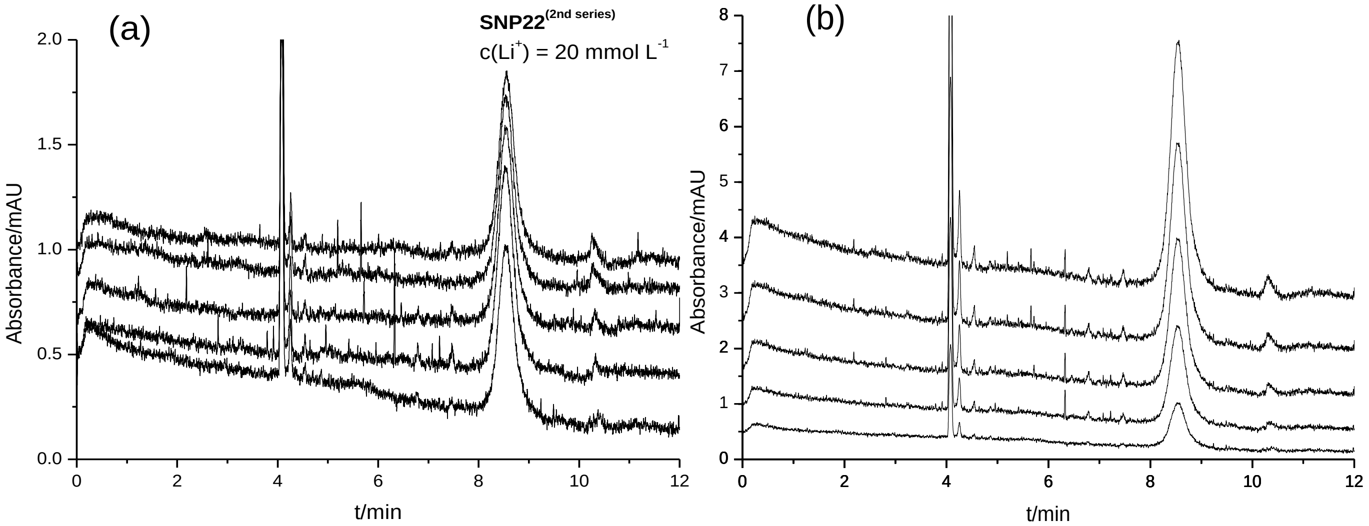
(a)
SNP22$^{(2nd\ series)}$
c(Li$^+$) = 20 mmol L^{-1}
Absorbance/mAU
0.0
0.5
1.0
1.5
2.0
t/min
0
2
4
6
8
10
12
(b)
Absorbance/mAU
0
1
2
3
4
5
6
7
8
t/min
0
2
4
6
8
10
12

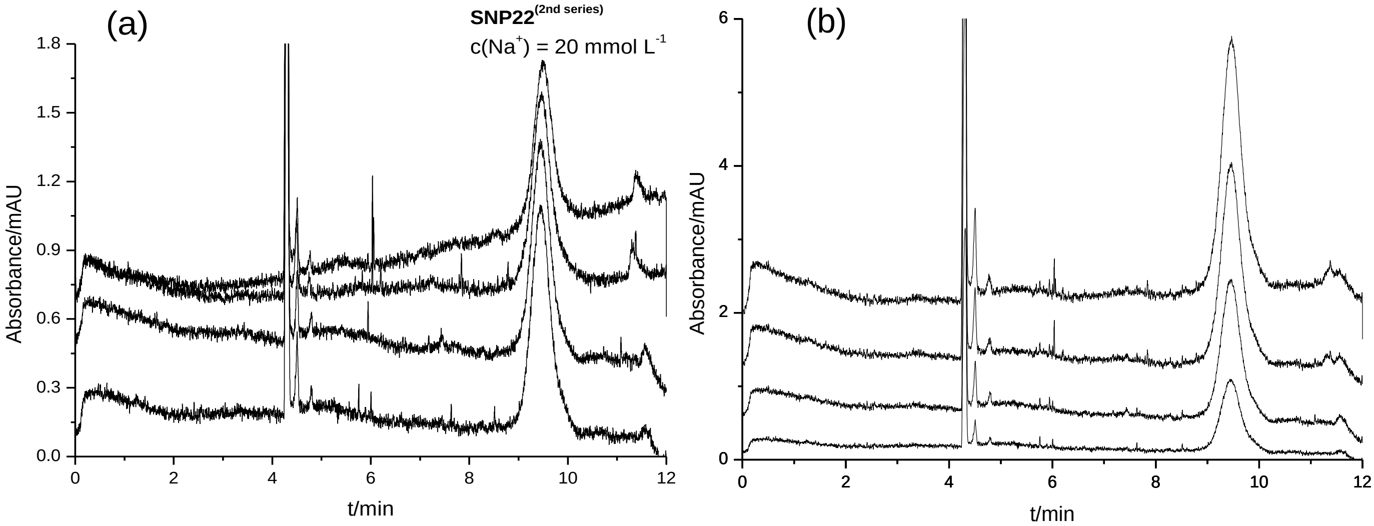
(a)
SNP22$^{(2nd\ series)}$
c(Na$^+$) = 20 mmol L^{-1}
Absorbance/mAU
0.0
0.3
0.6
0.9
1.2
1.5
1.8
t/min
0
2
4
6
8
10
12
(b)
Absorbance/mAU
0
2
4
6
t/min
0
2
4
6
8
10
12

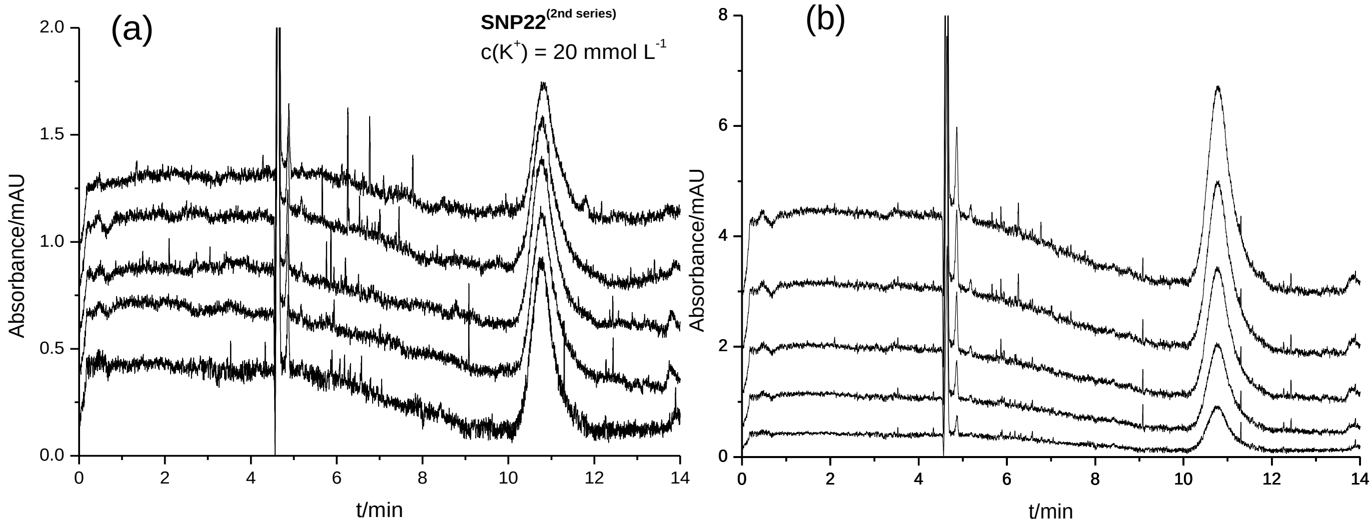
(a)
SNP22$^{(2nd\ series)}$
c(K$^+$) = 20 mmol L^{-1}
Absorbance/mAU
0.0
0.5
1.0
1.5
2.0
t/min
0
2
4
6
8
10
12
14
(b)
Absorbance/mAU
0
2
4
6
8
t/min
0
2
4
6
8
10
12
14

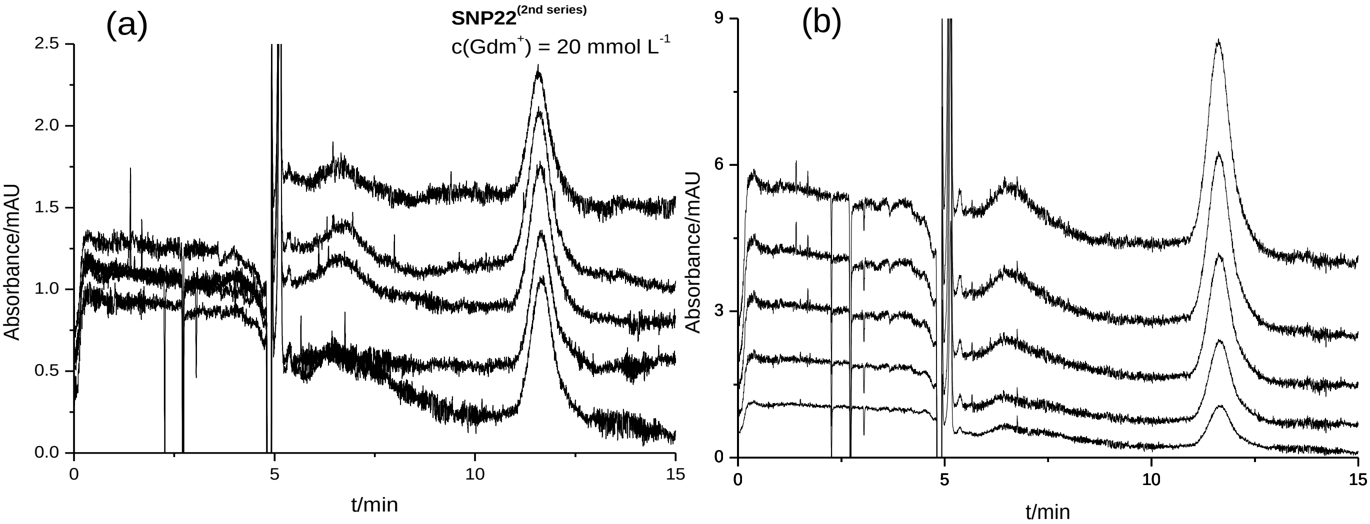
(a)
SNP22$^{(2nd\ series)}$
c(Gdm^{+}) = 20 mmol L^{-1}
Absorbance/mAU
0.0
0.5
1.0
1.5
2.0
2.5
0
5
10
15
t/min
(b)
Absorbance/mAU
0
3
6
9
0
5
10
15
t/min

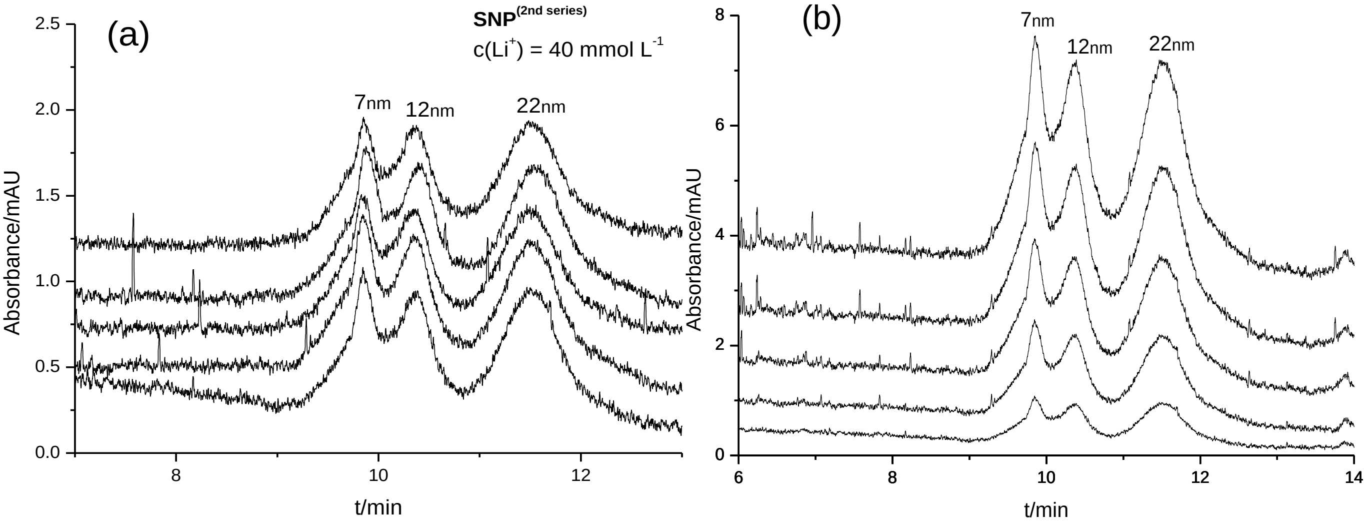
(a)
SNP$^{(2nd\ series)}$
c(Li^{+}) = 40 mmol L^{-1}
7nm
12nm
22nm
Absorbance/mAU
0.0
0.5
1.0
1.5
2.0
2.5
8
10
12
t/min
(b)
7nm
12nm
22nm
Absorbance/mAU
0
2
4
6
8
6
8
10
12
14
t/min

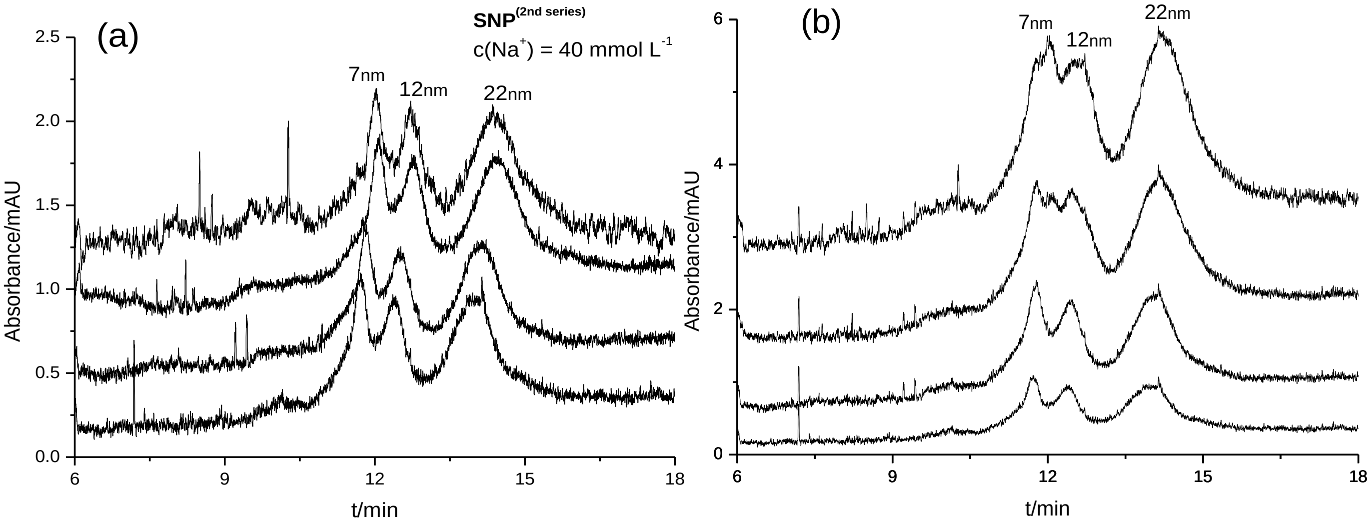
(a)
SNP$^{(2nd\ series)}$
c(Na^{+}) = 40 mmol L^{-1}
7nm
12nm
22nm
Absorbance/mAU
0.0
0.5
1.0
1.5
2.0
2.5
6
9
12
15
18
t/min
(b)
7nm
12nm
22nm
Absorbance/mAU
0
2
4
6
6
9
12
15
18
t/min

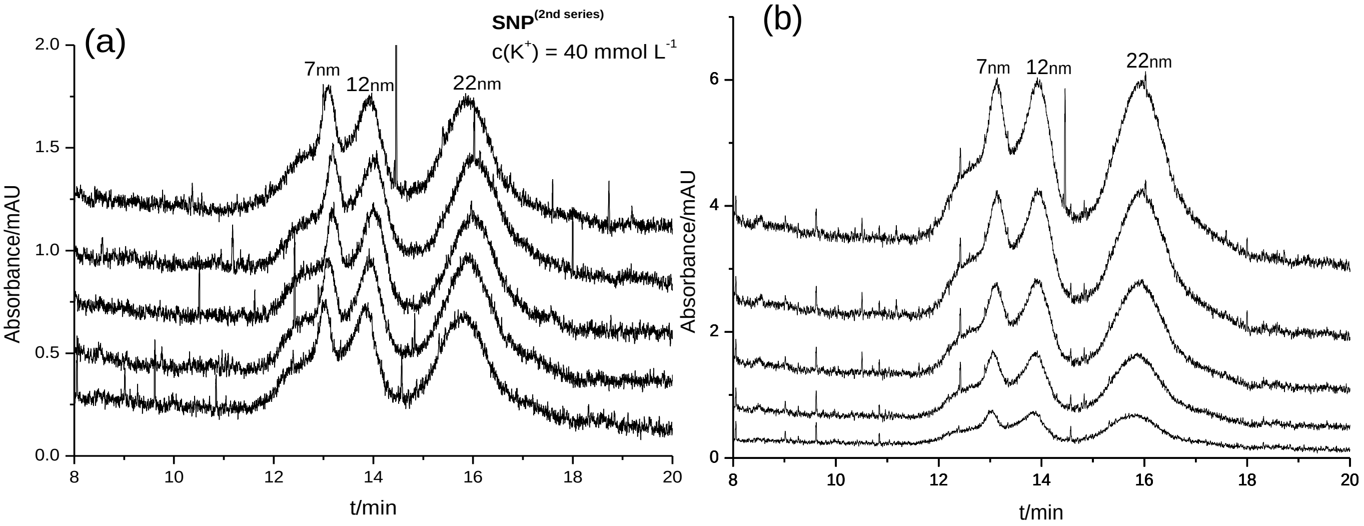
(a)
SNP$^{(2nd\ series)}$
c(K$^+$) = 40 mmol L^{-1}
7nm
12nm
22nm
Absorbance/mAU
t/min
(b)
7nm
12nm
22nm
Absorbance/mAU
t/min

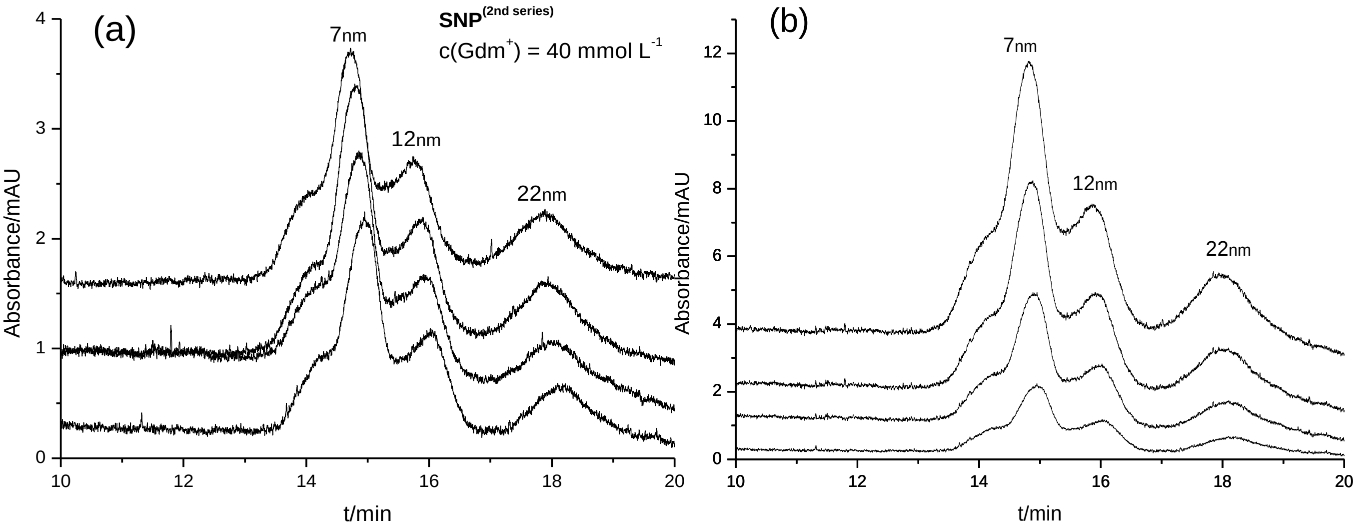
(a)
SNP$^{(2nd\ series)}$
c(Gdm$^+$) = 40 mmol L^{-1}
7nm
12nm
22nm
Absorbance/mAU
t/min
(b)
7nm
12nm
22nm
Absorbance/mAU
t/min

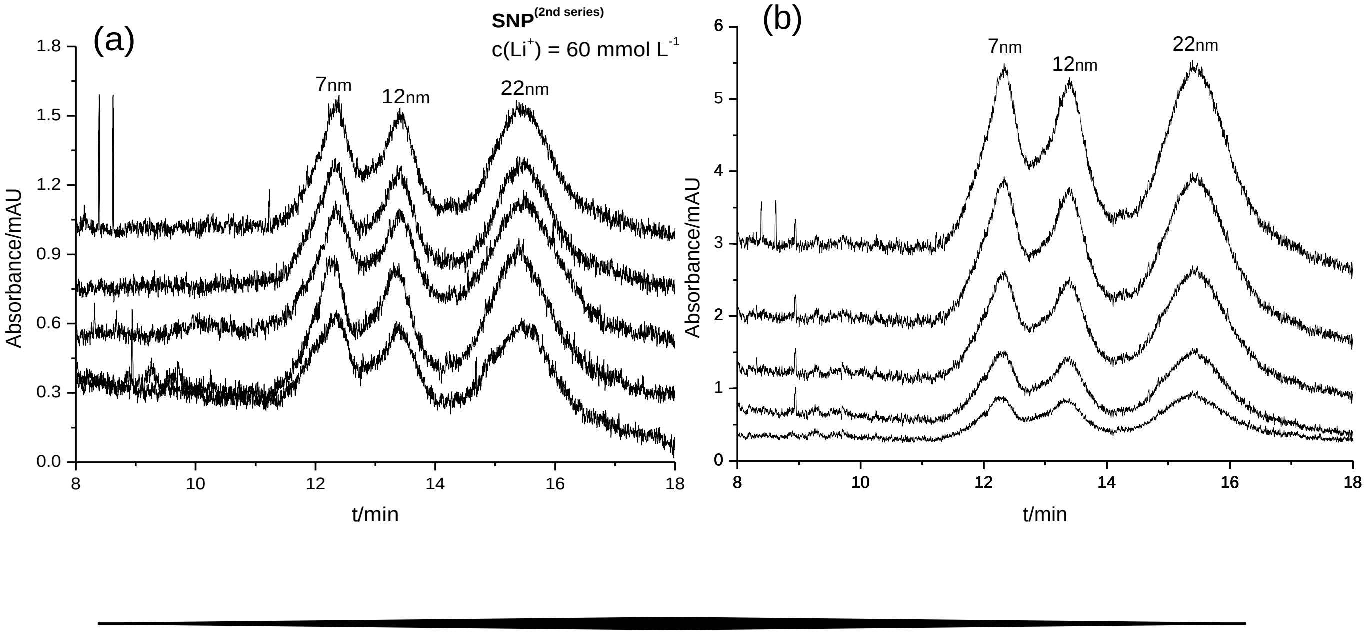
(a)
SNP$^{(2nd\ series)}$
c(Li$^+$) = 60 mmol L^{-1}
7nm
12nm
22nm
Absorbance/mAU
t/min
(b)
7nm
12nm
22nm
Absorbance/mAU
t/min

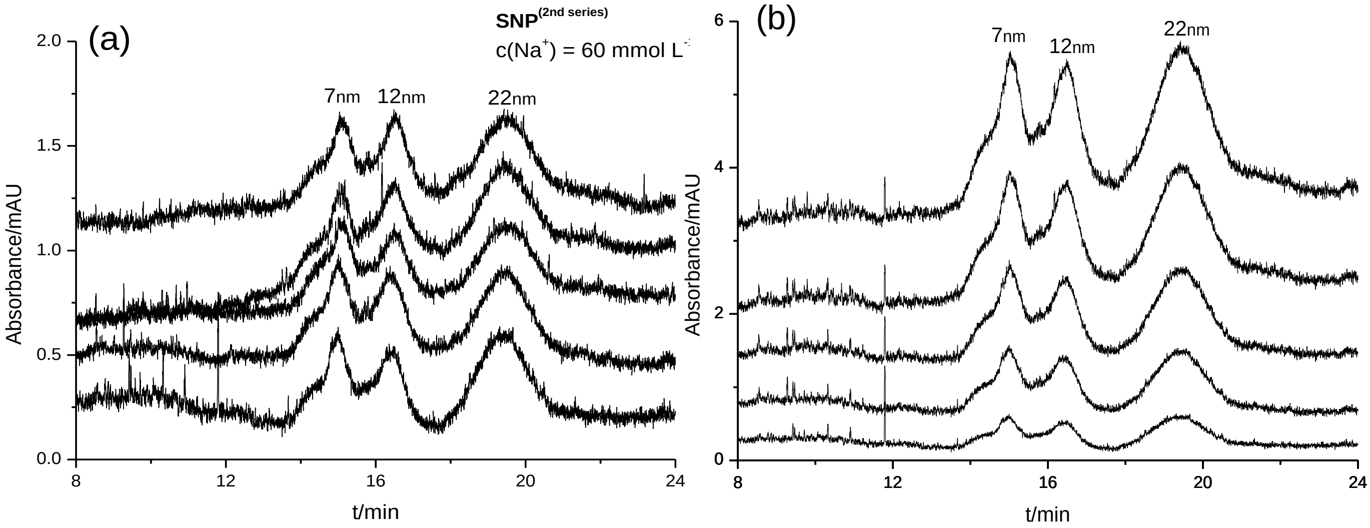
(a)
SNP$^{(2nd\ series)}$
c(Na$^+$) = 60 mmol L^{-}
7nm
12nm
22nm
Absorbance/mAU
0.0
0.5
1.0
1.5
2.0
8
12
16
20
24
t/min
(b)
7nm
12nm
22nm
Absorbance/mAU
0
2
4
6
8
12
16
20
24
t/min

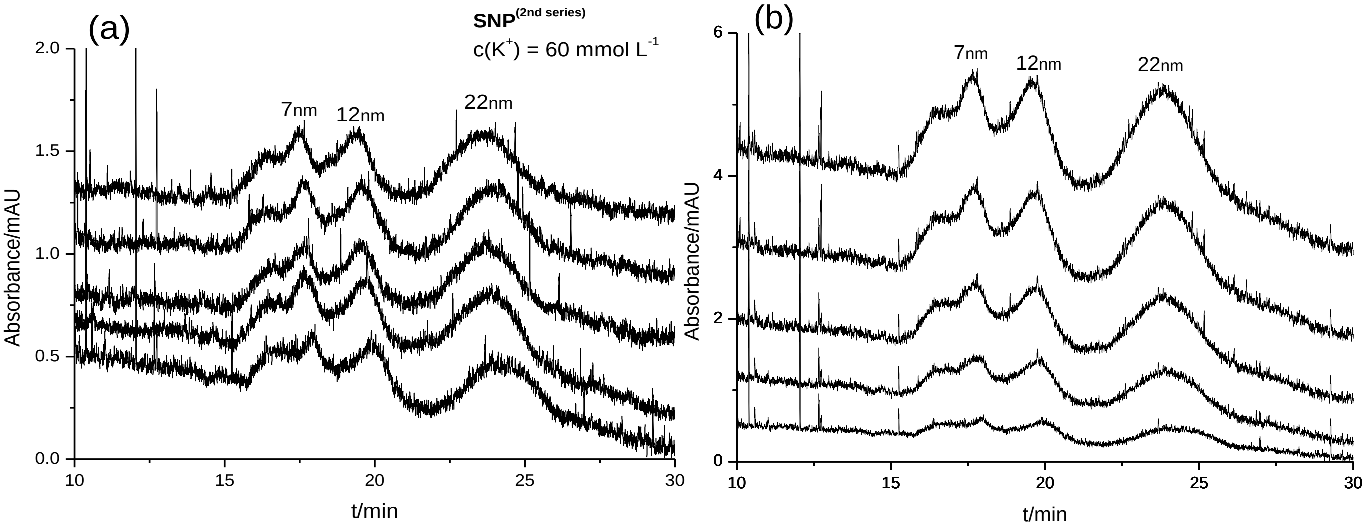
(a)
SNP$^{(2nd\ series)}$
c(K$^+$) = 60 mmol L^{-1}
7nm
12nm
22nm
Absorbance/mAU
0.0
0.5
1.0
1.5
2.0
10
15
20
25
30
t/min
(b)
7nm
12nm
22nm
Absorbance/mAU
0
2
4
6
10
15
20
25
30
t/min

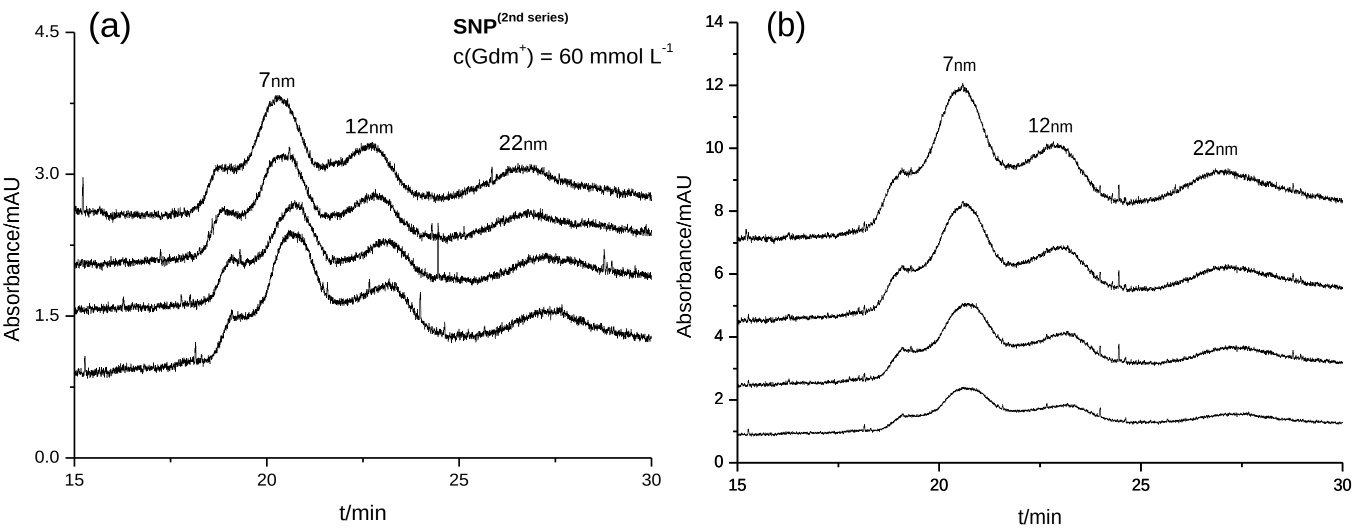
(a)
SNP$^{(2nd\ series)}$
c(Gdm$^+$) = 60 mmol L^{-1}
7nm
12nm
22nm
Absorbance/mAU
0.0
1.5
3.0
4.5
15
20
25
30
t/min
(b)
7nm
12nm
22nm
Absorbance/mAU
0
2
4
6
8
10
12
14
15
20
25
30
t/min

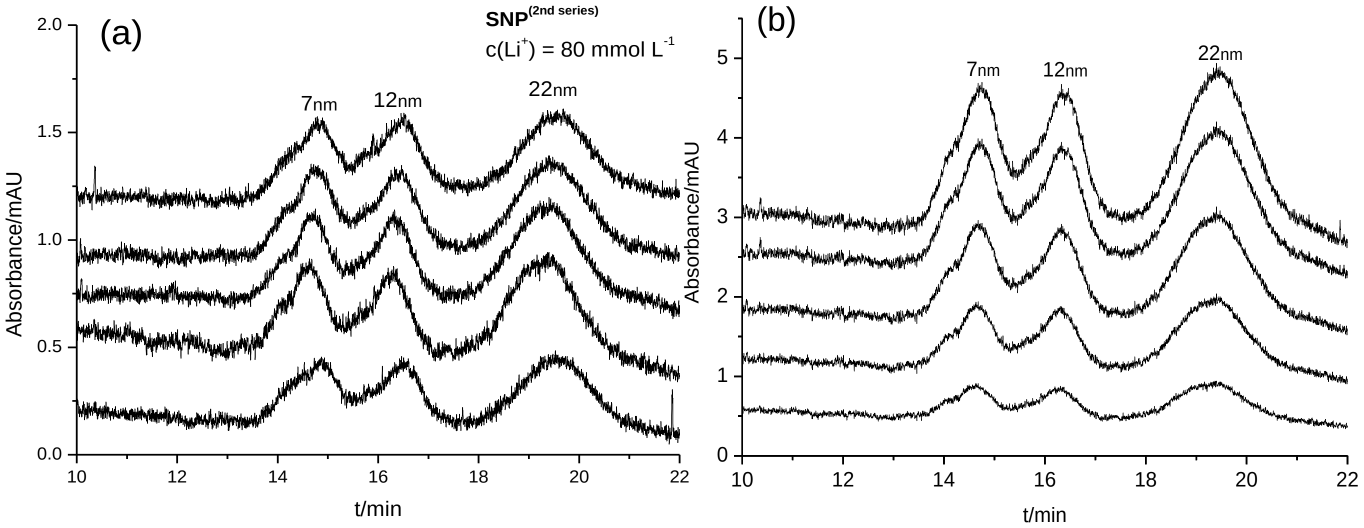
(a)
SNP$^{(2nd\ series)}$
c(Li$^+$) = 80 mmol L^{-1}
7nm
12nm
22nm
Absorbance/mAU
t/min
0.0
0.5
1.0
1.5
2.0
10
12
14
16
18
20
22
(b)
7nm
12nm
22nm
Absorbance/mAU
t/min
0
1
2
3
4
5

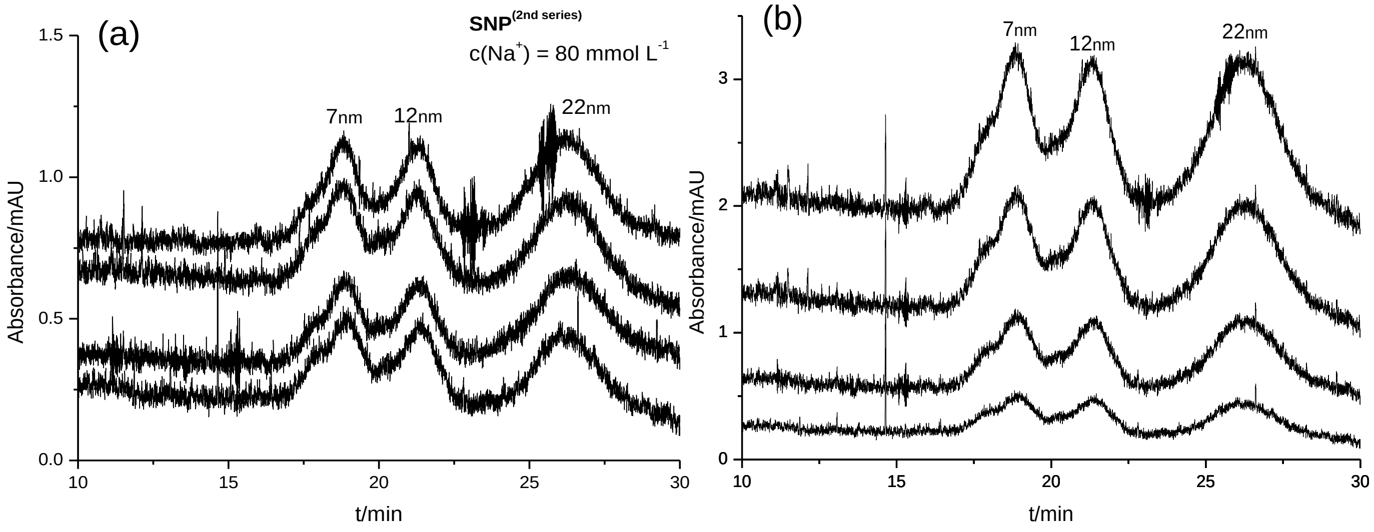
(a)
SNP$^{(2nd\ series)}$
c(Na$^+$) = 80 mmol L^{-1}
7nm
12nm
22nm
Absorbance/mAU
t/min
0.0
0.5
1.0
1.5
10
15
20
25
30
(b)
7nm
12nm
22nm
Absorbance/mAU
t/min
0
1
2
3

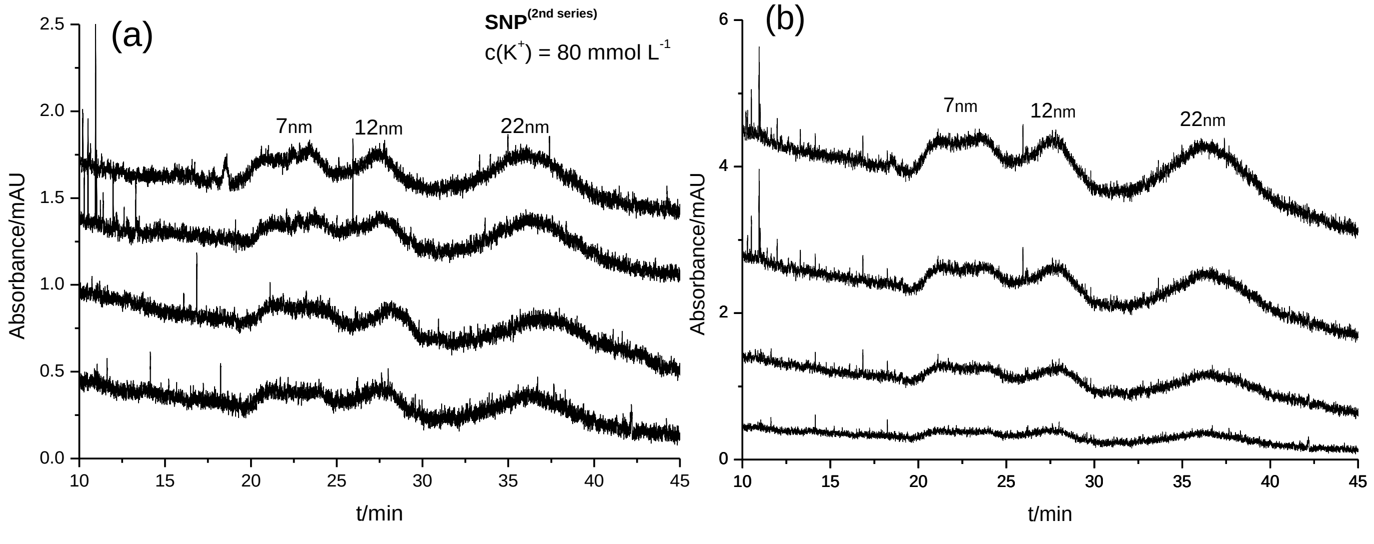
(a)
SNP$^{(2nd\ series)}$
c(K$^+$) = 80 mmol L^{-1}
7nm
12nm
22nm
Absorbance/mAU
t/min
0.0
0.5
1.0
1.5
2.0
2.5
10
15
20
25
30
35
40
45
(b)
7nm
12nm
22nm
Absorbance/mAU
t/min
0
2
4
6

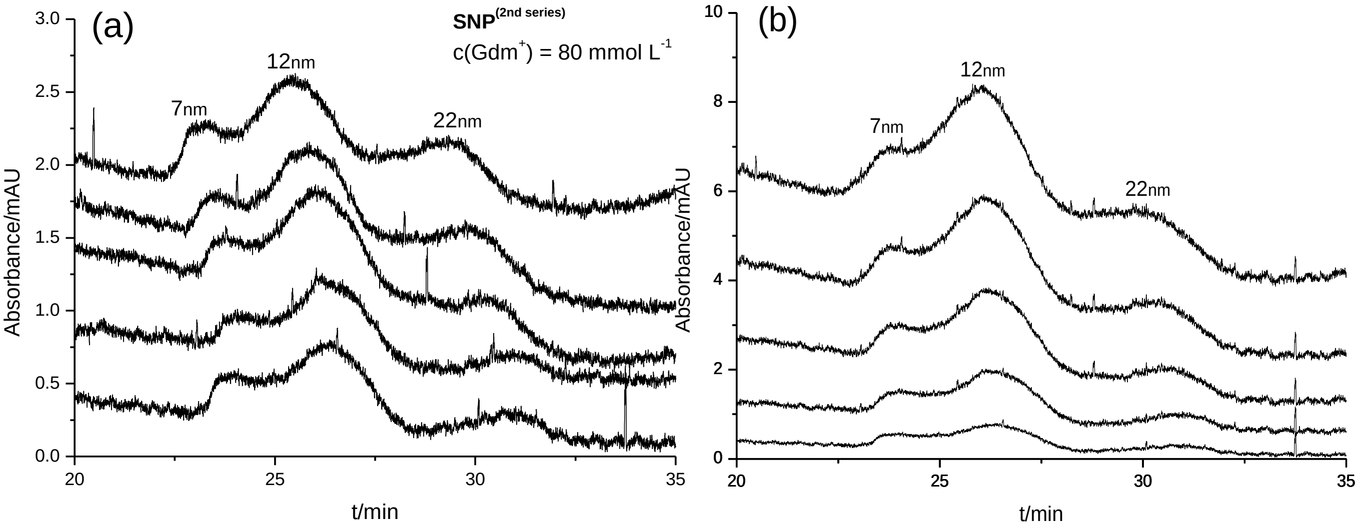
(a)
SNP(2nd series)
c(Gdm+) = 80 mmol L-1
7nm
12nm
22nm
Absorbance/mAU
0.0
0.5
1.0
1.5
2.0
2.5
3.0
20
25
30
35
t/min
(b)
7nm
12nm
22nm
Absorbance/mAU
0
2
4
6
8
10
20
25
30
35
t/min

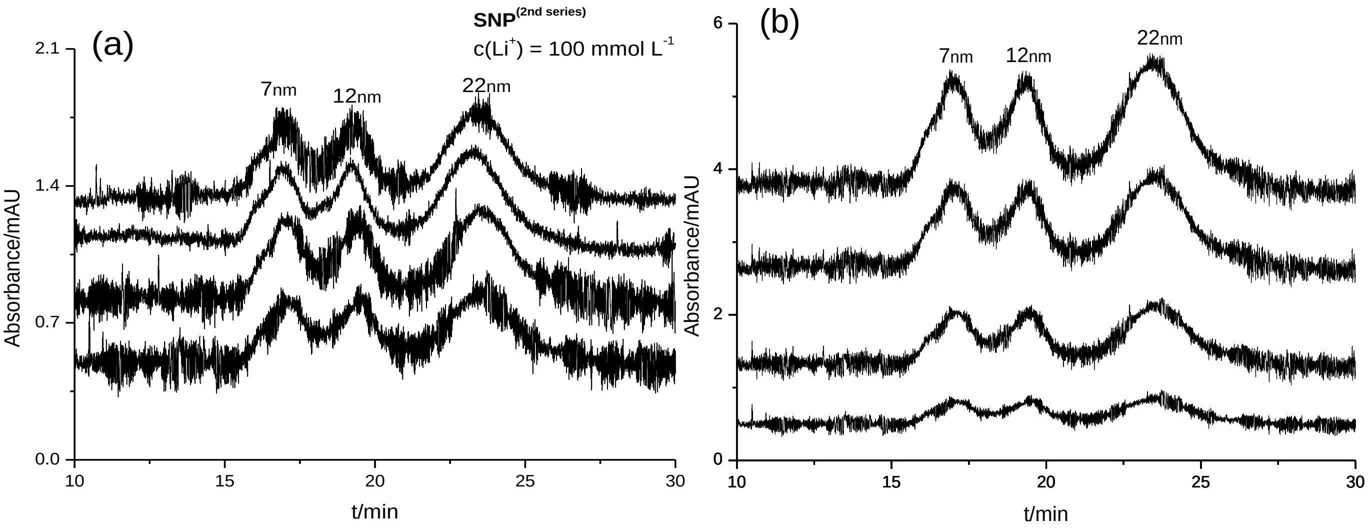
(a)
SNP(2nd series)
c(Li+) = 100 mmol L-1
7nm
12nm
22nm
Absorbance/mAU
0.0
0.7
1.4
2.1
10
15
20
25
30
t/min
(b)
7nm
12nm
22nm
Absorbance/mAU
0
2
4
6
10
15
20
25
30
t/min

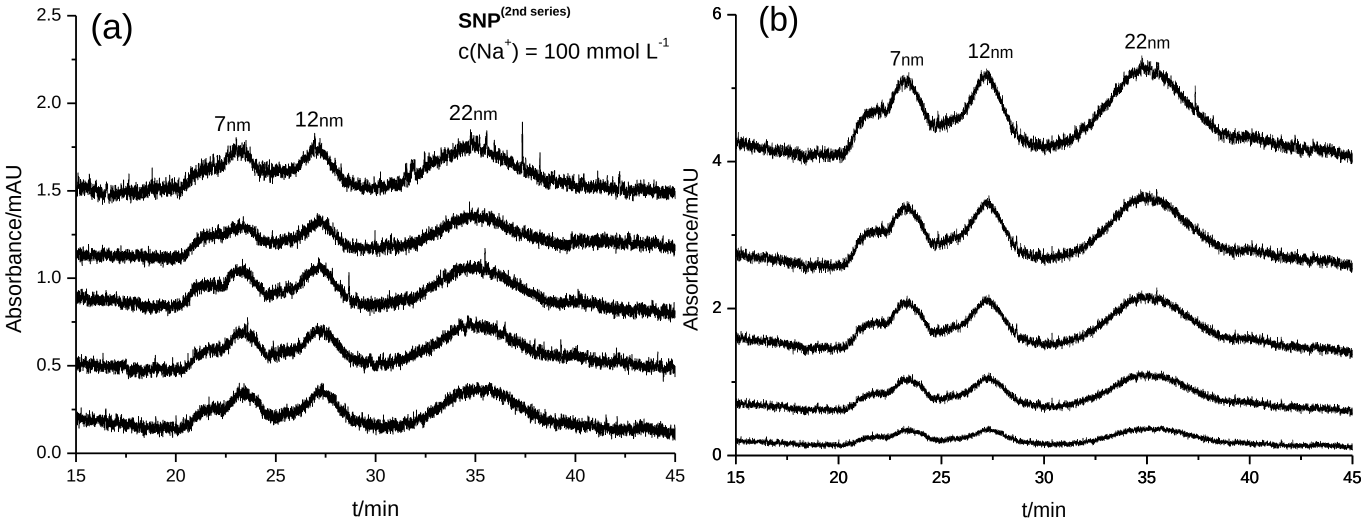
(a)
SNP(2nd series)
c(Na+) = 100 mmol L-1
7nm
12nm
22nm
Absorbance/mAU
0.0
0.5
1.0
1.5
2.0
2.5
15
20
25
30
35
40
45
t/min
(b)
7nm
12nm
22nm
Absorbance/mAU
0
2
4
6
15
20
25
30
35
40
45
t/min

Appendix A6

Calibration lines of SNPs in different monovalent counterions concentrations

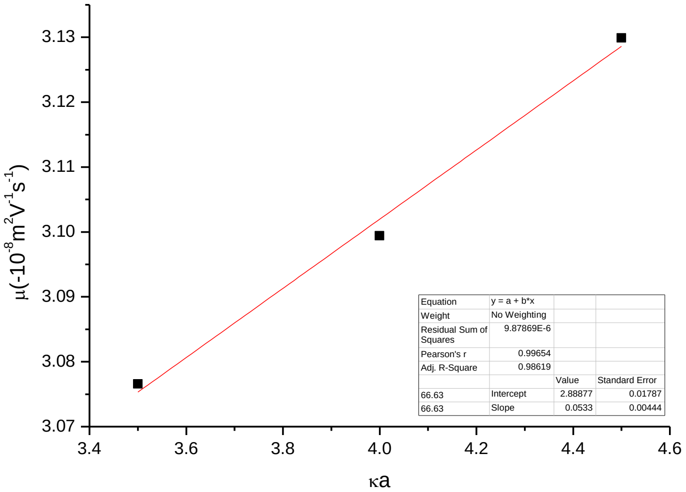

Equation	y = a + b*x		
Weight	No Weighting		
Residual Sum of Squares	9.87869E-6		
Pearson's r	0.99654		
Adj. R-Square	0.98619		
		Value	Standard Error
66.63	Intercept	2.88877	0.01787
66.63	Slope	0.0533	0.00444

Fig. 1: Calibration line for SNP7 (2nd series), c(Li^+) = 40 mmol L^{-1}, T = 25 °C.

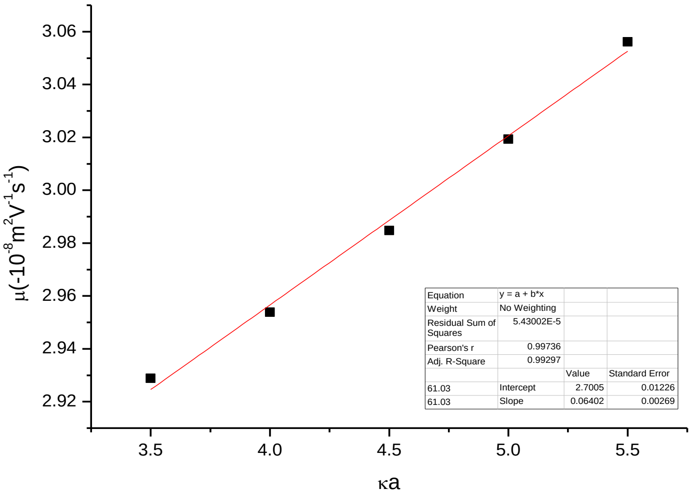

Equation	y = a + b*x		
Weight	No Weighting		
Residual Sum of Squares	5.43002E-5		
Pearson's r	0.99736		
Adj. R-Square	0.99297		
		Value	Standard Error
61.03	Intercept	2.7005	0.01226
61.03	Slope	0.06402	0.00269

Fig. 2: Calibration line for SNP7 (2nd series), c(Li^+) = 60 mmol L^{-1}, T = 25 °C.

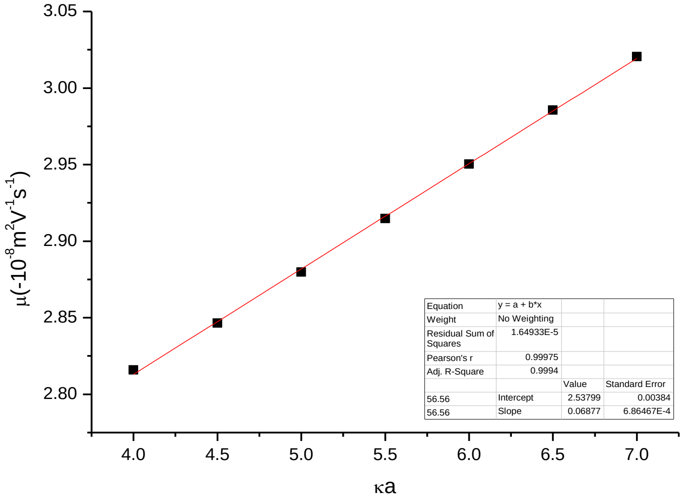

Equation	y = a + b*x		
Weight	No Weighting		
Residual Sum of Squares	1.64933E-5		
Pearson's r	0.99975		
Adj. R-Square	0.9994		
		Value	Standard Error
56.56	Intercept	2.53799	0.00384
56.56	Slope	0.06877	6.86467E-4

Fig. 3: Calibration line for SNP7 (2nd series), c(Li^+) = 80 mmol L^{-1}, T = 25 °C.

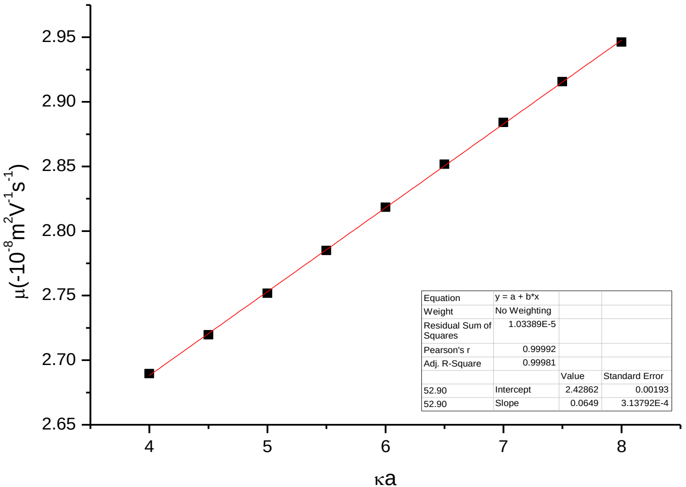

Equation	y = a + b*x		
Weight	No Weighting		
Residual Sum of Squares	1.03389E-5		
Pearson's r	0.99992		
Adj. R-Square	0.99981		
		Value	Standard Error
52.90	Intercept	2.42862	0.00193
52.90	Slope	0.0649	3.13792E-4

Fig. 4: Calibration line for SNP7 (2nd series), c(Li^+) = 100 mmol L^{-1},T = 25 °C.

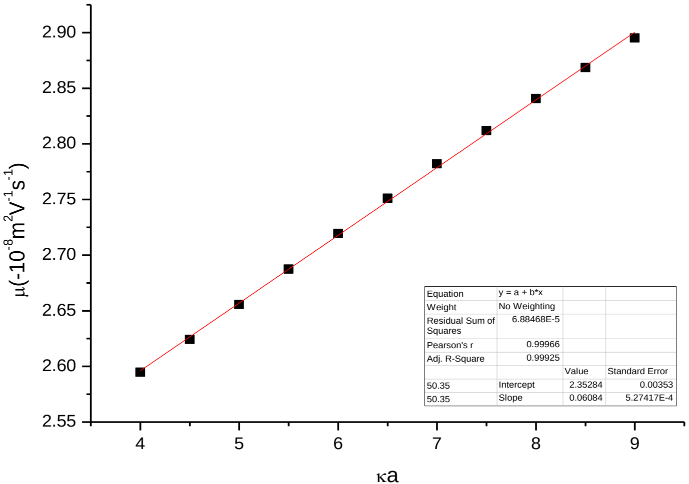

Equation	y = a + b*x		
Weight	No Weighting		
Residual Sum of Squares	6.88468E-5		
Pearson's r	0.99966		
Adj. R-Square	0.99925		
		Value	Standard Error
50.35	Intercept	2.35284	0.00353
50.35	Slope	0.06084	5.27417E-4

Fig. 5: Calibration line for SNP7 (2nd series), c(Li^+) = 120 mmol L^{-1}, T = 25 °C.

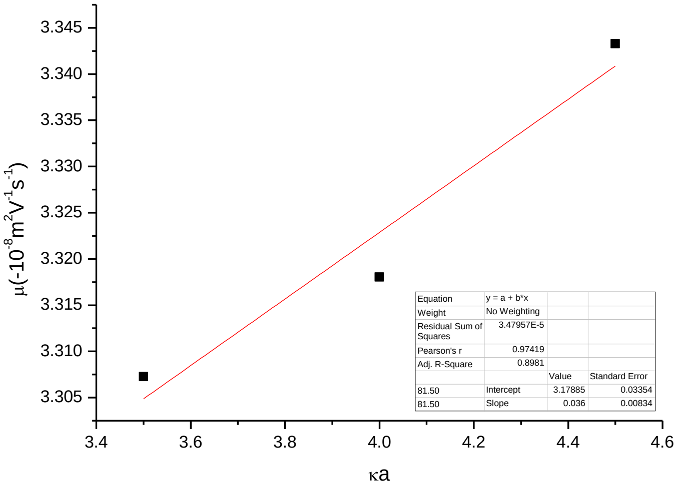

Equation	y = a + b*x		
Weight	No Weighting		
Residual Sum of Squares	3.47957E-5		
Pearson's r	0.97419		
Adj. R-Square	0.8981		
		Value	Standard Error
81.50	Intercept	3.17885	0.03354
81.50	Slope	0.036	0.00834

Fig. 6: Calibration line for SNP12 (2nd series), c(Li^+) = 20 mmol L^{-1},T = 25 °C.

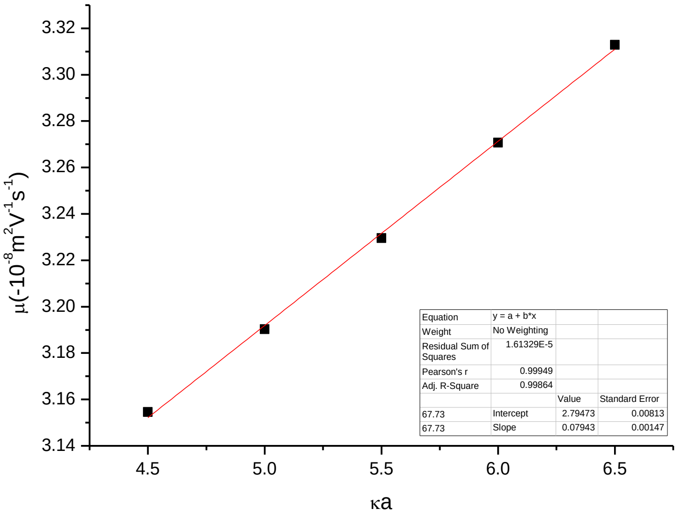

Fig. 7: Calibration line for SNP12 (2nd series), c(Li$^+$) = 40 mmol L^{-1}, T = 25 °C.

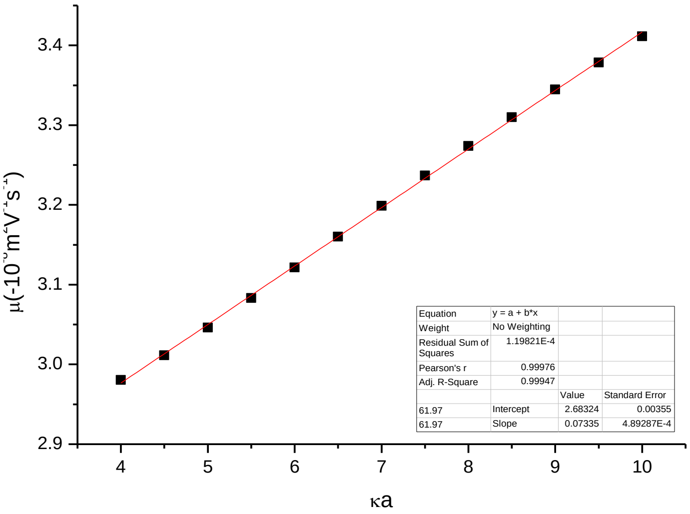

Fig. 8: Calibration line for SNP12 (2nd series), c(Li$^+$) = 60 mmol L^{-1}, T = 25 °C.

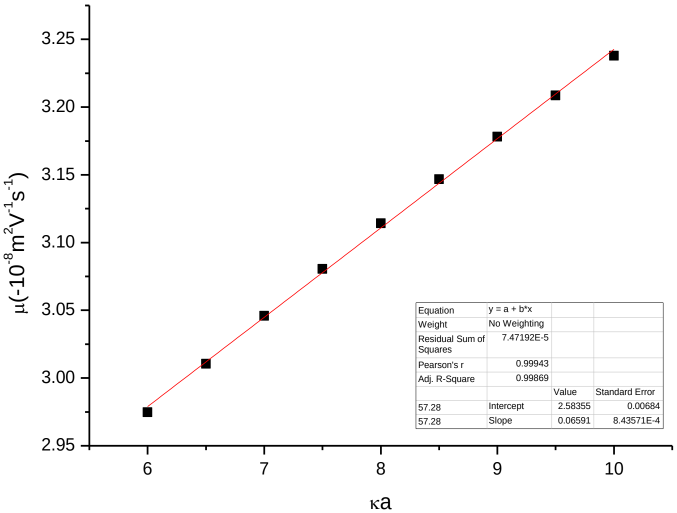

Fig.9: Calibration line for SNP12 (2nd series), c(Li$^+$) = 80 mmol L^{-1}, T = 25 °C.

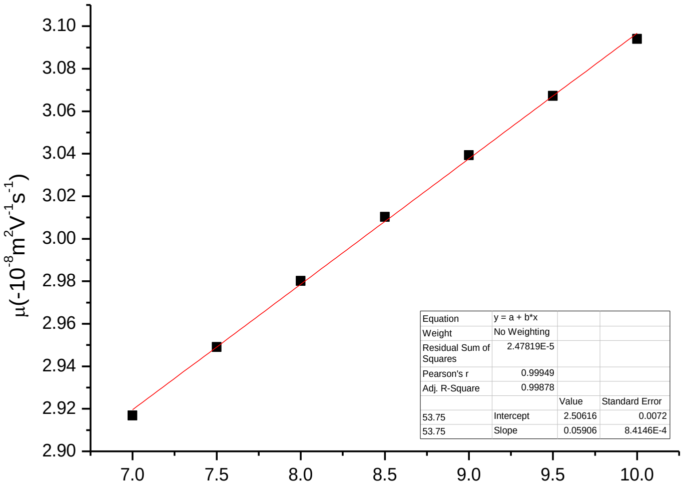

Fig. 10: Calibration line for SNP12 (2nd series), c(Li$^+$) = 100 mmol L^{-1},T = 25 °C.

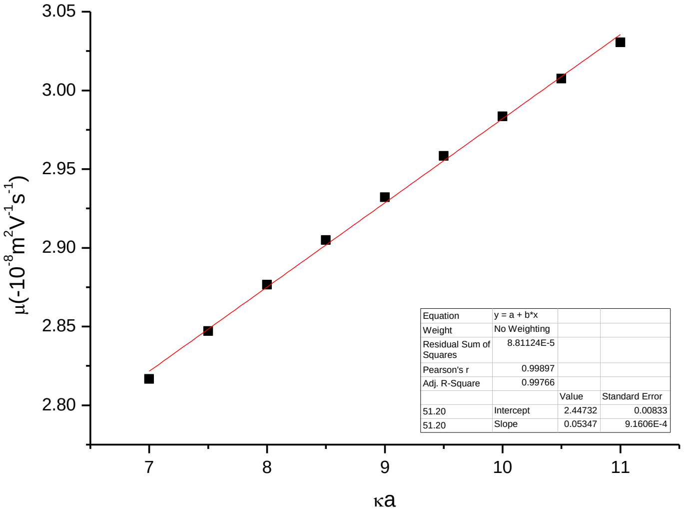

Fig. 11: Calibration line for SNP12 (2nd series), c(Li$^+$) = 120 mmol L^{-1}, T = 25 °C.

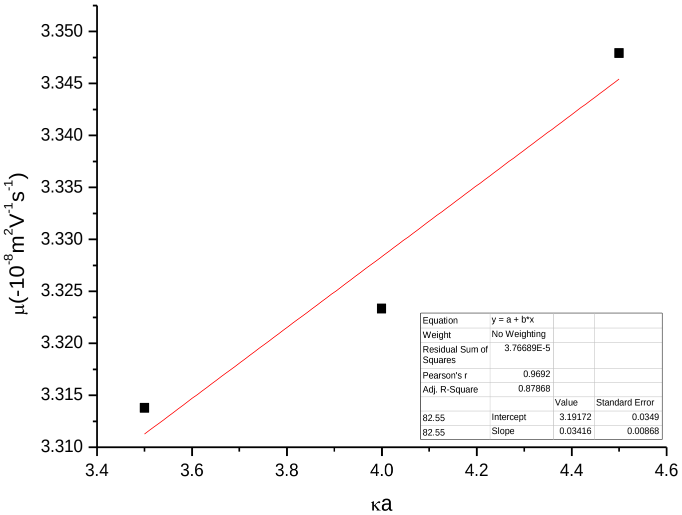

Fig. 12: Calibration line for SNP12 (1st series), c(Li$^+$) = 20 mmol L^{-1}, T = 25 °C.

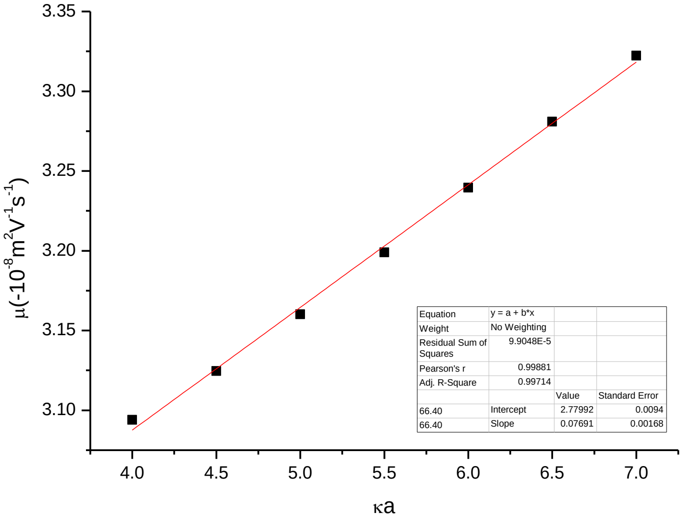

Equation	y = a + b*x		
Weight	No Weighting		
Residual Sum of Squares	9.9048E-5		
Pearson's r	0.99881		
Adj. R-Square	0.99714		
		Value	Standard Error
66.40	Intercept	2.77992	0.0094
66.40	Slope	0.07691	0.00168

Fig. 13: Calibration line for SNP12 (1st series), c(Li$^+$) = 40 mmol L^{-1}, T = 25 °C.

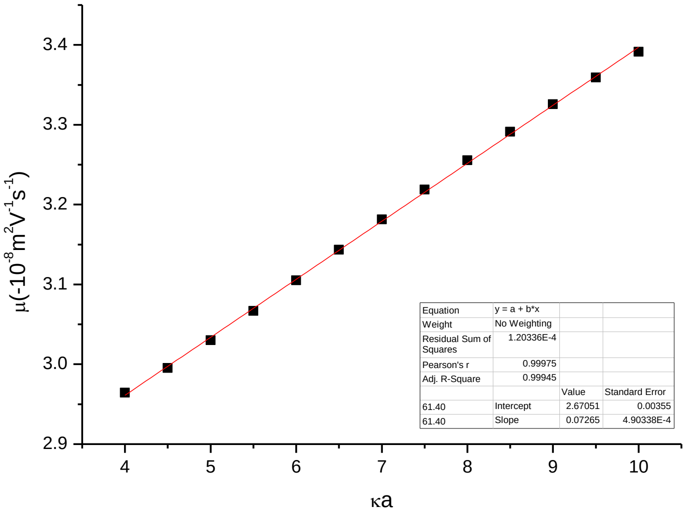

Equation	y = a + b*x		
Weight	No Weighting		
Residual Sum of Squares	1.20336E-4		
Pearson's r	0.99975		
Adj. R-Square	0.99945		
		Value	Standard Error
61.40	Intercept	2.67051	0.00355
61.40	Slope	0.07265	4.90338E-4

Fig. 14: Calibration line for SNP12 (1st series), c(Li$^+$) = 60 mmol L^{-1}, T = 25 °C.

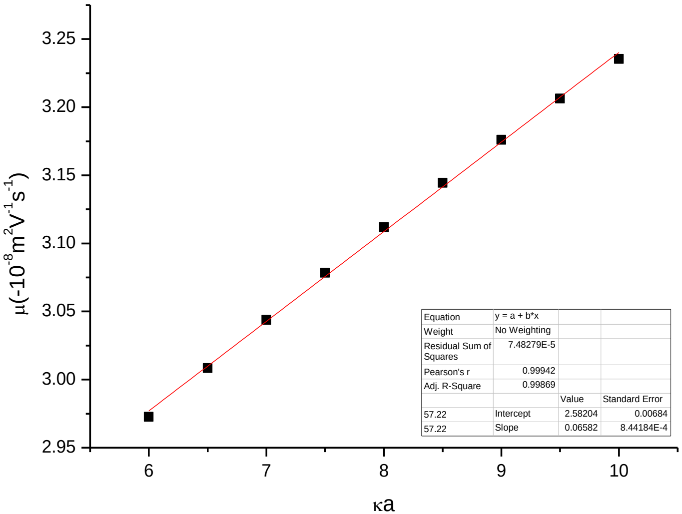

Equation	y = a + b*x		
Weight	No Weighting		
Residual Sum of Squares	7.48279E-5		
Pearson's r	0.99942		
Adj. R-Square	0.99869		
		Value	Standard Error
57.22	Intercept	2.58204	0.00684
57.22	Slope	0.06582	8.44184E-4

Fig. 15: Calibration line for SNP12 (1st series), c(Li$^+$) = 80 mmol L^{-1}, T = 25 °C.

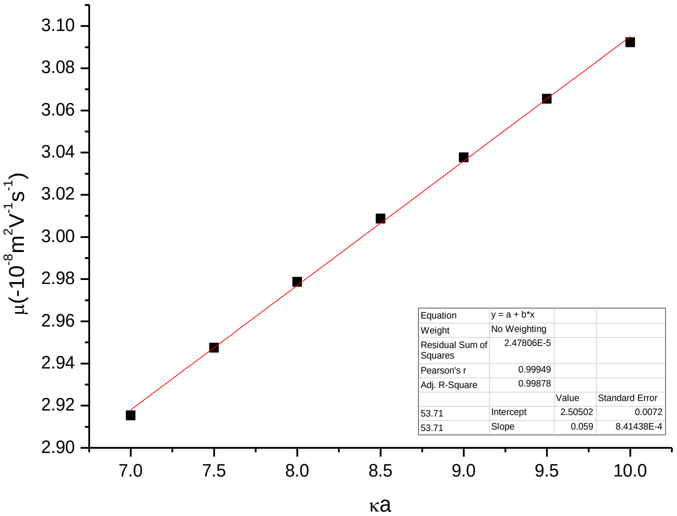

Equation	y = a + b*x		
Weight	No Weighting		
Residual Sum of Squares	2.47806E-5		
Pearson's r	0.99949		
Adj. R-Square	0.99878		
		Value	Standard Error
53.71	Intercept	2.50502	0.0072
53.71	Slope	0.059	8.41438E-4

Fig. 16: Calibration line for SNP12 (1st series), c(Li$^+$) = 100 mmol L^{-1}, T = 25 °C.

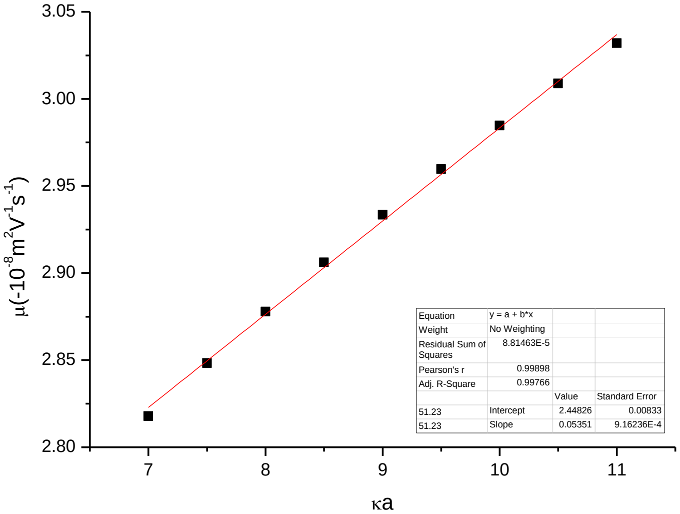

Equation	y = a + b*x		
Weight	No Weighting		
Residual Sum of Squares	8.81463E-5		
Pearson's r	0.99898		
Adj. R-Square	0.99766		
		Value	Standard Error
51.23	Intercept	2.44826	0.00833
51.23	Slope	0.05351	9.16236E-4

Fig. 17: Calibration line for SNP12 (1st series), c(Li$^+$) = 120 mmol L^{-1}, T = 25 °C.

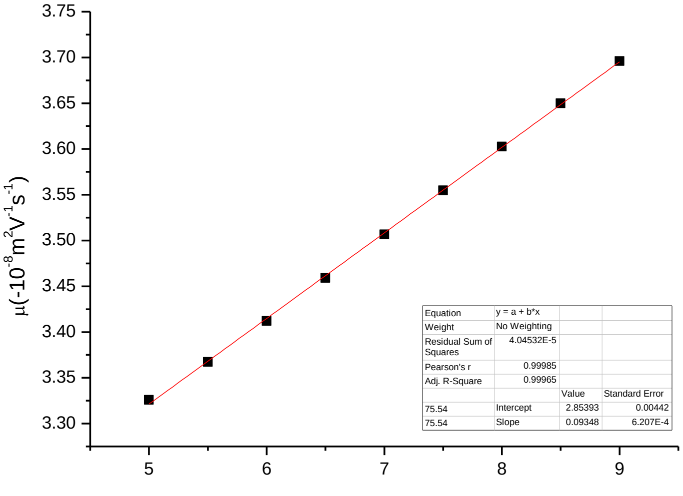

Equation	y = a + b*x		
Weight	No Weighting		
Residual Sum of Squares	4.04532E-5		
Pearson's r	0.99985		
Adj. R-Square	0.99965		
		Value	Standard Error
75.54	Intercept	2.85393	0.00442
75.54	Slope	0.09348	6.207E-4

Fig. 18: Calibration line for SNP22 (2nd series), c(Li$^+$) = 20 mmol L^{-1}, T = 25 °C.

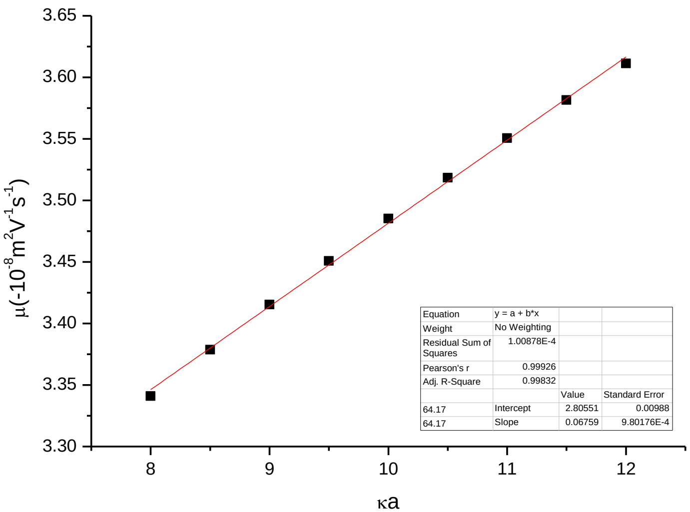

Equation	y = a + b*x		
Weight	No Weighting		
Residual Sum of Squares	1.00878E-4		
Pearson's r	0.99926		
Adj. R-Square	0.99832		
		Value	Standard Error
64.17	Intercept	2.80551	0.00988
64.17	Slope	0.06759	9.80176E-4

Fig. 19: Calibration line for SNP22 (2nd series), c(Li^{+}) = 40 mmol L^{-1}, T = 25 °C.

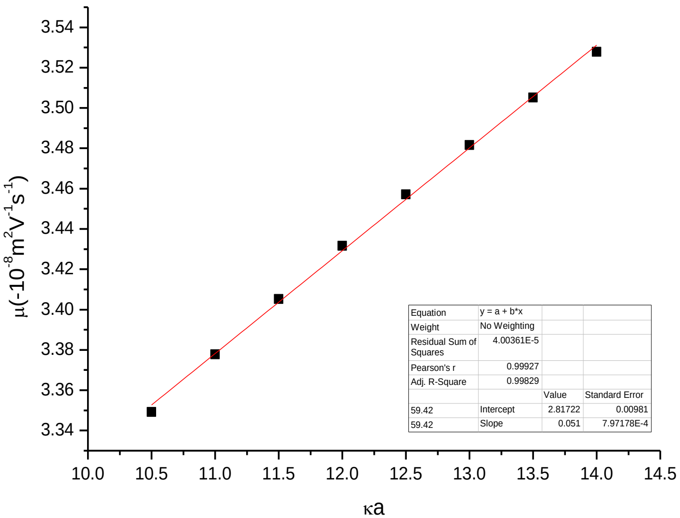

Equation	y = a + b*x		
Weight	No Weighting		
Residual Sum of Squares	4.00361E-5		
Pearson's r	0.99927		
Adj. R-Square	0.99829		
		Value	Standard Error
59.42	Intercept	2.81722	0.00981
59.42	Slope	0.051	7.97178E-4

Fig. 20: Calibration line for SNP22 (2nd series), c(Li^{+}) = 60 mmol L^{-1}, T = 25 °C.

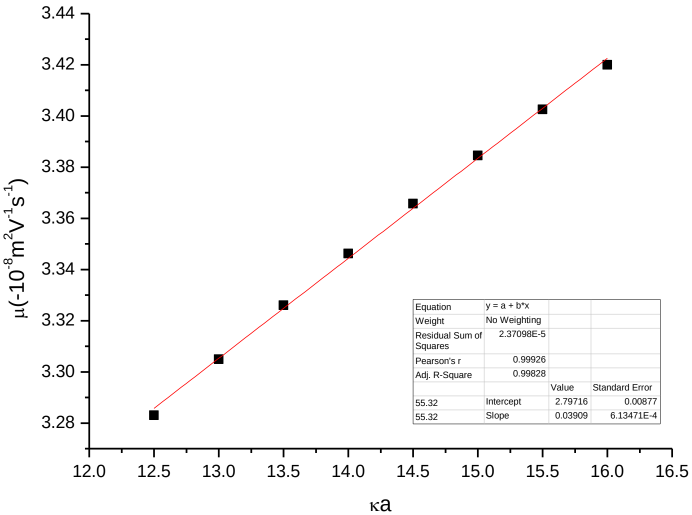

Equation	y = a + b*x		
Weight	No Weighting		
Residual Sum of Squares	2.37098E-5		
Pearson's r	0.99926		
Adj. R-Square	0.99828		
		Value	Standard Error
55.32	Intercept	2.79716	0.00877
55.32	Slope	0.03909	6.13471E-4

Fig. 21: Calibration line for SNP22 (2nd series), c(Li^{+}) = 80 mmol L^{-1}, T = 25 °C.

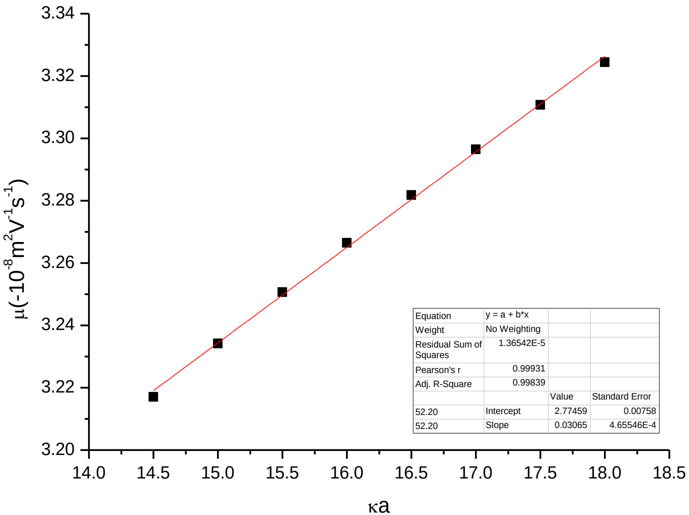

Equation	y = a + b*x		
Weight	No Weighting		
Residual Sum of Squares	1.36542E-5		
Pearson's r	0.99931		
Adj. R-Square	0.99839		
		Value	Standard Error
52.20	Intercept	2.77459	0.00758
52.20	Slope	0.03065	4.65546E-4

Fig. 22: Calibration line for SNP22 (2nd series), c(Li^{+}) = 100 mmol L^{-1}, T = 25 °C.

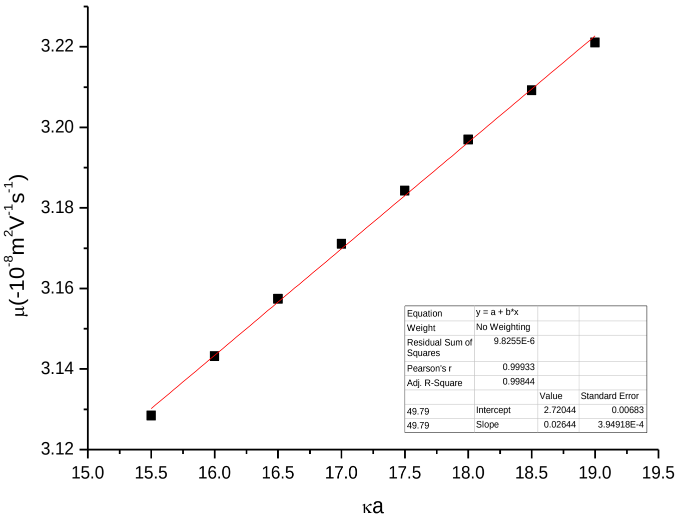

Equation	y = a + b*x		
Weight	No Weighting		
Residual Sum of Squares	9.8255E-6		
Pearson's r	0.99933		
Adj. R-Square	0.99844		
		Value	Standard Error
49.79	Intercept	2.72044	0.00683
49.79	Slope	0.02644	3.94918E-4

Fig. 23: Calibration line for SNP22 (2nd series), c(Li^{+}) = 120 mmol L^{-1}, T = 25 °C.

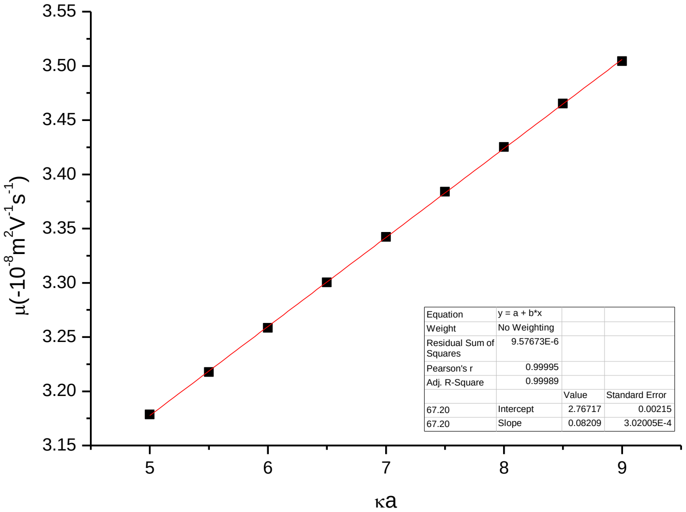

Equation	y = a + b*x		
Weight	No Weighting		
Residual Sum of Squares	9.57673E-6		
Pearson's r	0.99995		
Adj. R-Square	0.99989		
		Value	Standard Error
67.20	Intercept	2.76717	0.00215
67.20	Slope	0.08209	3.02005E-4

Fig. 24: Calibration line for SNP22 (1st series), c(Li^{+}) = 20 mmol L^{-1}, T = 25 °C.

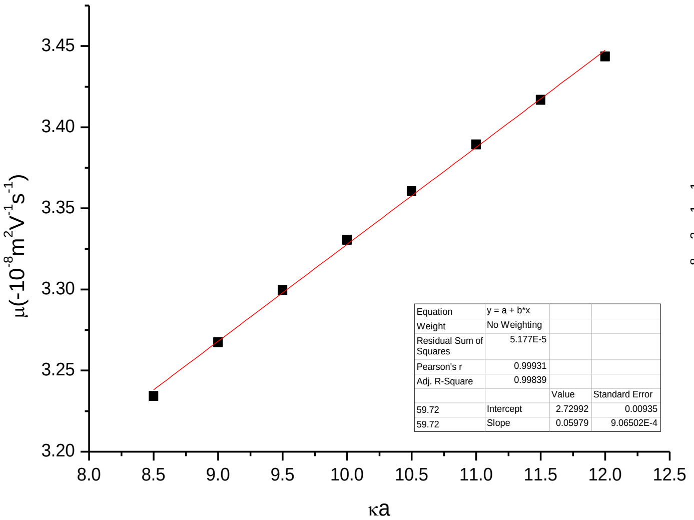

Equation	y = a + b*x		
Weight	No Weighting		
Residual Sum of Squares	5.177E-5		
Pearson's r	0.99931		
Adj. R-Square	0.99839		
		Value	Standard Error
59.72	Intercept	2.72992	0.00935
59.72	Slope	0.05979	9.06502E-4

Fig. 25: Calibration line for SNP22 (1^{st} series), c(Li^+) = 40 mmol L^{-1}, T = 25 °C.

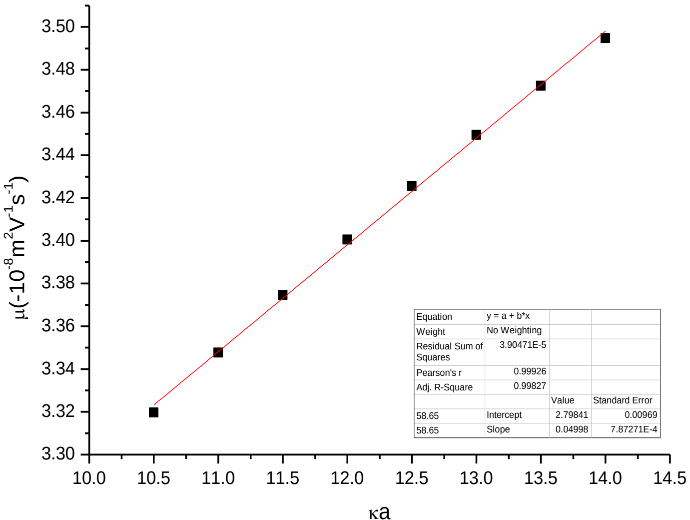

Equation	y = a + b*x		
Weight	No Weighting		
Residual Sum of Squares	3.90471E-5		
Pearson's r	0.99926		
Adj. R-Square	0.99827		
		Value	Standard Error
58.65	Intercept	2.79841	0.00969
58.65	Slope	0.04998	7.87271E-4

Fig. 26: Calibration line for SNP22 (1^{st} series), c(Li^+) = 60 mmol L^{-1}, T = 25 °C.

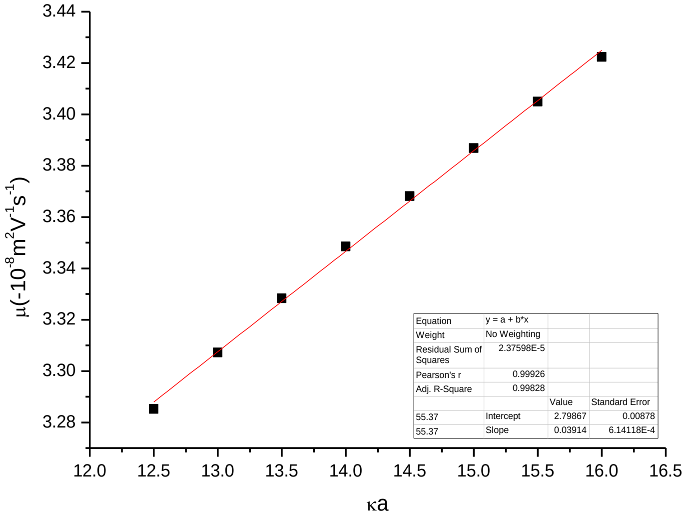

Equation	y = a + b*x		
Weight	No Weighting		
Residual Sum of Squares	2.37598E-5		
Pearson's r	0.99926		
Adj. R-Square	0.99828		
		Value	Standard Error
55.37	Intercept	2.79867	0.00878
55.37	Slope	0.03914	6.14118E-4

Fig. 27: Calibration line for SNP22 (1^{st} series), c(Li^+) = 80 mmol L^{-1}, T = 25 °C.

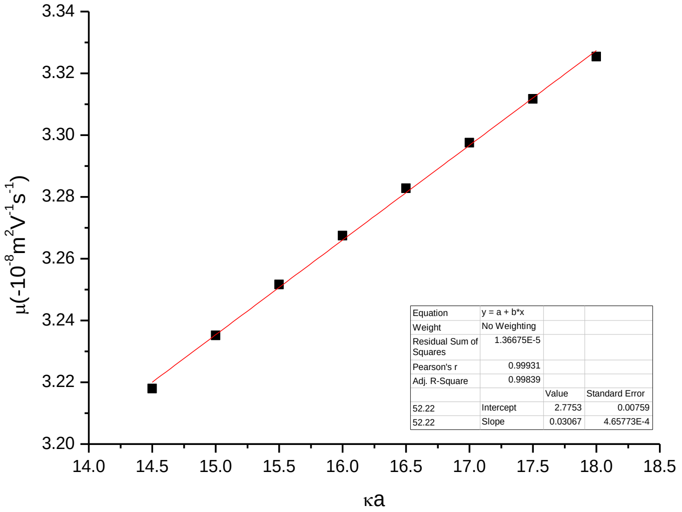

Equation	y = a + b*x		
Weight	No Weighting		
Residual Sum of Squares	1.36675E-5		
Pearson's r	0.99931		
Adj. R-Square	0.99839		
		Value	Standard Error
52.22	Intercept	2.7753	0.00759
52.22	Slope	0.03067	4.65773E-4

Fig. 28: Calibration line for SNP22 (1^{st} series), c(Li^+) = 100 mmol L^{-1}, T = 25 °C.

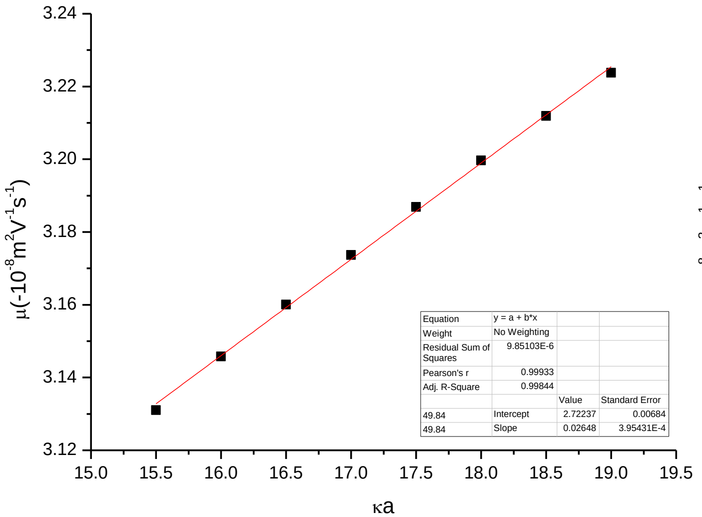

Equation	y = a + b*x		
Weight	No Weighting		
Residual Sum of Squares	9.85103E-6		
Pearson's r	0.99933		
Adj. R-Square	0.99844		
		Value	Standard Error
49.84	Intercept	2.72237	0.00684
49.84	Slope	0.02648	3.95431E-4

Fig. 29: Calibration line for SNP22 (1^{st} series), c(Li^+) = 120 mmol L^{-1}, T = 25 °C.

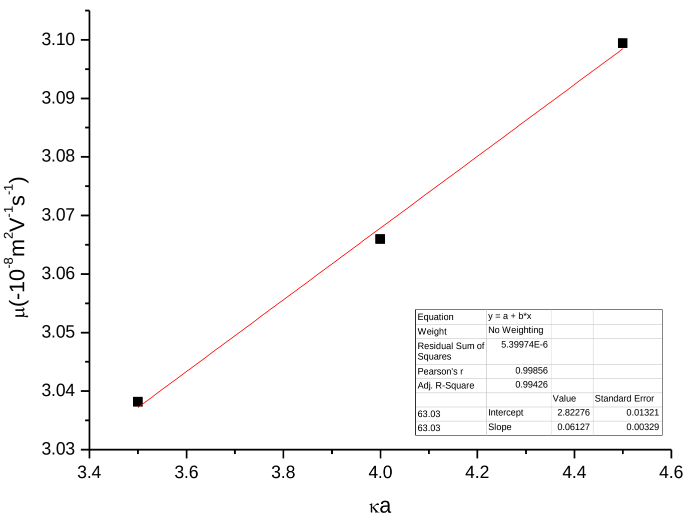

Equation	y = a + b*x		
Weight	No Weighting		
Residual Sum of Squares	5.39974E-6		
Pearson's r	0.99856		
Adj. R-Square	0.99426		
		Value	Standard Error
63.03	Intercept	2.82276	0.01321
63.03	Slope	0.06127	0.00329

Fig. 30: Calibration line for SNP7 (2^{nd} series), c(Na^+) = 40 mmol L^{-1}, T = 25 °C.

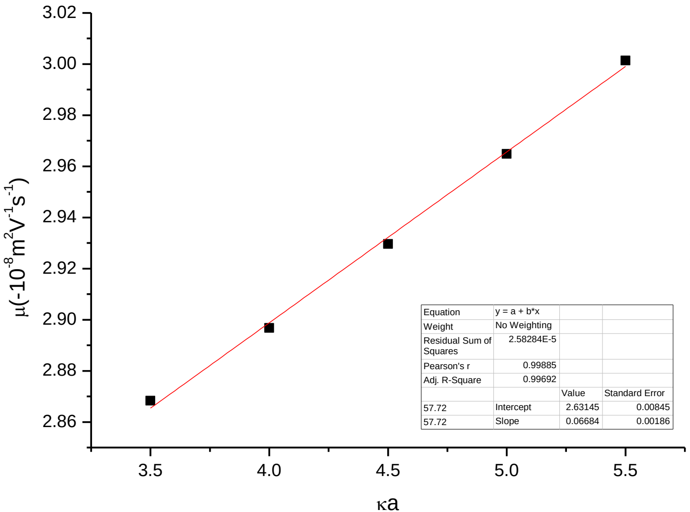

Fig. 31: Calibration line for SNP7 (2nd series), c(Na$^+$) = 60 mmol L^{-1},T = 25 °C.

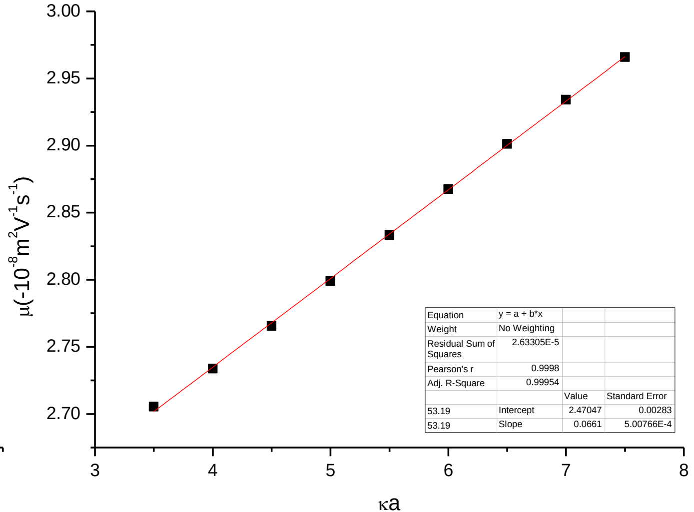

Fig. 32: Calibration line for SNP7 (2nd series), c(Na$^+$) = 80 mmol L^{-1},T = 25 °C.

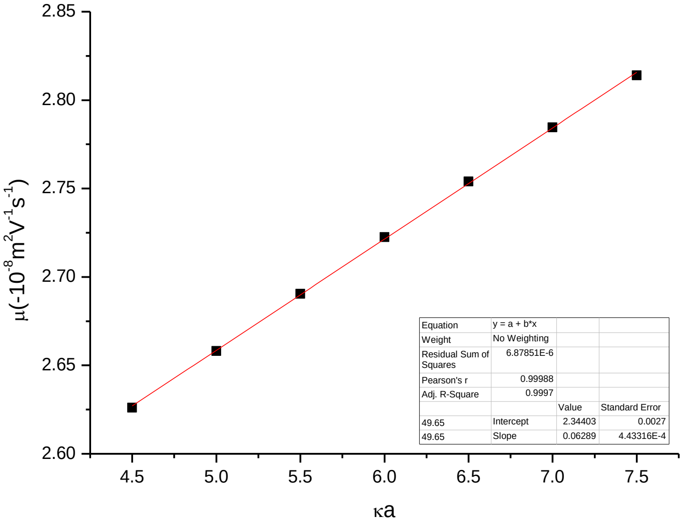

Fig. 33: Calibration line for SNP7 (2nd series), c(Na$^+$) = 100 mmol L^{-1}, T = 25 °C.

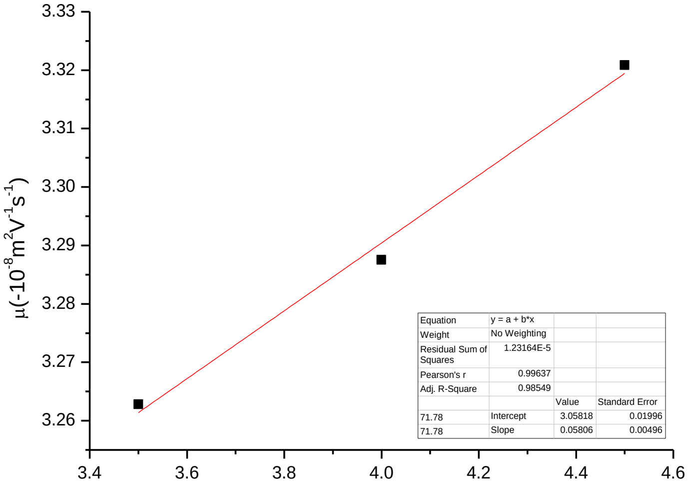

Fig. 34: Calibration line for SNP12 (2nd series), c(Na$^+$) = 40 mmol L^{-1}, T = 25 °C.

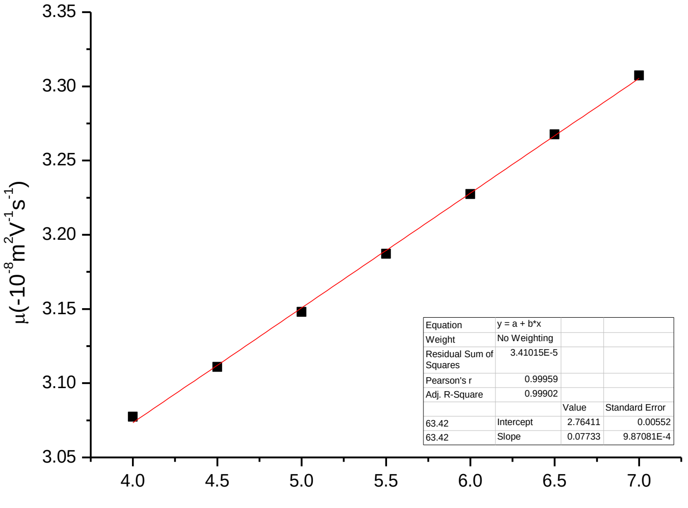

Fig. 35: Calibration line for SNP12 (2nd series), c(Na$^+$) = 40 mmol L^{-1}, T = 25 °C.

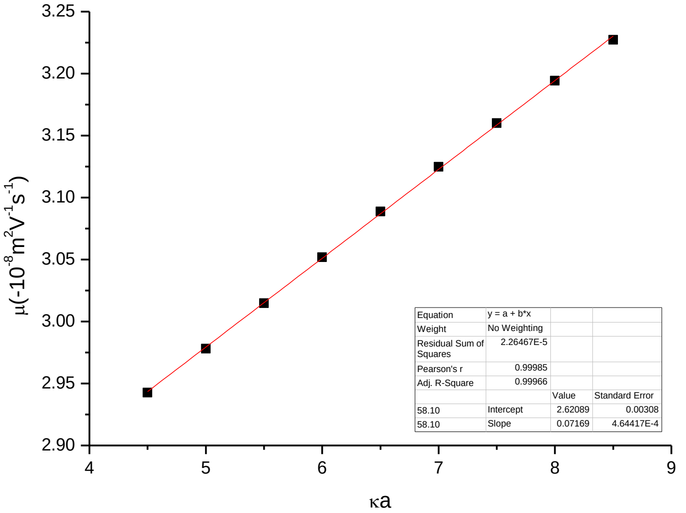

Fig. 36: Calibration line for SNP12 (2nd series), c(Na$^+$) = 60 mmol L^{-1}, T = 25 °C.

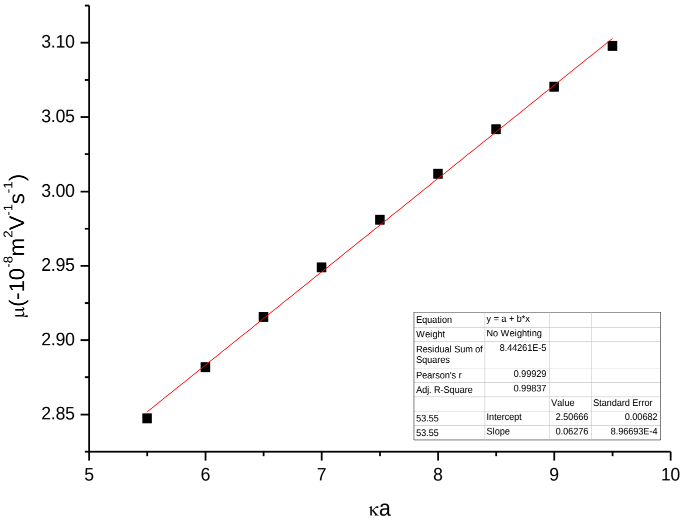

Equation	y = a + b*x		
Weight	No Weighting		
Residual Sum of Squares	8.44261E-5		
Pearson's r	0.99929		
Adj. R-Square	0.99837		
		Value	Standard Error
53.55	Intercept	2.50666	0.00682
53.55	Slope	0.06276	8.96693E-4

Fig. 37: Calibration line for SNP12 (2nd series), c(Na$^+$) = 80 mmol L^{-1}, T = 25 °C.

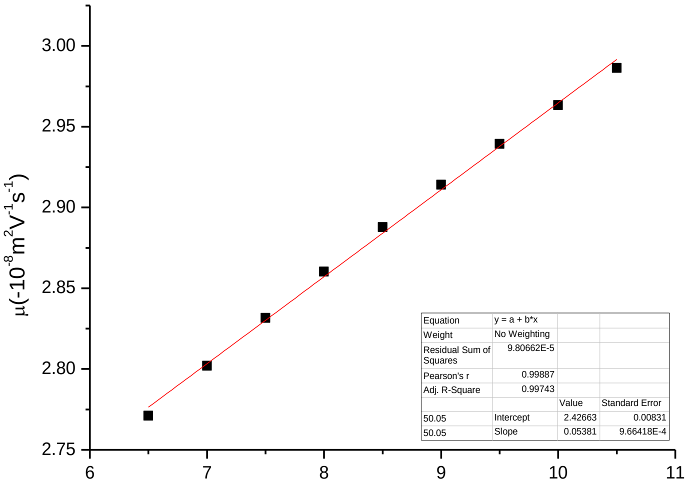

Equation	y = a + b*x		
Weight	No Weighting		
Residual Sum of Squares	9.80662E-5		
Pearson's r	0.99887		
Adj. R-Square	0.99743		
		Value	Standard Error
50.05	Intercept	2.42663	0.00831
50.05	Slope	0.05381	9.66418E-4

Fig. 38: Calibration line for SNP12 (2nd series), c(Na$^+$) = 100 mmol L^{-1},T = 25 °C.

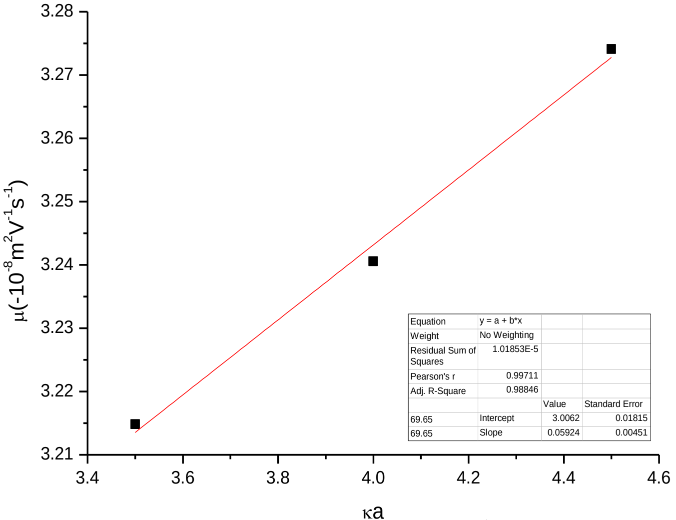

Equation	y = a + b*x		
Weight	No Weighting		
Residual Sum of Squares	1.01853E-5		
Pearson's r	0.99711		
Adj. R-Square	0.98846		
		Value	Standard Error
69.65	Intercept	3.0062	0.01815
69.65	Slope	0.05924	0.00451

Fig. 39: Calibration line for SNP12 (1st series), c(Na$^+$) = 20 mmol L^{-1}, T = 25 °C.

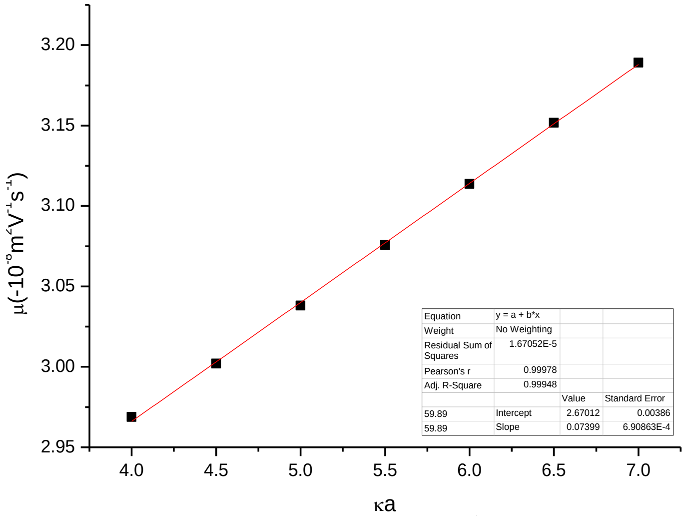

Equation	y = a + b*x		
Weight	No Weighting		
Residual Sum of Squares	1.67052E-5		
Pearson's r	0.99978		
Adj. R-Square	0.99948		
		Value	Standard Error
59.89	Intercept	2.67012	0.00386
59.89	Slope	0.07399	6.90863E-4

Fig. 40: Calibration line for SNP12 (1st series), (Na$^+$) = 40 mmol L^{-1}, T = 25 °C.

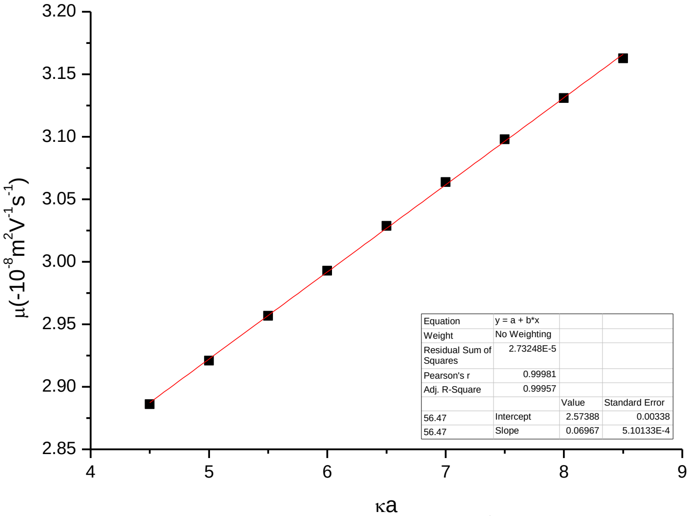

Equation	y = a + b*x		
Weight	No Weighting		
Residual Sum of Squares	2.73248E-5		
Pearson's r	0.99981		
Adj. R-Square	0.99957		
		Value	Standard Error
56.47	Intercept	2.57388	0.00338
56.47	Slope	0.06967	5.10133E-4

Fig. 41: Calibration line for SNP12 (1st series), c(Na$^+$) = 60 mmol L^{-1}, T = 25 °C.

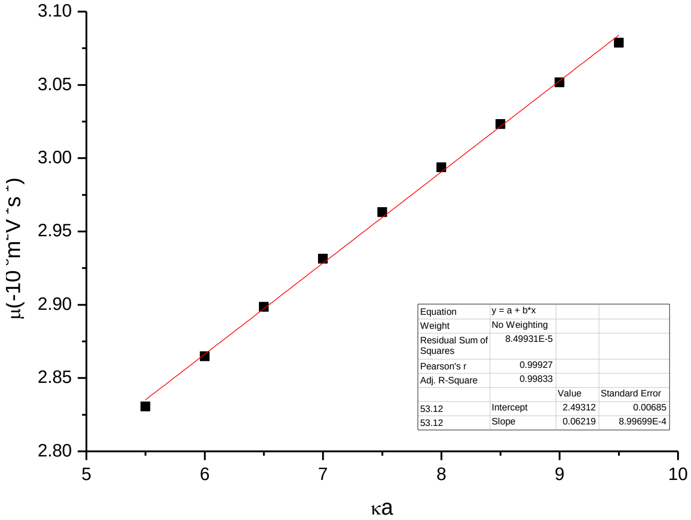

Equation	y = a + b*x		
Weight	No Weighting		
Residual Sum of Squares	8.49931E-5		
Pearson's r	0.99927		
Adj. R-Square	0.99833		
		Value	Standard Error
53.12	Intercept	2.49312	0.00685
53.12	Slope	0.06219	8.99699E-4

Fig. 42: Calibration line for SNP12 (1st series), c(Na$^+$) = 80 mmol L^{-1}, T = 25 °C.

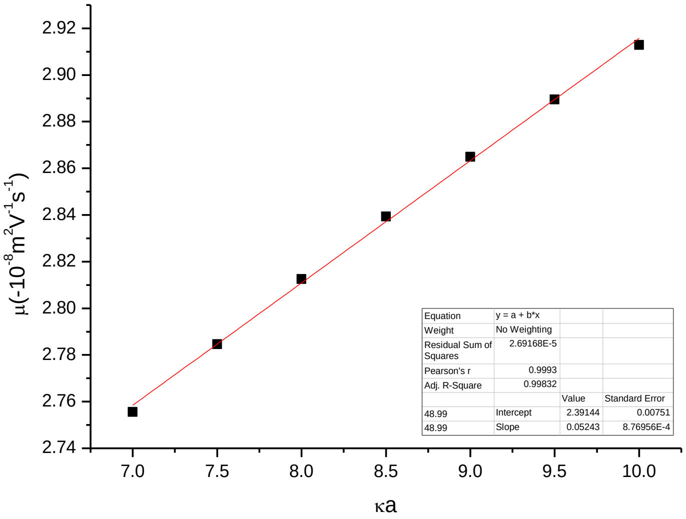

Equation	y = a + b*x		
Weight	No Weighting		
Residual Sum of Squares	2.69168E-5		
Pearson's r	0.9993		
Adj. R-Square	0.99832		
		Value	Standard Error
48.99	Intercept	2.39144	0.00751
48.99	Slope	0.05243	8.76956E-4

Fig. 43: Calibration line for SNP12 (1st series),
$c(Na^+)$ = 2100 mmol L^{-1}, T = 25 °C.

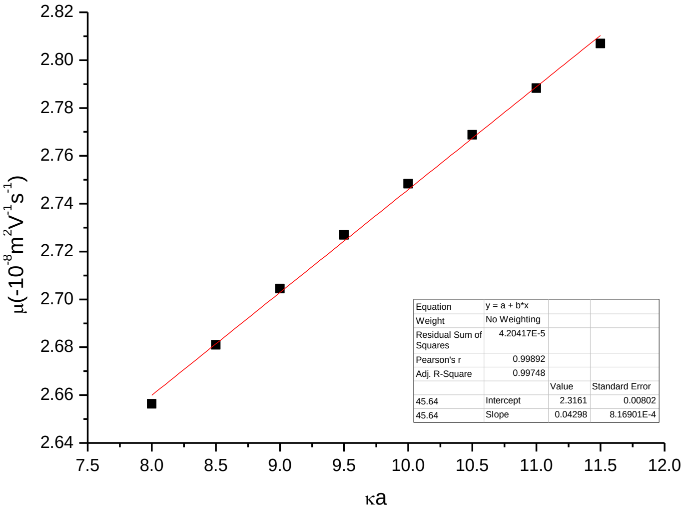

Equation	y = a + b*x		
Weight	No Weighting		
Residual Sum of Squares	4.20417E-5		
Pearson's r	0.99892		
Adj. R-Square	0.99748		
		Value	Standard Error
45.64	Intercept	2.3161	0.00802
45.64	Slope	0.04298	8.16901E-4

Fig. 44: Calibration line for SNP12 (1st series),
$c(Na^+)$ = 120 mmol L^{-1}, T = 25 °C.

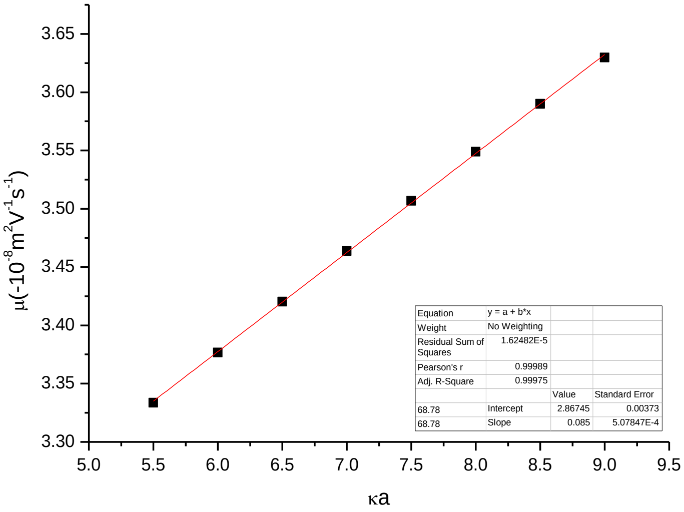

Equation	y = a + b*x		
Weight	No Weighting		
Residual Sum of Squares	1.62482E-5		
Pearson's r	0.99989		
Adj. R-Square	0.99975		
		Value	Standard Error
68.78	Intercept	2.86745	0.00373
68.78	Slope	0.085	5.07847E-4

Fig. 45: Calibration line for SNP22 (2nd series),
$c(Na^+)$ = 20 mmol L^{-1}, T = 25 °C.

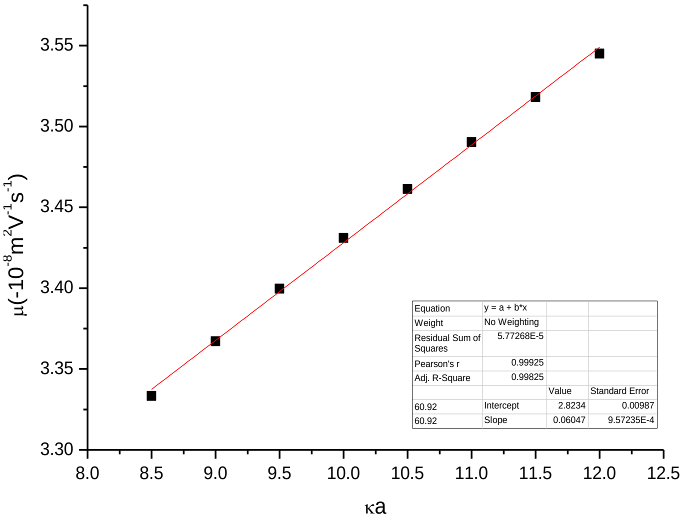

Equation	y = a + b*x		
Weight	No Weighting		
Residual Sum of Squares	5.77268E-5		
Pearson's r	0.99925		
Adj. R-Square	0.99825		
		Value	Standard Error
60.92	Intercept	2.8234	0.00987
60.92	Slope	0.06047	9.57235E-4

Fig. 46: Calibration line for SNP22 (2nd series),
$c(Na^+)$ = 40 mmol L^{-1}, T = 25 °C.

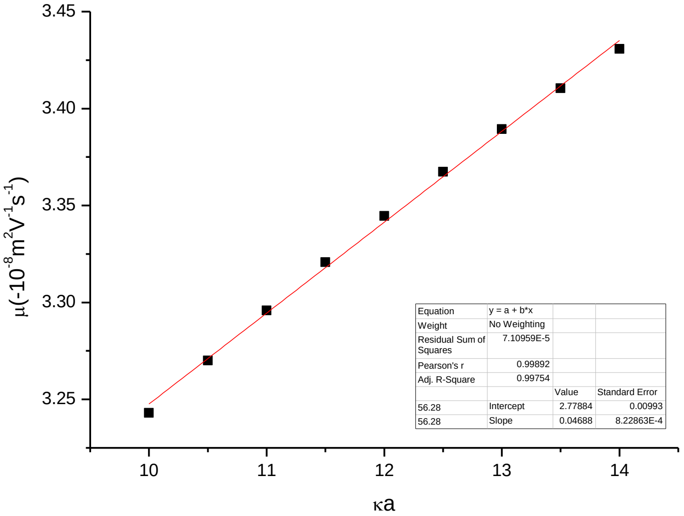

Equation	y = a + b*x		
Weight	No Weighting		
Residual Sum of Squares	7.10959E-5		
Pearson's r	0.99892		
Adj. R-Square	0.99754		
		Value	Standard Error
56.28	Intercept	2.77884	0.00993
56.28	Slope	0.04688	8.22863E-4

Fig. 47: Calibration line for SNP22 (2nd series),
$c(Na^+)$ = 60 mmol L^{-1}, T = 25 °C.

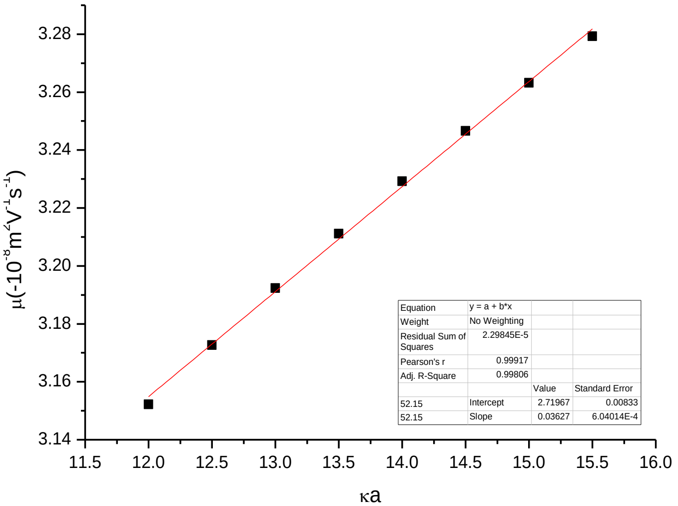

Equation	y = a + b*x		
Weight	No Weighting		
Residual Sum of Squares	2.29845E-5		
Pearson's r	0.99917		
Adj. R-Square	0.99806		
		Value	Standard Error
52.15	Intercept	2.71967	0.00833
52.15	Slope	0.03627	6.04014E-4

Fig. 48: Calibration line for SNP22 (2nd series),
$c(Na^+)$ = 80 mmol L^{-1},T = 25 °C.

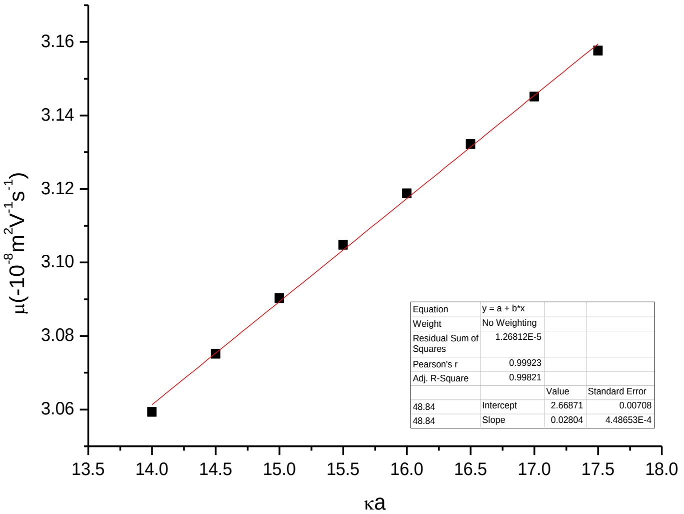

Fig. 49: Calibration line for SNP22 (2nd series), c(Na$^+$) = 100 mmol L^{-1}, T = 25 °C.

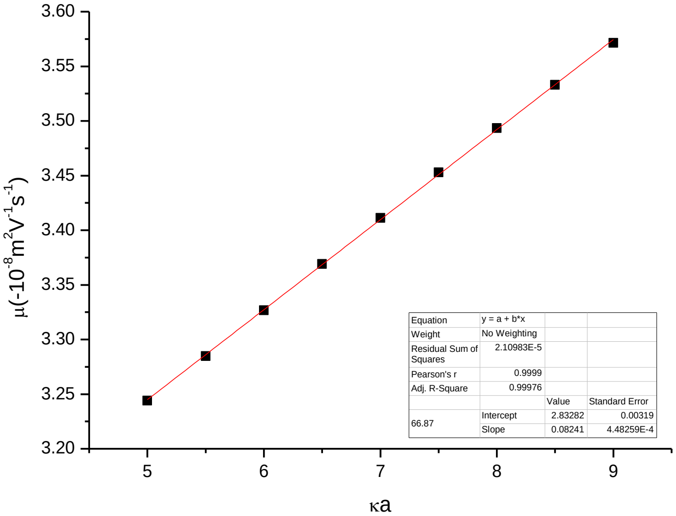

Fig. 50: Calibration line for SNP22 (1st series), c(Na$^+$) = 20 mmol L^{-1}, T = 25 °C.

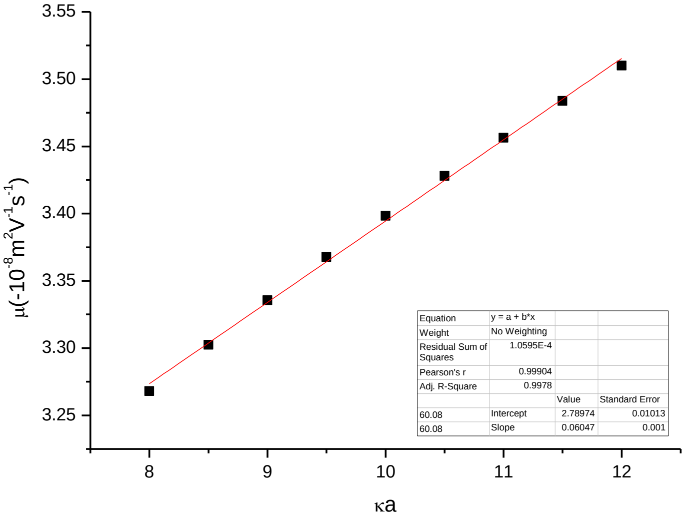

Fig. 51: Calibration line for SNP22 (1st series), c(Na$^+$) = 40 mmol L^{-1}, T = 25 °C.

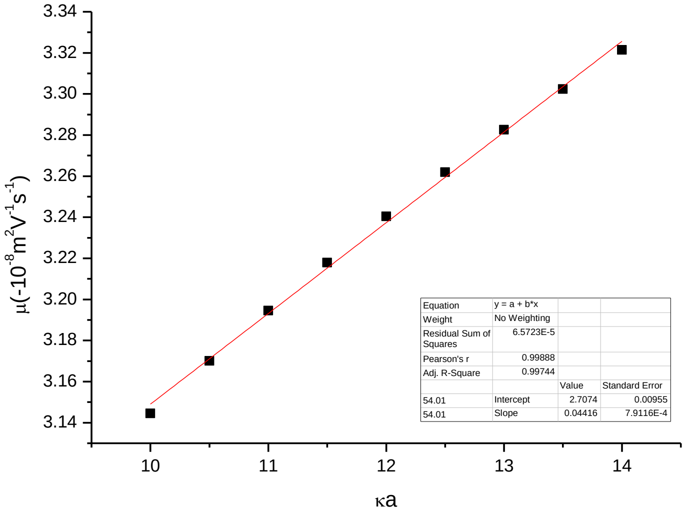

Fig. 52: Calibration line for SNP22 (1st series), c(Na$^+$) = 60 mmol L^{-1}, T = 25 °C.

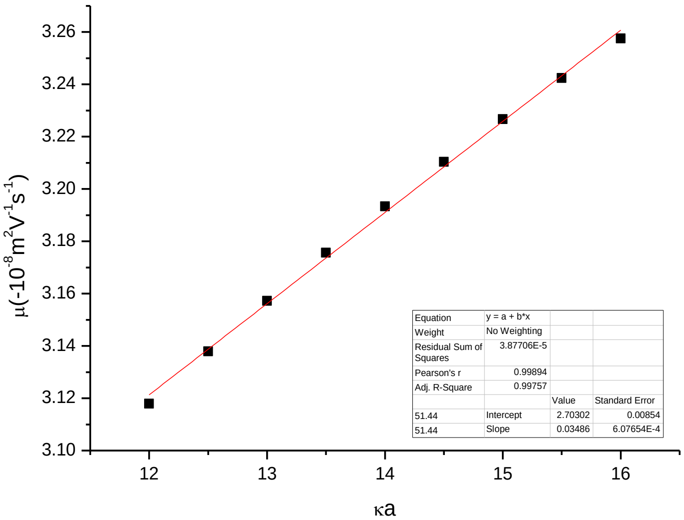

Fig. 53: Calibration line for SNP22 (1st series), c(Na$^+$) = 80 mmol L^{-1}, T = 25 °C.

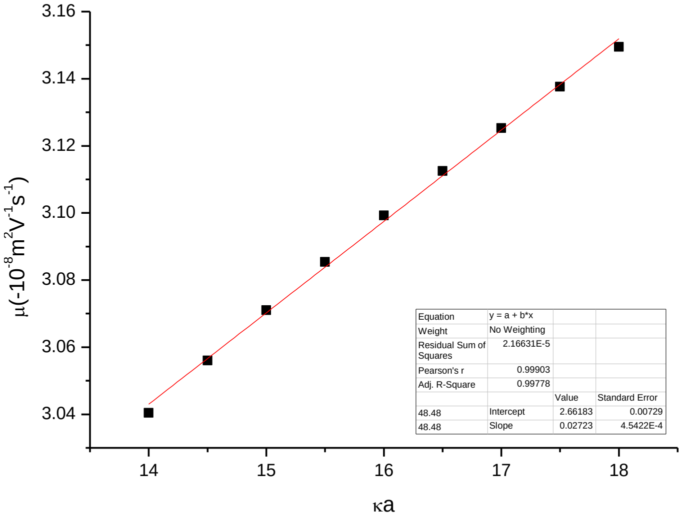

Fig. 54: Calibration line for SNP22 (1st series), c(Na$^+$) = 100 mmol L^{-1}, T = 25 °C.

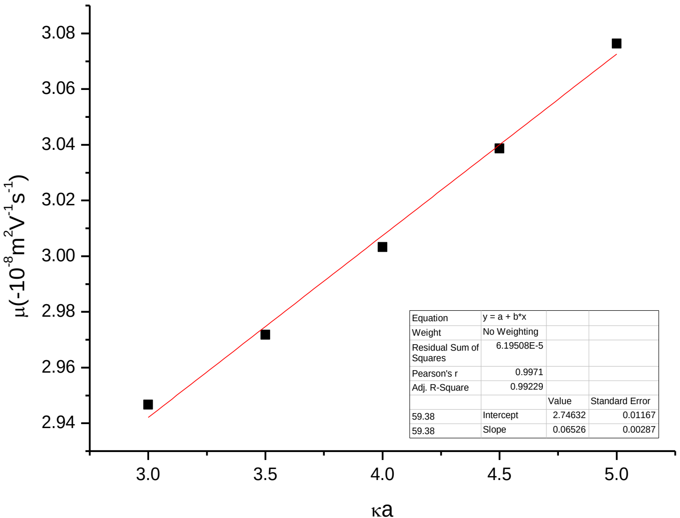

Equation	y = a + b*x		
Weight	No Weighting		
Residual Sum of Squares	6.19508E-5		
Pearson's r	0.9971		
Adj. R-Square	0.99229		
		Value	Standard Error
59.38	Intercept	2.74632	0.01167
59.38	Slope	0.06526	0.00287

Fig. 55: Calibration line for SNP7 (2^{nd} series), c(K^+) = 40 mmol L^{-1}, T = 25 °C.

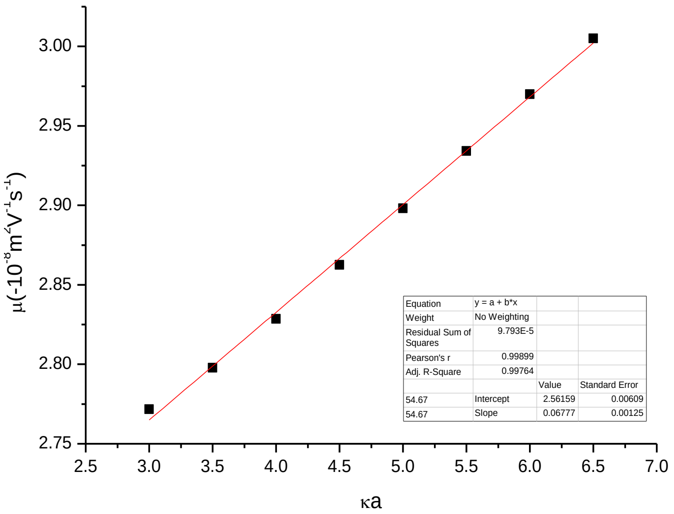

Equation	y = a + b*x		
Weight	No Weighting		
Residual Sum of Squares	9.793E-5		
Pearson's r	0.99899		
Adj. R-Square	0.99764		
		Value	Standard Error
54.67	Intercept	2.56159	0.00609
54.67	Slope	0.06777	0.00125

Fig. 56: Calibration line for SNP7 (2^{nd} series), c(K^+) = 60 mmol L^{-1}, T = 25 °C.

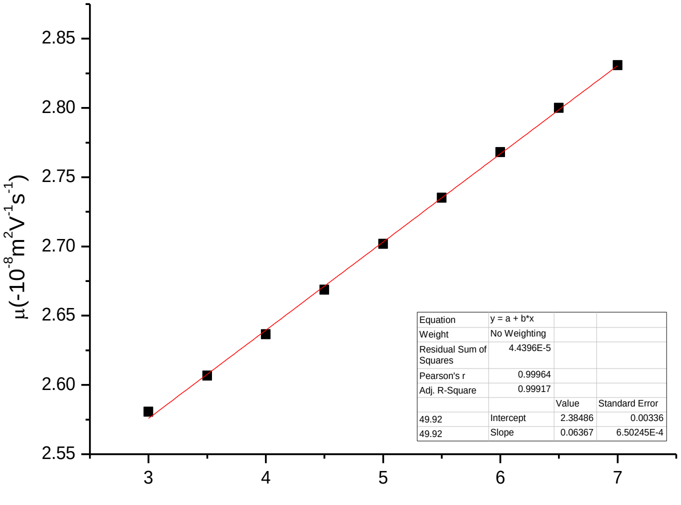

Equation	y = a + b*x		
Weight	No Weighting		
Residual Sum of Squares	4.4396E-5		
Pearson's r	0.99964		
Adj. R-Square	0.99917		
		Value	Standard Error
49.92	Intercept	2.38486	0.00336
49.92	Slope	0.06367	6.50245E-4

Fig. 57: Calibration line for SNP7 (2^{nd} series), c(K^+) = 80 mmol L^{-1}, T = 25 °C.

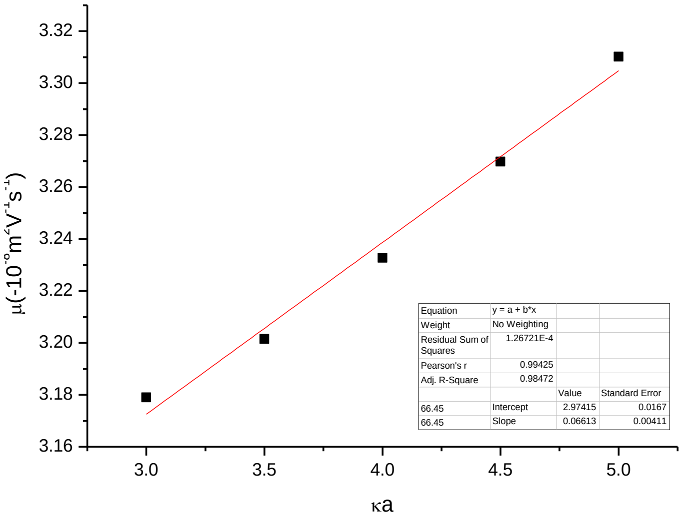

Equation	y = a + b*x		
Weight	No Weighting		
Residual Sum of Squares	1.26721E-4		
Pearson's r	0.99425		
Adj. R-Square	0.98472		
		Value	Standard Error
66.45	Intercept	2.97415	0.0167
66.45	Slope	0.06613	0.00411

Fig. 58: Calibration line for SNP12 (2^{nd} series), c(K^+) = 20 mmol L^{-1}, T = 25 °C.

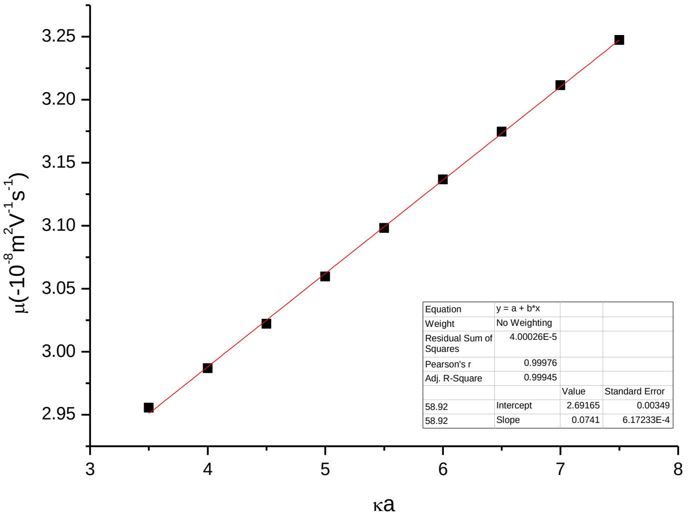

Equation	y = a + b*x		
Weight	No Weighting		
Residual Sum of Squares	4.00026E-5		
Pearson's r	0.99976		
Adj. R-Square	0.99945		
		Value	Standard Error
58.92	Intercept	2.69165	0.00349
58.92	Slope	0.0741	6.17233E-4

Fig. 59: Calibration line for SNP12 (2^{nd} series), c(K^+) = 40 mmol L^{-1}, T = 25 °C.

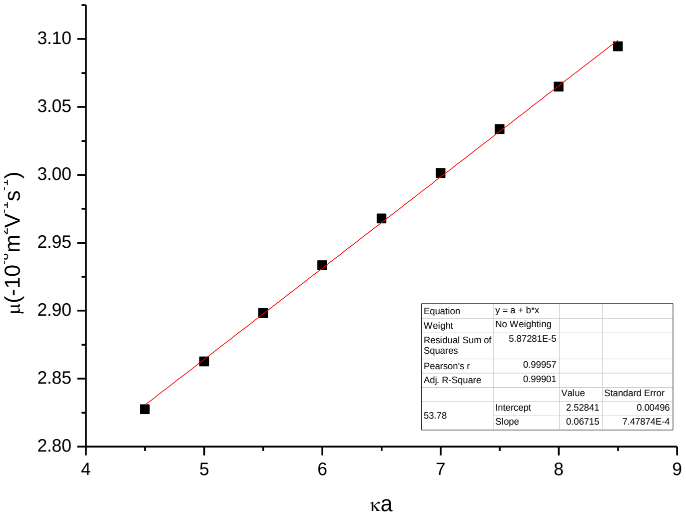

Equation	y = a + b*x		
Weight	No Weighting		
Residual Sum of Squares	5.87281E-5		
Pearson's r	0.99957		
Adj. R-Square	0.99901		
		Value	Standard Error
53.78	Intercept	2.52841	0.00496
	Slope	0.06715	7.47874E-4

Fig. 60: Calibration line for SNP12 (2^{nd} series), c(K^+) = 60 mmol L^{-1}, T = 25 °C.

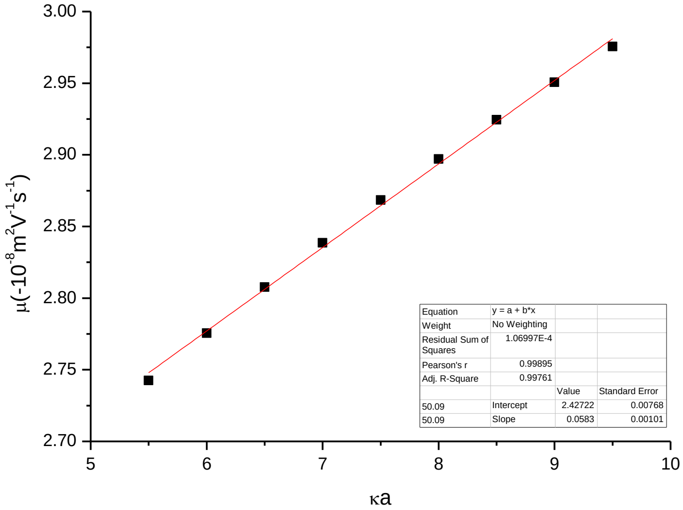

Fig. 61: Calibration line for SNP12 (2nd series), c(K$^+$) = 80 mmol L^{-1}, T = 25 °C.

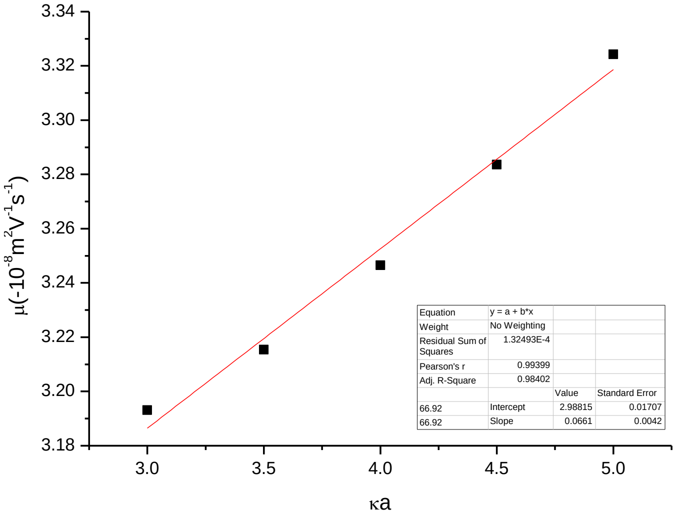

Fig. 62: Calibration line for SNP12 (1st series), c(K$^+$) = 20 mmol L^{-1}, T = 25 °C.

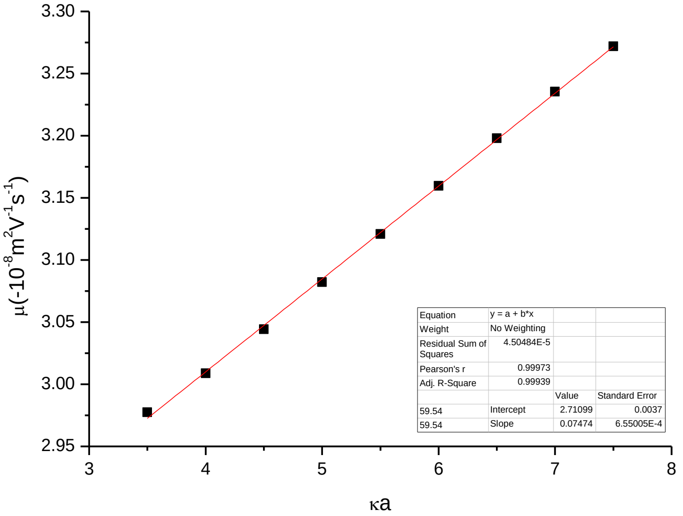

Fig. 63: Calibration line for SNP12 (1st series), c(K$^+$) = 40 mmol L^{-1}, T = 25 °C.

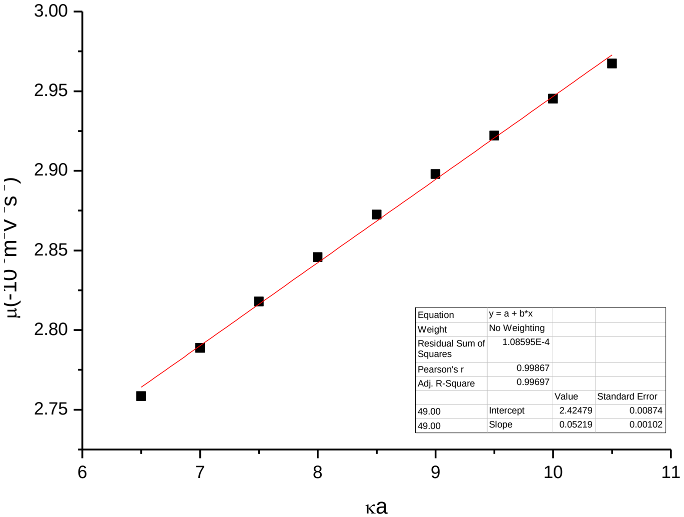

Fig. 64: Calibration line for SNP12 (1st series), c(K$^+$) = 100 mmol L^{-1}, T = 25 °C.

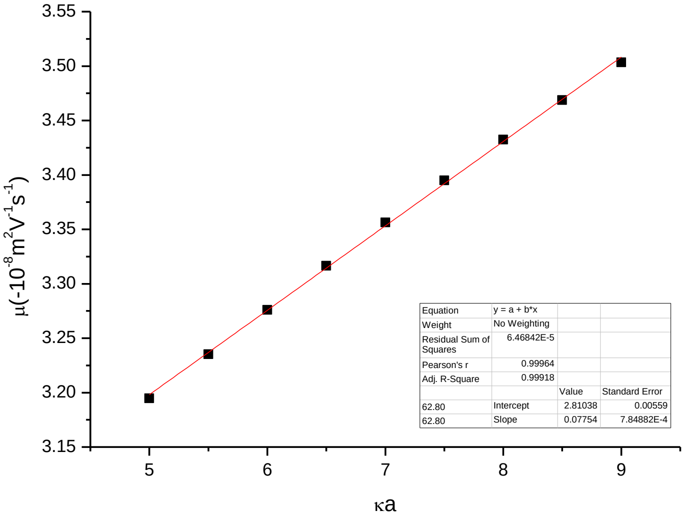

Fig. 65: Calibration line for SNP22 (2nd series), c(K$^+$) = 20 mmol L^{-1}, T = 25 °C.

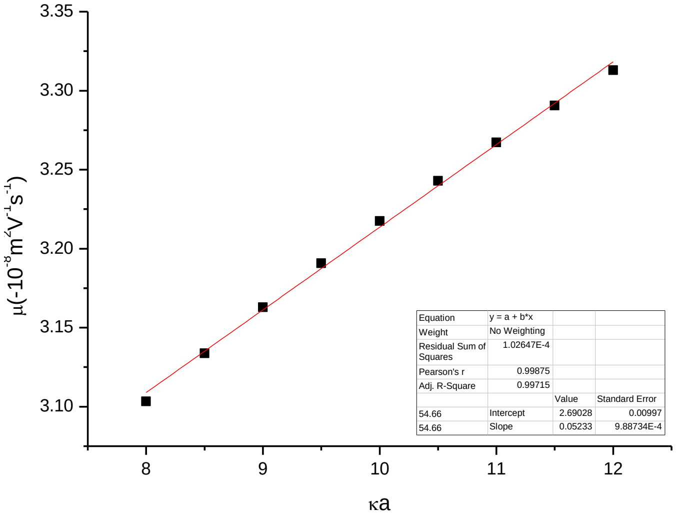

Fig. 66: Calibration line for SNP22 (2nd series), c(K$^+$) = 40 mmol L^{-1}, T = 25 °C.

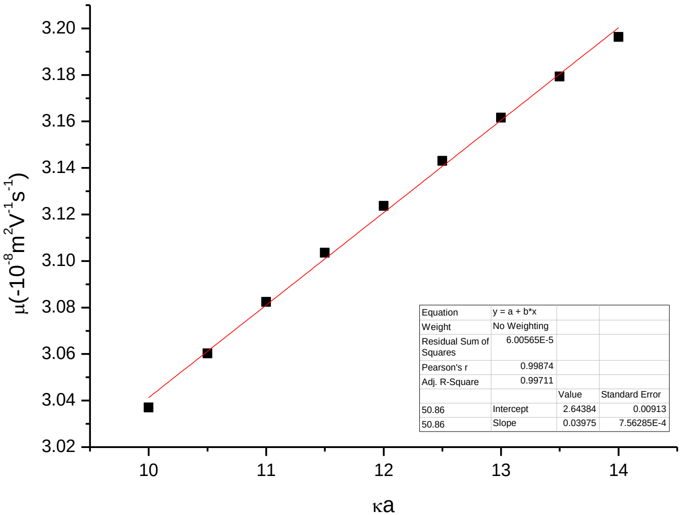

Fig. 67: Calibration line for SNP22 (2nd series), c(K^+) = 60 mmol L^{-1}, T = 25 °C.

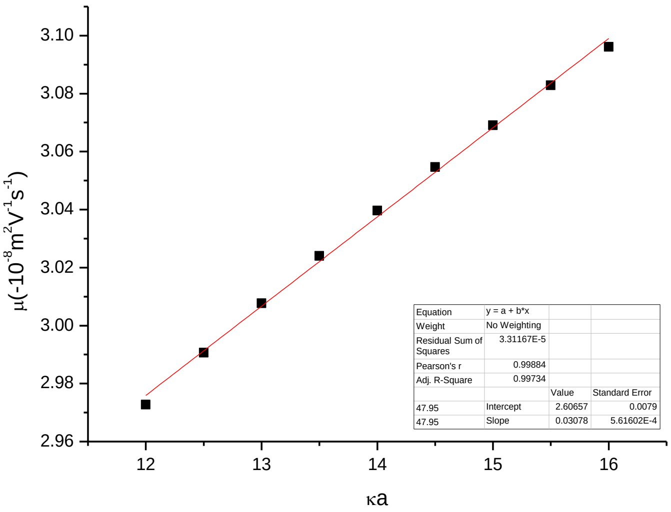

Fig. 68: Calibration line for SNP22 (2nd series), c(K^+) = 80 mmol L^{-1}, T = 25 °C.

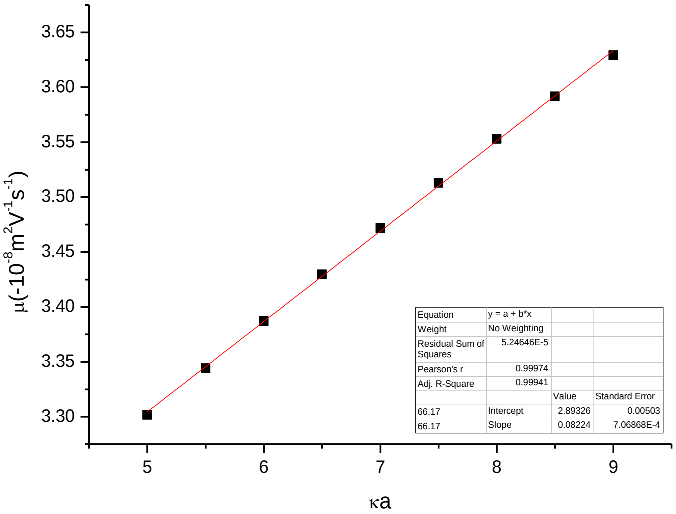

Fig. 69: Calibration line for SNP22 (1st series), c(K^+) = 20 mmol L^{-1}, T = 25 °C.

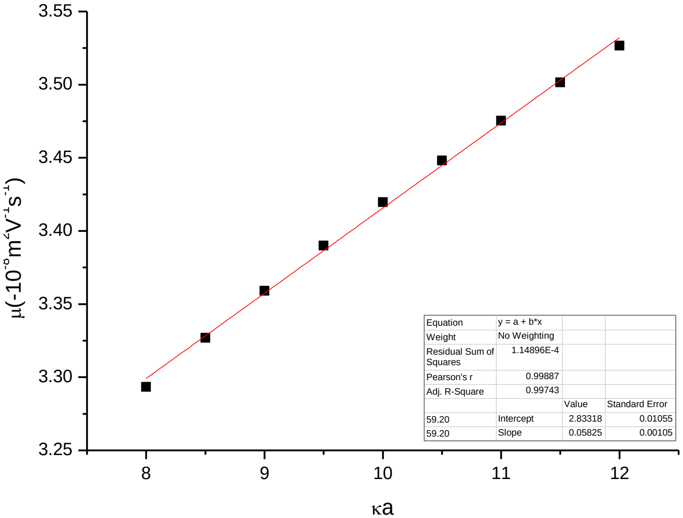

Fig. 70: Calibration line for SNP22 (1st series), c(K^+) = 40 mmol L^{-1}, T = 25 °C.

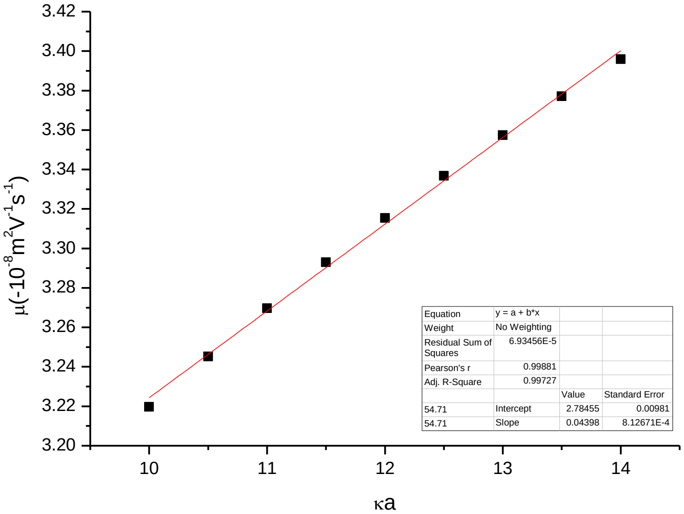

Fig. 71: Calibration line for SNP22 (1st series), c(K^+) = 60 mmol L^{-1}, T = 25 °C.

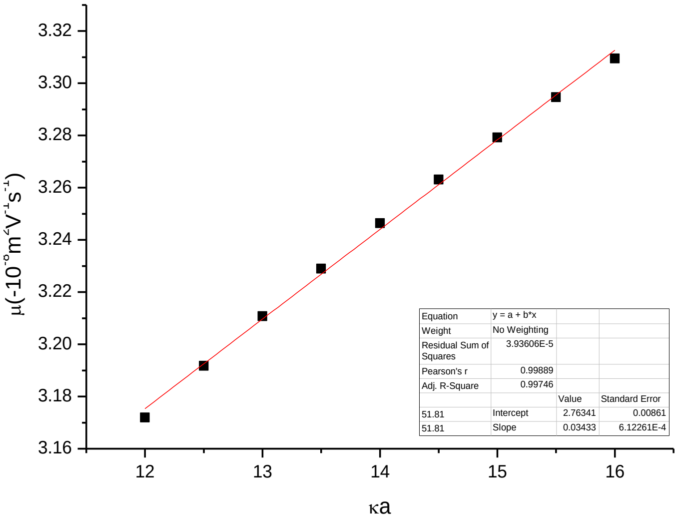

Fig. 72: Calibration line for SNP22 (1st series), c(K^+) = 80 mmol L^{-1}, T = 25 °C.

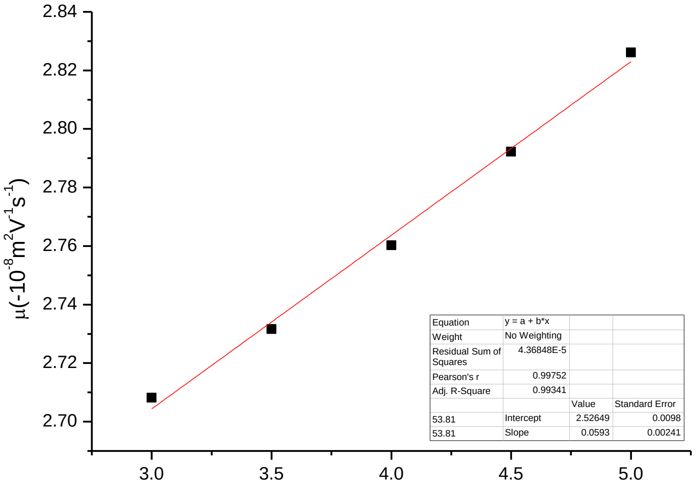

Equation	y = a + b*x		
Weight	No Weighting		
Residual Sum of Squares	4.36848E-5		
Pearson's r	0.99752		
Adj. R-Square	0.99341		
		Value	Standard Error
53.81	Intercept	2.52649	0.0098
53.81	Slope	0.0593	0.00241

Fig. 73: Calibration line for SNP7 (2nd series), c(Gdm$^+$) = 40 mmol L^{-1}, T = 25 °C.

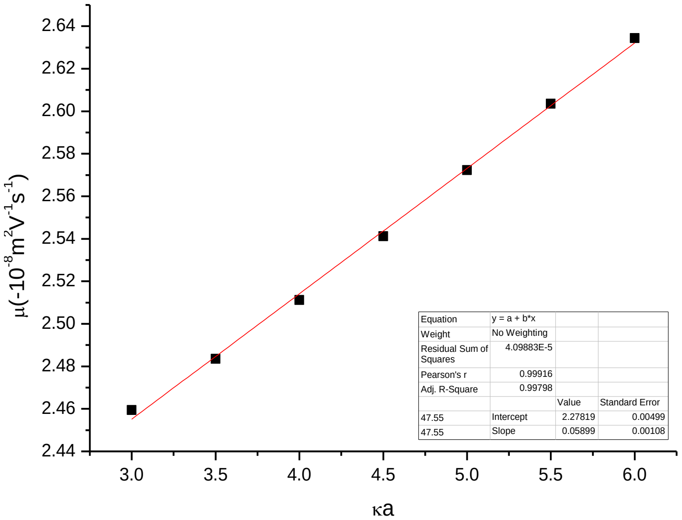

Equation	y = a + b*x		
Weight	No Weighting		
Residual Sum of Squares	4.09883E-5		
Pearson's r	0.99916		
Adj. R-Square	0.99798		
		Value	Standard Error
47.55	Intercept	2.27819	0.00499
47.55	Slope	0.05899	0.00108

Fig. 74: Calibration line for SNP7 (2nd series), c(Gdm$^+$) = 60 mmol L^{-1}, T = 25 °C.

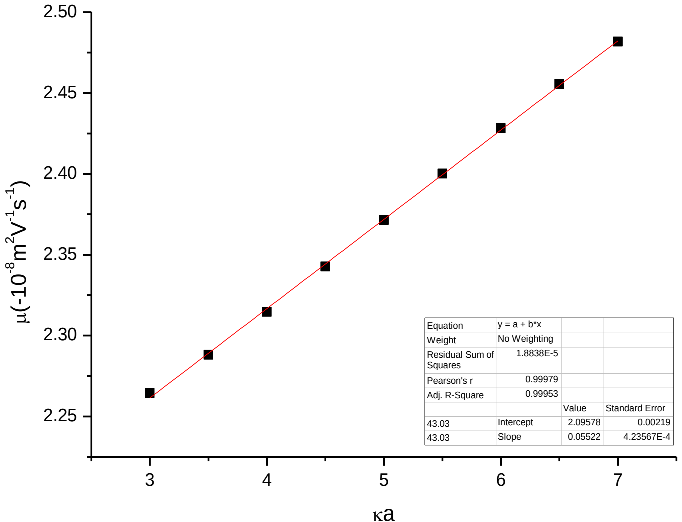

Equation	y = a + b*x		
Weight	No Weighting		
Residual Sum of Squares	1.8838E-5		
Pearson's r	0.99979		
Adj. R-Square	0.99953		
		Value	Standard Error
43.03	Intercept	2.09578	0.00219
43.03	Slope	0.05522	4.23567E-4

Fig. 75: Calibration line for SNP7 (2nd series), c(Gdm$^+$) = 80 mmol L^{-1}, T = 25 °C.

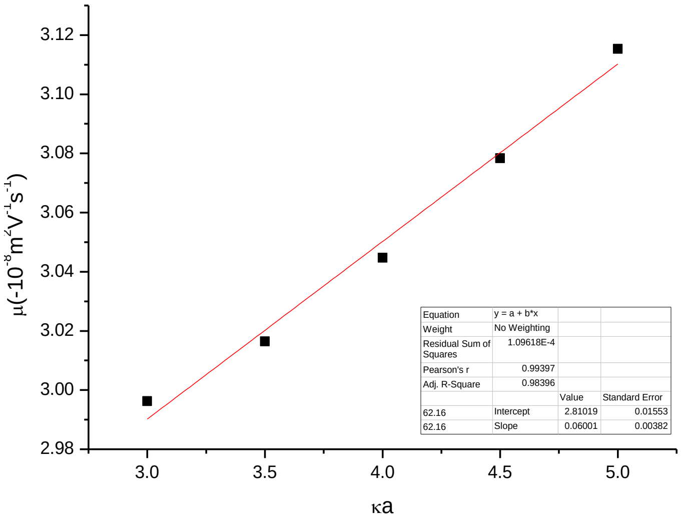

Equation	y = a + b*x		
Weight	No Weighting		
Residual Sum of Squares	1.09618E-4		
Pearson's r	0.99397		
Adj. R-Square	0.98396		
		Value	Standard Error
62.16	Intercept	2.81019	0.01553
62.16	Slope	0.06001	0.00382

Fig. 76: Calibration line for SNP12 (2nd series), c(Gdm$^+$) = 20 mmol L^{-1}, T = 25 °C.

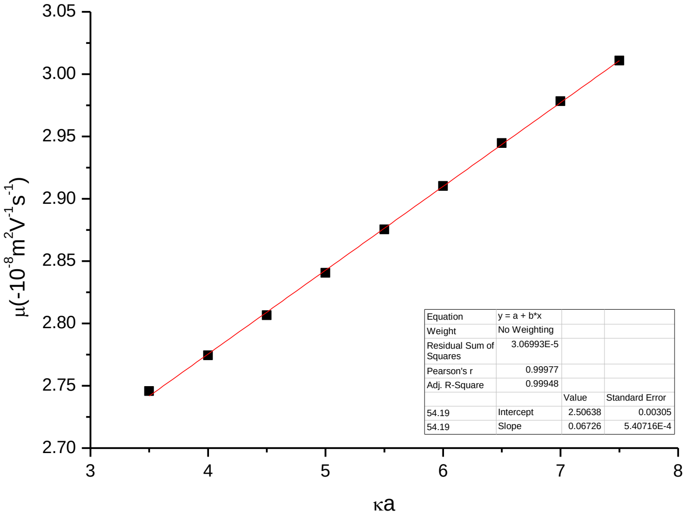

Equation	y = a + b*x		
Weight	No Weighting		
Residual Sum of Squares	3.06993E-5		
Pearson's r	0.99977		
Adj. R-Square	0.99948		
		Value	Standard Error
54.19	Intercept	2.50638	0.00305
54.19	Slope	0.06726	5.40716E-4

Fig. 77: Calibration line for SNP12 (2nd series), c(Gdm$^+$) = 40 mmol L^{-1}, T = 25 °C.

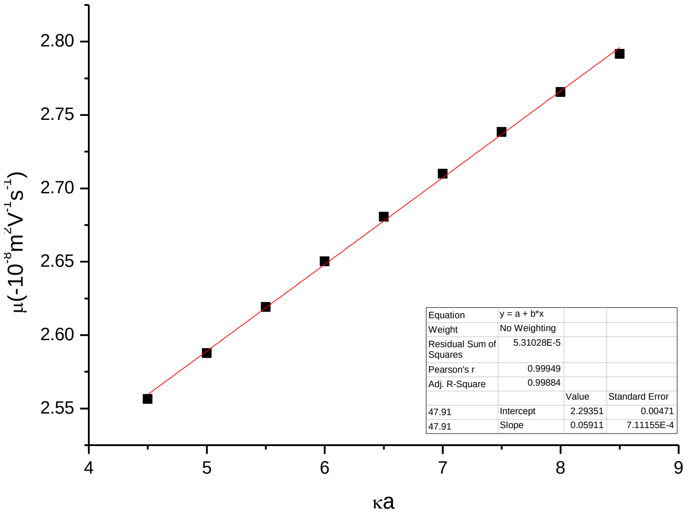

Equation	y = a + b*x		
Weight	No Weighting		
Residual Sum of Squares	5.31028E-5		
Pearson's r	0.99949		
Adj. R-Square	0.99884		
		Value	Standard Error
47.91	Intercept	2.29351	0.00471
47.91	Slope	0.05911	7.11155E-4

Fig. 78: Calibration line for SNP12 (2nd series), c(Gdm$^+$) = 60 mmol L^{-1}, T = 25 °C.

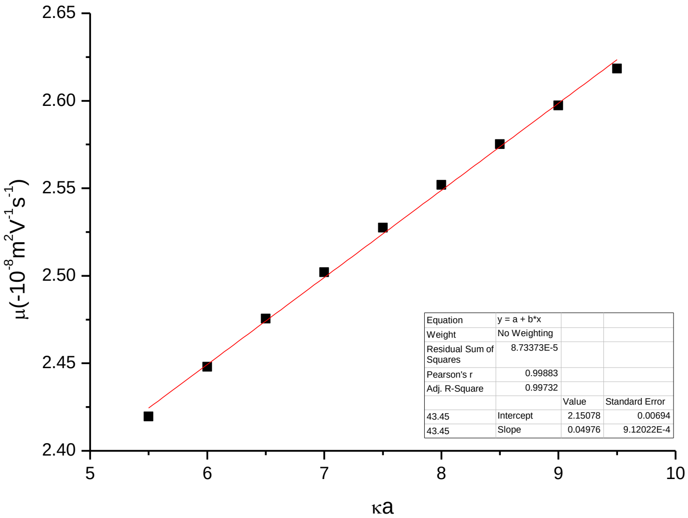

Fig. 79: Calibration line for SNP12 (2^{nd} series), c(Gdm$^+$) = 80 mmol L^{-1}, T = 25 °C.

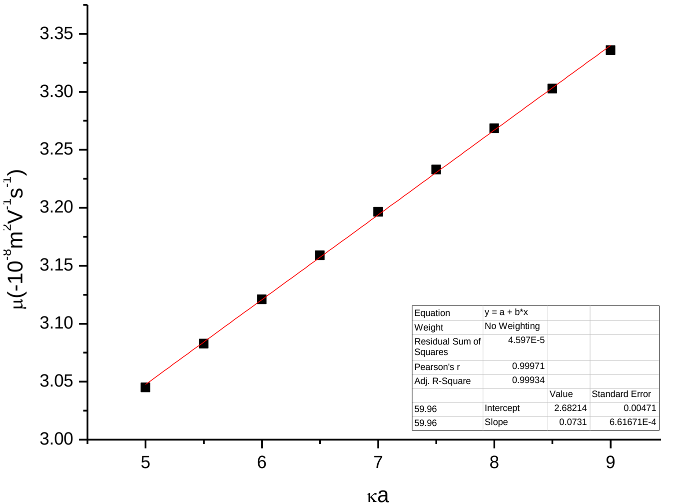

Fig. 80: Calibration line for SNP22 (2^{nd} series), c(Gdm$^+$) = 20 mmol L^{-1}, T = 25 °C.

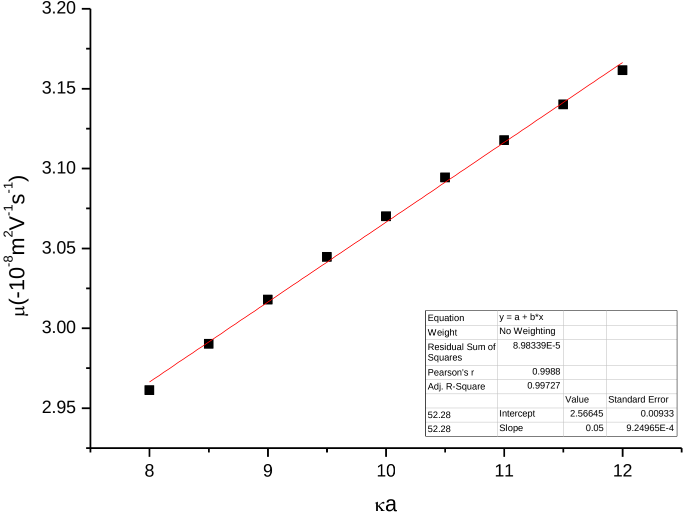

Fig. 81: Calibration line for SNP22 (2^{nd} series), c(Gdm$^+$) = 40 mmol L^{-1}, T = 25 °C.

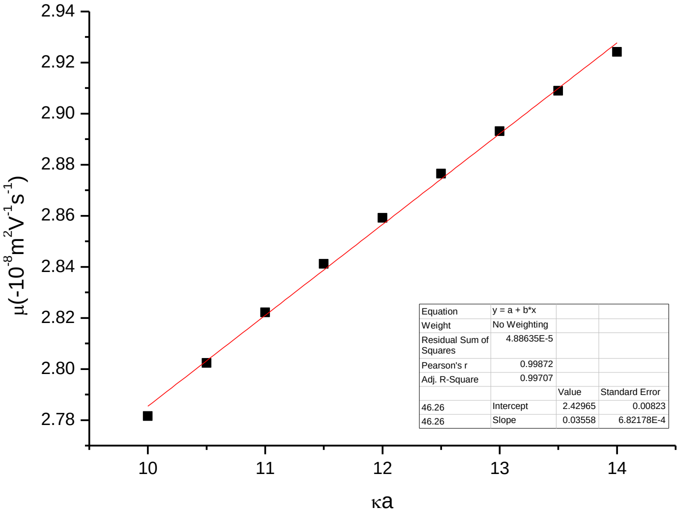

Fig. 82: Calibration line for SNP22 (2^{nd} series), c(Gdm$^+$) = 60 mmol L^{-1}, T = 25 °C.

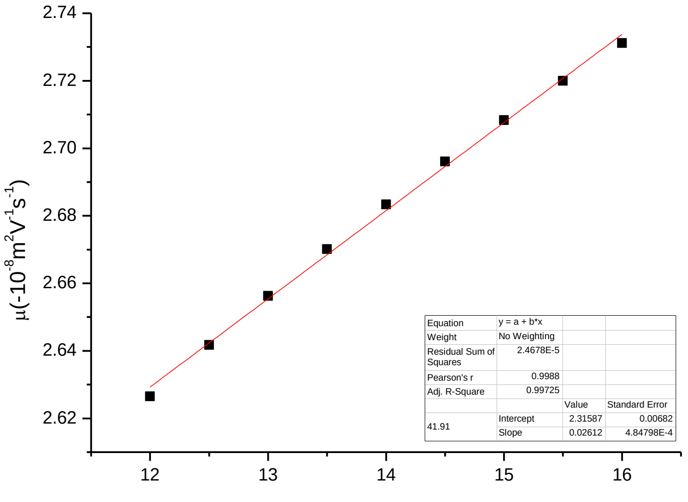

Fig. 83: Calibration line for SNP22 (2^{nd} series), c(Gdm$^+$) = 80 mmol L^{-1}, T = 25 °C.

Appendix A7

Calculated parameters of regression lines (for ranges of κ*a* refer to Appendix A6)

Cation counterion	**SNP**	**c(cation)/ (mmol L^{-1})**	**ζ/mV**	**R**	**SSE/ (m^2 V^{-1} s^{-1})**	**y-Intercept/ (10^{-8} m^2 V^{-1} s^{-1})**	**SE/ (10^{-8} m^2 V^{-1} s^{-1})**	**Slope/ (10^{-8} m^2 V^{-1} s^{-1})**	**SE/ (10^{-8} m^2 V^{-1} s^{-1})**
Li$^+$	**SNP7****	40	-66.63	0.98619	$9.87869\cdot10^{-6}$	2.88877	0.01787	0.05330	0.00444
		60	-61.03	0.99297	$5.43002\cdot10^{-5}$	2.70050	0.01226	0.06402	0.00269
		80	-56.56	0.99940	$1.64933\cdot10^{-5}$	2.53799	0.00384	0.06877	$6.86467\cdot10^{-4}$
		100	-52.90	0.99981	$1.03389\cdot10^{-5}$	2.42862	0.00193	0.06490	$3.13792\cdot10^{-4}$
		120	-50.35	0.99925	$6.88468\cdot10^{-5}$	2.35284	0.00353	0.06084	$5.27417\cdot10^{-4}$
	SNP12*	20	-82.55	0.87868	$3.76689\cdot10^{-5}$	3.19172	0.03490	0.03416	0.00868
		40	-66.40	0.99714	$9.90480\cdot10^{-5}$	2.77992	0.00940	0.07691	0.00168
		60	-61.40	0.99945	$1.20336\cdot10^{-5}$	2.67051	0.00355	0.07265	$4.90338\cdot10^{-4}$
		80	-57.22	0.99869	$7.48279\cdot10^{-5}$	2.58204	0.00684	0.06582	$8.44184\cdot10^{-4}$
		100	-53.71	0.99878	$2.47806\cdot10^{-5}$	2.50502	0.00720	0.05900	$8.41438\cdot10^{-4}$
		120	-51.23	0.99766	$8.81463\cdot10^{-5}$	2.44826	0.00833	0.05351	$9.16236\cdot10^{-4}$
	SNP12**	20	-81.50	0.89810	$3.47957\cdot10^{-5}$	3.17885	0.03354	0.03600	0.00834
		40	-67.73	0.99864	$1.61329\cdot10^{-5}$	2.79473	0.00813	0.07943	0.00147
		60	-61.97	0.99947	$1.19821\cdot10^{-4}$	2.68324	0.00355	0.07335	$4.89287\cdot10^{-4}$
		80	-57.28	0.99869	$7.47192\cdot10^{-5}$	2.58355	0.00684	0.06591	$8.43571\cdot10^{-4}$
		100	-53.75	0.99878	$2.47819\cdot10^{-5}$	2.50616	0.00720	0.05906	$8.41460\cdot10^{-4}$
		120	-51.20	0.99766	$8.81124\cdot10^{-5}$	2.44732	0.00833	0.05347	$9.16060\cdot10^{-4}$
	SNP22*	20	-67.20	0.99989	$9.57673\cdot10^{-6}$	2.76717	0.00215	0.08209	$3.02005\cdot10^{-4}$
		40	-59.72	0.99839	$5.17700\cdot10^{-5}$	2.72992	0.00935	0.05979	$9.06502\cdot10^{-4}$
		60	-58.65	0.99827	$3.90471\cdot10^{-5}$	2.79841	0.00969	0.04998	$7.87271\cdot10^{-4}$
		80	-55.37	0.99828	$2.37598\cdot10^{-5}$	2.79867	0.00878	0.03914	$6.14118\cdot10^{-4}$
		100	-52.22	0.99839	$1.36675\cdot10^{-5}$	2.77530	0.00759	0.03067	$4.65773\cdot10^{-4}$
		120	-49.84	0.99844	$9.85103\cdot10^{-6}$	2.72237	0.00684	0.02648	$3.95431\cdot10^{-4}$
	SNP22**	20	-75.54	0.99965	$4.04532\cdot10^{-5}$	2.85393	0.00442	0.09348	$6.20700\cdot10^{-4}$
		40	-64.17	0.99832	$1.00878\cdot10^{-4}$	2.80551	0.00988	0.06759	$9.80176\cdot10^{-4}$
		60	-59.42	0.99829	$4.00361\cdot10^{-5}$	2.81722	0.00981	0.05100	$7.97178\cdot10^{-4}$
		80	-55.32	0.99828	$2.37098\cdot10^{-5}$	2.79716	0.00877	0.03909	$6.13471\cdot10^{-4}$
		100	-52.20	0.99839	$1.36542\cdot10^{-5}$	2.77459	0.00758	0.03065	$4.65546\cdot10^{-4}$
		120	-49.79	0.99844	$9.82550\cdot10^{-6}$	2.72044	0.00683	0.02644	$3.94918\cdot10^{-4}$
Na$^+$	**SNP7****	40	-63.03	0.99426	$5.39974\cdot10^{-6}$	2.82276	0.01321	0.06127	0.00329
		60	-57.72	0.99692	$2.58284\cdot10^{-5}$	2.63145	0.00845	0.06684	0.00186
		80	-53.19	0.99954	$2.63305\cdot10^{-5}$	2.47047	0.00283	0.06610	$5.00766\cdot10^{-4}$
		100	-49.65	0.99970	$6.87851\cdot10^{-5}$	2.34403	0.00270	0.06289	$4.43316\cdot10^{-4}$
	SNP12*	20	-69.65	0.98846	$1.01853\cdot10^{-5}$	3.00620	0.01815	0.05924	0.00451
		40	-59.89	0.99948	$1.67052\cdot10^{-5}$	2.67012	0.00386	0.07399	$6.90863\cdot10^{-4}$
		60	-56.47	0.99957	$2.73248\cdot10^{-5}$	2.57388	0.00338	0.06967	$5.10133\cdot10^{-4}$
		80	-53.12	0.99833	$8.49931\cdot10^{-5}$	2.49312	0.00685	0.06219	$8.99699\cdot10^{-4}$
		100	-48.99	0.99832	$2.69168\cdot10^{-5}$	2.39144	0.00751	0.05243	$8.76956\cdot10^{-4}$
		120	-45.64	0.99748	$4.20417\cdot10^{-5}$	2.31610	0.00802	0.04298	$8.16901\cdot10^{-4}$

	SNP12**	20	-71.78	0.98549	$1.23164\cdot10^{-5}$	3.05818	0.01996	0.05806	0.00496
		40	-63.42	0.99902	$3.41015\cdot10^{-5}$	2.76411	0.00552	0.07733	$9.87081\cdot10^{-4}$
		60	-58.10	0.99966	$2.26467\cdot10^{-5}$	2.62089	0.00308	0.07169	$4.64417\cdot10^{-4}$
		80	-53.55	0.99837	$8.44261\cdot10^{-5}$	2.50666	0.00682	0.06276	$8.96693\cdot10^{-4}$
		100	-50.05	0.99743	$9.80662\cdot10^{-5}$	2.42663	0.00831	0.05381	$9.66418\cdot10^{-4}$
	SNP22*	20	-66.87	0.99976	$2.10983\cdot10^{-5}$	2.83282	0.00319	0.08241	$4.48259\cdot10^{-4}$
		40	-60.08	0.99780	$1.05950\cdot10^{-4}$	2.78974	0.01013	0.06047	0.00100
		60	-54.01	0.99744	$6.57230\cdot10^{-5}$	2.70740	0.00955	0.04416	$7.91160\cdot10^{-4}$
		80	-51.44	0.99757	$3.87706\cdot10^{-5}$	2.70302	0.00854	0.03486	$6.07654\cdot10^{-4}$
		100	-48.48	0.99778	$2.16631\cdot10^{-5}$	2.66183	0.00729	0.02723	$4.54220\cdot10^{-4}$
	SNP22**	20	-68.78	0.99975	$1.62482\cdot10^{-5}$	2.86745	0.00373	0.08500	$5.07847\cdot10^{-4}$
		40	-60.92	0.99825	$5.77268\cdot10^{-5}$	2.82340	0.00987	0.06047	$9.57235\cdot10^{-4}$
		60	-56.28	0.99754	$7.10959\cdot10^{-5}$	2.77884	0.00993	0.04688	$8.22863\cdot10^{-4}$
		80	-52.15	0.99806	$2.29845\cdot10^{-5}$	2.71967	0.00833	0.03627	$6.04014\cdot10^{-4}$
		100	-48.84	0.99821	$1.26812\cdot10^{-5}$	2.66871	0.00708	0.02804	$4.48653\cdot10^{-4}$
K^{+}	**SNP7****	40	-59.38	0.99229	$6.19508\cdot10^{-5}$	2.74632	0.01167	0.06526	0.00287
		60	-54.67	0.99764	$9.79300\cdot10^{-5}$	2.56159	0.00609	0.06777	0.00125
		80	-49.92	0.99917	$4.43960\cdot10^{-5}$	2.38486	0.00336	0.06367	$6.50245\cdot10^{-4}$
	SNP12*	20	-66.92	0.98402	$1.32493\cdot10^{-5}$	2.98815	0.01707	0.06610	0.00420
		40	-59.54	0.99939	$4.50484\cdot10^{-5}$	2.71099	0.00370	0.07474	$6.55005\cdot10^{-4}$
		100	-49.00	0.99697	$1.08595\cdot10^{-5}$	2.42479	0.00874	0.05219	0.00102
	SNP12**	20	-66.45	0.98472	$1.26721\cdot10^{-5}$	2.97415	0.01670	0.06613	0.00411
		40	-58.92	0.99945	$4.00026\cdot10^{-5}$	2.69165	0.00349	0.07410	$6.17233\cdot10^{-4}$
		60	-53.78	0.99901	$5.87281\cdot10^{-5}$	2.52841	0.00496	0.06715	$7.47874\cdot10^{-4}$
		80	-50.09	0.99761	$1.06997\cdot10^{-4}$	2.42722	0.00768	0.05830	0.00101
	SNP22*	20	-66.17	0.99941	$5.24646\cdot10^{-5}$	2.89326	0.00503	0.08224	$7.06868\cdot10^{-4}$
		40	-59.20	0.99743	$1.14896\cdot10^{-4}$	2.83318	0.01055	0.05825	0.00105
		60	-54.71	0.99727	$6.93456\cdot10^{-5}$	2.78455	0.00981	0.04398	$8.12671\cdot10^{-4}$
		80	-51.81	0.99746	$3.93606\cdot10^{-5}$	2.76341	0.00861	0.03433	$6.12261\cdot10^{-4}$
	SNP22**	20	-62.80	0.99918	$6.46842\cdot10^{-5}$	2.81038	0.00559	0.07754	$7.84882\cdot10^{-4}$
		40	-54.66	0.99715	$1.02647\cdot10^{-4}$	2.69028	0.00997	0.05233	$9.88734\cdot10^{-4}$
		60	-50.86	0.99711	$6.00565\cdot10^{-5}$	2.64384	0.00913	0.03975	$7.56285\cdot10^{-4}$
		80	-47.95	0.99734	$3.31167\cdot10^{-5}$	2.60657	0.00790	0.03078	$5.61602\cdot10^{-4}$
Gdm^{+}	**SNP7****	40	-53.81	0.99341	$4.36848\cdot10^{-5}$	2.52649	0.00980	0.05930	0.00241
		60	-47.55	0.99798	$4.09883\cdot10^{-5}$	2.27819	0.00499	0.05899	0.00108
		80	-43.03	0.99953	$1.88380\cdot10^{-5}$	2.09578	0.00219	0.05522	$4.23567\cdot10^{-4}$
	SNP12**	20	-62.16	0.98396	$1.09618\cdot10^{-4}$	2.81019	0.01553	0.06001	0.00382
		40	-54.19	0.99948	$3.06993\cdot10^{-5}$	2.50638	0.00305	0.06726	$5.40716\cdot10^{-4}$
		60	-47.91	0.99884	$5.31028\cdot10^{-5}$	2.29351	0.00471	0.05911	$7.11155\cdot10^{-4}$
		80	-43.45	0.99732	$8.73373\cdot10^{-5}$	2.15078	0.00694	0.04976	$9.12022\cdot10^{-4}$
	SNP22**	20	-59.96	0.99934	$4.59700\cdot10^{-5}$	2.68214	0.00471	0.07310	$6.61671\cdot10^{-4}$
		40	-52.28	0.99727	$8.98339\cdot10^{-5}$	2.56645	0.00933	0.05000	$9.24965\cdot10^{-4}$
		60	-46.26	0.99707	$4.88635\cdot10^{-5}$	2.42965	0.00823	0.03558	$6.82178\cdot10^{-4}$
		80	-41.91	0.99725	$2.46780\cdot10^{-5}$	2.31587	0.00682	0.02612	$4.84798\cdot10^{-4}$

R = correlation coefficient, SSE = sum of squared errors, SE = standard error.

Appendix A8

Superposition of size distribution functions for SNP7, SNP12 and SNP22 calculated from electropherograms (black solid line) with histograms (green) calculated from TEM data.

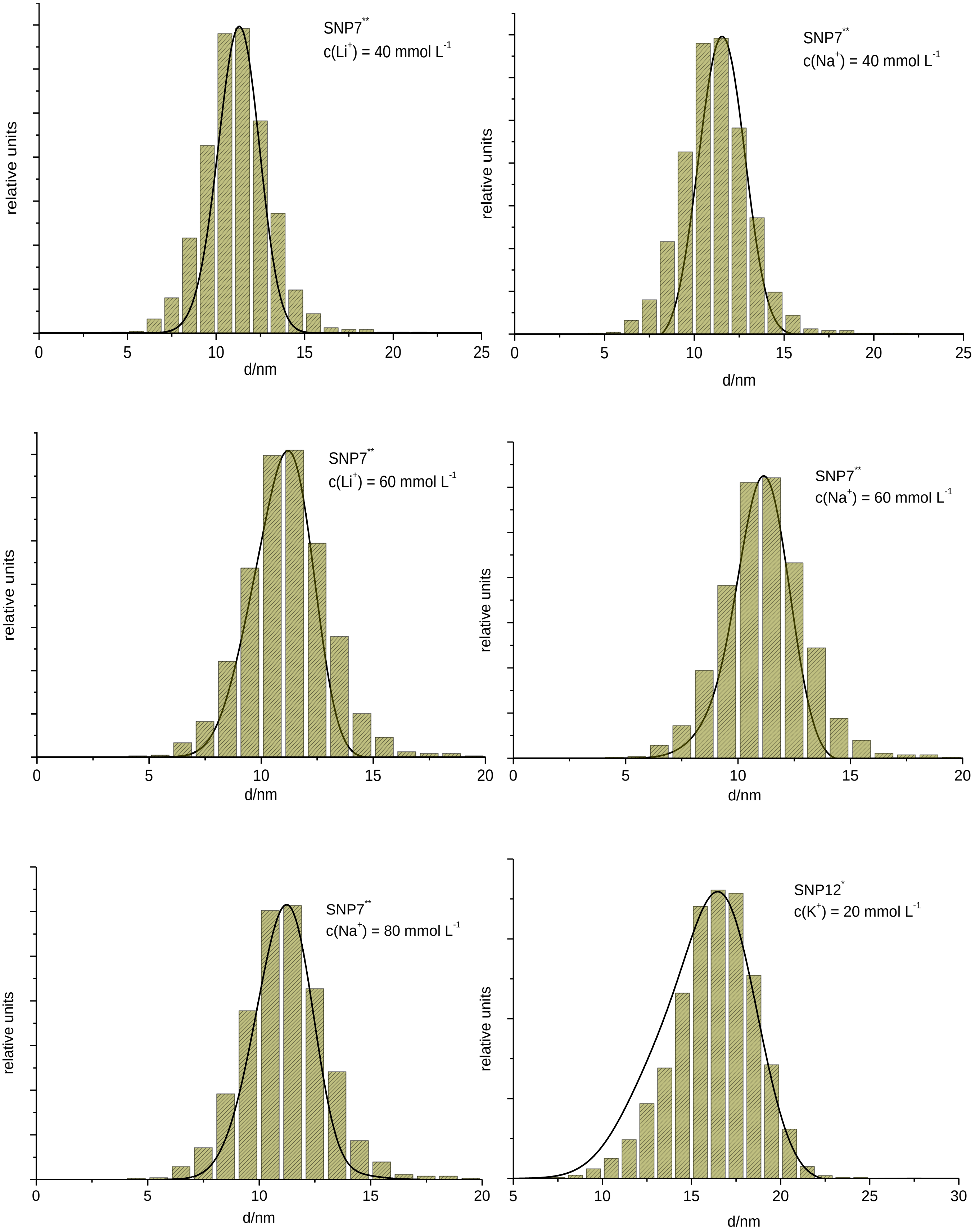

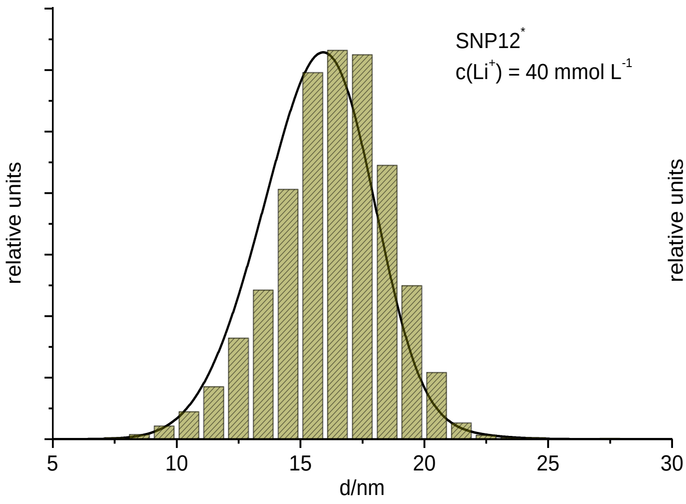
SNP12*
c(Li+) = 40 mmol L-1
relative units
5
10
15
20
25
30
d/nm

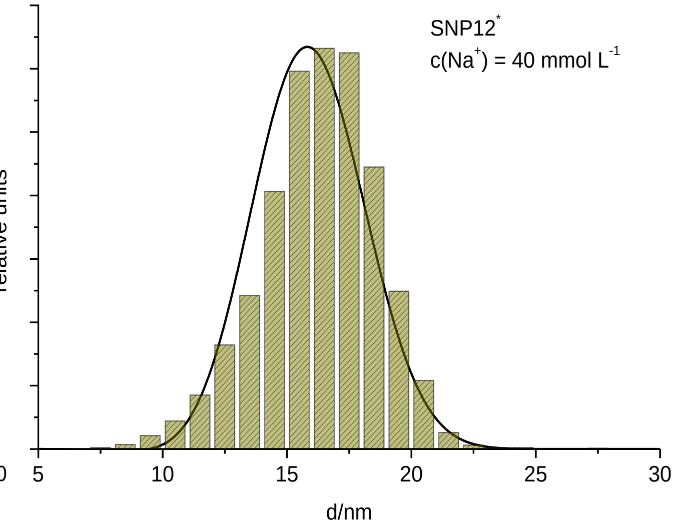
SNP12*
c(Na+) = 40 mmol L-1
relative units
5
10
15
20
25
30
d/nm

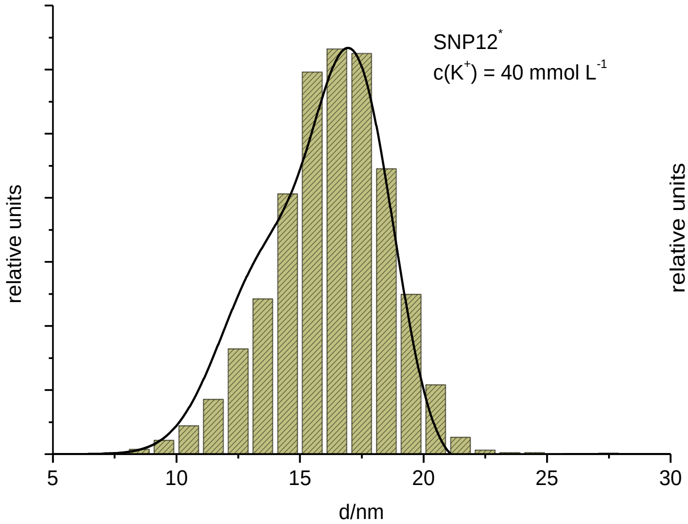
SNP12*
c(K+) = 40 mmol L-1
relative units
5
10
15
20
25
30
d/nm

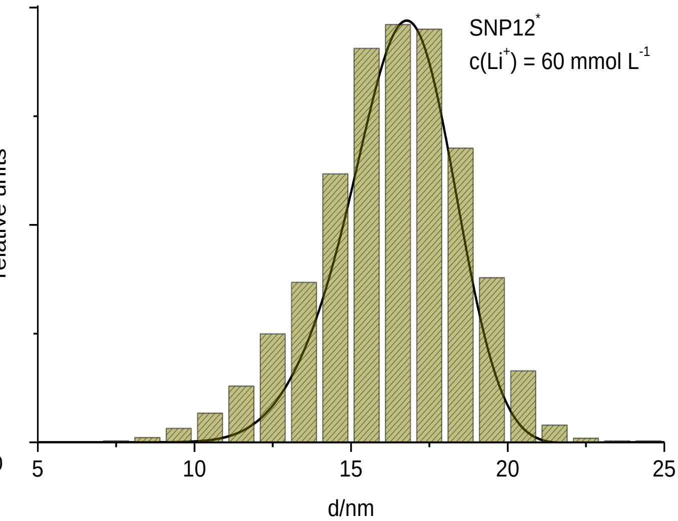
SNP12*
c(Li+) = 60 mmol L-1
relative units
5
10
15
20
25
d/nm

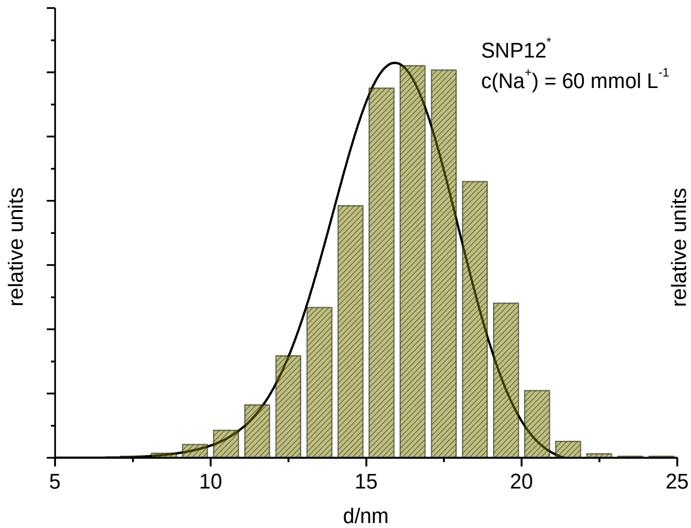
SNP12*
c(Na+) = 60 mmol L-1
relative units
5
10
15
20
25
d/nm

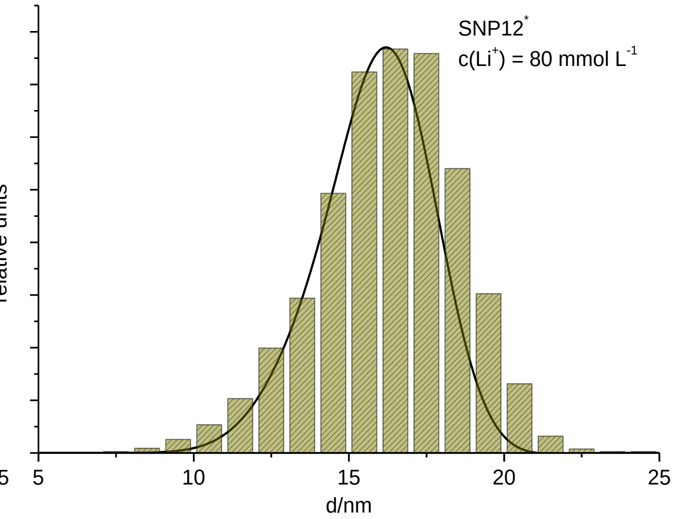
SNP12*
c(Li+) = 80 mmol L-1
relative units
5
10
15
20
25
d/nm

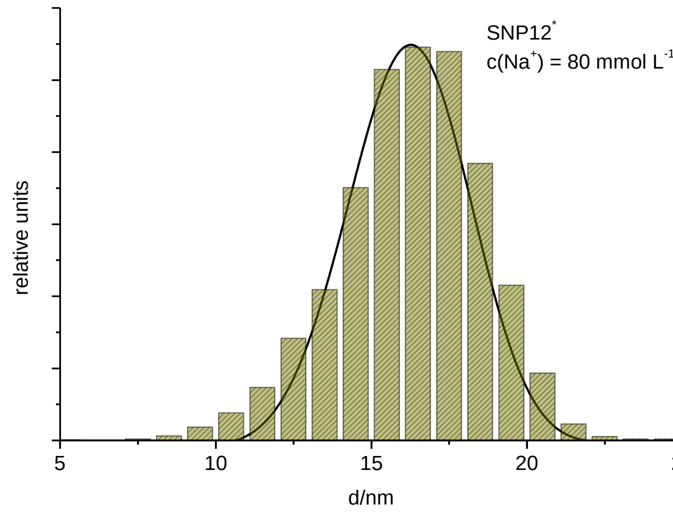
SNP12*
c(Na$^+$) = 80 mmol L^{-1}
relative units
d/nm
5
10
15
20
25

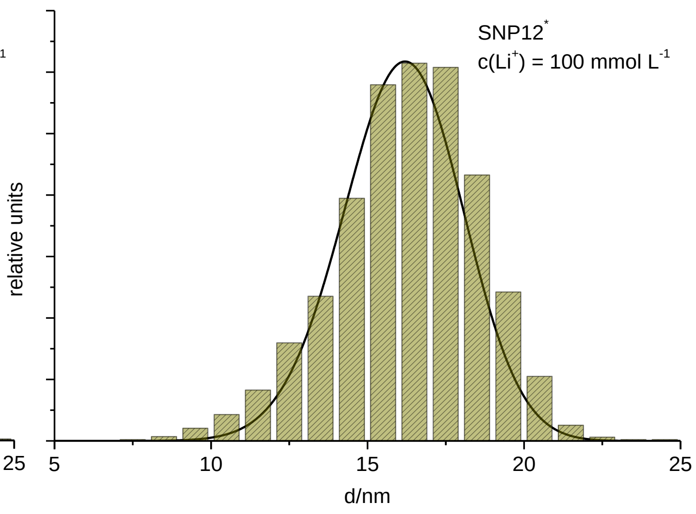
SNP12*
c(Li$^+$) = 100 mmol L^{-1}
relative units
d/nm
5
10
15
20
25

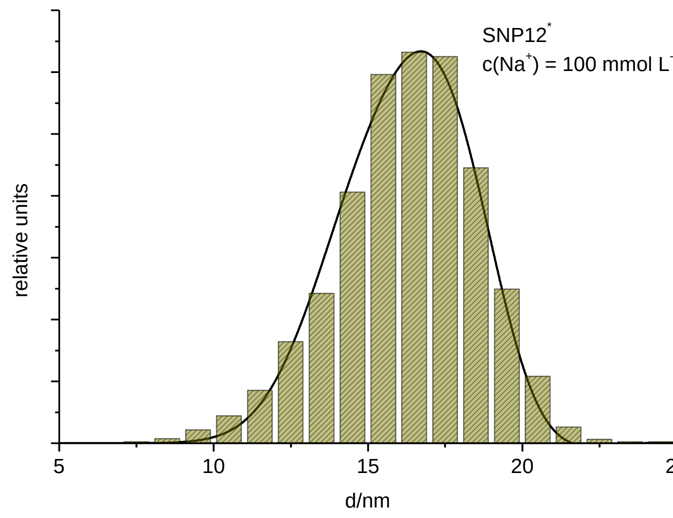
SNP12*
c(Na$^+$) = 100 mmol L^{-1}
relative units
d/nm
5
10
15
20
25

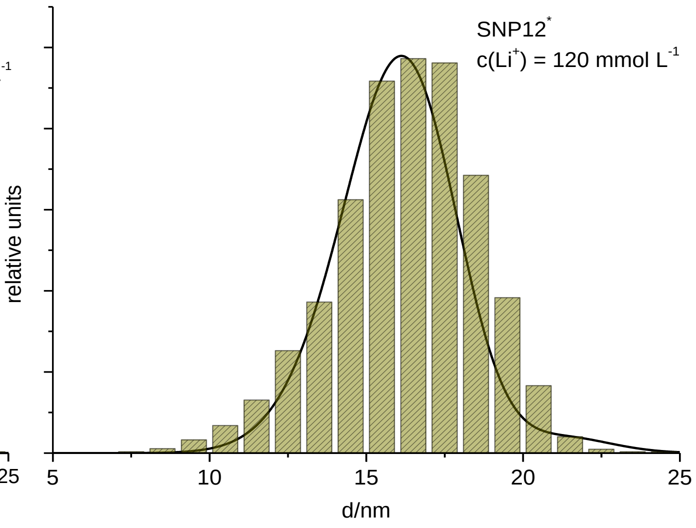
SNP12*
c(Li$^+$) = 120 mmol L^{-1}
relative units
d/nm
5
10
15
20
25

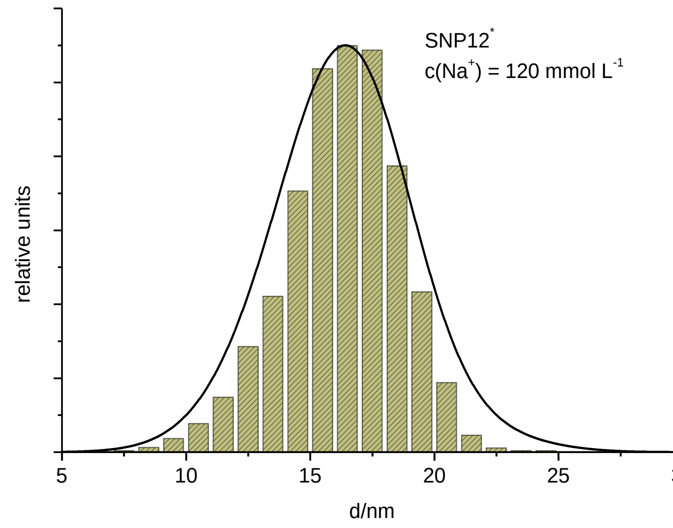
SNP12*
c(Na$^+$) = 120 mmol L^{-1}
relative units
d/nm
5
10
15
20
25
30

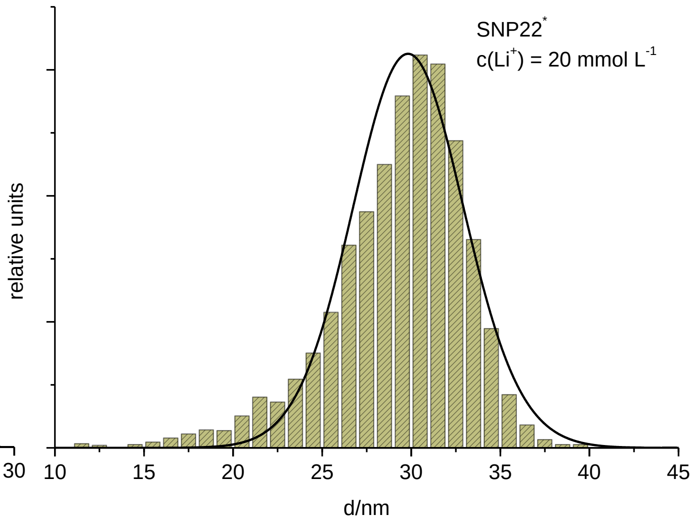
SNP22*
c(Li$^+$) = 20 mmol L^{-1}
relative units
d/nm
10
15
20
25
30
35
40
45

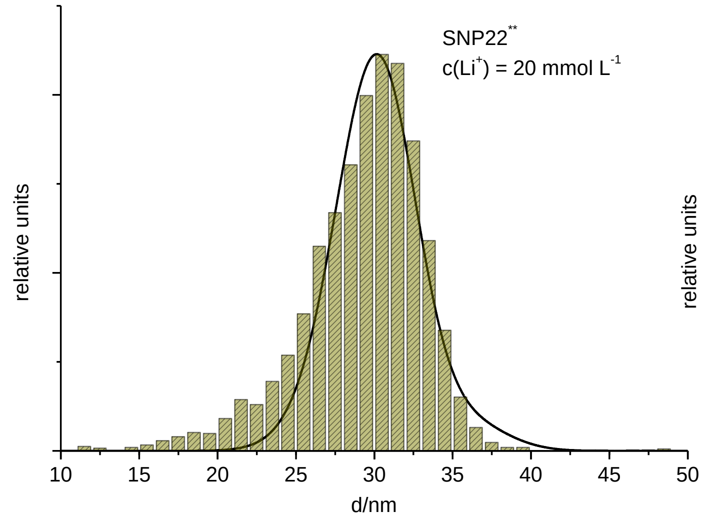
SNP22**
c(Li^{+}) = 20 mmol L^{-1}
relative units
10
15
20
25
30
35
40
45
50
d/nm

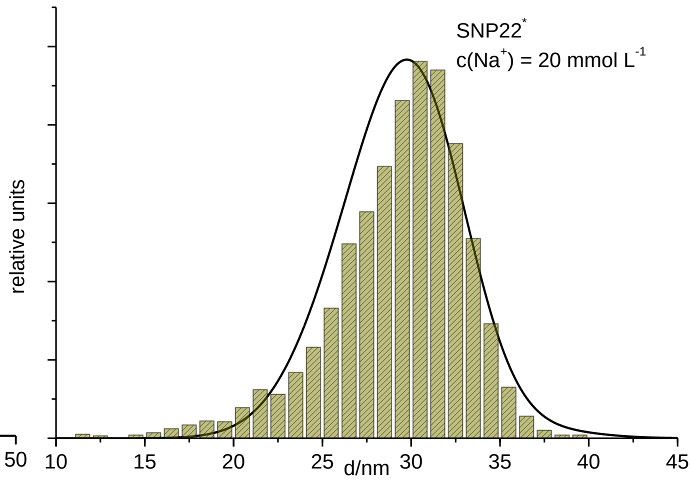
SNP22*
c(Na^{+}) = 20 mmol L^{-1}
relative units
10
15
20
25
30
35
40
45
d/nm

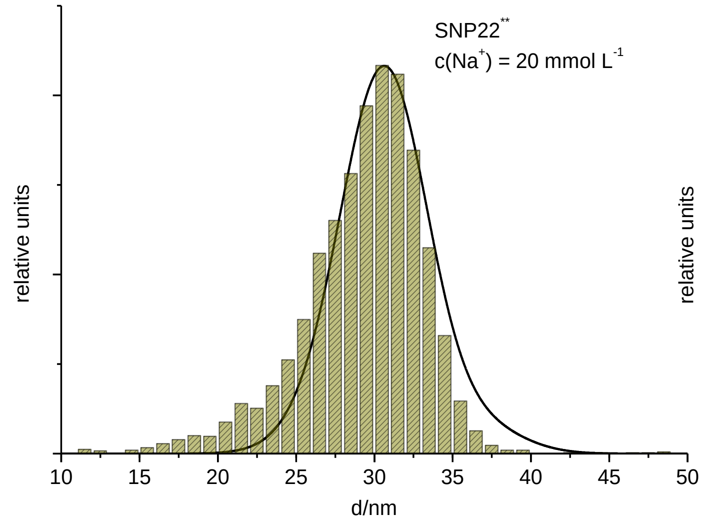
SNP22**
c(Na^{+}) = 20 mmol L^{-1}
relative units
10
15
20
25
30
35
40
45
50
d/nm

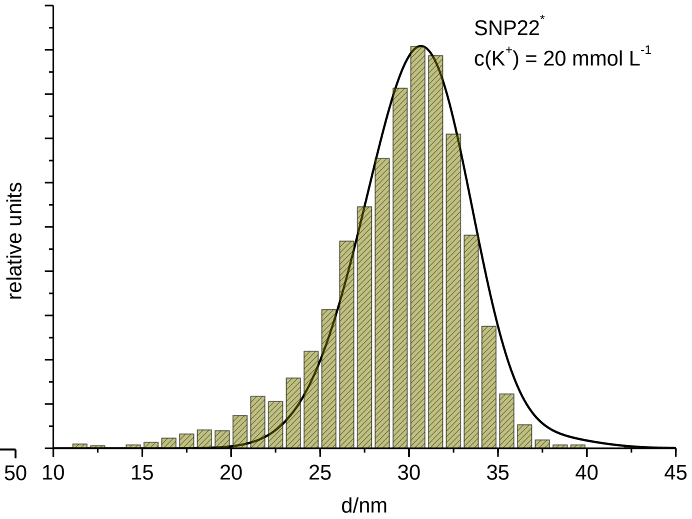
SNP22*
c(K^{+}) = 20 mmol L^{-1}
relative units
10
15
20
25
30
35
40
45
d/nm

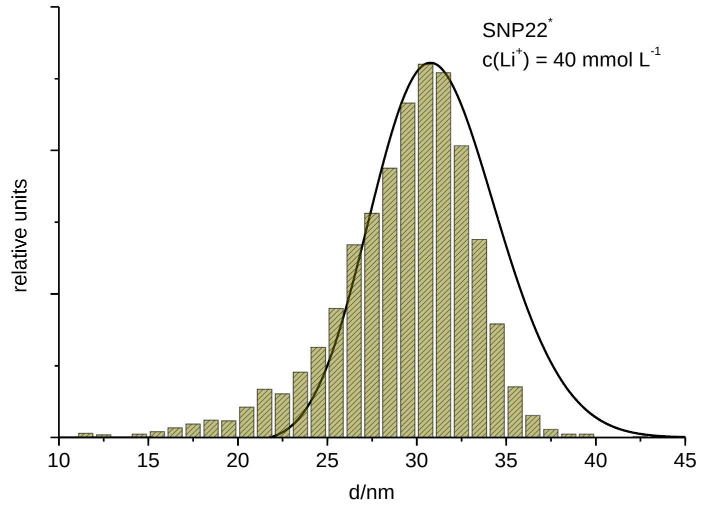
SNP22*
c(Li^{+}) = 40 mmol L^{-1}
relative units
10
15
20
25
30
35
40
45
d/nm

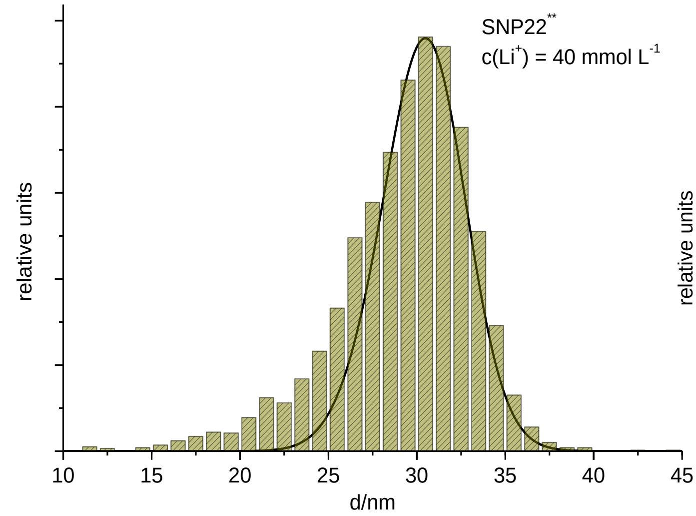
SNP22**
c(Li+) = 40 mmol L-1
relative units
d/nm
10
15
20
25
30
35
40
45

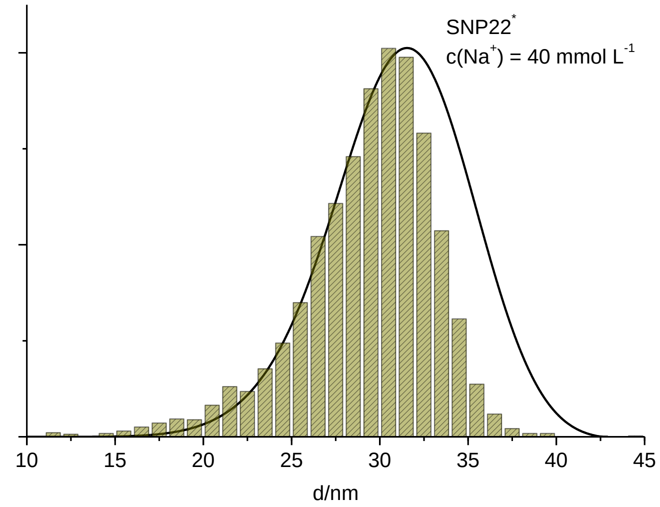
SNP22*
c(Na+) = 40 mmol L-1
relative units
d/nm
10
15
20
25
30
35
40
45

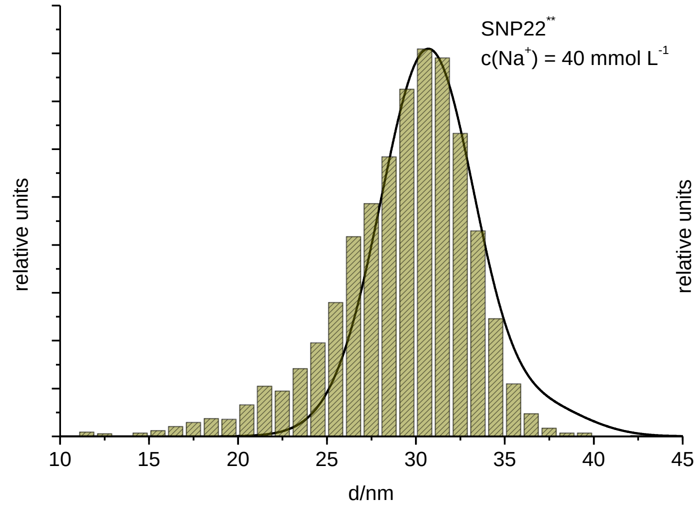
SNP22**
c(Na+) = 40 mmol L-1
relative units
d/nm
10
15
20
25
30
35
40
45

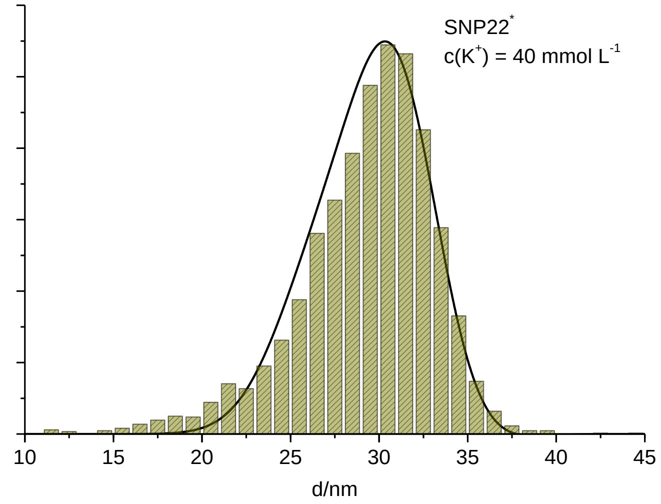
SNP22*
c(K+) = 40 mmol L-1
relative units
d/nm
10
15
20
25
30
35
40
45

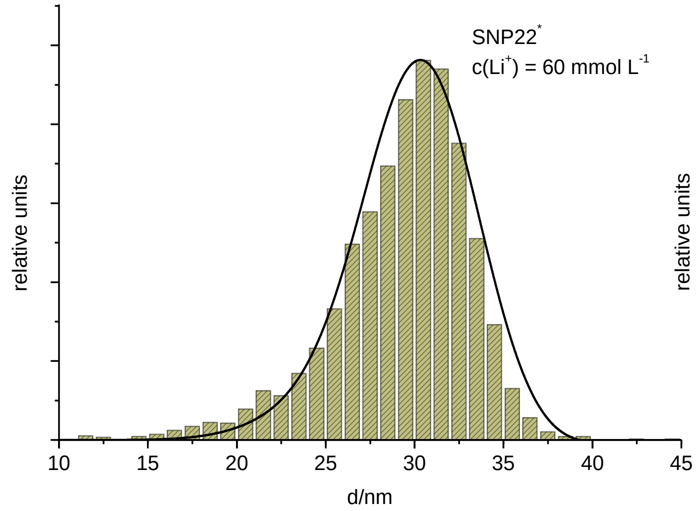
SNP22*
c(Li+) = 60 mmol L-1
relative units
d/nm
10
15
20
25
30
35
40
45

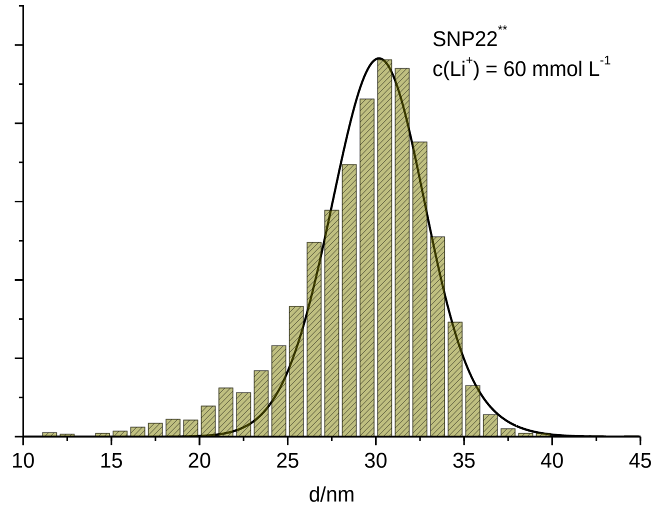
SNP22**
c(Li+) = 60 mmol L-1
relative units
d/nm
10
15
20
25
30
35
40
45

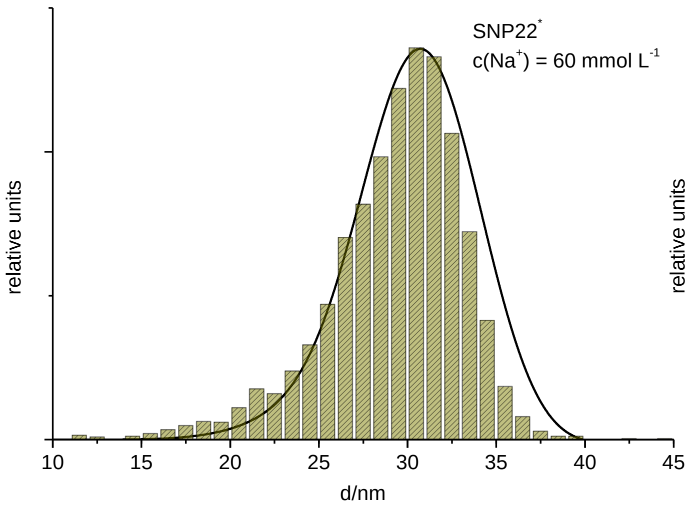
SNP22*
c(Na+) = 60 mmol L-1
relative units
d/nm
10
15
20
25
30
35
40
45

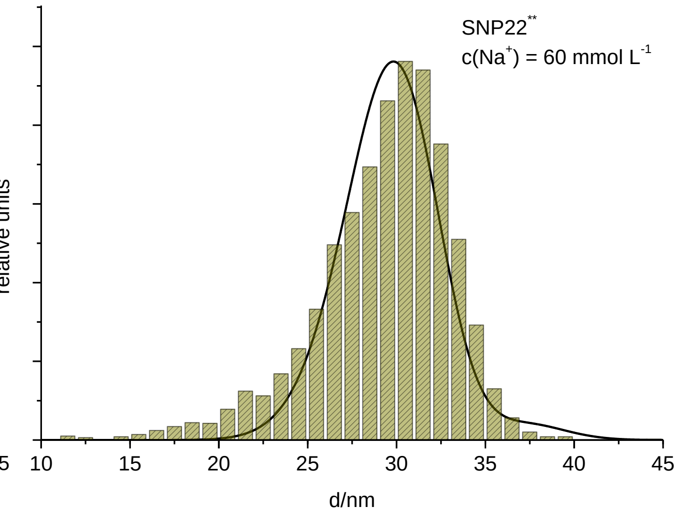
SNP22**
c(Na+) = 60 mmol L-1
relative units
d/nm
10
15
20
25
30
35
40
45

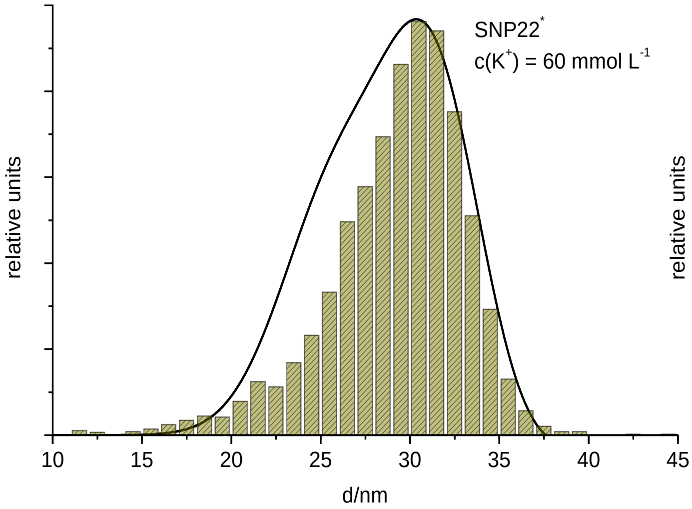
SNP22*
c(K+) = 60 mmol L-1
relative units
d/nm
10
15
20
25
30
35
40
45

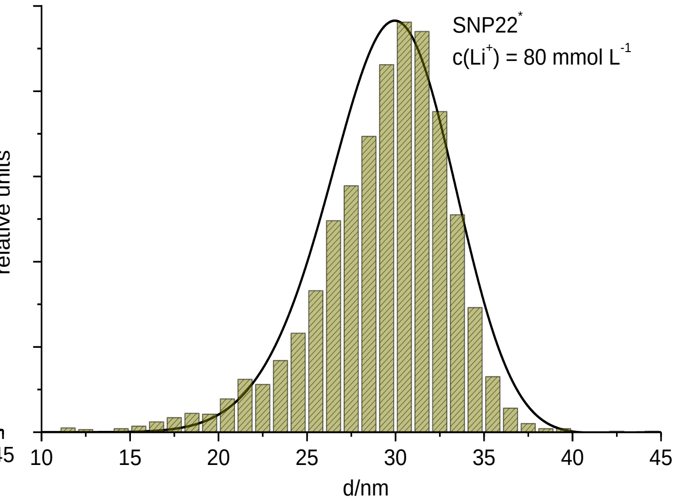
SNP22*
c(Li+) = 80 mmol L-1
relative units
d/nm
10
15
20
25
30
35
40
45

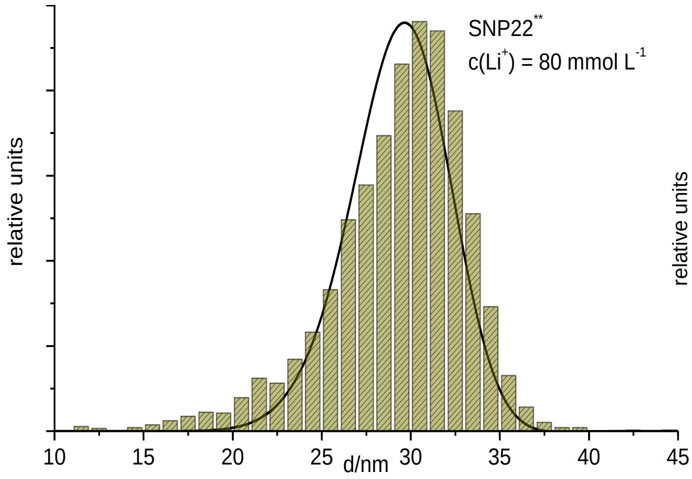
SNP22**
c(Li+) = 80 mmol L-1
relative units
d/nm
10
15
20
25
30
35
40
45

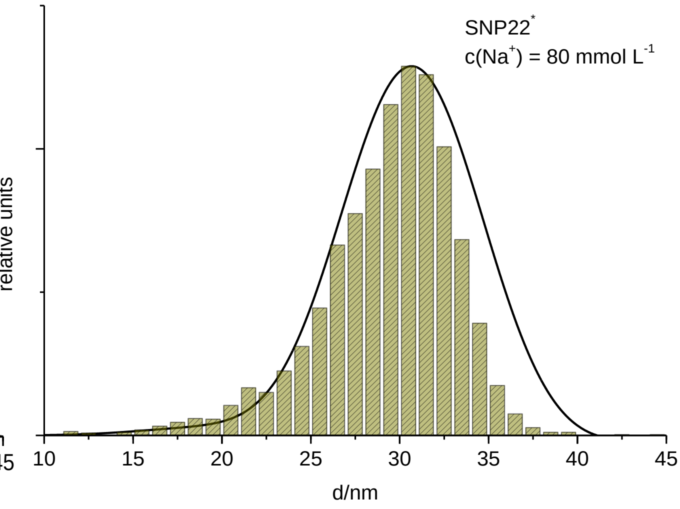
SNP22*
c(Na+) = 80 mmol L-1
relative units
d/nm
10
15
20
25
30
35
40
45

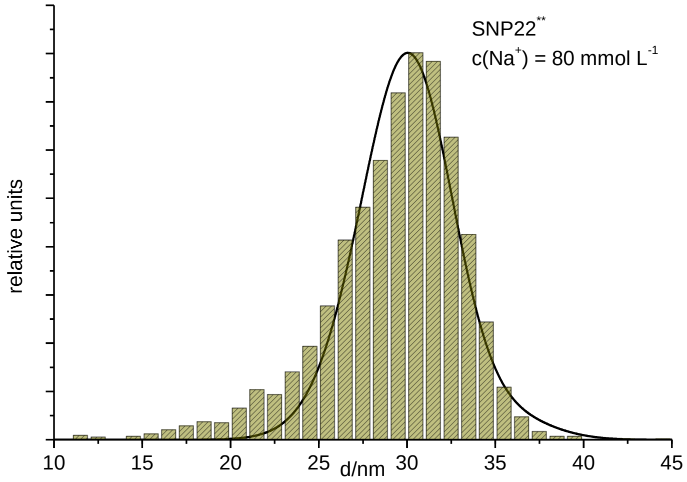
SNP22**
c(Na+) = 80 mmol L-1
relative units
10
15
20
25
30
35
40
45
d/nm

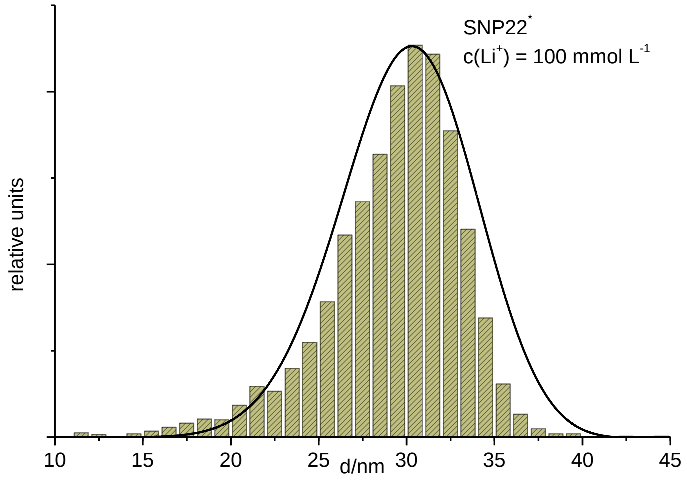
SNP22*
c(Li+) = 100 mmol L-1
relative units
10
15
20
25
30
35
40
45
d/nm

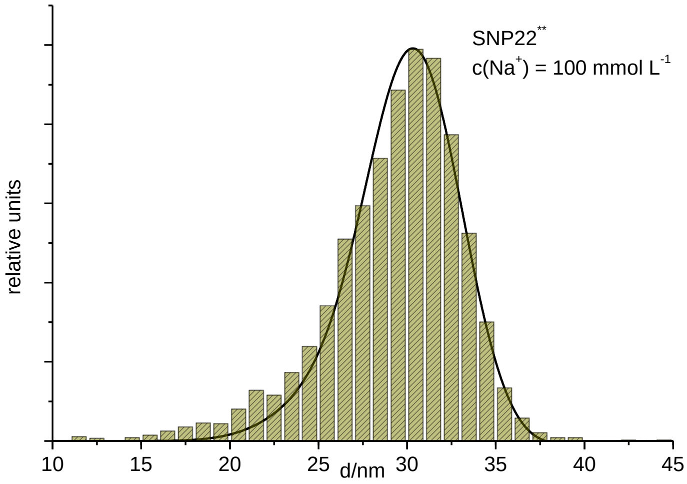
SNP22**
c(Na+) = 100 mmol L-1
relative units
10
15
20
25
30
35
40
45
d/nm

Appendix B1

The certificates of analysis for PSSL20, PSSL40, PSSL60, and PSSL80, respectively, were obtained from the manufacturing company.

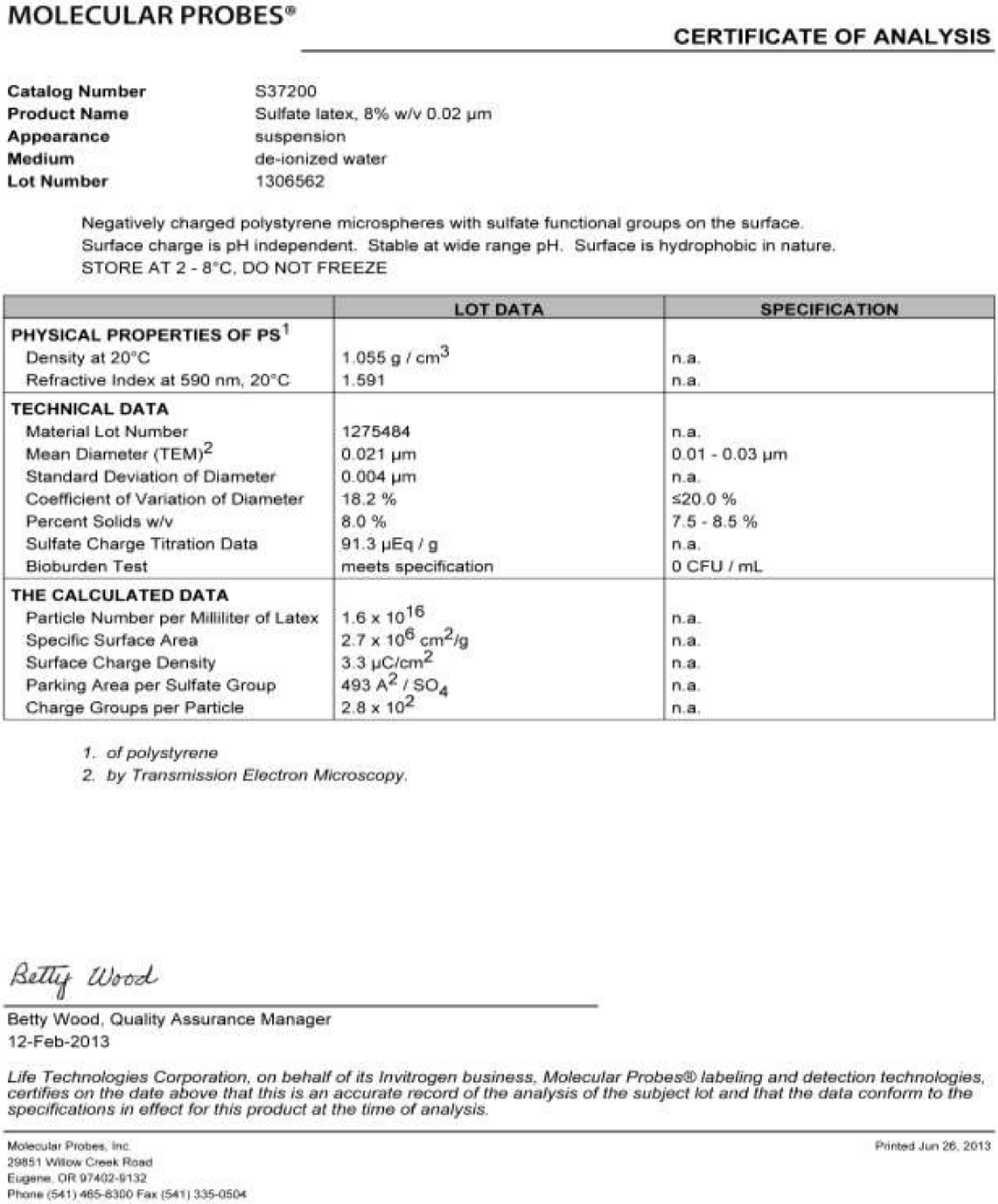

MOLECULAR PROBES®

CERTIFICATE OF ANALYSIS

Catalog Number	S37200
Product Name	Sulfate latex, 8% w/v 0.02 µm
Appearance	suspension
Medium	de-ionized water
Lot Number	1306562

Negatively charged polystyrene microspheres with sulfate functional groups on the surface.
Surface charge is pH independent. Stable at wide range pH. Surface is hydrophobic in nature.
STORE AT 2 - 8°C, DO NOT FREEZE

	LOT DATA	SPECIFICATION
PHYSICAL PROPERTIES OF PS[1]		
Density at 20°C	1.055 g / cm^3	n.a.
Refractive Index at 590 nm, 20°C	1.591	n.a.
TECHNICAL DATA		
Material Lot Number	1275484	n.a.
Mean Diameter (TEM)[2]	0.021 µm	0.01 - 0.03 µm
Standard Deviation of Diameter	0.004 µm	n.a.
Coefficient of Variation of Diameter	18.2 %	≤20.0 %
Percent Solids w/v	8.0 %	7.5 - 8.5 %
Sulfate Charge Titration Data	91.3 µEq / g	n.a.
Bioburden Test	meets specification	0 CFU / mL
THE CALCULATED DATA		
Particle Number per Milliliter of Latex	1.6×10^{16}	n.a.
Specific Surface Area	2.7×10^{6} cm^2/g	n.a.
Surface Charge Density	3.3 $\mu C/cm^2$	n.a.
Parking Area per Sulfate Group	493 A^2 / SO_4	n.a.
Charge Groups per Particle	2.8×10^{2}	n.a.

1. *of polystyrene*
2. *by Transmission Electron Microscopy.*

Betty Wood

Betty Wood, Quality Assurance Manager
12-Feb-2013

Life Technologies Corporation, on behalf of its Invitrogen business, Molecular Probes® labeling and detection technologies, certifies on the date above that this is an accurate record of the analysis of the subject lot and that the data conform to the specifications in effect for this product at the time of analysis.

Molecular Probes, Inc.
29851 Willow Creek Road
Eugene, OR 97402-9132
Phone (541) 465-8300 Fax (541) 335-0504

Printed Jun 26, 2013

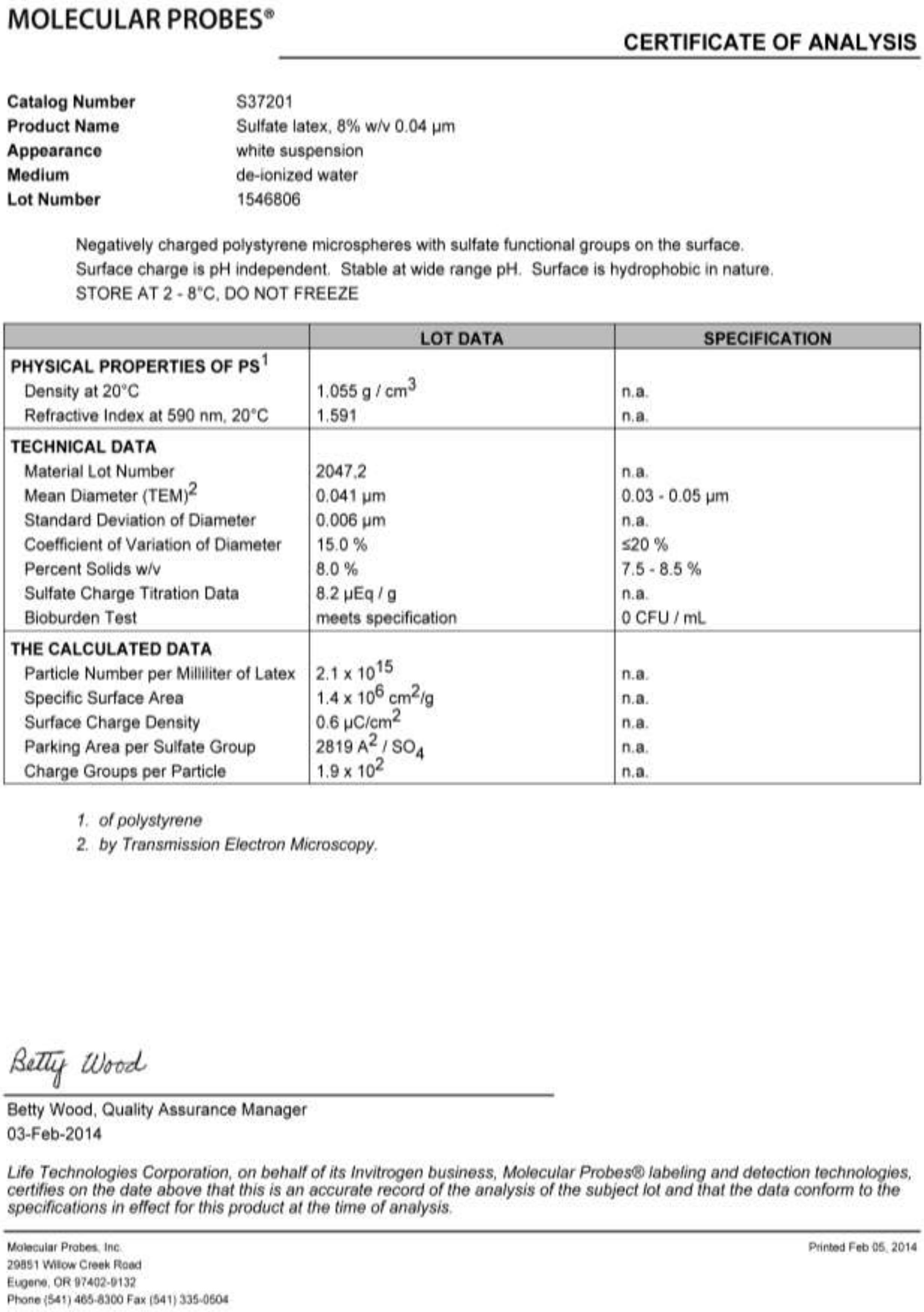

MOLECULAR PROBES®

CERTIFICATE OF ANALYSIS

Catalog Number	S37201
Product Name	Sulfate latex, 8% w/v 0.04 µm
Appearance	white suspension
Medium	de-ionized water
Lot Number	1546806

Negatively charged polystyrene microspheres with sulfate functional groups on the surface.
Surface charge is pH independent. Stable at wide range pH. Surface is hydrophobic in nature.
STORE AT 2 - 8°C, DO NOT FREEZE

	LOT DATA	SPECIFICATION
PHYSICAL PROPERTIES OF PS[1]		
Density at 20°C	1.055 g / cm^3	n.a.
Refractive Index at 590 nm, 20°C	1.591	n.a.
TECHNICAL DATA		
Material Lot Number	2047.2	n.a.
Mean Diameter (TEM)[2]	0.041 µm	0.03 - 0.05 µm
Standard Deviation of Diameter	0.006 µm	n.a.
Coefficient of Variation of Diameter	15.0 %	≤20 %
Percent Solids w/v	8.0 %	7.5 - 8.5 %
Sulfate Charge Titration Data	8.2 µEq / g	n.a.
Bioburden Test	meets specification	0 CFU / mL
THE CALCULATED DATA		
Particle Number per Milliliter of Latex	2.1×10^{15}	n.a.
Specific Surface Area	1.4×10^6 cm^2/g	n.a.
Surface Charge Density	0.6 µC/cm^2	n.a.
Parking Area per Sulfate Group	2819 A^2 / SO_4	n.a.
Charge Groups per Particle	1.9×10^2	n.a.

1. *of polystyrene*
2. *by Transmission Electron Microscopy.*

Betty Wood

Betty Wood, Quality Assurance Manager
03-Feb-2014

Life Technologies Corporation, on behalf of its Invitrogen business, Molecular Probes® labeling and detection technologies, certifies on the date above that this is an accurate record of the analysis of the subject lot and that the data conform to the specifications in effect for this product at the time of analysis.

Molecular Probes, Inc.
29851 Willow Creek Road
Eugene, OR 97402-9132
Phone (541) 465-8300 Fax (541) 335-0504

Printed Feb 05, 2014

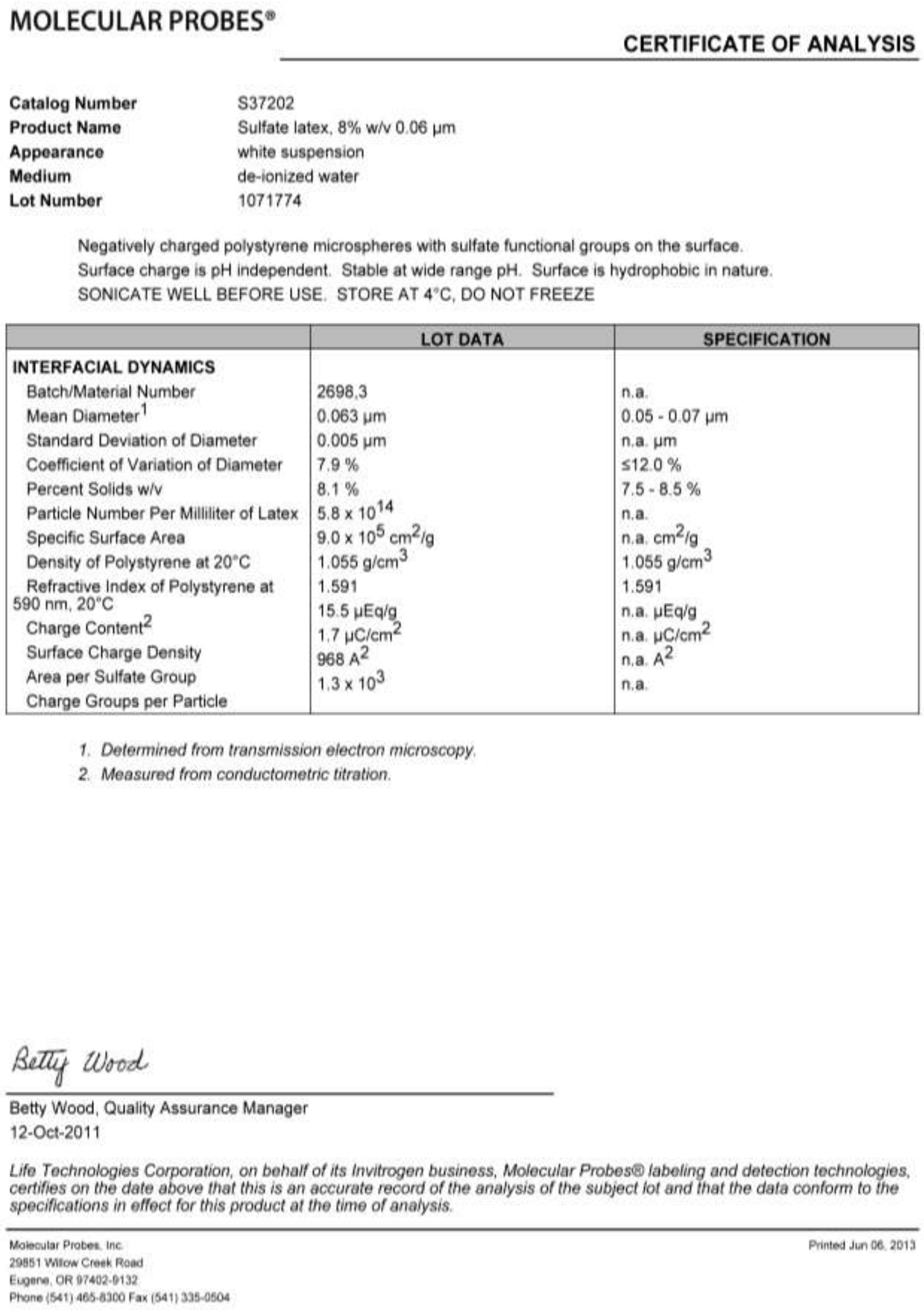

MOLECULAR PROBES®

CERTIFICATE OF ANALYSIS

Catalog Number	S37202
Product Name	Sulfate latex, 8% w/v 0.06 µm
Appearance	white suspension
Medium	de-ionized water
Lot Number	1071774

Negatively charged polystyrene microspheres with sulfate functional groups on the surface.
Surface charge is pH independent. Stable at wide range pH. Surface is hydrophobic in nature.
SONICATE WELL BEFORE USE. STORE AT 4°C, DO NOT FREEZE

	LOT DATA	SPECIFICATION
INTERFACIAL DYNAMICS		
Batch/Material Number	2698,3	n.a.
Mean Diameter[1]	0.063 µm	0.05 - 0.07 µm
Standard Deviation of Diameter	0.005 µm	n.a. µm
Coefficient of Variation of Diameter	7.9 %	≤12.0 %
Percent Solids w/v	8.1 %	7.5 - 8.5 %
Particle Number Per Milliliter of Latex	5.8×10^{14}	n.a.
Specific Surface Area	9.0×10^{5} cm^2/g	n.a. cm^2/g
Density of Polystyrene at 20°C	1.055 g/cm^3	1.055 g/cm^3
Refractive Index of Polystyrene at 590 nm, 20°C	1.591	1.591
Charge Content[2]	15.5 µEq/g	n.a. µEq/g
Surface Charge Density	1.7 $\mu C/cm^2$	n.a. $\mu C/cm^2$
Area per Sulfate Group	968 A^2	n.a. A^2
Charge Groups per Particle	1.3×10^{3}	n.a.

1. *Determined from transmission electron microscopy.*
2. *Measured from conductometric titration.*

Betty Wood

Betty Wood, Quality Assurance Manager
12-Oct-2011

Life Technologies Corporation, on behalf of its Invitrogen business, Molecular Probes® labeling and detection technologies, certifies on the date above that this is an accurate record of the analysis of the subject lot and that the data conform to the specifications in effect for this product at the time of analysis.

Molecular Probes, Inc.
29851 Willow Creek Road
Eugene, OR 97402-9132
Phone (541) 465-8300 Fax (541) 335-0504

Printed Jun 06, 2013

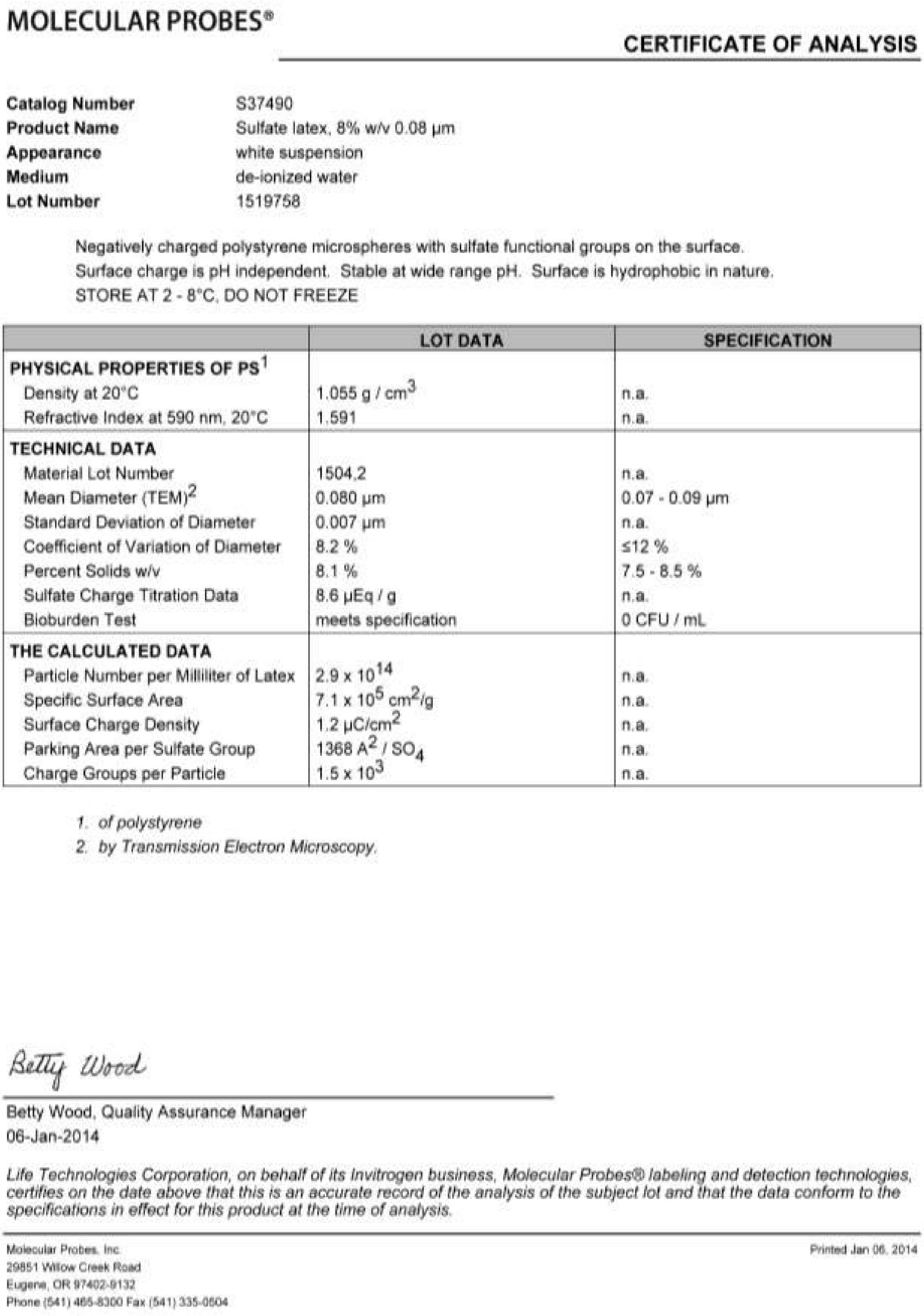

MOLECULAR PROBES®

CERTIFICATE OF ANALYSIS

Catalog Number	S37490
Product Name	Sulfate latex, 8% w/v 0.08 µm
Appearance	white suspension
Medium	de-ionized water
Lot Number	1519758

Negatively charged polystyrene microspheres with sulfate functional groups on the surface.
Surface charge is pH independent. Stable at wide range pH. Surface is hydrophobic in nature.
STORE AT 2 - 8°C, DO NOT FREEZE

	LOT DATA	SPECIFICATION
PHYSICAL PROPERTIES OF PS[1]		
Density at 20°C	1.055 g / cm^3	n.a.
Refractive Index at 590 nm, 20°C	1.591	n.a.
TECHNICAL DATA		
Material Lot Number	1504,2	n.a.
Mean Diameter (TEM)[2]	0.080 µm	0.07 - 0.09 µm
Standard Deviation of Diameter	0.007 µm	n.a.
Coefficient of Variation of Diameter	8.2 %	≤12 %
Percent Solids w/v	8.1 %	7.5 - 8.5 %
Sulfate Charge Titration Data	8.6 µEq / g	n.a.
Bioburden Test	meets specification	0 CFU / mL
THE CALCULATED DATA		
Particle Number per Milliliter of Latex	2.9×10^{14}	n.a.
Specific Surface Area	7.1×10^5 cm^2/g	n.a.
Surface Charge Density	1.2 $\mu C/cm^2$	n.a.
Parking Area per Sulfate Group	1368 A^2 / SO_4	n.a.
Charge Groups per Particle	1.5×10^3	n.a.

1. *of polystyrene*
2. *by Transmission Electron Microscopy.*

Betty Wood

Betty Wood, Quality Assurance Manager
06-Jan-2014

Life Technologies Corporation, on behalf of its Invitrogen business, Molecular Probes® labeling and detection technologies, certifies on the date above that this is an accurate record of the analysis of the subject lot and that the data conform to the specifications in effect for this product at the time of analysis.

Molecular Probes, Inc.
29851 Willow Creek Road
Eugene, OR 97402-9132
Phone (541) 465-8300 Fax (541) 335-0504

Printed Jan 06, 2014

Appendix B2

Recorded eluent traces (absorbance A at 214 nm versus time t) for: (1) PSSL20, (2) PSSL40, (3) PSSL60 and (4) PSSL80 in different concentrations: (a) 2 x 10^{-3} (% w/w), (b) 4 x 10^{-3} (% w/w), (c) 6 x 10^{-3} (% w/w) and (d) 8 x 10^{-3} (% w/w) with 8 mmol L^{-1} borax buffer; black = recorded trace, red = fitted curve.

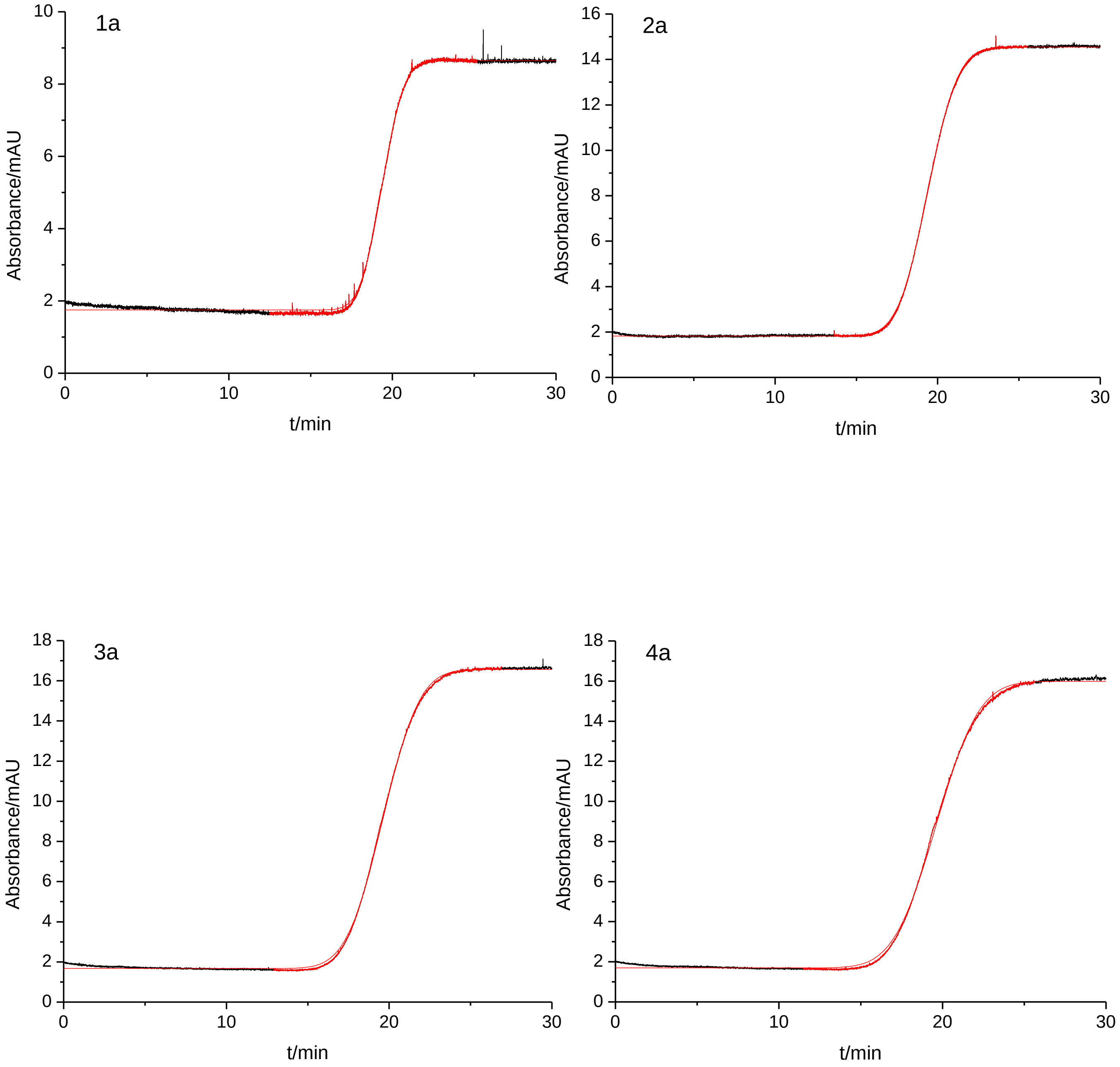

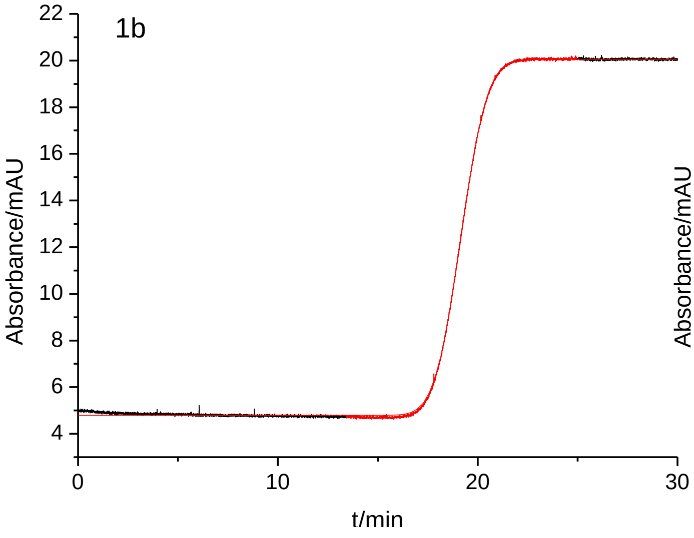
1b
Absorbance/mAU
22
20
18
16
14
12
10
8
6
4
0
10
20
30
t/min

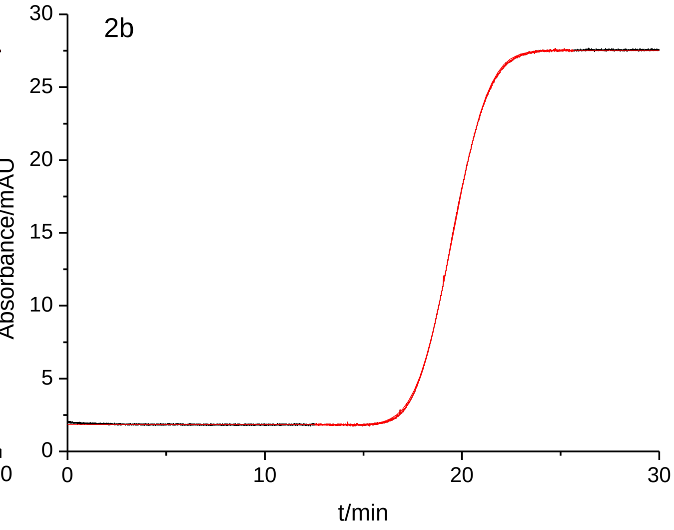
2b
Absorbance/mAU
30
25
20
15
10
5
0
0
10
20
30
t/min

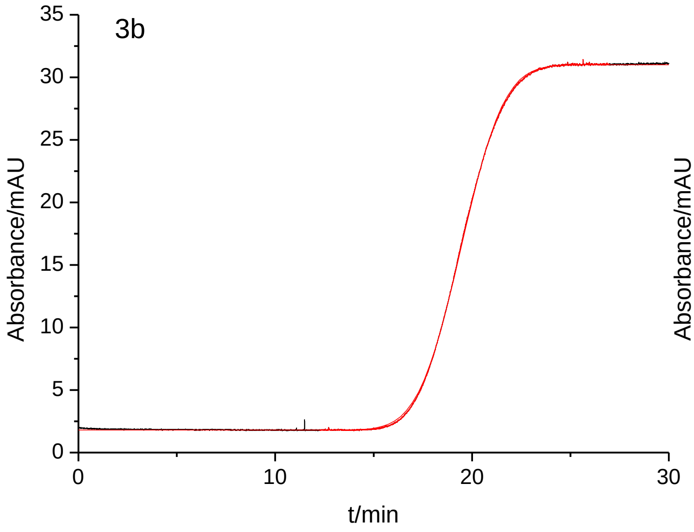
3b
Absorbance/mAU
35
30
25
20
15
10
5
0
0
10
20
30
t/min

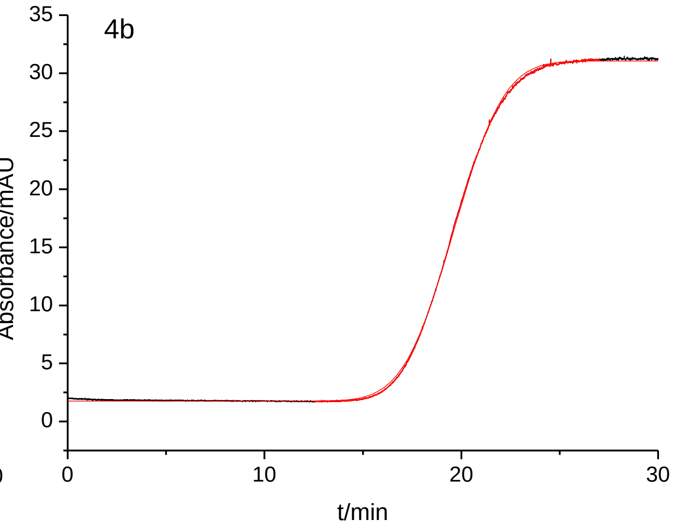
4b
Absorbance/mAU
35
30
25
20
15
10
5
0
0
10
20
30
t/min

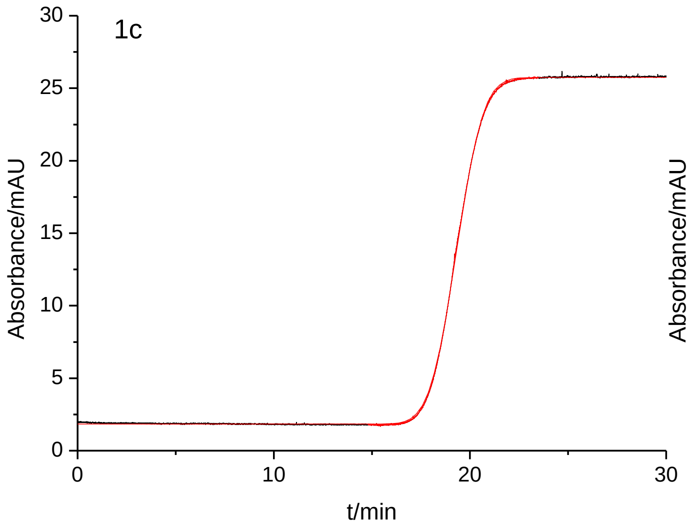
1c
Absorbance/mAU
30
25
20
15
10
5
0
0
10
20
30
t/min

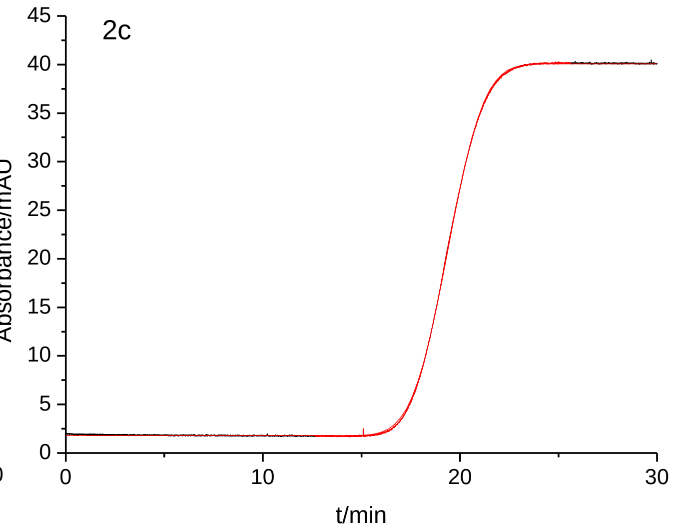
2c
Absorbance/mAU
45
40
35
30
25
20
15
10
5
0
0
10
20
30
t/min

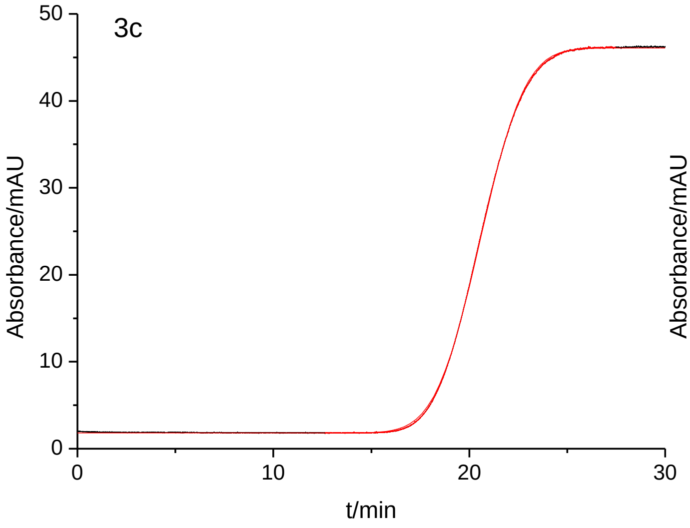
3c
Absorbance/mAU
0
10
20
30
40
50
t/min
0
10
20
30

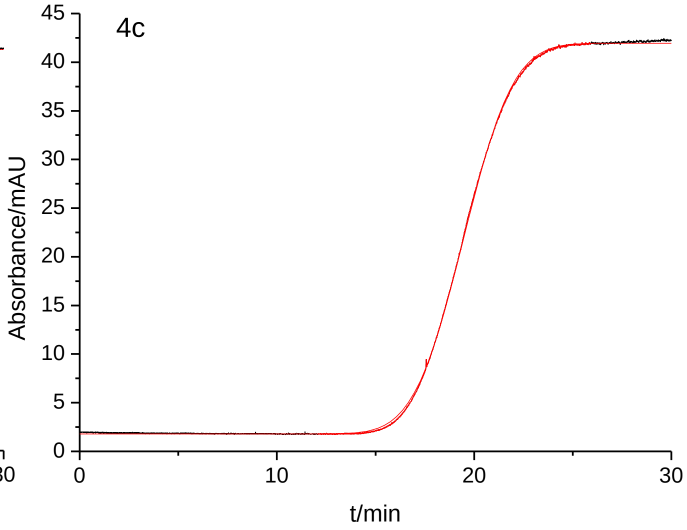
4c
Absorbance/mAU
0
5
10
15
20
25
30
35
40
45
t/min
0
10
20
30

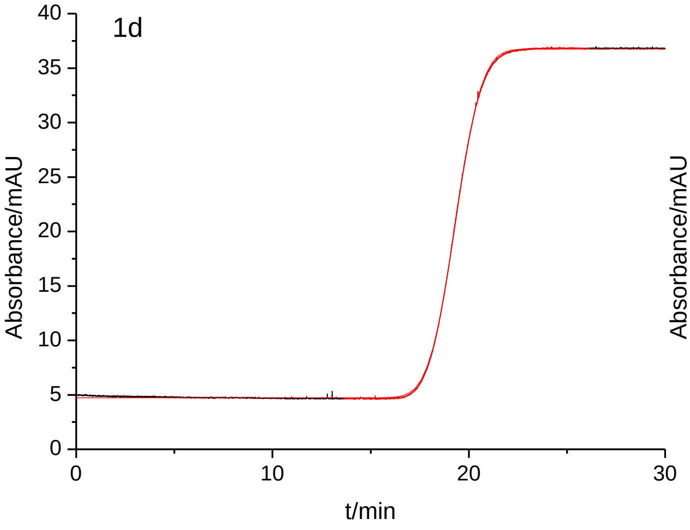
1d
Absorbance/mAU
0
5
10
15
20
25
30
35
40
t/min
0
10
20
30

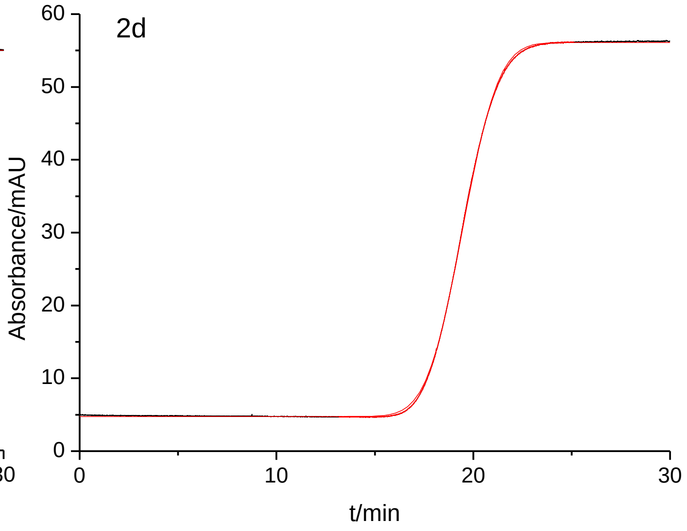
2d
Absorbance/mAU
0
10
20
30
40
50
60
t/min
0
10
20
30

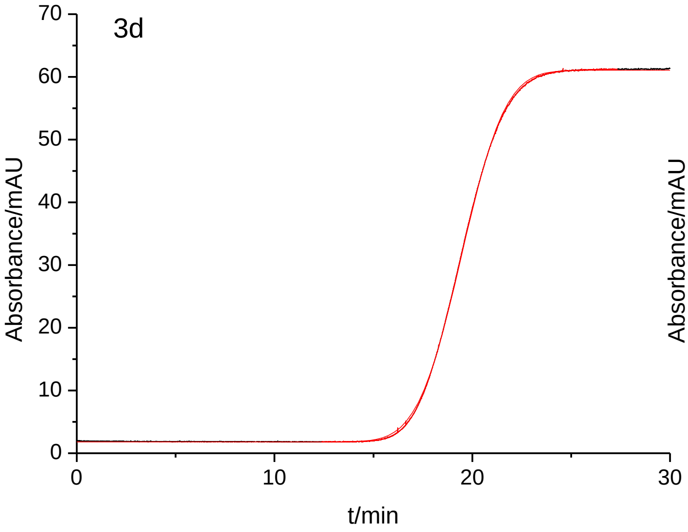
3d
Absorbance/mAU
0
10
20
30
40
50
60
70
t/min
0
10
20
30

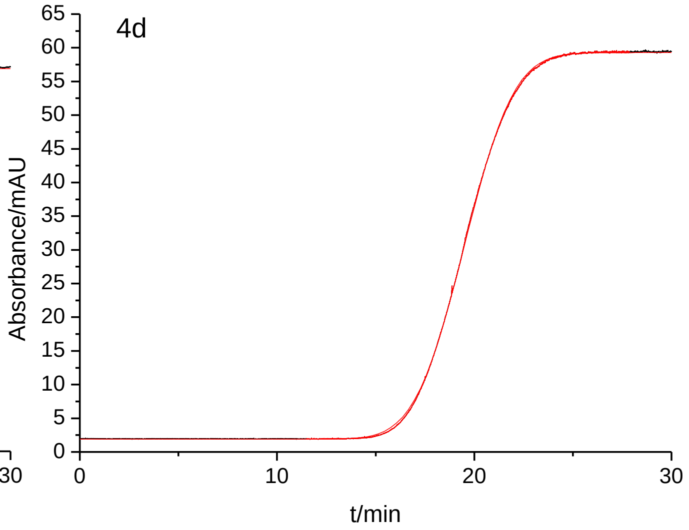
4d
Absorbance/mAU
0
5
10
15
20
25
30
35
40
45
50
55
60
65
t/min
0
10
20
30

Appendix B3

Recorded eluent traces (absorbance A at 214 nm versus time t) for: (1) PSSL20 and (2) PSSL40 with different ionic strength: (a) 4; (b) 8; (c) 12; (d) 16 and (e) 20 mmol L^{-1} borax buffer; black = recorded trace, red = fitted curve.

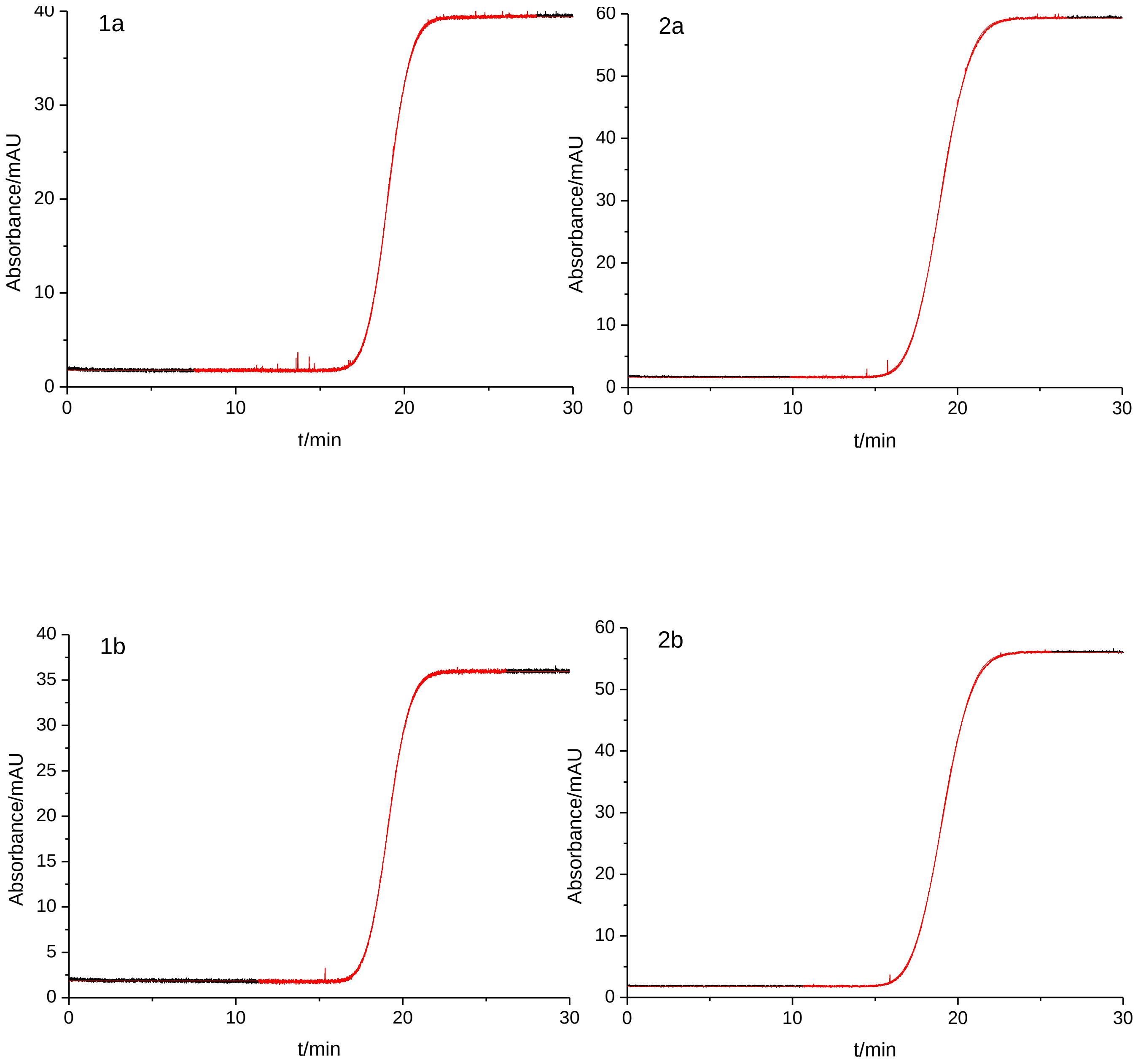

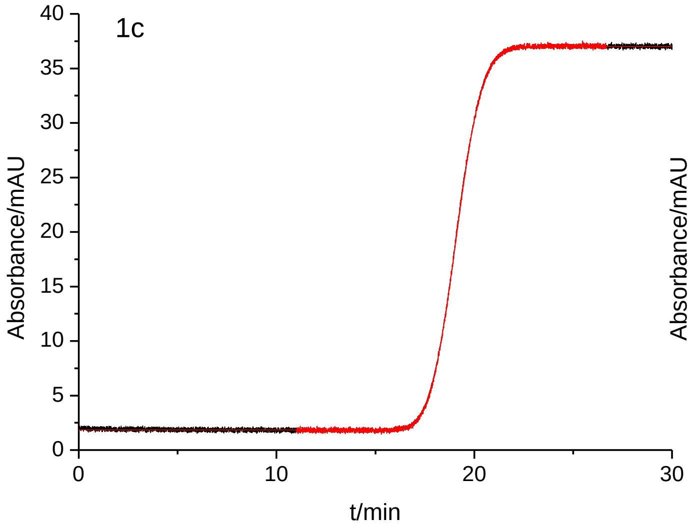
1c
Absorbance/mAU
t/min
0
5
10
15
20
25
30
35
40
0
10
20
30

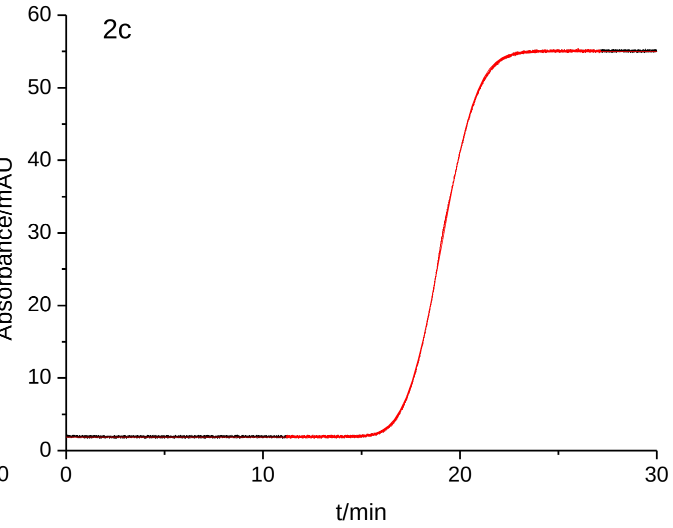
2c
Absorbance/mAU
t/min
0
10
20
30
40
50
60
0
10
20
30

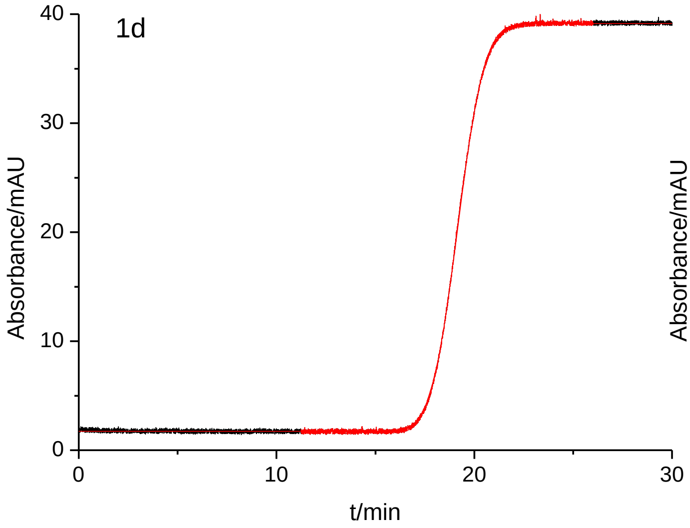
1d
Absorbance/mAU
t/min
0
10
20
30
40
0
10
20
30

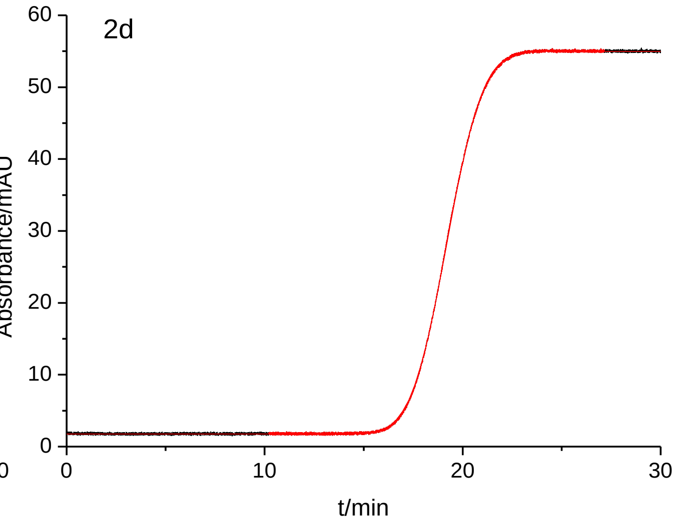
2d
Absorbance/mAU
t/min
0
10
20
30
40
50
60
0
10
20
30

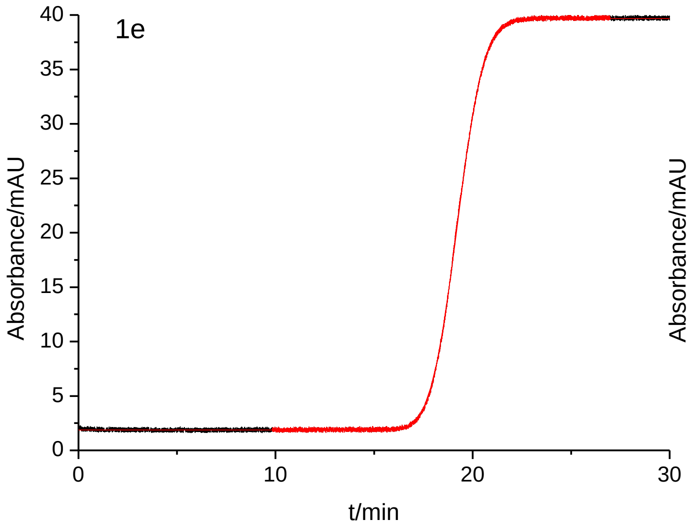
1e
Absorbance/mAU
t/min
0
5
10
15
20
25
30
35
40
0
10
20
30

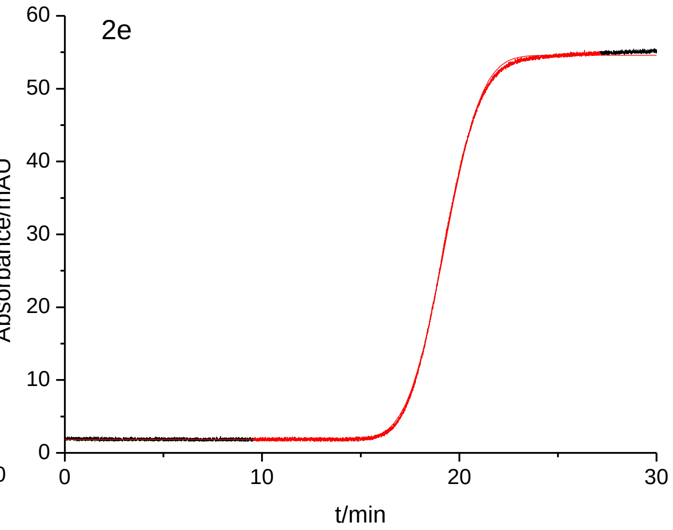
2e
Absorbance/mAU
t/min
0
10
20
30
40
50
60
0
10
20
30

Appendix B4

Superimposed electropherograms obtained in consecutive runs for different sizes of PSSL particles with a various concentrations of borax: (a) 5; (b) 10; (c) 20 and (d) 25 mmol L^{-1}; t_o= thiourea as a neutral marker. Experimental conditions: T= 20°C, total length of capillary = 60.7 cm, capillary length to detector = 50.5 cm, inner diameter of fused silica capillary = 76 μm, separation voltage 14 kV, sample injection 0.1 psi (6.89 mbar) 6 s, data rate 16 Hz, absorbance detection.

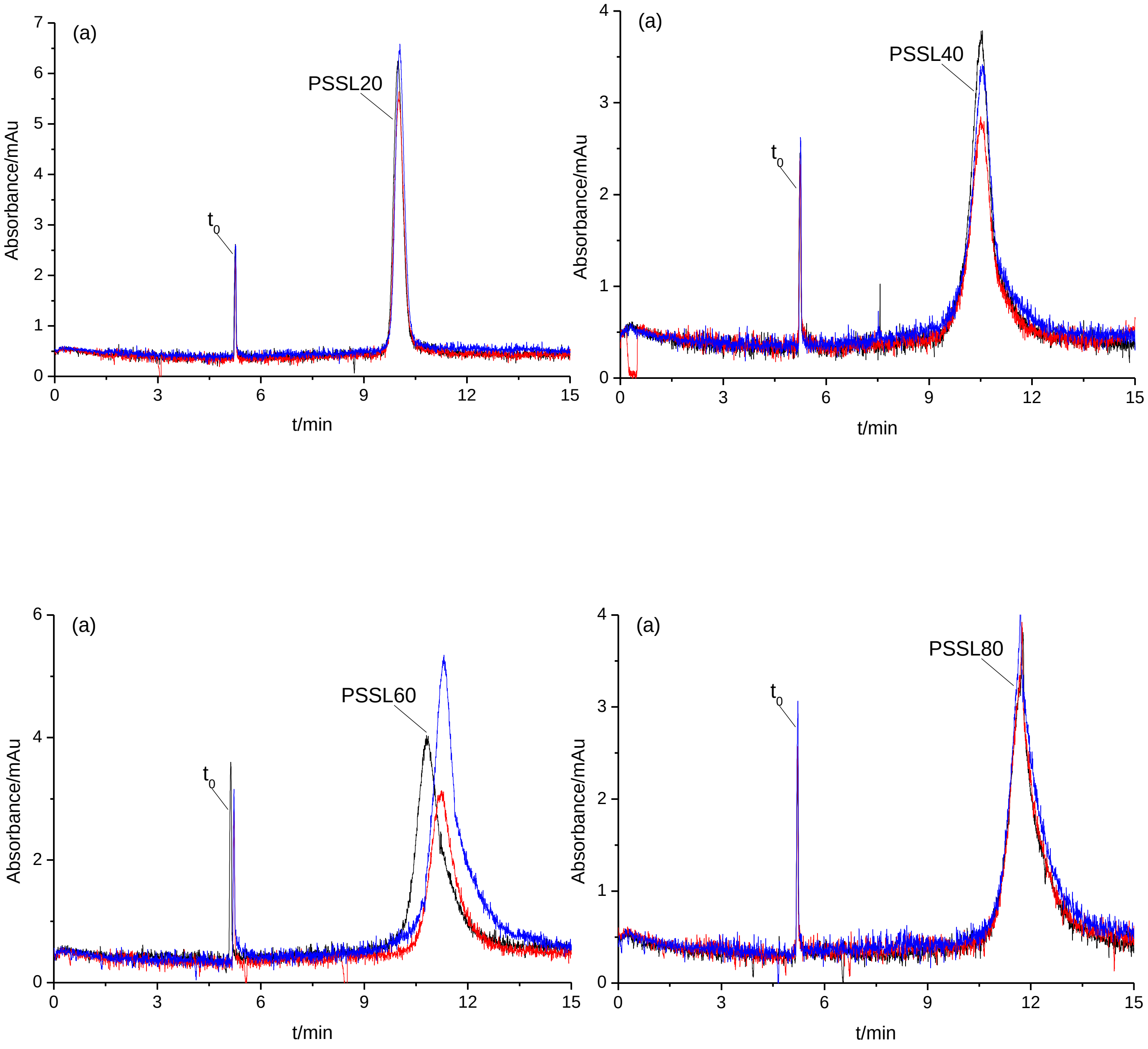

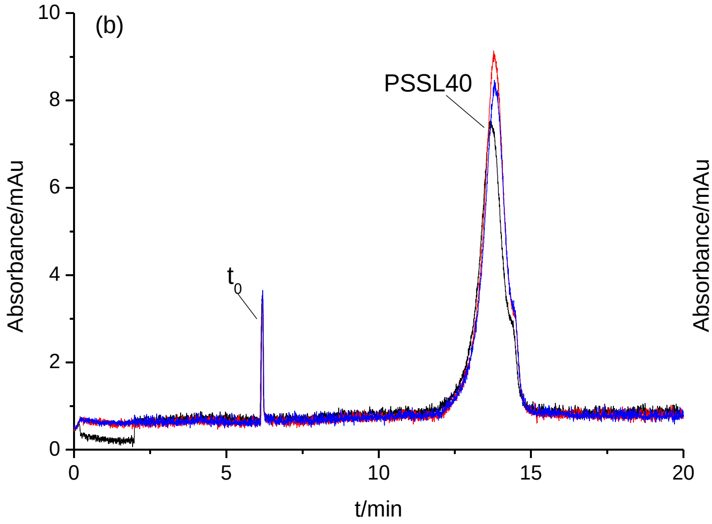
(b)
PSSL40
t0
Absorbance/mAu
t/min
0
2
4
6
8
10
0
5
10
15
20

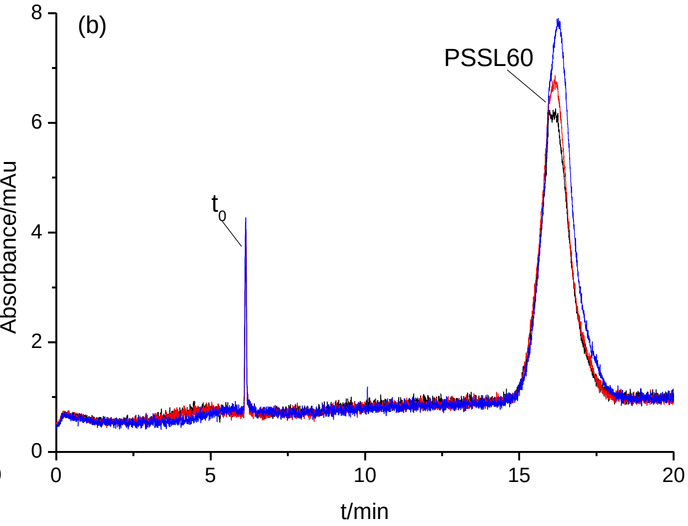
(b)
PSSL60
t0
Absorbance/mAu
t/min
0
2
4
6
8
0
5
10
15
20

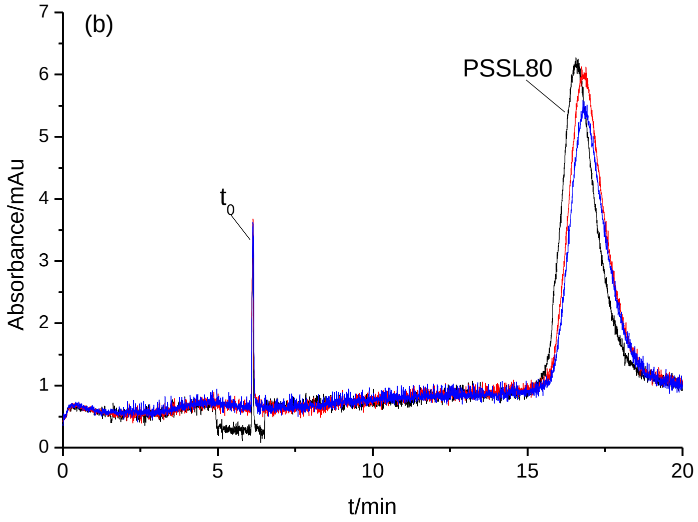
(b)
PSSL80
t0
Absorbance/mAu
t/min
0
1
2
3
4
5
6
7
0
5
10
15
20

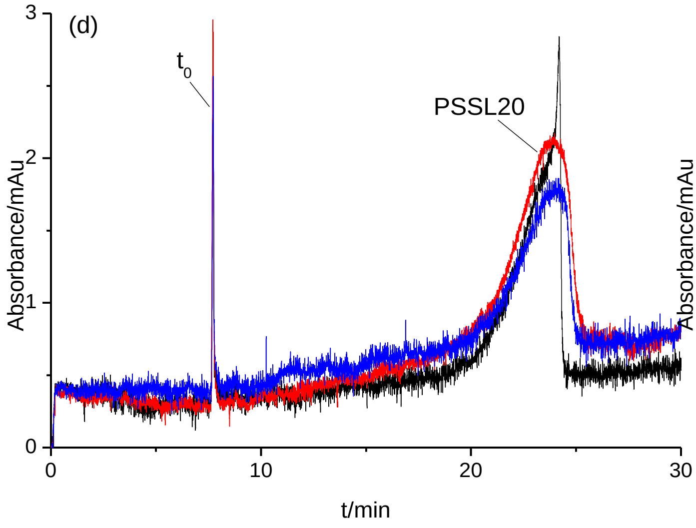
(d)
t0
PSSL20
Absorbance/mAu
t/min
0
1
2
3
0
10
20
30

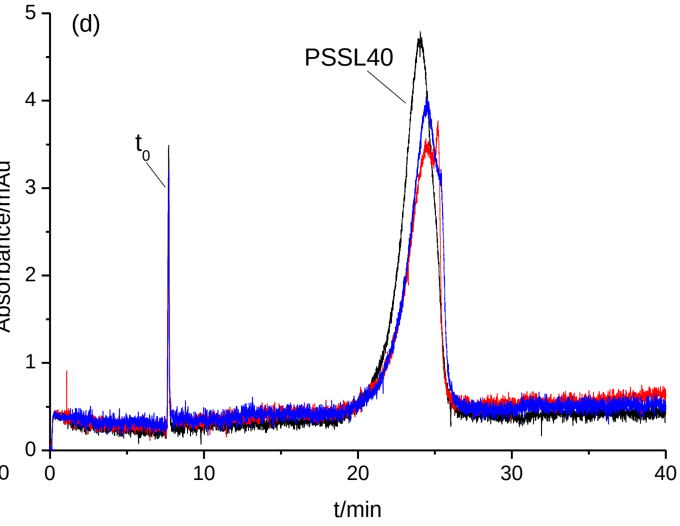
(d)
PSSL40
t0
Absorbance/mAu
t/min
0
1
2
3
4
5
0
10
20
30
40

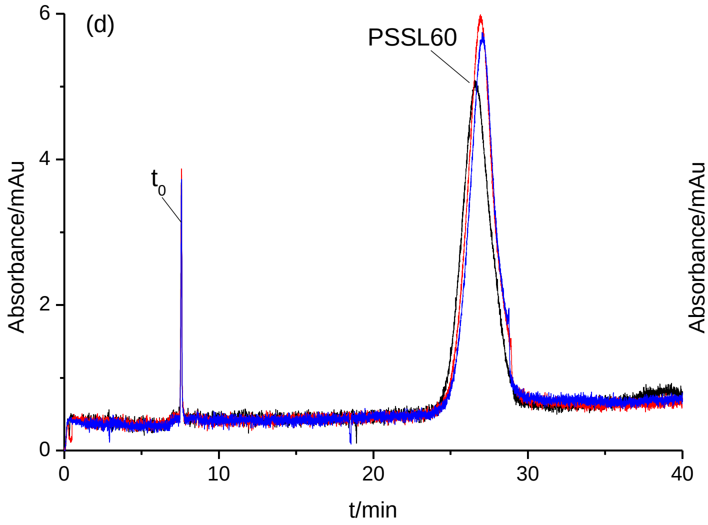
(d)
PSSL60
t0
Absorbance/mAu
t/min
0
2
4
6
0
10
20
30
40

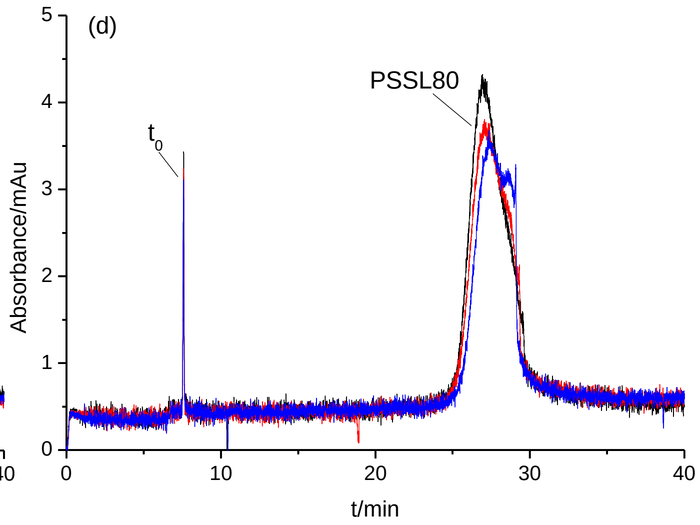
(d)
PSSL80
t0
Absorbance/mAu
t/min
0
1
2
3
4
5
0
10
20
30
40

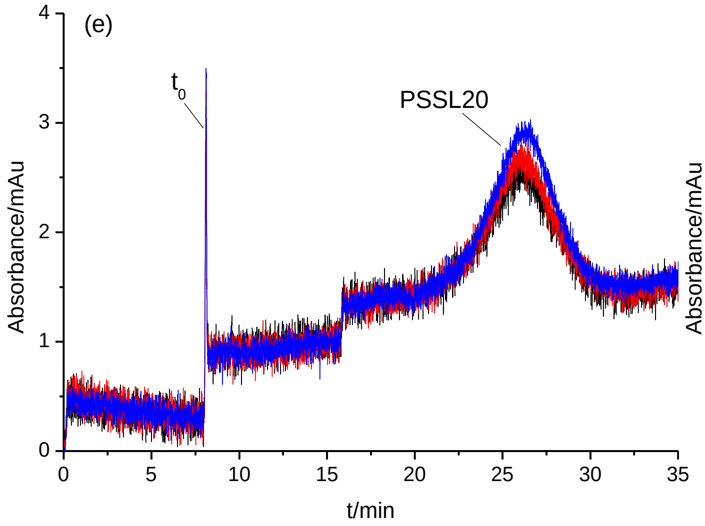
(e)
PSSL20
t0
Absorbance/mAu
t/min
0
1
2
3
4
0
5
10
15
20
25
30
35

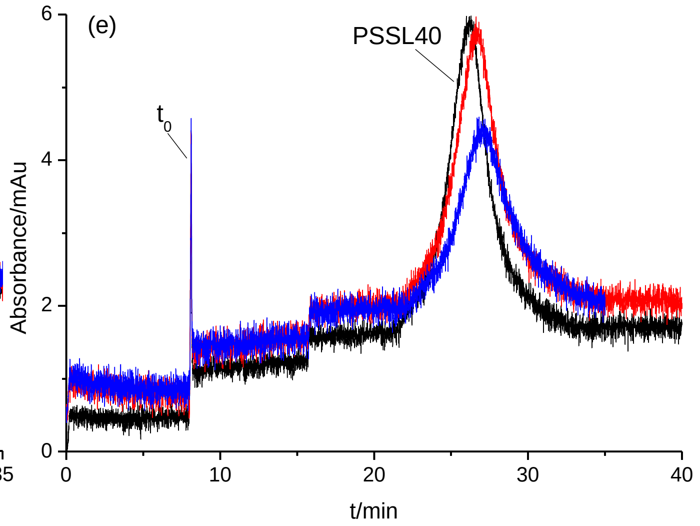
(e)
PSSL40
t0
Absorbance/mAu
t/min
0
2
4
6
0
10
20
30
40

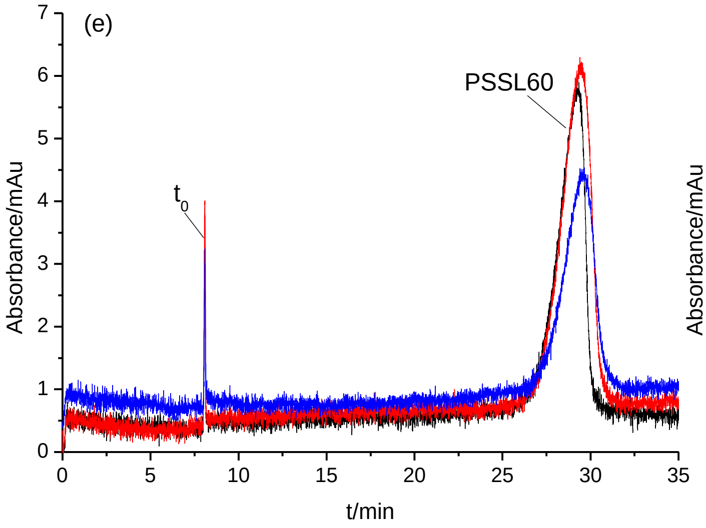
(e)
PSSL60
t0
Absorbance/mAu
t/min
0
1
2
3
4
5
6
7
0
5
10
15
20
25
30
35

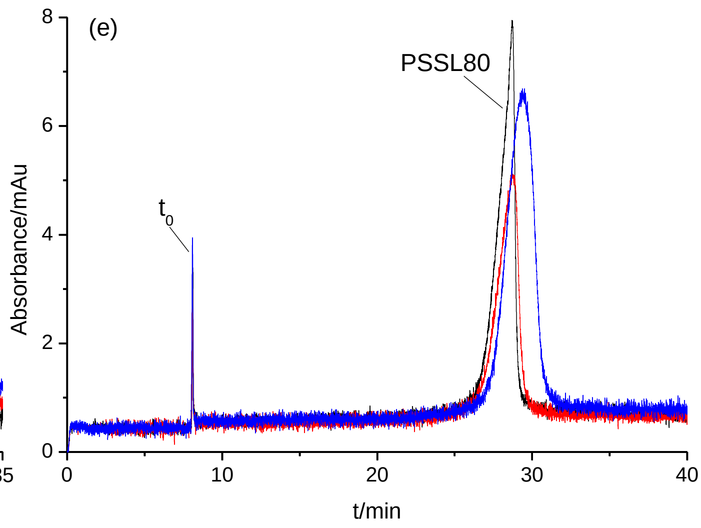
(e)
PSSL80
t0
Absorbance/mAu
t/min
0
2
4
6
8
0
10
20
30
40

Appendix B5

Measured electrophoretic mobilities μ_{ep} and electroosmotic mobilities μ_{eo} of different sizes for polystyrene sulfate latex (PSSL) with a various concentrations of borax, the following experimental conditions: T= 20°C, total length of capillary = 60.7 cm, capillary length to detector = 50.5 cm, inner diameter of fused silica capillary = 76 μm, separation voltage 14 kV, sample injection 0.1 psi (6.89 mbar) 6 s, data rate 16 Hz, absorbance detection.

PSSL		**PSSL20**		**PSSL40**		**PSSL60**		**PSSL80**	
buffet conc./ (mmol L^{-1})	**run**	**μ_{eo}/ (10^{-8} m^2 s^{-1} V^{-1})**	**μ_{ep}/ (10^{-8} m^2 s^{-1} V^{-1})**	**μ_{eo}/ (10^{-8} m^2 s^{-1} V^{-1})**	**μ_{ep}/ (10^{-8} m^2 s^{-1} V^{-1})**	**μ_{eo}/ (10^{-8} m^2 s^{-1} V^{-1})**	**μ_{ep}/ (10^{-8} m^2 s^{-1} V^{-1})**	**μ_{eo}/ (10^{-8} m^2 s^{-1} V^{-1})**	**μ_{ep}/ (10^{-8} m^2 s^{-1} V^{-1})**
5	1	6.9440	-3.2929	6.8691	-3.3680	7.1204	-3.7471	7.0037	-3.9038
	2	6.9358	-3.2938	6.8772	-3.3620	6.9870	-3.7333	6.9967	-3.8893
	3	6.9371	-3.3019	6.8786	-3.3510	6.9911	-3.7635	6.9856	-3.8657
Mw		6.9390	-3.2962	6.8750	-3.3603	7.0328	-3.7479	6.9953	-3.8863
SD		0.004	0.005	0.005	0.009	0.076	0.015	0.009	0.019
RSD		0.06%	0.15%	0.07%	0.26%	1.08%	0.40%	0.13%	0.49%
10	1	………[a]	………[a]	5.9177	-3.2588	5.9418	-3.6752	5.9559	-3.7573
	2	………[a]	………[a]	5.9057	-3.2645	5.9377	-3.6792	5.9468	-3.7779
	3	………[a]	………[a]	5.9037	-3.2701	5.9458	-3.7024	5.9488	-3.7820
Mw				5.9090	-3.2645	5.9418	-3.6856	5.9505	-3.7724
SD				0.008	0.006	0.004	0.015	0.005	0.013
RSD				0.13%	0.17%	0.07%	0.40%	0.08%	0.35%
15	1	5.2879	-3.2305	5.2879	-3.2125	5.2712	-3.6067	5.2475	-3.6120
	2	5.2887	-3.2268	5.2895	-3.2336	5.2744	-3.5901	5.2633	-3.6626
	3	5.2903	-3.2307	5.2887	-3.2546	5.2776	-3.6028	5.2641	-3.6510
Mw		5.2890	-3.2293	5.2887	-3.2336	5.2744	-3.5999	5.2583	-3.6419
SD		0.001	0.002	0.001	0.021	0.003	0.009	0.009	0.027
RSD		0.02%	0.07%	0.02%	0.65%	0.06%	0.24%	0.18%	0.73%

20	1	4.7258	-3.2179	4.7354	-3.2165	4.8128	-3.4417	4.8095	-3.4582
	2	4.7290	-3.2069	4.7277	-3.2331	4.8122	-3.4581	4.8108	-3.4646
	3	4.7233	-3.2122	4.7265	-3.2330	4.8122	-3.4648	4.8142	-3.4798
Mw		4.7260	-3.2124	4.7299	-3.2275	4.8124	-3.4548	4.8115	-3.4675
SD		0.003	0.006	0.005	0.010	0.000	0.012	0.002	0.011
RSD		0.06%	0.17%	0.10%	0.30%	0.01%	0.34%	0.05%	0.32%
25	1	4.4994	-3.1146	4.4937	-3.1012	4.5133	-3.2691	4.5023	-3.2316
	2	4.4994	-3.1154	4.5006	-3.1338	4.5110	-3.2736	4.5110	-3.2421
	3	4.4994	-3.1159	4.4960	-3.1464	4.5064	-3.2755	4.5128	-3.2704
Mw		4.4994	-3.1153	4.4967	-3.1271	4.5102	-3.2727	4.5087	-3.2480
SD		0.000	0.001	0.004	0.023	0.004	0.003	0.006	0.020
RSD		0.00%	0.02%	0.08%	0.75%	0.08%	0.10%	0.12%	0.62%

[a] Not determined.

Appendix B6

Measured absolute electrophoretic mobilities μ_{ep} and absolute electroosmotic mobilities μ_{eo} of PSSL20 and PSSL40 with a various concentrations of different counterion cations, the following experimental conditions: T= 20°C, total length of capillary = 39.5 cm, capillary length to detector = 29.1 cm, inner diameter of fused silica capillary = 76 µm, separation voltage 7 kV, sample injection 0.1 psi (6.89 mbar) 6 s, data rate 16 Hz, absorbance detection.

PSSL	**I (mmL^{-1})**	**run no.**	**t_0 (s)**			**t_m (s)**			**μ_{ep} (10^{-8} m^2 V^{-1} s^{-1})**			**μ_{eo} (10^{-5} m^2 V^{-1} s^{-1})**		
			Li$^+$	**Na$^+$**	**Gdm$^+$**	**Li$^+$**	**Na$^+$**	**Gdm$^+$**	**Li$^+$**	**Na$^+$**	**Gdm$^+$**	**Li$^+$**	**Na$^+$**	**Gdm$^+$**
PSSL20	40	1	300.75	331.88	401.19	612.00	788.38	762.94	2.7733	2.8614	1.9383	2.0112	1.8226	1.5077
		2	300.94	332.38	402.25	618.75	794.69	729.06	2.7991	2.8705	1.8276	2.0099	1.8198	1.5037
		3	301.31	332.19	402.38	617.06	798.13	725.31	2.7851	2.8821	1.8147	2.0074	1.8208	1.5032
		4	301.88	332.31	402.88	622.00	799.50	725.88	2.7960	2.8838	1.8114	2.0037	1.8202	1.5014
		Mw	301.22	332.19	402.17	617.45	795.17	735.80	2.7884	2.8744	1.8480	2.0081	1.8209	1.5040
		SD	0.496	0.223	0.709	4.173	4.963	18.169	0.012	0.011	0.061	0.003	0.001	0.003
		RSD	0.16	0.07	0.18	0.68	0.62	2.47	0.42	0.37	3.28	0.16	0.07	0.18
	60	1	338.00	372.50	464.38	669.50	822.06	863.00	2.4025	2.4077	1.6313	1.7895	1.6238	1.3025
		2	338.94	376.88	464.88	682.63	854.13	869.50	2.4361	2.4315	1.6417	1.7846	1.6049	1.3011
		3	340.19	380.69	465.75	680.13	874.50	877.38	2.4095	2.4326	1.6520	1.7780	1.5889	1.2987
		4	340.44	383.19	467.69	688.69	900.25	865.94	2.4360	2.4582	1.6127	1.7767	1.5785	1.2933
		Mw	339.39	378.31	465.67	680.23	862.73	868.95	2.4210	2.4325	1.6344	1.7822	1.5990	1.2989
		SD	1.136	4.664	1.459	8.009	33.036	6.212	0.018	0.021	0.017	0.006	0.020	0.004
		RSD	0.33	1.23	0.31	1.18	3.83	0.71	0.73	0.85	1.03	0.34	1.24	0.31
	80	1	376.69	431.81	570.38	820.56	809.75	802.81	2.3551	1.7726	0.8325	1.6057	1.4008	1.0605
		2	376.88	432.75	568.75	826.31	800.31	799.19	2.3668	1.7405	0.8314	1.6049	1.3977	1.0635
		3	376.56	433.88	570.13	832.44	824.00	802.75	2.3851	1.7896	0.8336	1.6063	1.3941	1.0609
		4	………[a]	434.13	570.31	………[a]	822.06	799.44	……...[a]	1.7827	0.8242	……...[a]	1.3933	1.0606
		Mw	376.71	433.58	569.73	826.44	814.03	801.05	2.3690	1.7714	0.8304	1.6057	1.3965	1.0614
		SD	0.157	0.732	0.853	5.938	11.112	2.005	0.015	0.022	0.004	0.001	0.003	0.001
		RSD	0.04	0.17	0.15	0.72	1.37	0.25	0.64	1.23	0.51	0.04	0.25	0.13
	100	1	405.19	468.81	627.63	737.50	798.50	1007.06	1.8238	1.4443	0.9845	1.4928	1.2902	0.9637

		2	406.31	469.44	626.13	738.56	807.19	1001.63	1.8158	1.4618	0.9819	1.4887	1.2885	0.9660
		3	407.06	470.06	626.06	742.31	811.88	999.44	1.8195	1.4689	0.9786	1.4859	1.2868	0.9661
		4	408.00	471.31	629.56	734.06	834.38	1009.19	1.7855	1.5141	0.9799	1.4825	1.2834	0.9608
		Mw	406.64	469.91	627.34	738.11	812.98	1004.33	1.8111	1.4723	0.9812	1.4875	1.2872	0.9642
		SD	1.189	1.067	1.646	3.397	15.299	4.558	0.017	0.030	0.003	0.004	0.003	0.003
		RSD	0.29	0.23	0.26	0.46	1.88	0.45	0.96	2.02	0.26	0.29	0.23	0.26
	120	1	439.88	………[a]	………[a]	928.25	………[a]	………[a]	1.9616	………[a]	………[a]	1.3751	………[a]	………[a]
		2	440.19	………[a]	………[a]	925.38	………[a]	………[a]	1.9534	………[a]	………[a]	1.3741	………[a]	………[a]
		3	441.31	………[a]	………[a]	939.13	………[a]	………[a]	1.9699	………[a]	………[a]	1.3706	………[a]	………[a]
		4	441.94	………[a]	………[a]	925.38	………[a]	………[a]	1.9387	………[a]	………[a]	1.3687	………[a]	………[a]
		Mw	440.83			929.53			1.9559			1.3721		
		SD	0.964			6.538			0.013			0.003		
		RSD	0.22			0.70			0.68			0.22		
PSSL40	40	1	300.63	328.50	406.13	630.81	776.13	685.06	2.8555	2.8793	1.6442	2.0120	1.8413	1.4894
		2	300.69	328.31	407.38	614.50	781.13	689.31	2.7853	2.8957	1.6466	2.0116	1.8423	1.4848
		3	301.69	329.00	408.00	623.19	784.31	697.13	2.8044	2.8938	1.6671	2.0049	1.8385	1.4825
		4	302.06	329.44	409.00	638.69	790.25	698.31	2.8616	2.9029	1.6613	2.0024	1.8360	1.4789
		Mw	301.27	328.81	407.63	626.80	782.95	692.45	2.8267	2.8929	1.6548	2.0078	1.8395	1.4839
		SD	0.721	0.508	1.203	10.356	5.918	6.341	0.038	0.010	0.011	0.005	0.003	0.004
		RSD	0.24	0.15	0.30	1.65	0.76	0.92	1.33	0.34	0.67	0.24	0.15	0.30
	60	1	337.38	369.56	478.75	769.94	708.25	729.94	2.7310	2.1221	1.1788	1.7929	1.6367	1.2634
		2	336.31	369.75	479.81	772.06	701.00	733.69	2.7522	2.0959	1.1827	1.7985	1.6359	1.2606
		3	337.06	370.75	480.81	751.00	715.00	761.81	2.6818	2.1298	1.2581	1.7945	1.6315	1.2580
		4	337.63	372.00	481.44	764.38	727.69	769.06	2.7119	2.15	1.2740	1.7915	1.63	1.2564
		Mw	337.09	370.52	479.79	764.34	712.98	748.63	2.7192	2.1257	1.2234	1.7944	1.6325	1.2596
		SD	0.569	1.118	1.032	9.468	11.347	19.697	0.030	0.024	0.050	0.003	0.005	0.003
		RSD	0.17	0.30	0.22	1.24	1.59	2.63	1.10	1.14	4.06	0.17	0.30	0.25

	80	1	373.88	436.00	570.38	732.38	910.19	803.38	2.1472	1.9596	0.8339	1.6178	1.3873	1.0605
		2	376.19	437.31	572.00	759.44	903.69	804.94	2.2000	1.9354	0.8297	1.6079	1.3831	1.0575
		3	375.88	438.56	573.13	799.25	911.75	806.38	2.3112	1.9407	0.8277	1.6092	1.3792	1.0554
		4	376.69	439.88	574.31	806.81	948.44	805.94	2.3210	1.9992	0.8207	1.6057	1.3751	1.0532
		Mw	375.66	437.94	572.45	774.47	918.52	805.16	2.2449	1.9587	0.8280	1.6102	1.3812	1.0566
		SD	1.234	1.662	1.677	34.919	20.251	1.331	0.085	0.029	0.006	0.005	0.005	0.003
		RSD	0.33	0.38	0.29	4.51	2.20	0.17	3.79	1.48	0.67	0.33	0.38	0.29
	100	1	397.88	468.13	634.94	656.38	848.63	1022.50	1.6233	1.5708	0.9790	1.5202	1.2921	0.9526
		2	400.63	470.75	655.69	648.94	828.13	1073.25	1.5664	1.5034	0.9731	1.5098	1.2849	0.9225
		3	402.25	471.50	669.63	654.69	846.50	1114.63	1.5720	1.5409	0.9778	1.5037	1.2829	0.9033
		4	403.63	472.38	683.82	662.75	872.63	1148.63	1.5886	1.5924	0.9705	1.4986	1.2805	0.8845
		Mw	401.09	470.69	661.02	655.69	848.97	1089.75	1.5876	1.5519	0.9751	1.5081	1.2851	0.9157
		SD	2.471	1.833	20.838	5.683	18.260	54.405	0.026	0.039	0.004	0.009	0.005	0.029
		RSD	0.62	0.39	3.15	0.87	2.15	4.99	1.61	2.49	0.41	0.62	0.39	3.17
	120	1	430.94	………[a]	………[a]	817.75	………[a]	………[a]	1.8001	………[a]	………[a]	1.4036	………[a]	………[a]
		2	432.88	………[a]	………[a]	829.81	………[a]	………[a]	1.8123	………[a]	………[a]	1.3973	………[a]	………[a]
		3	434.94	………[a]	………[a]	831.63	………[a]	………[a]	1.7986	………[a]	………[a]	1.3907	………[a]	………[a]
		4	437.75	………[a]	………[a]	842.13	………[a]	………[a]	1.7990	………[a]	………[a]	1.3818	………[a]	………[a]
		Mw	434.13			830.33			1.8025			1.3933		
		SD	2.917			9.989			0.007			0.009		
		RSD	0.67			1.20			0.36			0.67		

[a] Not determined.

Appendix B7

Regression lines for PSSL different size at 20 ^{o}C in borax: (e) and (g) 10 mmol L^{-1}; (a), (c) and (h) 15 mmol L^{-1}; (f) 20 mmol L^{-1}; (b) and (d) 25 mmol L^{-1}, respectively

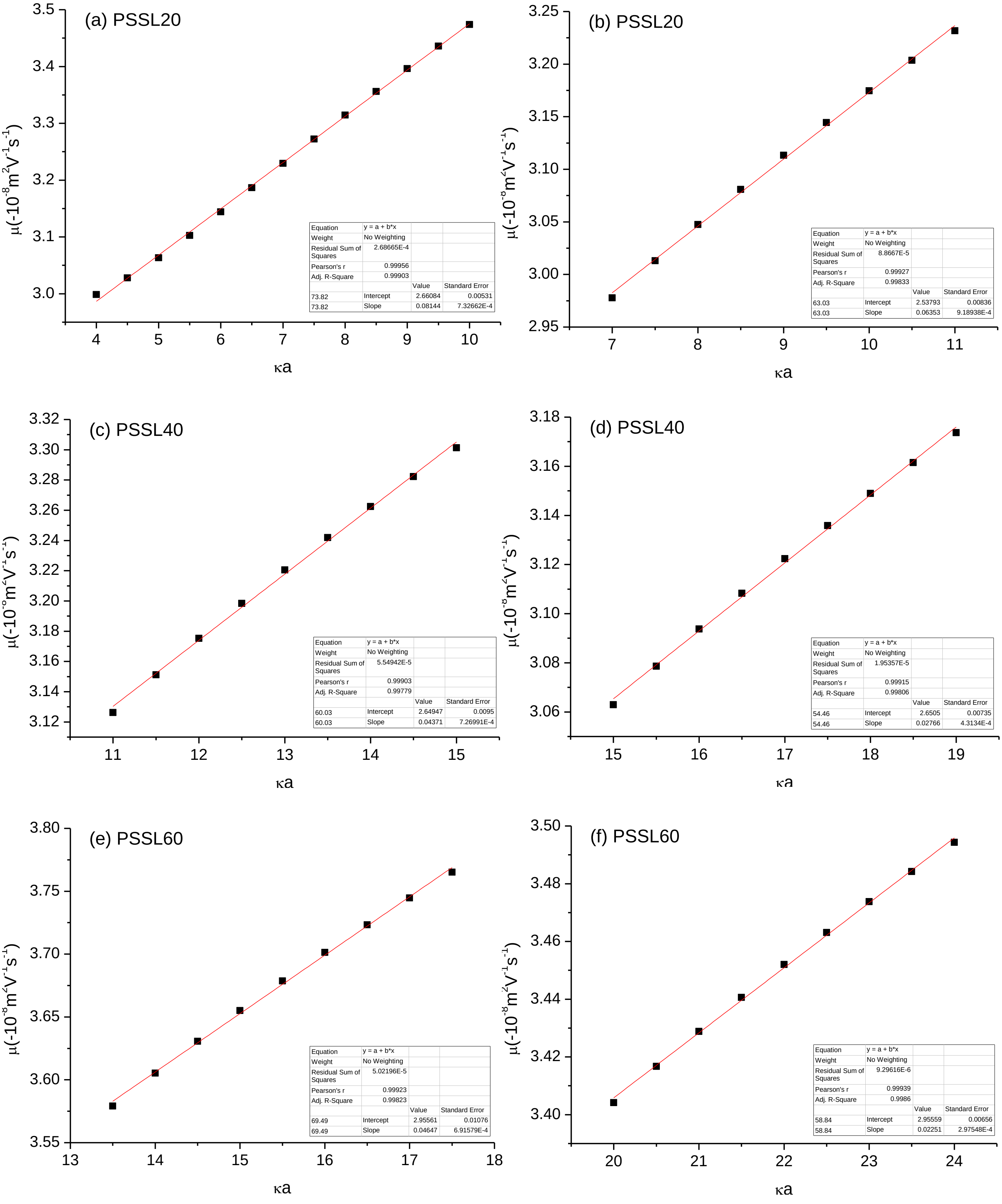

Equation	y = a + b*x		
Weight	No Weighting		
Residual Sum of Squares	2.68665E-4		
Pearson's r	0.99956		
Adj. R-Square	0.99903		
		Value	Standard Error
73.82	Intercept	2.66084	0.00531
73.82	Slope	0.08144	7.32662E-4

Equation	y = a + b*x		
Weight	No Weighting		
Residual Sum of Squares	8.8667E-5		
Pearson's r	0.99927		
Adj. R-Square	0.99833		
		Value	Standard Error
63.03	Intercept	2.53793	0.00836
63.03	Slope	0.06353	9.18938E-4

Equation	y = a + b*x		
Weight	No Weighting		
Residual Sum of Squares	5.54942E-5		
Pearson's r	0.99903		
Adj. R-Square	0.99779		
		Value	Standard Error
60.03	Intercept	2.64947	0.0095
60.03	Slope	0.04371	7.26991E-4

Equation	y = a + b*x		
Weight	No Weighting		
Residual Sum of Squares	1.95357E-5		
Pearson's r	0.99915		
Adj. R-Square	0.99806		
		Value	Standard Error
54.46	Intercept	2.6505	0.00735
54.46	Slope	0.02766	4.3134E-4

Equation	y = a + b*x		
Weight	No Weighting		
Residual Sum of Squares	5.02196E-5		
Pearson's r	0.99923		
Adj. R-Square	0.99823		
		Value	Standard Error
69.49	Intercept	2.95561	0.01076
69.49	Slope	0.04647	6.91579E-4

Equation	y = a + b*x		
Weight	No Weighting		
Residual Sum of Squares	9.29616E-6		
Pearson's r	0.99939		
Adj. R-Square	0.9986		
		Value	Standard Error
58.84	Intercept	2.95559	0.00656
58.84	Slope	0.02251	2.97548E-4

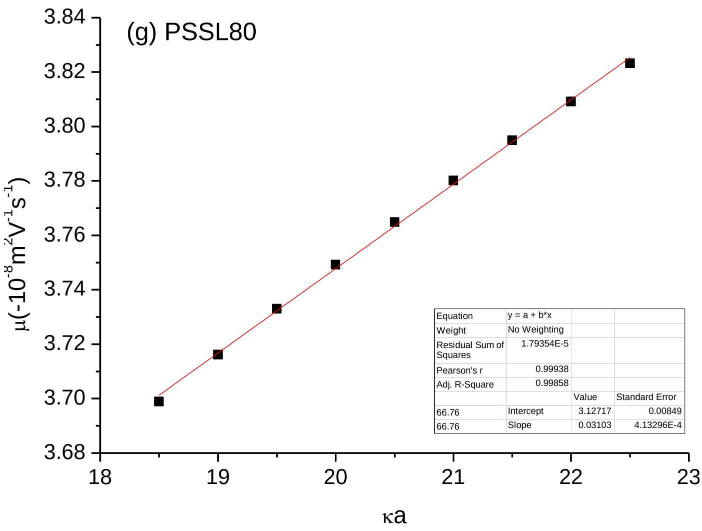

Equation	y = a + b*x		
Weight	No Weighting		
Residual Sum of Squares	1.79354E-5		
Pearson's r	0.99938		
Adj. R-Square	0.99858		
		Value	Standard Error
66.76	Intercept	3.12717	0.00849
66.76	Slope	0.03103	4.13296E-4

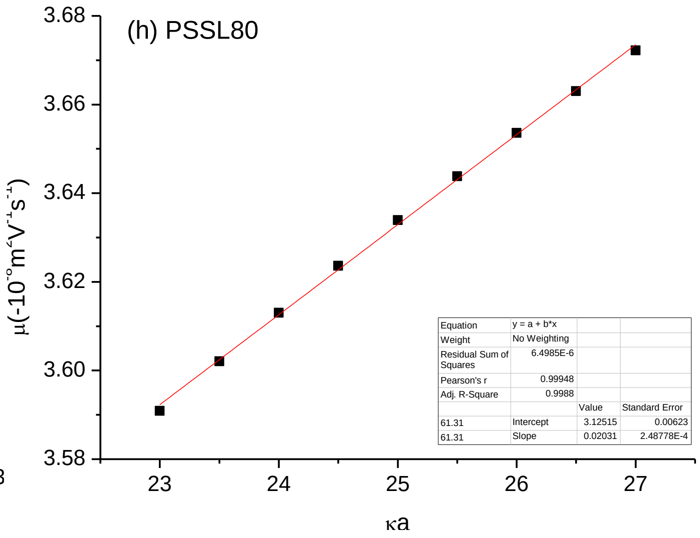

Equation	y = a + b*x		
Weight	No Weighting		
Residual Sum of Squares	6.4985E-6		
Pearson's r	0.99948		
Adj. R-Square	0.9988		
		Value	Standard Error
61.31	Intercept	3.12515	0.00623
61.31	Slope	0.02031	2.48778E-4

Appendix C

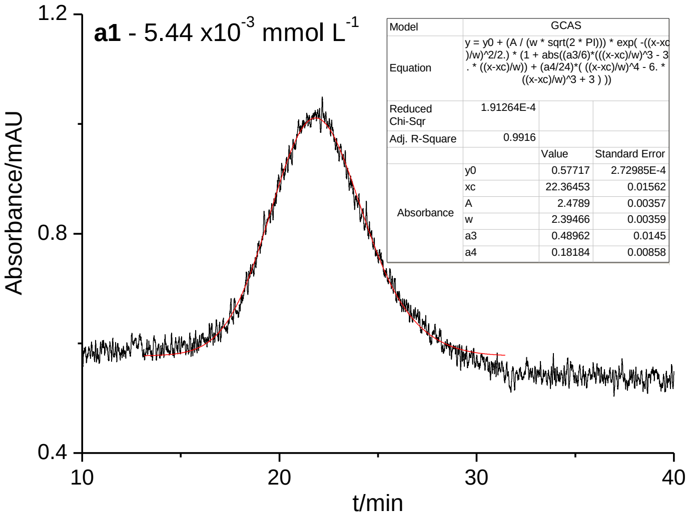

Model	GCAS		
Equation	y = y0 + (A / (w * sqrt(2 * PI))) * exp(-((x-xc)/w)^2/2.) * (1 + abs((a3/6)*(((x-xc)/w)^3 - 3 . * ((x-xc)/w)) + (a4/24)*(((x-xc)/w)^4 - 6. * ((x-xc)/w)^3 + 3)))		
Reduced Chi-Sqr	1.91264E-4		
Adj. R-Square	0.9916		
		Value	Standard Error
Absorbance	y0	0.57717	2.72985E-4
	xc	22.36453	0.01562
	A	2.4789	0.00357
	w	2.39466	0.00359
	a3	0.48962	0.0145
	a4	0.18184	0.00858

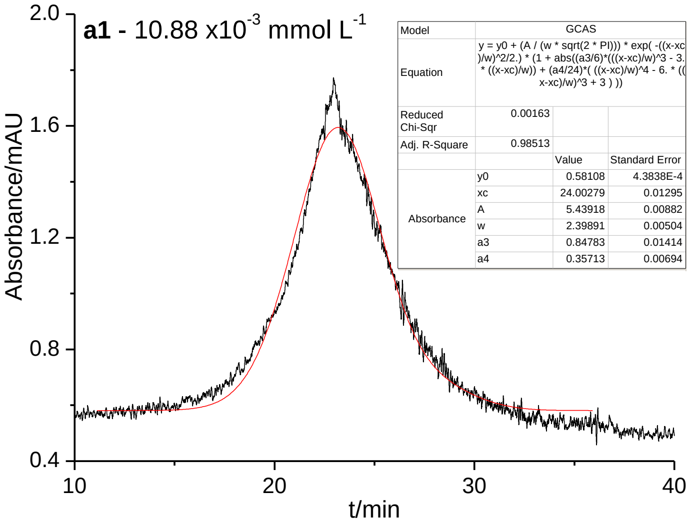

Model	GCAS		
Equation	y = y0 + (A / (w * sqrt(2 * PI))) * exp(-((x-xc)/w)^2/2.) * (1 + abs((a3/6)*(((x-xc)/w)^3 - 3. * ((x-xc)/w)) + (a4/24)*(((x-xc)/w)^4 - 6. * ((x-xc)/w)^3 + 3)))		
Reduced Chi-Sqr	0.00163		
Adj. R-Square	0.98513		
		Value	Standard Error
Absorbance	y0	0.58108	4.3838E-4
	xc	24.00279	0.01295
	A	5.43918	0.00882
	w	2.39891	0.00504
	a3	0.84783	0.01414
	a4	0.35713	0.00694

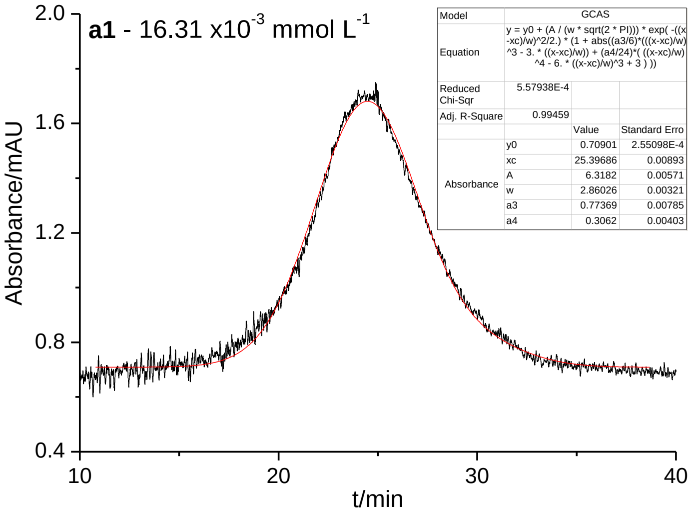

Model	GCAS		
Equation	y = y0 + (A / (w * sqrt(2 * PI))) * exp(-((x -xc)/w)^2/2.) * (1 + abs((a3/6)*(((x-xc)/w) ^3 - 3. * ((x-xc)/w)) + (a4/24)*(((x-xc)/w) ^4 - 6. * ((x-xc)/w)^3 + 3)))		
Reduced Chi-Sqr	5.57938E-4		
Adj. R-Square	0.99459		
		Value	Standard Erro
Absorbance	y0	0.70901	2.55098E-4
	xc	25.39686	0.00893
	A	6.3182	0.00571
	w	2.86026	0.00321
	a3	0.77369	0.00785
	a4	0.3062	0.00403

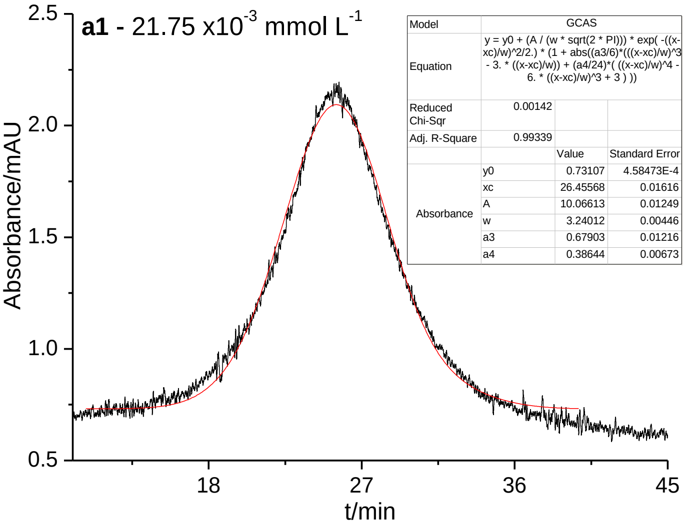

Model	GCAS		
Equation	y = y0 + (A / (w * sqrt(2 * PI))) * exp(-((x- xc)/w)^2/2.) * (1 + abs((a3/6)*(((x-xc)/w)^3 - 3. * ((x-xc)/w)) + (a4/24)*(((x-xc)/w)^4 - 6. * ((x-xc)/w)^3 + 3)))		
Reduced Chi-Sqr	0.00142		
Adj. R-Square	0.99339		
		Value	Standard Error
Absorbance	y0	0.73107	4.58473E-4
	xc	26.45568	0.01616
	A	10.06613	0.01249
	w	3.24012	0.00446
	a3	0.67903	0.01216
	a4	0.38644	0.00673

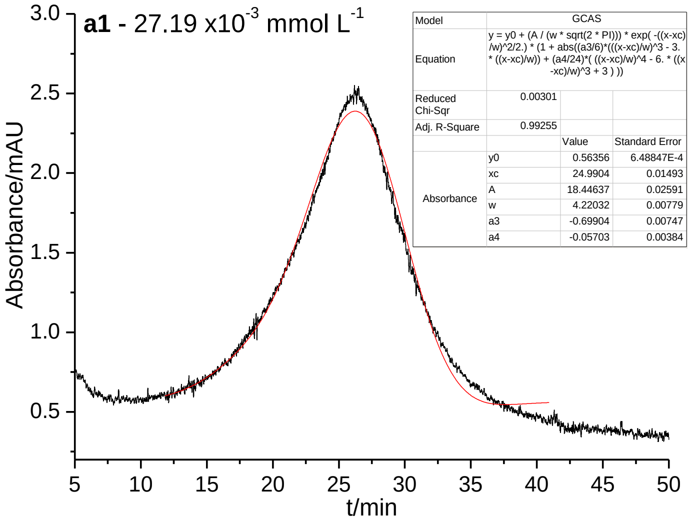

Model	GCAS		
Equation	y = y0 + (A / (w * sqrt(2 * PI))) * exp(-((x-xc) /w)^2/2.) * (1 + abs((a3/6)*(((x-xc)/w)^3 - 3. * ((x-xc)/w)) + (a4/24)*(((x-xc)/w)^4 - 6. * ((x -xc)/w)^3 + 3)))		
Reduced Chi-Sqr	0.00301		
Adj. R-Square	0.99255		
		Value	Standard Error
Absorbance	y0	0.56356	6.48847E-4
	xc	24.9904	0.01493
	A	18.44637	0.02591
	w	4.22032	0.00779
	a3	-0.69904	0.00747
	a4	-0.05703	0.00384

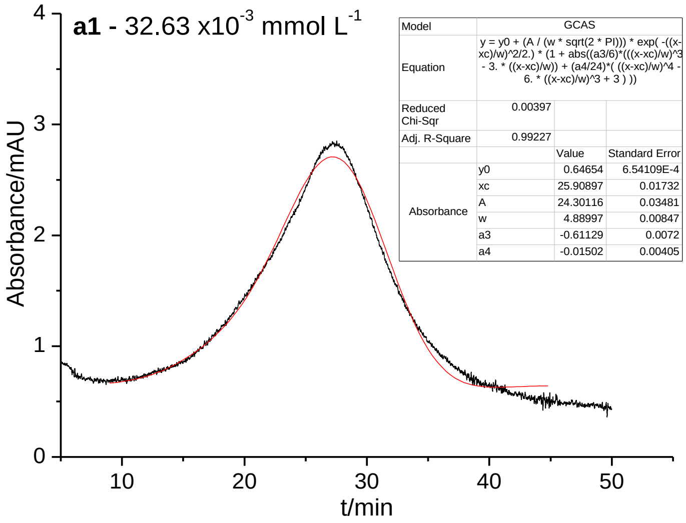

Model	GCAS		
Equation	y = y0 + (A / (w * sqrt(2 * PI))) * exp(-((x- xc)/w)^2/2.) * (1 + abs((a3/6)*(((x-xc)/w)^3 - 3. * ((x-xc)/w)) + (a4/24)*(((x-xc)/w)^4 - 6. * ((x-xc)/w)^3 + 3)))		
Reduced Chi-Sqr	0.00397		
Adj. R-Square	0.99227		
		Value	Standard Error
Absorbance	y0	0.64654	6.54109E-4
	xc	25.90897	0.01732
	A	24.30116	0.03481
	w	4.88997	0.00847
	a3	-0.61129	0.0072
	a4	-0.01502	0.00405

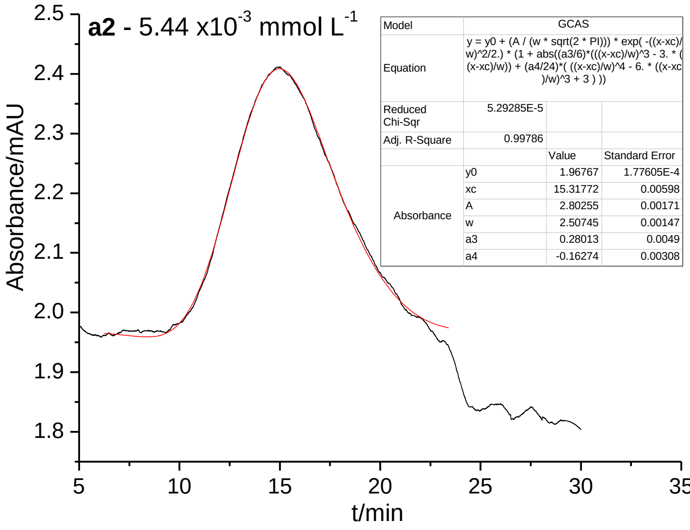

Model	GCAS		
Equation	y = y0 + (A / (w * sqrt(2 * PI))) * exp(-((x-xc)/w)^2/2.) * (1 + abs((a3/6)*(((x-xc)/w)^3 - 3. * ((x-xc)/w)) + (a4/24)*(((x-xc)/w)^4 - 6. * ((x-xc)/w)^3 + 3)))		
Reduced Chi-Sqr	5.29285E-5		
Adj. R-Square	0.99786		
		Value	Standard Error
Absorbance	y0	1.96767	1.77605E-4
	xc	15.31772	0.00598
	A	2.80255	0.00171
	w	2.50745	0.00147
	a3	0.28013	0.0049
	a4	-0.16274	0.00308

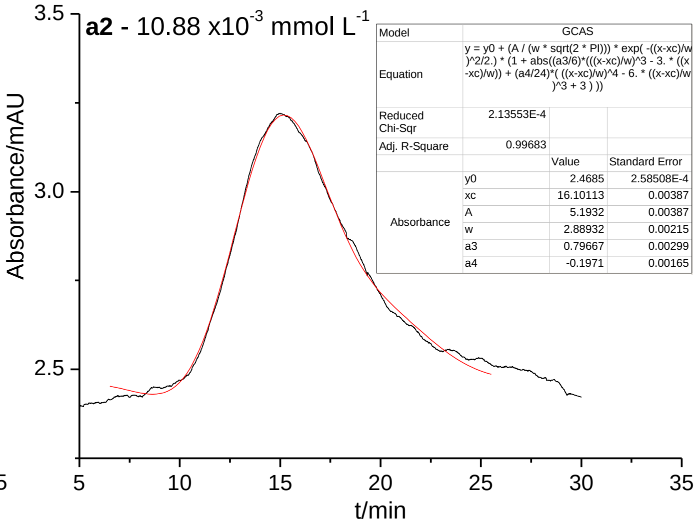

Model	GCAS		
Equation	y = y0 + (A / (w * sqrt(2 * PI))) * exp(-((x-xc)/w)^2/2.) * (1 + abs((a3/6)*(((x-xc)/w)^3 - 3. * ((x-xc)/w)) + (a4/24)*(((x-xc)/w)^4 - 6. * ((x-xc)/w)^3 + 3)))		
Reduced Chi-Sqr	2.13553E-4		
Adj. R-Square	0.99683		
		Value	Standard Error
Absorbance	y0	2.4685	2.58508E-4
	xc	16.10113	0.00387
	A	5.1932	0.00387
	w	2.88932	0.00215
	a3	0.79667	0.00299
	a4	-0.1971	0.00165

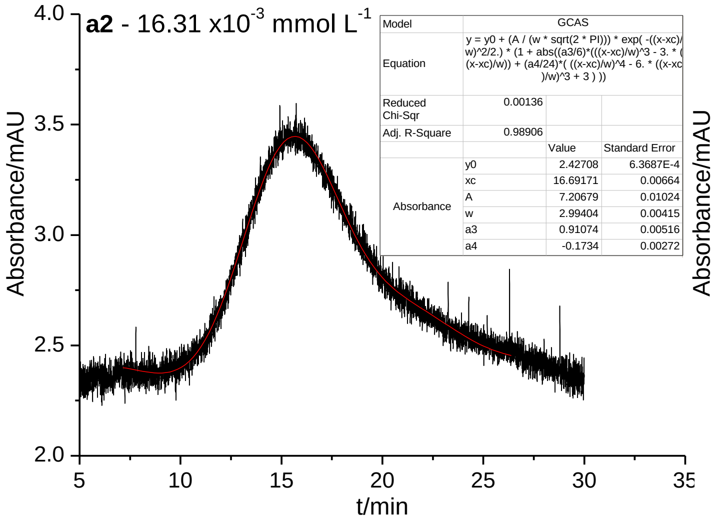

Model	GCAS		
Equation	y = y0 + (A / (w * sqrt(2 * PI))) * exp(-((x-xc)/w)^2/2.) * (1 + abs((a3/6)*(((x-xc)/w)^3 - 3. * ((x-xc)/w)) + (a4/24)*(((x-xc)/w)^4 - 6. * ((x-xc)/w)^3 + 3)))		
Reduced Chi-Sqr	0.00136		
Adj. R-Square	0.98906		
		Value	Standard Error
Absorbance	y0	2.42708	6.3687E-4
	xc	16.69171	0.00664
	A	7.20679	0.01024
	w	2.99404	0.00415
	a3	0.91074	0.00516
	a4	-0.1734	0.00272

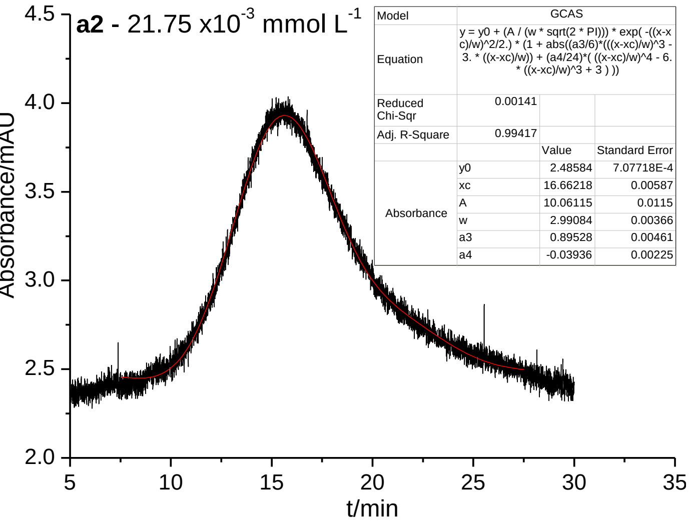

Model	GCAS		
Equation	y = y0 + (A / (w * sqrt(2 * PI))) * exp(-((x-xc)/w)^2/2.) * (1 + abs((a3/6)*(((x-xc)/w)^3 - 3. * ((x-xc)/w)) + (a4/24)*(((x-xc)/w)^4 - 6. * ((x-xc)/w)^3 + 3)))		
Reduced Chi-Sqr	0.00141		
Adj. R-Square	0.99417		
		Value	Standard Error
Absorbance	y0	2.48584	7.07718E-4
	xc	16.66218	0.00587
	A	10.06115	0.0115
	w	2.99084	0.00366
	a3	0.89528	0.00461
	a4	-0.03936	0.00225

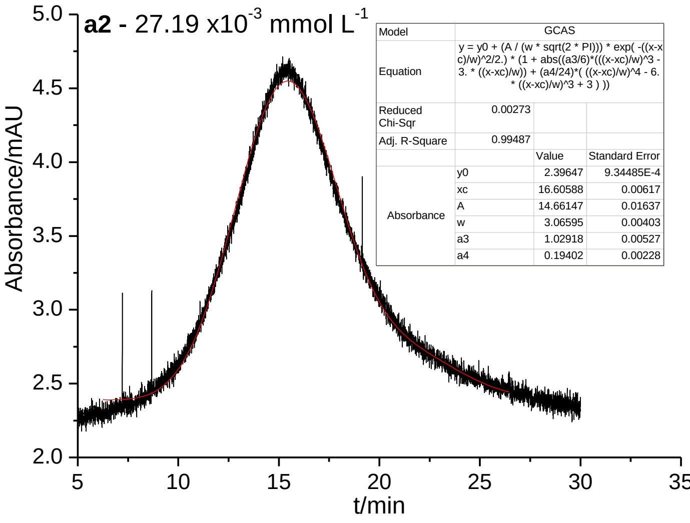

Model	GCAS		
Equation	y = y0 + (A / (w * sqrt(2 * PI))) * exp(-((x-xc)/w)^2/2.) * (1 + abs((a3/6)*(((x-xc)/w)^3 - 3. * ((x-xc)/w)) + (a4/24)*(((x-xc)/w)^4 - 6. * ((x-xc)/w)^3 + 3)))		
Reduced Chi-Sqr	0.00273		
Adj. R-Square	0.99487		
		Value	Standard Error
Absorbance	y0	2.39647	9.34485E-4
	xc	16.60588	0.00617
	A	14.66147	0.01637
	w	3.06595	0.00403
	a3	1.02918	0.00527
	a4	0.19402	0.00228

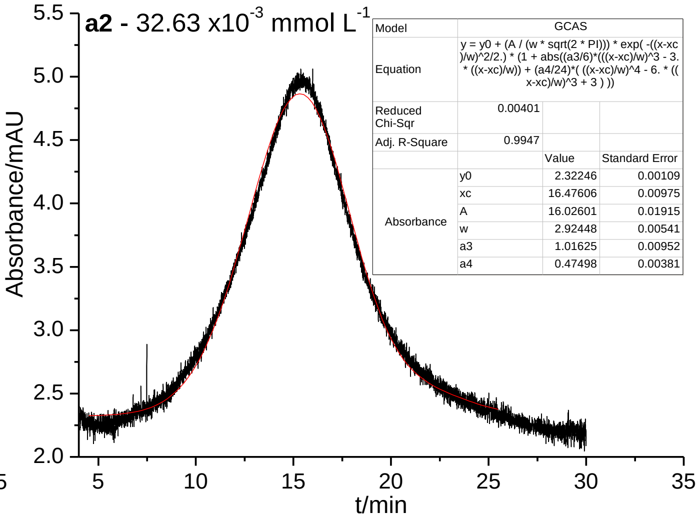

Model	GCAS		
Equation	y = y0 + (A / (w * sqrt(2 * PI))) * exp(-((x-xc)/w)^2/2.) * (1 + abs((a3/6)*(((x-xc)/w)^3 - 3. * ((x-xc)/w)) + (a4/24)*(((x-xc)/w)^4 - 6. * ((x-xc)/w)^3 + 3)))		
Reduced Chi-Sqr	0.00401		
Adj. R-Square	0.9947		
		Value	Standard Error
Absorbance	y0	2.32246	0.00109
	xc	16.47606	0.00975
	A	16.02601	0.01915
	w	2.92448	0.00541
	a3	1.01625	0.00952
	a4	0.47498	0.00381

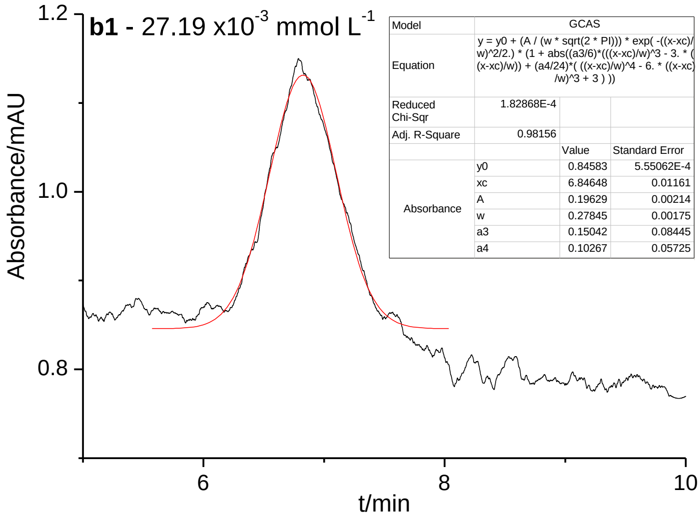

b1 - 27.19 x10^{-3} mmol L^{-1}

Model	GCAS		
Equation	y = y0 + (A / (w * sqrt(2 * PI))) * exp(-((x-xc)/w)^2/2.) * (1 + abs((a3/6)*(((x-xc)/w)^3 - 3. * ((x-xc)/w)) + (a4/24)*(((x-xc)/w)^4 - 6. * ((x-xc)/w)^3 + 3)))		
Reduced Chi-Sqr	1.82868E-4		
Adj. R-Square	0.98156		
		Value	Standard Error
Absorbance	y0	0.84583	5.55062E-4
	xc	6.84648	0.01161
	A	0.19629	0.00214
	w	0.27845	0.00175
	a3	0.15042	0.08445
	a4	0.10267	0.05725

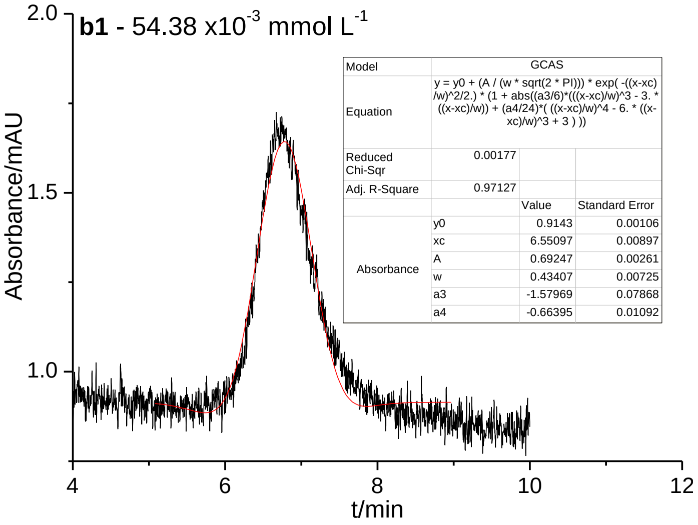

b1 - 54.38 x10^{-3} mmol L^{-1}

Model	GCAS		
Equation	y = y0 + (A / (w * sqrt(2 * PI))) * exp(-((x-xc)/w)^2/2.) * (1 + abs((a3/6)*(((x-xc)/w)^3 - 3. * ((x-xc)/w)) + (a4/24)*(((x-xc)/w)^4 - 6. * ((x-xc)/w)^3 + 3)))		
Reduced Chi-Sqr	0.00177		
Adj. R-Square	0.97127		
		Value	Standard Error
Absorbance	y0	0.9143	0.00106
	xc	6.55097	0.00897
	A	0.69247	0.00261
	w	0.43407	0.00725
	a3	-1.57969	0.07868
	a4	-0.66395	0.01092

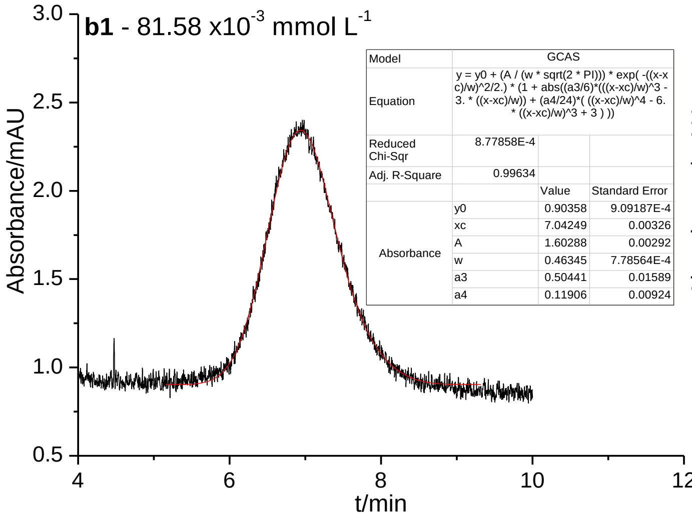

b1 - 81.58 x10^{-3} mmol L^{-1}

Model	GCAS		
Equation	y = y0 + (A / (w * sqrt(2 * PI))) * exp(-((x-xc)/w)^2/2.) * (1 + abs((a3/6)*(((x-xc)/w)^3 - 3. * ((x-xc)/w)) + (a4/24)*(((x-xc)/w)^4 - 6. * ((x-xc)/w)^3 + 3)))		
Reduced Chi-Sqr	8.77858E-4		
Adj. R-Square	0.99634		
		Value	Standard Error
Absorbance	y0	0.90358	9.09187E-4
	xc	7.04249	0.00326
	A	1.60288	0.00292
	w	0.46345	7.78564E-4
	a3	0.50441	0.01589
	a4	0.11906	0.00924

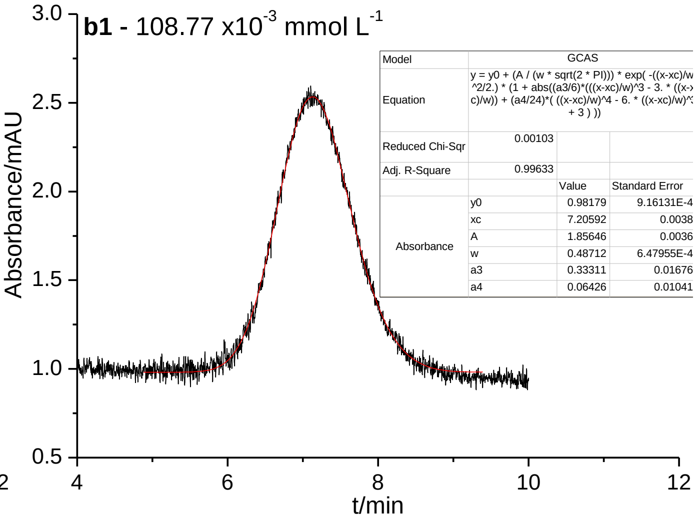

b1 - 108.77 x10^{-3} mmol L^{-1}

Model	GCAS		
Equation	y = y0 + (A / (w * sqrt(2 * PI))) * exp(-((x-xc)/w ^2/2.) * (1 + abs((a3/6)*(((x-xc)/w)^3 - 3. * ((x-x c)/w)) + (a4/24)*(((x-xc)/w)^4 - 6. * ((x-xc)/w)^ + 3)))		
Reduced Chi-Sqr	0.00103		
Adj. R-Square	0.99633		
		Value	Standard Error
Absorbance	y0	0.98179	9.16131E-4
	xc	7.20592	0.0038
	A	1.85646	0.0036
	w	0.48712	6.47955E-4
	a3	0.33311	0.01676
	a4	0.06426	0.01041

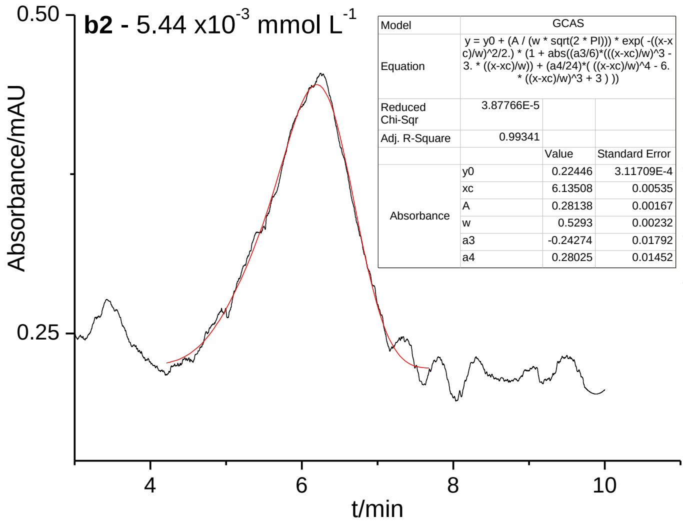

b2 - 5.44 x10^{-3} mmol L^{-1}

Model	GCAS		
Equation	y = y0 + (A / (w * sqrt(2 * PI))) * exp(-((x-xc)/w)^2/2.) * (1 + abs((a3/6)*(((x-xc)/w)^3 - 3. * ((x-xc)/w)) + (a4/24)*(((x-xc)/w)^4 - 6. * ((x-xc)/w)^3 + 3)))		
Reduced Chi-Sqr	3.87766E-5		
Adj. R-Square	0.99341		
		Value	Standard Error
Absorbance	y0	0.22446	3.11709E-4
	xc	6.13508	0.00535
	A	0.28138	0.00167
	w	0.5293	0.00232
	a3	-0.24274	0.01792
	a4	0.28025	0.01452

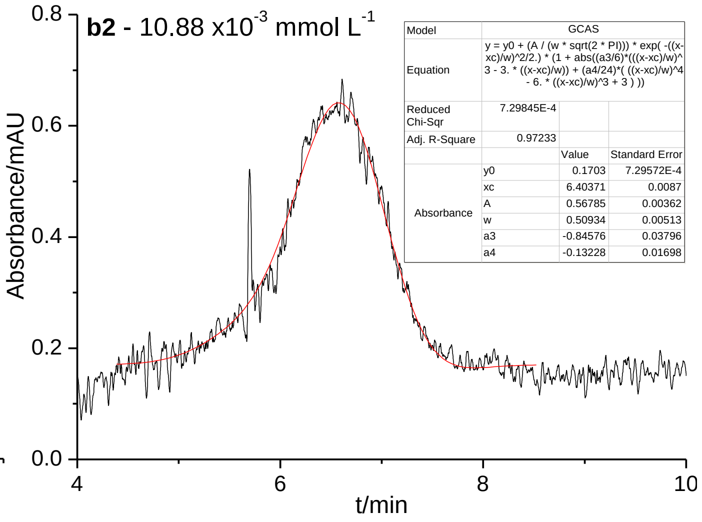

b2 - 10.88 x10^{-3} mmol L^{-1}

Model	GCAS		
Equation	y = y0 + (A / (w * sqrt(2 * PI))) * exp(-((x-xc)/w)^2/2.) * (1 + abs((a3/6)*(((x-xc)/w)^3 - 3. * ((x-xc)/w)) + (a4/24)*(((x-xc)/w)^4 - 6. * ((x-xc)/w)^3 + 3)))		
Reduced Chi-Sqr	7.29845E-4		
Adj. R-Square	0.97233		
		Value	Standard Error
Absorbance	y0	0.1703	7.29572E-4
	xc	6.40371	0.0087
	A	0.56785	0.00362
	w	0.50934	0.00513
	a3	-0.84576	0.03796
	a4	-0.13228	0.01698

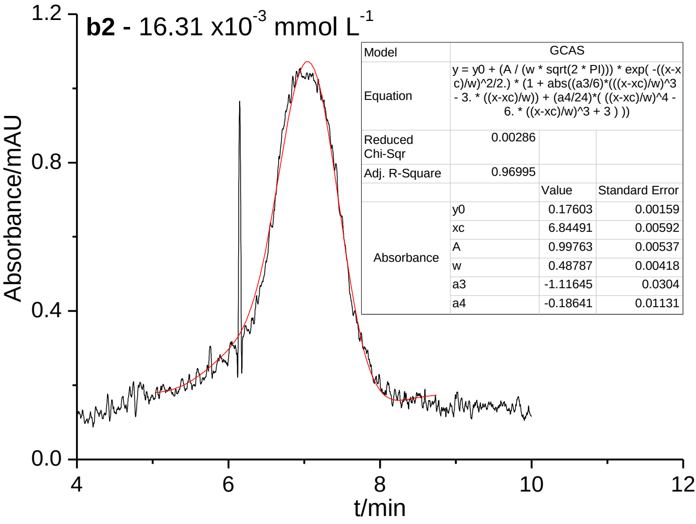

Model	GCAS		
Equation	y = y0 + (A / (w * sqrt(2 * PI))) * exp(-((x-xc)/w)^2/2.) * (1 + abs((a3/6)*(((x-xc)/w)^3 - 3. * ((x-xc)/w)) + (a4/24)*(((x-xc)/w)^4 - 6. * ((x-xc)/w)^3 + 3)))		
Reduced Chi-Sqr	0.00286		
Adj. R-Square	0.96995		
		Value	Standard Error
Absorbance	y0	0.17603	0.00159
	xc	6.84491	0.00592
	A	0.99763	0.00537
	w	0.48787	0.00418
	a3	-1.11645	0.0304
	a4	-0.18641	0.01131

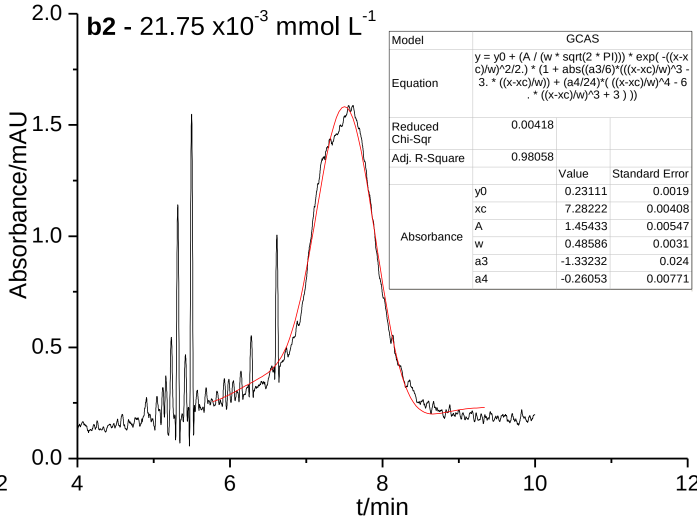

Model	GCAS		
Equation	y = y0 + (A / (w * sqrt(2 * PI))) * exp(-((x-xc)/w)^2/2.) * (1 + abs((a3/6)*(((x-xc)/w)^3 - 3. * ((x-xc)/w)) + (a4/24)*(((x-xc)/w)^4 - 6. * ((x-xc)/w)^3 + 3)))		
Reduced Chi-Sqr	0.00418		
Adj. R-Square	0.98058		
		Value	Standard Error
Absorbance	y0	0.23111	0.0019
	xc	7.28222	0.00408
	A	1.45433	0.00547
	w	0.48586	0.0031
	a3	-1.33232	0.024
	a4	-0.26053	0.00771

Curriculum Vitae

Curriculum Vitae

Academic Background

1998	Bachelor of Science (B.Sc.) in Chemistry, College of Science, Mosul University, Mosul, IRAQ.
2000	Master of Science (M.Sc.) in Physical Chemistry, College of Science, Mosul University, Mosul, IRAQ.

Scientific Publications

1. **Alaa H. Jalil**, Direct and Continuous Electrochemical Method for preparing Lead (II) Acetate from Local Sources. *M.Sc. Thesis,* Mosul University, IRAQ, 2000.
2. R. A. Khalil, **A. H. Jalil**, A. Y. Abd-Alrazzak, Application of a Schiff Base Derived from Sulfanilamide as an Acid- Base Indicator, *J. Iran. Chem. Soc.*, 6 (2), 345-352, 2009.
3. Rabah A. Khalil, **Alaa H. Jalil**, Use of Acetic Acid as an Electrolyte in Lead Electrorefining, *Mu'tah J. Res. Studies*, 26 (2), 2011.
4. **Alaa H. Jalil**, Surface Area Determination of Activated Carbons Produced from Waste tires via Adsorption from Solution, *Tikrit Journal of Pure Science*, 17 (2), 99-104, 2012.
5. Ute Pyell, **Alaa H. Jalil**, Christian Pfeiffer, Beatriz Pelaz, Wolfgang J. Parak, Characterization of Gold Nanoparticles with Different Hydrophilic Coating via Capillary Electrophoresis and Taylor Dispersion Analysis. Part I: Determination of the Zeta Potential Employing a Modified Analytic Approximation, *J. Colloid & Interface Science*, 450, 288-300, 2015.
6. Ute Pyell, **Alaa H. Jalil**, Dominic A. Urban, Christian Pfeiffer, Beatriz Pelaz, Wolfgang J. Parak, Characterization of Hydrophilic Coated Gold Nanoparticles via Capillary Electrophoresis and Taylor Dispersion Analysis. Part II: Determination of the Hydrodynamic Radius Distribution – Comparison with Asymmetric Flow Field-Flow Fractionation, *J. Colloid & Interface Science*, 457, 131-140, 2015.
7. Anna Fichtner, **Alaa Jalil**, and Ute Pyell, Determination of the Exact Particle Radius Distribution for Silica Nanoparticles via Capillary Electrophoresis and Modeling the Electrophoretic Mobility with a Modified Analytic Approximation, *Langmuir*, 33, 2325−2339, 2017.
8. **Alaa H. Jalil** and Ute Pyell, Quantification of Zeta-Potential and Electrokinetic Surface Charge Density for Colloidal Silica Nanoparticles Dependent on Type and Concentration of the Counterion: Probing the Outer Helmholtz Plane, *J. Phys. Chem. C*, 122, 4437−4453, 2018.